SPACE SCIENCES SERIES OF ISSI

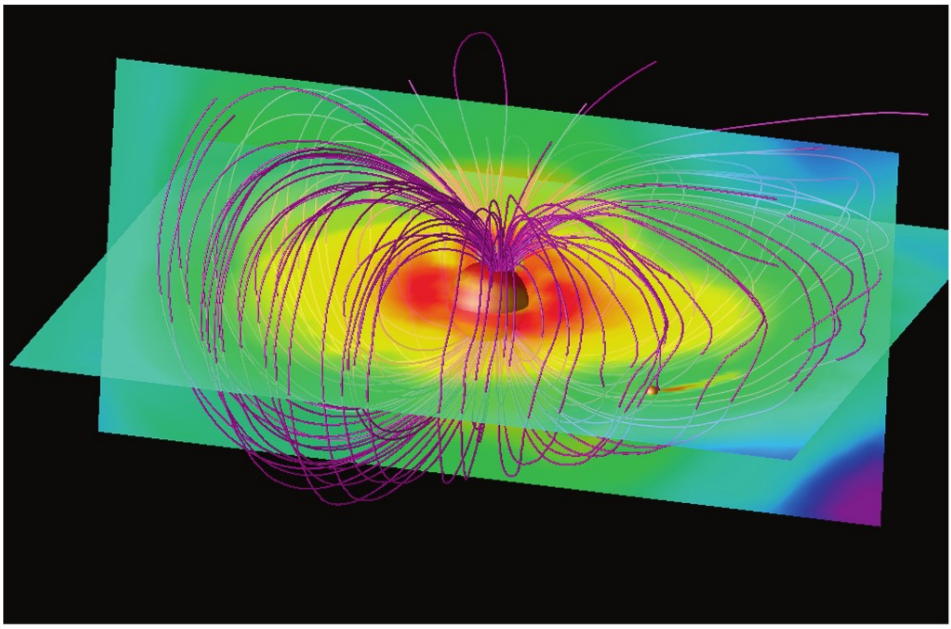

Karoly Szego *Editor*

Springer

Europlanet Research Infrastructure

INTERNATIONAL SPACE SCIENCE INSTITUTE

The Plasma Environment of Venus, Mars, and Titan

Space Sciences Series of ISSI

Volume 37

For further volumes:
www.springer.com/series/6592

Karoly Szego
Editor

The Plasma Environment of Venus, Mars, and Titan

Previously published in *Space Science Reviews* Volume 162, Issues 1–4, 2011

Springer

Editor
Karoly Szego
KFKI Research Institute for Particle and Nuclear Physics
Konkoly Thege Street 29 - 33
1121 Budapest
Hungary

ISSN 1385-7525 Space Sciences Series of ISSI
ISBN 978-1-4614-3289-0
Springer New York Dordrecht Heidelberg London

Library of Congress Control Number: 2012930942

Printed on acid-free paper

Springer is part of Springer Science+Business Media (www.springer.com)

Contents

Space Sci Rev (2011) 162:1–4
DOI 10.1007/s11214-011-9844-2

The Plasma Environment of Venus, Mars, and Titan, an Introduction

Karoly Szego · Ari-Matti Harri · Michel Blanc

Published online: 1 November 2011

In December 2009 the EUROPLANET Research Infrastructure, a project funded by the European Community under the Capacities programme of the Seventh Framework Programme (grant agreement number 228319) and the International Space Science Institute, organized a workshop in Bern to overview and summarize our current knowledge on the plasma environments of Venus, Mars, and Titan. This was the first workshop organized in the series of four planned in the networking activity NA-2 of Europlanet RI. Emphasis was on new results, since many excellent reviews were published recently. The comparison of the plasma environment of these three solar system objects was a primary focus of the workshop, which also aimed at defining directions for future research, through further use of existing data or development of new space missions.

In this introductory paper, we summarize the main results of this workshop, via an overview of the different chapters it contains.

Unlike the Earth, our neighbours Venus and Mars have no global magnetic fields, although Mars has small-scale crustal fields; and Titan, to our best knowledge, is also a non-magnetic body. These three objects are the only non-magnetic solar system bodies having a dense atmosphere. Venus and Mars have the supersonic and super-Alfvenic solar wind as their plasma environment. Titan, in contrast, is located inside Saturn's hot, rapidly rotating, subsonic, multicomponent magnetospheric flow (although it occasionally makes excursions into the magnetosheath) and its environment is highly variable in time. Accordingly,

K. Szego (✉)
KFKI Research Institute for Particle and Nuclear Research, Budapest, Hungary
e-mail: szego@rmki.kfki.hu

A.-M. Harri
Finnish Meteorological Institute, Helsinki, Finnland

M. Blanc
Ecole Polytechnique, Palaiseau and IRAP, Toulouse, France

M. Blanc
International Space Science Institute, Bern, Switzerland

these objects provide a wide parameter range for the investigations of the interaction of non-magnetized objects with their plasma environments. It is remarkable that their global structure is very similar, even if each obstacle has its own characteristics depending on the actual plasma regime.

In the last few years, European and international spacecraft have gathered significant new data on the interaction of these non-magnetized objects with their plasma environments. Cassini-Huygens[1] has accumulated data over 70 flybys of Titan; Mars Express[2] has over seven years of data from Mars, and Venus Express[3] over 4 years of data from Venus. This data bonanza will continue to accumulate during the extended phase of all of these missions, providing an ideal observational support to summarize, compare and analyse the similarities and differences of their plasma interaction. Cometary interaction with the solar wind also bears similarities with these objects; therefore the knowledge presented in this volume will be highly useful for the ROSETTA comet chaser (a mission of the European Space Agency) examining at close distance how a frozen comet is transformed by the heat of the Sun in the solar wind.

The basic processes of space plasma physics have been established by the scientific investigations during the past few decades. Currently the research is focused on the understanding of the evolution of planetary atmospheres and its effect on the climate evolution over geological time scales. That requires the study of the flow of energy and momentum from the solar wind through the different planetary plasma regions leading to the loss of planetary material; *mutatis mutandis*, the same holds for Titan.

Around non-magnetic solar system bodies the interaction of flowing plasma with an ionised obstacle creates a layered, onion-like structure in the plasma flow in front of the obstacle, and an elongated plasma formation behind it for typical interplanetary magnetic field (IMF) configurations. In front of the obstacle the magnetic field piles up forming a magnetic barrier. The magnetic field configuration behind the obstacle, in the tail, depends on the dynamic pressure of the flow. Recent investigations have revealed that when the IMF is parallel to the flow, a more complex plasma structure is generated around the obstacle, and the magnetic barrier is missing. The features of the interaction, including the nature and the features of the boundary layers, can be very different, depending upon the properties of the incident plasma and the nature of the obstacle. A particular role is played by the pickup processes. The pickup ion radius depends on the strength of the magnetic field which e.g. in the case of Titan is of the same order as the obstacle radius. The outer limit of the spatial volume which is under the control of ions originating from the obstacle is the boundary of the induced magnetosphere. The boundaries around the obstacles are of finite width. This is particularly important for the cometary bow shock, its considerable width allows neutrals to be ionized within the bow shock resulting in a new category of shocks, the mass loaded shock. The mass loading region is particularly extended around Titan, its width is a few Titan radii. As a consequence, the magnetic field and the pickup velocity are continuously changing in this region. For the non-magnetized planets the induced magnetosphere is not axially symmetric, due to the electric field induced by the magnetic field and flow velocity; this introduces asymmetry also in the structure of the tail.

[1]The Cassini-Huygens space mission is an international cooperative effort of NASA, the European Space Agency (ESA), the Italian Space Agency (ASI) and several separate European academic and industrial contributors.

[2]The Mars Express space mission is a cooperative effort of the European Space Agency.

[3]The Venus Express space mission is a cooperative effort of the European Space Agency.

The physical processes evidently involve electrons, which by definition account for half of the plasma population (except when multiply-charged ions are present). The electrons come from sources including the incoming plasma flow and the ionization processes (photo ionization and impact ionization) in the ionosphere of the object; they may also be produced in the region of the object by additional processes. The ionospheres are produced by solar radiation and precipitating electron impact (from the magnetosphere or shocked solar wind), or a combination of both. Electrons in the environment near non-magnetized objects can provide a source of energy for the atmosphere.

The papers of this volume describe first the upstream conditions, then the obstacles, the formation of the induced magnetospheres, ion acceleration and outflow; the special features derived from the observations of energetic neutrals, and a paper on modelling complement the description. Let us say a few words about each of them.

The paper by *Delva et al.* reviews the proton upstream waves reported for Venus and Mars, their generation mechanism and consequences for the planetary exospheres. *Arridge et al.* discuss the upstream parameters controlling the interaction of Titan and its effects on the chemistry of the ionosphere. The physics of Saturn's magnetosphere near Titan is also considered in this respect resulting in the high variability of the plasma environment. Titan has the most significant atmosphere of any moon in the solar system. The paper of *Coates et al*. reviews several recent advances in our description and understanding of Titan's ionosphere, and compares it to the ionospheres of Venus and Mars. The role of ionospheric photoelectrons is also considered. *Dubinin et al.* focus on the different channels through which planetary matter escapes. Forces responsible for energization in the various channels are special. The solar wind forcing of ion escape for Venus and Mars is the focal topic of the review paper of *Lundin*. The aim of this overview is to analyse the different acceleration processes associated with ion outflow. A broad description of the structure and properties of the induced magnetospheres and the boundaries of Venus, Mars an Titan is presented by *Bertucci et al.* The concept of fossil magnetic fields is also analyzed in depth. Analysis of energetic neutrals brings important information about the plasma environments and about the neutral exospheres; this novel technique is presented by *Yoshifumi et al*. Numerical modeling of the global plasma and neutral dynamics at Venus, Mars and Titan, presented by *Kallio et al.*, makes this volume complete.

A focal problem of the current research is to clarify the outflow channels of the planetary plasma and the planetary plasma loss as a result of the interaction with the impinging plasma flow. A part of the outflow takes place through the tail region; another part escapes through the boundary layer of the induced magnetosphere. The driver of the outflow is different in the different channels, this is also to be clarified in the future. The sophisticated instrumentation e.g. onboard of Mars-Express and Venus-Express makes it possible to measure the tail escape velocities. Presently the scientific community is debating on how the ionospheric outflow is made possible, and what is the role of thermal escape relative to the non-thermal escape processes. This requires the categorisation of the ionospheric structure, dynamics and chemistry. Outflow in the boundaries requires the identification of the boundaries and of the role of the different frictional effects, and the processes themselves that form the boundary regions and the tail. Additional work is necessary to quantify the pickup processes and associated wave excitations.

In summary, this volume gathers in a comprehensive and systematic way a comparison of the different features of the similarities and differences in the plasma interactions of Venus, Mars and Titan. From this comparison, one can explore a significant fraction of the parameter space of magnetized plasma flow interactions with non magnetized objects with

an atmosphere. Beyond the particular cases of Venus, Mars and Titan, this comparison partly addresses the comet-solar wind interaction, and the interaction of some of the exoplanets with their stellar wind.

Acknowledgements The editors here thank all the referees who reviewed the articles in this volume for their dedication to this work. Their contribution very much enhanced the value of this volume.

Space Sci Rev (2011) 162:5–24
DOI 10.1007/s11214-011-9828-2

Upstream Ion Cyclotron Waves at Venus and Mars

Magda Delva · Christian Mazelle · César Bertucci

Received: 10 February 2011 / Accepted: 29 August 2011 / Published online: 14 October 2011

Abstract The occurrence of waves generated by pick-up of planetary neutrals by the solar wind around unmagnetized planets is an important indicator for the composition and evolution of planetary atmospheres. For Venus and Mars, long-term observations of the upstream magnetic field are now available and proton cyclotron waves have been reported by several spacecraft. Observations of these left-hand polarized waves at the local proton cyclotron frequency in the spacecraft frame are reviewed for their specific properties, generation mechanisms and consequences for the planetary exosphere. Comparison of the reported observations leads to a similar general wave occurrence at both planets, at comparable locations with respect to the planet. However, the waves at Mars are observed more frequently and for long durations of several hours; the cyclotron wave properties are more pronounced, with larger amplitudes, stronger left-hand polarization and higher coherence than at Venus. The geometrical configuration of the interplanetary magnetic field with respect to the solar wind velocity and the relative density of upstream pick-up protons to the background plasma are important parameters for wave generation. At Venus, where the relative exospheric pick-up ion density is low, wave generation was found to mainly take place under stable and quasi-parallel conditions of the magnetic field and the solar wind velocity. This is in agreement with theory, which predicts fast wave growth from the ion/ion beam instability under quasi-parallel conditions already for low relative pick-up ion density. At Mars, where the relative exospheric pick-up ion density is higher, upstream wave generation may also take place under stable conditions when the solar wind velocity and magnetic field are quasi-perpendicular. At both planets, the altitudes where upstream proton cyclotron waves were observed (8 Venus and 11 Mars radii) are comparable in terms of the bow shock nose

M. Delva (✉)
Space Research Institute, Austrian Academy of Sciences, Schmiedlstrasse 6, 8042 Graz, Austria
e-mail: magda.delva@oeaw.ac.at
url: http://www.iwf.oeaw.ac.at

C. Mazelle
CESR/UPS-CNRS, Toulouse, France

C. Bertucci
Institute for Astronomy and Space Physics, IAFE, Buenos Aires, Argentina

distance of the planet, i.e. in terms of the size of the solar wind-planetary atmosphere interaction region. In summary, the upstream proton cyclotron wave observations demonstrate the strong similarity in the interaction of the outer exosphere of these unmagnetized planets with the solar wind upstream of the planetary bow shock.

Keywords Venus · Mars · Upstream · Cyclotron waves · Ion pick-up · Exosphere

1 Importance of Upstream Waves

The escape of particles, especially hydrogen, from planetary atmospheres is an important key towards understanding the atmospheres' composition and evolution over the lifetime of the solar system. In this context, plasma waves observed at the ion cyclotron frequency in the planetary frame are frequently used to prove the existence of specific ions in the neighborhood of planets and satellites. For an unmagnetized planet such as Venus or Mars, where the neutral exosphere extends into the flowing solar wind plasma, loss of pick-up ions upstream of the bow shock can play a significant role in the escape process. In general, planetary neutrals are ionized by photo-ionization, electron impact ionization and charge exchange (Zhang et al. 1993). The newborn ions form an unstable secondary ion species in the solar wind; interaction of these pick-up ions with the background plasma enables wave generation through different mechanisms. In velocity space, the pick-up ions form a specific distribution depending on the angle α_{VB} between the solar wind velocity $\boldsymbol{V}_{SW}$ and the magnetic field $\boldsymbol{B}$; in that context, the cone angle θ ($=$ angle$(-\boldsymbol{V}_{SW}, \boldsymbol{B})$ is also often used. For magnetic field perpendicular to the solar wind velocity (no parallel drift velocity) a pure ring distribution of pick-up ions develops, leading to left-hand polarized Alfven waves at the ion gyration frequency in the plasma frame (Huddleston and Johnstone 1992); for magnetic field parallel or anti-parallel to the solar wind velocity a pure field-aligned beam of pick-up ions forms, and the right-hand mode will be generated (Gary 1991). In reality, the configuration of the magnetic field and the solar wind will be neither of these extreme cases, so the general case for the ion distribution will be a ring-beam, generating waves observed at the specific ion's cyclotron frequency in the spacecraft frame. The cyclotron waves can theoretically be expected in magnetic field observations at any location where pick-up in adequate quantity from the neutral planetary atmosphere is possible; they propagate nearly parallel to the magnetic field and were reported at Mars (Russell et al. 1990b; Brain et al. 2002; Mazelle et al. 2004; Bertucci et al. 2005), at Saturn (Leisner et al. 2006), at Jupiter's satellites (e.g. Huddleston et al. 1997; Volwerk et al. 2001) and in the environment of active comets (e.g. Tsurutani and Smith 1986; Johnstone et al. 1987; Glassmeier et al. 1989). They were not observed at Titan; this was explained by a too long wave growth time compared to the convection time of background plasma through the interaction region (Cowee et al. 2010). Especially upstream of a planetary bow shock, the presence of ion cyclotron waves is a precursor of the approaching planet, demonstrating the existence of the specific neutral in the part of the planetary atmosphere which is unprotected by an intrinsic or induced magnetosphere. Many other types of waves are generated upstream, some of which are foreshock phenomena, i.e. occurring only in the region of space where the magnetic fieldlines are connected to the bowshock from solar wind particles reflected at the bowshock (e.g. Barabash and Lundin 1993). Other waves are generated by ions leaking through the bowshock (e.g. Crawford et al. 1993).

In this review, we concentrate on upstream waves observed at the cyclotron frequency in the spacecraft frame, generated by pick-up ions from locally-available planetary species because of their importance as tracers of the planetary exospheric composition.

2 Waves at the Ion Cyclotron Frequency

A spacecraft in orbit around a planet has approximately the planet's velocity relative to the solar wind, such that the planetocentric frame and the spacecraft frame are equivalent with respect to the solar wind frame.

A planetary neutral will be nearly at rest in the planet's frame and, neglecting its small initial velocity, will have a velocity $-\boldsymbol{V}_{SW}$ in the solar wind frame, where $\boldsymbol{V}_{SW}$ denotes the solar wind velocity and here is supposed to be radially outward from the Sun. At ionization the particle is injected into the solar wind flow, drifts with a velocity $\boldsymbol{V}_{\parallel}$ along the magnetic field B (where $V_{\parallel} = -V_{SW}\cos(\alpha_{VB})$ and α_{VB} is the angle between $\boldsymbol{V}_{SW}$ and $\boldsymbol{B}$) and gyrates around the magnetic field lines according to its velocity component $\boldsymbol{V}_{\perp}$ perpendicular to the magnetic field, with gyrofrequency $\Omega_i (\Omega_i = q/m_i B$; mass m_i, charge q, magnetic field strength B). Interaction of the beam of pick-up ions with the background solar wind plasma will take place and can lead to wave generation, if resonance with a wave in that plasma occurs. In the solar wind frame, the gyrating pick-up ions will be in resonance with a wave of frequency ω and wave vector $\boldsymbol{k}$, if

$$\omega - \boldsymbol{k}\cdot\boldsymbol{V}_{\parallel} \pm n\Omega_i = 0 \quad n = 1, 2, \ldots \tag{1}$$

Under this condition, the pick-up ions can exchange a significant amount of energy with the wave (Gary 1991). The resonant wave of frequency ω and propagating parallel to $\boldsymbol{B}$ (i.e. $\boldsymbol{k} = \boldsymbol{k}_{\parallel}$) will be observed in the spacecraft frame with a Doppler-shifted frequency:

$$\omega_{sc} = \omega + \boldsymbol{k}_{\parallel}\cdot\boldsymbol{V}_{SW} \tag{2}$$

Introducing the parallel velocity for planetary ions $V_{\parallel} = -V_{SW}\cos(\alpha_{VB})$ in (1) and using the parallel propagation property of the waves $\boldsymbol{k}_{\parallel}\cdot\boldsymbol{V}_{SW} = kV_{SW}\cos(\alpha_{VB})$ in (2), combination of both equations yields the frequency observed in the spacecraft frame

$$\omega_{sc} = \mp n\Omega_i \tag{3}$$

Resonance occurs mainly for the fundamental mode $n = 1$ (Brinca 1991). Therefore, parallel propagating waves generated from picked-up planetary particles with a negligible velocity relative to the planet and to the spacecraft will always be observed in the spacecraft frame exactly at the local ion frequency, regardless of the value of the angle α_{VB} between $\boldsymbol{V}_{SW}$ and $\boldsymbol{B}$. This fact immediately excludes confusion with ULF waves generated by solar wind protons back-streaming from the bow shock, which occur only within the foreshock and will be observed at the spacecraft at frequencies lower than the local proton cyclotron frequency due to their large velocity with respect to the spacecraft (Watanabe and Terasawa 1984; Gary 1991). The opposite signs in expression (3) account for the inversion of the polarization of the wave in the spacecraft frame with respect to the one observed in the solar wind frame; this effect is called "anomalous Doppler-effect" (Mazelle and Neubauer 1993). The local ion cyclotron frequency of the waves as observed in the spacecraft frame is the crucial criterion to identify them as generated by planetary ions and not by species of solar wind origin; furthermore, they are transverse left-hand polarized waves, propagating nearly parallel to the magnetic field (Mazelle et al. 2004).

Recently, left- and right hand polarized waves at frequencies f higher than the local proton cyclotron frequency f_p ($f \sim 1.4 f_p$ in the spacecraft frame, $f_p = (2\pi)^{-1}\Omega_p$) were reported in the solar wind at 1 AU from the STEREO spacecraft, occurring for nearly radially outward interplanetary magnetic field, i.e. parallel conditions of $\boldsymbol{V}_{SW}$ and $\boldsymbol{B}$. The high

frequency and the polarization (left- and right-handed) distinguish these waves from locally generated proton cyclotron waves; they were interpreted to be of solar wind origin (Jian et al. 2009).

In the plasma rest frame, the angle α_{VB} between $\boldsymbol{V}_{SW}$ and $\boldsymbol{B}$ is the important variable for wave generation, determining the resonant frequency ω (see (1)) and the growth rate of any unstable mode. Cyclotron resonance can generate two possible modes: the first is characterized by a left-hand polarization and a second mode with right-hand polarization, all in the plasma frame. The former mode is unstable only for $\alpha_{VB} \sim 90°$ and has low growth rate, whereas the latter is unstable for α_{VB} in the range 0–70° and has a large growth rate (Brinca 1991; Gary 1991); the instability of the mode is the wave driver. Therefore, under perpendicular conditions with a pure ring-distribution of pick-up protons in velocity space, left-hand polarized waves (in the plasma frame) at the local proton cyclotron frequency can be generated, but with slow wave growth. There, wave generation will only be efficient for high relative density of the pick-up ions to the background plasma and/or when stable conditions enable wave growth for sufficiently long times. The free energy of the ions in the ring acts as source for the ion cyclotron waves, e.g. at comets (see e.g. Coates et al. 1990), in the Io torus (Huddleston et al. 1997), at Mars (see e.g. Wei and Russell 2006) and other planets.

For a parallel or anti-parallel configuration of $\boldsymbol{V}_{SW}$ and $\boldsymbol{B}$, the newborn ions form a field-aligned beam of exospheric protons, with a low number density compared to the solar wind protons. For these conditions, the ion/ion resonant right-hand instability is dominant and wave growth is fast, whereas the left-hand mode cannot grow (Brinca 1991; Gary 1991). In velocity space, the pick-up ions have a beam distribution; the free energy is derived from the parallel drift velocity of the pick-up ions relative to the background plasma and ion cyclotron waves are efficiently generated from the ion/ion beam instability. The right-hand mode will be perceived at the local proton cyclotron frequency with a left-hand polarization in the spacecraft frame, due to the anomalous Doppler effect. This type of resonance has been discussed mainly for comets (Lee 1989; Brinca 1991; Tsurutani 1991) but also for Venus (Delva et al. 2011) and Mars (Mazelle et al. 2004).

For intermediate values of the angle α_{VB}, a ring-beam distribution is formed in velocity space and a transition from one generation mechanism to the other will take place with increasing values of α_{VB}, i.e. near $\alpha_{VB} = 70°$ (Gary 1991).

3 Hydrogen Ionization and Wave Generation

Upstream left-hand polarized waves observed in the spacecraft frame precisely at the local proton cyclotron frequency are indicator of pick-up of hydrogen with negligible velocity relative to the planet, i.e. of local hydrogen, and expected everywhere where sufficient pick-up of exospheric hydrogen is possible. Ionization processes have a solar zenith angle dependence in the upstream region, but are rotationally symmetric with respect to the Planet–Sun line. Observations of proton cyclotron waves (PCWs) from wave generation at first pick-up should show a similar rotational symmetric occurrence in space, and decrease with distance from the planet due to the decreasing exospheric density.

Another wave generation scenario was proposed from a limited set of Mars Global Surveyor (MGS) spacecraft observations (Wei and Russell 2006); details of these observations are discussed in a further paragraph. The authors suggest that PCW generation takes place at ionization of hydrogen from an asymmetric neutral hydrogen disk around the planet, formed by fast hydrogen. Since the planetary exosphere presumably does not reach far out,

planetary hydrogen should be first ionized and subsequently re-neutralized during the first part of the ion's gyration motion, such that at time of neutralization the particles continue their motion in direction of positive motional electric field ($\boldsymbol{E} = -\boldsymbol{V}_{SW} \times \boldsymbol{B}$) up to large distances from the planet. This should have the effect of creating a half space or thick exospheric disk of fast neutral hydrogen, in the preferred direction of positive electric field $\boldsymbol{E}$ and perpendicular to $\boldsymbol{B}$, with higher density at larger distance from the plane ($\boldsymbol{V}_{SW}$, $\boldsymbol{B}$). There, secondary ionization should take place and PCWs be generated, which are observed when the spacecraft crosses the region with enhanced density of fast neutral hydrogen in the exospheric disk. These PCWs should be observed as an intermittent feature, when the spacecraft is located within the neutral disk, at large distances to the side of the planet, with larger amplitudes at larger distances, and occur only in direction of positive electric field, i.e. in the $\boldsymbol{E}^+$ hemisphere.

In the following, the PCW observations at Venus and Mars will be discussed to enable insight into the possible wave generation mechanism at initial or at secondary ionization of local hydrogen.

The energy in the observed waves enables a prediction about the required ion density of the pick-up species in the generation area. In quasi-linear theory, it is expected that the wave energy is related to the rate of newly created ions, and therefore to the exospheric density (Huddleston and Johnstone 1992). This theory describes the transition from a ring-beam to an isotropic shell first by pitch-angle scattering and then to a thick shell by energy diffusion; the total free energy for wave generation in a pick-up ion ring distribution, in first approximation for small ratios V_A / V_{SW}, is given by the equation

$$E_{free} = \frac{1}{4} m_i n_i V_A V_{SW} [(1 + \cos \alpha_{VB})^2 + (1 - \cos \alpha_{VB})^2] \tag{4}$$

where m_i is the mass of the ion, n_i the number density, V_A the Alfven velocity, V_{SW} the solar wind velocity, and the pitch angle α_{VB}. Equaling the observed PCW energy to a fraction of the free energy in the ring-distribution ($E_{PCW} = \phi E_{free}$) leads to the required ion density n_i, where ϕ describes the efficiency of ring energy transfer to the waves ($\phi \leq 1$). Recent simulation studies indicate that a low value for the efficiency factor $\phi = 0.25$–0.30 is realistic (Cowee et al. 2007).

However, the relation can be much more complicated requiring a non-linear scenario: due to the existence of two ion populations (solar wind + planetary) with different densities, velocities and/or temperatures, a direct connection between wave amplitude at the cyclotron frequency and neutral density in the planetary exosphere may not exist (Mazelle et al. 2004).

4 Upstream Cyclotron Waves at Venus

4.1 Observations

At Venus, where the solar wind magnetic field is 5 to 40 nT, proton cyclotron waves are expected in a frequency range $f_p \sim 0.076$–0.610 Hz and with enhanced wave power in the left-hand polarized component of the transverse power.

The Venus upstream environment was observed by the Pioneer Venus Orbiter (PVO) from 1978 to 1992 with a magnetometer and a plasma instrument. The spacecraft orbit was highly elliptical with periapsis at low latitude in the Venus planetary frame; magnetometer observations are available for solar minimum and maximum conditions, however with variable time resolution throughout the mission. From the existence of a Venus hydrogen corona

(Nagy et al. 1990) the detection of ion cyclotron waves was expected from PVO observations, but never reported in the solar wind (Russell et al. 1990a); even recent new analysis of the PVO data could not reveal waves within 40% of the expected local proton frequency in the upstream region (Russell et al. 2006).

Since May 2005, the Venus Express spacecraft has been in a highly elliptical orbit around the planet with periapsis near the planetary north pole. The field and particle instrumentation is similar to PVO: a magnetometer MAG (Zhang et al. 2008) and plasma instrument ASPERA (Barabash et al. 2007) are onboard, both with a higher data-sampling rate than for PVO. The solar activity has been in a prolonged minimum state during the Venus Express mission up to end of 2009. PCWs upstream of the Venus bow shock were reported from the magnetometer observations on the Venus Express mission (Delva et al. 2008a, 2008c), i.e. left-hand polarized waves within the frequency range (0.8–1.0) f_p, where f_p is the local proton cyclotron frequency in the spacecraft frame.

4.2 Wave Characteristics

In recent work (Wei et al. 2010) a subset of the magnetometer data of Venus Express (34 orbits of 24 h in 2006) was investigated for upstream waves in a wider frequency range (0.15–4.0) f_p. The authors reported left- and right-handed polarized waves at higher frequencies ($f > 1.5 f_p$). Due to the frequency significantly larger than the local f_p, the waves were interpreted to be of solar wind origin, similar to waves in the solar wind at 1 AU observed by the STEREO spacecraft (Jian et al. 2009). Waves in the range (0.5–1.5) f_p were found to be left-handed polarized, mainly connected to the bow shock and occurring in opposite direction of the motional electric field; this is different from earlier findings at Mars (Wei and Russell 2006) where PCW occurrences were mainly in direction of positive electric field. Therefore, the authors conclude that at Venus the waves detected in the frequency range (0.5–1.5) f_p may be generated by solar wind ions backstreaming from the quasi-parallel shock and exospheric proton cyclotron wave production may be restricted to the magnetosheath.

A study of Venus Express magnetometer data from two Venus years (450 orbits of 24 h, 2006 May to 2007 Aug) in steps of 10 min intervals reported detection of upstream PCWs in the frequency range $[0.8(f_p - \Delta f_p), f_p + \Delta f_p]$, where $f_p = \kappa \mu(B_t)$ is the local proton cyclotron frequency in the spacecraft frame, the error range $\Delta f_p = \kappa(\sigma(B_t) + \Delta B)$ was determined from the mean total field $\mu(B_t)$ and standard deviation $\sigma(B_t)$ in a 10 min interval, and the data accuracy $\Delta B = \pm 1$ nT; $\kappa = (2\pi)^{-1} q/m_p$ with q and m_p charge and mass of the proton. Waves were found during 1% of the investigated upstream time-intervals, with mean amplitude 0.56 nT and wave durations from several minutes up to two hours. The waves were reported to be with and without connection to the bow shock, showing that they are not a foreshock related phenomenon and therefore interpreted to be generated by pick-up of protons from the extended Venus exosphere (Delva et al. 2008c). Figure 1a shows a typical example for the waveform in VSO coordinates (Venus Solar Orbital coordinate system, centered at Venus, x_{VSO} axis towards the Sun, z_{VSO} axis perpendicular to Venus' orbital plane and positive to ecliptic north, y_{VSO} axis completing the right-hand system) for 7 September 2006; the spacecraft was at a distance of 6.7 Venus radii (R_V). The period ~4.7 sec is clearly seen ($f_{pobs} \sim 0.21$ Hz, calculated local proton frequency $f_p = 0.23$ Hz); the spectrum in Fig. 1b shows the compressional and left- and right-hand polarized transverse power components; the strong enhancement of the power just below the calculated proton cyclotron frequency is only seen in the left-hand transverse component.

The left-handed polarized waves propagate with small angle to the magnetic field, they are highly elliptical (ellipticity = ratio of minor to major axis of the polarization ellipse, 0 =

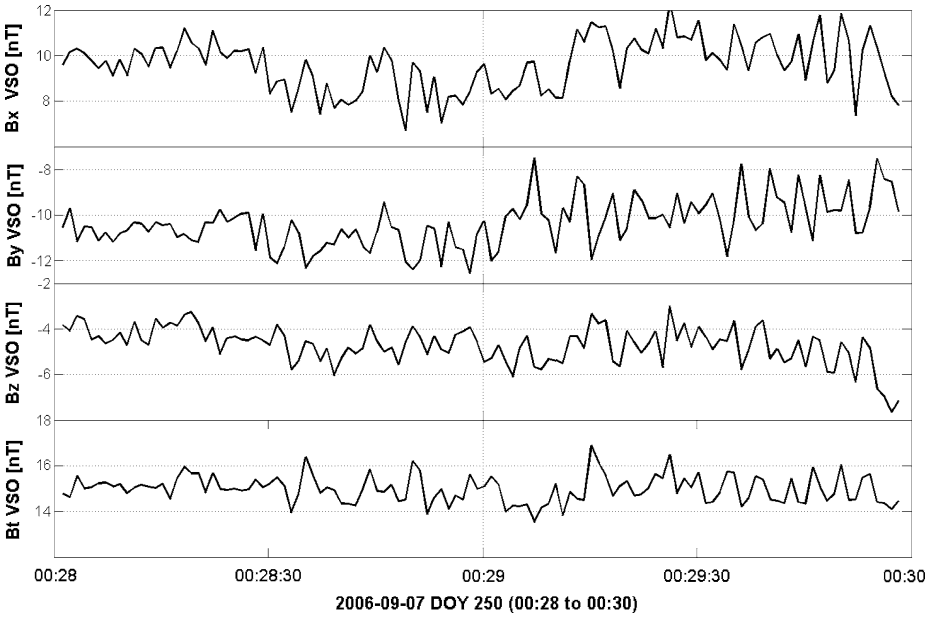

(a)

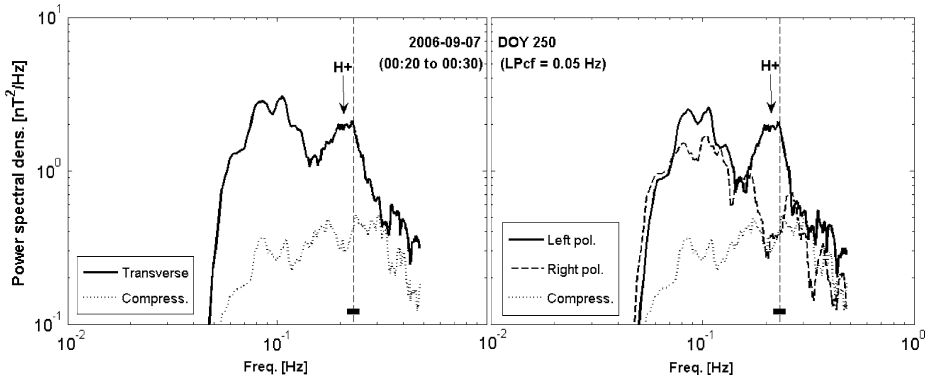

(b)

Fig. 1 Proton cyclotron waves observed by the Venus Express magnetometer on 2006-09-07 (from Delva et al. 2008b). (**a**) Waveform in VSO coordinates showing B_x, B_y, B_z, B_t; amplitude 0.65 nT, $f_{pcalc} = 0.23$ Hz, $f_{pobs} = 0.21$ Hz, ellipticity -0.55, polarization 55%; (**b**) Compressional power, left- and right-hand polarized transverse power as a function of frequency; *vertical dashed line* indicates f_{pcalc}, *horizontal bar* denotes the frequency range for $\mu(B_t) \pm \Delta B$ ($\Delta B = 1$ nT is the accuracy of the MAG data). The strong peak in the left-hand power at left of this line is the signature of proton cyclotron waves

linear, 1 = circular polarization; with negative sign for left-handed polarization), coherent and highly polarized, i.e. the criteria as known from upstream cyclotron waves at other planets or comets are well fulfilled here.

Figure 2 shows the positions of the wave observations in space; these are similar to Mars (Brain et al. 2002, and Fig. 6). PCWs are observed already at large upstream distance ($x_{VSO} = +4R_V$) from the planet and up to unexpectedly large distances of 9 R_V from the Venus–Sun line; the area covered by the spacecraft orbit stretches out to $\pm 4R_V$ in x_{VSO}

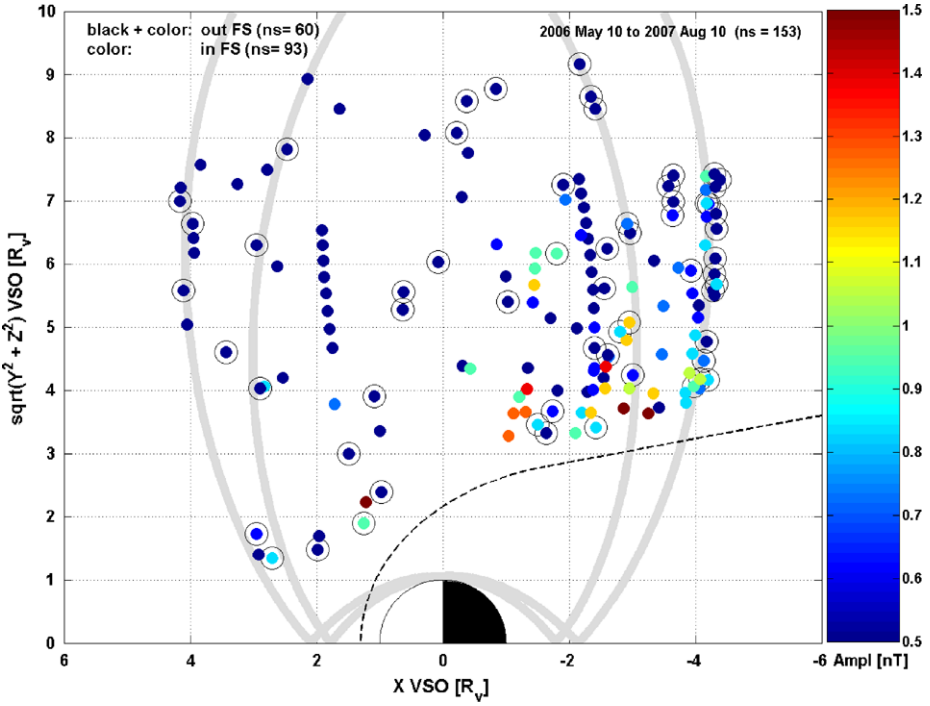

Fig. 2 Positions of observations of PCWs from two Venus-years in cylindrical VSO-coordinates. Colors are according to wave amplitude, *black circles* denote observations upstream of the foreshock region; *gray lines* denote approximately the limiting orbits of the spacecraft, regions outside of these lines were not accessed (from Delva et al. 2008c)

and to 12 R_V from the Venus–Sun line. The duration of observable PCWs is mainly short (up to 10 min) giving the impression of a short-lived feature; however, in 25% of the cases longer time-intervals (20 min up to 140 min) were observed ("trains" of subsequent observations in Fig. 2). Longer wave observations require similar wave generation conditions to be present in the large volume of space crossed by the spacecraft in the given time-interval. A difference between shorter and longer wave occurrences in terms of wave properties was reported: waves with longer duration have more pronounced wave characteristics, i.e. higher ellipticity, higher coherence and polarization (see histograms of these properties in Fig. 3).

4.3 Wave Generation and Exospheric Density

A study of the wave generation conditions from the Venus Express magnetometer data (Delva et al. 2011) revealed that a stable magnetic field was established for 20–30 min before the occurrence of observable PCWs, with specific quasi-parallel magnetic field and solar wind velocity; this means that the cone angle θ ($= \text{angle}(-\boldsymbol{V}_{SW}, \boldsymbol{B}) = \arccos(Bx_{VSO}/B_t)$) of the field is in the interval (0–60°) for parallel or (120–180°) for anti-parallel orientation, but independent of the clock angle $\psi = \arctan(Bz_{VSO}/By_{VSO})$. Maintenance of PCWs during longer time intervals was observed only if the specific conditions were stable for longer time, i.e. the same field conditions were valid over a large volume of space and similar waves were continuously generated within the volume crossed by the spacecraft (Fig. 4). Waves

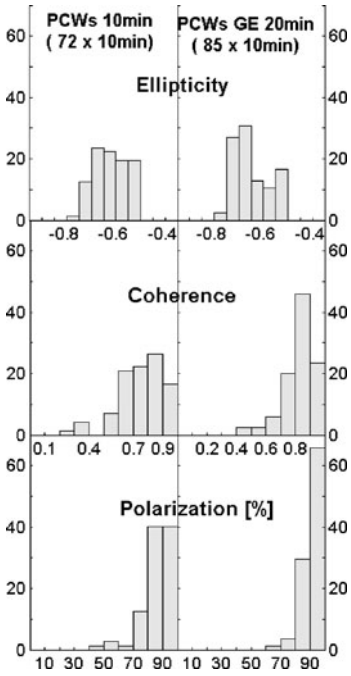

Fig. 3 Histograms (No. of cases in %) of wave parameters for short wave occurrences ($\leq$10 min, left) and for longer wave occurrences ($\geq$20 min, right), determined from 10 cyclotron periods. The specific characteristics for PCWs of high ellipticity (negative for left-hand polarized waves in the spacecraft frame), strong coherence and polarization are much more pronounced for longer-lasting waves (from Delva et al. 2011)

under quasi-perpendicular conditions were observed only beyond the terminator line, when the spacecraft had crossed through regions with higher neutral density.

In general, the hydrogen density in the Venus exosphere is expected to be low, although no in-situ observations of planetary ion densities are available at high altitudes in the solar wind, neither from the Pioneer Venus Orbiter (PVO) (Phillips and McComas 1991) nor from ASPERA on Venus Express (Barabash et al. 2007). Hybrid numerical simulations for quasi-parallel configuration of $\boldsymbol{V}_{SW}$ and $\boldsymbol{B}$ indicate that the observed waves could be produced when the pickup ion density is as low as $\sim$0.01% of the solar wind density (M. Cowee, personal communication, 2010) and also, that continual supply of pick-up ions under constant field conditions leads to faster wave growth and longer survival of the waves (Cowee et al. 2008).

The findings of more waves for stable specific quasi-parallel configurations of magnetic field and solar wind speed are in accordance with theory: for quasi-parallel configurations the ion/ion beam instability is the most effective wave generation mechanism, with fast wave growth rate even if the density of the planetary pick-up ions is low ($\leq$1%) with respect to the background solar wind plasma.

The positions of observations with no preferred direction of the motional electric field (Fig. 5) indicate that wave generation takes place at first ionization of slow local hydrogen. The waves are present up to large distances towards the Sun, proving that pick-up of planetary hydrogen takes place everywhere upstream of the bow shock from an extended reservoir of planetary origin. From the wave data, the existence of an extended Venus hydrogen exosphere with significant local neutral hydrogen densities was postulated, to enable generation of proton cyclotron waves with the observed energy (Delva et al. 2009). The nature of this extended exosphere with frequent high local densities is still an open issue.

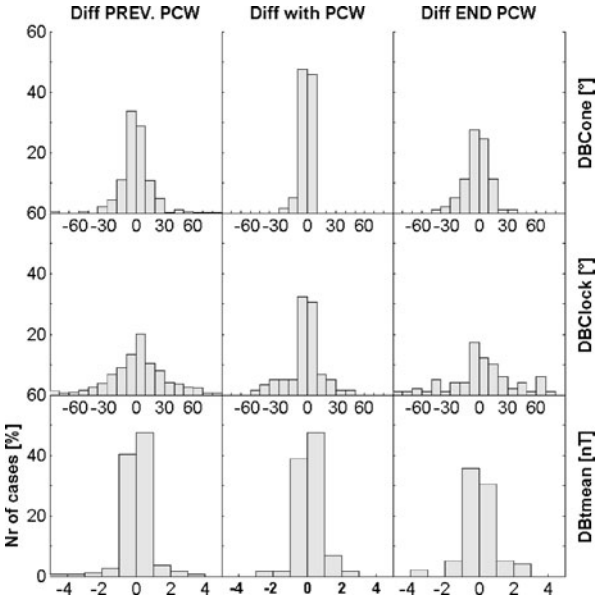

Fig. 4 Histograms (in %) of differences of field parameters one hour prior to the PCW occurrence (*left column*), during PCW occurrence (*middle column*) and from last interval with PCWs to first time interval without observable waves in the MAG data (*right column*); differences are from one 10 min interval to the next (from Delva et al. 2011)

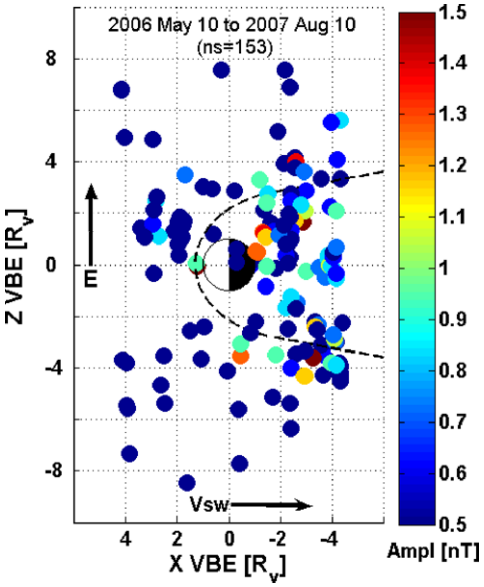

Fig. 5 Positions of observations of PCWs for two Venus-years in the $(x, z)_{VBE}$ plane of the electro-magnetic coordinate system VBE (x_{VBE} axis positive towards the Sun (and opposite to V_{SW}), y_{VBE} axis positive in direction of local mean magnetic field component perpendicular to Venus–Sun line, z_{VBE} axis positive in direction of local motional electric field $\boldsymbol{E} = -\boldsymbol{V}_{SW} \times \boldsymbol{B}$), where the mean magnetic field lines are always parallel to the $(x, y)_{VBE}$ plane and positive in the $+y_{VBE}$ direction. The *dashed line* denotes the bow shock. No asymmetry of PCW occurrence in direction of positive electric field is observed (from Delva et al. 2009)

5 Upstream Cyclotron Waves at Mars

5.1 Observations

At Mars, where the mean solar wind magnetic field is 3 to 10 nT, the local proton cyclotron frequency is in the range 0.04–0.15 Hz. From the Phobos-2 spacecraft magnetometer observations a first few cases of upstream proton cyclotron waves were reported (Russell et al. 1990b). The waves were observed near the subsolar bowshock (solar zenith angle 37–

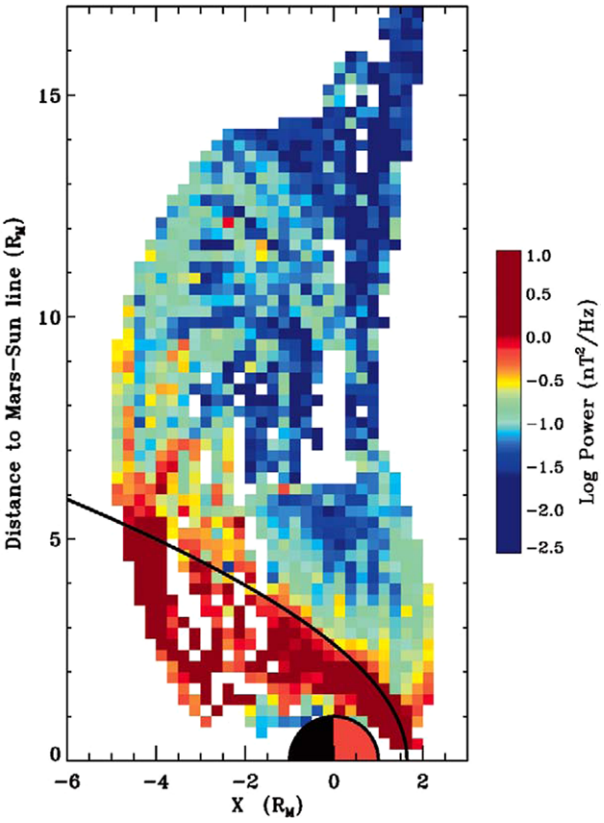

Fig. 6 Spatial distribution of power at the local proton gyrofrequency at Mars, from MGS observations. Average power is shown as a function of location for the x component of magnetic field in mean-field coordinates. The best fit bow shock is indicated in black (from Brain et al. 2002)

55°) of Mars at small distances (2–3 Mars-radii, $R_M = 3380$ km) and with low amplitudes ($\sim$0.15 nT) in a total field of $\sim$2.5 nT or $\delta B/B \sim 0.06$, left-hand polarized with eccentricities ~ -0.7 and propagating at low angle to the background field.

More PCWs were observed by the Mars Global Surveyor (MGS) spacecraft; their occurrence in space was studied in detail from a large data-set of 500 orbits (Brain et al. 2002). The authors found high concentrations of PCWs most sunward at lowest solar zenith angle (SZA) locations and for high SZA locations in tailward direction at the flanks of the bow shock; Fig. 6 shows the spatial distribution of the observed total power at the local proton cyclotron frequency for the x-component of the magnetic field. The wave amplitudes are generally larger than from the Phobos-2 spacecraft, $\delta B/B \sim 0.2$–0.56; eccentricities vary in the range -0.48 to -0.78 and propagation is at an angle $\sim$20° with respect to the background field. Table 1 lists the PCW characteristics as reported from MGS.

A further extensive study of the MGS data (Bertucci 2003; Mazelle et al. 2004; Bertucci et al. 2005) revealed more specific properties of the PCWs from a large set of orbits from different phases of the mission. Waves at the local proton cyclotron frequency were detected in the magnetometer data as well as in the electron fluxes during many orbits; Fig. 7 shows an example of the magnetic field in MSO coordinates (Mars Solar Orbital coordinate system, centered at Mars, x_{MSO} axis towards the Sun, z_{MSO} axis perpendicular to Mars' orbital plane and positive to ecliptic north, y_{MSO} axis completing the right-hand system) and simultaneous electron fluxes in different energy ranges. The oscillations have large amplitudes $\delta B/B \sim 0.3$, e.g. peak to peak amplitude up to 5 nT, and are extremely

Table 1 Upstream PCW characteristics ([a]) at Mars (from Brain et al. 2002)

Upstream waves	ω [Hz]	ω/Ω_c^+	A [nT]	$\delta B/B$	ε	θ_{kB} [°]
All waves	0.041–0.100	0.85–1.51	0.19–0.53	0.20–0.56	0.48–0.78	13.9–33.7
SPO1	0.044–0.081	0.87–1.27	0.13–0.33	0.15–0.26	0.61–0.83	10.6–22.5
AB1 "flank"	0.039–0.094	0.84–1.58	0.23–0.56	0.27–0.63	0.50–0.77	15.2–36.6

([a]) Each range denotes the quartiles around the median value

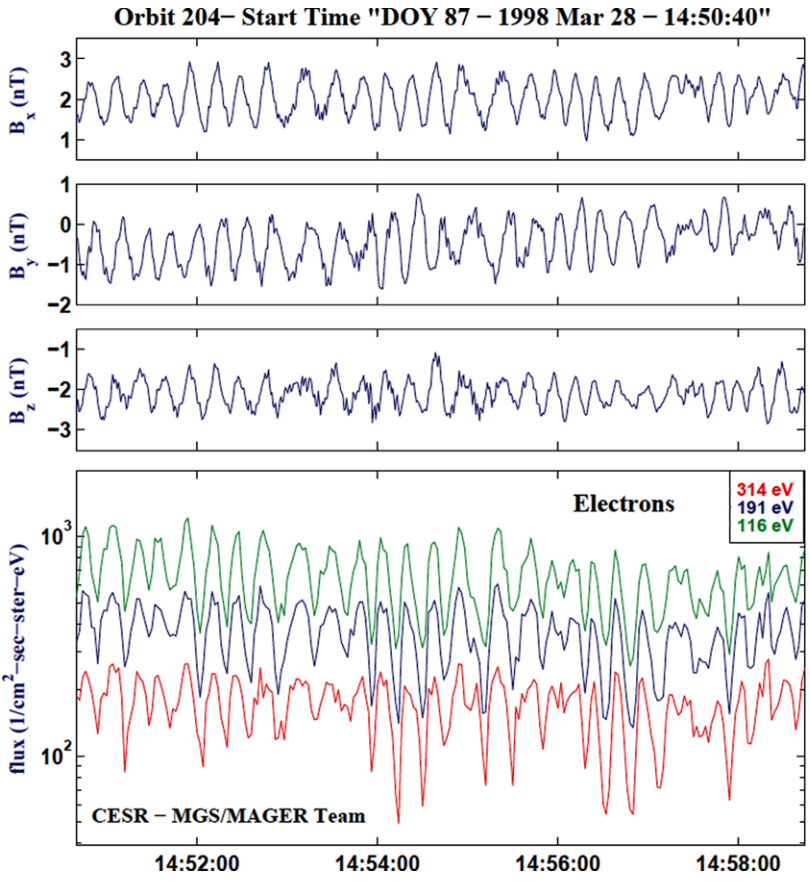

Fig. 7 Magnetic field and electron flux data from MGS orbit 204; the PCWs are present in both data-sets and have high coherence (from Bertucci 2003)

coherent. The polarization is highly left-hand circular (ellipticity ~ -1) and propagation is slightly oblique with respect to the background field. The waves were detected mainly for stable magnetic field conditions and as far as 11.3 R_M from the planet; at 5.5 R_M waves with large amplitudes $\delta B/B \sim 0.2$ were still observed. PCWs occurred during long times in the upstream part of the MGS orbit, with duration up several hours. Figure 8 shows an example of PCW occurrence for more than 3 hr for SZA of 25 to 75° on the Mars dayside, at altitude

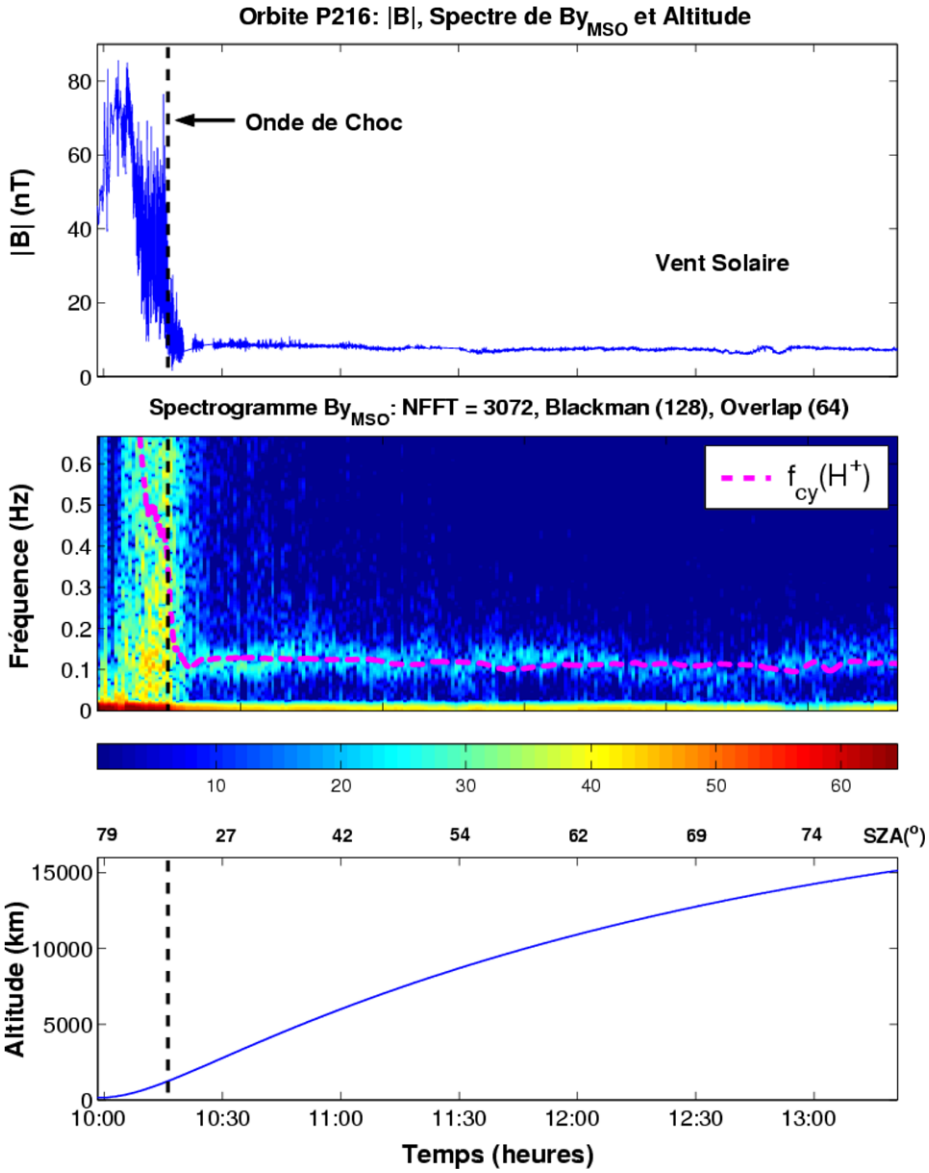

Fig. 8 PCWs observation for more than 3 hrs, occurring up to more than 5 R_M altitude, during Science Phase Orbit Phase 1 of MGS, where the orbital plane is fixed in space (from Bertucci 2003)

3000 to 15,000 km. In many cases, the waves are modulated by a lower frequency signal, and also the simultaneously observed suprathermal electron fluxes show the same superposed oscillation. The low frequency modulation has been explained through the existence of two ion populations with different densities, velocities and/or temperatures (Sauer et al. 2001); this implies that a direct connection between wave amplitude and neutral density in the planetary exosphere is not always ensured.

Another study (Wei and Russell 2006) analyzed magnetometer data from 9 of the pre-mapping orbits of MGS, during the first aerobraking phase (AB1) of the early MGS mission, where the spacecraft orbit evolved considerably and included observations at middle to high solar zenith angles and at large distances. The authors report mainly short occurrences of PCWs at large distances far from the planet (from 3 R_M up to 12 R_M), the waves last only for a few minutes to tens of minutes and are said to be intermittent.

5.2 Wave Generation and Exospheric Hydrogen

Also at Mars, the proton cyclotron waves are associated with pick-up protons from locally available planetary hydrogen, and therefore proof of the existence of planetary neutral hydrogen in the region upstream of the bowshock at the position of PCW observations.

From analysis of the vast majority of MGS orbits two groups of authors (Brain et al. 2002; Mazelle et al. 2004 and Bertucci et al. 2005) expect that the waves are generated at initial ionization, but with a non-linear correlation between wave energy and exospheric density; the wave energy is larger than expected from a linear correlation in (4). At initial ionization, different resonance mechanisms with different wave growths will be efficient depending on the quasi-parallel or quasi-perpendicular configuration of $\boldsymbol{B}$ and $\boldsymbol{V}_{SW}$. From the MGS data, the precise direction of the magnetic field is not always known, due to the contamination of the magnetometer data with a non-zero spacecraft field (up to 1 nT, Acuna et al. 2001). PCWs were continuously observed for hours during large parts of the upstream MGS orbit (Bertucci 2003). Since the IMF direction is in general not constant for such long times, it may be assumed that PCWs were observed for various directions of the IMF and, therefore both resonance mechanisms will contribute to wave generation. However, the contribution of each mechanism can be largely different, since in the quasi-parallel configuration, PCW generation is already efficient for very low densities of the pick-up ions relative to the plasma background (Cowee et al. 2008). Recent investigation of the MGS data for significant IMF values ($B_t \geq 5$ nT) and well defined field directions showed more PCW occurrences under quasi-parallel configurations (Mazelle et al. 2009).

As described in a previous chapter, another PCW generation scenario at secondary ionization from an asymmetric disk of re-neutralized planetary hydrogen was proposed, which should lead to PCW observations in the $\boldsymbol{E}^+$ hemisphere and only when the spacecraft crosses the disk. Wei and Russell (2006) analyzed a restricted data set of 9 pre-mapping orbits of MGS and reported PCWs far from the planet only for short times. From a data-set of 17 cases with strong $\boldsymbol{B}$-field, such that the uncertainty on the $\boldsymbol{B}$-direction is about $\pm 10°$ or less, the authors found wave observation positions to lay only in direction of positive electric field (Fig. 9), which lead to the proposed PCW generation at secondary ionization. The probability of either generation mechanism is discussed in the next chapter.

6 Comparison Venus–Mars

6.1 Wave Characteristics and Occurrence

The PCW amplitudes are clearly different from Venus to Mars. Whereas at Venus the amplitudes are weak (mean amplitude 0.56 nT), at Mars strong amplitudes in a weak background IMF are observed with $\delta B/B \sim 0.3$ to 0.5. Also, the waves at Mars appear to be even more left-hand polarized with an ellipticity close to -1 or almost circular, the coherence is also

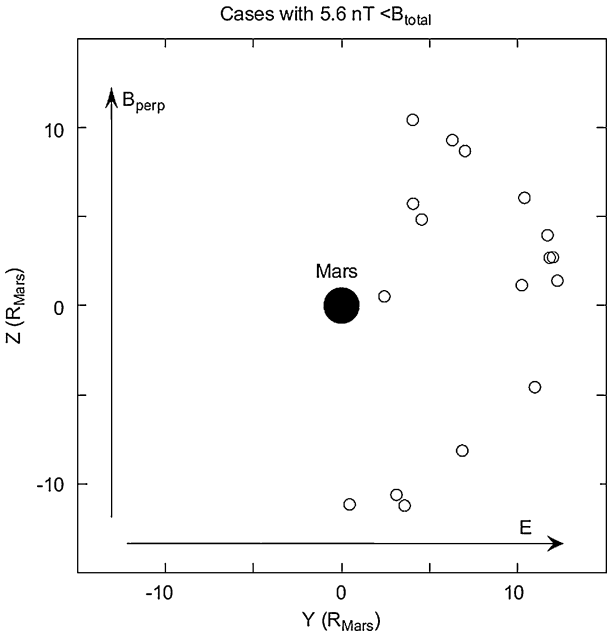

Fig. 9 Distribution of wave occurrences at Mars (from MGS) in an electric-magnetic coordinate system, whose interplanetary magnetic field B_t is large enough to neglect the inaccuracy of B_t. In this coordinate system, x-direction is from Mars to Sun, y direction is in $\boldsymbol{e}_x \times \boldsymbol{B}$ and z completes the right hand system. Thus by assuming the solar wind flow in x-direction, the y-axis is along the direction of interplanetary electric field; the z-axis lies along the direction of $\boldsymbol{B}_\perp$, perpendicular to $\boldsymbol{e}_x$ (from Wei and Russell 2006)

higher than at Venus. The majority of wave occurrences (75%) at Venus was of short duration ($\leq$10 min) but also longer cases up to 2 hours were reported; at Mars PCWs were generally observed to last for several hours, except for some short-lived cases at large distances from the planet. The occurrences in space show similar characteristics at Venus (Fig. 2) and Mars (Fig. 6): the waves were observed to have higher intensities at the flanks of the bow shock, and to occur up to large distances from the planet, further out than the respective neutral hydrogen exosphere was expected to reach.

At Venus, 25% of the cases have long duration and more pronounced specific wave characteristics in terms of ellipticity, polarization and coherence, which can develop only under favorable conditions for wave growth; at Mars, the majority of the cases has such pronounced characteristics. This means that, while favorable PCW generation conditions occur only during a minor part of the time at Venus, these seem to be available frequently and for long times at Mars.

From theory (e.g. Gary 1991) and numerical simulations (e.g. Cowee et al. 2008), it is known that PCW generation mainly depends on the relative density and velocity of the pick-up ion beam to the background plasma and on the geometrical configuration of the beam ions' velocity and the background IMF direction. In general a relative density of 0.01 to 1% is sufficient to enable PCW generation, where the lowest density is sufficient only under optimal conditions for wave growth. Therefore, quasi-parallel conditions of $\boldsymbol{B}$ and $\boldsymbol{V}_{SW}$ will enable sufficient wave growth towards observable waves already for very low relative density of the pick-up ions to the background plasma.

6.2 Exospheric Conditions

To get a better insight into the specific plasma and exospheric conditions at each planet, basic parameters are listed in Table 2. The dense atmosphere of Venus is confined to a small volume around the planet, leading to a small bow shock nose distance (1.32 R_V) on the

Table 2 Values of significant plasma and exospheric parameters at Venus and Mars

Parameter	Venus	Mars
Mass in units of Earth Mass [M_E]	0.857	0.107
Radius [km]	$R_V = 6052$	$R_M = 3380$
Exobase height [km]	200–220 [1]	220 [2]
BS nose distance from center in planetary radii	1.32 R_V [3]	1.65 R_M [4]
Neutral H number density at altitude [cm^{-3}]	~10–20 @ 12000 km ~5 @ 18000 km [5]	~0.5–20 @ 20000 km [6]
Distance from Sun [AU]	0.72	1.52
SW proton density [cm^{-3}]	15	3 [7]
Flux of SW protons [cm^{-2} s^{-1}]	5×10^8	10^8 [7]
EUV H ionization rate [s^{-1}]	~1.39×10^{-7} [8]	~0.35×10^{-7}
PCWs observed max altitude perpendicular to the Planet–Sun line [9]	~8R_V [from Fig. 2] ~6.1 × BS nose distance	~11R_M [from Fig. 6] ~6.7 × BS nose distance

[1] Lichtenegger, private communication; [2] Lichtenegger et al. (2006); [3] Zhang et al. (2008); [4] Vignes et al. (2000); [5] Gunell et al. (2005); [6] Galli et al. (2006); [7] Holmström and Kallio (2004); [8] Kallio et al. 2006; [9] Not limited by spacecraft orbital coverage in this direction

planet-Sun line; Mars with its low gravity has a thin atmosphere reaching further out in space, in terms of planetary radii the bow shock nose distance (1.65 R_M) is larger. If we use the bow shock nose distance as a measure for the solar wind interaction with the planetary atmosphere, we see that the PCWs are observed up to similar altitudes of 6.1 (for Venus) to 6.7 (for Mars) times that distance at each planet. This means that in terms of upstream hydrogen pick-up and proton cyclotron wave generation, the size of the interaction region is of similar size at both planets.

The parameters listed in Table 2 enable more comparisons. At Mars, the hydrogen exosphere is more extended and number densities at the same altitude are at least twice the value of Venus, but the total hydrogen ionization rate is only about 25–30% of the value at Venus (Zhang et al. 1993). Hence, the hydrogen ion density at the same altitude is similar at both planets, whereas the background solar wind plasma at Mars has only 20–25% of the density at Venus. Consequently the relative density of pick-up hydrogen to the background plasma is much higher at Mars and the critical minimum value for the relative density to enable PCW generation is easily reached, regardless of the angle between $\boldsymbol{B}$ and $\boldsymbol{V}_{SW}$. From the two resonant mechanisms which can generate PCWs, both can be effective at Mars, whereas at Venus with the lower relative pick-up ion density only the most efficient mechanism under quasi-parallel conditions may be effective. Indeed, from Venus it was reported that the majority of the PCWs and especially the long duration occurrences were observed under stable quasi-parallel conditions of the magnetic field and the solar wind velocity.

6.3 Discussion: Hydrogen Ionization and Wave Generation

The issue of wave generation at initial or at secondary ionization can now be discussed using the large amount of available PCW observations at both planets.

Different authors concluded from the majority of the observations at Venus and Mars, that initial ionization from exospheric hydrogen is the origin of the pick-up protons, which lead to cyclotron wave generation. Other authors proposed secondary ionization from a thick disk of fast neutral hydrogen only on the side of positive motional electric field of the planet, to explain intermittent wave occurrences at large distances from Mars.

In fact, since the solar wind and pick-up conditions from the exospheric properties of both planets are comparable, no principal differences exist and we can expect the same mechanism to be at work.

If in general PCW generation would take place from secondary pick-up from an asymmetric neutral hydrogen disk, PCW observations should have the following characteristics: be of short duration, occur mainly on the side or downstream of the terminator line, occur mainly within the neutral disk, at large distances to the side of the planet, and occur only in the $\boldsymbol{E}^+$ hemisphere; for strong $\boldsymbol{E}$-field occur preferably at large distances from the planet-Sun line and with the larger amplitudes further out. The large set of now available observations allows to check these characteristics.

From 450 orbits of Venus Express, it was reported that the waves mainly occur within the range 3–7.5 R_V from the Venus–Sun line for any value of the electric field (or $B_\perp$); no trend for larger PCW observation distances at larger $B_\perp$ was reported (see Fig. 5). Waves occur upstream as far as the spacecraft orbit reaches into the space towards the Sun ($x_{VSO} = +4R_V$) and not just at the flanks or behind the terminator line. This indicates that at Venus the waves are observed at initial ionization and not only at large distances after re-neutralization with subsequent secondary ionization. It was discussed that the time required for wave generation at secondary ionization is too long (Delva et al. 2011): neutralization frequency and ionization frequency are both low (Kallio et al. 1997, 2006) and the time needed for wave growth ($\sim$10 cyclotron periods) to obtain observable PCWs is not negligible. Therefore, the particles will be assimilated in the solar wind and swept away into the interplanetary space behind the planet, before any wave generation at secondary ionization could take place. Also, the density of the secondary pick-up ions will be extremely low, too low to account for the energy in the observed PCWs.

For Mars from the majority of MGS orbits, PCWs were observed for long times of several hours. In case of an existing neutral hydrogen disk, the spacecraft should have been permanently located within the disk, requiring constant clock angle of the IMF for these long times. From normal solar wind conditions, it is known that such stability is not existent, not for hours and certainly not frequently (see e.g. Ragot 2006).

Therefore, from PCW observations reported at Venus and from the majority of observations reported at Mars, we may conclude that the waves are generated at initial ionization from an extended hydrogen exosphere at each planet. The mechanism to transport neutral hydrogen to such high altitudes is not yet known.

7 Summary and Open Questions

Long term investigations of upstream waves at the local proton cyclotron frequency in the spacecraft frame at Venus and Mars were reviewed. The PCWs show similar occurrence positions with respect to the bow shocks, but stronger waves with larger $\delta B/B_0$ were seen at Mars. Occurrence and duration of the waves is significantly higher (during most spacecraft orbits and for several hours) at Mars, but long wave occurrences (up to 2 hours) were also reported for Venus under stable IMF conditions. The long lasting waves at Venus have pronounced properties of high ellipticity, polarization and coherence, and are therefore similar

to the majority of PCWs observed at Mars. The occurrence of the waves is reported mainly for stable conditions of the interplanetary magnetic field; at Venus the special configuration of quasi-parallel field and solar wind velocity is clearly dominant, but also at Mars, conditions with quasi-parallel magnetic field are often found.

For both planets, wave generation at initial ionization from local planetary hydrogen is found to be the basic mechanism. At Mars, the relative density of the pick-up ion beam to the background plasma is high enough to enable wave generation for various geometrical configurations of the magnetic field and solar wind velocity. At Venus with a low relative density, only the most efficient resonance mechanism for a quasi-field-aligned pick-up ion beam enables significant cyclotron wave generation. These results are consistent with theory and numerical simulations. The maximum distance of occurrence of observable PCWs from the planet-Sun line at both planets is 6–7 times the bow shock nose distance; at larger distances, pick-up ion densities are too low. This means that in terms of the size of the solar wind–planetary atmosphere interaction region, the planets are very similar also upstream and at the flanks of the bow shock.

Future research is needed to shed light on still open topics. Some tasks to be performed and questions to be answered are formulated here:

- Further investigation of waves observed near the local proton cyclotron frequency in the spacecraft frame at Venus, i.e. their connection to the bow shock, direction of propagation, wave parameters (coherence, degree of polarization, ellipticity) as function of the normalized frequency f_{obs}/f_p. This may enable a clear distinction between waves generated from locally picked up planetary hydrogen and waves generated by backstreaming solar wind protons;
- Search for the signature of upstream PCWs in other instruments of Venus Express, i.e. for waves at the local proton cyclotron frequency in the electron spectrometer ELS or for pick-up protons in the ion imager IMA, both parts of the ASPERA-4 plasma instrument; this would improve the knowledge at Venus. The problem is, that the time resolution of these sensors is partly lower than for MAG and that observations often are restricted to regions very close to or within the Venus bow shock;
- Detailed knowledge of the magnetic field conditions for long time observations at Mars would enable better comparison of the general PCW generation conditions with those found at Venus; this is difficult from the MGS data, due to the relatively large uncertainty on the field values. The study is not possible from the Mars Express data, because Mars Express carried no magnetometer. The upcoming mission MAVEN to Mars is very promising in this aspect;
- It is not known if the occurrence of PCWs is variable with the solar activity; a variable effect may be possible because the hydrogen coronae of Venus and Mars change significantly between minimum and maximum solar activity; the extension of the Venus Express mission to November 2012 may enable that type of study;
- The detection of ion cyclotron waves at planets (and satellites) has been the most sensitive method to predict the availability of the respective ion in the planetary (satellite) environment, long before any particles were directly measurable; however, the existence of slow exospheric neutrals at large distances from the planet is not yet understood. Further theoretical investigation and modeling may allow new insight into this exospheric question;
- In general, it is highly encouraged that new missions to planets may carry a magnetometer and plasma instrument, which sample simultaneously and with a comparable time resolution also far into the upstream region. Studies of ion cyclotron waves with the combined data-sets would act as very reliable detector for exospheric constituents.

Some of these questions may be answered from further investigation of existing data-sets, others require the design of new space missions with optimal plasma and magnetometer equipment. Any effort in these directions will increase our understanding of the physics of the exospheric environment of non-magnetized planets and its interaction with the solar wind.

References

M.H. Acuna et al., Magnetic field of Mars: summary of results from the aerobraking and mapping orbits. J. Geophys. Res. **106**(E10), 23403–23418 (2001)

S. Barabash, R. Lundin, Reflected ions near Mars: Phobos 2 observations. Geophys. Res. Lett. **20**, 787 (1993)

S. Barabash et al., The analyser of space plasmas and energetic atoms (ASPERA-4) for the Venus express mission. Planet. Space Sci. **55**, 1772 (2007)

C. Bertucci, Étude de l'interaction du vent solaire avec Mars: implications sur les méchanismes d'échappement atmosphérique. Ph.D. thesis, Univ. Paul Sabatier, Toulouse (2003)

C. Bertucci, C. Mazelle, M. Acuna, Interaction of the solar wind with Mars from Mars Global Surveyor MAG/ER observations. J. Atmos. Sol.-Terr. Phys. **67**, 1797 (2005)

D.A. Brain, F. Bagenal, M. Acuna et al., Observations of low-frequency electro-magnetic plasma waves upstream from the Martian shock. J. Geophys. Res. **107**, 1076 (2002). doi:10.1029/2000JA000416

A.L. Brinca, Cometary linear instabilities: from profusion to perspective, in "Cometary Plasma Processes". Geophys. Monogr. **61**, 211–221 (1991)

A.J. Coates, B. Wilken, A.D. Johnstone et al., Bulk properties and velocity distributions of water group ions at Comet Halley: Giotto measurements. J. Geophys. Res. **95**, 249 (1990)

M.M. Cowee, D. Winske, C.T. Russell, R. Strangeway, 1D hybrid simulation of planetary ion-pickup: energy partition. Geophys. Res. Lett. **34**, L02113 (2007). doi:10.1029/2006GL028285

M.M. Cowee, C.T. Russell, R.J. Strangeway, One-dimensional hybrid simulations of planetary ion pickup: effects of variable plasma and pickup conditions. J. Geophys. Res. **113**, A08220 (2008). doi:10.1029/2008JA013066

M.M. Cowee, S.P. Gary, H.Y. Wei, R.L. Tokar, C.T. Russell, An explanation for the lack of ion cyclotron wave generation by pickup ions at Titan: 1D hybrid simulation results. J. Geophys. Res. **115**, A10224 (2010). doi:10.1029/2010JA015769

G.K. Crawford, R.J. Strangeway, C.T. Russell, VLF emissions in the Venus foreshock: comparisons with terrestrial observations. J. Geophys. Res. **98**, 15305 (1993)

M. Delva, T.L. Zhang, M. Volwerk et al.. First upstream proton cyclotron wave observations at Venus. Geophys. Res. Lett. **35**, L03205 (2008a). doi:10.1029/2007GL032594

M. Delva, T.L. Zhang, M. Volwerk et al., Upstream proton cyclotron wave observations at Venus. Planet. Space Sci. **56**, 1293 (2008b). doi:10.1016/j.pss.2008.04.014

M. Delva, T.L. Zhang, M. Volwerk et al., Proton cyclotron waves in the solar wind at Venus. J. Geophys. Res. **113**, E00B06 (2008c). doi:10.1029/2008JE003148

M. Delva, M. Volwerk, C. Mazelle, J.Y. Chaufray, J.L. Bertaux et al., Hydrogen in the extended Venus exosphere. Geophys. Res. Lett. **36**, L01203 (2009). doi:10.1029/2008GL036164

M. Delva, C. Mazelle, C. Bertucci et al., Proton cyclotron wave generation mechanisms upstream of Venus. J. Geophys. Res. **116** (2011). doi:10.1029/2010JA015826

A. Galli, P. Wurz, H. Lammer et al., The hydrogen exospheric density profile measured with ASPERA-3/NPD. Space Sci. Rev. **126**, 447 (2006). doi:10.1007/s11214-006-9089-7

P. Gary, Electromagnetic ion/ion instabilities and their consequences in space plasmas: a review. Space Sci. Rev. **56**, 373 (1991)

K.H. Glassmeier, A.J. Coates, M.H. Acuna et al., Spectral characteristics of low-frequency plasma turbulence upstream of Comet P/Halley. J. Geophys. Res. **94**(A1), 37 (1989)

H. Gunell, M. Holmström, H.K. Biernat, N.V. Erkaev, Planetary ENA imaging: Venus and a comparison with Mars. Planet. Space Sci. **53**, 433 (2005)

M. Holmström, E. Kallio, The solar wind interaction with Venus and Mars: energetic neutral atom and X-ray imaging. Adv. Space Res. **33**, 187 (2004)

D.E. Huddleston, A.D. Johnstone, Relationship between wave energy and free energy from pick-up ions in the Comet Halley environment. J. Geophys. Res. **97**, 12217 (1992)

D.E. Huddleston, R.J. Strangeway, J. Warnecke et al., Ion cyclotron waves in the Io torus during the Galileo encounter: warm plasma dispersion analysis. Geophys. Res. Lett. **24**, 2143 (1997)

L.K. Jian, C.T. Russell, J.G. Luhmann, R.J. Strangeway, J.S. Leisner, A.B. Galvin, Ion-cyclotron waves in the solar wind observed by STEREO near 1 AU. Astrophys. J. **701**(2), L105–L109 (2009)
A.D. Johnstone, K.H. Glassmeier, M.H. Acuna et al., Waves in the magnetic field and solar wind flow outside the bow shock at Comet Halley. Astron. Astrophys. **187**, 47 (1987)
E. Kallio, J.G. Luhmann, S. Barabash, Charge exchange near Mars: the solar wind absorption and energetic neutral atom production. J. Geophys. Res. **102**, 22183 (1997)
E. Kallio, R. Järvinen, P. Janhunen, Venus–solar wind interaction: asymmetries and the escape of O^+ ions. Planet. Space Sci. **54**, 1472 (2006)
M. Lee, Ultra-low frequency waves at comets, in "Plasma waves and instabilities at comets and in magnetospheres". Geophys. Monogr. **53**, 13 (1989)
J.S. Leisner, C.T. Russell, M.K. Dougherty et al., Ion cyclotron waves in Saturn's E ring: initial Cassini observations. Geophys. Res. Lett. **33**, L11101 (2006). doi:10.1029/2005GL024875
H.I.M. Lichtenegger, H. Lammer, Y.N. Kulikov et al., Effects of low energetic neutral atoms on martian and Venusian dayside exospheric temperature estimations. Space Sci. Rev. **126**, 469 (2006). doi:10.1007/s11214-006-9082-1
C. Mazelle, F.M. Neubauer, Discrete wave packets at the proton cyclotron frequency at Comet P/Halley. Geophys. Res. Lett. **20**, 153 (1993)
C. Mazelle et al., Bow shock and upstream phenomena at Mars. Space Sci. Rev. **111**(1–2), 115 (2004)
C. Mazelle, C. Bertucci, J.G. Trotignon et al., Proton cyclotron waves at Mars revisited. In: AGU Fall Meeting 2009. Abstract #P11B-120 (2009)
A.F. Nagy, J. Kim, T.E. Cravens, Hot hydrogen and oxygen atoms in the upper atmospheres of Venus and Mars. Ann. Geophys. **8**, 251 (1990)
J.L. Phillips, D.L. McComas, The magnetosheath and magnetotail of Venus. Space Sci. Rev. **55**, 1 (1991)
B.R. Ragot, Distributions of magnetic field orientations in the turbulent solar wind. Astrophys. J. **651**, 1209–1218 (2006)
C.T. Russell, E. Chou, J.G. Luhmann et al., Solar cycle variations in the neutral exosphere inferred from the location of the Venus bow shock. Adv. Space Res. **10**, (5)3–(5)9 (1990a)
C.T. Russell, J.G. Luhmann, K. Schwingenschuh, W. Riedler, Upstream waves at Mars: Phobos observations. Geophys. Res. Lett. **17**, 897 (1990b)
C.T. Russell, S.S. Mayerberger, X. Blanco-Cano, Proton cyclotron waves at Mars and Venus. Adv. Space Res. **38**, 745 (2006)
K. Sauer, E. Dubinin, J.F. McKenzie, New type of soliton in bi-ion plasmas and possible implications. Geophys. Res. Lett. **28**, 3589 (2001)
B.T. Tsurutani, E.J. Smith, Hydromagnetic waves and instabilities associated with cometary pick-up: ICE observations. Geophys. Res. Lett. **13**, 263 (1986)
B.T. Tsurutani, Comets: a laboratory for plasma waves and instabilities, in "Cometary Plasma Processes". Geophys. Monogr. **61**, 189 (1991)
D. Vignes, C. Mazelle, H. Reme et al., The solar wind interaction with mars: locations and shapes of the bow shock and the magnetic pile-up boundary from the observations of the MAG/ER experiment onboard Mars Global Surveyor. Geophys. Res. Lett. **27**, 49 (2000)
M. Volwerk, M.G. Kivelson, K.K. Khurana, Wave activity in Europa's wake: implications for ion pickup. J. Geophys. Res. **106**, 26033 (2001)
Y. Watanabe, T. Terasawa, On the excitation mechanism of the low-frequency upstream waves. J. Geophys. Res. **89**, 26623 (1984)
H.Y. Wei, C.T. Russell, Proton cyclotron waves at Mars: exosphere structure and evidence for a fast neutral disk. Geophys. Res. Lett. 33 (2006). doi:10.1029/2006GL026244
H.Y. Wei, C.T. Russell, T.L. Zhang, X. Blanco-Cano, Comparative study of ion cyclotron waves at Mars, Venus and Earth. Planet. Space Sci. (2010). doi:10.1016/j.pss.2010.01.004
M.H.G. Zhang, J.G. Luhmann, A.F. Nagy et al., Oxygen ionization rates at Mars and Venus—relative contributions of impact ionization and charge exchange. J. Geophys. Res. **98**(E2), 3311 (1993)
T.L. Zhang et al., Initial Venus Express magnetic field observations of the Venus bow shock location at solar minimum. Planet. Space Sci. **56**, 785 (2008)

Space Sci Rev (2011) 162:25–83
DOI 10.1007/s11214-011-9849-x

Upstream of Saturn and Titan

C.S. Arridge · N. André · C.L. Bertucci · P. Garnier · C.M. Jackman · Z. Németh · A.M. Rymer · N. Sergis · K. Szego · A.J. Coates · F.J. Crary

Received: 28 February 2011 / Accepted: 12 October 2011 / Published online: 19 November 2011

C.S. Arridge (✉) · A.J. Coates
Mullard Space Science Laboratory, University College London, Dorking RH5 6NT, UK
e-mail: csa@mssl.ucl.ac.uk

C.S. Arridge · A.J. Coates
The Centre for Planetary Sciences at UCL/Birkbeck, Gower Street, London WC1E 6BT, UK

N. André
CNRS, Institut de Recherche en Astrophysique et Planétologie, 9 avenue du colonel Roche, BP 44346, 31028 Toulouse Cedex 4, France

N. André
UPS-OMP, Institut de Recherche en Astrophysique et Planétologie, Université de Toulouse, 9 avenue du colonel Roche, 31028 Toulouse, France

C.L. Bertucci
Instituto de Astronomía y Física del Espacio, Casilla de Correo 67, Sucursal 28, C1428ZAA Ciudad Autónoma de Buenos Aires, Argentina

P. Garnier
Swedish Institute of Space Physics, Box 537, 751 21 Uppsala, Sweden

C.M. Jackman
Space and Atmospheric Physics Group, The Blackett Laboratory, Imperial College London, South Kensington, London SW7 2AZ, UK

Z. Németh · K. Szego
KFKI Research Institute for Particle and Nuclear Physics, Konkoly Thege str. 29-33, Bldg. III, 1121 Budapest, Hungary

A.M. Rymer
Johns Hopkins University Applied Physics Laboratory, 11100 Johns Hopkins Road, Laurel, MD 20723-6099, USA

N. Sergis
Office of Space Research, Academy of Athens, 4 Soranou Efesiou Str, 11527 Athens, Greece

F.J. Crary
Southwest Research Institute, 6220 Culebra Road, P.O. Drawer 28510, San Antonio, TX 78228-0510, USA

Abstract The formation of Titan's induced magnetosphere is a unique and important example in the solar system of a plasma-moon interaction where the moon has a substantial atmosphere. The field and particle conditions upstream of Titan are important in controlling the interaction and also play a strong role in modulating the chemistry of the ionosphere. In this paper we review Titan's plasma interaction to identify important upstream parameters and review the physics of Saturn's magnetosphere near Titan's orbit to highlight how these upstream parameters may vary. We discuss the conditions upstream of Saturn in the solar wind and the conditions found in Saturn's magnetosheath. Statistical work on Titan's upstream magnetospheric fields and particles are discussed. Finally, various classification schemes are presented and combined into a single list of Cassini Titan encounter classes which is also used to highlight differences between these classification schemes.

Keywords Titan · Induced magnetosphere · Saturn · Plasma interaction

1 Introduction

Titan is Saturn's largest moon and the only moon in the solar system with a thick atmosphere and has an extended exosphere with an exobase located at approximately 1400 km (Sittler et al. 2009 and references therein). The atmosphere is characterised by an extremely rich and complex photochemically-driven N_2 and CH_4-based chemistry (Strobel et al. 2009; Waite et al. 2009, and references therein) that is important in Titan's interaction with its environment. Table 1 lists some of Titan's main properties. The formation of Titan's induced magnetosphere is the only known case in the solar system of a plasma-satellite interaction where the satellite has a substantial atmosphere with an exobase well above the planetary surface that interacts with magnetospheric (or magnetosheath/solar wind) plasma (Hunten et al. 1984). Thus the interaction between the plasma and the satellite is primarily an atmospheric-type interaction (as opposed to lunar-type interaction), although Titan may possess some weak magnetic field of internal origin it is almost certain to play a secondary role in the interaction (Neubauer et al. 1984). Cassini entered orbit around Saturn on 1 July 2004 and had encountered Titan 64 times before the end of 2009; none of these encounters found Titan in the solar wind and only two (Titan 32, otherwise known as T32, and T42) were in the magnetosheath.

Following the Voyager 1 flyby of Titan in 1980, Wolf and Neubauer (1982) discussed two main sources of variability in the interaction between Titan and its surrounding plasma environment: the solar wind and local time variations. Cassini observations have further illustrated how much more complex this interaction can be. Many aspects need to be included

Table 1 The physical and orbital parameters of Titan

Equatorial radius, R_T	2576 km
Semi-major axis	1 221 870 km (20.3 R_S where 1 $R_S = 60268$ km)
Orbital period	15.945 days
Spin period	Synchronous (15.945 days)
Mass	1.3452×10^{23} kg ($GM_T = 8.977 \times 10^{12}$ m^3 s^{-2})
Equatorial surface gravity	1.352 m s^{-2} (0.14 g)
Escape speed	2.639 km s^{-1}
Axial tilt	0°

if we want to obtain a full understanding and clearer picture of the moon-magnetosphere interaction.

Accurate models of Titan's atmospheric structure, chemistry, formation and loss rely on accurate knowledge of the local plasma environment, as a source of energy to the system, as well as possibly introducing variability in atmospheric interactions. In this paper we explore the upstream conditions that Titan is exposed to, both when inside and outside the magnetosphere. In Sect. 2 we consider the key processes involved in the formation of Titan's induced magnetosphere and in controlling its dynamics. This discussion leads us to a list of important plasma parameters that control the interaction. In Sect. 3 we describe the physics of Saturn's magnetosphere to build an understanding of how these important plasma parameters can be modulated by the physics of the system in which Titan is embedded. In Sect. 4 we discuss the solar wind and magnetosheath environment upstream of Saturn's magnetosphere, within which Titan is immersed under conditions of strong solar wind compression. In Sect. 5 the statistical properties of the magnetosphere are described which lead to a table of average plasma parameters, extending a similar table by Neubauer et al. (2006). In Sect. 6 we present various schemes for the classification of Titan's magnetospheric environment and combine these separate classifications into one table indicating the magnetospheric conditions near each Cassini encounter to date. Section 7 concludes this paper with a discussion of pre-Cassini open questions and new science questions.

2 Key Processes in the Formation of Titan's Induced Magnetosphere

To make a proper assessment of the effects of variability in upstream conditions on Titan's induced magnetosphere it is important to review the key processes and associated theoretical aspects that are important in the formation of the induced magnetosphere. In this section these features are considered with a view to building a list of the important parameters which will be discussed later in this paper.

Figure 1 contains a schematic of the interaction between Titan and Saturn's magnetosphere. The upstream (sub-)corotating magnetospheric plasma impinges on Titan from left to right, carrying with it Saturn's magnetospheric magnetic field. The electrically conducting ionosphere, produced from a variety of ionisation processes (as illustrated in Fig. 2), acts as an obstacle to the flowing magnetospheric plasma in a similar fashion to the solar wind interaction with Venus and Mars. Of course in the case of Venus and Mars the upstream flow is supersonic and so a bow shock stands upstream of the planet, but at Titan the flow is sub- and trans-sonic and no bow shock has been detected to date. At Titan the exosphere also plays a strong role in the interaction, in a similar fashion to the solar wind interaction with comets. The addition of exospheric ions to the magnetospheric flow plays a strong role in slowing and deflecting the magnetospheric flow and forming a magnetic barrier from the pile up of magnetic flux.

The most distinctive signature of Titan's plasma interaction is the absence of a significant intrinsic global magnetic field (Ness et al. 1982; Backes et al. 2005; Wei et al. 2010). A dipole moment of 0.78 ± 2.2 nT R_T^3 was reported by Wei et al. (2010) hence consistent with Titan being unmagnetised. For this reason the central element in the formation of Titan's induced magnetosphere is its ionosphere, produced from Titan's atmosphere and exosphere by photoionisation, charge-exchange and electron impact ionisation from precipitating magnetospheric plasma, energetic particles, and galactic cosmic rays. The ionosphere is the final obstacle to the external magnetised plasma flow. Because the ionosphere is a conductor currents are induced in the upstream magnetoplasma flow to prevent the magnetised

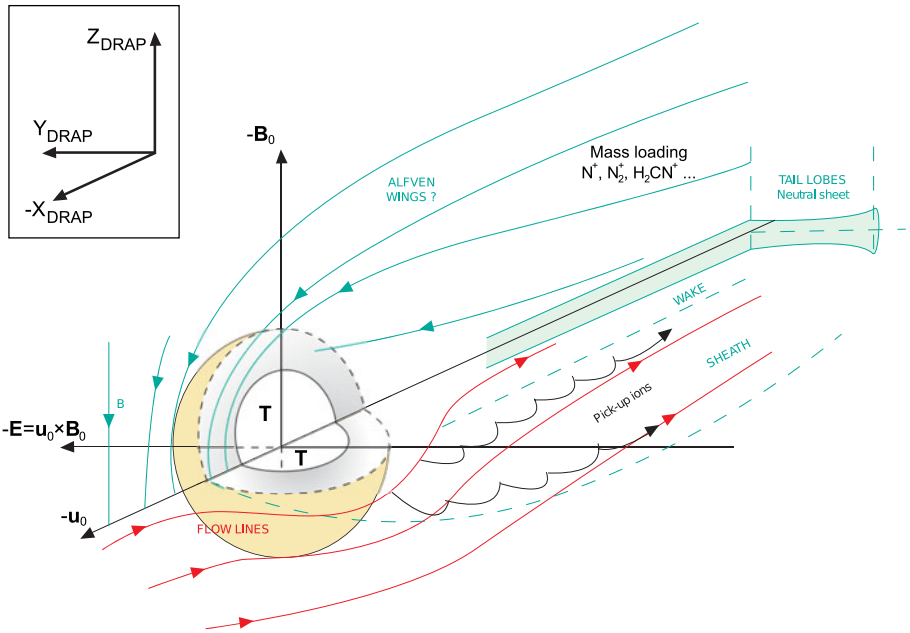

Fig. 1 Schematic illustration of the interaction between Saturn's magnetosphere and Titan. The coordinate axes are defined by the background field $\mathbf{B}_0$ and flow $\mathbf{u}_0$ and hence convection electric field $\mathbf{E}$. Under Voyager 1 conditions the background field is essentially dipolar and perpendicular to Saturn's equatorial plane, and the upstream flow is in the corotation direction, and hence the convection electric field is points radially outward from Saturn. The *inset* shows the definition of draping coordinates, which are equivalent to Titan Interaction System (TIIS) coordinates, as defined by Backes et al. (2005), for the Voyager 1 case. This figure is modified from the figure in Blanc et al. (2002)

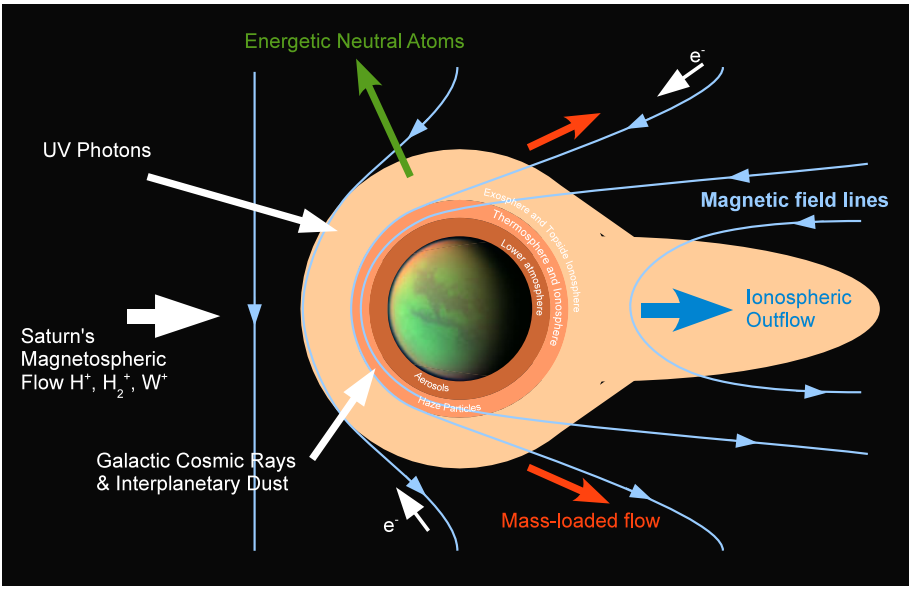

Fig. 2 Illustration of energy deposition processes in the various layers of Titan's atmosphere. After Sittler et al. (2009)

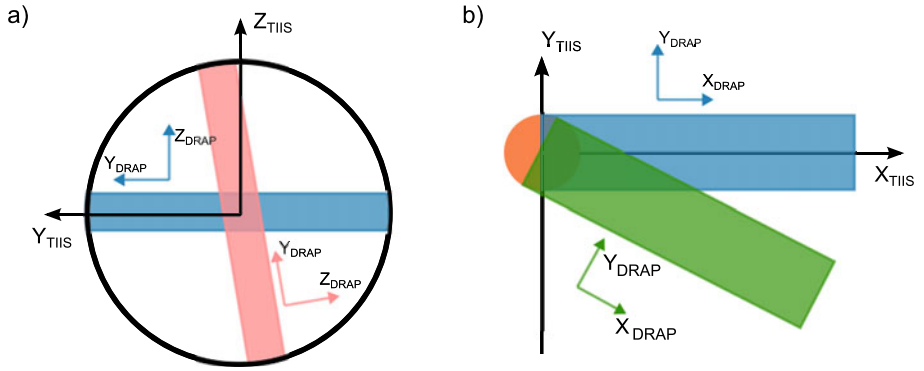

Fig. 3 Illustration of the difference between the Titan Interaction System (TIIS) and draping (DRAP) coordinates for three different upstream flow and field configurations. The *blue segments* show the location of the induced tail current sheet (**a**) and induced tail (**b**) when the upstream field is aligned with the Z axis of the TIIS coordinate system, corresponding to a dipolar upstream configuration, and the flow is along the nominal corotation direction (X axis of TIIS). The *pink* current sheet reflects a rotation of the upstream field so that it is nearly parallel to the orbital plane of Titan but the whole tail retains the same orientation (the current sheet merely rotates in along the tail axis). The *green* induced tail reflects a deflection of the flow direction so that the magnetospheric flow now has a component away from Saturn. The tail current sheet may still lie in the nominal (*blue*) orientation or it may be rotated depending on the upstream field orientation

fluid from penetrating the conducting obstacle. As long as the field orientation remains unsteady the ionosphere will remain an effective obstacle but when the field becomes steady it will diffuse through the ionosphere. As we will see, the Titan's upstream field orientation is highly unsteady. A pressure boundary called the ionopause, similar to the magnetopause at a magnetised planet, forms where the pressure of the upstream flow balances the pressure in the ionosphere. The plasma flowing past Titan then drapes the magnetic field around Titan forming an induced magnetosphere. An induced magnetotail forms in the tail/wake region of the magnetosphere. The orientation of the induced magnetotail rotates around the flow vector according to the orientation of the upstream field, but is parallel to the upstream plasma flow vector. To account for this Israelevich et al. (1994) introduced the draping (DRAP) coordinate system (illustrated in Fig. 3) which is widely and successfully used in the study of induced magnetospheres (e.g., Bertucci et al. 2003a, 2003b; Neubauer et al. 2006). In this coordinate system the X axis is parallel to the direction of the flow, the $-Z$ axis points along the mean external magnetic field perpendicular to the flow direction, and the Y axis is parallel to the cross product of the Z and X unit vectors to give a right-handed triad. In this system then, the draping effect occurs on the XZ plane, adding a negligible effect to the Y component, and the tail current sheet is then parallel to the XY plane. Hence the orientation of the upstream field is important in establishing the location of the induced tail (Simon et al. 2007; Winglee et al. 2009) and can also generate asymmetries in the induced tail (Simon and Motschmann 2009).

Exospheric ions whose capture by the external plasma begins several planetary radii away from the moon (Sittler et al. 2009 and references therein) are also an important element in the formation of Titan's induced magnetosphere and in the loss of Titan's atmosphere. The ring distributions of exospheric pickup ions drive various plasma instabilities (see Szego et al. 2000 and references therein) and this process can be extremely important in the plasma interaction. These waves are also dependent on the upstream parameters, for example the Alfvén speed can have an effect on the growth and evolution of ion cyclotron waves. The

orientation of the upstream magnetic field and the flow direction establish the orientation of the convection electric field and hence the location of pickup ions from Titan (e.g., Simon and Motschmann 2009). The location of pickup ions also results in enhanced slowing of the upstream flow in that region of the induced magnetosphere (Hartle et al. 2006). The gyroradii of pickup ions is larger when Titan is immersed in Saturn's magnetospheric current sheet hence the loss of Titan's atmosphere and pickup ion induced heating of the atmosphere can be enhanced when in a current sheet regime (Johnson et al. 2009).

Magnetospheric plasma, magnetic field and energetic particles are an important source of energy for Titan's atmosphere (Sittler et al. 2009) and are a key mechanism for the ionisation of low-altitude atmospheric layers (Kliore et al. 2008; Cravens et al. 2008) and may participate in the complex chemistry producing heavy positive and negative ions (Coates et al. 2007; Waite et al. 2007; Sittler et al. 2009). Enhancements in the dynamic pressure can increase the loss rate from Titan's atmosphere similar to that found at Mars and Venus (Ma et al. 2006; Ma and Nagy 2007; Johnson et al. 2008, and references therein). Energetic particles charge-exchange in Titan's exosphere and so the flux of energetic particles is not only important in ionising and heating the atmosphere but also in modulating the loss of the atmosphere to Saturn's magnetosphere (Sittler et al. 2009, and references therein). The composition of the upstream flow has been shown to have a significant affect on the extent of Titan's induced magnetosphere (Sillanpää et al. 2011). Whilst the magnetic field can be a barrier to the injection of charged particles into Titan's atmosphere it can also channel charged particles such as magnetospheric electrons into different layers of the atmosphere. The gyroradii of these particles, hence their energy spectra and the upstream magnetic field, is important in understanding where these particles will deposit their energy and hence how they might affect the energetics and loss of Titan's atmosphere (Sittler et al. 2009, and references therein). The position of the various plasma boundaries in Titan's induced magnetosphere are strongly affected by the temperature of the upstream ions (Simon et al. 2007).

Based on these considerations and the more thorough discussions in (Bertucci et al., Coates et al., Delva et al., Dubinin et al., Kallio et al., Yoshifumi et al., this issue) one can compile a list of the important quantities to characterise in order to probe the development of Titan's induced magnetosphere. Table 2 contains a list of these parameters. Numerical modelling of Titan's plasma interaction has been used since the early 1990s and is reviewed in detail by Kallio et al. (this issue) and also Ledvina et al. (2008). Knowledge of the upstream field and plasma flow orientation, composition, density and temperature, and derived quantities such as pressure and Mach numbers are important boundary conditions for the accurate modelling of Titan's interaction with its environment. In this paper we will investigate how these parameters vary at Titan's orbit, not only when Titan is located inside the magnetosphere but also when Titan is in the magnetosheath and solar wind.

It has long been recognised that the parameters in Table 2 are inherently variable and it is worthwhile to consider briefly the impact of such variability. Simon et al. (2010a) discuss three time scales which control Titan's magnetospheric interaction. The first is the lifetime of fossil fields in the ionosphere which has been estimated to lie between 20 minutes and three hours from simulations and observations of the T32 encounter (Ma et al. 2009; Bertucci et al. 2008). The second is the duration of stationary upstream conditions which is estimated from data to be not greater than five hours (Simon et al. 2010a). Finally, the third is due to periodic magnetospheric current sheet oscillations, which again seems to be around five hours, as estimated from Titan data by Simon et al. (2010a), which is about half of Saturn's magnetospheric oscillation period, suggesting a strong relationship to periodicities in the magnetosphere (e.g. Arridge et al. 2008a, 2011b; Khurana et al. 2009). A key question to address is the effects of periodic modulation of the key parameters involved in controlling Titan's plasma interaction. Very few observational studies have addressed such periodicities in

Table 2 List of parameters that are important in the physics of Titan's induced magnetosphere

Parameter	Influence
Electron density and temperature	Formation of ionosphere due to charge-exchange.
Electron velocity distributions	Atmospheric loss.
	Energy input into atmosphere/ionosphere.
Incident flow velocity	Ion pick-up.
	Induced tail orientation.
	Convection electric field.
	Development of ionopause on ram side.
Plasma pressure	High energetic particle pressure drives chemistry.
Plasma beta	
Ram pressure	Exospheric ion escape.
Ion distributions	Formation of ionopause.
Ion composition	Ram and plasma pressure.
Alfvén speed	Growth and evolution of ion cyclotron waves associated with ion pickup.
Mach numbers	Presence of shocks upstream of the interaction.
	Development of Alfvén wings.
Field orientation	Ion pick-up.
	Convection electric field.
	Generation of induction field in interior.
	Orientation of induced tail current sheet.

the trans-Titan environment but such a discussion is particularly relevant given the discovery and thorough characterisation of global magnetospheric periodicities (e.g., Southwood and Kivelson 2007; Carbary et al. 2007, 2008a; Arridge et al. 2008a, 2011b; Andrews et al. 2008; Burch et al. 2009) at periods longer than the assumed rotation period of Saturn. Such periodicities will be discussed in Sect. 3 but for now we simply comment on several scenarios where periodicities might represent important drivers.

Periodicities in Titan's upstream magnetic field might play an important role in generating an induced internal field at Titan due to the inductive response from a sub-surface ocean. Such an induction field is generated at Jupiter's moon Europa from periodic magnetic field oscillations produced by the Jovian magnetospheric current sheet oscillating over the moon twice every rotation period (Khurana et al. 1998; Saur et al. 2009). One key difference between Titan and Europa however, is that Titan has a thick atmosphere and a significant ionosphere which may shield the lower altitudes and interior from such external field perturbations; see Saur et al. (2009) for a review. A further complicating factor is the magnetic memory of Titan's atmosphere and the timescales for diffusion of the magnetic field in the atmosphere (Bertucci et al. 2008). Nevertheless this represents an important process and the detection and characterisation of periodic magnetic field perturbations is an important goal.

The periodic oscillation of Saturn's magnetic equator and magnetospheric plasma sheet (e.g. Khurana et al. 2009; Jackman et al. 2009; Arridge et al. 2011c) about Titan's location can also produce strong changes in the charged particle environment in which Titan is em-

bedded, and strong rotations in the convection electric field. The motion of the plasma sheet implies strong changes in the plasma density and hence ram and plasma pressure. Periodicities in the dynamic pressure of the incident flow could produce periodic ion loss from Titan's exosphere (Ma et al. 2006).

3 Structure and Physics of Saturn's Magnetosphere Near Titan

The structure of the Saturnian magnetosphere depends both on several independent spatial coordinates (radial distance, latitude, longitude, local time, and the orbital phase of the Saturnian moons, in particular that of Enceladus and Titan), as well as on the time variability of its neutral/dust/plasma sources, the solar wind, and the various transport and physical and chemical processes that take place in this complicated multiphase environment (e.g., André et al. 2008). In this section we introduce the structure and physics of Saturn's magnetosphere particularly focusing on the region near Titan's orbit at 20.3 R_S. For detailed recent reviews of the Saturnian magnetosphere and its configuration we refer the reader to André et al. (2008), Gombosi et al. (2009) and Arridge et al. (2011c). The basic configuration and physics of Saturn's magnetosphere is presented in Sect. 3.1. In Sect. 3.2 we discuss the dynamics of the magnetopause, in Sect. 3.3 we describe latitudinal structure in the magnetosphere and the implications for the centrifugal force with a complex multi-component plasma as found at Saturn. In Sect. 3.4 we use the material developed in the preceding sections to discuss rotational and longitudinal variability in the magnetosphere.

3.1 Basic Configuration of Saturn's Magnetosphere Near 20 R_S

At the core of Saturn's intrinsic magnetosphere is Saturn's internally generated magnetic field which is an almost axisymmetric field that is offset along the spin axis by $+0.0361$ R_S and has a dipole surface field strength of 21136 nT (Burton et al. 2011). The Saturnian magnetosphere is dominated by neutrals originating from the icy satellites and ring system and which outnumber the ions by a factor of 10–100 (Arridge et al. 2011c). These neutrals are ionised by photoionisation, electron impact ionisation and charge-exchange processes in the inner and middle magnetosphere producing a plasma sheet composed of protons, H_2^+, and a population of heavy ions termed the water group W^+ (O^+, OH^+, H_2O^+, H_3O^+). The equatorial magnetosphere is strongly coupled to the ionosphere and atmosphere via Birkeland currents which transport angular momentum from the atmosphere to the equatorial magnetosphere and forces the magnetospheric plasma to at least partially corotate with the ionosphere. Because Saturn is a rapidly rotating planet the resulting velocity of the plasma is quite rapid, varying from $\sim$30 km s^{-1} near Enceladus at 4 R_S, to 130 km s^{-1} near 15 R_S, and up to 170 km s^{-1} at 20 R_S where the velocity becomes approximately constant with radial distance (Thomsen et al. 2010, Arridge et al. 2011c). No information on the local-time variation of this flow profile is available. The centrifugal force associated with this rapid rotation is important in both the radial and vertical force balance in the plasma and confines the colder plasma into a fairly thin $\sim$1 R_S plasma sheet about the equatorial plane (see Sect. 3.3 for further discussion of this aspect).

An azimuthal current system flows within this plasma sheet and is due to a variety of mechanical stresses (centrifugal forces, pressure gradients and pressure anisotropy) existing within the plasma sheet. At distances greater than 16 R_S from Saturn the magnetic field due

to this current system stretches out Saturn's dipolar internal field into a thin current sheet-like configuration known as the magnetodisc. The currents that flow in the more dipolar region are often termed the ring current. When the magnetosphere is in a fairly expanded state, corresponding to low solar wind dynamic pressures, the magnetodisc only has a fairly modest local time asymmetry, being slightly less stretched on the dayside. However, under more intense compression a strong local time asymmetry develops with the magnetodisc essentially disappearing on the dayside, being replaced with a more dipolar configuration typical of the Voyager 1 observations (Arridge et al. 2008c). The solar wind also changes the geometry of the plasma and current sheet. During the Cassini nominal mission the solar wind flowed obliquely to the plasma sheet, which applies stress lifting the plasma and current sheet out of the equatorial plane (Arridge et al. 2008b). This effect wasn't observed on the Voyager 1 encounter with Titan, probably due to seasonal effects.

The upstream magnetic field also has a component parallel to Titan's orbital motion (B_φ in a Saturn-centred polar coordinate system) which is described as sweep-back or sweep-forward depending on the configuration. This azimuthal field component reverses sign about the magnetic equator such that for a swept-back configuration the radial and azimuthal field components are in anti-phase, below (above) the equator $B_r < 0$, $B_\varphi > 0$ ($B_r > 0$, $B_\varphi < 0$). At Saturn this is produced largely by magnetosphere-ionosphere (M-I) coupling currents which enforce partial corotation on the magnetospheric plasma and produce a swept-back configuration much like the Parker spiral in the solar wind. To first order this configuration should be symmetric in local-time. Sweep-back and sweep-forward is also produced by magnetopause currents but this effect is strongly local-time dependent, producing sweep-back on the dawn flank, sweep-forward on the dusk flank, and changing sign at the noon-midnight meridian. In the dawn sector these two effects combine to give strongly swept-back fields (strong B_φ) and in the dusk sector they oppose with the actual orientation of the field being determined by the relative contributions from internal and solar wind forcing. Observationally the field is found to be swept-back over much of the magnetosphere but with some swept-forward configurations found in the dusk sector (A. Masters and C.S. Arridge, private communication).

The net effect of this field-line stretching and warping is that Titan's upstream field is not in a quasi-dipolar north-south configuration but often points radially towards Saturn and in a prograde direction during the epoch of the Cassini nominal mission.

Saturn's magnetospheric regions are dynamically and chemically coupled, through an efficient recycling of mass: the plasma is transported outwards from its main plasma source regions located deep inside the magnetosphere to remote regions close to the magnetospheric boundaries and in the magnetotail where plasma is lost after mass-loaded flux tubes break open (Vasyliūnas 1983). During plasma transport this plasma is heated by non-adiabatic processes, such as Coulomb collisions (e.g., Rymer et al. 2007), to achieve temperatures of around 100 eV for H^+ and 1000 eV for W^+ (McAndrews et al. 2009). However, blobs of cold plasma are still observed in the trans-Titan environment and might be the result of rapid cross-L transport which does not afford the time for the ions to non-adiabatically heat due to (slow) Coulomb collisions (Arridge et al. 2009b) or due to local pickup (Rymer et al. 2009). These cold blobs were also studied by McAndrews et al. (2009) who interpreted these observations in the context of a Vasyliūnas-type cycle, with sufficiently mass-loaded flux tubes breaking open down the magnetotail, returning to the dayside and in the inner magnetosphere (André et al. 2007) with their heavy-ion depleted residual plasma, and interspersing with other mass-loaded flux tubes moving outwards. The immediate implication for the Titan interaction with its surrounding plasma is that the upstream flow direction is not strictly corotational and is affected by the passage of these interchanging fingers of plasma

(Winglee et al. 2009). This dependence on flow direction has possibly been illustrated in the case of the T9 flyby where the plasma flow and magnetic field directions in the distant plasma environment of the moon were distinctly different from the other flybys (Szego et al. 2007).

Hot ions are also found in the trans-Titan environment and represent the suprathermal tail of the lower energy populations described by McAndrews et al. (2009) measured in the CAPS (Cassini Plasma Spectrometer) ion energy range. The intensity and latitudinal distribution of these energetic ions was found to be asymmetric between the dayside and nightside, with more intense and latitudinally extended populations on the dayside (Krimigis et al. 2007). Such a thickness asymmetry has also been reported just inside of Titan's orbit by Morooka et al. (2009). Electrons have a typical temperature (mean kinetic energy) of 200 eV but sometimes have a bi-modal distribution of cold ∼10 eV blobs and warm ∼200 eV plasma sheet electrons, or warm and hot ∼1000 eV electrons. The hot electrons are probably the result of dynamics in the outer magnetosphere, possibly related to reconnection (Arridge et al. 2009b). Apart from the bi-modal nature of the measured electron distributions, the energy distributions of each population are generally found to be non-thermal in nature with significant power-law tails which can be well modelled by Kappa distributions (Arridge et al. 2009b; Rymer et al. 2009).

3.2 Location of the Magnetopause

Cassini measurements have shown that Saturn's magnetopause responds unusually strongly to changes in solar wind dynamic pressure (Arridge et al. 2006; Kanani et al. 2010) Achilleos et al. (2008) also statistically investigated the subsolar standoff distance of the magnetopause and found a bimodal probability distribution for its standoff distance with means at ∼22 and ∼27 R_S more likely to represent compressed and extended configurations of the magnetosphere, with both external and internal influences as discussed later. The immediate implication of this observation for Titan's interaction with its surrounding environment is that the orbit of Titan is located most of the time within Saturn's magnetosphere. It is nevertheless possible that near noon Titan can interact with the shocked solar wind during periods of high solar wind dynamic pressure, as observed during the T32 Cassini encounter (Bertucci et al. 2008).

In a different separate study, Lundberg et al. (2005) propagated solar wind data from ∼1 AU out to Saturn and used the resulting solar wind parameters to investigate the resulting magnetopause and bow shock standoff distributions. When Titan was located at the subsolar point they calculated that Titan should be located in the magnetosphere 56.7% of the time, 42.1% of the time in the magnetosheath, and 1.3% in the solar wind. In separate studies Bertucci et al. (2009) found a probability of 5.5% for Titan being outside the magnetosphere at 1200 Saturn Local Time (SLT) and Garnier et al. (2010) found a probability of 23% for Titan being located in the magnetosheath between 1000 and 1400 SLT.

However, these statistics do not account for the possible perturbations introduced by the presence of Titan inside the magnetosphere. Wei et al. (2009) used Cassini observations to test this point and found that near noon SLT Titan is more frequently located inside the magnetosphere than the statistics of Lundberg et al. (2005) suggest. Near noon SLT (0900–1500), Cassini was located in the magnetosheath on 10.37% of cases when passing through Titan's orbital distance, however Titan has only been observed in the magnetosheath on 3.37% of cases. This is a statistically significant difference. Wei et al. (2009) suggested that Titan locally reduces the compressibility of the magnetosphere, possibly by anchoring the magnetic field in the magnetosphere, or by locally mass-loading the magnetosphere,

or from fast neutrals transferring momentum from the magnetospheric plasma. Wahlund et al. (2005) and Garnier et al. (2009) have also suggested that the exo-ionospheric thermal pressure may easily exceed 0.02 nPa ($\sim$100 eV cm^{-3}) and exert additional plasma pressure when the moon is located near the magnetopause thus affecting the equilibrium location of the magnetopause (see Fig. 6 in Achilleos et al. 2008) and push out the boundary by 1 or 2 R_S.

3.3 Latitudinal Structure and the Effects of Centrifugal Forces

The centrifugal force along magnetic field-lines acts to confine heavy ions towards the equatorial plane. For a single species the (exponential) scale height is proportional to $(k_B\ \mathrm{T/m})^{1/2}$ and so colder heavier ions have smaller scale heights than hotter lighter ions (Hill and Michel 1976). Because of their small mass, for the same temperature electrons essentially fill the magnetic field lines and must have a temperature of the order m_e/m_i smaller than that of the ions to have the same scale height as an ion species. However, the introduction of an electron population produces a charge imbalance problem along the field line since the heavy ion population will be confined about the equator and the electrons will fill the field lines. To restore quasi-neutrality field-aligned polarisation (ambipolar) electric fields are set up to confine the electrons near the equator and to balance the heavy ion charge density that is centrifugally confined to the equator (e.g., Persson 1966; Maurice et al. 1997). In a complex multi-species plasma, for example with one electron population and two ion populations (H^+ and O^+ for example), the problem is significantly more complex. The field-aligned force balance between pressure gradients and field-aligned electric fields, and the condition of quasi-neutrality must be solved for simultaneously (e.g., Maurice et al. 1997). The consequences of such a force balance are that the heavy ion population is concentrated about the equator but the light ion population "floats" off the equator, with the electrons providing a neutralising component with a scale height somewhat larger than that of the heavy ions. These effects introduce structure into the dependence of the ion composition as a function of latitude.

This latitudinal structure in ion composition combined with warping and periodic motion (see Sect. 3.4 and Arridge et al. 2008a) provide a mechanism for considerable variability in the ion composition of the plasma in which Titan is immersed. The incident ion composition is dominated by protons when Titan is below or above the plasmasheet and by heavy water-group ions when Titan is close to the centre of the plasmasheet, owing to the mass-dependent influence of the centrifugal force on the field-aligned distribution of ions in a multispecies plasma (see also Szego et al. 2011).

The thickness of the magnetodisc and its plasma sheet has been investigated by a number of authors (Kellett et al. 2009; Sergis et al. 2011) and has shown that the plasma sheet thickness differs between different populations of particles in accordance with the above discussion. Sergis et al. (2011) have studied the thickness of the energetic ion and thermal electron plasma sheets and the current sheet near Titan's orbit and found a plasma sheet where the energetic ion plasma sheet was around a factor of two thicker than the electron plasma sheet and both were much thicker than the current sheet. These thicknesses exhibited considerable variability.

To investigate the thickness of the thermal ion plasma sheet the ion (H^+ and W^+) density was examined (Szego et al. 2011) near Titan's orbit using the B_r component of the magnetic field to determine the proximity of the spacecraft to the current sheet centre where $B_r = 0$. This was carried out on a total of 30 encounters with Titan on near-equatorial and highly inclined passes through the magnetodisc. These formed three groups in Saturn local time: the nightside (between 0200–0300 hours SLT, T9, T11, T16–24), the dayside (1000–1200

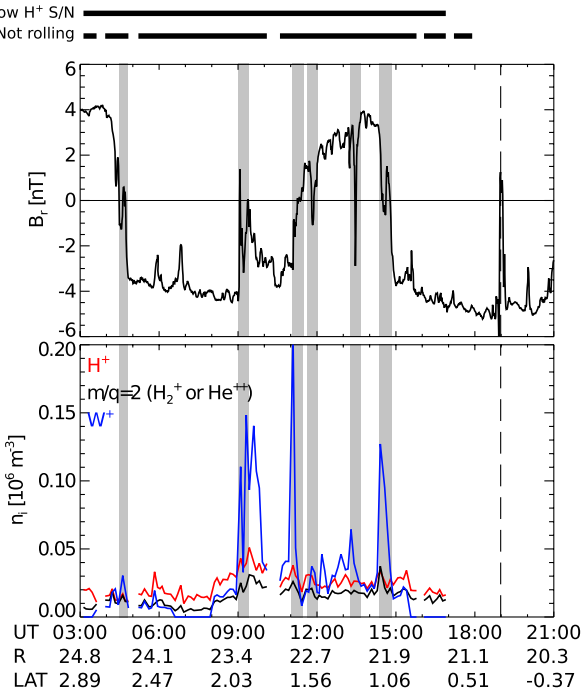

Fig. 4 Magnetic field and ion moments for the T18 flyby on 23 September 2006. The *top panel* shows the radial component (in KRTP coordinates) of the magnetic field, and the *bottom panel* shows the ion densities in units of m^{-3}. The *red line* indicates proton number densities, the *black line* the number density of the $m/q = 2$ species, and the *blue line* the W^+ number densities. The closest approach to Titan is indicated by the *dashed vertical line*. Approaches to the centre of the current sheet are denoted by *grey bars* and it can be seen that they line up with increases in the W^+ density. The *solid bars above the figure* indicate moment quality flags where a gap indicates a reduction in quality. A *gap in the top bar* indicates poor H^+ signal-to-noise and in the *bottom bar a gap* indicates when the spacecraft is rolling, potentially aliasing the distributions

hours T35–T44 and 1300–1400 hours T25–T33), and the dusk side (T34). The data from these flybys are highly variable but these passes exhibit the basic properties of the plasma sheet. The dayside and nightside passes are visibly different with more dense plasma present on the dayside passes.

Figure 4 presents data from the T18 encounter on the nightside showing ion densities from Thomsen et al. (2010) and magnetometer data following a similar presentation in Szego et al. (2011). The spacecraft trajectory was inclined to Saturn's equatorial plane by about 30°. The plasma density maximises near $B_r = 0$ (see also Arridge et al. 2009b). The half-thickness of the heavy ion plasma sheet was estimated as 0.25–0.3 R_S with some additional evidence of a very narrow plasma sheet at the crossing near 1400 UT. The crossings on T34 on the dusk flank were a factor of two larger than the nightside T18 crossings. The sheet on the dayside was found to be somewhat thinner and a half-thickness of 0.2 R_S was derived.

3.4 Rotational and Longitudinal Variability

Like Jupiter, Saturn is a rapidly rotating planet and the planetary rotation influences the magnetospheric structure and drives dynamics, to some extent, in the outer magnetosphere where Titan orbits. Despite the fact that Saturn's intrinsic magnetic field is symmetric about the planet's spin axis, the magnetic field strength and direction (e.g., André et al. 2008) has been observed in the whole magnetosphere to be modulated "internally" at periods close to the planetary radio rotation period. Radio emissions, known as Saturn Kilometric Radiation (SKR), have also been shown to pulse at the same period. Moreover, this period is known to be slowly varying in time. The time-dependent period of these radio emissions have been used to construct a longitude system known as the Saturn Longitude System (SLS, and its subsequent revisions SLS2 and SLS3) which has been shown to organise fields and particles data inside Saturn's magnetosphere (e.g., Kurth et al. 2008, and references therein).

Clarke et al. (2006, 2010a) found that the Saturnian magnetopause also undergoes spin-periodic oscillations in response to oscillations in the magnetospheric total pressure. Estimates of the amplitude of the magnetopause oscillations yield typical values of 1–2 R_S, with extreme amplitudes occasionally reaching 4–5 R_S (Clarke et al. 2010a), hence providing one of the two internal influences on the probability distribution discussed by Achilleos et al. (2008). Similar oscillations were also found in the Saturnian bow shock (Clarke et al. 2010b). Outward excursions of the Saturnian magnetopause were found to map back along spiral phase fronts into both the rotating plasma bulge in the outer magnetosphere reported by Burch et al. (2009) and Morooka et al. (2009) and the longitudinally-restricted plasma density maximum (around 330° in SLS3) in the inner Enceladus torus observed by Gurnett et al. (2007). The first immediate implication for the Titan interaction with its surrounding plasma is that its orbit is located closer to the magnetopause and, hence, may be preferentially embedded within the Saturnian magnetosheath in a particular longitudinal magnetospheric sector where the total magnetospheric pressure is reduced.

Observations show that the outer magnetospheric plasma sheet flaps (e.g., Arridge et al. 2008a, 2009b, 2011b; Khurana et al. 2009) and a variety of mechanisms have been proposed to explain this flapping, from the interaction between a rotationally asymmetric lobe field and the solar wind (Khurana et al. 2009) to the generation of a tilted dipole field signature by a shell of field-aligned currents (Southwood and Kivelson 2007). Arridge et al. (2008a) further analysed the longitudinal organisation of electron densities and temperatures at 20 ± 2 R_S in Saturn's outer magnetosphere. They found evidence for a density minimum in a restricted longitudinal sector (around 170° in SLS3 longitude) which corresponds to the sector with similar properties identified by Gurnett et al. (2007) in the Enceladus torus. Arridge et al. (2008a) also examined the properties of the magnetic field and found that the B_r and B_φ components reached local maxima near the regions with low electron flux and reached local minima (varying in an anti-phase manner), often reaching zero, when the electron flux maximised. They interpreted this apparent periodicity in density with a vertical flapping of the plasma sheet. Németh et al. (2011) also found a periodicity in the heavy ion count rate but where they required a small shift in period from that of SKR during the period of validity of the SLS3 system.

Figure 5 is taken from Arridge et al. (2008a) and illustrates an example of this behaviour. In particular panel (e) shows the distance of the Cassini from the centre of the magnetodisc current sheet (normalised to the current sheet thickness) and shows that the spacecraft reaches nearly a full scale height away from the centre (at least several R_S according to the modelling results of Kellett et al. 2009). Arridge et al. (2011b) have investigated these flapping motions in more detail and found definite phase relationships between the phase of plasma sheet flapping and SKR. Morooka et al. (2009) have also investigated these motions and found that periodic variations in plasma sheet thickness are required to interpret the high-latitude flapping observations away from the transverse motions of the plasma sheet studied by Arridge et al. (2008a, 2011b).

The implication of the observed longitudinal plasma and magnetic asymmetry in the outer magnetosphere of Saturn for Titan's interaction with the surrounding plasma is that significant periodic pressure variations, of up to three orders of magnitude over half a Saturn rotation period, occur upstream of Titan. This makes the magnetospheric energy input at Titan highly variable, both in longitude as discussed here and in local time as discussed previously.

An additional implication relates to the orientation of the convection electric field near Titan. The prevailing pre-Cassini view, based on the observed near-azimuthal plasma flow and dipolar magnetic field, was that the convection electric field **E** in Titan's rest frame

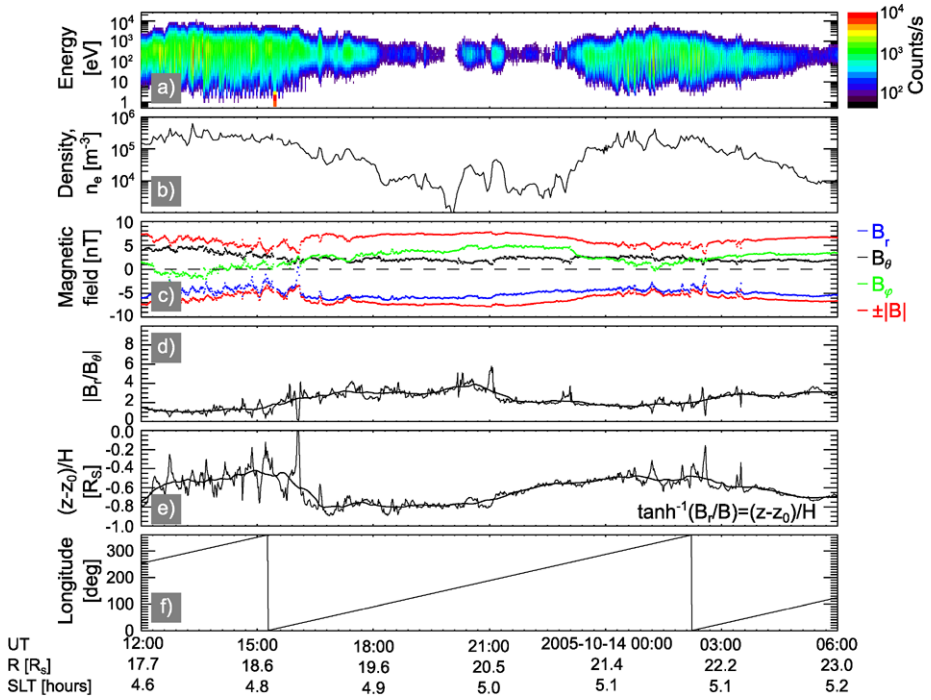

Fig. 5 Thermal electrons and magnetic fields from a crossing of Titan's semi-major axis from 13–14 October 2005. Panel (**a**) shows a time-energy electron spectrogram, (**b**) the electron number density, (**c**) the magnetic field in KRTP coordinates, (**d**) the ratio B_r/B_θ which increases when the spacecraft moves away from the centre of the current sheet, (**e**) the distance from the centre of the current sheet, normalised by the current sheet thickness, obtained from B_r using a Harris profile: $(z-z_0)/H = \tanh^{-1}(B_r/B_{\max})$, and (**f**) is the sub-spacecraft SLS3 longitude. The *smooth curves* in panels (**d**) and (**e**) show 60-minute sliding averages of each parameter. From Arridge et al. (2008a) and used by permission of the American Geophysical Union

pointed radially away from Saturn. We now know that the magnetic field can have a dominantly radial component which produces important vertical components to the convection electric field (see also Sect. 5.3 for statistics of the convection electric field). Coupled with periodic vertical flapping this can clearly produce large amplitude periodic modulations in the convection electric field. The implications of this periodic modulation were investigated by Arridge et al. (2011a) who found that in the environment of a highly stretched magnetodisc undergoing significant vertical flapping motions one can expect rapid changes in the convection electric field strength and direction at Titan on timescales of around one hour. They also found that significant changes in the orientation of **E** could be obtained whilst Titan was immersed in the current sheet. This has important consequences for the classification of Titan's upstream environment where although the upstream environment may be jointly classified as current sheet (e.g., Simon et al. 2010a) and plasma sheet (e.g., Rymer et al. 2009), which might lead to assumptions regarding the orientation of the convection electric field (i.e., assumed to be radial), the actual electric field may have a significant north-south component and may be highly variable. It is important to note that this does not devalue these classification criteria but does draw attention to the fact that caution must be used in their application.

Table 3 Magnetic moments and upstream flow parameters for Mars, Venus and Titan

	Mars[a,b]	Venus[c,d]	Titan[e]		
			M' sphere[f]	M' sheath[g]	Solar wind[g]
$\|M\|$ (T m^3)	$<2 \times 10^{11}$	$<3 \times 10^{11}$	$<2 \times 10^{11}$		
n (10^6 m^{-3})		∼20	0.029	0.5–1.0	0.80 (0.54, 1.52)
$\|\mathbf{u}\|$ (km s^{-1})	410	∼400	90	100	520 (540, 630)
$\|\mathbf{B}\|$ (nT)	2.8	11–12	4.1	<10	1.4 (1.2, 3.1)
M_A	7–8	7	0.6	0.3–1	24 (16, 13)
M_S	6–7	6	0.5	0.4–0.7	14 (14, 12)
β	2–3	1–2	1.7	0.5–4	6.9 (1.6, 1.6)
T_e (eV)	8	17	130	30–40	1–2
T_i (eV)	11	9	2000	200	1–2

[a]Acuña et al. (1998); [b]Slavin and Holzer (1981); [c]Luhmann et al. (1993); [d]Pilipp et al. (1990); [e]Neubauer et al. (1984); [f]This work, Sect. 5; [g]This work, Sect. 4.2, where the values in brackets indicate the minimum and maximum values

4 Titan in the Magnetosheath or Solar Wind: Properties of Saturn's Upstream Region and Comparisons with Venus and Mars

The orbital distance of Titan is just smaller than the average distance of the sub-solar point of Saturn's magnetopause. As all objects in the solar system, Saturn interacts with the solar wind which partially drives magnetospheric dynamics (compressions/expansions) and possibly triggers major magnetospheric disturbances when solar wind perturbations hit the magnetosphere. Saturn orbits the Sun at a heliocentric distance of ∼9.5 AU and consequently the number density, Mach number, ram pressure and field strength have varied strongly from their values in the inner solar system near Venus and Mars. In this section we examine the solar wind medium upstream of Saturn's magnetosphere leading to an understanding of Titan's upstream parameters when Titan is located in the solar wind or magnetosheath. Table 3 illustrates these parameters and compares them with the upstream environments of Venus and Mars. One can see that the solar wind upstream environment of Titan is similar to that of Mars.

In this paper we do not address more exotic and unique influences, such as have been reported during the Voyager 2 encounter with Saturn, but we mention it here for completeness. During most of the Voyager 2 flyby it was possible that Saturn was immersed in Jupiter's magnetotail or encountered Jovian tail filaments, Saturn being almost aligned with the Jupiter-Sun line at that time. Estimates of the length of the Jovian magnetotail range from at least 4.4 AU (Lepping et al. 1983) up to 6.5 AU, which allow Saturn to pass through Jupiter's tail. The inferred (from in situ measurements) effects in Saturn's outer magnetosphere include greatly enhanced energetic particle fluxes, an overall inflation and reconfiguration of the magnetospheric field, and a sharp decrease of SKR emissions that lasted for several days (e.g., Behannon et al. 1983). Saturn is therefore possibly the only planet in the solar system whose magnetospheric dynamics is controlled over certain time intervals by the extended magnetotail of another planet (Desch 1983).

4.1 Large Scale Structure of the Heliosphere Near Saturn

An understanding of the large-scale structure of the interplanetary magnetic field (IMF) upstream of the planet is crucial for understanding magnetospheric dynamics. The IMF struc-

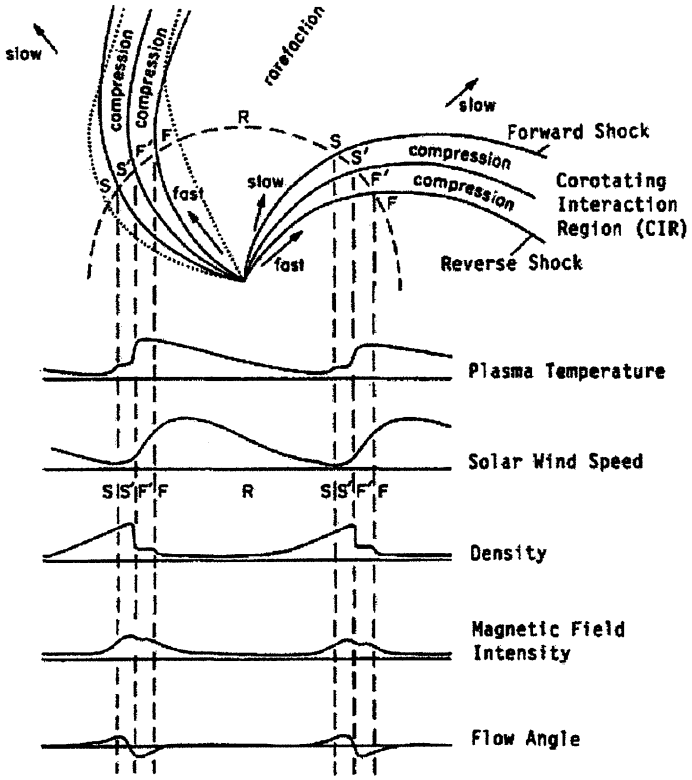

Fig. 6 Schematic diagram of two CIRs corotating with the Sun, along with the associated solar wind and magnetic field signatures at 1 AU. From Kunow (2001)

ture is highly dependent on the phase of the solar cycle. Pioneer 11, Voyager 1 and Voyager 2 all visited Saturn at or near to solar maximum, thus sampling a particular character of IMF near Saturn. By contrast, Cassini's approach to Saturn took place during the declining phase of the solar cycle. During such a period the Sun's magnetic field takes the form of a tilted dipole (e.g. Gosling and Pizzo 1999). In this configuration, the closed field arcades from which the slow ($\sim$400 km s^{-1}) solar wind emanates straddle the magnetic equator, while the fast ($\sim$750 km s^{-1}) solar wind emerges from open coronal holes situated at higher magnetic latitudes. The heliospheric current sheet (HCS) marks the boundary between field lines that point toward or away from the Sun. Streams of fast and slow solar wind constantly flow away from the Sun, with the solar magnetic field frozen into the plasma. As the Sun rotates, the fast and slow streams come into contact with each other. When fast wind follows slow, a compression region is formed as the flow speed rises, while when slow wind follows fast, a rarefaction region is formed. The resulting pattern of compressions and rarefactions is termed a "corotating interaction region" (CIR), and two such regions are illustrated schematically in Fig. 6. Compressional waves driven by fast wind catching up with slow wind can steepen into forward- and reverse-propagating shock waves (e.g. Hundhausen and Gosling 1976).

Jackman et al. (2004) studied the effect of CIRs on the structure of the IMF during the period in 2003–2004 when Cassini was upstream of Saturn, taking continuous magnetic field measurements. As expected for the declining phase of the solar cycle, they found that

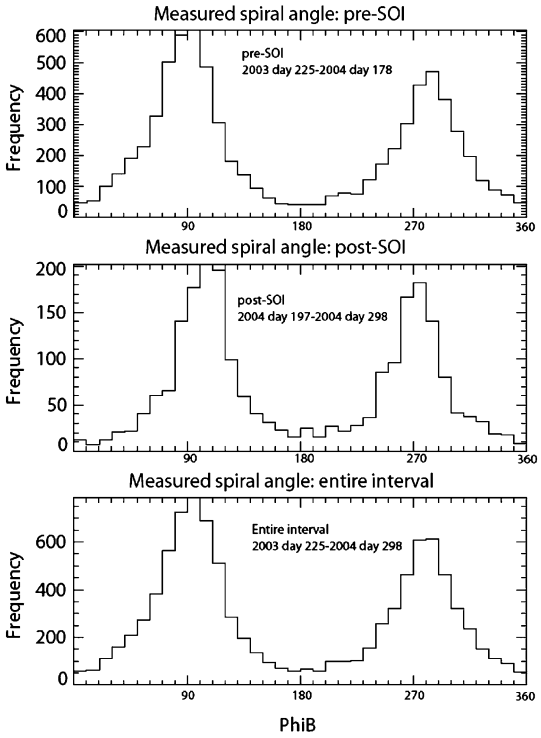

Fig. 7 Plot showing three histograms of measured spiral angle. The *top* represents the period pre-SOI from day 225 of 2003 to day 178 of 2004. The *middle* shows the post-SOI period from day 197 to day 298 of 2004. The *bottom* is the sum of the top and the middle and shows the data from the entire interval

the IMF consisted of two sectors per solar rotation, with crossings of the HCS embedded within two compression regions, and separated by plasma and field rarefactions. However, we note that on occasion, the pattern of CIR compressions and rarefactions can be disturbed by strong solar activity.

While the solar wind outflow is purely radial, the IMF field lines are frozen to this flow and the foot of each field line is rooted to the rotating Sun. Thus the streamline of interconnecting particles emerging from a fixed source takes the form of an Archimedean spiral, which is located along the locus of all plasma elements emitted from a given source region on the Sun's surface (Parker 1958). The theoretical Parker spiral angle is dependent on the local solar wind velocity, the heliocentric distance and the heliographic longitude. The real azimuthal angle can be estimated from *in situ* spacecraft measurements, and compared with the theoretical value to determine whether the interplanetary field obeys the predictions of the Parker model. Jackman et al. (2008) studied the IMF measurements for several months prior to Cassini Saturn Orbit Insertion (SOI) and several months afterwards where the spacecraft trajectory took it out into the solar wind again. Figure 7 shows the summary of their results. The overall mean azimuthal angle was found to be $93.2° \pm 0.3°$, corresponding to a mean spiral angle of $86.8° \pm 0.3°$. This compares to a predicted spiral angle over that radial range of $\sim 83°$.

From this large-scale structure we can see that for periods when Titan is located in the magnetosheath or solar wind the Saturnian magnetosphere is likely to be immersed in a CIR. When Titan is embedded in the solar wind/magnetosheath the field will be oriented close to Titan's equator thus forming a north-south induced tail current sheet (see Fig. 3). However, it is also known that the field in CIRs is highly variable in direction (Jackman et al. 2004).

4.2 Titan in the Solar Wind and Magnetosheath

To estimate the density and temperature of the solar wind when Titan is upstream of the bow shock, one can use the bow shock model of Masters et al. (2008). This empirical model gives the subsolar standoff distance of Saturn's bow shock: $R_{SN} = (17 \pm 1) P_{SW}^{-1/(5.7\pm0.5)}$. For Titan to be located in the solar wind the bow shock stand-off distance must be inside Titan's orbit $R_{SN} < 19.7\ R_S$ (the distance of Titan from Saturn at noon SLT). From this condition one can obtain a constraint on the ram pressure and the density of the solar wind such that $P_{SW} > 0.29$ nPa. Jackman and Arridge (2011) have investigated the solar wind conditions upstream of Saturn and using their results with this dynamic pressure range we can place constraints on the other solar wind parameters. From this constraint on the solar wind dynamic pressure the solar wind proton and He^{++} density must be larger than 3.4 and 0.13×10^5 m^{-3} respectively with a mass density larger than 3.9×10^5 amu m^{-3}. Because derived quantities such as plasma beta and Mach number are dependent on other quantities it is misleading to simply quote median values for each quantity. For example, the median values of pressure and field strength may not yield a quoted median plasma beta. To account for this we obtained the full set of solar wind plasma and field parameters at the median dynamic pressure (0.36 nPa) for solar wind dynamic pressures larger than the limit given above, and also at the minimum (0.29 nPa) and maximum (1.1 nPa) recorded dynamic pressures. These full results are given in Table 3 whereas here we focus on the median results.

The proton and He^{++} number densities were found to be 7.7 and 0.31×10^5 m^{-3} producing a mass density of 8.9×10^5 amu m^{-3}. The field strength and plasma pressure were found to be 1.4 nT and 0.0013 nPa respectively giving a plasma beta of 6.9. Using these parameters with the flow speed of 590 km s^{-1} gives Alfvén and sonic Mach numbers of 24 and 14 respectively. Hence when Titan is in the solar wind the flow is highly supersonic and super-Alfvénic with a high plasma beta which contrasts strongly with the environments of Mars and Venus. Complementing these values typical solar wind electron and ion temperatures in the solar wind near Saturn are 1–2 eV (Achilleos et al. 2006; Slavin et al. 1985).

Bertucci et al. (2008) presented data from the T32 flyby when Titan was located in the magnetosheath. From the results of Bertucci et al. (2008) we can see that the field strength was <10 nT, the plasma density was between 0.5 and 1×10^6 m^{-3} the electron temperature was 30–40 eV. Measurements of the flow speed and ion temperature were not available during this flyby but we estimate the ion temperature to be 200 eV and the flow velocity to be ∼100 km s^{-1} from the results of Richardson (2002). From these values we estimate the total plasma pressure as 0.02–0.04 nPa, the plasma beta as ∼0.5–4, the Alfvén and sonic Mach numbers as 0.3–1 and 0.4–0.7 respectively.

5 Statistical Properties of Titan's Magnetospheric Background

A quantitative understanding of Titan's magnetospheric background is required as an input for modelling studies and to evaluate magnetospheric driving of Titan. Statistical studies are valuable in understanding the typical upstream parameters for such studies but also in characterising the variability in the upstream environment to address the issues raised in Sects. 2 and 3.4. The effects of such variability can be revealed in the range or standard deviation of important quantities. There are three principal physical motivations that drive a quantitative understanding of the upstream environment, as discussed in Sect. 2. Firstly the central element involved in the formation of Titan's induced magnetosphere is Titan's

ionosphere, which is partly generated by impact ionisation and charge exchange with the incident magnetospheric plasma flow. Secondly, the upstream field orientation and flow direction are essential in understanding both the orientation of the induced magnetosphere (and construction of a draping coordinate system with which to interpret flyby data) and the direction of the convection electric field which is essential in understanding the trajectories of pickup ions and the acceleration of ionospheric photoelectrons, thirdly exospheric ion escape is very sensitive to the upstream dynamic pressure and so establishing typical values of the dynamic pressure and its variability are crucial in understanding the evolution of Titan's atmosphere and exosphere. Perhaps one of the most important reasons for gaining a statistical understanding of Titan's magnetospheric background is that it provides a quantitative context for the various qualitative classification schemes that are discussed in Sect. 6. In this section we describe statistical studies of magnetic fields (Sect. 5.1), energetic particles and the suprathermal particle pressure (Sect. 5.2), and combined magnetic field, plasma and energetic particles studies (Sect. 5.3).

5.1 Magnetic Fields at Titan's Orbit

Bertucci et al. (2009) used magnetometer data to study the large-scale structure of the magnetic field near Titan. Data from the first 52 orbits of Cassini (day 180 of 2004 to 325 of 2007) within the range $19 < \rho < 21\ R_S$ and $|z| < 0.5\ R_S$ were used. Data from within the magnetosheath and around Titan encounters was removed before the analysis was carried out. The data was analysed in cylindrical polar coordinates in the Kronocentric Solar Magnetic (KSMAG) frame.

In addition to studying the field components, they also calculated sweepback angles $\text{atan}(B_\varphi/B_\rho)$ and stretch angles $\text{atan}(-B_\rho/B_z)$. The sweepback angle describes the degree to which the field is swept out of the meridional plane, such that negative sweepback angles describe a swept-back field (opposite the direction of planetary rotation). The stretch angle measures the deviation of the meridional field component from a north-south orientation. Large values of this angle describe field lines that are stretched, with the magnetic field pointing either toward (negative) or away (positive) from Saturn, and indicate if the spacecraft is below or above the magnetic equator. See also the discussion in Sect. 3.1.

5.1.1 Magnetodisc and Solar Wind Influences

Figure 8 presents the radial component of the magnetic field with distance from the kronographic equator. Near-zero values of the field indicate crossings of the magnetodisc and the data clearly shows that the radial component is significantly negative at $z = 0$, showing that Titan is usually below (south of) Saturn's magnetodisc and that the magnetodisc is typically located up to 2 R_S above the equator (e.g., Arridge et al. 2008b). This behaviour holds for all observed Saturn local times. Variability in B_ρ can be interpreted in terms of global magnetospheric periodicities and in short-time variations introduced by the solar wind or impulsive processes inside the magnetosphere. Figure 9 shows the stretch and sweepback angles as a function of Saturn local time. The larger stretch angles in the dusk, midnight and dawn sectors indicate more highly stretched fields compared to the noon sector. The large variability in the noon sector reveals the higher sensitivity of the disc's structure to changes in solar wind pressure, as suggested by Arridge et al. (2008c). The variability in the dusk sector is real and is not strongly affected by the trajectory of the spacecraft in that sector. Table 4 summarises the magnetic field observations in different local time sectors.

In contrast to the stretch angle, the sweepback angle exhibits less variation in local time and is consistently negative, with a minimum of $-7°$ at dusk and a maximum of $-24°$

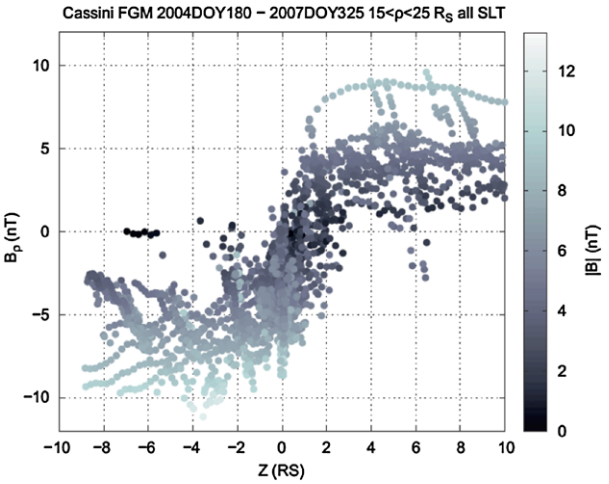

Fig. 8 Radial (cylindrical) component of the magnetic field versus the vertical distance from the kronographic equator, between 15 and 25 R_S in Saturn's magnetosphere. The colour scale indicates the magnetic field strength. From Bertucci et al. (2009)

Table 4 Mean and standard deviation of the field strength, and stretch and sweepback angles in various local time sectors of the magnetosphere. From Bertucci et al. (2009)

	Dawn (3–9 SLT)	Noon (9–15 SLT)	Dusk (15–21 SLT)	Midnight (21–3 SLT)
Field strength (nT)	5.3 ± 1.7	4.4 ± 1.6	3.7 ± 1.4	4.8 ± 1.8
Stretch angle (°)	-58 ± 20	-32 ± 19	-18 ± 32	-56 ± 33
Sweepback angle (°)	-24 ± 16	-10 ± 25	-7 ± 41	-18 ± 23

at dawn. An inspection of Fig. 9 also shows that the sweepback angle does not change sign about the noon-midnight meridian implying that the origin of the azimuthal field is related to the production and transport of plasma in the magnetosphere, and not due to the interaction between the magnetosphere and the solar wind. Bertucci et al. (2009) also assert that these observations are incompatible with the possibility that in the midnight sector Titan may interact with the magnetotail of Saturn, under which circumstances one would expect the stretch angle to be near 90° and the sweepback angle near 0°. Under such conditions the magnetic field would be highly stretched and no longer strongly influenced by the rotation of the planet so that the azimuthal field is not related to magnetosphere–ionosphere coupling processes.

5.1.2 Periodic Influences

To examine the magnetic field data for evidence of magnetospheric periodicities, and their effects on variability in the data, Bertucci et al. (2009) examined data within a 0400–0600 SLT and between $19 < \rho < 21$ R_S and $|z| < 0.5$ R_S which was selected because this region is the least affected by the influence of the solar wind. Data at a cadence of 1 minute was selected for the analysis to reduce the scatter in the data. They found clear structure in the stretch angle where larger stretch angles were found near SLS3 longitude of 140° and smaller stretch angles were found near 320° (see also Fig. 5). There was some evidence for larger field strengths at larger stretch angles. Very little evidence for an SLS3 dependence on the sweepback angle was found in the data with no dependence on the field strength. This invariance of the sweepback angle with SLS3 is to be expected if the current sheet is indeed

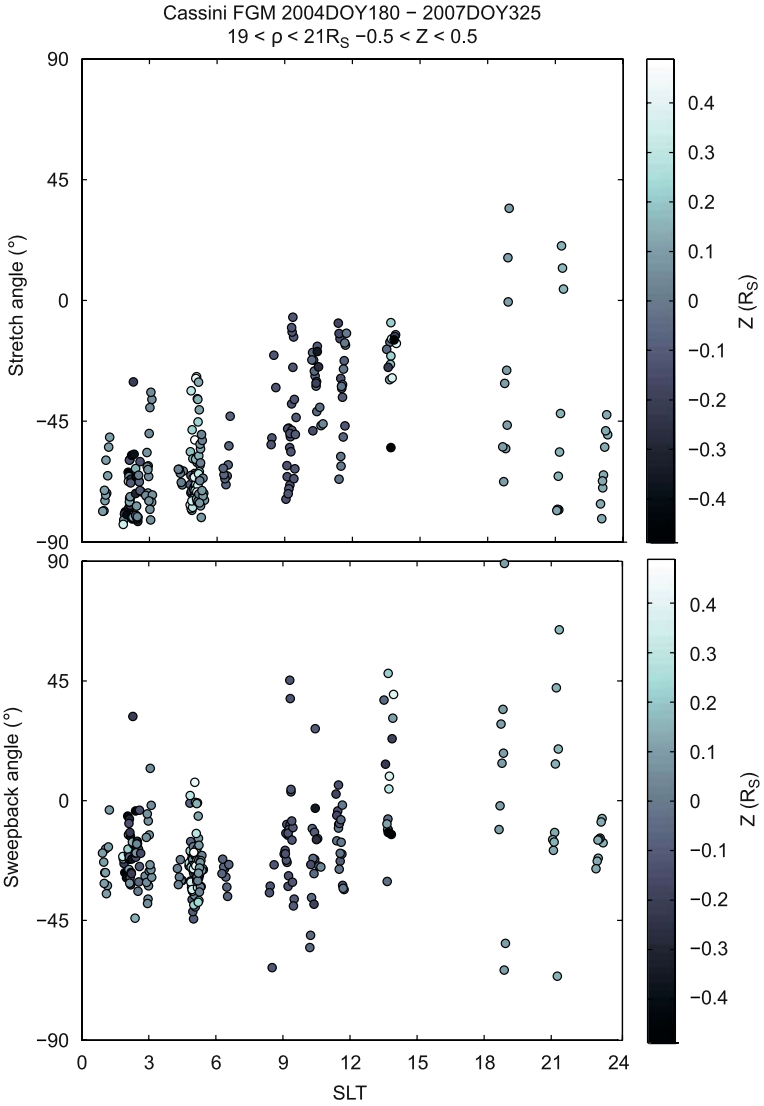

Fig. 9 Stretch (*top*) and sweepback angles (*bottom*) as a function of Saturn Local time and where the *colour* indicates the kronographic z distance. From Bertucci et al. (2009)

executing vertical periodic motion as the B_r and B_φ components of the field vary in anti-phase about a current sheet with both radial and azimuthal field components (corresponding to a stretched and swept-back or swept-forward field configuration). As demonstrated in Fig. 5 taken from Arridge et al. (2008c) the B_ρ and B_φ components both approach zero from $-B_{\rho(\text{lobe})}$ and $+B_{\varphi(\text{lobe})}$ respectively. Under this relationship we can say that $B_\rho \propto B_\varphi$ and hence $\text{atan}(B_\rho/B_\varphi) \sim \text{atan}(\text{const}) \sim \text{const}$ (assuming that $B_r \approx B_\rho$). At Titan's orbit these SLS3-dependent SKR-related periodicities manifest themselves as compressive fluctuations in the magnetic field with a change of $|\Delta B|/B \sim 0.5$. These modulations can account for the difference in magnetic field strength measured inbound and outbound from Titan as reported

by a number of authors (e.g., Backes et al. 2005; Neubauer et al. 2006). These SKR-related modulations will also be discussed in the Sect. 5.2.

5.2 Energetic Particles and Suprathermal Particle Pressure at Titan's Orbit

In this section we utilise energetic particle and magnetic field measurements to determine the long-term characteristics of the energetic particle environment along the orbit of Titan, as revealed through the equatorial plane orbits of Cassini and as captured by energetic neutral atom (ENA) imaging during its high latitude passes. The energetic proton environment at Titan's orbit will be described based on analyses of Cassini MIMI (Magnetospheric Imaging Instrument) data by Garnier (2007), Garnier et al. (2010) and Dialynas et al. (2009). The suprathermal particle pressure analysis is based on energetic particle pressures calculated from the MIMI/CHEMS (Charge Energy Mass Spectrometer) instrument by Sergis et al. (2009).

5.2.1 Energetic Protons

The energetic component of the plasma was first described by Krimigis et al. (1981, 1983) and MacLennan and Lanzerotti (1983) from Voyager LECP (Low Energy Charged Particle) data. The distributions of the proton population were best fitted by kappa distributions Vasyliūnas (1968), which are similar to Maxwellians but have extended power law tails. The κ parameter of these distributions was found to range between 4–6 in the outer magnetosphere and was highly variable. The anisotropies were also given, with proton pitch angle distributions peaking around 90°.

Garnier et al. (2007, 2010) studied the background energetic proton environment of Titan, providing MIMI-LEMMS (Low Energy Magnetospheric Measurements System) intensities for 27–255 keV protons during all the moon's orbit crossings by Cassini until 1 January 2008. This corresponds to the LEMMS A0–A3 channels for 72 events in the equatorial plane (absolute latitudes above 10° were removed), among them were 39 close Titan flybys. A summary of the main statistical parameters is given in Table 5 with the overall mean and maximum flux values, as well as their spread between the orbit crossings. Quantitatively, the mean flux values are very similar to the Voyager 1 Saturnian data for overlapping energies but larger than Voyager 2 results (Krimigis et al. 1981, 1983). Garnier et al. (2010) have shown that the energetic proton pitch angle distributions are quasi-isotropic at Titan's orbit and on the timescale of Titan flybys. This justifies the use of the LEMMS proton fluxes after the platform rotation stopped, since they can be roughly considered as omnidirectional fluxes for macro-scale processes. However, small-scale anisotropies are present which may be strongly affected by the presence of Titan, which induces a draping of the kronian magnetic field and may lead to an evolution of the pitch angle distribution of energetic protons which cannot strictly follow the rotation of the field (Garnier 2007).

The flybys were categorised between magnetosphere/magnetosheath and LEMMS rotating/non-rotating events. The different flux values between the latter categories are essentially due to the low number of events where LEMMS was rotating (four) rather than being the consequence of a reduced pitch angle coverage after the LEMMS platform stopped rotating, since the pitch angle distributions appear to be quasi isotropic (see Sect. 5.2.3). The mean magnetospheric flux values are larger than in the magnetosheath, as expected from the respective plasma temperatures $k_B T_e \sim 200$ eV in the magnetosphere compared with 50 eV in the magnetosheath (Bertucci et al. 2008; Garnier et al. 2009). Moreover, the proton fluxes are 50% larger on the dayside than in

Table 5 [From Garnier et al. (2010)] Statistical parameters for the proton flux at the Titan orbit ($(cm^2\,s\,sr\,keV)^{-1}$) from the LEMMS channels A0 (27–35 keV), A1 (35–56 keV), A2 (56–106 keV) and A3 (106–255 keV)

Energy channel	A0	A1	A2	A3
Mean flux	113.4	40.1	13.5	2.0
Maximum flux	748.6	252.8	85.8	25.2
Dispersion (standard deviation/mean)	1.1	1.2	1.4	2.0
Mean flux in magnetosheath	72.2	26.9	8.9	1.0
Mean flux in magnetosphere (MSPH)	115.5	41.1	13.8	2.1
Mean flux in MSPH, LEMMS rotating	64.9	8.2	1.8	0.1
Mean flux in MSPH, LEMMS not rotating	119.7	43.1	14.6	2.2
Mean flux dayside MSPH	147.3	50.5	16.5	2.4
Mean flux nightside MSPH	90.6	33.2	11.6	1.8

the nightside magnetosphere, since Titan's orbit regularly crosses the energetic plasmasheet which is more extended in latitude on the dayside (Sergis et al. 2009).

Figure 10 shows proton temperatures and spectral indices for suprathermal (30.7–2300 keV) protons measured by MIMI between 5 and 20 R_S from Dialynas et al. (2009). Globally, the results obtained by Dialynas et al. (2009) are in good agreement with the Voyager results published by Krimigis et al. (1981, 1983), in particular in the outer magnetosphere. Both temperature and spectral index increase with decreasing L values, with a power law trend for the temperature profile (blue line) showing that energetic protons are accelerated adiabatically towards the inner magnetosphere where the magnetic field strength is enhanced. The proton spectra at the Titan orbit exhibit a large variability, with a large temperature range of 1–100 keV and high energy spectral indices (denoted γ_1) between approximately 2.5 and 5. The distinction of a high energy spectral index accounts for any break in the spectrum where the fluxes become softer at very high energies and thus characterised by a different spectral index (denoted γ_2) (Dialynas et al. 2009).

5.2.2 Energetic Particle Composition

Figure 11 shows a comparison of the average H^+ and W^+ (dominated by O^+) spectra for two local time sectors near the equatorial plane ($|z| \leq 0.5\ R_S$) and at radial distance between 19 and 21 R_S as measured by the MIMI/CHEMS instrument. These spectra were obtained from 5-minute averages of CHEMS spectra which has been shown to provide reliable statistics and detailed spatial resolution for the region of interest. The energetic ions appear more intense as we move towards the dayside. In addition, W^+ ions appear somehow more energised in the dayside, following, however, a power law of spectral index between 2.1 and 2.3, as the spectrum becomes slightly harder. Nevertheless, we should note that the sampling is not sufficient enough for a solid conclusion to be drawn, especially when the observed differences are not significant. The analysis of simultaneously obtained CHEMS measurements of H^+ and W^+ ions permits a direct comparison of the partial contribution of each ion species to the local (suprathermal) density and pressure. In agreement with conditions in the inner magnetosphere, the results verify the importance of W^+ ions and show that they hold on average $\approx$67% of the number density and carry $\approx$65% of the corresponding pressure.

The pre-Cassini belief that Titan would be a major supplier of nitrogen ions was not confirmed by the comprehensive measurements during the repeated Cassini flybys or passes

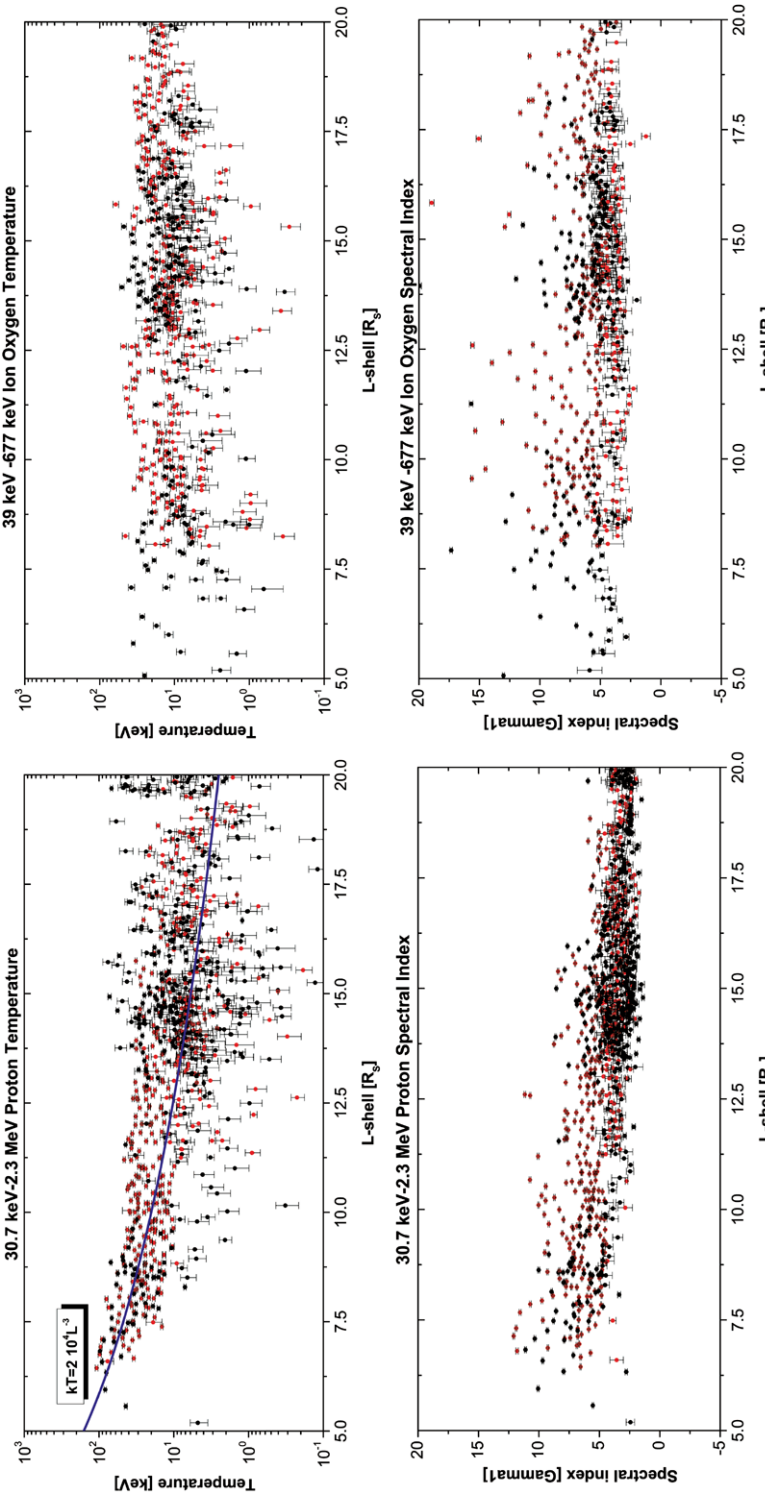

Fig. 10 [From Dialynas et al. (2009)] (*Upper panel*) Proton temperature profile (in keV) as a function of L shell ($5 < L < 20\ R_S$). The *blue line* is a power law fit at L values (*a reference line*) that describes the observed trend in the proton temperatures with L shell; (*lower panel*) Proton spectral index (γ_1) as a function of L shell ($5 < L < 20\ R_S$)

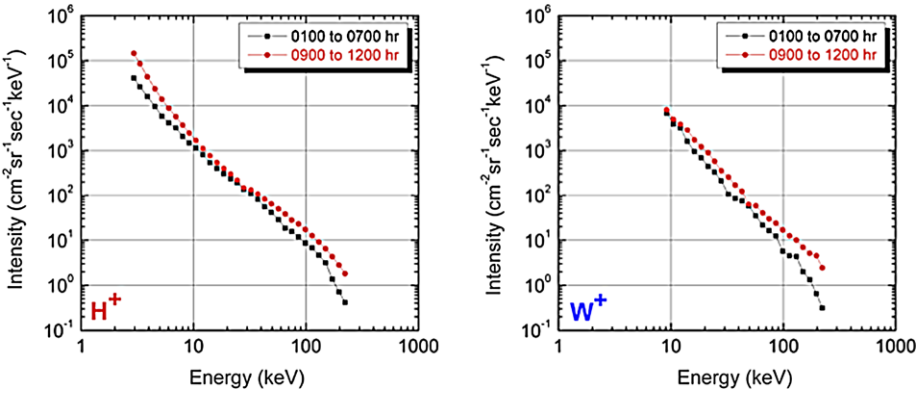

Fig. 11 A comparison between average energy spectra for the two major energetic ion species (H^+ on the *left* and W^+ on the *right*) taken along the orbit of Titan (with Titan absent) for the indicated local time sectors (0100–0700 hr in *black* and 0900–1200 in *red*). The average intensity appears increased in the dayside for both species, while for the W^+ the intensity remains relatively stable but the spectrum becomes slightly harder

through Titan's L-shell. The analysis of ion plasma measurements from the CAPS/IMS (Ion Mass Spectrometer), has shown that Enceladus is likely the dominant nitrogen source for Saturn's inner magnetosphere, although Titan might account for a fraction of the observed nitrogen ions at larger radial distances (Smith et al. 2008). However, MIMI/CHEMS has not shown so far any evidence of increased energetic nitrogen ions at Titan's orbit (D.C. Hamilton, private communication).

5.2.3 Suprathermal Pressure

A key element in order to understand the average energetic particle conditions along Titan's orbit is the computation of the local particle pressure. The measurements provided by the MIMI suite offer the opportunity to accurately calculate the suprathermal component of the particle pressure (Sergis et al. 2007, 2009). The question that naturally emerges is how the suprathermal pressure compares to the total particle pressure. The analyses done so far (Sergis et al. 2009, 2010; Thomsen et al. 2010) indicate that near the orbit of Titan the suprathermal component is on average (at least) comparable to the thermal plasma pressure, i.e. MIMI captures at least half of the total particle pressure.

Data from the equatorial plane ($|z| \leq 0.5\ R_S$) and at radial distances between 19 and 21 R_S were combined to analyse the statistics of the suprathermal pressure near Titan's orbit while Titan was not present (flybys were excluded). Despite the fact that all available data from SOI (2004) to 2009 have been included, the coverage is still partial and non-uniform, with the dawn to noon sector (0100 to 1400 hr) sampled better than the rest of the orbit. It should be mentioned, however, that through the Cassini mission, this part of the Saturnian magnetosphere is for the first time sampled sufficiently enough for a statistical study to be attempted. Figure 12 shows the statistical distribution of the suprathermal pressure along the orbit of Titan. The considerable broadness of the distribution (full width half maximum of $\sim 1.8 \times 10^{-2}$ nPa), reveals the increased variability of the pressure conditions that Titan is expected to encounter along its path. During 87% of the total time that Cassini spent there from 2004 to 2009, the energetic particle pressure varied between 0.001 and 0.05 nPa, while for 28% of the cases it exceeded 0.01 nPa. The causes that could at least partially explain the observed variability are discussed in the following section.

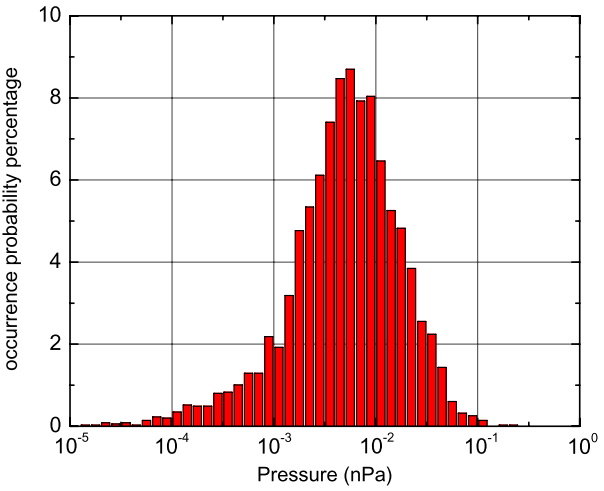

Fig. 12 Statistical distribution of the suprathermal (>3 keV) pressure along the orbit of Titan during periods that Titan was not present. For 87% of the total sampled time from SOI to 2009, the energetic particle pressure varied between 10^{-11} and 5×10^{-10} dyne cm^{-2}, while for 28% of the cases it exceeded 10^{-10} dyne cm^{-2}. The considerable broadness of the distribution indicates the increased variability of the pressure conditions that Titan encounters along its orbit

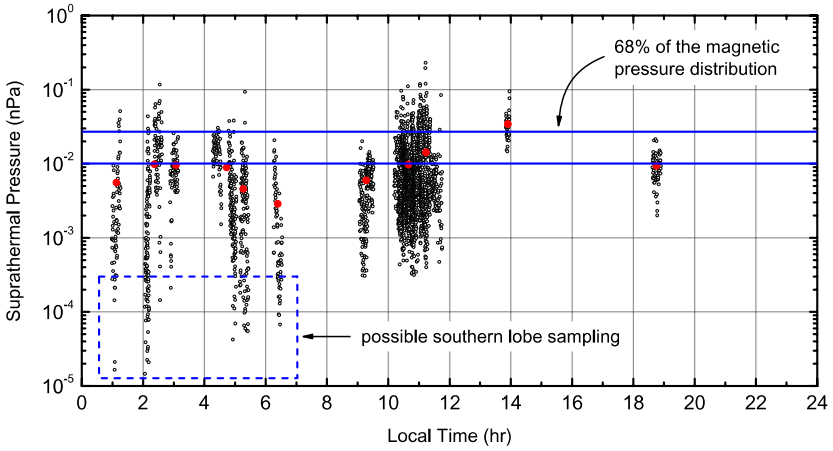

Fig. 13 The measured suprathermal pressure at the orbit of Titan vs. local time. The *big red circles* correspond to the average values per 1-hr bin. The *two blue horizontal lines* form roughly a $1-\sigma$ (68%) band of the magnetic pressure distribution, while the *dashed square in the lower left corner* brackets measurements that most likely correspond to the southern night side lobe

The distribution of the energetic particle pressure in local time for all measurements obtained at the orbit of Titan (with Titan itself not present), is presented in Fig. 13, together with the averages per local time bin. The suprathermal pressure appears (on average) increased in the dayside. The comparison to the distribution of the magnetic pressure (blue horizontal band) reveals that high (>1) plasma β values are mainly expected in the dayside, perhaps due to the steadily growing mass loading. It should be noted however, that the difference in the averages are almost masked by the strong natural scatter of the data that reveal the intense dynamics that characterise the energetic particle population. The blue square at the midnight-to-dawn sector groups low pressure values extending beyond the typical scatter, and are presumed to correspond to Cassini sampling the southern or northern lobe due to the northward tilt of the thinner night side plasma sheet.

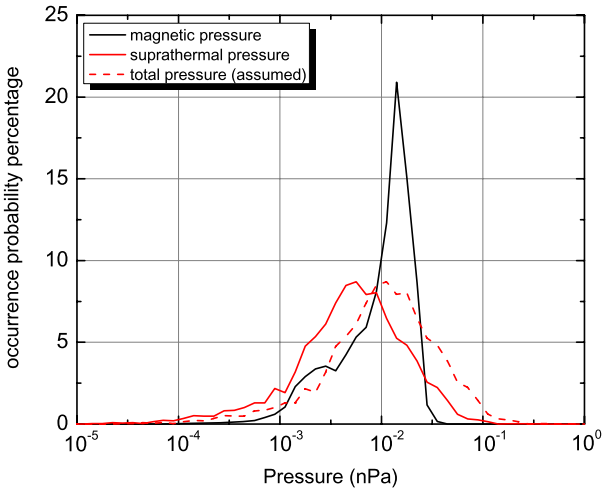

Fig. 14 Statistical distribution of the magnetic pressure (*black line*), the suprathermal pressure (*red solid line*) and the total particle pressure (*red dashed line*), for the orbit of Titan (as shown in Fig. 1). The total particle pressure is estimated assuming that half of the total pressure is contributed by the energetic particles. For ∼28% of the time, Titan's orbit is statistically expected to be in a $\beta > 1$ plasma environment

Figure 14 shows a direct comparison between the statistical distribution of the suprathermal pressure (in red) and the magnetic pressure (in black) at the orbit of Titan. The red dashed line corresponds to the estimated total particle pressure, under the assumption that the suprathermal particles carry approximately half of the total pressure. It is evident that the magnetic pressure has a rather narrow distribution compared to the energetic particles (as also indicated by Fig. 13). However, the most significant conclusion emerging from this comparison is that there is a noteworthy part of the distribution (∼28 %) for which the total particle pressure exceeds the magnetic pressure (particle $\beta > 1$). A high β regime for the Saturnian magnetosphere has also been reported by Sergis et al. (2009), with somewhat lower values as it did not include the thermal plasma pressure, but it is now the first time that data are selectively analysed and a conclusion is drawn for this particular part of the magnetosphere.

5.2.4 Energetic Particle Dynamics

Although the early missions to Saturn (Pioneer, Voyager) provided important information about the plasma distribution and dynamics in Saturn's magnetosphere, it is Cassini that with its multiple passes and continuous sampling since 2004 that has offered an expanded spatial and temporal coverage of magnetospheric properties. Several studies have revealed the intense dynamic behaviour of the energetic particle population throughout the Saturnian magnetosphere (Carbary et al. 2007, 2008a, 2008b; Krimigis et al. 2007; Dialynas et al. 2009; Kane et al. 2009; Krupp et al. 2009; Mitchell et al. 2009; Sergis et al. 2009, 2010). Even though in their majority these studies focus mostly on the general magnetospheric environment, their conclusions often apply beyond the middle magnetosphere, covering the vicinity of Titan's path.

The energetic proton population was confirmed to be highly variable at Titan's orbit between 2004 and 2008, as previously emphasised by Krimigis et al. (1983) for the Voyager period. Firstly, the flux values may vary, from a crossing to another, from the instrument background up to 750, 250, 85 and 25 $\mathrm{cm^2\,s^{-1}\,sr^{-1}\,keV^{-1}}$ for the A0, A1, A2 and A3 LEMMS energy channels respectively. Then, the intensities are also dynamic at the timescale of a single crossing, with a mean variability of a factor of between 5 and 10 (but as large as 100) between minimum and maximum fluxes during a one hour time interval.

The variability may be estimated through the timescale of the flux gradient, whose value is of the order of only 5–10 minutes. The dynamics of the proton flux is suggested to be larger in the magnetosheath than in the magnetosphere, due to turbulence, as seen in the terrestrial environment (e.g. Cai et al. 2009). Garnier et al. (2010) estimated the mean energy deposition by energetic protons between 0.001 and 0.002 nPa at a peak altitude of 700–750 km which lies between estimates previously given by Luna et al. (2003) and Smith et al. (2009). The proton flux was also found to be highly variable, even over the duration of a single Cassini flyby of Titan thus introducing a strong dynamical nature to the energy deposition.

Finally, Dialynas et al. (2009) showed that the energy spectra were highly variable at the L shell of Titan, through both the temperature and the spectral index parameter (see Sect. 5.2.3). The rapid evolution of the proton plasma conditions have, in particular, important consequences for the Titan interaction, with a very dynamic energy deposition by the plasma into the moon's atmosphere (see Smith et al. (2009) for a case study). The suprathermal particle pressure was found to be much more variable than the magnetic pressure. Even though the 5-min resolution used is sufficient to keep the measurement uncertainties low, the suprathermal pressure changes are within a factor of 20, while the magnetic pressure remains comparatively stable, varying roughly by a factor of 3.

ENA images taken by the wide field of view camera of MIMI/INCA (Ion Neutral Camera) during the high latitude orbits of Cassini, offer a unique opportunity to capture both the spatial and the temporal variability of the near equatorial magnetosphere in the keV energy range. In Fig. 15 we present a three hour sequence of six INCA images, obtained while Cassini was at a latitude of $\approx 63^\circ$. The field of view of INCA is wide enough to capture a large part of the equatorial magnetosphere (as far as the orbit of Titan), thus providing an excellent overview of (almost) global magnetospheric activity during that time. As this wide top view reveals, there is a strong and evolving variability, primarily seen as a hot plasma "blob" that tends to rotate with the planet. This particular sequence of ENA images illustrates the almost instantaneous energetic (24–55 keV) particle conditions at the orbit of Titan for approximately half of its full path. It is evident that, at a given moment, the ENA intensity along the orbit of Titan varies more than a factor of 10. As this energised "blob" rotates, and provided it does not considerably deform, it is expected to encounter and interact with Titan (shown as a dot at the lower left corner of each frame), for 2 or 3 hours. During this time, Titan will experience a radical change of the surrounding plasma environment and will emerge in a significantly hotter and much more variable particle population, in contrast to the relatively quiet conditions outside the energised region.

5.3 Statistical Properties of Titan's Upstream Magnetospheric Plasma

To date, estimates and small collections of the important plasma and field parameters (see Table 3) have been published (e.g., Neubauer et al. 1984, 2006) but no comprehensive statistical survey of these parameters has been attempted. To solve this issue, and provide a statistical understanding of the plasma and field variability in the vicinity of Titan, Arridge et al. (2011d) used a data set derived from magnetic field, energetic particle, and plasma measurements made in Saturn's magnetosphere by the Cassini CAPS, MIMI, and MAG (magnetometer) instruments.

5.3.1 Data Processing and Selection

The energetic particle pressure was obtained from the MIMI CHEMS and LEMMS data by a direct integration over the particle distributions (e.g., Sergis et al. 2007). Ion moments

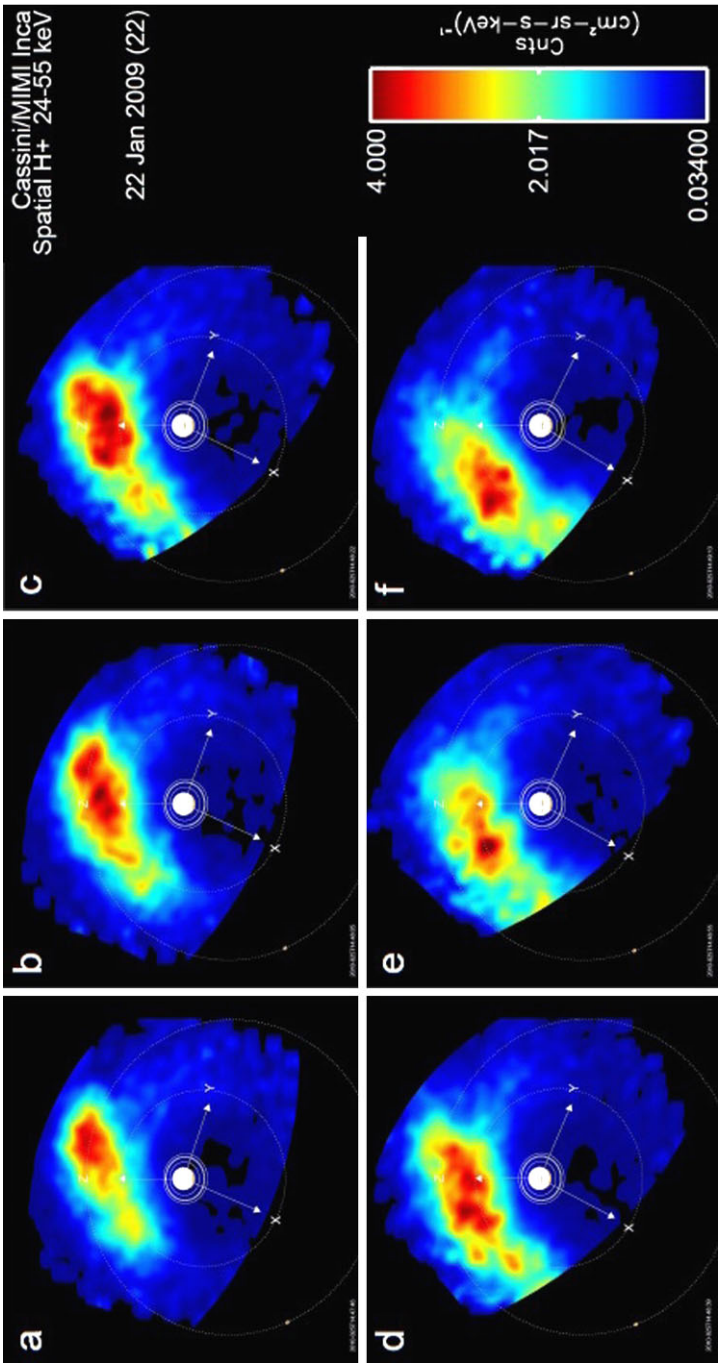

Fig. 15 Sequence of six continuous (**a** to **f**) ENA images in neutral hydrogen in the range 24 to 55 keV, obtained by MIMI/INCA on 22 January 2009. Cassini was located at ~63° latitude and ~13.7 R_S from Saturn at local time ~15:35. The whole sequence covers approximately 3 hours. Saturn is at the centre, the x axis is pointing approximately in the solar direction, y is pointing towards dusk, and z is pointing along Saturn's spin vector. The *two dotted lines* show the orbits of Rhea (8.7 R_S), and Titan (20.2 R_S) in proper perspective. Sharp edges on the frames are attributable to the limit of INCA's field of view

(density, temperature, bulk velocity) for the lower energy populations (<52 keV/q) were obtained from the CAPS IMS data by direct numerical integration over the observed distributions (e.g., Thomsen et al. 2010). Moments were obtained for three main ion species: H^+, W^+ (water group ions), and ions with an m/q of 2 which is assumed to be H_2^+ although evidence exists for the presence of He^{++}. Finally, electron moments (number density and temperature) were obtained from the measured CAPS/ELS (Electron Spectrometer) spectra by numerical integration (Lewis et al. 2008; Arridge et al. 2009a) assuming that the measured distributions were isotropic in the spacecraft frame. All vector quantities (magnetic fields **B**, flow velocities **u**, and convection electric fields **E**) were represented in Kronocentric Radial-Theta-Phi (KRTP) coordinates which is a Saturn-centred spherical polar coordinate system.

Usable data from 2004–2008 were extracted for radial distances between 18 and 22 R_S and at kronographic latitudes less than 10°. This data selection procedure reduced the total number of ion moments from ∼280000 to 842. The selected data points were found to come predominantly from the dayside magnetosphere, with smaller groups of points at midnight and dusk.

5.3.2 Statistical Results

The distribution of number densities were found to peak near 2×10^4, 3×10^4, 3×10^4 and 10^4 m^{-3} for electrons, O^+, H^+, and $m/q = 2$ (H_2^+) respectively (see Fig. 2 of Arridge et al., to be submitted). The distribution of the partial pressures of each population show that the CAPS water group ion and MIMI energetic ion pressures peak at similar pressures but with CAPS (MIMI) extending to lower (higher) pressures. The electron and $m/q = 2$ pressure distributions also peak at similar values. The proton pressure distribution peaks in between the electron and water group ion pressure peaks. The total pressure distribution peaks at ∼0.01 nPa (10 pPa) which is similar to the peaks in the distribution of both the ram and magnetic pressures. The plasma beta is illustrated in Fig. 16 (from Arridge et al., to be submitted) where the distribution peaks near unity, but has a narrow distribution between ∼0.5 and 10 and extends between 0.1 and 100. As expected, larger values of plasma beta were found in the centre of the current sheet. The bulk plasma velocity is generally dominated by the azimuthal flow of Saturn's magnetospheric plasma, which was found to be subcorotating by around 50% with a speed of 100 km s^{-1}. The radial and polar components of the bulk flow velocity have distributions centred about zero and instrumental considerations suggest that these are the most uncertain given the viewing constraints of CAPS. The distribution of bulk flow speed was found to generally reflect the distribution of azimuthal plasma velocities.

The Mach numbers confirm the Voyager 1 picture that Titan's upstream environment is sub-sonic and sub-magnetosonic but trans-Alfvénic. The distributions of each Mach number are illustrated in Fig. 17 (from Arridge et al., in preparation) and show that the fast magnetosonic Mach number peaks near 0.4 with only 10% of points above 1, and that the sonic Mach number peaks near 0.6 with only 20% of points above 1, thus demonstrating that upstream bow shocks should be an infrequent feature of Titan's magnetospheric interaction. The peak in the distribution of the Alfvén Mach number lies near 0.8 with a significant fraction of points above 1 in the super-Alfvénic regime. Some evidence was found for variation in the Alfvén Mach number with the B_r component of the magnetic field where larger Mach numbers were found in the centre of the current sheet.

The picture of a north-south (quasi-dipolar) background field and azimuthal plasma flow, developed from the Voyager flyby, produces a nominal convection electric field in the radial

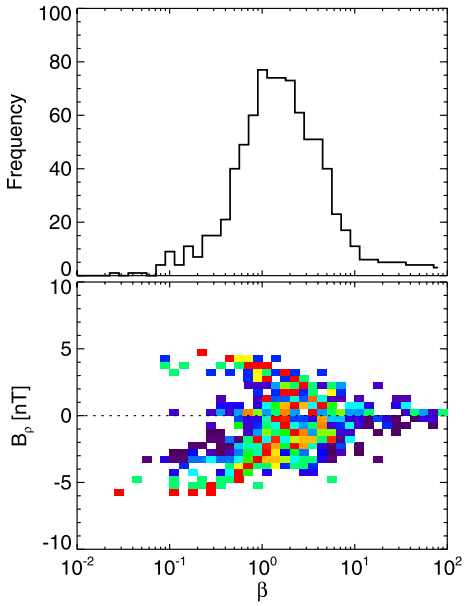

Fig. 16 Histogram of the total plasma beta (*top*) and then the dependence of plasma beta on the B_ρ component of the magnetic field, used as a proxy for distance from the centre of the current sheet (*bottom*), where the colour scale shows the number of points in that bin, normalised to the maximum number in that B_ρ range (from 0 = *black* to 1 = *red*). From Arridge et al. (in preparation)

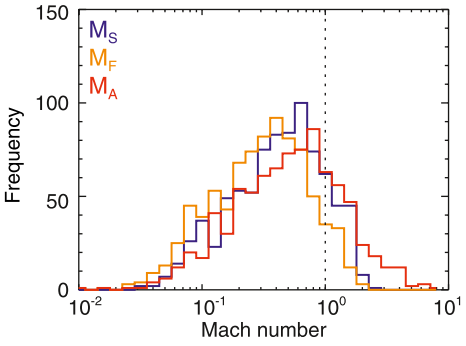

Fig. 17 Histogram of sonic (*blue*), fast-mode (*orange*), and Alfvén (*red*) Mach numbers. The vertical dotted line indicates a Mach number of one. From Arridge et al. (in preparation)

direction with a value of between 0.5 and 1.0 mV m^{-1} corresponding to a 5 nT background magnetic field at half and full corotation speed respectively. Figure 18 shows the distribution of the three components of the calculated convection electric field. Arridge et al. (to be submitted) found that the distribution of E_ρ peaked near 0.1 mV m^{-1}, somewhat smaller than the nominal value from the Voyager 1 dataset (but such high values are observed). The azimuthal component of the convection electric field shows a symmetric distribution about 0 and since the axial and radial flow speeds are the most poorly constrained components of the flow, the azimuthal component of **E** is similarly the most poorly determined. The axial component of the convection electric field similarly exhibits an almost symmetric distribution about zero, but Arridge et al. (to be submitted) argued that here the axial convection electric field should be well determined. In examining the B_ρ dependence of each component of the convection electric field (see Fig. 19), Arridge et al. (2011d) found that the E_z component was linearly dependent on the radial component of the magnetic field. Indeed they went on to fit an equation to the data, allowing an estimate of the axial convection electric field from upstream measurements of the magnetic field: $E_z = (-0.01 \pm 0.05) + (-0.07 \pm 0.03) \times B_\rho$

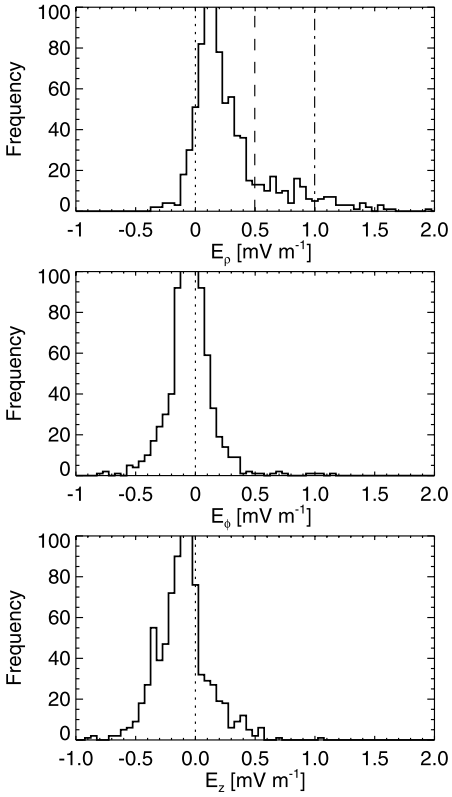

Fig. 18 Histograms of estimated convection electric fields in spherical polar coordinates. Zeros are indicated by *horizontal dotted lines*. The *dot-dashed line* in E_ρ histogram indicates the value expected from a "nominal" Voyager 1 electric field due to ideal plasma corotation and a dipolar magnetic field with a field strength of 5 nT. The *dashed line* indicates the same conditions but with the plasma moving at half ideal corotation speed. From Arridge et al. (2011d)

and where the error in E_z is given by $0.03(1 + B_\rho^2)^{1/2}$. The distributions of E_z and E_ρ presented by Arridge et al. (2011d) showed that there could be periods where the polar convection electric field dominates. This is clearly of importance for modelling and understanding Titan's magnetospheric interaction.

As stated above, the aims of the Arridge et al. (2011d) study was to extend the table of upstream field and plasma parameters presented by Neubauer et al. (1984, 2006). Table 6 presents this expanded table, comparing these Cassini-era results with the Voyager 1 values. Both the median values, and the upper (75%) and lower (25%) quartiles are quoted. Interestingly, the particle number densities, mass densities, pressures and the plasma beta are all smaller in the Cassini dataset by an order of magnitude, and wave speeds were found to be somewhat larger than the Voyager 1 measurements; although by inspection of the histograms one finds that the Voyager 1 values can be found in the tails of the Cassini-era distributions. This supports the idea that the Voyager 1 values were obtained during a fairly rare configuration of the magnetosphere and are atypical of the magnetosphere near Titan's orbit.

Arridge et al. (to be submitted) showed numerous examples of systematic variations in some of these parameters with distance from the centre of the current sheet. Simon et al. (2010a) developed a definition of current sheet-type and lobe-type regions based on the radial component of the magnetic field (see Sect. 6.4). Arridge et al. (2011d) used this scheme to organise their field and plasma parameters into values from the current sheet and lobe regions.

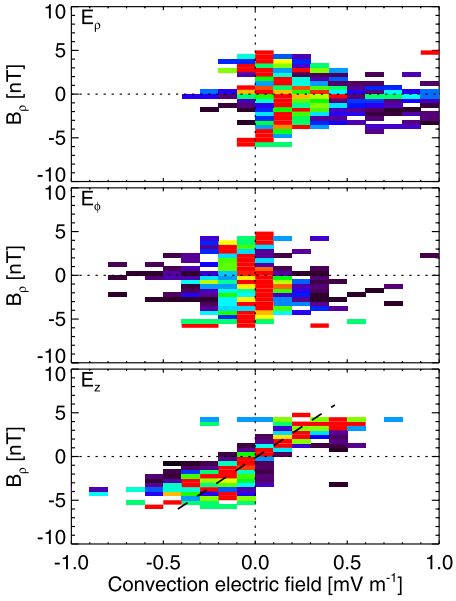

Fig. 19 Dependence of the B_ρ magnetic field component on the convection electric field in cylindrical polar coordinates, following a similar format to the bottom panel in Fig. 6. The panels show the radial (*top*), polar (*middle*), and azimuthal (*bottom*) components

6 Titan Encounter Classifications

Given the numerous encounters Cassini has now made with Titan, recent studies have surveyed in situ data during Titan encounters in order to explore to what extent the magnetospheric environment near Titan might be qualitatively characterised on an encounter-to-encounter basis. Four studies have attempted to do this separately using low-energy electron (Rymer et al. 2009) and ion data (Németh et al. 2011), magnetic field data (Simon et al. 2010a), and energetic particle data (Garnier et al. 2010). These studies provide helpful information on the characteristics of particular passes and are highly valuable for modelling studies of particular Cassini Titan encounters. Such studies are required to resolve many of the apparent inconsistencies between predictions and observations of Titan and its interactions with the surrounding plasma environment. In this section we discuss the classifications from Rymer et al. (2009) and a study using ion data to confirm these classifications (Sect. 6.1), Simon et al. (2010a) (Sect. 6.2) and Garnier et al. (2010) (Sect. 6.3). We combine these classifications into a single encounter-by-encounter table in Sect. 6.4.

6.1 Electron and Ion Classification: Rymer et al. (2009) and Németh et al. (2011)

Rymer et al. (2009) used electron (ELS and LEMMS) data to classify each encounter and focused on the electron environment because electron-impact interactions with Titan's atmosphere and ionosphere are important near Titan and, due to their high thermal speed with respect to the local magnetospheric flow speed, are well sampled irrespective of spacecraft pointing. Bertucci et al. (2008) and Ma et al. (2009) show that Titan's "magnetic memory" (that is the extent to which the Titan atmosphere displays the magnetic properties "fossil fields" of a magnetic environment it was embedded in earlier) is a function of altitude and is typically on the order of a few tens of minutes to a few (<3) hours. Therefore Rymer et al. (2009) considered data ±3 hours from Cassini closest approach to Titan. Németh et al. (2011) have also used CAPS ion data to study the features of ion distributions (1–52 keV/q)

Table 6 Various important plasma and field parameters with pre-Cassini (Voyager 1) estimates and the medians and quartiles of each value as estimated from Cassini measurements in this study. From Arridge et al. (in preparation)

Parameter	Median	Quartiles (25%, 75%)	Voyager 1
Electron number density, n_e [m^{-3}]	2.9×10^4	$(1.6, 5.9) \times 10^4$	3.0×10^5
Mass density, ρ [amu m^{-3}]	2.9×10^5	$(0.82, 8.1) \times 10^5$	2.9×10^6
Electron temperature, T_e [eV]	130	(71, 250)	200
Magnetic field strength, B [nT]	4.1	(3.2, 5.0)	5
Ram pressure, p_{ram} [pPa]	4.6	(1.1, 14)	70
Electron pressure, p_e [pPa]	0.76	(0.47, 1.1)	9.6
Ion pressure, p_i [pPa]	9.5	(5.1, 20)	96
Magnetic pressure, p_m [pPa]	6.6	(4.0, 10)	∼10.0
Plasma β	1.7	(0.70, 3.7)	∼11
Alfvén speed, v_A [km s^{-1}]	420	(95, 340)	64
Sound speed, v_S [km s^{-1}]	410	(120, 350)	210
Fast-mode speed, v_F [km s^{-1}]	610	(170, 520)	220
Alfvén Mach number, M_A	0.60	(0.28, 1.1)	1.9
Sonic Mach number, M_S	0.50	(0.25, 0.86)	0.57
Fast mode Mach number, M_F	0.36	(0.17, 0.62)	0.55
Convection electric field [mV m^{-1}]			
Radial, E_ρ	0.22	(0.10, 0.41)	0.6
Azimuthal, E_φ	−0.011	(−0.11, 0.062)	0
Axial, E_z	−0.083	(−0.21, 0.017)	0
Plasma bulk velocity [km s^{-1}]			
Azimuthal, u_φ	89	(55, 120)	120
Radial, u_ρ	11	(−18, 44)	−41
Axial, u_z	3.4	(−13, 23)	0

in these classifications to see if the ion data support the results of Rymer et al. (2009) or whether they suggest a different classification scheme. They used the same 3 hour windows as Rymer et al. (2009) but also expanded the window to 12 hours to examine the wider region surrounding each encounter.

6.1.1 Classification Scheme

The encounters were characterised into four broad types: “plasma sheet”, “lobe-like”, “magnetosheath” and “bimodal”. Despite many encounters occurring close to the magnetopause only two encounters to date were predominantly in the magnetosheath (T32 and T42). Bimodal encounters contain two distinct electron populations, the low energy component of the bi-modal populations were apparently associated with local water group products. Additionally, they noted that a hot lobe-like environment was occasionally observed which they suggested might be associated with increased local pick-up. Although a statistical study of such populations found that they were observed at a wide variety of kronocentric radial distances in the outer magnetosphere and were consistent with heating due to reconnection processes in the magnetotail. Rymer et al. (2009) found that 34 of 54 encounters analysed were associated with one of these groups while the remaining encounters exhibited a com-

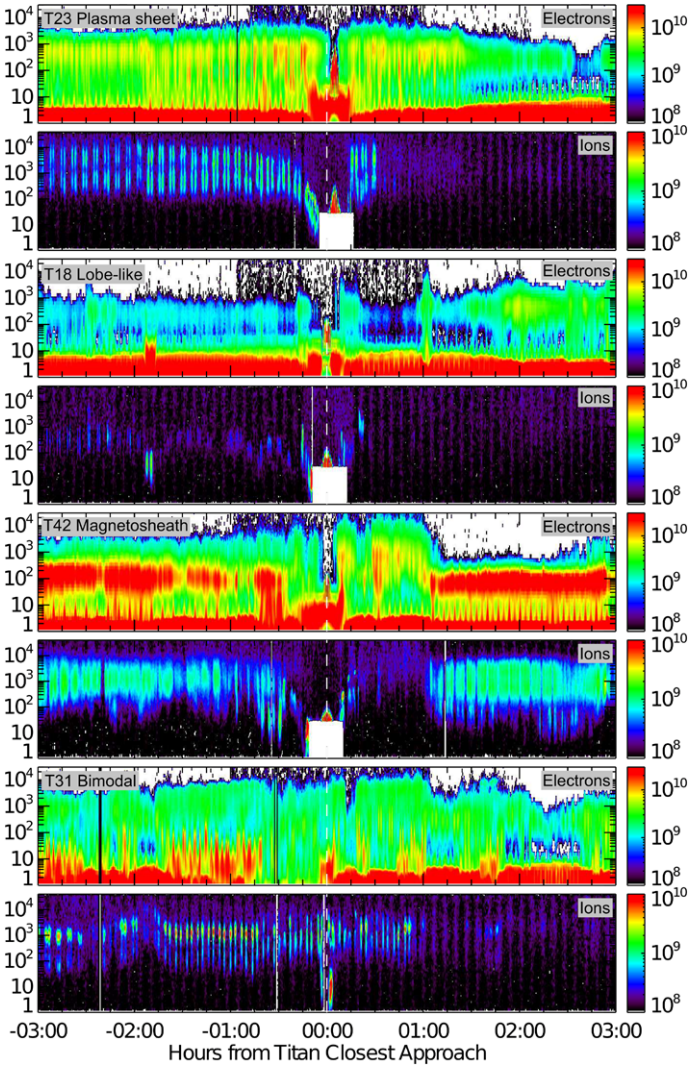

Fig. 20 Energy-time spectrograms for plasma electrons and ions (∼±3 hours of closest approach to Titan) showing examples of the four different categories of magnetospheric background observed during Cassini-Titan encounters along with their associated Titan encounter number. The spectrograms are in units of differential energy flux (eV m^{-2} s^{-1} sr^{-1} eV^{-1}). After Rymer et al. (2009) and Németh et al. (2011)

bination of these environments and provided typical electron properties and spectra for each plasma regime and a list of the encounters appropriate to each.

Figure 20 shows four energy-time spectrograms of electron and ion differential energy flux measured by CAPS/ELS and CAPS/IMS following similar figures from Rymer et al. (2009) and Németh et al. (2011). Each panel shows six hours of data, within three hours either side of Cassini's closest approach to Titan. The electron population below ∼10 eV at the bottom of each panel consists of trapped spacecraft photoelectrons. At the centre of each panel is the closest approach to Titan (indicated by the apparent discontinuity in the spectra). Near Titan the ambient (ionospheric) electron populations can be sufficient to charge Cassini

Table 7 Classification scheme from Rymer et al. (2009)

	Peak energy (eV)	Peak flux (10^{10} m^{-2} s^{-1} sr^{-1})
Plasma sheet (e.g., T23, 13 January 2007)	120–600	0.35–1.2
Lobe-like (e.g., T18, 23 September 2006)	150–820	0.053–0.24
Magnetosheath (e.g., T32, 13 June 2007)	∼50 eV	1
Bimodal (e.g., T31, 28 May 2007)	200–3400	0.09–0.24
	5.3–16.3	0.57–1.6

to a negative potential. Photoelectrons produced from the surface of Cassini are no longer trapped and are accelerated away from the spacecraft and thus are not observed by ELS. In this situation the measured electron energy is smaller than in the ambient plasma due to the negative potential. Regions near the ionospheric interaction region were not considered in the Rymer et al. (2009) classification.

After compiling all available electron energy-time spectrograms for 54 Titan encounters from October 2004 to May 2009 it was determined that over half of the encounters are broadly associated with one of the four categories ("plasma sheet", "lobe-like", "magnetosheath" and "bimodal"). The definition of this classification scheme is reproduced in Table 7. Rymer et al. (2009) noted that the nomenclature for category two was not completely accurate, they use the term "lobe-like" because the hot tenuous nature of the Earth's lobe regions is similar to these low density regions near Titan. The ion spectra counterparts show broadly the same structure, and the ion energy distribution and composition are significantly different between the two types.

The "bi-modal" category is a particularly interesting category because it corresponds to two very different superposed electron populations. The more energetic population appears to be either plasma sheet or hot electrons while the less energetic but more dense population is similar to the cold electron population produced in Saturn's inner magnetosphere by pickup from the neutral cloud (Rymer et al. 2007; Sittler et al. 2008; Wilson et al. 2008). The ion distributions in the bi-modal intervals are shifted towards lower energies (around 250 and 1500 eV for H^+ and W^+ respectively) and the heavy ion distribution has a larger peak and is much narrower indicating a colder more dense heavy ion population. Thus, from the point of view of the ion measurements, this plasma type cannot be called "bimodal", but the encounters dominated by this "heavy rich" plasma coincide with that classified as bimodal based on the electron measurements. The origin of these cold electrons and dense cold ion populations is not clear and may be related to in situ photoionisation of water (Rymer et al. 2009) or rapid plasma transport from the inner magnetosphere as found at Jupiter (Arridge et al. 2009b, and references therein).

In addition to these clear categories Rymer et al. (2009) provided a "mixed" category in which we list the encounters that did not occur solely in one of the four plasma environments identified and an "unclassified" category in which plasma distributions not included in any of our categories are observed occasionally, but not throughout. For example a high energy electron distribution (peaking around and above 10 keV with electron energy flux at the peak of few times 10^8 eV m^{-2} s^{-1} sr^{-1} eV^{-1}) is occasionally observed during Titan encounters. Since no encounter occurs exclusively in this type of environment they did not designated it to a separate category. They noted that most of the encounters in the 'Unclassified' category show evidence of both very high energy electrons and the cold 'pick-up' population—perhaps indicative of additional ionisation energy being provided by sporadic energetic electron distributions. From the point of view of the ions, Németh et al. (2011)

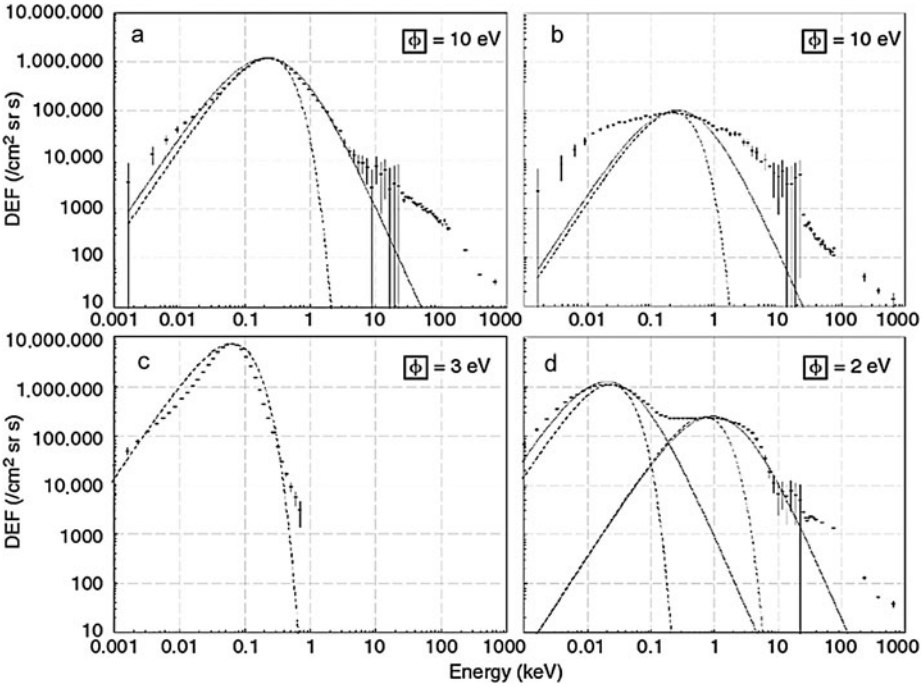

Fig. 21 Example combined CAPS-MIMI electron differential energy flux versus energy spectra for the four regions identified. (**a**) An example plasma sheet spectra observed during T13. (**b**) A low density lobe-like population observed during T8. (**c**) A magnetosheath spectra from T32. (**d**) A bi-modal example spectra observed during T31. *Dashed and solid lines* are Maxwellian and kappa fits to the data, respectively. The spacecraft potential correction (ϕ) applied to each spectra is indicated in the *top right hand corner*. From Rymer et al. (2009)

Table 8 Summary of fit parameters from Fig. 21. From Rymer et al. (2009)

Region	Maxwellian		Kappa		
	n (10^5 m^{-3})	T (eV)	n (10^5 m^{-3})	T (eV)	κ
Plasma sheet	0.39	112	0.50	130	4
Lobe-like	0.03	112	0.04	150	4
Magnetosheath	4.35	31	n/a	n/a	n/a
Bi-modal (cold, hot)	1.12, 0.04	12, 350	1.70, 0.05	12, 570	4, 4

found that in reality all encounters are somewhat mixed. There are few hour-long upstream measurements that could be characterised by a single type, as found for the magnetic field measurements by Simon et al. (2010a).

6.1.2 Spectra

Figure 21 shows examples of combined CAPS-MIMI/LEMMS electron spectra for each category. Each spectrum has been corrected to remove spacecraft photoelectrons and noise. Panel 1 (top left) shows an example plasma sheet spectrum observed during T13 from 19:00 to 19:10 UT 30 April 2006; panel 2 (top right) shows a typical low density lobe-like popu-

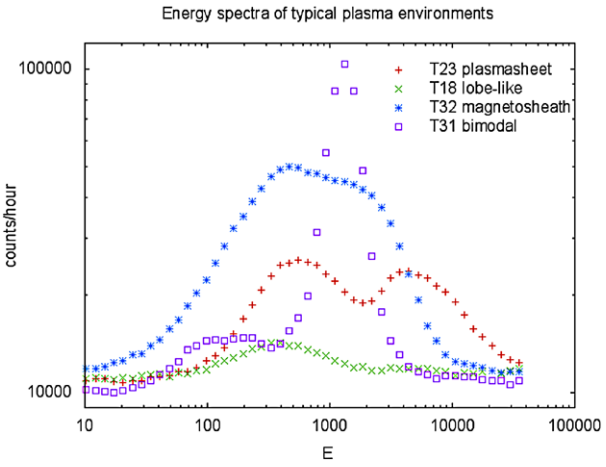

Fig. 22 Ion-energy spectra of typical plasma environments. From Németh et al. (2011)

lation observed during T8 from 03:00 to 03:10 UT 28 October 2005; panel 3 (bottom left) shows a magnetosheath spectra observed during T32 from 19:00 to 19:10 UT 13 June 2007 and panel 4 (bottom right) shows an example of a bi-modal electron spectra observed during T31 from 17:30 to 17:40 UT 28 May 2007. The approximate boundary between CAPS and MIMI is at 20 keV, the discontinuity in the lobe-like and magnetosheath spectra at this energy can be understood as the CAPS-ELS signal falling to its instrument background levels at the higher end of its energy range while the LEMMS signal is still above its instrument background level. Long dashed and solid lines are Maxwellian and kappa fits to the data, respectively. The parameters of these fits are listed in Table 8. Rymer et al. (2009) note that the lobe-like distribution is not well fit by either a kappa or a Maxwellian distribution and that it is not possible to fit the higher energy tails of the distributions using this method, although such issues may be the result of poor signal to noise and longer summations may produce good quality fits.

Figure 22 shows examples of ion spectra for the four categories. Plasma sheet encounters are characterised by a clear double-peaked energy/charge spectrum. A lower energy peak corresponding to the proton group can be found around 400–600 eV, and a higher energy peak corresponding to the heavier ions can be found around 4400 eV. The intensities of the two peaks are similar with a signal of 15000–20000 counts/hour for both populations. The lobe encounters have similar characteristic energies but the higher energy peak is highly suppressed relative to the proton peak. A few thousand counts/hour is typical for the low energy peak and the high energy peak is much smaller. Magnetosheath spectra show a very broad intense peak in the energy/charge spectrum around 1000 eV, with count rates as high as 50000 counts/hour, and a small peak near 400 eV. This distribution is the superposition of H^+ and He^{++} where the small 400 eV peak corresponds to H^+. In the bimodal categories the very large and narrow peak near 1000 eV dominates the spectrum and these are thus categorised (in the ion data) as "heavy-rich" indicating the dominance of heavy ions in the spectra.

6.1.3 Results

Rymer et al. (2009) found that the majority of Titan encounters occurred in an environment similar to one (or a combination of) the electron spectra shown in Fig. 20. The classifications from TA-T55 from Rymer et al. (2009) are included in Table 11 along with classifications from Simon et al. (2010a) (see Sect. 6.3), Németh et al. (2011) and Garnier et al. (2010) (see

Sect. 6.4). Where an encounter within ±3 hours of closest approach is clearly associated with one region a single identification code is listed in the appropriate column in Table 11. These codes are: "PS" for plasma sheet, "LL" for lobe-like, "MS" for magnetosheath, "BM" for bimodal, "U" for unknown/unclassifiable, and "Mx" for a mixture of types. For passes where there are brief occurrences of other plasma types this is indicated with a set of additional codes in brackets, for example "LL (PS)" indicates that the encounter is mainly lobe-like but with occurrences of plasma sheet electrons. The mixed class Mx indicates that an encounter was split into different classes, for example "Mx (PS, LL)" indicates that the encounter was split, in chronological order, between plasma sheet and lobe-like environments. The unclassified categorisation refers to encounters that typically contain elements of the above regions, but also contain electron spectra which were difficult to classify.

This categorisation is supported by an analysis of ion data (Németh et al. 2011). In this study they found that the most important type (found most frequently during our analysis) is the "mixed" type which are combinations of the clear types. In reality the few hour-long upstream measurements cannot be characterised by a single type, it is always a combination of shorter time intervals showing plasma properties of a few different clear classes. Thus clear classification is only possible for shorter time intervals; half an hour is short enough for most cases. Overall the ion and electron classifications were in good agreement with some difference between the mixed and lobe-like categories.

The Rymer et al. (2009) analysis indicates that 34 of the 54 Cassini Titan encounters analysed can be mainly associated with one of the four environment categories, with 19 plasma sheet encounters, eight encounters in what we have referred to as a lobe-like region, two encounters that were predominantly in the magnetosheath and five encounters consisting of predominantly bi-modal electron signatures.

Titan encounters were mostly found to lie within the plasma sheet category. Titan encounters in the magnetosheath were found to be rare, despite numerous Cassini-Titan flybys near noon (see Sect. 3.2 for a discussion of the location of the magnetopause). Intervals of sheath type plasma were seen during several encounters (T22, T29, T32, T36, T39) however encounters T32 (e.g. Bertucci et al. 2008) and T42 are the only encounters to date that are predominantly close to or in the magnetosheath. However, we also note that solar activity has been rather low during the observed portion of the Cassini tour so it is possible that Titan may be exposed more often to the magnetosheath as solar activity increases and pushes the magnetosheath Saturn-ward (e.g., Jackman and Arridge 2011). There seems to be a tendency for the "unclassified" encounters to occur post noon and so might be associated with a more disturbed dusk flank region of the magnetosphere.

6.2 Magnetic Field Classification: Simon et al. (2010a)

As discussed in Sect. 5.1 Bertucci et al. (2009) characterised the global features of Saturn's magnetospheric field at 20.3 R_S and described the different field regimes encountered by Titan. However, they did not go on to apply their findings and develop a classification scheme for each flyby. Furthermore, they did not investigate whether the conceptual picture of a quiet homogeneous upstream field is valid for understanding Titan's magnetospheric interaction when observations show the upstream field to be highly variable. Simon et al. (2010a) have carried out such an investigation and classification using the Cassini magnetometer data. They not only characterised the upstream field as either current sheet-like or lobe-like, but also investigated: (a) the importance of vertical flapping motions on Titan's upstream field, (b) to what degree the idealised Voyager picture of a homogeneous constant upstream field is valid in the Cassini epoch, (c) could the length of time that Titan is exposed to a quasi-stationary field be estimated, (d) could groups of flybys from particular local time

sectors also be grouped by their environment type, and (e) the extent of any evidence for seasonal variations in Titan's magnetic environment. They also used data to calculate the average background field before and after closest approach (when embedded in quiet lobe-type fields) and calculate the stretch and sweep-back angles of the field in a similar fashion to Bertucci et al. (2009). For more details see Simon et al. (2010a), Table 5.

6.2.1 Length of Time Interval for Classification

Simon et al. (2010a) chose to analyse magnetometer data within ±8 hours of closest approach to Titan, somewhat longer than the ±3 hours selected by Rymer et al. (2009) and Wei et al. (2009). They highlighted the importance of choosing a time interval that reflects the characteristic time scales of Titan's local plasma interaction. This time scale is defined by the lifetime of "fossil" magnetic fields in Titan's ionosphere. Neubauer et al. (2006) discussed the formation of such fossil fields in terms of the slow and dense heavy ion plasma below an altitude of ∼1700 km "trapping" the upstream field as a fossil in the ionosphere. A magnetic flux tube which enters this region will remain trapped in this region until it can convect out of the ionosphere. Because the convection speeds may be as low as 100 $\mathrm{m\,s^{-1}}$ the flux tubes might be trapped for several hours. Thus, changes in the upstream field can be trapped in the ionosphere, potentially for several hours.

Observational evidence for such fossil fields was obtained during the T32 encounter (Bertucci et al. 2008) and this flyby scenario was also modelled by Ma et al. (2009). These studies suggested a lifetime of fossil fields of between 20 minutes and 3 hours; hence the selection of ±3 hours by Rymer et al. (2009) and Wei et al. (2009). Although, as Simon et al. (2010a) point out, the lifetime of fossil fields may exceed these estimates (obtained from a single flyby) and physically the longest possible time of residence of fossil fields in the ionosphere is controlled by the longest possible convection time through the ionosphere. Furthermore, this estimate was obtained from a particular type of scenario where Titan moves from the magnetosphere into the magnetosheath, carrying with it the magnetic memory of its previous magnetospheric environment. Simon et al. (2010a) point out that even when Titan is located continuously inside the magnetosphere, the fossil fields from partial or complete current sheet crossings may accumulate and "contaminate" Titan's ionospheric field. In support of a longer fossil field lifetime, Simon et al. (2010a) commented that in addition to the convection timescale, diffusion becomes more important in the deeper regions of the ionosphere which probably lengthens the fossil field lifetime, and that the T32 observations were from a particular location with respect to Titan and longer fossil field lifetimes should be found in the central wake compared to other locations.

In the absence of more detailed simulations and further data-driven case studies, Simon et al. (2010a) adopted a time range of ±8 hours from closest approach in order to account for the potentially longer fossil field lifetimes, but they paid particular attention to the data collected within ±3 hours. The selection of ±8 hours was also valuable for estimating the length of time during which Titan may be embedded in a quasi-stationary magnetospheric background. Also, and perhaps more importantly, data from a ±3 hour window have frequently been shown to contain an incomplete and possibly even a misleading snapshop of the large-scale magnetospheric processes involved in shaping Titan's magnetic environment. An example of this is a single current sheet crossing observed in a ±3 hour window might give the impression of a lone current sheet crossing with a quasi-stationary location away from the current sheet crossing, whereas the ±8 hour window might reveal the presence of significant periodic flapping motions.

Table 9 Classification criteria according to Simon et al. (2010a)

Classification	Mnemonic	Criteria
Magnetodisc lobe	L^N and L^S	$\lvert B_y\rvert/B > 0.6, \delta B_y/B \leq 0.05$
Lobe with current sheet features	L_{Sh}, L^N_{Sh}, L^S_{Sh}	$\lvert B_y\rvert/B > 0.6, 0.05 < \delta B_y/B \leq 0.2$
Current sheet	*Sh*	$\lvert B_y\rvert/B < 0.6, \delta B_y/B > 0.2$

6.2.2 Classification Scheme

Simon et al. (2010a) used 10 second averages of the high resolution magnetometer data in TIIS coordinates (Titan Interaction System—$\mathbf{e}_x$ is along the corotation direction, $\mathbf{e}_y$ is toward Saturn, and $\mathbf{e}_z$ is perpendicular to the equator). These data were binned into 1 hour intervals and the mean B_j $(j = x, y, z)$ and standard deviation δB_j for each field component and the total field strength B were calculated within each bin. The region near Titan, where the field was distorted by the local interaction between the plasma and the moon, was neglected; the exact identification of this region was challenging for some flybys.

Simon et al. (2010a) defined three basic upstream environment classes: magnetodisc lobes (L), lobe with current sheet features (L_{Sh}), and current sheet-like (Sh). Table 9 lists the criteria used to define these classes. For the magnetodisc lobe criteria the field is highly stretched and quiet (distorted by proximity to the current sheet) giving a dominant B_y and small δB_y. In the lobes there are often intervals that are distorted by current sheet fields which leads to the L_{Sh} classification, essentially allowing more variability δB_y than the lobe class. Current sheet fields are quite different and are identified by a weakened B_y and increased field fluctuations. In applying these criteria, Simon et al. (2010a) found a few cases where $\delta B_y/B \gg 0.2$ and $|B_y|/B \approx 0.95$ which are assigned to the Sh category. The robustness of this scheme and criteria was tested with respect to the time resolution of the data and the length of the binning intervals. They found that changes in the bin interval length (e.g., from 1 hour to 2 hours) didn't change the classification, but reducing the time resolution of the magnetometer data resulted in a loss of information. For example, short duration current sheet encounters would not be fully resolved by 1 minute averages and so lobe-type fields with minor current sheet signatures would be wrongly characterised as purely lobe-type fields.

Simon et al. (2010a) demonstrated the application of these classification criteria to three selected flybys, all of which contained frequent transitions between the different classification regimes, thus providing an excellent opportunity to test the classification technique. One of their tests of this scheme (T21) is reproduced in Fig. 23 and is discussed in Sect. 6.4.

In their classification scheme the order of the symbols indicate the temporal sequence of regions encountered by Cassini. The last symbol in the outbound column and the first symbol in the inbound column characterise the region within 3 hours of closest approach and thus are most directly comparable to the classification from Rymer et al. (2009).

6.2.3 Results

The classifications for TA–T62 inclusive are included in Table 11 along with the classifications from Rymer et al. (2009), Németh et al. (2011) and Garnier et al. (2010) (see also Sect. 6.4 for a discussion of these combined classifications). Quiet lobe-type fields both inbound and outbound were only observed on 10 flybys out of 62 and only nine of these were lobe-type fields of the same polarity (sign of B_y). Current sheet-type fields both inbound

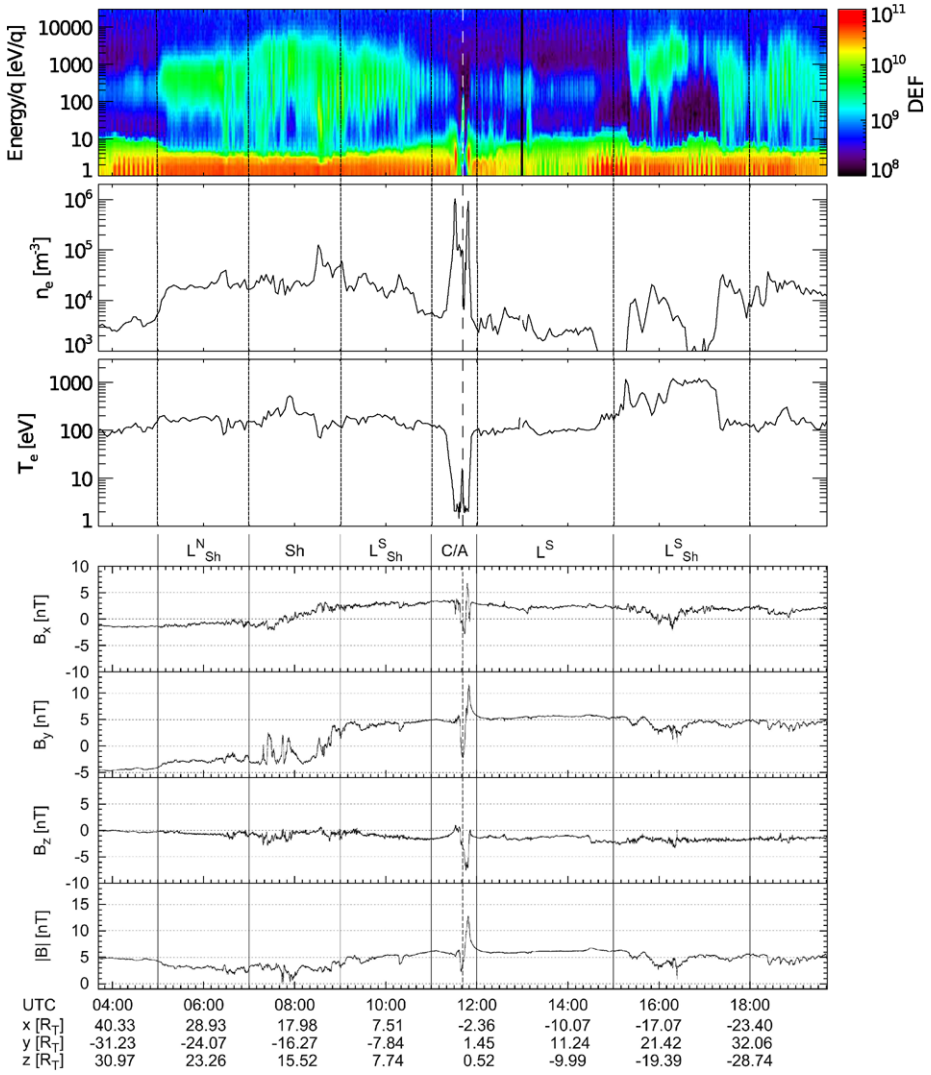

Fig. 23 Magnetometer data from Simon et al. (2010a) (their Fig. 7) evaluating their upstream classification environment for the T21 flyby compared with electron spectra and moments for the same period

and outbound were observed on 22 flybys out of 62. Two Titan encounters occurred near the magnetopause.

The flybys that occurred in the post-midnight magnetosphere (T16–T24) showed that a mixture of lobe and current sheet fields were found above Titan's orbital plane, whereas the field southward of the moon mainly belonged to the lobe category, supporting the warped magnetodisc picture of Arridge et al. (2008b). From this model one would expect that the current sheet near equinox would be flat and unwarped and so Titan should encounter pure current sheet signatures with a vanishing B_y component. However the observations from T52–T62 presented a very different view showing that the picture of a quasi-stationary magnetodisc is not suitable for understanding Titan's magnetic environment near equinox. The

Table 10 Classification of Titan flybys according to three protons flux models, based on the LEMMS channels A0, A1 and A2. From Garnier et al. (2010) and Table 11 (this work). For entries from Table 11 where the classification is joint, for example high/medium, we take the highest flux classification for this table, for example high/medium is recorded as high for this table

	Low flux	Medium flux	High flux
Titan flybys	3 7 8 16 22 25	A B 5 9 12 13 14 15 23 26 29 30 34 37 38 40 41 45 46 47 49 54 58 59 62	6 10 11 17 18 19 20 21 27 28 31 32 33 35 36 39 42 43 44 48 50 51 52 53 55 56 57 61

entire series of flybys were found to contain frequent current sheet crossing signatures so that the highly stretched lobe fields do not play a role in the moon's local plasma interaction. Instead, Titan is exposed to alternating lobe polarities separated by current sheet crossings. In the dawn magnetosphere (T4–T7) the bowl-shaped model of the magnetodisc is confirmed by the generally lobe-type fields encountered by Cassini. In this regard the T4 encounter is of particular note as it is among the few encounters where lobe-type fields of the same polarity were detected both before and after the flyby.

In the noon magnetosphere, flybys of Titan have typically been associated with immersion in the current sheet (Bertucci et al. 2009; Simon et al. 2010a) and the near noon encounters T25–T33 (post-noon) and T35–51/TA–T3 (pre-noon) show that the magnetic environment near noon is completely different from that near midnight. Although fields near noon are clearly more dipolar than the nightside, the Voyager 1 picture of Titan being embedded in a constant quasi-dipolar field is not valid due to the high level of variability. The presence of current sheet fields near local noon is exactly what was expected from near-equinox flybys T52–T62 in the pre-midnight magnetosphere but which was not observed. Simon et al. (2010a) noted that current sheet crossings observed in the nightside magnetosphere appear much more rapid compared to noon which suggests that the current sheet is thinner on the nightside. Thus the larger thickness of the dayside plasma sheet may also play a role in the field variability observed near noon.

In many cases current sheet fields were observed on one side of the encounter with lobe-type on the other. In such strongly variable situations fossil magnetic fields will be important in the magnetometer data collected near closest approach. Furthermore the large-scale features of Titan's pick up tail will also be strongly disrupted by such an inhomogeneous environment.

6.3 Energetic Particle Classification: Garnier et al. (2010)

Garnier et al. (2010) also discussed the flux spectra of 27–255 keV protons, during all magnetospheric crossings of the Titan orbit by the Cassini spacecraft before 2008. This revealed a trimodal distribution when frequencies are given as a function of differential flux intervals: two main peaks appear with an order of flux magnitude between them, and a third one can be considered, for low flux and background dominated events. Table 10 taken from Garnier et al. (2010) shows a classification of Titan flybys according to three proton flux modes, based on the LEMMS channels A0, A1 and A2. Two arbitrary limits, $l1$ and $l2$, bound the low ($F < l1$), medium ($l1 < F < l2$) and high ($F > l2$) flux cases, with different values for each of the A0, A1 and A2 LEMMS channels. The $l1$ limits are equal to 8, 3.6 and 0.5 $cm^{-2}\ s^{-1}\ sr^{-1}\ keV^{-1}$ for A0, A1, and A2 respectively, and the $l2$ limits are equal to 57.5, 21.5, and 8.8 $cm^{-2}\ s^{-1}\ sr^{-1}\ keV^{-1}$.

These classifications are also repeated in Table 11 where we combine the classification schemes of Rymer et al. (2009), Simon et al. (2010a), Németh et al. (2011) and Garnier

Table 11 Compilation of classifications from Rymer et al. (2009), Simon et al. (2010a), Garnier et al. (2010), and Németh et al. (2011). The magnetic field codes indicate: *Sh* (current sheet), L^N (northern lobe), L^S (southern lobe), L^N_{Sh} (northern lobe with brief current sheet fields), L^S_{Sh} (southern lobe with brief current sheet fields), Sh^N_L (current sheet with brief northern lobe), Sh_{L^S} (current sheet with brief southern lobe), *Msh* (magnetosheath), * (unclassified, perhaps extended features from the Titan interaction). The electron codes indicate: PS (plasma sheet), LL (lobe-like), BM (bimodal), MS (magnetosheath), Mx (mixed, with components in brackets), U (unclassified). The ion classification follows the same as for the electrons except HR indicates "heavy-rich" events. The energetic proton flux classification is discussed in Sect. 6.4 and Table 5

Flyby	Date	SLT	Subsolar latitude	Magnetic field		Plasma		Energetic protons
				Inbound	Outbound	Electrons	Ions	
TA	30 Oct 2004	10.6	−23.2°	*Msh*, *Sh*	L^S_{Sh}, *Sh*	PS	PS	Medium
TB	13 Dec 2004	10.5	−22.8°	*Sh*	L^S_{Sh}	Mx (PS, LL)	Mx	Medium
TC			N/A	N/A	N/A	N/A	N/A	N/A
T3	15 Feb 2005	10.3	−22.3°	L^S_{Sh}	*Sh*	LL (PS, BM)	LL	Low
T4	31 Mar 2005	5.3	−22.1°	L^S_{Sh}	L^S_{Sh}	LL (PS)	LL	High
T5	16 Apr 2005	5.3	−22.0°	L^S_{Sh}, *Sh*	L^S_{Sh}	PS	PS	Medium
T6	22 Aug 2005	5.0	−20.7°	L^S_{Sh}	Sh_{L^S}, L^S_{Sh}	Mx (LL, BM)	Mx	High
T7	07 Sep 2005	5.0	−20.5°	N/A	N/A	N/A	N/A	Low
T8	28 Oct 2005	9.3	−19.6°	L^S_{Sh}	L^S_{Sh}, *Sh*, L^S_{Sh}	LL	LL	Low
T9	26 Dec 2005	3.0	−19.1°	L^S_{Sh}, (*)	L^S_{Sh}	PS	PS	Medium
T10	15 Jan 2006	8.5	−18.8°	L^S_{Sh}	Sh_{L^S}	LL	LL	High
T11	27 Feb 2006	1.1	−18.2°	L^S, (*)	L^S	PS	PS	High
T12	19 Mar 2006	6.4	−18.2°	*Sh*, L^S_{Sh}	L^S_{Sh}	Mx (PS, LL)	Mx	Medium
T13	30 Apr 2006	23.2	−17.3°	L^S_{Sh}, *Sh*	*Sh*, L^S	PS	PS	Medium
T14	20 May 2006	4.4	−17.4°	L^S_{Sh}	L^S, L^S_{Sh}	LL (BM, LL)	LL	Medium
T15	02 Jul 2006	21.2	−16.6°	L^S_{Sh}, *Sh*	*Sh*, L^S_{Sh}	PS (BM)	PS	Medium
T16	22 Jul 2006	2.4	−16.5°	(*)	L^S_{Sh}	U (PS)	U	Low
T17	07 Sep 2006	2.3	−15.8°	*Sh*	L^S	U (BM)	U	High
T18	23 Sep 2006	2.3	−15.6°	L^N_{Sh}, *Sh*, L^S	L^S_{Sh}	LL	LL	High

Table 11 (*Continued*)

Flyby	Date	SLT	Subsolar latitude	Magnetic field		Plasma		Energetic protons
				Inbound	Outbound	Electrons	Ions	
T19	09 Oct 2006	2.2	−15.4°	L^S_{Sh}, (*)	*Sh*, L^S_{Sh}	PS (BM, U)	PS	High
T20	25 Oct 2006	2.2	−15.2°	*Sh*	L^S, L^S_{Sh}	Mx (PS, LL)	Mx	High
T21	12 Dec 2006	2.1	−14.5°	L^N_{Sh}, *Sh*, L^S_{Sh}	L^S, L^S_{Sh}	Mx (PS, LL)	Mx	High
T22	28 Dec 2006	2.0	−14.3°	L^N_{Sh}, *Sh*, L^S	*Sh*, L^S_{Sh}	Mx (PS, MS, LL, BM)	U	Low
T23	13 Jan 2007	2.0	−14.1°	(*)	L^S	PS (BM)	PS	Medium
T24	29 Jan 2007	1.9	−13.8°	L^N_{Sh}, *Sh*	L^S_{Sh}	Mx (PS, LL)	Mx	High
T25	22 Feb 2007	13.9	−13.5°	Data gap, *Sh*	*Sh*	U	U	Low
T26	10 Mar 2007	13.8	−13.3°	L^S_{Sh}	*Sh*	BM (PS)	HR	Medium
T27	26 Mar 2007	13.8	−13.1°	L^S_{Sh}, *Sh*	*Sh*	U (BM)	Mx	High
T28	10 Apr 2007	13.7	−12.8°	*Sh*	*Sh*	Mx (LL, BM, U)	Mx	High
T29	26 Apr 2007	13.7	−12.6°	*Sh*	*Sh*, *MSh*, *Sh*	PS (MS)	PS	Medium
T30	12 May 2007	13.6	−12.4°	Sh_{L^S}, *Sh*	*Sh*	Mx (LL, BM, U)	Mx	Medium
T31	28 May 2007	13.6	−12.1°	*Sh*	*Sh*	BM (PS)	HR	High
T32	13 Jun 2007	13.6	−11.9°	*Msh*, *Sh*	*Msh*	MS (PS)	MS	High
T33	29 Jun 2007	13.6	−11.7°	*Sh*	*Sh*	PS (BM)	PS	High
T34	19 Jul 2007	18.8	−11.5°	*Sh*	*Sh*	PS (BM)	PS	Medium
T35	31 Aug 2007	11.5	−10.6°	*Sh*, L^S_{Sh}	*Sh*, L^S_{Sh}	U (BM)	Mx	High
T36	02 Oct 2007	11.5	−10.1°	*Sh*	*Sh*	PS (BM, MS)	PS	High
T37	19 Nov 2007	11.4	−9.4°	*Sh*, L^S_{Sh}	Data gap	U (BM)	U	Medium
T38	05 Dec 2007	11.4	−9.2°	*Sh*	*Sh*	U (BM)	Mx	Medium
T39	20 Dec 2007	11.4	−8.9°	*Sh*	*Sh*	PS (MS)	PS	High
T40	05 Jan 2008	11.3	−8.7°	(*)	*Sh*	BM (PS, LL, U)	HR	Medium

Table 11 (*Continued*)

Flyby	Date	SLT	Subsolar latitude	Magnetic field		Plasma		Energetic protons
				Inbound	Outbound	Electrons	Ions	
T41	22 Feb 2008	11.2	−8.0°	*Sh*, L^S_{Sh}	L^S_{Sh}, *Sh*	LL	LL	Medium/Low
T42	25 Mar 2008	11.1	−7.5°	*Sh*, *Msh*, *Sh*	*Msh*, *Sh*	MS (PS)	MS	High
T43	12 May 2008	11.0	−6.7°	L^S_{Sh}	L^S_{Sh}, *Sh*	LL (BM)	Mx	High/Medium
T44	28 May 2008	10.9	−6.5°	*Sh*	*Sh*	PS	PS	High
T45	31 Jul 2008	10.7	−5.5°	L^S_{Sh}	*Sh*	U (BM)	U	Medium
T46	03 Nov 2008	10.5	−4.0°	L^S_{Sh}	*Sh*	BM (LL)	HR	Medium
T47	19 Nov 2008	10.4	−3.8°	L^S_{Sh}, *Sh*	*Sh*	BM (LL, U)	HR	Medium
T48	05 Dec 2008	10.4	−3.6°	L^S_{Sh}, *Sh*	*Sh*	U (BM)	U	High/Medium
T49	21 Dec 2008	10.3	−3.3°	*Sh*	*Sh*	PS	PS	Medium
T50	07 Feb 2009	10.2	−2.6°	L^S_{Sh}, *Sh*	*Sh*	Mx (BM, PS, U)	Mx	High
T51	27 Mar 2009	10.1	−1.8°	*Sh*	*Sh*	PS (BM, U)	PS	High
T52	04 Apr 2009	22.1	−1.7°	L^N_{Sh}, *Sh*	*Sh*, L^S_{Sh}	PS (BM)	PS	High
T53	20 Apr 2009	22.0	−1.5°	L^N_{Sh}, *Sh*	L^S_{Sh}, L^S	PS	PS	High
T54	05 May 2009	22.0	−1.2°	L^N_{Sh}, *Sh*, L^S_{Sh}	L^N_{Sh}, *Sh*, L^S	Mx (LL, PS)	Mx	Medium
T55	21 May 2009	22.0	−1.0°	L^N_{Sh}, *Sh*	*Sh*, L^S_{Sh}, L^S	PS (BM)	PS	High/Medium
T56	06 Jun 2009	21.9	−0.7°	L^N_{Sh}, *Sh*, L^S_{Sh}	*Sh*, L^S_{Sh}	Mx (LL, PS)		High
T57	22 Jun 2009	21.9	−0.5°	L^N, L^N_{Sh}, *Sh*	L^S_{Sh}	Mx (BM, PS)		High/Medium
T58	08 Jul 2009	21.8	−0.2°	L^N_{Sh}, *Sh*, L^S_{Sh}	*Sh*, L^N_{Sh}, *Sh*, L^S_{Sh}	PS (BM)		Medium
T59	24 Jul 2009	21.8	0.0°	L^N, *Sh*	L^S_{Sh}, *Sh*	Mx (PS, BM, LL)		Medium
T60	09 Aug 2009	21.7	0.2°	*Sh*	*Sh*	N/A		N/A
T61	25 Aug 2009	21.7	0.5°	*Sh*, L^N_{Sh}, *Sh*	L^S_{Sh}, *Sh*, L^N_{Sh}	LL (PS, BM)		High/Medium
T62	12 Oct 2009	21.6	1.2°	L^S_{Sh}, *Sh*, L^N_{Sh}	*Sh*, L^S_{Sh}, *Sh*	Mx (LL, BM, PS)		Medium

et al. (2010). One can see that the plasma classifications do not correspond exactly to the energetic proton classes. In particular the mean energetic proton fluxes during the flybys identified by Rymer et al. (2009) as plasma sheet or lobe-like environments differ in their fluxes by a factor of between 5 and 10.

6.4 Combined Classifications

In Table 11 we combine the classifications from Rymer et al. (2009) and the ion data from Németh et al. (2011) (Sect. 6.1), Simon et al. (2010a) (Sect. 6.2) and Garnier et al. (2010) (Sect. 6.3) to provide a combined reference for the classification of the upstream environment Titan encounters. This table also exposes differences between these classification schemes, a particular example of which is T11 where the electron classification suggests the encountered occurred whilst Titan was in the plasma sheet (Rymer et al. 2009) with high energetic proton fluxes (Garnier et al. 2010) but from the magnetic point of view the encounter occurred in the southern lobe (Simon et al. 2010a). However, in performing such comparisons one must bear in mind the different time ranges used to establish the classification for each flyby and that the classifications from Rymer et al. (2009) are only strictly comparable with the "inner" classifications from Simon et al. (2010a).

In Fig. 24 we show the magnetic field and electron data for the T11 encounter to highlight the origins of this discrepancy. The field structure in the regions beyond ± 3 of closest approach shows evidence of lobe-like fields confirming the L^S classification of Simon et al. (2010a). Although the field orientation is relatively steady there are persistent field fluctuations (almost transverse to the field and thus present in the B_θ and B_φ components). The plasma data in these regions shows evidence of steady 100 eV electron populations, characteristic of the plasma sheet (Arridge et al. 2009b) but at fairly low densities. Jointly, the field and plasma observations thus suggest that outside of ± 3 hours of closest approach the spacecraft was located in the outer layers of the plasma sheet (Arridge et al. 2009b) and not in the lobes. Two intervals where the spacecraft probably closely approached the lobes were around ≈ -6 hours inbound and ≈ 4 hours outbound. However, in both these cases the ELS instrument still recorded significant fluxes indicating that the spacecraft was probably on closed field lines at a large field-aligned distance from the centre of the plasma sheet and thus not on open field lines.

Inside the ± 3 hour window adopted by Rymer et al. (2009) the inbound data shows evidence of the plasma sheet, confirming their identification and both the B_r and B_φ components of the field weaken in anti-phase demonstrating that the spacecraft approaches the current sheet. Therefore the field could be characterised as current sheet within 3 hours inbound. The field perturbation observed roughly one hour after closest approach is reminiscent of a current sheet approach, with B_r and B_φ components falling to near zero values coincident with intensifications in the electron flux, although the perturbation is sufficiently close to the interaction that one cannot be certain of its origin. After this perturbation, between 2 and 3 hours outbound, both the field and plasma are indicative of outer plasma sheet or close to the southern lobe. Therefore this pass exposes difference in the classification schemes and the importance of structure on timescales of one hour.

Encounters T8 and T10 are lobe-like according to the classification of Rymer et al. (2009) but the energetic proton fluxes from the classification of Garnier et al. (2010) are very different between the two passes. Furthermore the classification from Simon et al. (2010a) shows the presence of lobe fields with the appearance of current sheet fields. This latter point is supported by the electron data which shows the transient appearance of plasma sheet electrons and suggests that Cassini is located in the outer plasma sheet/lobe interface region. An

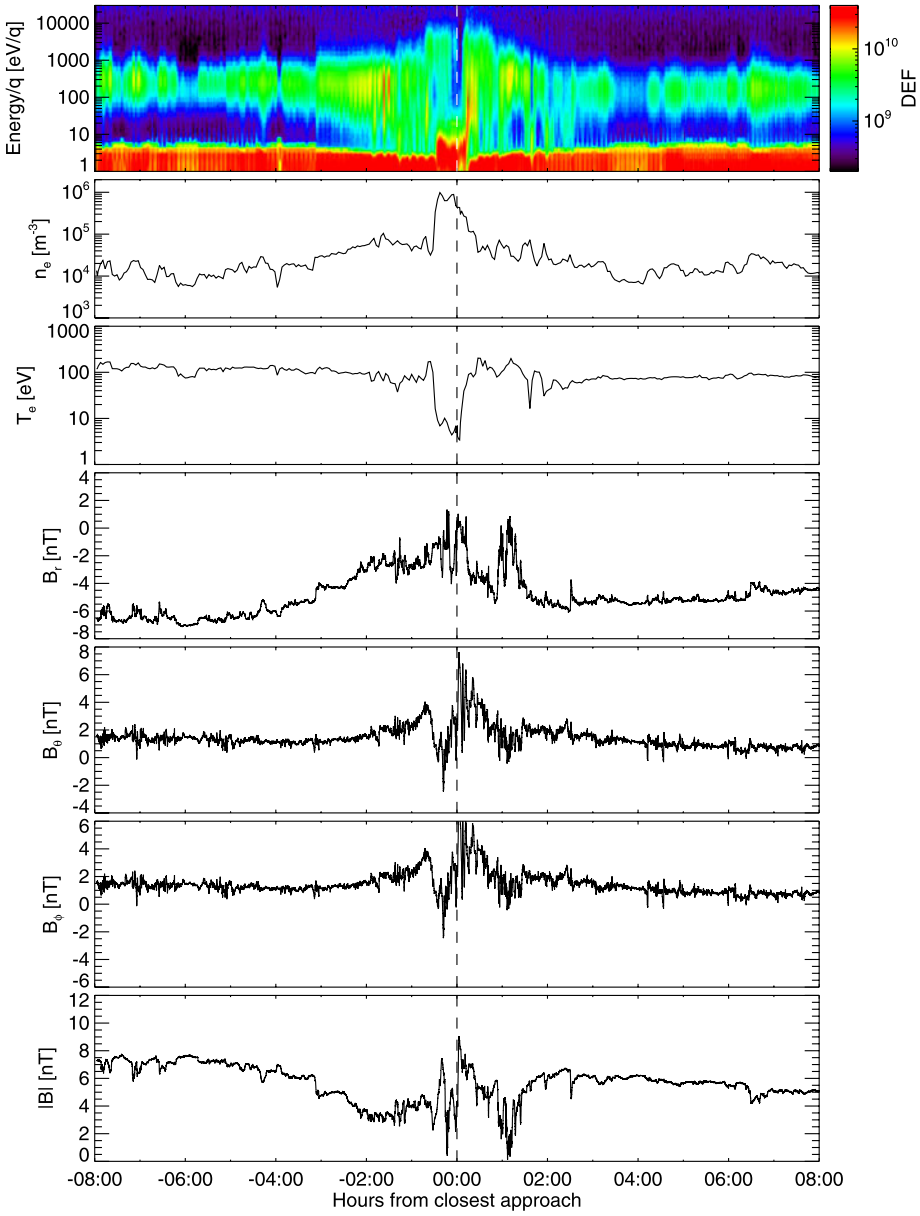

Fig. 24 Electron and magnetic field data illustrating the upstream environment during Cassini's T11 flyby of Titan. The *first panel* shows a energy-time spectrogram of electron fluxes measured by CAPS/ELS in units of differential energy flux (eV m^{-2} s^{-1} sr^{-1} eV^{-1}), the *second* and *third panels* show electron number densities and temperatures estimated from the CAPS/ELS spectra, panels *four–six* show three components of the magnetic field in spherical polar KRTP coordinates, and the *final panel* shows the field magnitude. The *central dashed line* indicates closest approach to Titan. The whole plot covers the interval considered by Simon et al. (2010a)

examination of the electron data out to ±8 hours from closest approach shows that energetic electrons with an energy of ∼1 keV are observed on both T8 and T10. Such electron populations were observed in the magnetotail by Arridge et al. (2009b) and attributed to magnetospheric dynamics and might suggest that the magnetosphere was more disturbed during these flybys. This does not explain the relative difference in the energetic proton flux between T8 and T10 which may be due to the exact intervals used by Garnier et al. (2010) and how they relate to those used by Rymer et al. (2009) and Simon et al. (2010a). This indicates the fundamental importance of understanding the exact time intervals used by different classification schemes, and for future classifications to use multiple datasets.

Simon et al. (2010a) tested their classification scheme for T21 and in Fig. 23 we reproduce their figure and also include electron spectrometer data for comparison. For this flyby, Rymer et al. (2009) consider this to be a mixed category with the appearance of both plasma sheet and lobe-like plasma. Cassini starts the interval in a lobe-type regime as confirmed by the magnetometer and electron data. From the significant electron fluxes we can see that Cassini is probably on closed field lines mapping into the plasma sheet but still defined as lobe since the spacecraft is probably many field-aligned scale heights from the centre of the plasma sheet. Between 0500 and 0700 UT the classification criteria suggests that Cassini is in a lobe-type environment with some current sheet signatures, but a comparison with the plasma data shows that the environment is essentially the outer part of the plasma and current sheet, possibly well outside of the bulk of the current carrying region. The current sheet region between 0700 and 0900 UT is corroborated by the electron data, with evidence of cold bimodal distributions in the centre of the current sheet near 0830 UT. Similar to the L^N_{Sh} region, the L^S_{Sh} region from 0900 to 1100 UT might be more properly characterised as the outer plasma sheet but outside of the bulk of the current layer. The LS lobe-type region between 1200 and 1500 UT is consistent between the two datasets. Although the region between 1500 and 1800 UT is classified as L^S_{Sh} the electron data suggests evidence for magnetospheric dynamics with hot electron populations rather than a simple encounter with the plasma sheet although there is a clear change in the plasma properties at 1730 UT back to nominal plasma sheet conditions. Regarding the statement from Simon et al. (2010a) that current sheet may be thinner on T21 compared to T20, the current sheet on T21 is clearly filled with cold plasma which is absent on most of the current sheet signatures on T20. Such an abundance of cold plasma may result in a thinner sheet thus supporting the suggestion of Simon et al. (2010a).

We envisage that this table will be useful in understanding the effects of the upstream environment on Titan's magnetospheric interaction and atmosphere. Westlake et al. (2011) compared the temperature of Titan's atmosphere to the classification from Rymer et al. (2009). The list in Table 11 will be useful in further studies of this nature and enables effects on Titan's atmosphere to be compared with more than one classification. This list will provide a temporary multi-instrumental classification of Titan's environment until such a true classification is available. For such uses it is important to recognise the different time intervals used for each classification scheme.

7 Discussion

The studies thus far carried out into Titan's upstream environment show a picture of Titan generally located below the centre of the magnetodisc in agreement with the displacement inferred by Arridge et al. (2008b). This implies that for most of Titan's orbit the moon is located in fields typical of the southern magnetodisc lobe which are depleted of thermal plasma

compared to the centre of the plasma sheet. Such a scenario will modulate the particle energy input into Titan's ionosphere such that inside the plasma sheet the energy deposition rate will be high, whereas in the lobes it will be low. The noon and late dusk sectors are exceptions to this rule where the fields are generally found to be less stretched and more variable. In the noon sector the solar wind is thought to contribute to the dipolarisation of the dayside field (e.g. Arridge et al. 2008c) thus it is more likely that Titan will be immersed in the plasma sheet that has thickened in response to the dipolarisation. It must be pointed out that thus far most Cassini observations of Titan have been carried out during Saturn's southern summer season. All the Titan encounters up to T60 were during this season, with T60 and T61 bracketing equinox on 10 August 2009. The findings described above are consistent with and reflect this seasonal bias. In Sects. 7.1.2 and 7.2.4 we comment on the effect the changing seasons will have on Titan's upstream environment.

In the late dusk sector there are intervals of clear swept-forward fields that are characteristic of super-corotating plasma. This intriguing feature is not associated with Titan flybys and significantly complicates the interpretation of the moon's interaction, especially if concurrent changes in the plasma flow are observed. The probability of Titan being exposed to these different scenarios depends on SLT because of the asymmetrical shape of Saturn's "bowl-shaped" magnetodisc and the confining effect of the solar wind (which depends on the solar wind pressure) and the phase of Saturn's global magnetospheric periodicities. Variations in ion composition have been found as a function of magnetic latitude producing large changes in dynamic pressure as the plasma sheet moves vertically with respect to Titan. Cold dense ions and bimodal electron distributions are often found at or near the centre of the current sheet and are thought to be trapped deep within the centrifugal potential well produced by the rapid rotation of the plasma sheet.

The picture of a quasi-static upstream environment where either the spacecraft is in a constant homogeneous lobe or current sheet field configuration does not appear to be valid in the Cassini era. The picture now emerging from various studies is that of a current and plasma sheet in constant motion, with both long (near the planetary rotation period) and short period (due to magnetospheric dynamics driven by internal processes and solar wind variability) motions. This indicates the fundamental importance of understanding the exact time intervals used by different classification schemes. The various discrepancies between different classification schemes highlight the need to develop categorisations which take advantage of the multiple datasets available from Cassini and the unique collaboration within the magnetospheric and plasma science community. That being said, from these classifications one can see that both electron (Rymer et al. 2009) and magnetic field (Simon et al. 2010a) classifications suggest that Titan was located in the current/plasma sheet near closest approach on flybys: TA, T5, T13, T15, T19, T29, T33, T34, T36, T39, T44, T49, T50, T51, T52, T53 and T55. Similarly, both classifications support a lobe-type flyby on T4, T8, T14, T18, T41, T43 and T54 and transitions between types on encounters TB, T12, T20, T21, T22, and T24 (Simon et al. 2010a).

From published statistics on the solar wind properties, the probabilities of finding Titan in the magnetosheath or solar wind do not compare favourably with the observed frequencies. Some authors (e.g. Wei et al. 2009) have suggested that this is due to Titan's effect on the magnetosphere, providing additional mass loading and magnetospheric pressure which contributes to standing off the solar wind to a larger degree than would otherwise be found if Titan was absent. Future work on the question of Titan's effect on the magnetosphere is clearly needed.

7.1 Pre-Cassini Open Questions on the Effects of Upstream Conditions on Titan

Before the arrival of Cassini-Huygens at Saturn, Blanc et al. (2002) reviewed the state of the art in magnetospheric and plasma science understanding at Saturn and posed a number of open questions relating to the interaction between Titan and Saturn's magnetosphere. We now consider the relevant open questions in the light of the studies presented and reviewed in this section.

7.1.1 What Is the Variability of Titan's Ionosphere, and to What Extent Is It Controlled by Magnetospheric Effects (Importance and Variability of Energetic Charged Particles as Plasma Sources, of Its Magnetisation by the Surrounding Plasma Flow, etc.)?

The observed variability in Titan's upstream environment and in particular its dependence on Saturn local time has made it difficult to understand to what extent the ionosphere is controlled by magnetospheric effects. However it is known that the magnetospheric thermal electrons determine the structure of the nightside ionosphere (Agren et al., 2009) and that energetic ions may create ionospheric layers at low altitudes (Cravens et al. 2008). Future work and future Titan flybys are required to shed further light on the control of Titan's ionosphere.

7.1.2 What Is the Basic Geometry of the Interaction of Titan's Atmosphere with Saturn's Magnetised Plasma Flow? How Does It Vary with Changing Conditions in the Upstream Flow Characteristics and with the Geometry of Local Ionisation Sources?

The first Cassini Titan flyby showed that Titan's induced magnetosphere was rotated about its axis in response to deviations in the upstream field away from the idealised north-south Voyager 1 case (e.g., Backes et al. 2005). The tail was also found to be displaced due to non-azimuthal flows during the T9 flyby (e.g., Simon et al. 2007). The effects of radial and axial (vertical) flows and radial and azimuthal magnetic fields on the orientation of the tail are now reasonably well established. The variability in upstream conditions have made it difficult to assess the role played by the geometry of local ionisation sources (particularly since variability in the upstream conditions also varies with Saturn local time) but work in this area is ongoing. The ongoing Cassini mission will show us how the geometry of Titan's magnetospheric interaction changes as Saturn's magnetosphere transitions from southern hemisphere summer to northern hemisphere summer during the Cassini Solstice Mission.

7.2 Open Questions

From these questions and the theoretical and observational work discussed in this paper we might pose further questions to be addressed in the Cassini Solstice Mission and/or future missions to Titan and the Saturn system.

7.2.1 Periodicities in Upstream Conditions: Do They Simply Produce Periodic Modulations in the Induced Magnetosphere or Are There Resonances or Non-linearities That Produce More Profound Changes?

Given that Titan may be periodically exposed to alternating high- and low-flux plasma environments, are there some periods that can drive the Titan atmosphere-exosphere-ionosphere system more strongly. Or can small changes in the incident particle and energy flux dramatically change Titan's induced ionosphere?

7.2.2 Does Titan Exert Some Level of Control on the Vertical Motion of the Current Sheet?

Simon et al. (2010a) have shown that during encounters T17, T20, T24 the background conditions abruptly changed from current sheet-like to lobe-like around closest approach. Magnetohydrodynamic modelling results (Kidder et al., private communication) support the idea that Titan can perturb the location of the current sheet up to large distances from Titan, although further work by Simon et al. (2010b) appears to contradict this. Further attention from observations and modelling is required to shed light on this.

7.2.3 How Does Titan Influence Its Local and Global Magnetospheric Environment?

Observational (Wei et al. 2009; Russell et al. 2008), and modelling studies (Winglee et al. 2009) have suggested that Titan influences the magnetosphere, perhaps by introducing additional mass into the system and modifying local force balance. What are the exact physical processes involved in this situation and how do they vary with local time, global magnetospheric periodicities and with the exact upstream conditions?

7.2.4 How Does Titan's Magnetospheric Background Vary with Season?

Cassini measurements from SOI through to August 2009 provide a very valuable dataset for evaluating the seasonal change in Titan's upstream environment. Simon et al. (2010a) have searched this dataset for evidence of such effects and have identified the effect of the change in warp of the current sheet (also corroborated by Sergis et al. 2011). As Saturn moves away from equinox and approaches northern summer solstice we should expect that Titan will be exposed to more northern lobe-type fields, and the impinging particle fluxes should reduce compared to equinox. The amplitude and period of the oscillation may also change from equinox to solstice (e.g., Sergis et al. 2011).

But in general how does the magnetospheric background change with time? In terms of upstream conditions there does not seem to be a Cassini Titan encounter similar to the Voyager 1 encounter, does this imply that the Voyager 1 flyby occurred during a special period, perhaps hinting at secular changes in the magnetosphere? The Cassini Solstice Mission (CSM) will be invaluable in evaluating these effects as Saturn moves to northern summer solstice.

7.3 Future Work

Studies of Titan's upstream environment have shown it to be highly variable and one focus of future work should be to attempt to evaluate the effects of such variability on Titan's induced magnetosphere. Simon et al. (2008) and Simon and Motschmann (2009) have presented the first attempts at a series of local hybrid simulations, exposing Titan to non-stationary magnetospheric environment and alternative approach has been developed by Winglee et al. (2009) who embed a Titan simulation within a global simulation of Saturn's magnetosphere. These studies should be continued to address the variability issues discussed in Sects. 2 and 3.

Future work aimed at developing more detailed and multi-instrumental upstream environment classifications is also necessary with rigorous quantitative connections to a statistical understanding of the environment.

Acknowledgements The authors thank the staff at the International Space Science Institute for their hospitality. CSA wishes to thank A. Wellbrock and H.T. Smith for useful discussions and assistance. The authors would like to thank N. Krupp for use of MIMI-LEMMS data, M. Kusterer (JHU/APL) for assistance with the data reduction, M. Dougherty for the use of MAG data, and S.M. Krimigis for MIMI data. We are grateful to Cassini/MIMI and Cassini/CAPS colleagues for comments that improved this study. We thank the many individuals at JPL, NASA, ESA and numerous PI and Co-I institutions who have contributed to making the Cassini project an outstanding success. CSA was supported by an STFC post-doctoral fellowship under grant ST/G007462/1, AMR was supported by NASA-JPL contract NAS5-97271 between the NASA Goddard Space Flight Center and Johns Hopkins University for the MIMI investigation and by NASA-JPL contract 1243218 for the CAPS program at the Southwest Research Institute. Work at JHU/APL was supported by NASA and by subcontracts at the UMD and the Academy of Athens. The German contribution of MIMI/LEMMS was financed by the Bundesministerium für Bildung und Forschung through the Deutsches Zentrum für Luft und Raumfahrt and by the Max-Planck-Gesellschaft. The French co-authors acknowledge support from the French space agency CNES. The authors acknowledge the support of EUROPLANET RI project (Grant agreement no.: 228319) funded by EU; and also the support of the International Space Science Institute (Bern). CAPS operations at Mullard Space Science Laboratory, UCL, and MAG operations at Imperial College London are supported in the UK by the Science and Technology Facilities Council and the European Space Agency.

References

N. Achilleos, C. Bertucci, C.T. Russell, G.B. Hospodarsky, A.M. Rymer, C.S. Arridge, M.E. Burton, M.K. Dougherty, S. Hendricks, E.J. Smith, B.T. Tsurutani, Orientation, location, and velocity of Saturn's bow shock: initial results from the Cassini spacecraft. J. Geophys. Res. **111**, A03201 (2006). doi:10.1029/2005JA011297

N. Achilleos, C.S. Arridge, C. Bertucci, C.M. Jackman, M.K. Dougherty, K.K. Khurana, C.T. Russell, F.J. Crary, D.T. Young, Large-scale dynamics of Saturn's magnetopause: observations by Cassini. J. Geophys. Res. **113**, A11209 (2008). doi:10.1029/2008JA013265

M.H. Acuña, J.E.P. Connerney, P. Wasilewski, R.P. Lin, K.A. Anderson, C.W. Carlson, J. McFadden, D.W. Curtis, D. Mitchell, H. Reme, C. Mazelle, J.A. Sauvaud, C. d'Uston, A. Cros, J.L. Medale, S.J. Bauer, P. Cloutier, M. Mayhew, D. Winterhalter, N.F. Ness, Magnetic field and plasma observations at Mars: initial results of the Mars Global Surveyor mission. Science **29**(5357), 1676–1680 (1998). doi:10.1126/science.279.5357.1676

N. André, A.M. Persoon, J. Goldstein, P. Louarn, G.R. Lewis, A.M. Rymer, A.J. Coates, W.S. Kurth, E.C. Sittler, M.F. Thomsen, F.J. Crary, M.K. Dougherty, D.A. Gurnett, D.T. Young, Magnetic signatures of plasma-depleted flux tubes in the Saturnian inner magnetosphere. Geophys. Res. Lett. **34**, L14108 (2007). doi:10.1029/2007GL030374

N. André, M. Blanc, S. Maurice, P. Schippers, E. Pallier, T.I. Gombosi, K.C. Hansen, D.T. Young, F.J. Crary, S. Bolton, E.C. Sittler, H.T. Smith, R.E. Johnson, R.A. Baragiola, A.J. Coates, A.M. Rymer, M.K. Dougherty, N. Achilleos, C.S. Arridge, S.M. Krimigis, D.G. Mitchell, N. Krupp, D.C. Hamilton, I. Dandouras, D.A. Gurnett, W.S. Kurth, P. Louarn, R. Srama, S. Kempf, H.J. Waite, L.W. Esposito, J.T. Clarke, Identification of Saturn's magnetospheric regions and associated plasma processes: synopsis of Cassini observations during orbit insertion. Rev. Geophys. **46**, RG4008 (2008). doi:10.1029/2007RG000238

D.J. Andrews, E.J. Bunce, S.W.H. Cowley, M.K. Dougherty, G. Provan, D.J. Southwood, Planetary period oscillations in Saturn's magnetosphere: phase relation of equatorial magnetic field oscillations and Saturn kilometric radiation modulation. J. Geophys. Res. **113**, A09205 (2008). doi:10.1029/2007JA012937

C.S. Arridge, N. Achilleos, M.K. Dougherty, K.K. Khurana, C.T. Russell, Modeling the size and shape of Saturn's magnetopause with variable dynamic pressure. J. Geophys. Res. **111**, A11227 (2006). doi:10.1029/2005JA011574

C.S. Arridge, N. André, N. Achilleos, K.K. Khurana, C.L. Bertucci, L.K. Gilbert, G.R. Lewis, A.J. Coates, M.K. Dougherty, Thermal electron periodicities at 20 R_S in Saturn's magnetosphere. Geophys. Res. Lett. **35**, L15107 (2008a). doi:10.1029/2008GL034132

C.S. Arridge, K.K. Khurana, C.T. Russell, D.J. Southwood, N. Achilleos, M.K. Dougherty, A.J. Coates, H.K. Leinweber, Warping of Saturn's magnetospheric and magnetotail current sheets. J. Geophys. Res. **113**, A08217 (2008b). doi:10.1029/2007JA012963

C.S. Arridge, C.T. Russell, K.K. Khurana, N. Achilleos, S.W.H. Cowley, M.K. Dougherty, D.J. Southwood, E.J. Bunce, Saturn's magnetodisc current sheet. J. Geophys. Res. **113**, A04214 (2008c). doi:10.1029/2007JA012540

C.S. Arridge, L.K. Gilbert, G.R. Lewis, E.C. Sittler, G.H. Jones, D.O. Kataria, A.J. Coates, D.T. Young, The effect of spacecraft radiation sources on electron moments from the Cassini CAPS electron spectrometer. Planet. Space Sci. **57**(7), 854–869 (2009a). doi:10.1016/j.pss.2009.02.011

C.S. Arridge, H.J. McAndrews, C.M. Jackman, C. Forsyth, A.P. Walsh, E.C. Sittler, L.K. Gilbert, G.R. Lewis, C.T. Russell, A.J. Coates, M.K. Dougherty, G.A. Collinson, A. Wellbrock, D.T. Young, Plasma electrons in Saturn's magnetotail: structure, distribution and energisation. Planet. Space Sci. **57**(14–15), 2032–2047 (2009b). doi:10.1016/j.pss.2009.09.007

C.S. Arridge, N. Achilleos, P. Guio, Electric field variability and classifications of Titan's magnetoplasma environment. Ann. Geophys. **29**, 1253–1258 (2011a). doi:10.5194/angeo-29-1253-2011

C.S. Arridge, N. André, K.K. Khurana, C.T. Russell, S.W.H. Cowley, G. Provan, D.J. Andrews, C.M. Jackman, A.J. Coates, E.C. Sittler, M.K. Dougherty, D.T. Young, Periodic motion of Saturn's nightside plasma sheet. J. Geophys. Res. **116**, A11205 (2011b). doi:10.1029/2011JA016827

C.S. Arridge, N. André, H.J. McAndrews, E.J. Bunce, M.H. Burger, K.C. Hansen, H.-W. Hsu, R.E. Johnson, G.H. Jones, S. Kempf, K.K. Khurana, N. Krupp, W.S. Kurth, J.S. Leisner, C. Paranicas, E. Roussos, C.T. Russell, P. Schippers, E.C. Sittler, H.T. Smith, M.F. Thomsen, M.K. Dougherty, Mapping magnetospheric equatorial regions at Saturn from Cassini prime mission observations, Space Sci. Rev., accepted manuscript (2011c)

C.S. Arridge et al., A statistical analysis of plasma parameters near Titan's orbit, manuscript to be submitted to J. Geophys. Res. (2011d)

H. Backes, F.M. Neubauer, M.K. Dougherty, N. Achilleos, N. André, C.S. Arridge, C. Bertucci, G.H. Jones, K.K. Khurana, C.T. Russell, A. Wennmacher, Titan's magnetic field signature during the first Cassini encounter. Science **308**, 992 (2005). doi:10.1126/science.1109763

K.W. Behannon, R.P. Lepping, N.F. Ness, Structure and dynamics of Saturn's outer magnetosphere and boundary regions. J. Geophys. Res. **88**, 8791 (1983)

C. Bertucci, C. Mazelle, D.H. Crider, D. Vignes, M.H. Acuña, D.L. Mitchell, R.P. Lin, J.E.P. Connerney, H. Rème, P.A. Cloutier, N.F. Ness, D. Winterhalter, Magnetic field draping enhancement at the Martian magnetic pileup boundary from Mars global surveyor observations. Geophys. Res. Lett. **30**(2), 1099 (2003a). doi:10.1029/2002GL015713

C. Bertucci, C. Mazelle, J.A. Slavin, C.T. Russell, M.H. Acuña, Magnetic field draping enhancement at Venus: evidence for a magnetic pileup boundary. Geophys. Res. Lett. **30**(17), 1876 (2003b). doi:10.1029/2002GL015713

C. Bertucci, N. Achilleos, M.K. Dougherty, R. Modolo, A.J. Coates, K. Szego, A. Masters, Y. Ma, F.M. Neubauer, P. Garnier, J.-E. Wahlund, D.T. Young, The magnetic memory of Titan's ionized atmosphere. Science **321**(5895), 1475 (2008). doi:10.1126/science.1159780

C. Bertucci, B. Sinclair, N. Achilleos, P. Hunt, M.K. Dougherty, C.S. Arridge, The variability of Titan's magnetic environment. Planet. Space Sci. **57**(14–15), 1813–1820 (2009). doi:10.1016/j.pss.2009.02.009

M. Blanc, S. Bolton, J. Bradley, M.E. Burton, T.E. Cravens, I. Dandouras, M.K. Dougherty, M.C. Festou, J. Feynman, R.E. Johnson, T.G. Gombosi, W.S. Kurth, P.C. Liewer, B.H. Mauk, S. Maurice, D. Mitchell, F.M. Neubauer, J.D. Richardson, D.E. Shemansky, E.C. Sittler, B.T. Tsurutani, P. Zarka, L.W. Esposito, E. Grün, D.A. Gurnett, A.J. Kliore, S.M. Krimigis, D.J. Southwood, J.H. Waite, D.T. Young, Magnetospheric and plasma science with Cassini-Huygens. Space Sci. Rev. **104**(1), 253–346 (2002)

J.L. Burch, A.D. DeJong, J. Goldstein, D.T. Young, Periodicity in Saturn's magnetosphere: plasma cam. Geophys. Res. Lett. **36**, L14203 (2009). doi:10.1029/2009GL039043

M.E. Burton, M.K. Dougherty, C.T. Russell, Saturn's internal planetary magnetic field. Geophys. Res. Lett. **37**, L24105 (2011). doi:10.1029/2010GL045148

C.L. Cai, I. Dandouras, H. Rème, J.B. Cao, G.C. Zhou, C. Shen, G.K. Parks, D. Fontaine, Magnetosheath excursion and the relevant transport process at the magnetopause. Ann. Geophys. **27**(8), 2997–3005 (2009). doi:10.5194/angeo-27-2997-2009

J.F. Carbary, D.G. Mitchell, S.M. Krimigis, D.C. Hamilton, N. Krupp, Charged particle periodicities in Saturn's outer magnetosphere. J. Geophys. Res. **112**, A06246 (2007). doi:10.1029/2007JA012351

J.F. Carbary, D.G. Mitchell, P. Brandt, E.C. Roelof, S.M. Krimigis, Periodic tilting of Saturn's plasma sheet. Geophys. Res. Lett. **35**, L24101 (2008a). doi:10.1029/2008GL036339

J.F. Carbary, D.G. Mitchell, P. Brandt, E.C. Roelof, S.M. Krimigis, Statistical morphology of ENA emissions at Saturn. J. Geophys. Res. **113**, A05210 (2008b). doi:10.1029/2007JA012873

K.E. Clarke, N. André, D.J. Andrews, A.J. Coates, S.W.H. Cowley, M.K. Dougherty, G.R. Lewis, H.J. McAndrews, J.D. Nichols, T.R. Robinson, D.M. Wright, Cassini observations of planetary-period oscillations of Saturn's magnetopause. Geophys. Res. Lett. **33**, L23104 (2006). doi:10.1029/2006GL0278212006

K.E. Clarke, D.J. Andrews, C.S. Arridge, A.J. Coates, S.W.H. Cowley, Magnetopause oscillations near the planetary period at Saturn: occurrence, phase, and amplitude. J. Geophys. Res. **115**, A08209 (2010a). doi:10.1029/2009JA014745

K.E. Clarke, D.J. Andrews, A.J. Coates, S.W.H. Cowley, A. Masters, Magnetospheric period oscillations of Saturn's bow shock. J. Geophys. Res. **115**, A05202 (2010b). doi:10.1029/2009JA015164

A.J. Coates, F.J. Crary, G.R. Lewis, D.T. Young, J.H. Waite, E.C. Sittler, Discovery of heavy negative ions in Titan's ionosphere. Geophys. Res. Lett. **34**, L22103 (2007). doi:10.1029/2007GL030978

T.E. Cravens, I.P. Robertson, S.A. Ledvina, D. Mitchell, S.M. Krimigis, J.H. Waite, Energetic ion precipitation at Titan. Geophys. Res. Lett. **35**, L03103 (2008). doi:10.1029/2007GL032451

M. Desch, Radio emission signature of Saturn immersions in Jupiter's magnetic tail. J. Geophys. Res. **88**, 6904 (1983)

K. Dialynas, S.M. Krimigis, D.G. Mitchell, D.C. Hamilton, N. Krupp, P.C. Brandt, Energetic ion spectral characteristics in the Saturnian magnetosphere using Cassini/MIMI measurements. J. Geophys. Res. **114**, A01212 (2009). doi:10.1029/2008JA013761

P. Garnier, The exosphere of Titan and its interaction with the kronian magnetosphere, with the use of MIMI data onboard Cassini. Ph.D. thesis, Universite Toulouse III, 2007

P. Garnier, J.-E. Wahlund, L. Rosenqvist, R. Modolo, K. Ågren, N. Sergis, P. Canu, M. Andre, D.A. Gurnett, W.S. Kurth, S.M. Krimigis, A. Coates, M. Dougherty, J.H. Waite, Titan's ionosphere in the magnetosheath: Cassini RPWS results during the T32 flyby. Ann. Geophys. **27**, 4257–4272 (2009). doi:10.5194/angeo-27-4257-2009

P. Garnier, I. Dandouras, D. Toublanc, E.C. Roelof, P.C. Brandt, D.G. Mitchell, S.M. Krimigis, N. Krupp, D.C. Hamilton, J.-E. Wahlund, Statistical analysis of the energetic ion and ENA data for the Titan environment. Planet. Space Sci. **58**(14–15), 1811–1822 (2010). doi:10.1016/j.pss.2010.08.009

T.I. Gombosi, T.P. Armstrong, C.S. Arridge, K.K. Khurana, S.M. Krimigis, N. Krupp, A.M. Persoon, M.F. Thomsen, Saturn's magnetospheric configuration, in *Saturn from Cassini-Huygens*, ed. by M.K. Dougherty, L.W. Esposito, S.M. Krimigis (Springer, Berlin, 2009), pp. 203–255. doi:10.1007/978-1-4020-9217-6_9

J.T. Gosling, V.J. Pizzo, Formation and evolution of corotating interaction regions and their three dimensional structure. Space Sci. Rev. **89**, 21 (1999)

D.A. Gurnett, A.M. Persoon, W.S. Kurth, J.B. Groene, T.F. Averkamp, M.K. Dougherty, D.J. Southwood, The variable rotation period of the inner region of Saturn's plasma disk. Science **316**(5823), 442 (2007). doi:10.1126/science.1138562

R.E. Hartle, E.C. Sittler Jr., F.M. Neubauer, R.E. Johnson, H.T. Smith, F. Crary, D.J. McComas, D.T. Young, A.J. Coates, D. Simpson, S. Bolton, D. Reisenfeld, K. Szego, J.J. Berthelier, A. Rymer, J. Vilppola, J.T. Steinberg, N. André, Initial interpretation of Titan plasma interaction as observed by the Cassini plasma spectrometer: comparisons with Voyager 1. Planet. Space Sci. **54**, 1211–1224 (2006). doi:10.1016/j.pss.2006.05.029

T.W. Hill, F.C. Michel, Heavy ions from the Galilean satellites and the centrifugal distortion of the Jovian magnetosphere. J. Geophys. Res. **81**, 4561–4565 (1976). doi:10.1029/JA081i025p04561

A.J. Hundhausen, J.T. Gosling, Solar wind structure at large heliocentric distances; an interpretation of Pioneer 10 observations. J. Geophys. Res. **81**, 1436 (1976)

D.M. Hunten, M.G. Tomasko, F.M. Flasar, R.E. Samuelson, D.F. Strobel, D.J. Stevenson, Titan, in *Saturn*, ed. by T. Gehrels, M.S. Matthews (University of Arizona Press, Tucson, 1984), pp. 671–759

P.L. Israelevich, F.M. Neubauer, A.I. Ershkovich, The induced magnetosphere of comet Halley: interplanetary magnetic field during Giotto encounter. J. Geophys. Res. **99**, 6575–6583 (1994). doi:10.1029/93JA03199

C.M. Jackman, N. Achilleos, E.J. Bunce, S.W.H. Cowley, M.K. Dougherty, G.H. Jones, S.E. Milan, E.J. Smith, Interplanetary magnetic field at ∼9 AU during the declining phase of the solar cycle and its implications for Saturn's magnetospheric dynamics. J. Geophys. Res. **109**, A11203 (2004). doi:10.1029/2004JA010614

C.M. Jackman, R.J. Forsyth, M.K. Dougherty, The overall configuration of the interplanetary magnetic field upstream of Saturn as revealed by Cassini observations. J. Geophys. Res. **113**, A08114 (2008). doi:10.1029/2008JA013083

C.M. Jackman, C.S. Arridge, H.J. McAndrews, M.G. Henderson, R.J. Wilson, Northward field excursions in Saturn's magnetotail and their relationship to magnetospheric periodicities. Geophys. Res. Lett. **36**, L16101 (2009). doi:10.1029/2009GL039149

C.M. Jackman, C.S. Arridge, Solar cycle effects on the dynamics of Jupiter's and Saturn's magnetospheres. Sol. Phys. (2011). doi:10.1007/s11207-011-9748-z

R.E. Johnson, M.R. Combi, J.L. Fox, W.-H. Ip, F. Leblanc, M.A. McGrath, V.I. Shematovich, D.F. Strobl, J.H. Waite Jr., Exospheres and atmospheric escape. Space Sci. Rev. **139**, 355–397 (2008). doi:10.1007/s11214-008-9415-3

R.E. Johnson, O.J. Tucker, M. Michael, E.C. Sittler, H.T. Smith, D.T. Young, J.H. Waite, Mass loss processes in Titan's upper atmosphere, in *Titan from Cassini-Huygens*, ed. by R.H. Brown, J.-P. Lebreton, J. Hunter Waite (Springer, Berlin, 2009), pp. 373–391. Chapter 15

S.J. Kanani, C.S. Arridge, G.H. Jones, A.N. Fazakerley, H.J. McAndrews, N. Sergis, S.M. Krimigis, M.K. Dougherty, A.J. Coates, D.T. Young, K.C. Hansen, N. Krupp, A new form of Saturn's magnetopause using a dynamic pressure balance model, based on in-situ, multi instrument Cassini measurements. J. Geophys. Res. **115**, A06207 (2010). doi:10.1029/2009JA014262

M. Kane, D.G. Mitchell, J.F. Carbary, S.M. Krimigis, F.J. Crary, Plasma convection in Saturn's outer magnetosphere determined from ions detected by the Cassini INCA experiment. Geophys. Res. Lett. **35**, L04102 (2009). doi:10.1029/2007GL032342

S. Kellett, E.J. Bunce, A.J. Coates, S.W.H. Cowley, Thickness of Saturn's ring current determined from north-south Cassini passes through the current layer. J. Geophys. Res. **114**, A04209 (2009). doi:10.1029/2008JA013942

K.K. Khurana, M.G. Kivelson, D.J. Stevenson, G. Schubert, C.T. Russell, R.J. Walker, C. Polanskey, Induced magnetic fields as evidence for subsurface oceans in Europa and Callisto. Nature **395**(6704), 777–780 (1998)

K.K. Khurana, D.G. Mitchell, C.S. Arridge, M.K. Dougherty, C.T. Russell, C. Paranicas, N. Krupp, A.J. Coates, Sources of rotational signals in Saturn's magnetosphere. J. Geophys. Res. **114**, A02211 (2009). doi:10.1029/2008JA013312

A.J. Kliore, A.F. Nagy, E.A. Marouf, R.G. French, M.F. Flasar, N.J. Rappaport, A. Anabttawi, S.W. Asmar, D.S. Kahann, E. Barbinis, G.L. Goltz, D.U. Fleischman, D.J. Rochblatt, First results from the Cassini radio occultations of the Titan ionosphere. J. Geophys. Res. **113**, A09317 (2008). doi:10.1029/2007JA012965

S.M. Krimigis, T.P. Armstrong, W.I. Axford, C.O. Bostrom, G. Gloekler, E.P. Keath, L.J. Lanzerotti, J.F. Carbary, D.C. Hamilton, E.C. Roelof, Low-energy charged particles in Saturn's magnetosphere: results from Voyager 1. Science **212**, 225–231 (1981)

S.M. Krimigis, J.F. Carbary, E.P. Keath, T.P. Armstrong, L.J. Lanzerotti, G. Gloeckler, General characteristics of hot plasma and energetic particles in the Saturnian magnetosphere: results from the Voyager spacecraft. J. Geophys. Res. **88**(A11), 8871–8892 (1983)

S.M. Krimigis, N. Sergis, D.G. Mitchell, D.C. Hamilton, N. Krupp, A dynamic, rotating ring current around Saturn. Nature **450**(7172), 1050–1053 (2007). doi:10.1038/nature06425

N. Krupp, E. Roussos, A. Lagg, J. Woch, A.L. Müller, S.M. Krimigis, D.G. Mitchell, E.C. Roelof, C. Paranicas, J. Carbary, G.H. Jones, D.C. Hamilton, S. Livi, T.P. Armstrong, M.K. Dougherty, N. Sergis, Energetic particles in Saturn's magnetosphere during the Cassini nominal mission (July 2004–July 2008). Planet. Space Sci. **57**(14–15), 1754–1768 (2009). doi:10.1016/j.pss.2009.06.010

H. Kunow, Solar wind: Corotating interaction region, in *Encyclopedia of Astronomy and Astrophysics*, vol. 4 (Institute of Physics, Bristol, 2001), p. 2825

W.S. Kurth, T.F. Averkamp, D.A. Gurnett, J.B. Groene, A. Lecacheux, An update to a Saturnian longitude system based on kilometric radio emissions. J. Geophys. Res. **113**(5), A05222 (2008). doi:10.1029/2007JA012861

S.A. Ledvina, Y.-J. Ma, E. Kallio, Modeling and simulating flowing plasmas and related phenomena. Space Sci. Rev. **139**(1–4), 143–189 (2008). doi:10.1007/s11214-008-9384-6

R.P. Lepping, M.D. Desch, E.C. Sittler Jr., K.W. Behannon, L.W. Klein, J.D. Sullivan, W.S. Kurth, Structure and other properties of Jupiter's distant magnetotail. J. Geophys. Res. **88**, 8801–8815 (1983)

G.R. Lewis, N. André, C.S. Arridge, A.J. Coates, L.K. Gilbert, D.R. Linder, A.M. Rymer, Derivation of density and temperature from the Cassini-Huygens CAPS electron spectrometer. Planet. Space Sci. **56**, 901–912 (2008). doi:10.1016/j.pss.2007.12.017

J.G. Luhmann, T.-L. Zhang, S.M. Petrinec, C.T. Russell, P. Gazis, A. Barnes, Solar cycle 21 effects on the interplanetary magnetic field and related parameters at 0.7 and 1.0 AU. J. Geophys. Res. **98**(A4), 5559–5572 (1993). doi:10.1029/92JA02235

N. Luna, M. Michael, M.B. Shah, R.E. Johnson, C.J. Latimer, J.W. McConkey, Dissociation of N_2 in capture and ionization collisions with fast H^+ and N^+ ions and modeling of positive ion formation in the Titan atmosphere. J. Geophys. Res. **108**, 5033 (2003). doi:10.1029/2002JE001950

E.T. Lundberg, K.C. Hansen, T.I. Gombosi, G. Toth, Statistical study of the probability of Titan being in the solar wind or in Saturn's magnetosheath. Eos Trans. AGU **86**(52), Fall Meet. Suppl., abstract P43A-0957 (2005)

Y.-J. Ma, A.F. Nagy, Ion escape fluxes from Mars. Geophys. Res. Lett. **34**, L08201 (2007). doi:10.1029/2006GL029208

Y. Ma, A.F. Nagy, T.E. Cravens, I.V. Sokolov, K.C. Hansen, J.-E. Wahlund, F.J. Crary, A.J. Coates, M.K. Dougherty, Comparisons between MHD model calculations and observations of Cassini flybys of Titan. J. Geophys. Res. **111**, A05207 (2006). doi:10.1029/2005JA011481

Y.-J. Ma, C.T. Russell, A.F. Nagy, G. Toth, C. Bertucci, M.K. Dougherty, F.M. Neubauer, A. Wellbrock, A.J. Coates, P. Garnier, J.-E. Wahlund, T.E. Cravens, F.J. Crary, Time-dependent global MHD simulations of Cassini T32 flyby: from magnetosphere to magnetosheath. J. Geophys. Res. **114**, A03204 (2009). doi:10.1029/2008JA013676

C.G. MacLennan, L.J. Lanzerotti, Low-energy particles at the bow shock, magnetopause, and outer magnetosphere of Saturn. J. Geophys. Res. **88**, 8817–8830 (1983)

A. Masters, N. Achilleos, M.K. Dougherty, J.A. Slavin, G.B. Hospodarsky, C.S. Arridge, A.J. Coates, An empirical model of Saturn's bow shock: Cassini observations of shock location and shape. J. Geophys. Res. **113**, A10210 (2008). doi:10.1029/2008JA013276

S. Maurice, M. Blanc, R. Prangé, E.C. Sittler, The magnetic-field-aligned polarization electric field and its effects on particle distribution in the magnetospheres of Jupiter and Saturn. Planet. Space Sci. **45**(11), 1449–1465 (1997)

H.J. McAndrews, M.F. Thomsen, C.S. Arridge, C.M. Jackman, R.J. Wilson, M.G. Henderson, R.L. Tokar, K.K. Khurana, E.C. Sittler, A.J. Coates, M.K. Dougherty, Plasma in Saturn's nightside magnetosphere and the implications for global circulation. Planet. Space Sci. **57**(14–15), 1714–1722 (2009). doi:10.1016/j.pss.2009.03.003

D.G. Mitchell, S.M. Krimigis, C. Paranicas, P.C. Brandt, J.F. Carbary, E.C. Roelof, W.S. Kurth, D.A. Gurnett, J.T. Clarke, J.D. Nichols, J.C. Gérard, D.C. Grodent, M.K. Dougherty, W.R. Pryor, Recurrent energization of plasma in the midnight-to-dawn quadrant of Saturn's magnetosphere and its relationship to auroral UV and radio emissions. Planet. Space Sci. **57**(14–15), 1732–1742 (2009). doi:10.1016/j.pss.2009.04.002

M.W. Morooka, R. Modolo, J.-E. Wahlund, M. André, A.I. Eriksson, A.M. Persoon, D.A. Gurnett, W.S. Kurth, A.J. Coates, G.R. Lewis, K.K. Khurana, M. Dougherty, The electron density of Saturn's magnetosphere. Ann. Geophys. **27**(7), 2971–2991 (2009). doi:10.5194/angeo-27-2971-2009

Z. Németh, K. Szego, Z. Bebesi, G. Erdős, L. Foldy, A. Rymer, E.C. Sittler, A.J. Coates, A. Wellbrock, Ion distributions of different Kronian plasma regions. J. Geophys. Res. **116**, A09212 (2011). doi:10.1029/2011JA016585

N.F. Ness, M.H. Acuna, K.W. Behannon, The induced magnetosphere of Titan. J. Geophys. Res. **87**, 1369–1381 (1982). doi:10.1029/JA087iA03p01369

F.M. Neubauer, D. Gurnett, J.D. Scudder, R.E. Hartle, Titan's magnetospheric interaction, in *Saturn*, ed. by T. Gehrels, M.S. Matthews (University of Arizona Press, Tucson, 1984)

F.M. Neubauer, H. Backes, M.K. Dougherty, A. Wennmacher, C.T. Russell, A. Coates, D. Young, N. Achilleos, N. André, C.S. Arridge, C. Bertucci, G.H. Jones, K.K. Khurana, T. Knetter, A. Law, G.R. Lewis, J. Saur, Titan's near magnetotail from magnetic field and electron plasma observations and modeling: Cassini flybys TA, TB, and T3. J. Geophys. Res. **111**, A10220 (2006). doi:10.1029/2006JA011676

E.N. Parker, Dynamics of the interplanetary magnetic field. Astrophys. J. **128**, 664 (1958)

H. Persson, Electric field parallel to the magnetic field in a low-density plasma. Phys. Fluids **9**, 1090 (1966). doi:10.1063/1.1761807

W.G. Pilipp, K.-H. Muehlhaeuser, H. Miggenrieder, H. Rosenbauer, R. Schwenn, Large-scale variations of thermal electron parameters in the solar wind between 0.3 and 1 AU. J. Geophys. Res. **95**, 6305–6329 (1990). doi:10.1029/JA095iA05p06305

J.D. Richardson, The magnetosheaths of the outer planets. Planet. Space Sci. **50**(5–6), 503–517 (2002). doi:10.1016/S0032-0633(02)00029-6

C.T. Russell, C.M. Jackman, H.-Y. Wei, C. Bertucci, M.K. Dougherty, Titan's influence on Saturnian substorm occurrence. Geophys. Res. Lett. **35**, L12105 (2008). doi:10.1029/2008GL034080

A.M. Rymer, B.H. Mauk, T.W. Hill, C. Paranicas, N. André, E.C. Sittler Jr., D.G. Mitchell, H.T. Smith, R.E. Johnson, A.J. Coates, D.T. Young, S.J. Bolton, M.F. Thomsen, M.K. Dougherty, Electron sources in Saturn's magnetosphere. J. Geophys. Res. **112**, A02201 (2007). doi:10.1029/2006JA012017

A.M. Rymer, H.T. Smith, A. Wellbrock, A.J. Coates, D.T. Young, Discrete classification and electron energy spectra of Titan's varied magnetospheric environment. Geophys. Res. Lett. **36**, L15109 (2009). doi:10.1029/2009GL039427

J. Saur, F.M. Neubauer, K.-H. Glassmeier, Induced magnetic fields in solar system bodies. Space Sci. Rev. **152**(1–4), 391–421 (2009). doi:10.1007/s11214-009-9581-y

N. Sergis, S.M. Krimigis, D.G. Mitchell, D.C. Hamilton, N. Krupp, B.M. Mauk, E.C. Roelof, M. Dougherty, Ring current at Saturn: energetic particle pressure in Saturn's equatorial magnetosphere measured with Cassini/MIMI. Geophys. Res. Lett. **34**, L09102 (2007). doi:10.1029/2006GL029223

N. Sergis, S.M. Krimigis, D.G. Mitchell, D.C. Hamilton, N. Krupp, B.H. Mauk, E.C. Roelof, M.K. Dougherty, Energetic particle pressure in Saturn's magnetosphere measured with the magnetospheric imaging instrument on Cassini. J. Geophys. Res. **114**, A02214 (2009). doi:10.1029/2008JA013774

N. Sergis, S.M. Krimigis, E.C. Roelof, C.S. Arridge, A.M. Rymer, D.G. Mitchell, D.C. Hamilton, N. Krupp, M.F. Thomsen, M.K. Dougherty, A.J. Coates, D.T. Young, Particle pressure, inertial force, and ring current density profiles in the magnetosphere of Saturn, based on Cassini measurements. Geophys. Res. Lett. **37**, L02102 (2010). doi:10.1029/2009GL041920

N. Sergis, C.S. Arridge, S.M. Krimigis, D.G. Mitchell, A.M. Rymer, D.C. Hamilton, N. Krupp, M.K. Dougherty, A.J. Coates, Dynamics and seasonal variations in Saturn's magnetospheric plasma sheet, as measured by Cassini. J. Geophys. Res. **116**, A04203 (2011). doi:10.1029/2010JA016180

I. Sillanpää, D.T. Young, F. Crary, M. Thomsen, D. Reisenfeld, J.-E. Wahlund, C. Bertucci, E. Kallio, R. Jarvinen, P. Janhunen, Cassini plasma spectrometer and hybrid model study on Titan's interaction: effect of oxygen ions. J. Geophys. Res. **116**, A07223 (2011). doi:10.1029/2011JA016443

S. Simon, G. Kleindienst, A. Boesswetter, T. Bagdonat, U. Mtschmann, K.-H. Glassmeier, J. Schuele, C. Bertucci, M.K. Dougherty, Hybrid simulation of Titan's magnetic field signature during the Cassini T9 flyby. Geophys. Res. Lett. **34**(24), L24S08 (2007). doi:10.1029/2007GL029967

S. Simon, U. Motschmann, K.-H. Glassmeier, Influence of non-stationary electromagnetic field conditions on ion pick-up at Titan: 3-D multispecies hybrid simulations. Ann. Geophys. **26**(3), 599–617 (2008). doi:10.5194/angeo-26-599-2008

S. Simon, U. Motschmann, Titan's induced magnetosphere under non-ideal upstream conditions: 3D multispecies hybrid simulations. Planet. Space Sci. **57**(14–15), 2001–2015 (2009). doi:10.1016/j.pss.2009.08.010

S. Simon, F.M. Neubauer, C.L. Bertucci, H. Kriegel, J. Saur, C.T. Russell, M.K. Dougherty, Titan's highly dynamic magnetic environment: a systematic survey of Cassini magnetometer observations from flybys TA–T62. Planet. Space Sci. **58**(10), 1230–1251 (2010a). doi:10.1016/j.pss.2010.04.021

S. Simon, A. Wennmacher, F.M. Neubauer, C.L. Bertucci, H. Kriegel, C.T. Russell, M.K. Dougherty, Dynamics of Saturn's magnetodisk near Titan's orbit: comparison of Cassini magnetometer observations from real and virtual Titan flybys. Planet. Space Sci. **58**(12), 1625–1635 (2010b). doi:10.1016/j.pss.2010.08.006

E.C. Sittler, N. André, M. Blanc, M. Burger, R.E. Johnson, A.J. Coates, A. Rymer, D. Reisenfeld, M.F. Thomsen, A. Persoon, M. Dougherty, H.T. Smith, R.A. Baragiola, R.E. Hartle, D. Chornay, M.D. Shappirio, D. Simpson, D.J. McComas, D.T. Young, Ion and neutral sources and sinks within Saturn's inner magnetosphere: Cassini results. Planet. Space Sci. **56**(1), 3–19 (2008). doi:10.1016/j.pss.2007.06.006

E.C. Sittler, R.E. Hartle, C. Bertucci, A. Coates, T. Cravens, I. Dandouras, D. Shemansky, Energy deposition processes in Titan's upper atmosphere and its induced magnetosphere, in *Titan from Cassini-Huygens*, ed. by R.H. Brown, J.-P. Lebreton, J. Hunter Waite (Springer, Berlin, 2009), pp. 393–453. Chapter 16

J.A. Slavin, R.E. Holzer, Solar wind flow about the terrestrial planets. I—modeling bow shock position and shape. J. Geophys. Res. **86**, 11401–11418 (1981). doi:10.1029/JA086iA13p11401

J.A. Slavin, E.J. Smith, J.R. Spreiter, S.S. Stahara, Solar wind flow about the outer planets—gas dynamic modeling of the Jupiter and Saturn bow shocks. J. Geophys. Res. **90**, 6275–6286 (1985). doi:10.1029/JA090iA07p06275

H.T. Smith, M. Shappirio, R.E. Johnson, D. Reisenfeld, E.C. Sittler, F.J. Crary, D.J. McComas, D.T. Young, Enceladus, a potential source of ammonia products and molecular nitrogen for Saturn's magnetosphere. J. Geophys. Res. **113**, A11206 (2008). doi:10.1029/2008JA013352

H.T. Smith, D.G. Mitchell, R.E. Johnson, C. Paranicas, Investigation of energetic proton penetration in Titan's atmosphere using the Cassini INCA instrument. Planet. Space Sci. **57**(13), 1539–1546 (2009). doi:10.1016/j.pss.2009.03.013

D.J. Southwood, M.G. Kivelson, Saturnian magnetospheric dynamics: elucidation of a camshaft model. J. Geophys. Res. **112**, A12222 (2007). doi:10.1029/2007JA012254

D.F. Strobel, S.K. Atreya, B. Bézard, F. Ferri, F.M. Flasar, M. Fulchignomi, E. Lellouch, I. Müller-Wodarg, Atmospheric structure and composition, in *Titan from Cassini-Huygens*, ed. by R.H. Brown, J.-P. Lebreton, J. Hunter Waite (Springer, Berlin, 2009), pp. 235–258. Chapter 10

K. Szego, K.-H. Glassmeier, R. Bingham, A. Bogdanov, C. Fischer, G. Haerendel, A. Brinca, T. Cravens, E. Dubinin, K. Sauer, L. Fisk, T. Gombosi, N. Schwadron, P. Isenberg, M. Lee, C. Mazelle, E. Möbius, U. Motschmann, V.D. Vitali, B. Tsurutani, G. Zank, Physics of mass loaded plasmas. Space Sci. Rev. **94**(3/4), 429–671 (2000)

K. Szego, Z. Bebesi, C. Bertucci, A.J. Coates, F. Crary, G. Erdös, R. Hartle, E.C. Sittler, D.T. Young, Charged particle environment of Titan during the T9 flyby. Geophys. Res. Lett. **34**, L24S03 (2007). doi:10.1029/2007GL030677

K. Szego, Z. Nemeth, G. Erdos, L. Foldy, M.F. Thomsen, D.M. Delapp, The plasma environment of Titan: the magnetodisk of Saturn near the encounters as derived from ion densities measured by the Cassini/CAPS plasma spectrometer. J. Geophys. Res. **116**, A10219 (2011). doi:10.1029/2011JA016629

M.F. Thomsen, D.B. Reisenfeld, D.M. Delapp, R.L. Tokar, D.T. Young, F.J. Crary, E.C. Sittler, M.A. McGraw, J.D. Williams, Survey of ion plasma parameters in Saturn's magnetosphere. J. Geophys. Res. **115**, A10220 (2010). doi:10.1029/2010JA015267

V.M. Vasyliūnas, A survey of low-energy electrons in the evening sector of the magnetosphere with OGO 1 and OGO 3. J. Geophys. Res. **73**, 2839 (1968)

V.M. Vasyliūnas, Plasma distribution and flow, in *Physics of the Jovian Magnetosphere*. Cambridge Planetary Science Series, ed. by A.J. Dessler (Cambridge University Press, Cambridge, 1983),

J.-E. Wahlund, R. Boström, G. Gustafsson, D.A. Gurnett, W.S. Kurth, A. Pedersen, T.F. Averkamp, G.B. Hospodarsky, A.M. Persoon, P. Canu, F.M. Neubauer, M.K. Dougherty, A.I. Eriksson, M.W. Morooka, R. Gill, M. André, L. Eliasson, I. Müller-Wodarg, Cassini measurements of cold plasma in the ionosphere of Titan. Science **308**(5724), 986–989 (2005). doi:10.1126/science.1109807

J.H. Waite, D.T. Young T.E. Cravens, A.J. Coates, F.J. Crary, B. Magee, J. Westlake, The process of tholin formation in Titan's upper atmosphere. Science **316**(5826), 870–875 (2007). doi:10.1126/science.1139727

J.H. Waite, D.T. Young, J. Westlake, J.L. Lunine, C.P. McKay, W.S. Lewis, High-altitude production of Titan's aerosols, in *Titan from Cassini-Huygens*, ed. by R.H. Brown, J.-P. Lebreton, J.H. Waite (Springer, Berlin, 2009), pp. 201–214. Chapter 8

H.Y. Wei, C.T. Russell, A. Wellbrock, M.K. Dougherty, A.J. Coates, Plasma environment at Titan's orbit with Titan present and absent. Geophys. Res. Lett. **36**, L23202 (2009). doi:10.1029/2009GL041048

H.Y. Wei, C.T. Russell, M.K. Dougherty, F.M. Neubauer, Y.J. Ma, Upper limits on Titan's magnetic moment and implications for its interior. J. Geophys. Res. **115**, E10007 (2010). doi:10.1029/2009JE003538

J.H. Westlake, J.M. Bell, J.H. Waite Jr., R.E. Johnson, J.G. Luhmann, K.E. Mandt, B.A. Magee, A.M. Rymer, Titan's thermospheric response to various plasma environments. J. Geophys. Res. **116**, A03318 (2011). doi:10.1029/2010JA016251

R.J. Wilson, R.L. Tokar, M.G. Henderson, T.W. Hill, M.F. Thomsen, D.H. Pontius Jr., Cassini plasma spectrometer thermal ion measurements in Saturn's inner magnetosphere. J. Geophys. Res. **113**, A12218 (2008). doi:10.1029/2008JA013486

R.M. Winglee, D. Snowden, A. Kidder, Modification of Titan's ion tail and the kronian magnetosphere: coupled magnetospheric simulations. J. Geophys. Res. **114**, A05215 (2009). doi:10.1029/2008JA013343

D.A. Wolf, F.M. Neubauer, Titan's highly variable plasma environment. J. Geophys. Res. **87**, 881–885 (1982)

Space Sci Rev (2011) 162:85–111
DOI 10.1007/s11214-011-9826-4

Recent Results from Titan's Ionosphere

A.J. Coates · J.-E. Wahlund · K. Ågren · N. Edberg · J. Cui · A. Wellbrock · K. Szego

Received: 11 February 2011 / Accepted: 22 August 2011 / Published online: 1 October 2011

Abstract Titan has the most significant atmosphere of any moon in the solar system, with a pressure at the surface larger than the Earth's. It also has a significant ionosphere, which is usually immersed in Saturn's magnetosphere. Occasionally it exits into Saturn's magnetosheath. In this paper we review several recent advances in our understanding of Titan's ionosphere, and present some comparisons with the other unmagnetized objects Mars and Venus. We present aspects of the ionospheric structure, chemistry, electrodynamic coupling and transport processes. We also review observations of ionospheric photoelectrons at Titan, Mars and Venus. Where appropriate, we mention the effects on ionospheric escape.

Keywords Ionosphere · Titan · Mars · Venus

1 Introduction

The purpose of this paper is to provide an update on progress in several topics within Titan's ionosphere, since the comprehensive review by Cravens et al. (2009) in the 'Titan from Cassini-Huygens' book, and others (see below).

A.J. Coates (✉) · A. Wellbrock
Department of Space and Climate Physics, Mullard Space Science Laboratory, University College London, Holmbury St. Mary, Dorking RH5 6NT, UK
e-mail: ajc@mssl.ucl.ac.uk

J.-E. Wahlund · K. Ågren · N. Edberg
Swedish Institute of Space Physics, Box 537, 751 21 Uppsala, Sweden

J. Cui
Department of Astronomy & Key Laboratory of Modern Astronomy and Astrophysics in Ministry of Education, Nanjing University, Nanjing 210093, China

K. Szego
Research Institute for Particle and Nuclear Physics, Hungarian Academy of Sciences, KFKI-RMKI, Budapest, Hungary

The upper part of any atmosphere (or any exosphere or gas plume) in the solar system may become partially ionized by the action of solar EUV, X- and γ-ray radiation, and by energetic impacting plasma (electrons and ions) from nearby regions of space. Cosmic radiation with origin far outside the solar system may also play a role. The result is an ionization layer or ionosphere (e.g., Banks and Kockarts 1973; Rees 1989; Schunk and Nagy 2009). The radiation in question must be energetic enough to overcome the ionization energy threshold of the atmospheric species. Metallic ion layers may also arise due to meteoritic bombardment within the atmosphere. In this case an ionization layer is produced by meteor ablation. The consequent concentration may be produced by either neutral wind shears, by convection electric fields perpendicular to magnetic fields that are oblique to the vertical atmospheric structure, or by corpuscular impact ionization of the atmospheric dust particles (e.g., Whitehead 1970; Derblom 1981; Nygrén et al. 1984; Turunen et al. 1985; Von Zahn et al. 1987). Note that meteor-induced ionospheric layers have also been detected at Mars and Venus (Pätzold et al. 2005, 2009).

The ionosphere (a partially ionized plasma region) has at least three major impacts on its plasma environment:

- *Electrodynamic coupling*: An ionosphere in the collisional regime is electrically conducting perpendicular to any magnetic field (e.g., Boström 1964; Schunk and Nagy 2009; Kelley 2009; Withers 2008). An ionosphere may therefore act as an electro-dynamic dynamo region for electric currents, and set up an electric circuit that couples it to the surrounding plasma environment through magnetic field aligned currents into the conducting ionosphere, thereby creating electric current layers in the ionosphere. The ability of the ionosphere to conduct an electrical current also plays an important role in the dynamics and energetics of the ionospheres as it leads to coupling of plasma convection to the neutral atmosphere and, thus, energy dissipation. It is also a controlling factor for magnetic field diffusion.
- *Atmospheric erosion*: Apart from direct exospheric Jeans escape of the neutral medium to space, the external plasma flow (usually the solar wind) induces an electro-dynamic interaction that leads to a significant escape of ionospheric plasma downstream from the planetary body in question (e.g., Chappell et al. 1987; Lundin et al. 2004; Moore and Horwitz 2007; Ma and Nagy 2007; Engwall et al. 2009). One general problem is how these interactions, which are complex in nature and to a large extent unknown, cause topside ionospheric outflows of plasma into the (induced) magnetosphere and its tail, where it can be further accelerated (cf. Fig. 1). Depending on the external plasma flow conditions the erosion rate can be large and is therefore one key factor for understanding the evolution of the climate of planetary bodies over geological timescales.
- *Atmospheric composition change*: The ionized component of the ionosphere produced by the energetic radiation is chemically reactive, and drives a catalytic-like chemistry in the atmosphere through fast ion-molecule reactions. This has significant long-term compositional effects especially if coupled to ionospheric erosion (e.g., Kasting and Catling 2003; Lundin and Barabash 2004; Lammer et al. 2003, 2007; Ribas et al. 2005; Kulikov et al. 2006; Yamauchi and Wahlund 2007) and may explain the variation in water abundance in terrestrial planetary atmospheres (Venus, Earth, and Mars). In the case of Titan, the ionospheric chemistry may even give rise to the observed global orange-brown aerosol layer, affect the climate and induce pre-biotic organic and nitrile chemistry (e.g., Coates et al. 2007a; Waite et al. 2007; Wahlund et al. 2009; Sittler et al. 2009a, 2009b).

Titan's ionosphere, induced magnetosphere, mass loss processes and interaction with the external plasma flow of Saturn's magnetosphere have recently been reviewed (see Cravens

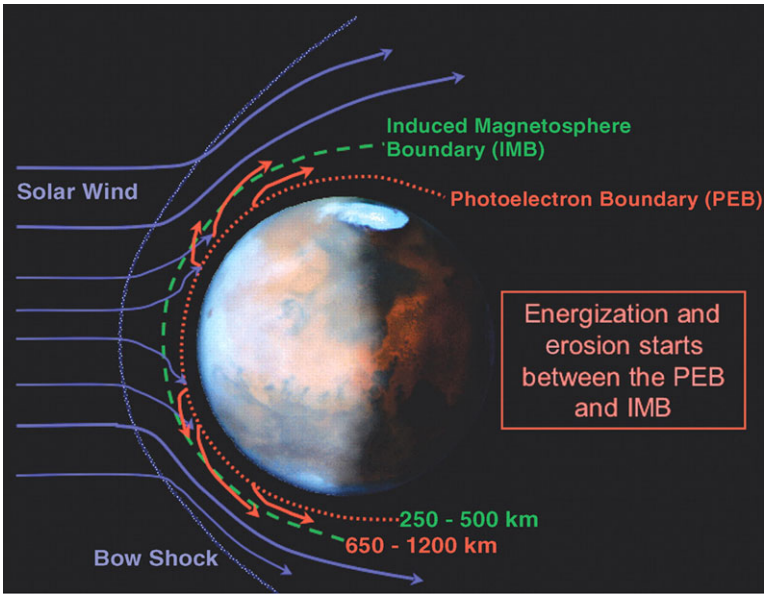

Fig. 1 A cartoon of the topside ionospheric outflows that erode the atmosphere of Mars (picture from Lundin et al. 2004)

et al. 2009; Johnson et al. 2009; Sittler et al. 2009a, 2009b; Coates 2009 respectively) using results from the *Cassini-Huygens* mission. In this paper, our intention is not to provide a comprehensive review of Titan's ionosphere, but rather to complement the reviews cited above. We will present the results of recent progress on several aspects of Titan's ionosphere, and also make some comparisons with Mars and Venus. The subjects we cover here are recent results on:

- Titan's ionospheric structure,
- Titan's ionospheric chemistry,
- Titan's ionospheric electro-dynamic coupling,
- Titan's ionospheric transport processes,
- Photoelectrons at Venus, Mars and Titan.

The discussion relates to some ionospheric processes at Mars and Venus where appropriate.

2 Titan's Ionospheric Structure

In the case of Titan, several ionization processes determine the ionospheric structure. Although the first detection of an ionosphere at Titan was made by Voyager-1 radio occultation measurements (Bird et al. 1997) during one single and remote flyby, the Cassini detailed in situ measurements by several instruments (e.g., Wahlund et al. 2005; Waite et al. 2005; Coates et al. 2007b; Crary et al. 2009) have up to now made extensive studies of Titan's ionosphere based on over 70 flybys. Most of these flybys passed directly through the dominant ionospheric peak situated at altitudes between 950–1300 km, and the deepest flyby has so far occurred at 850 km altitude. The Cassini mission will continue until 2017 and by

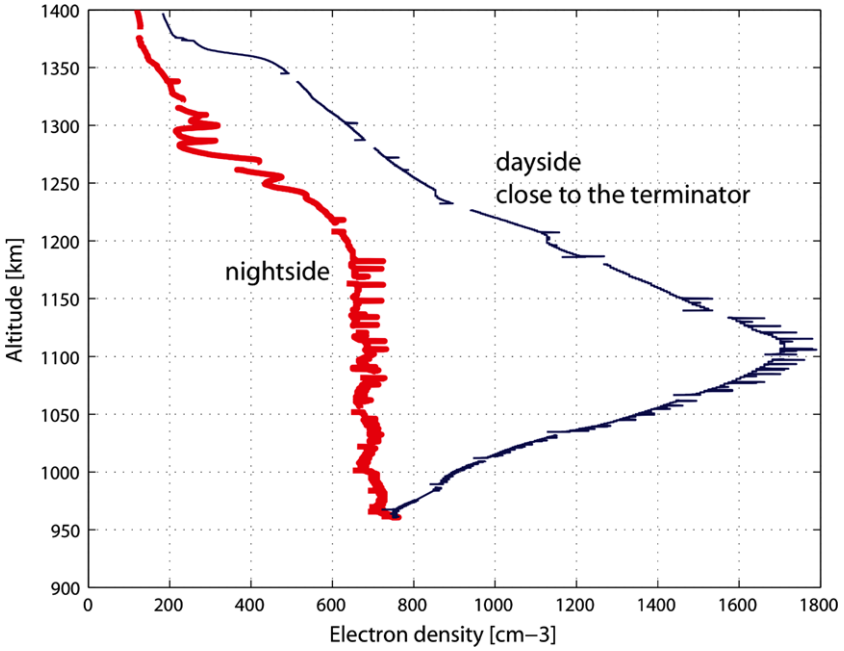

Fig. 2 Typical day and nightside ionospheric density profiles at Titan measured by the Cassini RPWS Langmuir probe 20 Hz sampling mode during the T18 flyby. The solar zenith angle at closest approach was 88°. The superposed one-sample spikes are instrumental (from Ågren et al. 2009)

then have passed Titan around 130 times at a range of latitudes, solar zenith angles (SZA), and external plasma flow conditions. The lower ionosphere was monitored by the Huygens probe during its landing in early 2005. Radio occultation monitoring by Cassini has complemented the in situ measurements by probing the altitude region below the region down to ∼850 km where in-situ measurements are possible (Kliore et al. 2008). In particular, these measurements provide vertical electron density profiles of the near-terminator ionosphere, from ∼3000 km down to ∼250 km.

The dominant ionospheric peak is associated with plasma number densities between 2500–3500 cm^{-3} on the dayside and 400–1000 cm^{-3} on the nightside (see Fig. 2, Ågren et al. 2009). Other prominent ionospheric peaks have been identified at 500–600 km altitude (Kliore et al. 2008; Cravens et al. 2008a, 2008b) and at 60–80 km altitude (López-Moreno et al. 2008), and mainly reflect the different ionization sources acting on Titan's atmosphere at different altitudes (see below). The ionization levels remain high (100–1000 cm^{-3}) throughout the atmosphere where measurements have been made. It is worth noting that it is critical to make measurements of both the electron and ion number densities for both low and high masses separately, since they differ due to the presence of substantial amounts of multiply charged ions and aerosol particles (Wahlund et al. 2009).

The energy of any radiation (electromagnetic or corpuscular), together with the absorption cross section of the atmospheric constituents, determine the depth of the ionization into the atmosphere. More energetic radiation may reach lower atmospheric layers or even the surface. The consensus is that the main ionospheric peak can be accounted for by solar EUV radiation and associated photoelectrons for solar zenith angles out past the terminator to about 100° SZA (see Fig. 3) due to the extended nature of Ti-

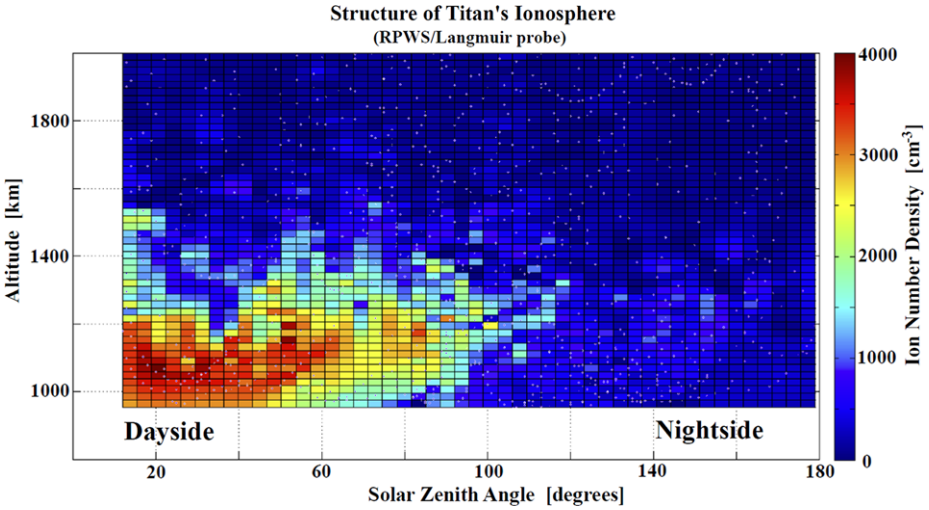

Fig. 3 The ionospheric "ion" density of Titan (altitude versus solar zenith angle, SZA) as measured by the Cassini RPWS Langmuir probe (ion current part) based on 55 flybys (110 altitude profiles). Each *dot* is a measurement

tan's atmosphere (see Cravens et al. 2009; and references therein). On Earth, several different ionospheric layers arise (D-, E-, F2-, and F1-layers) because different molecular or atomic ions dominate at different altitudes due mostly to the effects of atmosphere-ionosphere chemistry. Titan shows a dominance of H_2CN^+ and $C_2H_5^+$ in the upper ionosphere (e.g., Cravens et al. 2006), while the lower ionosphere shows an incredibly complex display of poly-aromatic hydrocarbon and nitrile molecular ions with masses up to 50,000 atomic mass units (amu) (e.g., Coates et al. 2007a, 2009; Vuitton et al. 2007; Waite et al. 2007; Crary et al. 2009; Sittler et al. 2009a, 2009b; Vuitton et al. 2009; Wahlund et al. 2009). It is therefore unsurprising that deviations from a true Chapman-like altitude profile are at times encountered (e.g., Figs. 2 and 4). Solar electromagnetic radiation varies also both with the synodic solar rotation (about 27 days), where active regions of the Sun come into view of the planetary body periodically, and over the solar cycle (about 11 years), which in turn cause similar variations in the ionosphere.

The ionization beyond 100° SZA is, at these altitudes, dominated by precipitation of electrons with energies of a few hundred eV, and by associated secondary electrons produced in the atmosphere during the impact process. The energetic, hot electrons are from the external plasma in Saturn's magnetosphere passing Titan with a bulk speed of about 120 km/s. Their thermal velocity is much higher than the bulk speed (e.g., Coates et al. 2007b; Ågren et al. 2007; Cravens et al. 2008a; Galand et al. 2010). Both the bulk plasma flow and the high energy particle intensities in Saturn's magnetosphere, which the atmosphere of Titan experiences, varies with 2–3 orders of magnitude and is connected to the Saturn rotation period of about 10.7 hours (Bertucci et al. 2009; Morooka et al. 2009; Rymer et al. 2009; Andrews et al. 2010). There are also transient solar phenomena (e.g., CME) that may provide temporary effects on the ionization.

The prominent ionospheric peak near 500–600 km altitude is intermittent and believed to be caused by energetic ion precipitation (Cravens et al. 2008b) consistent with the variable behavior of Saturn's magnetosphere. The macro-molecular organic rich species found here should readily be ionized. However, metallic ion layers due to meteoritic impacts cannot yet

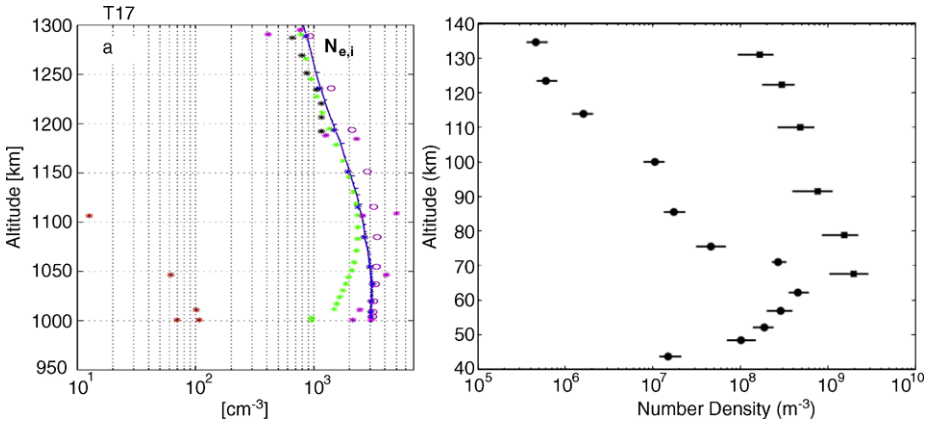

Fig. 4 Plasma number density estimates for inbound of the T17 flyby (*left panel*, from Wahlund et al. 2009). Plasma number densities are the electron number density by RPWS/LP (*blue*) and RPWS/E (*black*), the total ion number density by CAPS/IBS (*magenta stars*) and RPWS/LP (*magenta circles*) as well as INMS (green stars, <100 amu), the heavy (>100 amu) ion number densities by and CAPS/IBS (*red stars*). The *right panel* (from López-Moreno et al. 2008) shows the electron number densities (*circles*) and ion number densities (*squares*) measured during the Huygens probe descent. Significant differences in electron and ion number densities or between ion densities for low mass and high mass numbers can at times be detected throughout the main regions of the ionosphere (70–1100 km altitude). Negatively charged ions or aerosol and/or very massive ions up to several thousand amu can cause such differences

be ruled out as the source for this ionospheric peak (Molina-Cuberos et al. 2001). The deepest ionospheric regions near 70 km can only be produced by the most energetic radiation, cosmic rays.

The solar EUV and X-rays cause ionization only on the dayside and give rise to Chapman-like layers (notably with large variability), while the external plasma flow causes a dominant effect on the ram-side. For Titan (most often orbiting within Saturn's magnetosphere) the source direction cyclically varies with its orbit period of about 16 days. Sometimes the solar wind pressure is strong enough and the location of Titan favorable, such that Titan becomes directly immersed in the solar wind or the magneto-sheath (which happened during the T32 flyby, see e.g., Bertucci et al. 2008; Garnier et al. 2009; see Fig. 5). To compare with Mars and Venus, two other unmagnetized planetary bodies, the ram flow is then in a similar orientation to the electromagnetic radiation.

The gradient in plasma pressure that arises between the day and night ionosphere may cause a day-to-night plasma flow, as has been shown for Venus and possibly for Titan (e.g., Cui et al. 2009; see further below).

One can divide an ionosphere into a transport controlled (topside part) and a chemistry controlled (deeper part) region, and the boundary between these is related to the amount of collisions between the ionospheric plasma and the neutral gas in the atmosphere. On Titan such a boundary has been identified to be near ∼1300 km altitude (Ma et al. 2006, see also Galand et al. 2010), below which the effective electron dissociative recombination coefficient (a few times 10^{-7} to 10^{-6} cm^3 s^{-1}) can be determined (see Fig. 6). The rather large value for the recombination coefficients of heavy molecular organic ions is confirmed by laboratory measurements simulating Titan conditions (Vigren 2010).

Unlike the Earth, Titan has no detectable global magnetic field or small-scale crustal fields as occur at Mars (Neubauer et al. 1984; Backes et al. 2005; Bertucci et al. 2007, 2008). Therefore, the external plasma flow interacts more directly with the atmosphere,

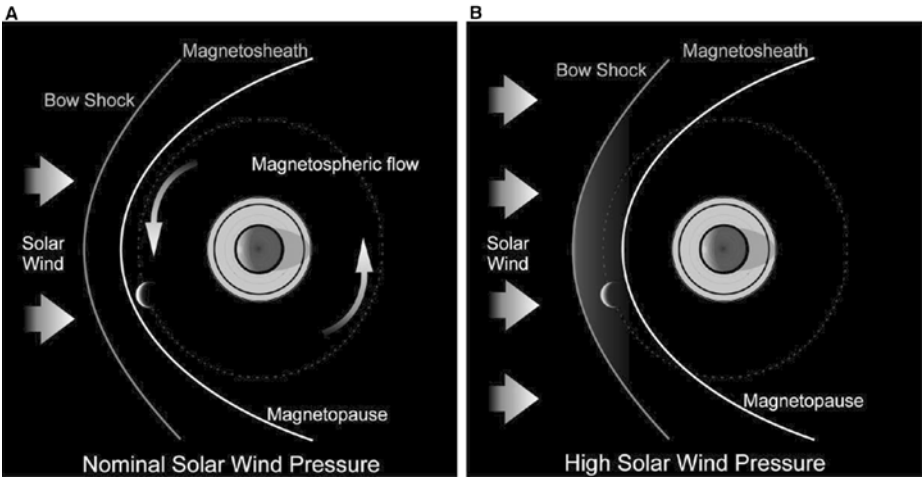

Fig. 5 The importance of direction of ionizing radiation and the location of Titan in its orbit around Saturn for the ionospheric structure (after Bertucci et al. 2008)

exosphere and ionosphere of unmagnetized Titan. The external plasma flow is mostly the highly dynamic magnetosphere of Saturn (e.g., Bertucci et al. 2009; Morooka et al. 2009; Rymer et al. 2009; Andrews et al. 2010), or occasionally the solar wind during active solar conditions (Bertucci et al. 2008; Garnier et al. 2009).

In the case of Titan, with a well-developed ionosphere, this interaction leads to the formation of an induced magnetosphere engulfing the planetary body with a pileup of magnetic field upstream and a draped magnetic tail-like configuration downstream (e.g., Ness et al. 1982), which mediates the escape of the ionospheric plasma to the surrounding space and contributes to the atmospheric erosion (Wahlund et al. 2005; Ma et al. 2006; Modolo et al. 2007a, 2007b; Szego et al. 2007; Wei et al. 2007; Sittler et al. 2009a, 2009b). Depending on the external plasma flow conditions the erosion rate can be large and is therefore the key for understanding the evolution of the atmosphere of Titan (and other similar unmagnetized bodies) over geological timescales. One different feature of Titan's ionosphere interaction, as compared to the cases at Mars and Venus, is that the external pressures (magnetic, dynamic, energetic plasma) most often are larger than the ionospheric plasma pressure (Garnier et al. 2009; Edberg et al. 2010). This causes the magnetic pile-up region on the ram-side to be close to the ionospheric peak, and plasma collisions with the neutral atmosphere need be taken into account to enforce pressure balance (see Fig. 7).

3 Titan's Ionospheric Chemistry

On the first close (1174 km altitude) flyby by Cassini of Titan, the Ion and Neutral Mass Spectrometer (INMS) found a remarkably complex spectrum of neutral species (Waite et al. 2005, 2007) in Titan's upper atmosphere and ionosphere. Later flybys (down to 950 km altitude) confirmed the neutral observations and showed that positive ion species were also present, with a highly complex spectrum observed up to the 100 amu/q mass limit of INMS (Cravens et al. 2006; Waite et al. 2007, see Fig. 8). The CAPS ion instruments also showed a rich diversity of ions when the spacecraft was oriented in the ram direction (e.g. Coates

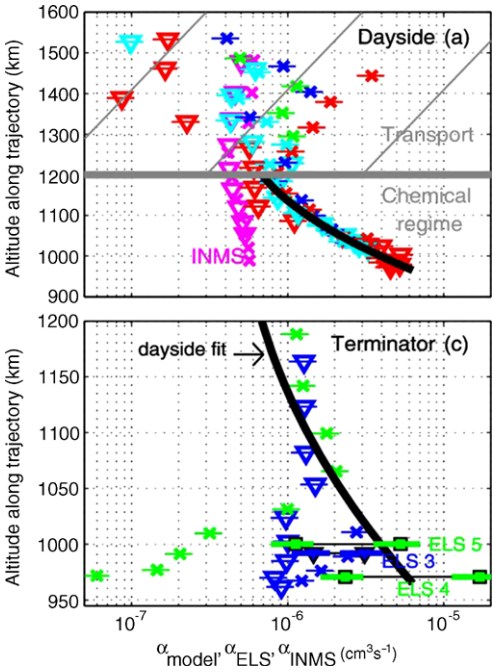

Fig. 6 (*Upper panel*) Altitude profiles of the modeled effective recombination coefficient during dayside conditions (SZA < 85°) (T18 in *blue*, T32 in *green*, T39 in *red*, and T40 in *cyan*). *Open triangles* correspond to inbound, and crosses correspond to outbound. The *thick*, *solid*, *black line* represents the best fit of the modeled effective recombination coefficient below 1200 km. (*Lower panel*) Altitude profiles of the modeled effective recombination coefficient for T18 (*blue*) and T32 (*green*) for terminator conditions (85° < SZA < 110°) (from Galand et al. 2010)

et al., AGU Fall meeting 2004, Crary et al., Dynamics and Composition of Plasma in and around Titan, unpublished manuscript, 2005). The CAPS IBS data showed evidence for heavy positive ions with masses up to at least 350 amu/q (Waite et al. 2007). In addition, the RPWS Langmuir probe also reported data consistent with the presence of heavy positive ions (Wahlund et al. 2005).

The picture became even more complex with the discovery of heavy negative ions in Titan's ionosphere (Coates et al. 2007a; Waite et al. 2007). In addition to the complex positive ions, these negative ions were observed every time Cassini flew through Titan's ionosphere with CAPS oriented in the ram direction at altitudes below ∼1400 km (Coates et al. 2007a, 2009; Coates 2009). Using the CAPS electron spectrometer, the ∼6 km/s relative flyby speed means that cold ions observed while the instrument is pointed in the ram direction have an energy per charge E_{eV} which can be related to their mass per charge m_{amu}, using $m_{amu} = c(E_{eV} - V_{sc})$ with $c = 5.32$ amu/eV and the spacecraft potential $V_{sc} \sim -0.5$ V (see Coates et al. 2010). The spacecraft potential may be determined from the peak in the IBS data corresponding to $HCNH^+$ (e.g. Coates et al. 2007a, 2007b; Cravens et al. 2006) or from the Langmuir probe (Wahlund et al. 2005).

The observations showed that negative ions are seen with a range of masses, corresponding to the observed peaks in the energy spectrum, with a broad, unresolved peak at high mass. On one encounter, the mass was clearly higher than 8,000 amu/q (Waite et al. 2007) and reanalysis showed that the maximum mass was over 10,000 amu/q (Coates et al. 2007a) and can reach as high as 13,800 amu/q (Coates et al. 2009, 2010), see Fig. 9. The mass may in fact be larger than this as the charge state is not determined; a simple charging argument shows that q may be as high as 5 (Coates et al. 2007a) thus the observed mass may be a factor 5 higher than the mass per charge.

The altitude and latitude dependence of these negative ions was studied during 23 encounters (Coates et al. 2009), indicating that the heaviest positive ions are observed at the

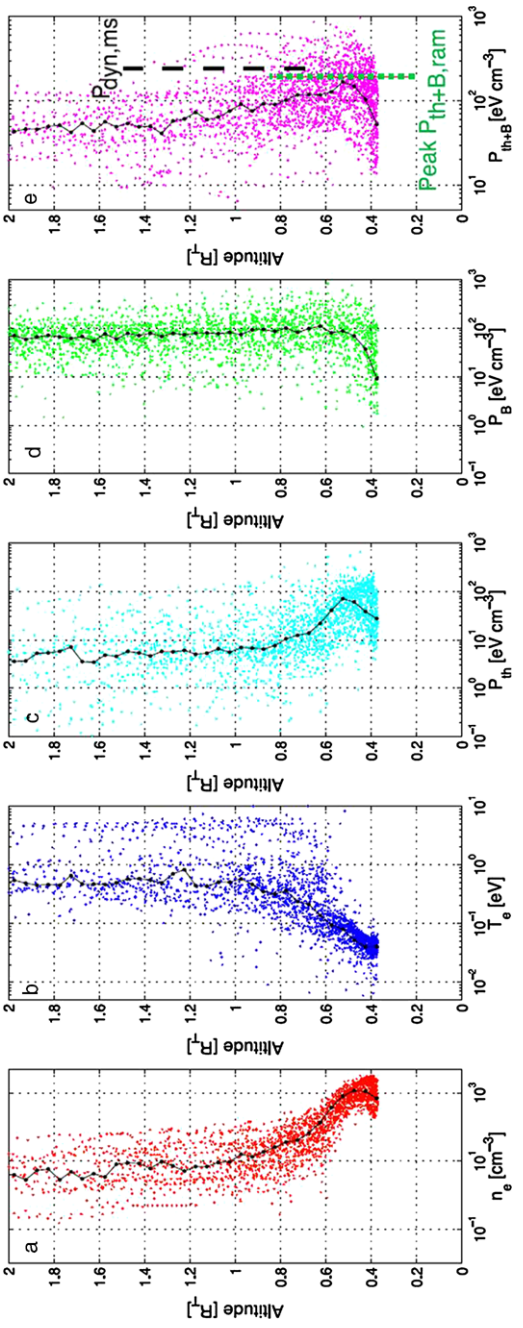

Fig. 7 Combined observed altitude profiles of (**a**) the electron density, (**b**) the electron temperature, (**c**) the thermal pressure, (**d**) the magnetic pressure and (**e**) thermal plus magnetic pressure. The *black solid lines* show the median values. The *black dashed line* in panel (**e**) shows the approximate magnetospheric ram pressure and the *green dotted line* shows the average peak pressure when only including ram side data (from Edberg et al. 2010)

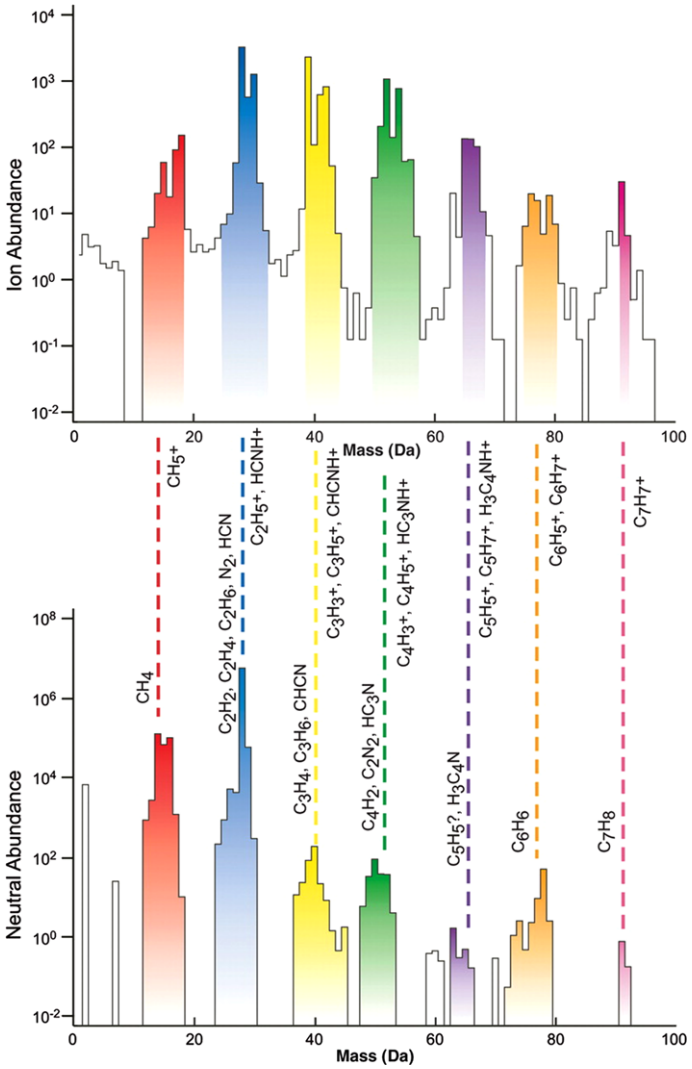

Fig. 8 Ion (*upper panel*) and neutral (*lower panel*) data from INMS during the T19 encounter showing the chemical complexity in Titan's ionosphere (from Waite et al. 2007)

lowest altitudes. In addition, it was found that the heaviest ions are seen at high latitudes and near the terminator. This has implications for the formation and destruction processes. The formation of the heaviest ions is more efficient, or destruction processes least efficient, when sunlight is weak or absent. The ions appear to build up in size with decreasing altitude, though it is not yet clear whether they are formed at higher altitudes and grow or at lower altitudes and dissociate (Coates et al. 2010; Waite et al. 2008). However it is likely that the particles descend through the atmosphere to form Titan's haze and becoming tholins which reach the surface (e.g., Sagan et al. 1993); this is also consistent with haze observations from Cassini UVIS up to 950 km (Liang et al. 2007).

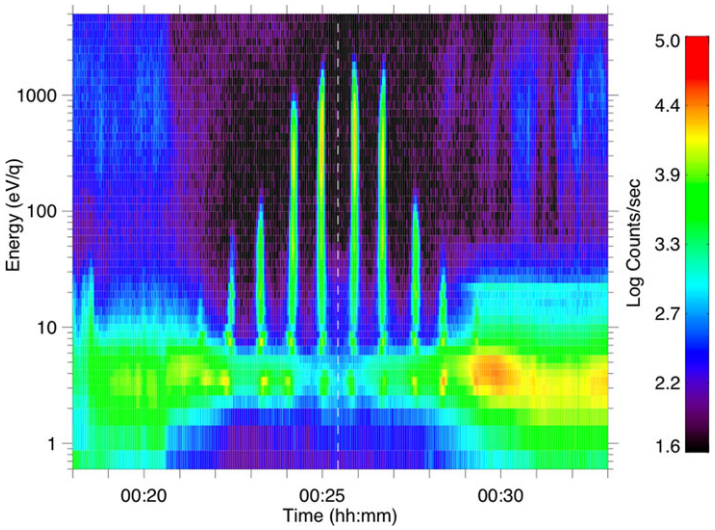

Fig. 9 CAPS ELS data from T16, showing the observation of negative ion peaks when the CAPS actuator sweeps the ELS field of view through the ram direction. Negative ions are seen at energies up to 13,800 amu/q on this encounter (from Coates et al. 2010)

Furthermore, the effect of solar radiation on the negative ion densities is currently under investigation. At the altitude range of 950–1050 km initially studied, the solar radiation can reach the ions at solar zenith angles (SZA) of up to 135°. This is demonstrated in Fig. 10. At such high angles, however, the amount of solar radiation may be very small. Results from two data sets are shown here. The first data set (Figs. 10B and 10D) is from 22 encounters where negative ions were observed. The second data set (Figs. 10C and 10E) is from one encounter only (T57). It was possible during this encounter to obtain a continuous set of measurements because the actuator was fixed. This flyby took place around a SZA of 135° and hence allowed observing the difference in densities of ions exposed to no solar radiation ('in shadow' symbols in figures) and ions exposed to the small amount of solar radiation available at this high SZA.

Two different mass groups are shown: Light ions (10–30 amu, Figs. 10B and 10C) and heavier ions (110–200 amu, Figs. 10D and 10E). Density measurements are indicated on the horizontal axes of Figs. 10B–E. Due to uncertainties in the absolute calibration of the CAPS-ELS instrument for negative ions, the values should be treated as relative densities at present.

The densities of the light ion mass group are highest when exposed to large amounts of solar radiation. This suggests that photochemical reactions yield the highest production rates for this mass group. The heavier ion densities are highest on the night side where chemical reactions that do not involve solar radiation take place. Photochemical reactions that break up larger ions are also not present here. Both mass groups have a density minimum in the terminator region where only a small amount of solar radiation is present.

In addition to the negative ion studies, the positive ions were studied in detail by Crary et al. 2009. Using CAPS and INMS data they were able to determine the spacecraft potential, and in addition the ion temperature and a component of the wind speed in Titan's ionosphere. The ion temperature (110 K at 1200 km) was less than the neutral temperature at that altitude, perhaps indicating decoupling of the ionized and neutral components, though there

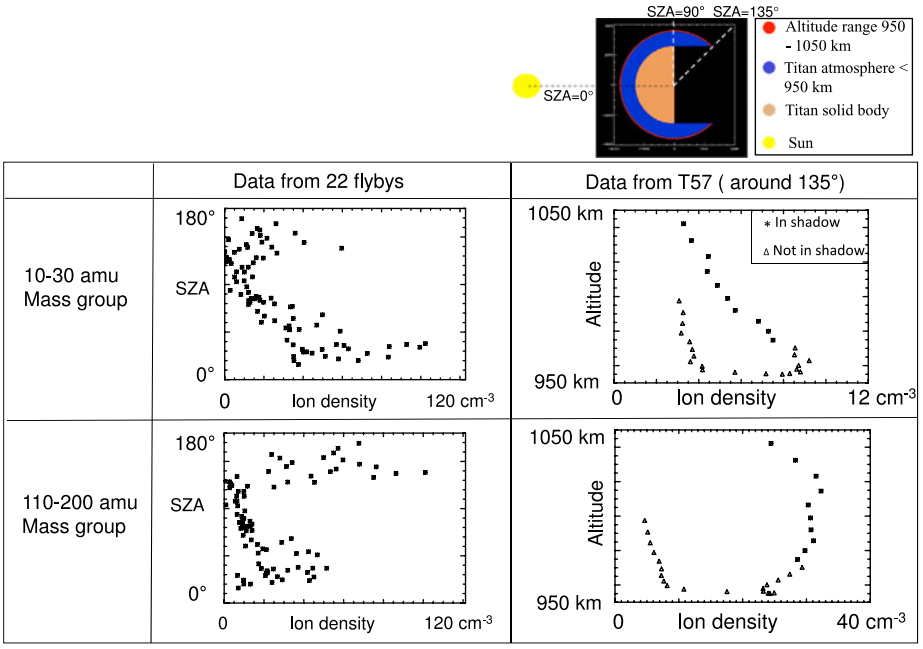

Fig. 10 A, schematic of Titan's ionosphere and (B-D) CAPS ELS data on negative ion density in different mass groups

may also be significant errors in the determination of the ion temperature. Strong ion winds of 100–260 m/s are consistent with estimates at lower altitudes. Also, they found persistent positive ion peak occurrence up to at least 200 amu/q, with peak spacing of 12–14 amu/q, indicating hydrocarbon and/or nitrile chemistry. Note that detailed ionospheric models had also predicted complex positive ion species in Titan's ionosphere (Fox and Yelle 1997; Keller et al. 1998). Such ions are always present in the data below 1200 km and can dominate the ion population. Crary et al. conclude that PAH species, some with two or three benzene rings, are the most likely identification for the heavy positive ions. Examples of IBS and ELS data, which show the completely unexpected negative ions at these altitudes, are shown in Fig. 11.

A number of chemical models have been produced for Titan's ionosphere. Before Cassini, Wilson and Atreya (2004) presented a detailed model of the anticipated positive ion chemistry. Vuitton et al. (2007) presented a more detailed model based on INMS data. Later, Vuitton et al. (2009) presented the first chemical model of Titan's ionosphere to include negative ions. Based on the production and loss rates assumed, the main production mechanism is expected to be dissociative electron attachment, and the main loss process associative detachment with some photodetachment. They concluded that the main low mass negative ion peaks are consistent with CN^-, C_3N^-, and C_5N^-. However the higher mass negative ions, which in association with the positive ions may form the source for Titan's haze (Waite et al. 2007; Coates et al. 2007a) are not fully explained as yet.

Due to the limited mass resolution of the electron spectrometer (Linder et al. 1998; Young et al. 2004), it is impossible to determine from the measurements whether the high mass negative ions are rings, chains or even fullerenes (the latter suggested by Sittler et al. 2009a, 2009b). The fullerene possibility is interesting as it may provide a mechanism for

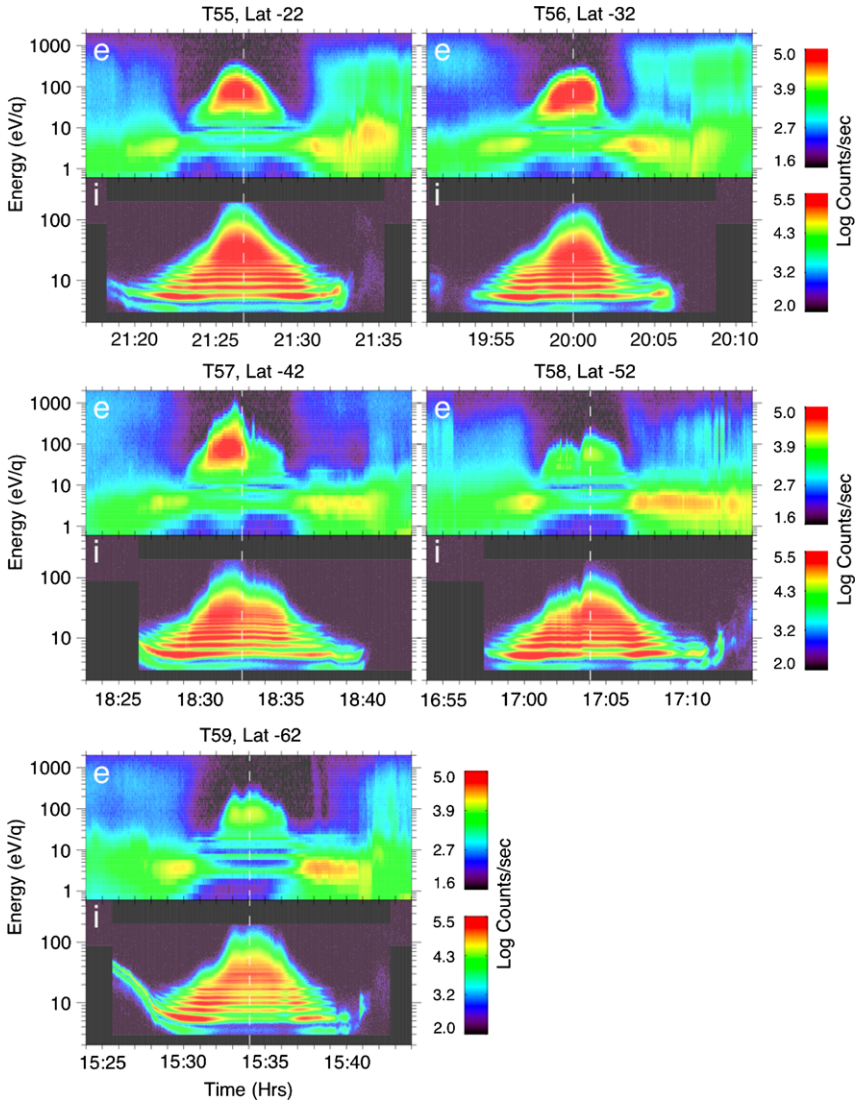

Fig. 11 CAPS ELS and IBS data, showing the complexity of the positive and negative ion data (from Coates et al. 2010)

transporting magnetospheric oxygen from the top of the atmosphere to Titan's surface where it would provide the possibility of oxidation. In addition, Michael et al. (2011) modeled the negative ion populations and concluded that the particles are aerosols with size <10 nm and are likely to be singly charged.

Further analysis of the RPWS Langmuir probe data, with that of CAPS and INMS, has shown that the amount of heavy organic compounds that falls through Titan's atmosphere may be as high as 01.–1 Mt/y (Wahlund et al. 2009)—providing a sizeable source for Titan's haze. It was also suggested that heavy particles would dominate in the unobserved region of Titan's atmosphere between 400 and 950 km. In addition, the presence of heavy negative

ions has recently been confirmed using the RPWS LP data (Wahlund et al., paper presented at Alfven conference, 2010).

4 Titan's Ionospheric Electro-Dynamic Coupling

The altitude region between 800 and 1500 km is the most electrically conductive region with conductivities perpendicular to the magnetic field (Hall and Pedersen) between 10^{-3}–10^{-1} S/m (Rosenqvist et al. 2009). This region therefore readily couples electro-dynamically to the external magnetized plasma flow (Saturn's magnetosphere or solar wind) past Titan (e.g., Ness et al. 1982; Blanc et al. 2002, which set up ionospheric current systems (10–100 nA/m^2) and associated convection electric fields (0.5–3 μV/m) that may lead to energy deposition by Joule heating and/or ion collisional heating with the atmosphere (Ågren et al. 2011; see Fig. 12). The latter form of ion heating has possibly already been detected (Crary et al. 2009), where the inferred ion temperature enhancements above 1200 km altitude correspond well in magnitude with the expected ion Joule, or frictional, heating by ionospheric electric fields. An alternative driving mechanism of the observed ionospheric currents might be thermosphere neutral winds that cause a drag on the plasma and generate electrical currents in the conductive ionospheric plasma.

The external plasma flow induces an electro-dynamic interaction with the ionosphere. Convection electric fields are set up in the interaction, which generate both plasma flows in the non-collisional part of the ionosphere, as well as electrical current systems in the conductive (collisional) part of the ionosphere. The currents and the drag between ions and neutrals cause Joule (frictional) heating, which in turn generate thermal gradients and expansion through ambipolar diffusion. The currents below the exobase (≈1400 km) are principally parallel and Hall in nature, i.e. they are flowing parallel to the magnetic field and/or perpendicular to both the magnetic and the electric field, respectively, whereas the Pedersen current, flowing perpendicular to the magnetic field and parallel to the electric field, is negligible in comparison.

The waves in the external plasma flow, like ion cyclotron waves and Alfvén waves in the ULF range, propagate into the ionosphere, are reflected or absorbed there and cause additional heating/expansion and direct acceleration of ionospheric plasma by their inherent wave electric fields. Quasi-static electric fields may also arise, accelerating and energizing the ionospheric plasma. In the Earth's auroral region it is known that such waves break up, become broadband and energize the ionospheric plasma causing an ionospheric outflow along the magnetic field lines toward the magnetosphere (e.g., Louarn et al. 1994; Wahlund et al. 1994, 1998; Stasiewicz et al. 2000; Barakat and Schunk 2006; Chaston et al. 2007; Horwitz and Zeng 2009, and references therein). Similar processes may occur in the ionosphere of Titan near structured magnetic field regions in the draped tail. On Titan, the waves can propagate directly from the external plasma flow (e.g., Saturn magnetospheric flow turbulence) into the ionosphere.

5 Titan's Ionospheric Transport Processes

Since Titan has a low gravity, it is not surprising that the ions in Titan's upper atmosphere are constantly escaping from this moon. We present in this section observational evidences for ion loss on Titan, as revealed by Cassini.

First, a measurement of the ion velocity was made with the Langmuir Probe (LP) of the Cassini Radio and Plasma Wave Science (RPWS) instrument. Multiplied by the measured

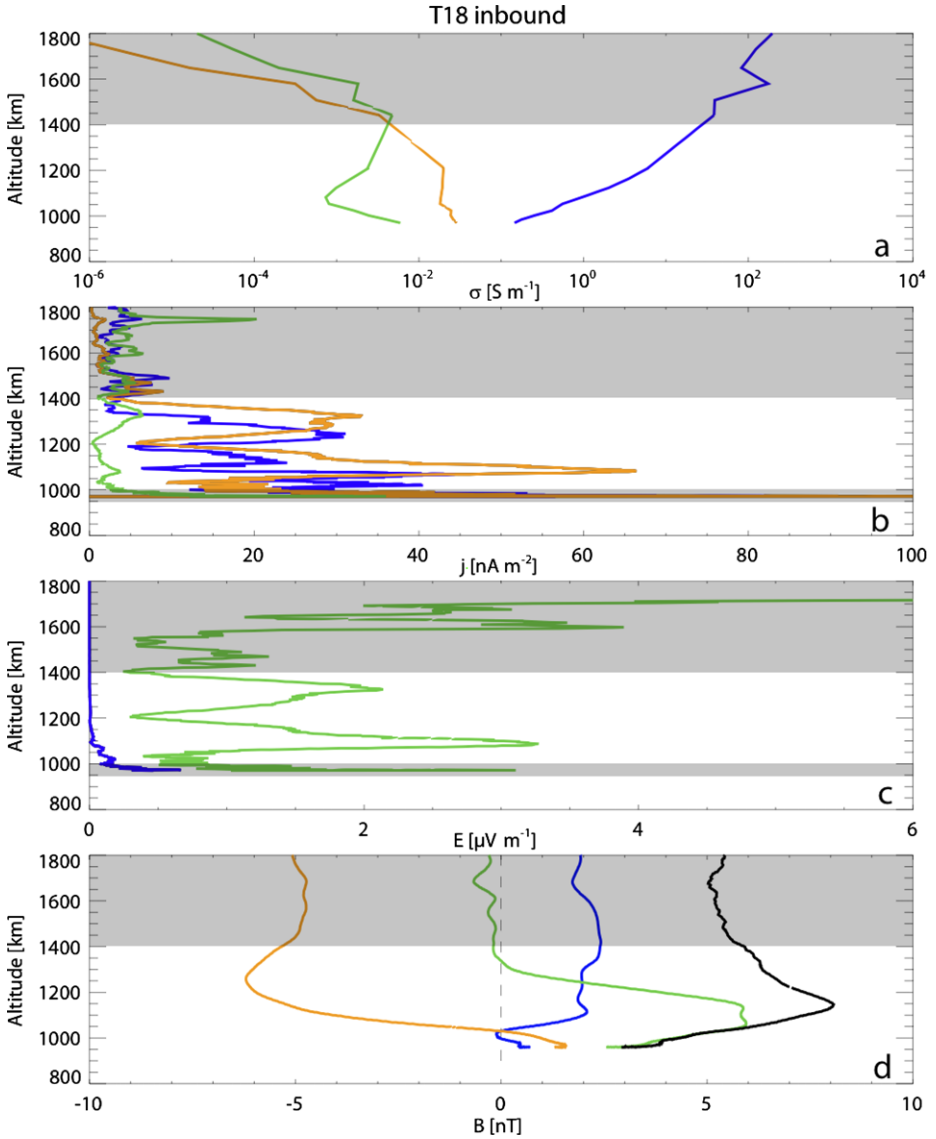

Fig. 12 Data from the inbound leg of flyby T18. Altitude profiles of (**a**) parallel (*blue*), Pedersen (*green*) and Hall (*orange*) conductivities, (**b**) parallel (*blue*), Pedersen (*green*) and Hall (*orange*) currents, (**c**) parallel (*blue*) and perpendicular (*green*) electric fields and (**d**) magnetic field components in Titan-centered spherical coordinates (B_r in *blue*, B_θ in *green* and B_φ in *orange*) and total field strength in *black*. (From Ågren et al. 2011)

electron density and assuming cylindrical geometry for the wake region, the total ion loss rate from Titan was estimated to be $\sim 10^{25}$ ions/s for the first Titan flyby of Cassini (known in project parlance as TA, Wahlund et al. 2005). This is significantly higher than the value of 1.2×10^{24} ions/s estimated from Voyager 1 observations based on simple pressure balance considerations (Gurnett et al. 1982). However, it should be emphasized that the TA estimate

was based on the assumption of interpreting the measured total ion velocity as a direct representation of the escaping velocity.

Second, indirect evidence for ion transport in planetary atmospheres was obtained by comparing the observed ion distribution with that inferred from the diffusive equilibrium condition. Such a method has been extensively used in the studies of the Venus and Mars ionospheres (e.g. Whitten et al. 1982; Cravens et al. 1983; Brannon et al. 1993; Tanaka and Murawski 1997). The diffusive equilibrium distribution is derived from the plasma momentum equation by assuming force balance for the ions. On Titan, the vertical component of the plasma momentum equation can be written as

$$\frac{1}{N_e}\frac{\partial N_e}{\partial r}+\frac{1}{T_p}\frac{\partial T_p}{\partial r}+\frac{1}{H_p}+\frac{1}{N_e k T_p}\frac{\partial}{\partial r}\left(\frac{B_h^2}{8\pi}\right)=\sum_n \frac{\overline{M}\nu_n U_n}{kT_p}$$

where $T_p = T_e + T_i$ is the plasma temperature with T_e and T_i being the electron and ion temperatures, N_e is the electron density, M is the mean ion mass, $H_p = (kT_p)/(Mg)$ is the plasma scale height with g being the local gravity and k being the Boltzmann constant, B_h is the magnitude of the horizontal B-field, ν_n is the mean ion-neutral collision frequency, and U_n is the neutral drift velocity. To solve for the diffusive equilibrium electron (or total ion) densities, N_e, we adopted here the mean ion mass and ion temperature (assuming identical to the neutral temperature) measured by the Cassini Ion Neutral Mass Spectrometer (INMS) (e.g., Cui et al. 2009), the electron temperature measured by RPWS LP (e.g., Wahlund et al. 2005), and the magnetic field measured by the Cassini Magnetometer (MAG) (e.g., Neubauer et al. 2006). The other parameters such as the neutral drift velocity and the ion-neutral collision frequency can also be obtained from the Cassini INMS data (e.g., Yelle et al. 2008). The diffusive equilibrium electron distribution thus obtained can then be compared with the observed distribution (see Fig. 13), with the difference between the two providing information on the actual state of ion flow on Titan.

In Cui et al. (2010), such an analysis was made based on the global averaged measurements made during 9 close encounters of Cassini with Titan. We present in Fig. 13a a comparison between the observed electron (or total ion) distribution (solid circles) and that expected in diffusive equilibrium (solid line). Ions are observed eroded with respect to the diffusive equilibrium values, especially above 1400 km. This implies the presence of ion outflow on Titan, i.e. ions are escaping from the satellite. The ion velocity profile was also inferred from the difference between the observed profile and that in diffusive equilibrium, which gives an estimate of the global average ion escape rate of 1.7×10^{25} ions/s (Cui et al. 2010), comparable with the value reported by Wahlund et al. (2005). This value lies between the ion loss rate of $\sim(3\text{–}7)\times10^{24}$ ions/s predicted by MHD models (e.g., Nagy et al. 2001; Ma et al. 2006) and the value of $\sim(1.5\text{–}6)\times10^{25}$ ions/s predicted by hybrid simulations (e.g., Sillanpää et al. 2006; Modolo and Chanteur 2008).

A byproduct of the above analysis is the evaluation of the actual force balance in Titan's ionosphere, from which we can obtain information on how ions are accelerated. This is presented in Fig. 13b, with different line-styles giving the global average altitude profiles of various force terms, including the plasma pressure gradient, the gravitational force, the magnetic force as well as the neutral drag force. The dominant forces are the upward plasma pressure gradient and downward gravity. The extended nature of Titan's atmosphere is characterized by a moderate decrease in the plasma pressure gradient as compared with the gravity, leading to a net upward force in the upper ionosphere of Titan.

The general properties of ion flow on Titan are not only characterized by a trend of global ion loss, but also characterized by horizontal ion transport. To investigate this, we divided the

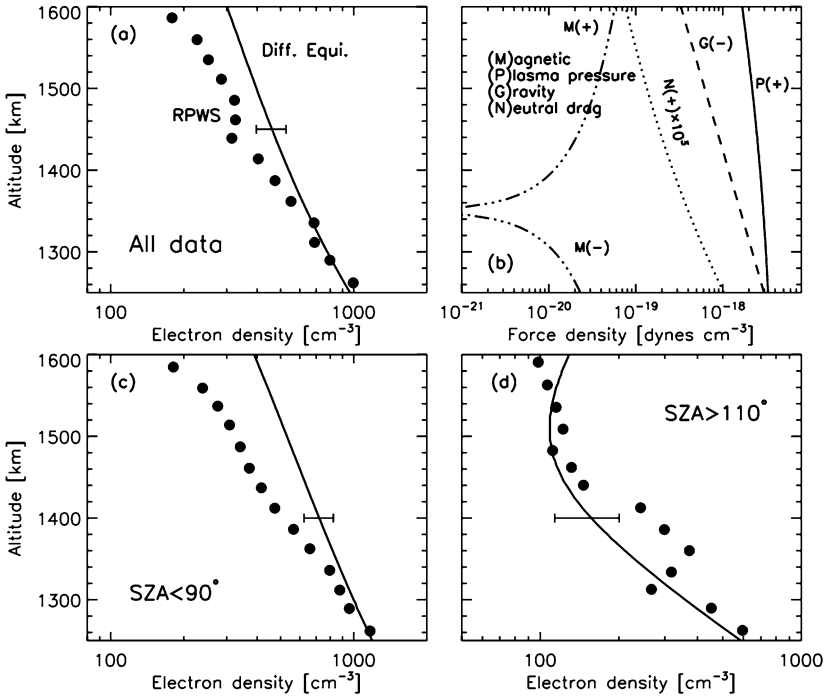

Fig. 13 (**a**) Comparison between the observed RPWS electron density profile with that in diffusive equilibrium, in the global average sense. (**b**) The altitude profiles of various terms in the plasma momentum equation, including the plasma pressure gradient term, the gravitational term, the magnetic field term and the neutral drag term. The neutral drag term is amplified by a factor of 1000. Positive and negative signs represent upward and downward forces. (**c**)–(**d**) Same as panel (**a**) but averaged over the dayside and nightside subsamples, respectively. Adapted from Cui et al. (2010)

available Cassini dataset into two subsamples, one averaged over the dayside and the other one averaged over the nightside. A comparison of the observed electron distribution with the diffusive equilibrium distribution is presented in Fig. 13c for the dayside subsample and in Fig. 13d for the nightside subsample. On the one hand, similar to the global average case, the dayside electron distribution is observed eroded, indicating ion outflow from Titan's dayside ionosphere. On the other hand, an inverse trend is clearly revealed by the nightside subsample, which could be interpreted as the presence of ion inflow at night. The diurnal difference in the behaviors of ion transport on Titan can be interpreted as a signature of day-to-night ion transport on this satellite (Cui et al. 2010). This is probably not surprising since it has been revealed by Cui et al. (2009) that although ions are generally found to be depleted at the nightside of Titan (as compared with the dayside), there is a clear trend of strong depletion for short-lived ions (e.g. CH_5^+ and $C_2H_5^+$) but only modest depletion for long-lived ones (e.g., $C_2H_5^+$ and $C_2H_3CNH^+$, see Fig. 14 for several examples).

Such a fact may significantly influence our understanding of the formation of nightside ions on Titan, which has been previously believed to be due to electron precipitation from Saturn's magnetosphere only (e.g., Cravens et al. 2008a, 2008b; Ågren et al. 2007, 2009). However, it appears from the Cassini observations that the transport of ions created at Titan's dayside may play an important role (Cui et al. 2009, 2010). Finally, it should be emphasized that such a scenario has to be distinguished from that of Venus on which the day-to-night

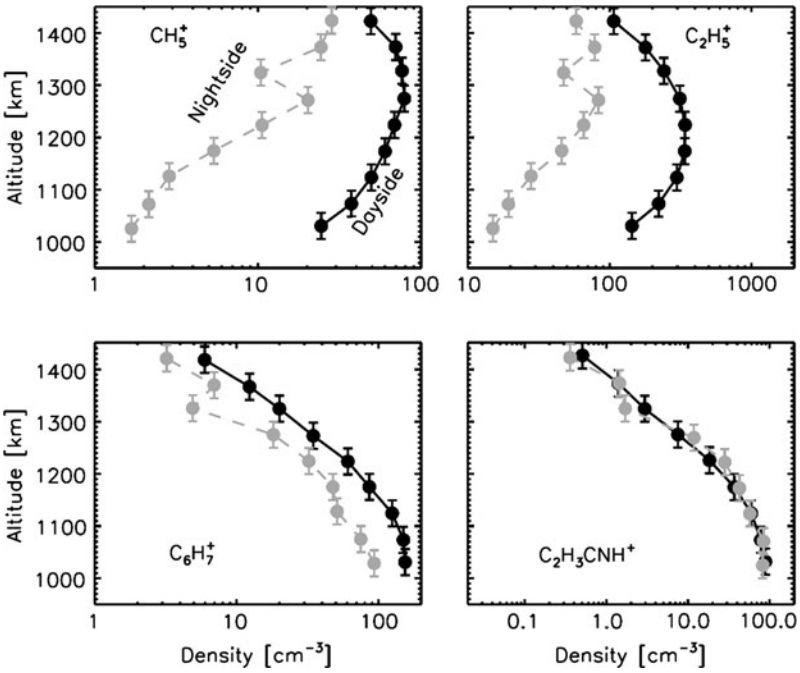

Fig. 14 The observed diurnal variations of several representative ion species. *Black* and *grey circles* represent the ion density profiles on Titan's dayside and nightside, respectively. All species in the *upper panels*, with short chemical time constants, show clear nightside depletion at low altitudes, whereas those in the *lower panels*, with long chemical time constants, present modest nightside depletion at all altitudes. Adapted from Cui et al. (2009)

ion transport is probably driven by strong horizontal thermal winds in response to pressure gradients from the large diurnal temperature difference (Elphic et al. 1984; Witten et al. 1984; Nagy et al. 1991), while on Titan, this could be either associated with the solid-body rotation of the satellite or enhanced by super-rotating horizontal neutral winds (e.g., Müller-Wodarg et al. 2000, 2008).

6 Photoelectrons at Venus, Mars and Titan

Ionospheric photoelectrons are a key component of planetary ionospheres. They are a product of photoionization, which is the major ionization source in sunlit ionospheres. The spectrum of solar radiation plays a key role in determining the resultant energy spectrum of ionospheric photoelectrons. The intense solar HeII 30.4 nm radiation line, with energy 40.79 eV, is one of the principal energy sources for ionization, and it produces photoelectrons with distinct energies. A number of theoretical and experimental studies have been performed for Earth, Mars, Venus and Titan, which have calculated the anticipated spectrum at the different objects (e.g., Nagy and Banks 1970; Mantas and Hanson 1979; Fox and Dalgarno 1979; Haider 1986; Gan et al. 1992; Galand et al. 2006; Schunk and Nagy 2009).

Based on the anticipated important species in each ionosphere, Coates et al. (2011) identified the most prominent expected peaks at the four objects (see Table 1). These peaks, which have been observed at Earth (e.g. Lee et al. 1980a, 1980b), Mars (Frahm et al. 2006a,

Table 1 Some dominant photoelectron energies from 30.4 nm solar UV illumination (40.79 eV); from Coates et al. (2011)

Earth		Mars		Venus		Titan	
Transition	Energy (eV)	Transition	Energy (eV)	Transition	Energy (eV)	Transition	Energy (eV)
$N_2\ X^2\Sigma_g$	25.2	$CO_2\ X^2\Pi_g$	27.02	$O\ ^2P$	22.29	$N_2\ A^2\Pi_u$	24.09
$O\ ^2P$	22.29	$CO_2\ B^2\Sigma_u$	22.69	$O\ ^4S$	27.17		
$N_2\ A^2\Pi_u$	24.09	$O\ ^2P$	22.29	$O\ ^2D$	23.69		

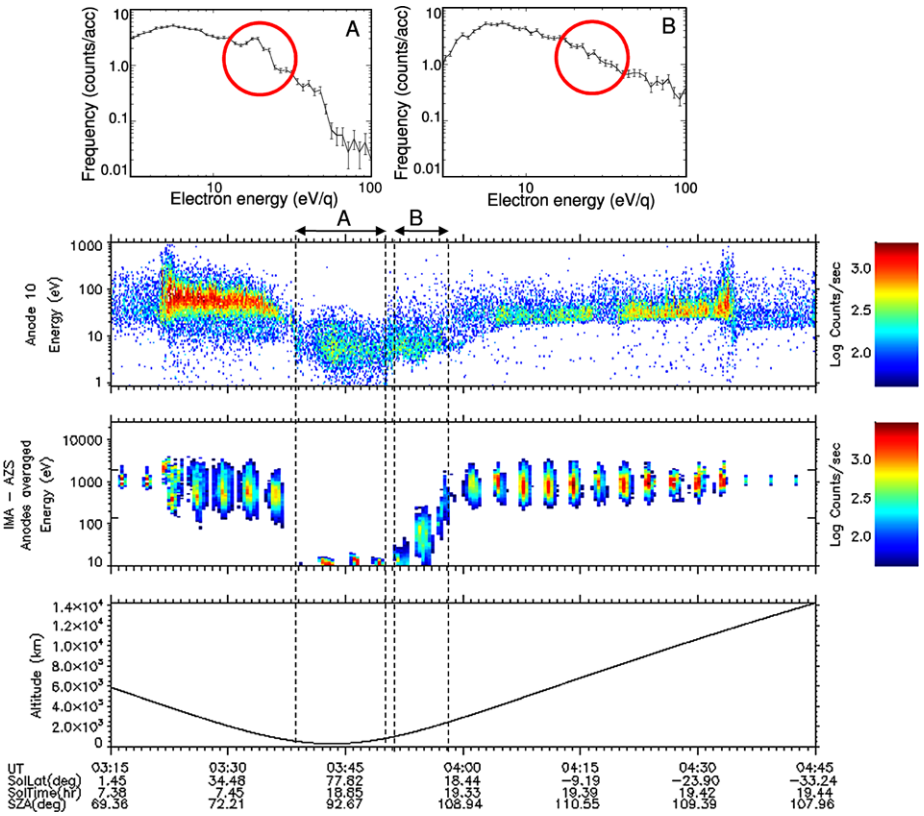

Fig. 15 Photoelectron example at Venus (from Coates et al. 2011)

2006b), Venus (Coates et al. 2008) and Titan (Coates et al. 2007b), are characteristic 'fingerprints' of the dayside planetary ionosphere. Although collisions, particularly at lower altitudes, broaden the primary photoelectron spectrum, clearly the fingerprints may still be present in the spectrum; the resulting electron energy spectrum can be calculated (e.g. Gan et al. 1990, 1992; Cravens et al. 1980, 2005; Galand et al. 2006).

In addition, a reduction in the energy spectrum of photoelectrons is expected at ∼60 eV. This is due to a drop in the solar input spectrum near 16 nm. This provides a second type of spectral signature, which can be used to infer the presence of photoelectrons.

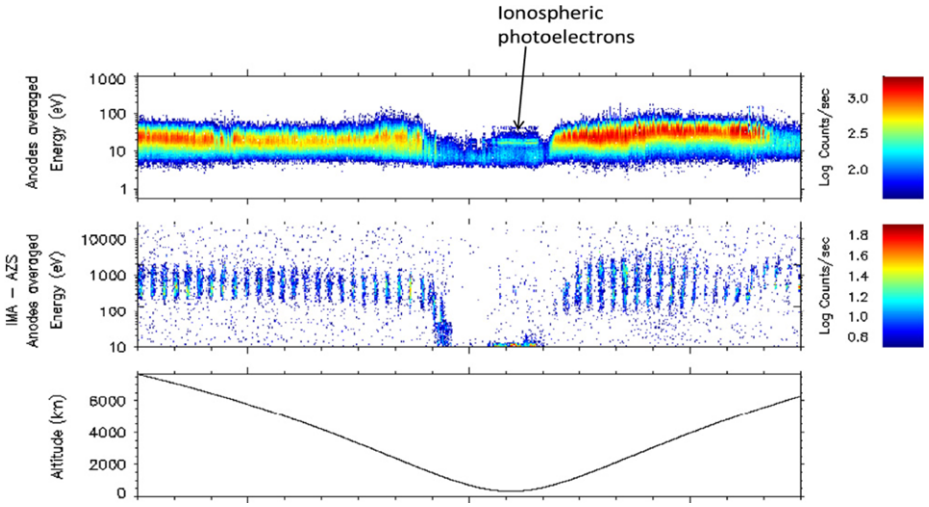

Fig. 16 Photoelectron example at Mars (from Coates et al. 2011)

Coates et al. (2011) presented a summary of observations in the dayside ionospheres. They also summarized existing and new observations of ionospheric photoelectrons at remote locations from the observation point at each of the objects (examples of data in the dayside ionosphere and at remote locations are shown in Figs. 15, 16 and 17). At the remote observation points, the low local neutral density means that local production of photoelectrons at the remote locations will be negligible. At Earth, the remote location is the equatorial magnetosphere at 7 R_E (Coates et al. 1985); at Mars, in the tail at distances up to the Mars Express apoapsis, ~3 R_M (Frahm et al. 2006a, 2006b); at Venus, in the tail at 1.45 R_V (Coates et al. 2008, 2011) and at Titan in the tail at up to 6.8 R_T (Coates et al. 2007b).

Clearly, at all of the objects considered, observations of photoelectrons in remote locations from their primary production point (the dayside ionospheres of the objects), provide a valuable diagnostic of the magnetic connection to their production point. The observations are summarized in Table 2 (from Coates et al. 2011).

The observation of photoelectrons at remote locations, and the magnetic connection to the observation point (see illustration in Fig. 18), raises the possibility that an ambipolar electric field may be set up by the mobile, energetic photoelectrons, as was suggested by Coates et al. (2007b). This may lead to a polar wind-type mechanism of ion escape from the ionospheres involved. Observations at Mars, Venus and Titan support this idea (Coates et al. 2011) and it has also been confirmed as a possibility using observations taken during recent Cassini flybys (Edberg et al. 2011).

Despite the different conditions at Earth, Mars, Venus and Titan, there are a number of similarities in the processes at work involving ionospheric photoelectrons (IPE) at these objects.

1. IPE are seen clearly in the dayside ionospheres with suitable instrumentation.
2. The energy spectrum of IPE is distinctive, acting as a 'fingerprint' for ionization processes.
3. IPE can, at times, be seen at large distances from the dayside ionospheres, e.g. in Earth's magnetosphere, and in the tails of Mars, Venus and Titan.

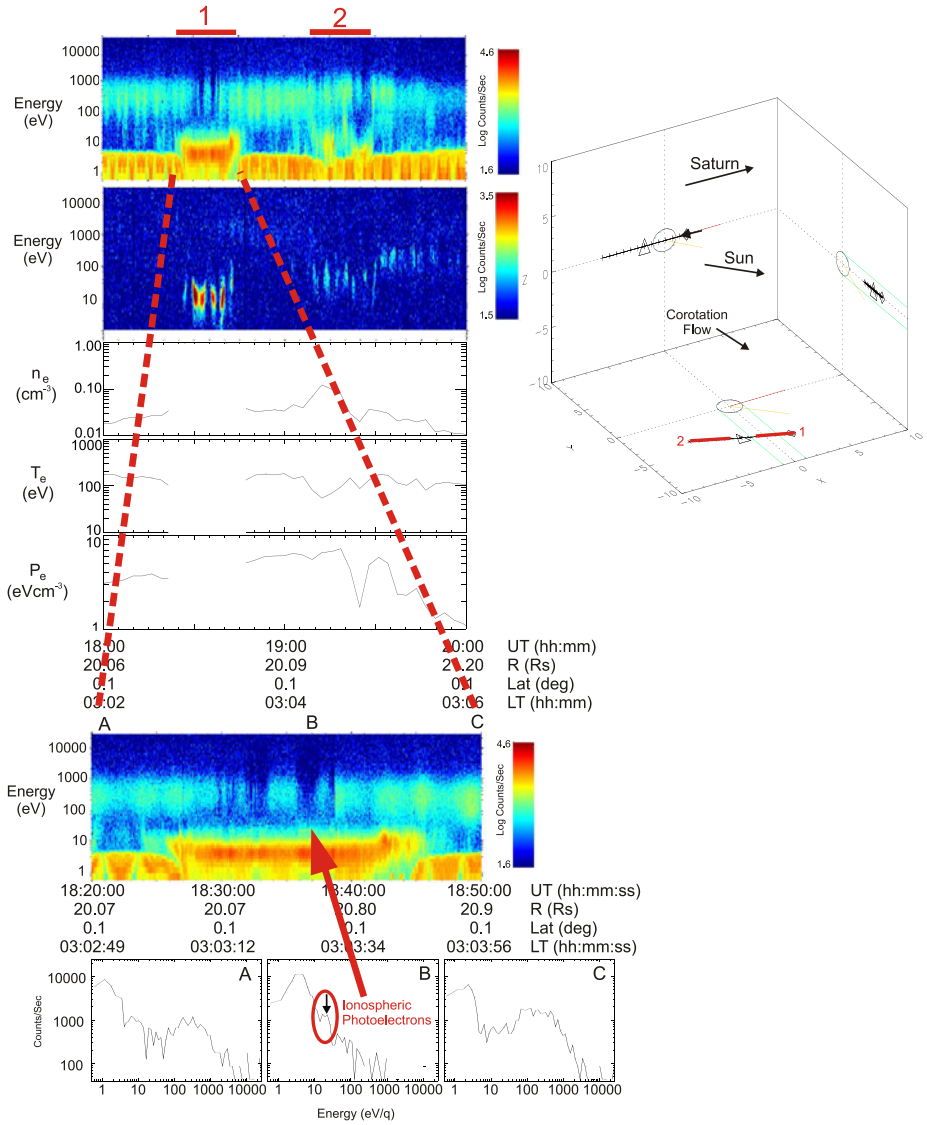

Fig. 17 Photoelectron example at Titan (from Coates 2009)

4. IPE are a sensitive diagnostic 'tracer' of a magnetic connection to the production location, namely the dayside ionospheres.
5. IPE may play a role in setting up an ambipolar electric field at the top of the ionosphere which would enhance ionospheric escape, in a mechanism analogous to the Earth's polar wind (e.g., Ganguli 1996, and references therein), enhancing pressure-driven plasma escape. A similar mechanism was suggested at Venus (Hartle and Grebowsky 1995), and a polar wind-related electric field escape mechanism at Titan was modeled by Keller and Cravens (1984).

Table 2 Summary of unmagnetized body interactions and of observations of ionospheric photoelectrons

	Venus	Earth	Mars	Titan
Interaction	Solar wind	Solar wind	Solar wind	Saturn magnetosphere
Intrinsic magnetic field	No	Ye—dipole	Localized crustal magnetization associated with heavily-cratered Southern highlands	No
Species associated with dominant photoelectron peaks (dayside, high altitude)	O	N_2, O	CO_2, O	N_2, (CH_4)
Location of ionospheric photoelectrons seen remotely from dayside ionosphere	Tail	Magnetosphere	Tail	Tail
Related ion escape?	Y (Fig. 15)	Y (polar wind)	Y (Fig. 16)	Y (Fig. 17)

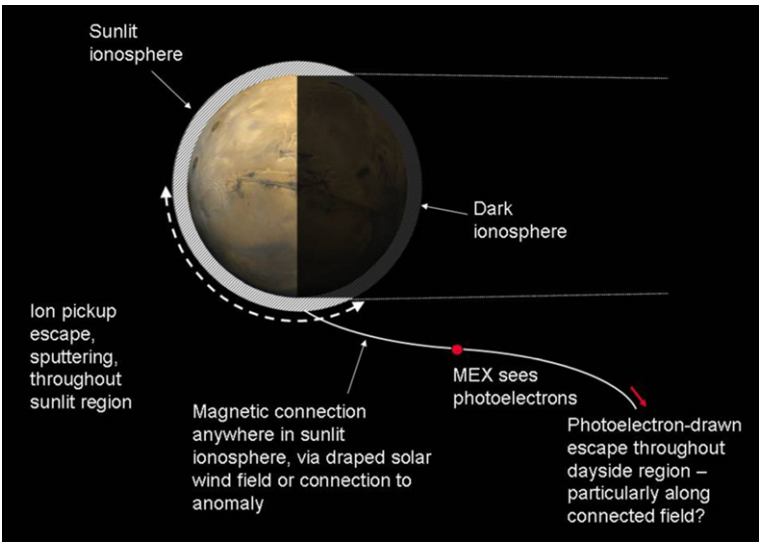

Fig. 18 Illustration of remotely observed photoelectrons, magnetic field connection and enhancement of escape (from Coates et al. 2011)

7 Conclusions

In this paper we have reviewed some recently studied aspects of the ionosphere of Titan, and in some cases compared with similar effects at Mars and Venus. The Cassini mission is currently approximately half way through its encounters with Titan, and following the extension of the mission we expect significant additional information on Titan's ionosphere until 2017.

Acknowledgements The authors acknowledge the support of EUROPLANET RI project (Grant agreement no. 228319) funded by the EU; and also the support of the International Space Science Institute (Bern). We

acknowledge support of the CAPS ELS operations and software team by STFC (to 2010) and by ESA via UK Space Agency (from 2011). The Swedish National Space Board (SNSB) supports the RPWS/LP instrument on board Cassini.

References

K. Ågren, J.-E. Wahlund, R. Modolo, D. Lummerzheim, M. Galand, I. Müller-Wodarg, P. Canu, W.S. Kurth, T.E. Cravens, R.V. Yelle, J.H. Waite Jr., A.J. Coates, G.R. Lewis, D.T. Young, C. Bertucci, M.K. Douherty, On magnetospheric impact ionization and dynamics in Titan's ram-side and polar ionosphere – a Cassini case study. Ann. Geophys. **25**, 2359 (2007)

K. Ågren, J.-E. Wahlund, P. Garnier, R. Modolo, J. Cui, M. Galand, I. Müller-Wodarg, The ionospheric structure of Titan. Planet. Space Sci. **57**, 1821 (2009)

K. Ågren, D.J. Andrews, S.C. Buchert, A.J. Coates, S.W.H. Cowley, M.K. Dougherty, N.J.T. Edberg, P. Garnier, G.R. Lewis, R. Modolo, H. Opgenoorth, G. Provan, L. Rosenqvist, D.L. Talboys, J.-E. Wahlund, A. Wellbrock, Detection of currents and associated electric fields in Titan's ionosphere from Cassini data, J. Geophys. Res. **116** (2011). CiteID A04313

D.J. Andrews, S.W.H. Cowley, M.K. Dougherty, G. Provan, Magnetic field oscillations near the planetary period in Saturn's magnetosphere: Variation of amplitude and phase with radial distance and local time. J. Geophys. Res. **115**(A14), A04212 (2010)

H. Backes et al., Titan's magnetic field signature during the first Cassini encounter. Science **308**, 992 (2005)

P.M. Banks, G. Kockarts, *Aeronomy, Parts A and B* (Academic Press, San Diego, 1973)

A.R. Barakat, R.W. Schunk, A three-dimensional model of the generalized polar wind. J. Geophys. Res. **111**, A12314 (2006)

C. Bertucci et al., Structure of Titan's mid-range magnetic tail: Cassini magnetometer observations during the T9 flyby. Geophys. Res. Lett. **34**, L24S02 (2007)

C. Bertucci et al., The magnetic memory of Titan's ionized atmosphere. Science **321** (2008)

C. Bertucci et al., The variability of Titan's magnetic environment. Planet. Space Sci. **57**, 1813 (2009)

M.K. Bird, R. Dutta-Roy, S.W. Asmar, T.A. Rebold, Detection of Titan's ionosphere from Voyager 1 radio occultation observations. Icarus **130**, 426–436 (1997)

M. Blanc, S. Bolton, J. Bradley, M. Burton, T.E. Cravens, I. Dandouras, M.K. Dougherty, M. Festou, J. Feynman, R.E. Johnson, T. Gombosi, W.S. Kurth, P.C. Liewer, B.H. Mauk, S. Maurice, D. Mitchell, F.M. Neubauer, J.D. Richardson, D.E. Shemansky, E.C. Sittler, B.T. Tsurutani, Ph. Zarka, L.W. Esposito, E. Grün, D.A. Gurnett, A. Kliore, S.M. Krimigis, D. Southwood, J.H. Waite, D.T. Young, Magnetospheric and plasma science with Cassini-Huygens. Space Sci. Rev. **104**, 253–346 (2002)

R. Boström, A model of the auroral electrojets. J. Geophys. Res. **69**, 4983 (1964)

J.F. Brannon, J.L. Fox, H.S. Porter, Evidence for day-to-night ion transport at low solar activity in the Venus pre-dawn ionosphere. Geophys. Res. Lett. **20**, 2739–2742 (1993)

C.R. Chappell, T.E. Moore, J.H. Waite, The ionosphere as a fully adequate source of plasma for the Earth's magnetosphere. J. Geophys. Res. **92**, 5896 (1987)

C.C. Chaston, A.J. Hull, J.W. Bonnell, C.W. Carlson, R.E. Ergun, R.J. Strangeway, J.P. McFadden, Large parallel electric fields, currents, and density cavities in dispersive Alfven waves above the aurora. J. Geophys. Res. **112**, A05215 (2007)

A.J. Coates, A.D. Johnstone, J.F.E. Johnson, J.J. Sojka, G.L. Wrenn, Ionospheric photoelectrons observed in the magnetosphere at distances of up to 7 Earth radii. Planet. Space Sci. **33**, 1267–1275 (1985)

A.J. Coates, F.J. Crary, G.R. Lewis, D.T. Young, J.H. Waite Jr., E.C. Sittler Jr., Discovery of heavy negative ions in Titan's ionosphere. Geophys. Res. Lett. **34**, L22103 (2007a)

A.J. Coates, F.J. Crary, D.T. Young, K. Szego, C.S. Arridge, Z. Bebesi, E.C. Sittler Jr., R.E. Hartle, T.W. Hill, Ionospheric electrons in Titan's tail: plasma structure during the Cassini T9 encounter. Geophys. Res. Lett. **34**, L24S05 (2007b)

A.J. Coates et al., Ionospheric photoelectrons at Venus: initial observations by ASPERA-4 ELS. Planet. Space Sci. **56**, 802–806 (2008)

A.J. Coates, Interaction of Titan's ionosphere with Saturn's magnetosphere. Philos. Trans. R. Soc. A **367**, 773–788 (2009)

A.J. Coates, A. Wellbrock, G.R. Lewis, G.H. Jones, D.T. Young, F.J. Crary, J.H. Waite Jr., Heavy negative ions in Titan's ionosphere: altitude and latitude dependence. Planet. Space Sci. **57**, 1866–1871 (2009)

A.J. Coates, A. Wellbrock, G.R. Lewis, G.H. Jones, D.T. Young, F.J. Crary, J.H. Waite, R.E. Johnson, T.W. Hill, E.C. Sittler Jr., Negative ions at Titan and Enceladus: recent results. Faraday Discuss. **147**(1), 293–305 (2010)

A.J. Coates, S.M.E. Tsang, A. Wellbrock, R.A. Frahm, J.D. Winningham, S. Barabash, R. Lundin, D.T. Young, F.J. Crary, Ionospheric photoelectrons: comparing Venus, Earth, Mars and Titan. Planet. Space Sci. **59**, 1019–1027 (2011)

F.J. Crary, B.A. Magee, K. Mandt, J.H. Waite Jr., J. Westlake, Heavy ions, temperatures and winds in Titan's ionosphere: combined Cassini CAPS and INMS observations. Planet. Space Sci. **57**, 1847–1856 (2009)

T.E. Cravens, T.I. Gombosi, J. Kozyra, A.F. Nagy, L.H. Brace, W.C. Knudsen, Model calculations of the dayside ionosphere of Venus: Energetics. J. Geophys. Res. **85**, 7778–7786 (1980)

T.E. Cravens, S.L. Crawford, A.F. Nagy, T.I. Gombosi, A two-dimensional model of the ionosphere of Venus. J. Geophys. Res. **88**, 5595–5606 (1983)

T.E. Cravens, I.P. Robertson, J. Clark, J.-E. Wahlund, J.H. Waite Jr., S.A. Ledvina, H.B. Niemann, R.V. Yelle, W.T. Kasprzak, J.G. Luhmann, R.L. McNutt, W.-H. Ip, V. De La Haye, I.C.F. Müller-Wodarg, D.T. Young, A.J. Coates, Titan's ionosphere: Model comparisons with Cassini Ta data. Geophys. Res. Lett. **32**, L12108 (2005)

T.E. Cravens, I.P. Robertson, J.H. Waite Jr., R.V. Yelle, W.T. Kasprzak, C.N. Keller, S.A. Ledvina, H.B. Niemann, J.G. Luhmann, R.L. McNutt, W.-H. Ip, V. De La Haye, I. Mueller-Wodarg, J.-E. Wahlund, V.G. Anicich, V. Vuitton, Composition of Titan's ionosphere. Geophys. Res. Lett. **33**, L07105 (2006)

T.E. Cravens, I.P. Robertson, J.H. Waite Jr., R.V. Yelle, V. Vuitton, A.J. Coates, J.-E. Wahlund, K. Ågren, M.S. Richard, V. De La Haye, A. Wellbrock, F.M. Neubauer, Model-data comparisons for Titans nightside ionosphere. Icarus **199**, 174–188 (2008a)

T.E. Cravens et al., Energetic ion precipitation at Titan. Geophys. Res. Lett. **35**, L03103 (2008b)

T.E. Cravens, R.V. Yelle, J.-E. Wahlund, D.E. Shemansky, A.F. Nagy, Composition and structure of the ionosphere and thermosphere, in *Titan form Cassini-Huygens*, ed. by R.H. Brown, J.-P. Lebreton, J.H. Waite (Springer, Berlin, 2009). Chapter 11

J. Cui, M. Galand, R.V. Yelle, V. Vuitton, J.-E. Wahlund, P.P. Lavvas, I.C.F. Müller-Wodarg, T.E. Cravens, W.T. Kasprzak, J.H. Waite Jr., Diurnal variations of Titan's ionosphere. J. Geophys. Res. **114**, A06310 (2009)

J. Cui, M. Galand, R.V. Yelle, J.-E. Wahlund, K. Ågren, J.H. Waite Jr., M.K. Dougherty, Ion transport in Titan's upper atmosphere. J. Geophys. Res. **115**, A06314 (2010)

H. Derblom, Non-sporadic properties of sporadic E. Internal Report UIO-SR-81-03, Uppsala Ionosphere Obs., Uppsala, Sweden (1981)

N.J.T. Edberg et al., Electron density and temperature measurements in the cold plasma environment of Titan: implications for atmospheric escape. Geophys. Res. Lett. **37**, L20105 (2010)

N.J.T. Edberg, K. Agren, J.-E. Wahlund, M.W. Morooka, D.J. Andrews, S.W.H. Cowley, A. Wellbrock, A.J. Coates, C. Bertucci, M.K. Dougherty, Structured ionospheric outflow during the Cassini Titan flybys T55-T59. Planet. Space Sci. **59**, 788–797 (2011)

R.C. Elphic, H.G. Mayr, R.F. Theis, L.H. Brace, K.L. Miller, W.C. Knudsen, Nightward ion flow in the Venus ionosphere—implications of momentum balance. Geophys. Res. Lett. **11**, 1007–1010 (1984)

E. Engwall, A.I. Eriksson, C.M. Cully, M. André, R. Torbert, H. Vaith, Earth's ionospheric outflow dominated by hidden cold plasma. Nat. Geosci. **2**(1), 24 (2009)

J.L. Fox, R.V. Yelle, Hydrocarbon ions in the ionosphere of Titan. Geophys. Res. Lett. **24**, 2179–2182 (1997)

J.L. Fox, A. Dalgarno, Ionization, luminosity, and heating of the upper atmosphere of Mars. J. Geophys. Res. **84**, 7315–7333 (1979)

R.A. Frahm, J.D. Winningham, J.R. Sharber, J.R. Scherrer, S.J. Jeffers, A.J. Coates, D.R. Linder, D.O. Kataria, R. Lundin, S. Barabash, M. Holmström, H. Andersson, M. Yamauchi, A. Grigoriev, E. Kallio, H. Koskinen, T. Säles, P. Riihela, W. Schmidt, J.U. Kozyra, J.G. Luhmann, E.C. Roelof, D.J. Williams, S. Livi, C.C. Curtis, K.C. Hsieh, B.R. Sandel, M. Grande, M. Carter, J.-A. Sauvaud, A. Fedorov, J.-J. Thocaven, S. McKenna-Lawler, S. Orsini, R. Cerulli-Irelli, M. Maggi, P. Wurz, P. Bochsler, N. Krupp, J. Woch, M. Fraenz, K. Asamura, C. Dierker, Carbon dioxide photoelectron peaks at Mars. Icarus **182**, 371–382 (2006a)

R.A. Frahm, J.R. Sharber, J.D. Winningham, P. Wurz, M.W. Liemohn, E. Kallio, M. Yamauchi, R. Lundin, S. Barabash, A.J. Coates, D.R. Linder, J.U. Kozyra, M. Holmström, S.J. Jeffers, H. Andersson, S. McKenna-Lawlor, Locations of atmospheric photoelectron energy peaks within the Mars environment. Space Sci. Rev. **126**, 389–402 (2006b)

M. Galand, R.V. Yelle, A.J. Coates, H. Backes, J.-E. Wahlund, Electron temperature of Titan's sunlit ionosphere. Geophys. Res. Lett. **33**, L21101 (2006)

M. Galand et al., Ionization sources in Titan's deep ionosphere. J. Geophys. Res. **115**, A07312 (2010)

L. Gan, C.N. Keller, T.E. Cravens, Electrons in the ionosphere of Titan. J. Geophys. Res. **97**, 12,137–12,151 (1992)

L. Gan, T.E. Cravens, M. Horanyi, Electrons in the ionopause boundary layer of Venus. J. Geophys. Res. **95**(A11), 19,023–19,035 (1990)

S.B. Ganguli, The polar wind. Rev. Geophys. **34**, 311–348 (1996)

D.A. Gurnett, F.L. Scarf, W.S. Kurth, The structure of Titan's wake from plasma wave observations. J. Geophys. Res. **87**, 1395–1403 (1982)
P. Garnier et al., Titan's ionosphere in the magnetosheath: Cassini RPWS results during the T32 flyby. Ann. Geophys. **27**, 5257 (2009)
S.A. Haider, Some molecular nitrogen emission from Titan–solar EUV interaction. J. Geophys. Res. **91**, 8998–9000 (1986)
R.E. Hartle, J.M. Grebowsky, Planetary loss from light ion escape on Venus. Adv. Space Res. **15**(4), 117–122 (1995)
J.L. Horwitz, W. Zeng, Physics-based formula representations of high-latitude ionospheric outflows: H^+ and O^+ densities, flow velocities, and temperatures versus soft electron precipitation, wave-driven transverse heating, and solar zenith angle effects. J. Geophys. Res. **114**, A01308 (2009)
R.E. Johnson et al., Mass loss processes in Titan's upper atmosphere, in *Titan form Cassini-Huygens*, ed. by R.H. Brown, J.-P. Lebreton, J.H. Waite (Springer, Berlin, 2009). Chapter 15
J.F. Kasting, D. Catling, Evolution of a habitable planet. Annu. Rev. Astron. Astrophys. **41**, 429 (2003)
C.N. Keller, T.E. Cravens, One-dimensional multispecies hydrodynamic models of the wakeside ionosphere of Titan. J. Geophys. Res. **99**, 6527–6536 (1984)
C.N. Keller, V.G. Anicich, T.E. Cravens, Model of Titan's ionosphere with detailed hydrocarbon ion chemistry. Planet. Space Sci. **46**, 1157–1174 (1998)
M.C. Kelley, *The Earth's Ionosphere* (Academic Press, San Diego, 2009)
A.J. Kliore, A.F. Nagy, E.A. Marouf, R.G. French, F.M. Flasar, N.J. Rappaport, A. Anabttawi, S.W. Asmar, D.S. Kahann, E. Barbinis, G.L. Goltz, D.U. Fleischman, D.J. Rochblatt, First results from the Cassini radio occultations of the Titan ionosphere. J. Geophys. Res. **113**, A09317 (2008)
Yu.N. Kulikov et al., Atmospheric and water loss from early Venus. Planet. Space Sci. **54**, 1425 (2006)
H. Lammer, H.I.M. Lichtenegger, C. Kolb, I. Ribas, E.F. Guinan, R. Abart, S.J. Bauer, Loss of water from Mars: implications for the oxidation of the soil. Icarus **165**, 9 (2003)
H. Lammer et al., Coronal mass ejection (CME) activity of low mass M start's as an important factor for the habitability of terrestrial exoplanets. II. CME-induced ion pickup of Earth-like exoplanets in close-in habitable zones. Astrobiology **7**, 185 (2007)
J.S. Lee, J.P. Doering, T.A. Potemra, L.H. Brace, Measurement of the ambient photoelectron spectrum from AE. I: AE-E measurements below 300 km in solar minimum conditions. Planet. Space Sci. **28**, 947 (1980a)
J.S. Lee, J.P. Doering, T.A. Potemra, L.H. Brace, Measurements of the ambient photoelectron spectrum from AE.II: AE-E measurements between 300 and 1000 km in solar minimum conditions. Planet. Space Sci. **28**, 973 (1980b)
M.-C. Liang, Y.L. Yung, D.E. Shemansky, Photolytically generated aerosols in the mesosphere and thermosphere of Titan. Astrophys. J. Lett. **661**, L199–L202 (2007)
D.R. Linder, A.J. Coates, R.D. Woodliffe, C. Alsop, A.D. Johnstone, M. Grande, A. Preece, B. Narheim, K. Svenes, D.T. Young, The Cassini CAPS electron spectrometer, in *Measurement Techniques in Space Plasmas: Particles*, ed. by R.E. Pfaff, J.E. Borovsky, D.T. Young. AGU Geophysical Monograph, vol. 102 (AGU, Washington DC, 1998), pp. 257–262
J.J. López-Moreno, G.J. Molina-Cuberos, M. Hamelin, R. Grard, F. Simões, R. Godard, K. Schwingenschuh, C. Béghin, J.J. Berthelier, V.J.G. Brown, P. Faulkner, F. Ferri, M. Fulchignoni, I. Jernej, J.M. Jerónimo, R. Rodrigo, R. Trautner, Structure of Titan's low altitude ionized layer from relaxation probe onboard Huygens. Geophys. Res. Lett. **35**, L22104 (2008)
P. Louarn, J.E. Wahlund, T. Chust, H. de Feraudy, A. Roux, B. Holback, P.O. Dovner, A.I. Eriksson, G. Holmgren, Observation of kinetic Alfven waves by the FREJA spacecraft. Geophys. Res. Lett. **21**, 1847–1850 (1994)
R. Lundin, S. Barabash, Evolution of the martian atmosphere and hydrosphere: solar wind erosion studied by ASPERA-3 on Mars Express. Planet. Space Sci. **52**, 1059 (2004)
R. Lundin et al., Solar wind-induced atmospheric erosion at Mars: First results from ASPERA-3 on Mars Express. Science **305**, 1933 (2004)
Y.-J. Ma, A.F. Nagy, T.E. Cravens, I.V. Sokolov, K.C. Hansen, J.-E. Wahlund, F.J. Crary, A.J. Coates, M.K. Dougherty, Comparisons between MHD model calculations and observations of Cassini flybys of Titan. J. Geophys. Res. **111**, A05207 (2006)
Y.J. Ma, A.F. Nagy, Ion escape fluxes from Mars, Geophys. Res. Lett., L08201 (2007)
G.P. Mantas, W.B. Hanson, Photoelectron fluxes in the Martian ionosphere. J. Geophys. Res. **84**, 369–385 (1979)
M. Michael, S.N. Tripathi, P. Arya, A. Coates, A. Wellbrock, D.T. Young, High-altitude charged particles in the atmosphere of Titan. Planet. Space Sci. **59**, 880–885 (2011)
R. Modolo et al., Far plasma wake of Titan from RPWS observations: a case study. Geophys. Res. Lett. **34**, L24S04 (2007a)

R. Modolo et al., Plasma environment in the wake of Titan from hybrid simulation: a case study. Geophys. Res. Lett. **34**, L24S07 (2007b)
R. Modolo, G.M. Chanteur, A global hybrid model for Titan's interaction with the Kronian plasma: Application to the Cassini Ta flyby. J. Geophys. Res. **113**, A01317 (2008)
G.J. Molina-Cuberos, H. Lammer, W. Stumptner, K. Schwingenschuh, H.O. Rucker, J.J. Lopez-Moreno, R. Rodrigo, T. Tokano, Ionospheric layer induced by meteoric ionization in Titan's atmosphere. Planet. Space Sci. **49**, 143–153 (2001)
T.E. Moore, J.L. Horwitz, Stellar ablation of planetary atmospheres. Rev. Geophys. **45**, RG3002 (2007)
M.W. Morooka et al., The electron density of Saturn's magnetosphere. Ann. Geophys. **27**, 2971 (2009)
I.C.F. Müller-Wodarg, R.V. Yelle, M. Mendillo, L.A. Young, A.D. Aylward, The thermosphere of Titan simulated by a global three-dimensional time-dependent model. J. Geophys. Res. **105**, 20833–20856 (2000)
I.C.F. Müller-Wodarg, R.V. Yelle, J. Cui, J.H. Waite Jr., Horizontal structures and dynamics of Titan's thermosphere. J. Geophys. Res. **113**, E10005 (2008)
A.F. Nagy, P.M. Banks, Photoelectron fluxes in the ionosphere. J. Geophys. Res. **75**, 6260–6270 (1970)
A.F. Nagy, A. Korosmezev, J. Kim, T.I. Gombosi, A two dimensional shock capturing, hydrodynamic model of the Venus ionosphere. Geophys. Res. Lett. **18**, 801–804 (1991)
A.F. Nagy, Y. Liu, K.C. Hansen, K. Kabin, T.I. Gombosi, M.R. Combi, D.L. DeZeeuw, K.G. Powell, A.J. Kliore, The interaction between the magnetosphere of Saturn and Titan's ionosphere. J. Geophys. Res. **106**, 6151–6160 (2001)
N.F. Ness et al., The induced magnetosphere of Titan. J. Geophys. Res. **87**, 1369 (1982)
F.M. Neubauer, D.A. Gurnett, J.D. Scudder, R.E. Hartle, Titan's magnetospheric interaction, in *Saturn*, ed. by T. Gehrels, M.S. Matthews (Univ. Arizona Press, Tucson, 1984), pp. 760–787
F.M. Neubauer, H. Backes, M.K. Dougherty, A. Wennmacher, C.T. Russell, A. Coates, D. Young, N. Achilleos, N. André, C.S. Arridge, C. Bertucci, G.H. Jones, K.K. Khurana, T. Knetter, A. Law, G.R. Lewis, J. Saur, Titan's near magnetotail from magnetic field and electron plasma observations and modeling: Cassini flybys TA, TB, and T3. J. Geophys. Res. **111**, A10220 (2006)
T. Nygrén, L. Jalonen, J. Oksman, T. Turunen, The role of electric field and neutral wind direction in the formation of sporadic E-layers. J. Atmos. Sol.-Terr. Phys. **46**, 373 (1984)
M. Pätzold, S. Tellmann, B. Häusler, D. Hinson, R. Schaa, G.L. Tyler, A sporadic third layer in the ionosphere of Mars. Science **310**, 837–839 (2005)
M. Pätzold, S. Tellmann, B. Häusler, M.K. Bird, G.L. Tyler, A.A. Christou, P. Withers, A sporadic layer in the Venus lower ionosphere of meteoric origin. Geophys. Res. Lett. **36**, L05203 (2009)
M.H. Rees, *Physics and Chemistry of the Upper Atmosphere* (Cambridge University Press, Cambridge, 1989)
I. Ribas, E.F. Guinan, M. Gudel, M. Audard, Evolution of the solar activity over time and effects on planetary atmospheres I: High-energy irradiances (1–1700 Å). Astrophys. J. **622**, 680 (2005)
L. Rosenqvist et al., Titan ionospheric conductivities from Cassini measurements. Planet. Space Sci. **10**, 1016 (2009)
A.M. Rymer, H.T. Smith, A. Wellbrock, A.J. Coates, D.T. Young, Discrete classification and electron energy spectra of Titan's varied magnetospheric environment. Geophys. Res. Lett. **36**, 799 (2009)
C. Sagan, B.N. Khare, W.R. Thompson, G.D. McDonald, M.R. Wing, J.L. Bada, T. Vo-Dinh, E.T. Arakawa, Polycyclic aromatic hydrocarbons in the atmospheres of Titan and Jupiter. Astrophys. J. **414**(1), 399–405 (1993)
R.W. Schunk, A.F. Nagy, *Ionospheres—Physics, Plasma Physics, and Chemistry* (Cambridge University Press, Cambridge, 2009)
I. Sillanpää, E. Kallio, P. Janhunen, W. Schmidt, K. Mursula, J. Vilppola, P. Tanskanen, Hybrid simulation study of ion escape at Titan for different orbital positions. Adv. Space Res. **38**, 799–805 (2006)
E.C. Sittler Jr., A. Ali, J.F. Cooper, R.E. Hartle, R.E. Johnson, A.J. Coates, D.T. Young, Heavy ion formation in Titan's ionosphere: magnetospheric introduction of free oxygen and a source of Titan's aerosols?. Planet. Space Sci. **57**, 1547–1557 (2009a)
E.C. Sittler et al., Energy deposition processes in Titan's upper atmosphere and its induced magnetosphere, in *Titan form Cassini-Huygens*, ed. by R.H. Brown, J.-P. Lebreton, J.H. Waite (Springer, Berlin, 2009b). Chapter 16
K. Stasiewicz, Y. Khotyaintsev, M. Berthomier, J.-E. Wahlund, Identification of widespread turbulence of dispersive Alfven waves. Geophys. Res. Lett. **27**, 173–176 (2000)
K. Szego et al., Charged particle environment of Titan during the T9 flyby. Geophys. Res. Lett. **34**, L24S03 (2007)
T. Tanaka, K. Murawski, Three-dimensional MHD simulation of the solar wind interaction with the ionosphere of Venus: Results of two-component reacting plasma simulation. J. Geophys. Res. **102**, 19805–19822 (1997)
T. Turunen, J. Silén, T. Nygrén, L. Jalonen, Observation of a thin E_S-layer by the EISCAT radar. Planet. Space Sci. **33**, 1407 (1985)

E. Vigren, Dissociative recombination of organic molecular ions of relevance for interstellar clouds and Titan's upper atmosphere. PhD Thesis, Stockholm University (2010). ISBN 978-91-7447-133-5
U. Von Zahn, P. von der Gathen, G. Hansen, Forced release of sodium from upper atmosphere dust particles. Geophys. Res. Lett. **8**, 65 (1987)
V. Vuitton, P. Lavvas, R.V. Yelle, M. Galand, A. Wellbrock, G.R. Lewis, A.J. Coates, J.-E. Wahlund, Negative ion chemistry in Titan's upper atmosphere. Planet. Space Sci. **57**, 1558–1572 (2009)
V. Vuitton, R.V. Yelle, M.J. McEwan, Ion chemistry and N-containing molecules in Titan's upper atmosphere. Icarus **191**, 722–742 (2007)
J.E. Wahlund, P. Louarn, T. Chust, H. de Feraudy, A. Roux, B. Holback, P.-O. Dovner, G. Holmgren, On ion acoustic turbulence and the nonlinear evolution of kinetic Alfven waves in aurora. Geophys. Res. Lett. **21**, 1831–1834 (1994)
J.-E. Wahlund, A.I. Eriksson, B. Holback, M.H. Boehm, J. Bonnel, P.M. Kintner, C.E. Seyler, J.H. Clemmons, L. Eliasson, D.J. Knudsen, P. Norqvist, L.J. Zanetti, Broadband ELF plasma emission during auroral energization 1. Slow ion acoustic waves. J. Geophys. Res. **103**, 4343–4375 (1998)
J.-E. Wahlund, R. Boström, G. Gustafsson, D.A. Gurnett, W.S. Kurth, A. Pedersen, T.F. Averkamp, G.B. Hospodarsky, A.M. Persoon, P. Canu, F.M. Neubauer, M.K. Dougherty, A.I. Eriksson, M.W. Morooka, R. Gill, M. André, L. Eliasson, I. Müller-Wodarg, Cassini measurements of cold plasma in the ionosphere of Titan. Science **308**, 986–989 (2005)
J.-E. Wahlund, M. Galand, I. Müller-Wodarg, J. Cui, R.V. Yelle, F.J. Crary, K. Mandt, B. Magee, J.H. Waite Jr., D.T. Young, A.J. Coates, P. Garnier, K. Ågren, M. André, A.I. Eriksson, T.E. Cravens, V. Vuitton, D.A. Gurnett, W.S. Kurth, On the amount of heavy molecular ions in Titan's ionosphere. Planet. Space Sci. **57**, 1857–1865 (2009)
J.D. Whitehead, Production and prediction of sporadic E. Rev. Geophys. **8**, 65 (1970)
R.C. Whitten, B. Baldwin, W.C. Knudsen, K.L. Miller, K. Spenner, The Venus ionosphere at grazing incidence of solar radiation—Transport of plasma to the night ionosphere. Icarus **51**, 261–270 (1982)
E.H. Wilson, S.K. Atreya, Current state of modeling the photochemistry of Titan's mutually dependent atmosphere and ionosphere. J. Geophys. Res. **109**, E06002 (2004)
P. Withers, Theoretical models of ionospheric electrodynamics and plasma transport. J. Geophys. Res. **113**, A07301 (2008)
J.H. Waite, H. Niemann, R.V. Yelle, W.T. Kasprzak, T.E. Cravens, J.G. Luhmann, R.L. McNutt, W.-H. Ip, D. Gell, V. De La Haye, I. Müller-Wordag, B. Magee, N. Borggren, S. Ledvina, G. Fletcher, E. Walter, R. Miller, S. Scherer, R. Thorpe, J. Xu, B. Block, K. Arnett, Ion neutral mass spectrometer results from the first flyby of Titan. Science **308**, 982–986 (2005)
J.H. Waite Jr., D.T. Young, T.E. Cravens, A.J. Coates, F.J. Crary, B. Magee, J. Westlake, The process of Tholin formation in Titan's upper atmosphere. Science **316**, 870–875 (2007)
J.H. Waite Jr., D.T. Young, A.J. Coates, F.J. Crary, B.A. Magee, K.E. Mandt, J.H. Westlake, The source of heavy organics and aerosols in Titan's atmosphere. Proc. Int. Astron. Union **4**, 321–326 (2008)
H.Y. Wei et al., Cold ionospheric plasma in Titan's magnetotail. Geophys. Res. Lett. **34**, L24S06 (2007)
R.C. Witten, P.T. McCormick, D. Merritt, K.W. Thompson, R.R. Brynswold, C.J. Eich, W.C. Knudsen, K.L. Miller, Dynamics of the Venus ionosphere: a two-dimensional model study. Icarus **60**, 317–326 (1984)
M. Yamauchi, J.-E. Wahlund, Role of the ionosphere for the atmospheric evolution of planets. Astrobiology **7**, 5 (2007)
R.V. Yelle, J. Cui, I.C.F. Müller-Wodarg, Methane escape from Titan's atmosphere. J. Geophys. Res. **113**, E10003 (2008)
D.T. Young, J.-J. Berthelier, M. Blanc, J.L. Burch, A.J. Coates, R. Goldstein, M. Grande, T.W. Hill, R.E. Johnson, V. Kelha, D.J. McComas, E.C. Sittler, K.R. Svenes, K. Szegv, P. Tanskanen, K. Ahola, D. Anderson, S. Bakshi, R.A. Baragiola, B.L. Barraclough, R. Black, S. Bolton, T. Booker, R. Bowman, P. Casey, G. Dirks, N. Eaker, J.T. Gosling, H. Hannula, C. Holmlund, H. Huomo, J.-M. Illiano, P. Jensen, M.A. Johnson, D. Linder, T. Luntama, S. Maurice, K. McCabe, B.T. Narheim, J.E. Nordholt, A. Preece, J. Rutzki, A. Ruitberg, K. Smith, S. Szalai, M.F. Thomsen, K. Viherkanto, T. Vollmer, T.E. Wahl, M. Wuest, T. Ylikorpi, C. Zinsmeyer, Cassini plasma spectrometer investigation. Space Sci. Rev. **114**, 1–112 (2004)

Space Sci Rev (2011) 162:113–171
DOI 10.1007/s11214-011-9845-1

The Induced Magnetospheres of Mars, Venus, and Titan

C. Bertucci · F. Duru · N. Edberg · M. Fraenz · C. Martinecz · K. Szego · O. Vaisberg

Received: 2 March 2011 / Accepted: 22 September 2011 / Published online: 26 November 2011

Abstract This article summarizes and aims at comparing the main features of the induced magnetospheres of Mars, Venus and Titan. All three objects form a well-defined induced magnetosphere (IM) and magnetotail as a consequence of the interaction of an external wind of plasma with the ionosphere and the exosphere of these objects. In all three, photoionization seems to be the most important ionization process. In all three, the IM displays a clear outer boundary characterized by an enhancement of magnetic field draping and massloading, along with a change in the plasma composition, a decrease in the plasma temperature, a deflection of the external flow, and, at least for Mars and Titan, an increase of the total density. Also, their magnetotail geometries follow the orientation of the upstream magnetic field and flow velocity under quasi-steady conditions. Exceptions to this are fossil fields observed at Titan and the near Mars regions where crustal fields dominate the magnetic topology. Magnetotails also concentrate the escaping plasma flux from these three objects and similar acceleration mechanisms are thought to be at work. In the case of Mars and Titan, global reconfiguration of the magnetic field topology (reconnection with the crustal sources and exits into Saturn's magnetosheath, respectively) may lead to important losses of

C. Bertucci (✉)
Institute for Astronomy and Space Physics (IAFE), CONICET/UBA, Buenos Aires, Argentina
e-mail: cbertucci@iafe.uba.ar

F. Duru
Department of Astronomy, The Unversity of Iowa, Iowa City, USA

N. Edberg
Swedish Space Science Institute, Uppsala, Sweden

M. Fraenz · C. Martinecz
Max Planck Institute for Solar System Research, Klatenburg-Lindau, Germany

K. Szego
KFKI-RMKI, Budapest, Hungary

O. Vaisberg
Space Research Institute, Russian Academy of Sciences, Moscow, Russian Federation

plasma. Finally, an ionospheric boundary related to local photoelectron signals may be, in the absence of other sources of pressure (crustal fields) a signature of the ultimate boundary to the external flow.

Keywords Induced magnetospheres · Mars · Venus · Titan · Boundaries · Draping · Massloading

1 Introduction

The presence of an unmagnetized planetary body surrounded by an atmosphere in a flow of collisionless, magnetized plasma generates, via ionizing processes, a perturbation in the upstream plasma and the magnetic field. As the perturbation in the magnetic field is generated from currents induced from the differential motion between the external and the planetary particle populations, these perturbed regions are usually referred to as 'induced magnetospheres', in opposition to 'intrinsic magnetospheres' where the perturbation is originating in the planet's intrinsic magnetic field.

Mars, Venus and Titan are three distinct examples of unmagnetized objects (Acuña et al. 1998; Russell et al. 1979; Wei et al. 2011) possessing an atmosphere. In spite of the differences in their atmospheric composition, size, ionization/flow conditions, and upstream magnetic field variability, the perturbations that they generate in the surrounding plasma (solar wind, Saturn's magnetospheric plasma) display remarkable similarities, indicating that common processes operate in spite of their distinct position in the parameter space.

An induced magnetosphere is the result of the collisionless transfer of energy and momentum from the plasma flow surrounding an unmagnetized body into its induced magnetosphere and atmosphere.

The interaction can start several planetary radii away from these objects, where exospheric particles are ionized, mostly by photoionization. Photoionization adds a small amount of energy to the neutral particles and therefore these 'newborn ions' have the same temperature as their parent neutral (a few eVs). As soon as a newborn ion is formed, it becomes sensitive to the electric fields associated to the incoming flow (convective, electric fields arising from plasma microinstabilities), whose forces intend to restore the thermodynamical equilibrium, accelerating the ion. As the flow approaches the object, an increasing number of cold exospheric newborn ions are picked up in this way and lead to significant massloading which decelerates the flow in agreement with momentum conservation.

In addition to massloading, the presence of an obstacle represented by a current layer (e.g. ionopause), a collision-dominated diffusion region within the body's ionosphere, or the object itself contributes to the diversion of the flow. In regions where the collisionless regime holds, the external magnetic field frozen into the plasma piles up around the flow 'stagnation' region, and drapes around the object as the flow is diverted around the body (Alfven 1957). This defines an induced magnetic tail formed by two lobes of opposite magnetic polarity separated by a neutral sheet.

As a result, a well-defined region filled with perturbed, massloaded external plasma is formed. This region is called 'induced magnetosphere'.

The external plasma loses its momentum and energy to the local plasma both abruptly and gradually. This defines respectively the boundaries and regions within an induced magnetosphere. Several permanent, well-defined regions and boundaries emerge in most observations:

- A collisionless bow shock (BS)
- Magnetosheath
- Induced magnetospheric boundary (IMB)
- Induced magnetosphere (including magnetotail)
- Ionospheric boundary/ionopause

A boundary has to be 'thin' with respect to the regions surrounding it, a measure of its extent being given by local particle lengthscales such as local ion gyroradius or inertial length, where strong current systems, which modify the external magnetic field occur. Conversely, regions have dimensions of several of these lengthscales.

The understanding of the processes occurring in induced magnetospheres requires the characterization of the following parameters: upstream plasma (solar or planetary), local superthermal and cold populations, and magnetic field. Since the beginning of space exploration, spacecraft have measured these quantities. The measurements of these quantities, have dramatically increased in number over the last two decades, enabling not only deeper analyses of the structures at each object, but also, and for the first time, thorough inter-object comparisons.

Limitations on these comparisons will come from two main elements: first, the scarce availability of simultaneous measurements of basic plasma parameters, and second, the absence of multipoint observations. As a result, observations taken at different epochs and locations are usually used assuming steady state interactions.

The present review intends to be an initial effort in summarizing the most relevant results on the study of the induced magnetospheres of Mars, Venus and Titan and comparing their main features in order to identify common physical processes operating at these objects.

The choice of these three bodies follows the topics covered by the rest of the articles in this issue. However, observations around active comets—a special case of an induced magnetosphere entirely created and sustained by massloading—will be included in the comparison section.

Finally, it is the intention of the authors to focus on observations, as the analyses and discussion of numerical simulations are treated in the comprehensive review by Kallio et al. (this issue).

The article is structured as follows: First, a summary of the characteristics of the induced magnetospheres and related structures at Mars, Venus and Titan is given in Sects. 2, 3 and 4 respectively. These results are then discussed and compared in Sect. 5, followed by conclusions.

2 Mars

Since the very beginning of space exploration, several spacecraft visited planet Mars, revealing the properties of its plasma environment. Following the encounters by Mariner 4, 6 and 7, Mars 2, 3, and Mariner 9. Mars 2 and 3 were probably the first spacecraft to enter the Martian induced magnetosphere (Vaisberg and Bogdanov 1974) in the tail sector (i.e. plasma and magnetic tail), although at the time of those observations, the nature (i.e. intrinsic or inteplanetary) of the magnetic field observed close to the planet had not been unveiled (Dolginov et al. 1976; Russell 1978a, 1978b). This issue would not be resolved until the arrival of Mars Global Surveyor (MGS) (Albee et al. 2001), which provided in situ magnetic field measurements below the ionospheric density peak for the first time. These measurements revealed that, aside from the crustal sources of remnant magnetization, there was no global intrinsic magnetic field (Acuña et al. 1992).

The absence of a global intrinsic magnetic field at Mars led to the re-interpretation of part of previous plasma measurements, in particular those obtained by the Phobos-2 mission (see, e.g., special issue of Nature, 341, 1989). A comprehensive review on the comparison between MGS and Phobos-2 plasma observations within the induced magnetosphere of Mars can be found in Nagy et al. (2004). Following a ∼1.5 year phase consisting of elliptical orbits, where the induced magnetosphere was explored at different altitudes and solar zenith angles (except the subsolar region), MGS was set into a 400 km altitude, 2AM-2PM local-time circular orbit (mapping mission phase). Although the magnetic field and the superthermal (mostly solar wind) electron population were efficiently characterized by the magnetometer and electron reflectometer (MAG/ER) (Acuña et al. 1992), MGS did not carry instruments capable of measuring either cold (planetary) ions, cold (planetary) electrons, or superthermal (solar wind/planetary) ions. The MGS MAG/ER investigation comprises a magnetometer (MAG), which provides, wide range, fast (32 Hz) magnetic field vector measurements, and an electron spectrometer used as a reflectometer (ER), which measures the fluxes of electrons in the energy range 10 eV–20 keV with a maximum resolution of 2 s.

With an overlap of a few years with MGS (which stopped taking measurements in late 2006) and while it was on a circular orbit at 400 km altitude, Mars Express (MEX) (Chicarro et al. 2004; Picardi et al. 2004) began its observations around Mars in 2003 from a highly elliptical orbit (∼270 km and ∼10000 km altitude periapsis and apoapsis, respectively), providing the first comprehensive picture of solar wind, and cold and superthermal planetary particle populations around Mars. This was made possible by the ASPERA-3 instrument, which consists of an electron spectrometer (ELS) and an ion mass analyzer (IMA) (Barabash et al. 2006). ELS measures electrons in the energy range 10 eV–20 keV. IMA measures ions in the energy range 10 eV/q–30 keV/q and can resolve the masses of the main ion species (1, 2, 4, 8, 16 and 32 amu/q).

Unfortunately, MEX does not carry a magnetometer. Nevertheless, for some orbits, the magnetic field strength and the electron density within the induced magnetosphere can be deduced from the Mars Advanced Radar for Subsurface and Ionospheric Sounding (MARSIS) measurements (Gurnett et al. 2005). One capability of the ionospheric sounding mode of MARSIS onboard MEX is the measurement of the local plasma frequency in the vicinity of the spacecraft by means of the detection of local plasma oscillations. Summaries of MEX plasma results can be found in review articles by Franz et al. (2006a) and Dubinin et al. (2006a).

More recently, the Rosetta spacecraft performed a flyby around Mars (March 2007), but only the lander magnetometer (Auster et al. 2007) was on while the orbiter, with all its instruments off, flew through the Martian induced magnetosphere (e.g. Edberg et al. 2008).

Apart from the plasma waves generated by the pick up of exospheric ions, the first perturbation generated by Mars in the supermagnetosonic solar wind flow is the bow shock. This bow shock, will decelerate, heat and compress the solar wind plasma which populates the magnetosheath. The end of the turbulent regime of the magnetosheath is the induced magnetosphere boundary or IMB (referred to as the magnetic pileup boundary in Fig. 1), which precedes a region of highly draped magnetic field local plasma-dominated region: the induced magnetosphere (IM). The IMB extends out into the downstream sector where it becomes the outer boundary of the magnetic tail. The IMB has several subregions. On the dayside, the region below the IMB and above the ionospheric boundary is referred to as the magnetic pileup region (MPR). At low magnetic latitudes, the interplanetary magnetic field (IMF) within the MPR is connected to tail lobe fields. The ionospheric boundary marks the lower end of the MPR on the dayside. Usually referred to it as photoelectron boundary (PEB), this boundary is usually associated with the upper limit of the collisional ionosphere.

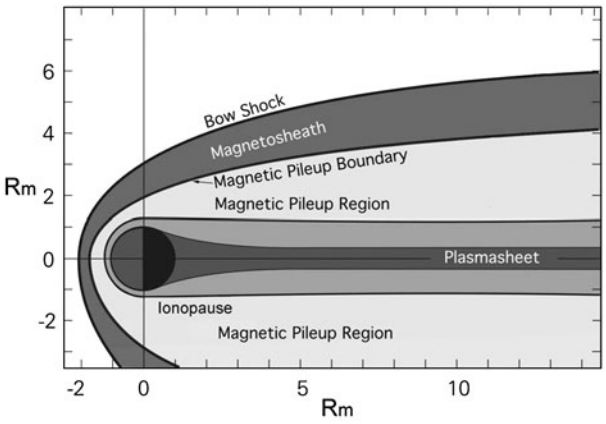

Fig. 1 Approximate locations and shapes of major plasma boundaries found around Mars according to Nagy et al. (2004)

The PEB and to a lesser extent the IMB locations are influenced by the magnetic fields from the crustal sources. In the downstream sector, a tail plasma sheet separating both tail lobes is observed. The plasma structure of the plasma sheet close to the planet is still under scrutiny with a strong effect of the crustal magnetic sources in the nightside.

2.1 The Martian Bow Shock

The most distinctive features of the Martian bow shock are its relatively small size and the signatures produced by pick up of exospheric ions (Moses et al. 1988; Dubinin et al. 1993a).

In opposition to Venus, the small size of Mars combined with a weaker IMF makes the Larmor radius of solar wind protons comparable to the size of the Martian shock, and therefore kinetic effects become important (Lembège and Savoini 2002).

In addition, the large extent of the Martian exosphere (Chaufray et al. 2008) results in the presence of pick up ions that generate low frequency waves (Brain et al. 2002; Mazelle et al. 2004; Wei and Russell 2006) well beyond the shock. These waves are convected downstream by the solar wind and interact with the shock structure, leading to a more disturbed signature.

Initial in situ plasma and magnetic field measurements established the existence of a bow shock at Mars (see e.g. Vaisberg et al. 1973; Slavin et al. 1980). In particular, Phobos-2 explored in detail the structure of the Martian shock in the terminator and post terminator regions and its substructures were investigated. These include a foot, ramp, and overshoot, whose size ranges between 0.5 and 2.5 proton gyroradii (2–8 c/ω_{pi}) and whose amplitude scales with the magnetosonic Mach number (Tatrallyay et al. 1997) as predicted for fast magnetosonic shock waves. A comprehensive review of Phobos-2 shock observations can be found in Mazelle et al. (2004).

The observations by MGS MAG/ER provided a description of the magnetic structure of the Martian shock on the dayside. Figure 2 shows a typical shock crossing by MGS (around 07:10 UT) characterized by an increase in the magnetic field magnitude and variability, followed by a compression of the plasma related to the increase in the superthermal electron fluxes. In MEX/ASPERA-3 data the BS is observed inbound as a sudden increase in fluxes of both electrons and ions in the ELS and IMA data sets.

As mentioned above, the Martian bow shock is also characterized by the presence of a strong wave activity regardless of shock angle. Figure 3 shows MGS MAG profiles of the magnetic field strength for a quasi-perpendicular crossing (top), an intermediate case,

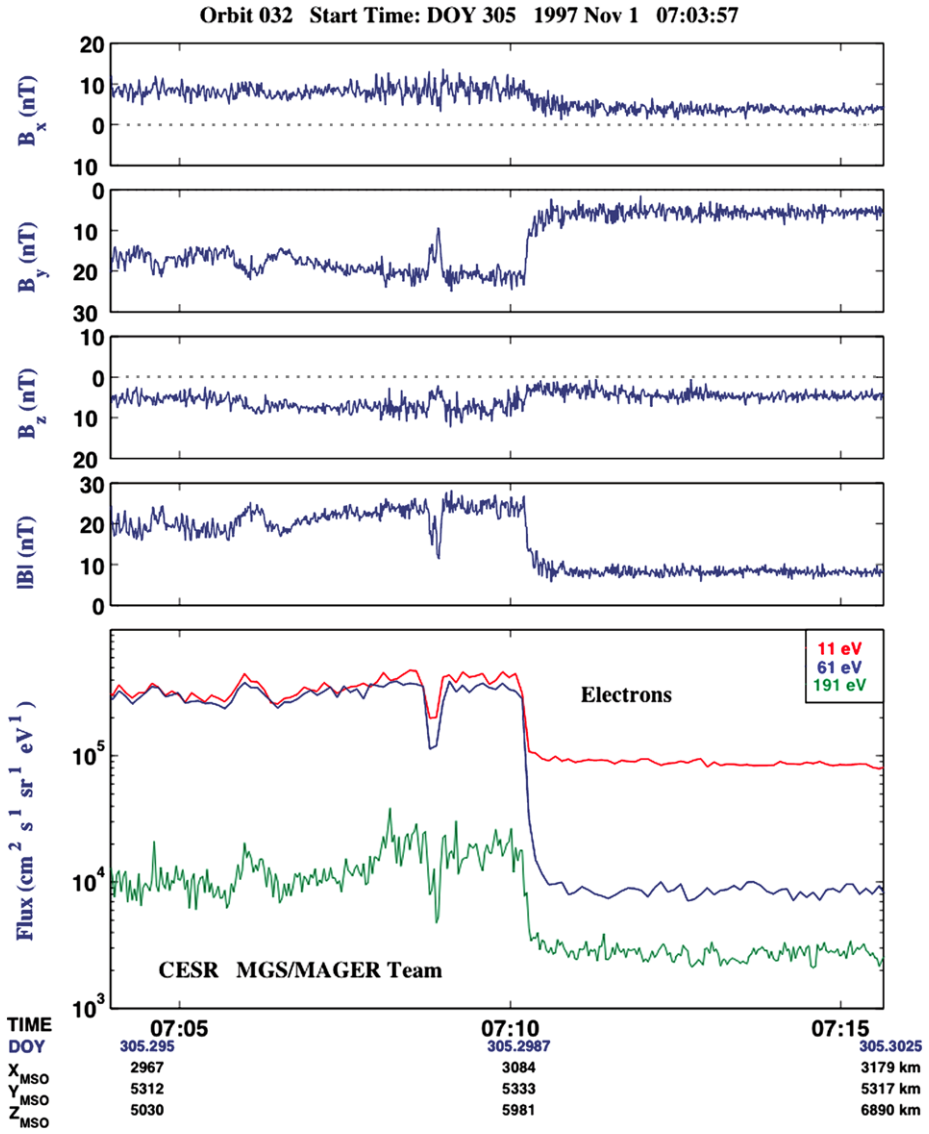

Fig. 2 Magnetic field in MSO coordinates and electron fluxes between 10 and 190 eV measured by MGS MAG/ER during a Martian bow shock crossing (Bertucci et al. 2005b)

and a quasi-parallel-like shock crossing (bottom). In the upper panel, the shock ramp and overshoot are clearly visible. In the middle panel an important wave activity precludes the identification of the ramp. The bottom panel shows a quasi-parallel shock crossing extended over a very large region (12:30–13:00 UT) where no steep ramp can be identified because of the presence of high amplitude, non-linear waves (Bertucci et al. 2005b). Bow shock's averaged shape, size and controlling factors are covered in Sect. 2.3.2, where they are compared with the IMB.

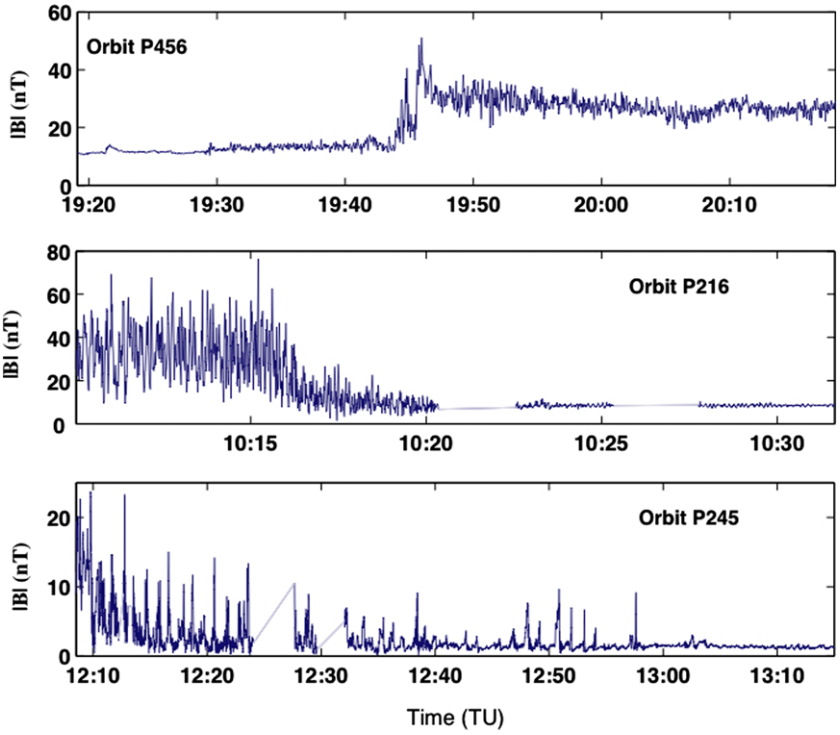

Fig. 3 MGS/MAG magnetic field strength profiles of the Martian bow shock for three different types of bow shock geometries (Bertucci et al. 2005b)

2.2 Magnetosheath

As for the shock, the distinct characteristic of the Marian magnetosheath is its exiguous extent. Moses et al. (1988) pointed out that the distance between the Martian bow shock and the so-called obstacle is of the order of a solar wind proton gyroradius and therefore there is no room for solar wind thermalization. Dubinin et al. (1993a) indicate that not only solar wind but also planetary proton thermalization would require a region extending from the shock including the induced magnetosphere.

The Martian magnetosheath is also filled with ultra low frequency plasma waves which are observed up to the induced magnetosphere boundary. In a study comprising 282 MGS magnetosheath passes, Bertucci et al. (2004) reported linearly polarized ultra low frequency magnetic field and superthermal electron fluctuations within the Martian magnetosheath in 48% of the time. These compressive magnetic field oscillations were found to be anticorrelated to the superthermal electron density suggesting that they are mirror mode waves. This purely kinetic mode is stationary in the plasma frame ($\omega_r = 0$) for a homogeneous media and is generated from temperature anisotropies in the particle distribution function in a high beta plasma (Hasegawa 1975). Possible sources for these anisotropies are the heating of the ion population downstream from quasi-perpendicular shocks and/or distributions (likely non-gyrotropic) of heavy (O^+) pickup ions. Another possibility is that these waves be related to the occurrence of the IMB itself. Similar observations were reported against the IMB at comets P/Halley (Mazelle et al. 1991), and P/Giacobini–Zinner (Tsurutani et al. 1999) seem

to support this idea. A global study by Espley et al. (2004) confirmed the observations by Bertucci et al. (2004).

2.3 The Induced Magnetosphere Boundary (IMB)

At Mars, the outer edge of the induced magnetosphere revealed itself as a distinct, sharp discontinuity, of which one of the most predominant signatures is the increase in the magnetic field strength by a factor of 2 to 3 (Acuña et al. 1998). This feature appeared so evident in the first in situ magnetic field measurements well above the collisional ionosphere that it was interpreted as an intrinsic magnetopause (e.g., Dolginov et al. 1976). However, contemporary interpretations also suggested its atmospheric origin (e.g., Russell 1978a, 1978b).

2.3.1 Identification and Structure

Mars' IMB was first unambiguously detected by spacecraft Mars-5 (Vaisberg 1976) and systematically studied by spacecraft Phobos 2 (Yeroshenko et al. 1990; Grard et al. 1989; Trotignon et al. 1996, 2006; Sauer et al. 1992), followed by MGS (Vignes et al. 2000; Bertucci et al. 2003a, 2004, 2005a, 2005b) and Mars Express (Dubinin et al. 2006a, 2008a, 2008b; Fränz et al. 2006a). The features that usually characterize the dayside IMB and its surrounding on the dayside are:

(a) Sharp increase in the magnetic field strength by a factor of 2–3.
(b) Sharp Decrease in the magnetic field fluctuations.
(c) Sharp enhancement of the magnetic field draping.
(d) Decrease in the temperature of electrons.
(e) Increase in the total electron density.
(f) Decrease in the solar wind ion (H^+ and He^{++}) densities.

The sudden increase in the IMF strength followed by the reduction of magnetic field fluctuations is the most noticeable signature of the IMB. Figure 4a shows MAGER magnetic field orientation in MSO spherical coordinates, magnetic field strength, altitude and electron fluxes for energies between 40 and 120 eV for the outbound leg of a MGS orbit. From right to left, MGS crosses the shock around 0732 UTC, and stays in the magnetosheath until 0703. The shocked plasma there is characterized by highly fluctuating, weak magnetic fields and enhanced and, also variable, electron fluxes. The IMB is crossed around 0702 UTC where $|B|$ varies from around 15 to 30 nT in less than a minute and the fluctuations in the magnetic field strength and direction fade out. At the same time, 40 eV electron fluxes fall from 2×10^6 to 2×10^5 s^{-1} cm^{-2} sr^{-1} eV^{-1}. This decrease is smaller but still noticeable for higher energies in agreement with the predicted cross section for electron impact ionization (Crider et al. 2000). As it will be shown later, this does not imply a decrease of the total electron density but an increase, followed by a decrease of the fluxes of superthermal electrons. At times earlier than 0702, MGS explores the magnetic pileup region or induced magnetosphere, where fields remain strong and quiet.

Figure 4b shows Phobos-2 solar wind proton density, their velocity vector MSO X and Y components, and the magnetic field strength, MSO elevation and azimuth (after Sauer et al. 1992). In the Mars Solar Orbital (MSO) system, the x-axis is directed toward the Sun, the z-axis is directed along the Mars orbital angular momentum vector and the y-axis completes the right-handed system. As observed in MGS data, the magnetic field fluctuations are strongly damped inside the IMB. However, the increase in the magnetic field strength is gradual. This can be interpreted as a spatial effect as Phobos-2 (whose periapsis was at

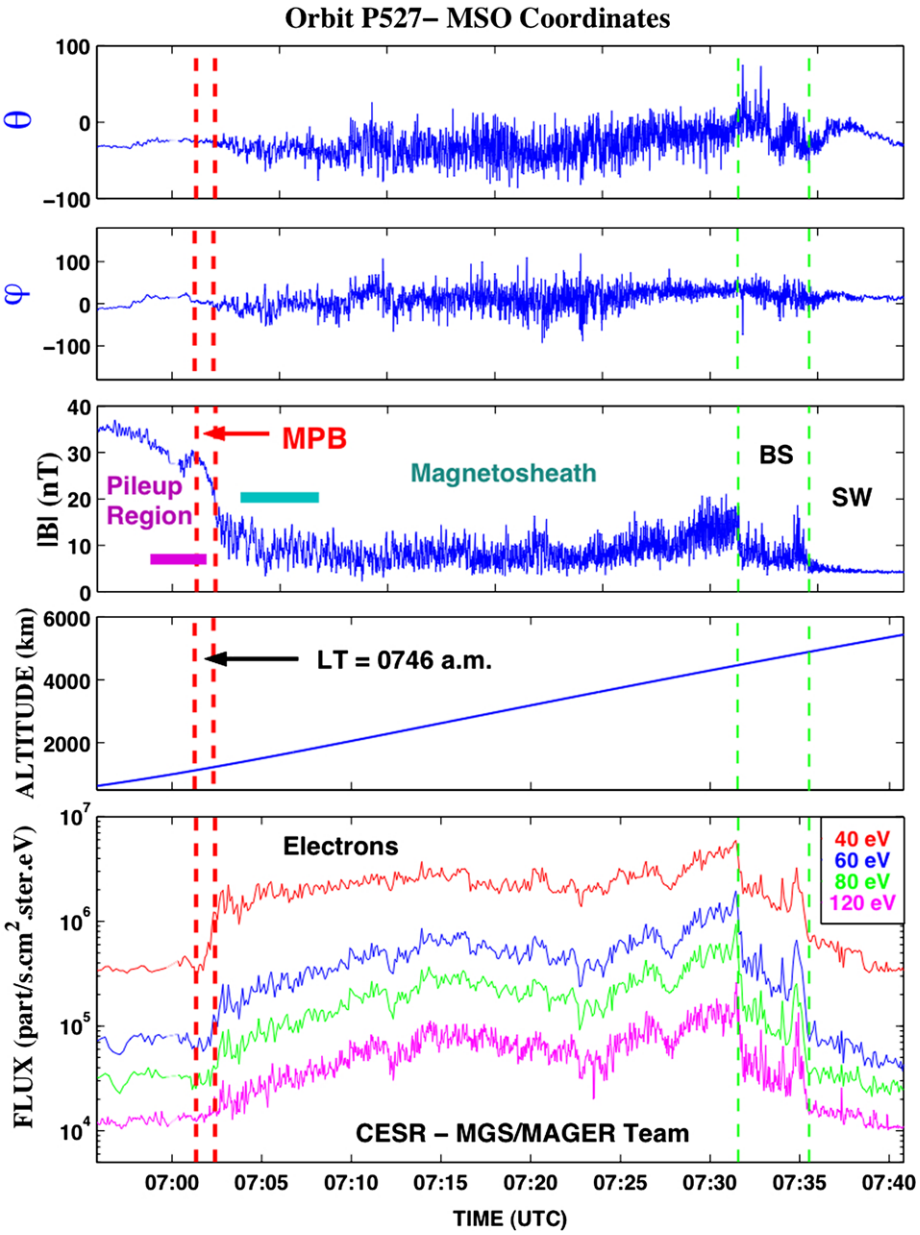

Fig. 4a From top to bottom, MGS Magnetic field in MSO spherical coordinates: elevation ($\theta = 0$ means ecliptic), azimuth ($\varphi = 0$ means noon) (Adapted from Bertucci et al. 2003a)

865 km, very close to the IMB location) orbital velocity near the IMB was rather horizontal. The upper panel shows the decrease in the solar wind proton density as Phobos 2 passes from the magnetosheath into the induced magnetosphere (from ~2.5 cm^{-3} to near-zero values). This behavior was confirmed by ASPERA measurements not only for solar wind protons but also for alpha particles (Fränz et al. 2006a).

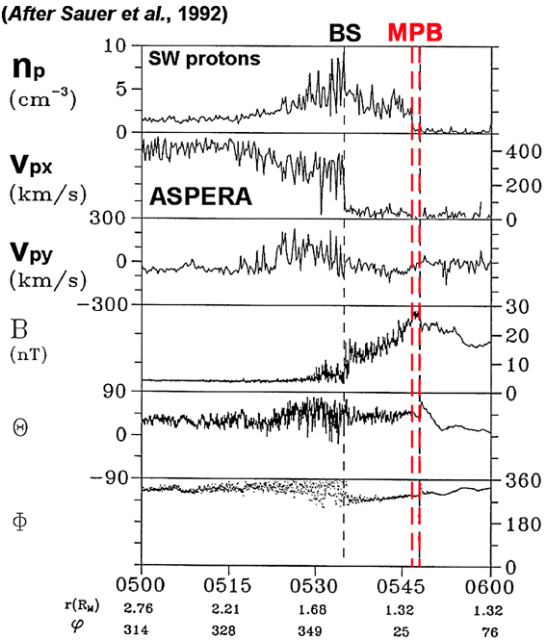

Fig. 4b From top to bottom, Phobos-2 proton density, proton velocity components XMSO and YMSO and magnetic field in MSO spherical coordinates (Adapted from Sauer et al. 1992)

Figure 5 shows MEX ASPERA/MARSIS measurements along the outbound leg of an orbit on July 9, 2007 as the spacecraft emerges from the Martian ionosphere into the unshocked solar wind (Dubinin et al. 2008a, 2008b). On the left end of the figure panels, the ionosphere is well recognized from the appearance of the energy peaks in the range between 20 and 30 eV on the electron spectrograms (Frahm et al. 2006), followed and the ∼20–30 eV O^+ and O_2^+ with energies also recorded by ASPERA-3. The superimposed curves of solar wind ($E_e > 5$ eV) electron density measured by ASPERA-3 (white) and the total electron density measured by MARSIS (black) begin to diverge at the IMB in coincidence with the decrease in the fluxes of superthermal electrons observed on MGS/ER data. As anticipated earlier, this indicates an increase in the total plasma density driven by the increase in the planetary cold electron density, as the solar wind electrons fade out. The IMB is indeed a thin layer (∼25 km ∼0.4 c/ω_{pi}) where there is also a sudden jump of the magnetic field strength. It is noteworthy, however, the fact that this abrupt increase in the magnetic field pileup is not always present (e.g. Bertucci et al. 2003a; Dubinin et al. 2008a, 2008b). In such cases, the IMB is still well identified by the drop in solar wind electrons and the increase of draping. The IMB is also the place where the thermal pressure in the magnetosheath balances the magnetic pressure in the induced magnetosphere (Dubinin et al. 2008a, 2008b).

Another characteristic of the IMB is the enhancement observed in the magnetic field draping (Bertucci et al. 2003a). This enhancement was detected from the correlation between the MSO aberrated (4°) flow-aligned and cross flow components of the magnetic field: $B_{x'} = B_{XMSO'}$ and $B_r = (B^2_{YMSO'} + B^2_{ZMSO'})^{1/2}$. Whereas outside the IMB, inside the magnetosheath, both components are poorly correlated, this correlation significantly improves inside the IMB.

The IMB comprises a layer where the magnetic field rotates defining a directional discontinuity. The structure of such discontinuity was studied by Bertucci et al. (2005a), who applied minimum variance analysis (MVA, Sonnerup and Scheible (1998)) on Martian IMB crossings by MGS. The study showed that the normal component of the magnetic field

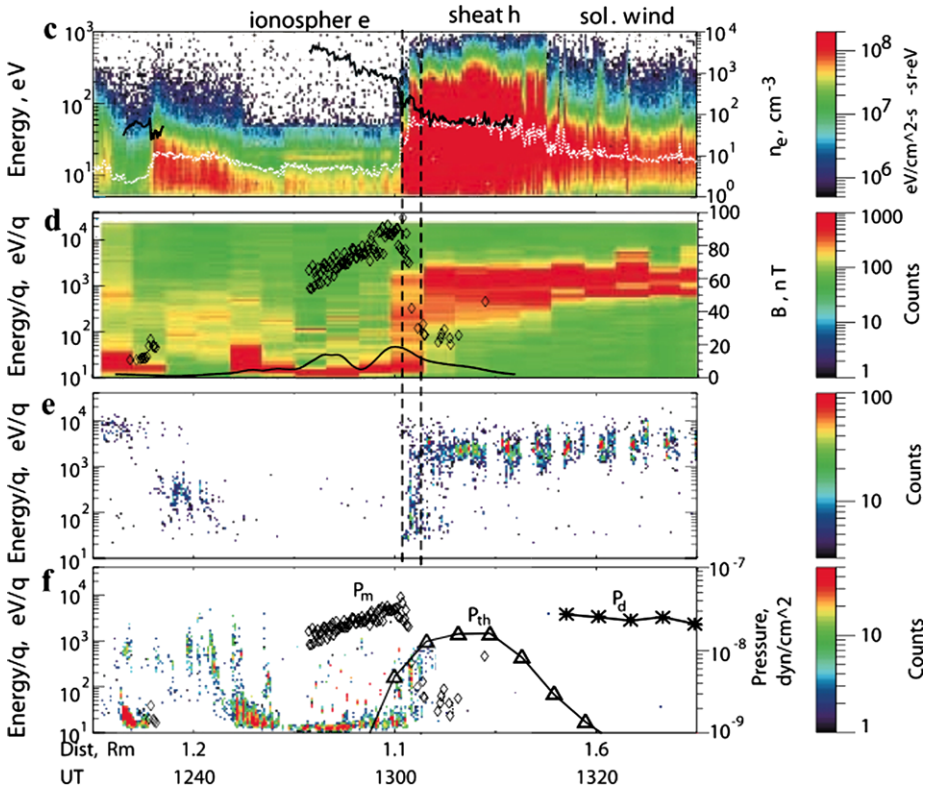

Fig. 5 MEX ASPERA/MARSIS measurements on July 9, 2007 from Dubinin et al. (2008a). The *dashed curve* corresponds to the averaged position of the IMB. Energy-time spectrograms of the (**c**) electrons with the imposed curves of ne from ASPERA (*white*) and MARSIS (*black*) and (**d**) all ion species, (**e**) He++, and (**f**) heavy ($m/q > 16$) ions. Imposed curves are: the magnetic field value from the MARSIS observations (*diamonds*) and Cain et al. (2003) crustal field model (*solid*) (**d**), the magnetic pressure P_m (*diamonds*), the thermal proton pressure P_{th} (*triangles*), and the solar wind ram pressure P_d (*asterisks*)

at the IMB is usually negligible (Fig. 6), as in a MHD tangential discontinuity. However, the changes in the dominant population occurring at the IMB make the comparison with single fluid plasma theory discontinuity properties a simplification. In agreement with ASPERA measurements mentioned above, Bertucci et al. (2005a) find a thickness of 80 km for the current layer within the IMB along which an estimated volume current density $|J_V| = 81$ nA m^{-2} flows. The IMB extends into the downstream sector where it becomes the magnetotail boundary and similar criteria are used to identify it Vignes et al. (2000), Edberg et al. (2009a).

2.3.2 Comparison of Martian IMB and Bow Shock Sizes, Shapes and Controlling Factors

The shape and location of the Martian BS and IMB have been studied in the past by e.g. Slavin and Holzer (1981), Vignes et al. (2000), Bertucci et al. (2005b), Trotignon et al. (2006) and Edberg et al. (2008). During the Phobos 2 mission the number of bow shock and IMB crossings were 127 and 41, whereas during the MGS mission, 573 (Trotignon et al. 2006) and 1149 (Bertucci et al. 2005b), respectively. In the data set of MEX/ASPERA-3 from 2004 until 2008 have 5014 IMB crossings and 3277 BS crossings been identified

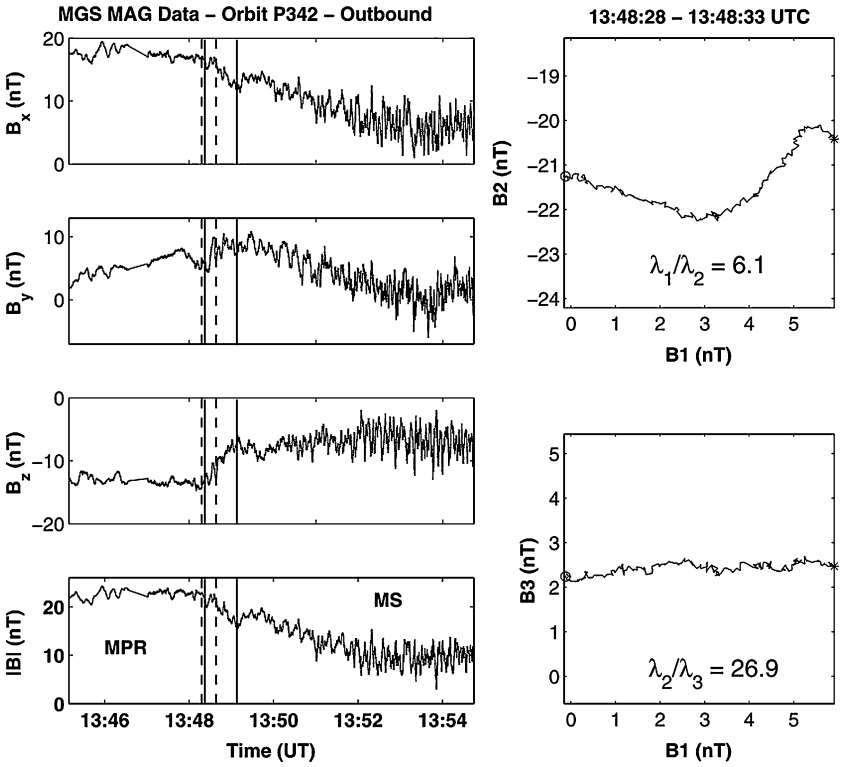

Fig. 6 High-resolution (32 s^{-1}) MGS MAG data (MSO coordinates) for a Martian MPB crossing (*solid lines*) on orbit P342 around 63° SZA. MVA is applied between 1348:18 and 1348:38 UTC (*dashed lines*). Magnetosheath (MS) and the magnetic pileup region (MPR) are indicated for reference. On the right, two hodograms show the magnetic field projection on the minimum variance planes (e1, e2) and (e1, e3) between 1348:28 and 1348:33 UTC. Start and the end of the hodograms are marked with *circles* and *stars*, respectively. Eigenvalue ratios are also indicated

(Edberg et al. 2009b). The number of crossings during the overlapping mission time between MGS and MEX (Feb 2004–Nov 2006) is 2500 and 1840, respectively.

Figure 7 shows the position of all BS (red dots) and IMB (green dots) crossings from MEX 2004–2008 and MGS-derived fits to the boundaries from Edberg et al. (2008). The shape of both the BS and the IMB have been shown to be well represented by conic sections $r = L/(1 + \varepsilon \cos(\theta))$, where r and ε are polar coordinates with origin at X_0 referenced to the MSO x-axis and θ and L are the eccentricity and semi-latus rectum, respectively. This particular shape has been determined from statistical studies using single-spacecraft measurements and recently confirmed through two-spacecraft study using near-simultaneous MEX and Rosetta measurements during the Rosetta Mars flyby in February 2007 (Edberg et al. 2009a). The BS is on average located at an altitude of $0.58R_M$ (∼2000 km) and the IMB at an altitude of $0.33R_M$ (∼1100 km) at the subsolar point. On the terminator plane, the BS is on average at an altitude of $1.6R_M$ (∼5400 km) and the IMB at $0.45R_M$ (∼1500 km).

The factors that have been studied for possible effects on the location of these boundaries include the IMF direction (Vignes et al. 2002; Brain et al. 2005), the crustal magnetic fields (Crider et al. 2002; Dubinin et al. 2006a; Fränz et al. 2006a; Edberg et al. 2008, 2009b), the solar wind dynamic pressure (Crider et al. 2002; Brain et al. 2005; Edberg et al. 2009b), the

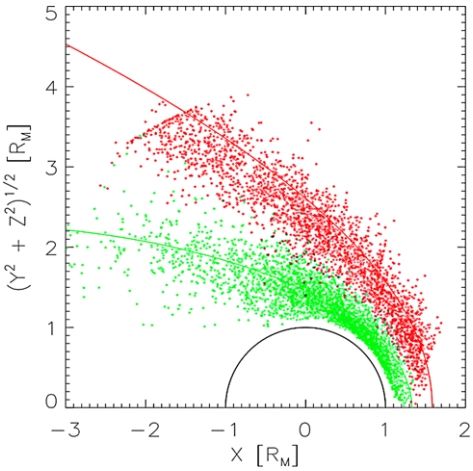

Fig. 7 The position of all BS (*red dots*) and MPB (*green dots*) crossings by MEX from 2004 until 2008. The *red* and *green lines* are previously obtained best fits to the boundaries derived from MGS measurements from Edberg et al. (2008)

EUV flux and solar cycle (Vignes et al. 2000; Edberg et al. 2009b), and the magnetosonic Mach number (Edberg et al. 2010).

Measurements of and Proxies for the Controlling Factors The instruments and orbits of three spacecraft have been relevant for describing which factors that control the location of plasma boundaries at Mars: MGS, MEX and the ACE spacecraft. ACE is in orbit around the L1 Lagrange point upstream of Earth and continuously measures the solar wind proton density, temperature and velocity as well as the vector magnetic field.

Crider et al. (2002) and Brain et al. (2005) have developed proxies for both the solar wind dynamic pressure and the IMF direction from MGS/MAG measurements. The proxies have been formulated in terms of measurements of the average magnetic field strength and draping azimuth at 400 km altitude. The field strength is assumed to balance, and therefore be a proxy for, the solar wind dynamic pressure. The pressure proxy is given by the magnetic field strength B_{proxy} which can be converted to magnetic pressure $P_B = B^2_{\text{proxy}}/2\mu_0$.

The solar EUV flux proxy has been determined from the F10.7 radio flux at 2–200 nm measurements at Earth extrapolated to Mars (Mitchell 2001).

The solar wind (proton) velocity v and density n moments can be calculated from MEX/IMA measurements outside of the BS which is a more direct measurement of the solar wind dynamic pressure $P_{\text{dyn}} = m_p n v^2$, where m_p is the proton mass. For details regarding the moment calculations from MEX/ASPERA-3, see Fränz et al. (2006b). The pressure determined from MEX that is described here is calculated as a mean over 10 min of measurements exterior to a BS crossing.

Influence of the Solar Wind Dynamic Pressure Figure 8, panel (a), shows the extrapolated (Vignes et al. 2002; Crider et al. 2002) terminator distances R_T of the BS crossings as a function of upstream solar wind dynamic pressure $P_{\text{dyn,IMA}}$ as measured by MEX/IMA (Edberg et al. 2009b). The crossings are binned into $0.05 R_M$ bins and the mean values of the dynamic pressure upstream of all crossings in each bin are calculated. The error bars show standard error on the mean (standard deviation divided by number of samples in each bin). There is a trend to smaller radial distance for higher dynamic pressure, with a correlation coefficient of -0.51. An exponential curve (solid line) is fitted to the data points. Panel (b) shows the terminator radius of the IMB as a function of $P_{\text{dyn,IMA}}$. Again, there is a clear trend

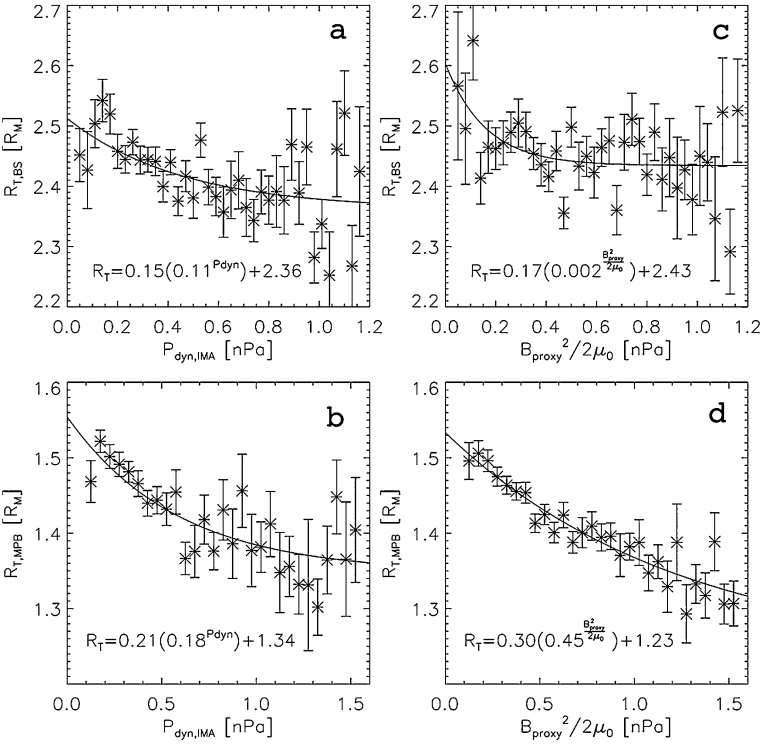

Fig. 8 The influence of the dynamic pressure on the BS and MPB. The panels show (**a**) the altitude of the BS extrapolated to the terminator plane as a function of the dynamic pressure measured by IMA on MEX, (**b**) the terminator altitude of the MPB as a function of $P_{\mathrm{dyn,IMA}}$, (**c**) the terminator altitude of the BS as function of the MGS pressure proxy and (**d**) the terminator altitude of the MPB as a function of the MGS pressure proxy. Reproduced from Edberg et al. (2009b)

to smaller radial distances for higher $P_{\mathrm{dyn,IMA}}$ with a correlation coefficient of -0.74, and the same type of exponential curve is fitted to the data points. The error bars at low radial distance tend to increase which could be an effect of the stronger influence of the crustal fields at lower altitudes. However, it could also be an effect of fewer data points in these bins. The results visualized in these two panels clearly show that the solar wind dynamic pressure has an influence on the location of the boundaries.

These results were also compared to those obtained when the MGS pressure proxy is used, rather than $P_{\mathrm{dyn,IMA}}$. Panel (c) and (d) show the terminator radius of the BS and IMB, respectively, as a function of the MGS pressure proxy $P_B = B^2_{\mathrm{proxy}}/2\mu_0$. The pressure proxy values are linearly interpolated to the time of the boundary crossings. Surprisingly, there is no obvious trend for the variation of the BS radius (correlation coefficient of -0.41) whereas the trend for the IMB is very similar to that in panel (b) (correlation coefficient of -0.93). The lack of a trend for the BS crossings could be explained by the time difference between the time of the pressure proxy measurement and the BS crossings, which can be as long as 1 hour. The BS is expected to move on time scales much shorter than that. For the IMB the same problem with the time difference should arise but the results in panel (b) and (d) are still very similar, which rather disproves the argument above, if the BS and IMB move on the same timescales. It is also likely that the IMB and the BS can simply

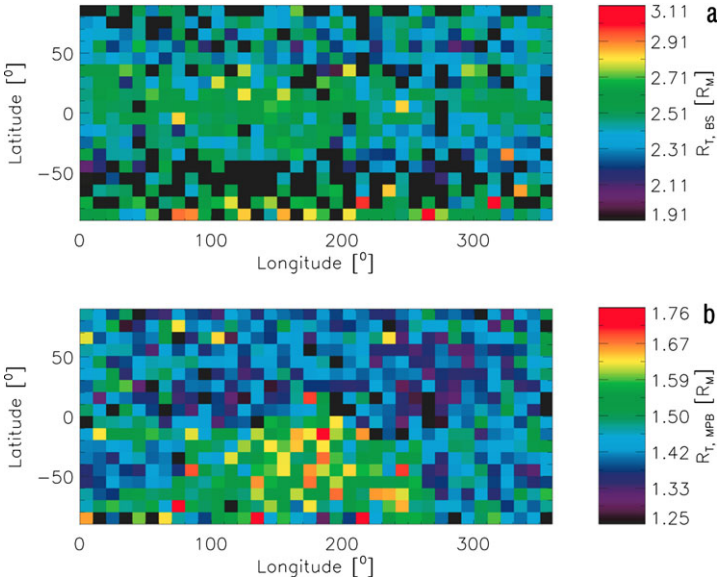

Fig. 9 The influence of the crustal magnetic field on the BS and MPB. The panels show color-coded the mean extrapolated terminator altitude of the (**a**) BS and the (**b**) (MPB) in longitude-latitude bins. Reproduced from Edberg et al. (2009b)

respond differently to changes in the solar wind dynamic pressure. The pressure proxy and the measured pressure values do not match up perfectly and this could be an indication of an unknown compression factor between the solar wind dynamic pressure outside the BS/IMB and the magnetic pressure inside the IMB.

It is also possible that when the BS is at very low radial distances the crustal magnetic fields become more important while at the same time the dynamic pressure becomes less important. The dynamic pressure can only push the boundary down to a certain altitude before the magnetic pressure from the crustal fields together with the plasma pressure inside of the BS become too high and the trend of a lower radial distance for a higher dynamic pressure vanishes. Similarly, when the BS is at very high radial distances the IMF direction could become more important while at the same time the dynamic pressure becomes less important.

Influence of the Crustal Magnetic Fields The crustal fields have been shown to influence the boundaries by using MGS and MEX measurements (Crider et al. 2002; Brain et al. 2005; Fränz et al. 2006a; Edberg et al. 2008, 2009b). Panel (a) and (b) in Fig. 9 (from Edberg et al. 2009b) show two global 10° × 10° longitude-latitude maps color coded by the radial distance of the BS and IMB, respectively. All crossings from 2004 until 2008 from the dayside of Mars are used and the mean of the radial distance of all crossings within each bin are shown. Bins with less than two crossings are colored black. The strongest crustal fields are located in the southern hemisphere at longitudes between 90° and 270° (Connerney et al. 2005). The map of the BS crossings, panel (a), shows no distinct influence of the crustal magnetic fields on the altitude of BS, i.e. there is no specific region where the boundary is at larger radial distance than elsewhere and which also corresponds to a region of strong crustal fields. There are, unfortunately, many empty bins at southern latitudes where the crustal fields are strongest. However, the mean value of RT of all the dayside BS crossings in the northern

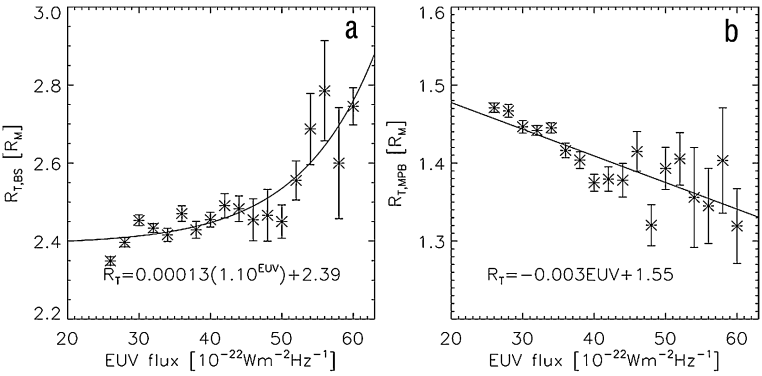

Fig. 10 The influence of the EUV flux on the (**a**) BS and (**b**) MPB. The EUV flux is determined through a proxy using the F10.7 measurements at Earth and then extrapolated to Mars. Reproduced from Edberg et al. (2009b)

hemisphere is $2.45R_M$ compared to $2.49R_M$ in the southern hemisphere and in the bottom rows of panel (a), at southern latitudes, there is a weak tendency that the crossings are at higher distances. The difference is statistically significant according to a Student's t-test at 95% confidence level. This difference is smaller than the difference presented in Edberg et al. (2008) where MGS crossings where used. The accuracy in this study should, however, be better due to the much larger data set.

The influence of the crustal magnetic fields on the IMB is much clearer. In panel (b) of Fig. 9 there is a large area at southern latitudes between longitudes from ∼90° to ∼270°, where the IMB occurs at larger radial distances than elsewhere. This region corresponds very closely to the region where the strongest crustal fields are located. Also, at latitudes above −30° and at longitudes between 0° and 90° there is a less prominent but still visible area of higher IMB which corresponds to a region of intermediately strong crustal fields.

Results show that the IMB is strongly affected by the crustal fields, but the BS to a much lesser extent. The influence on the BS is still somewhat ambiguous due to a lack of sufficiently many BS crossings over the southern crustal magnetic anomalies. Vignes et al. (2002) found that the BS was not influenced while Edberg et al. (2008) found evidence that it was indeed influenced, both using MGS measurements.

Influence of the Solar EUV Flux Figure 10 from the study by Edberg et al. (2009b) depicts the results on the dependence of BS and IMB with respect to the solar EUV flux. The crossings are divided into 2.0×10^{-22} W m^{-2} Hz^{-1} bins and the mean of the radial distance for all crossings within each bin is calculated. There is a clear trend of a larger BS radius for a higher EUV flux and it seems to increase exponentially. For the BS an exponential curve is fitted to the data points. The IMB on the other hand clearly decreases in radius when the solar EUV flux increases and it seems to decrease linearly as the fit in panel (b) shows. Modolo et al. (2006) used a hybrid simulations to study the influence of the EUV flux on the plasma boundary and found that the BS was pushed outward at the subsolar point but moved in at the terminator plane when going from solar minimum to maximum conditions, while the IMB only moved inward at the terminator, in agreement with this study. The data used in this study are all taken during the declining phase of the solar cycle and during solar minimum (2004–2008) and therefore it cannot be yet determined how the EUV flux at solar maximum will affect the boundaries. However, comparisons between the BS and IMB fits

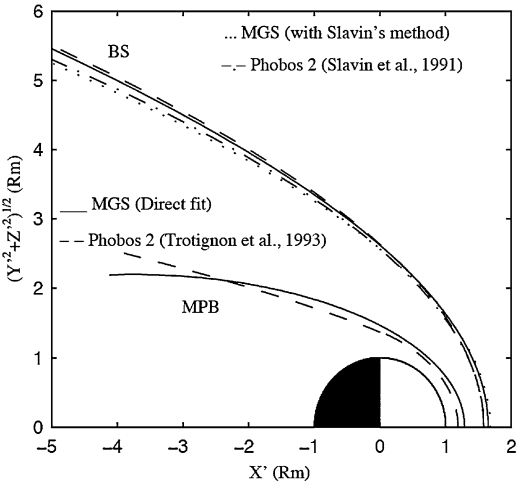

Fig. 11 Martian BS and IMB fits from MGS and Phobos 2 (Vignes et al. 2000)

from Phobos-2 (Slavin et al. 1991; Trotignon et al. 1993) and MGS observations (Fig. 11) suggest that the position of both boundaries is not sensitive to solar cycle phase (Vignes et al. 2000).

Influence of Magnetosonic Mach Number Vennerstrom et al. (2003) extrapolated Earth upstream conditions to Mars by studying the magnetic field measured by ACE and compared that to the MGS measured fields at Mars during an interval in 1999 when Mars and Earth were close to being aligned on a Parker spiral. To perform such an extrapolation a time shift had to be applied to the ACE measurements which took into account the radial distance as well as the longitudinal distance between the two planets (Vennerstrom et al. 2003).

Two intervals when Mars and Earth are in the same solar wind sector have occurred since MEX arrived at Mars, starting in 2005 and in 2007, and were used by Edberg et al. (2010) for studying the effect of the magnetosonic Mach number.

In Fig. 12 the terminator distances of the BS crossings from these two intervals are plotted as a function of the magnetosonic Mach number, as measured by ACE and extrapolated to Mars. The mean distance is calculated in Mach number bins of 0.25, ranging from Mach number 6.1 to 10.5. Outside of this interval there are too few data points in each bin (<10). Crossings that take place outside the SZA range 40°–110° are removed in order to avoid any orbital bias. A linear curve is fitted to the mean values and there is a clear trend of a lower BS altitude for an increasing Mach number. Clearly, when the Mach number is higher than average, the BS becomes compressed. When the Mach number drops, the BS moves to higher altitudes.

Edberg et al. (2010) results show that the Martian BS altitude decreases near-linearly with increasing Mach number calculated from ACE, which is similar to results obtained for the Venus BS by the Pioneer Venus Orbiter mission (Slavin et al. 1980). The IMB on the other hand does not seem to be affected by the Mach number.

Influence of IMF Direction/Upstream Convective Electric Field Edberg et al. (2009b) also studied how the boundaries reacted to different directions of the convective electric field. It was, however, found that the IMF direction had a very weak influence on the boundaries if compared the other factors. This is not to say that the IMF direction is unimportant but rather that the method of using the MGS derived proxy for the IMF direction is not sufficiently

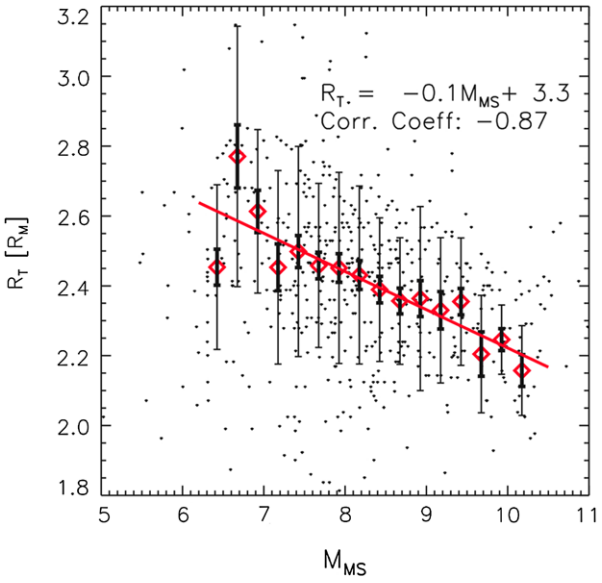

Fig. 12 The influence of the magnetosonic Mach number on the BS. The Mach number is determined from ACE measurements of the solar wind parameters at Earth and then extrapolated to Mars (Edberg et al. 2010)

good or accurate. Vignes et al. (2002) showed that the IMF does have an influence on the boundary locations. This is also observed in simulations (see e.g. Modolo et al. 2006).

2.4 The Induced Magnetosphere

The induced magnetosphere is the region populated by draped external field lines and largely dominated by planetary plasma (especially O^+ and O_2^+). But also, the induced magnetosphere is the place where most of the transfer of energy and momentum from the solar wind to the Martian plasma occurs (Dubinin et al. 2006a, 2006b). Several authors point at the boundary layer and the tail rays as the substructures where escaping local plasma are concentrated (Lundin et al. 1991; Lundin and Dubinin 1992, Dubinin et al. 2006b, 2006c).

On the dayside, the induced magnetosphere is a region of a few hundred kilometers thick with highly piled up fields which form a more or less efficient barrier against the protrusion of the external plasma. In spite of the low beta that characterizes the dayside induced magnetosphere (referred to it as magnetic pileup region, MPR), compressive (i.e. correlated with plasma density oscillations), quasi-monochromatic, linearly polarized waves were observed by MGS (Bertucci et al. 2004). The oscillations also display a wave vector normal to the background magnetic field. All these signatures suggest that these oscillations are fast magnetosonic waves. As mentioned above, these waves are sometimes accompanied by mirror-mode waves in the magnetosheath (Fig. 13) where the magnetic oscillations are anti-correlated to the plasma density. A survey of 282 IMB crossings by MGS shows that fast magnetosonic waves occur at least 27%. Fast magnetosonic (IMB) and mirror mode (magnetosheath) waves coincide in at least 18% of the observations. Finally, at least 11% of the observations show neither of them.

Far from regions where crustal magnetic fields dominate, the IMF clock angle seems to play an important role in spatially defining the subregions where escaping plasma channels are located. Near the terminator, the strongest magnetic stresses will be observed in the magnetic polar regions (where field lines try to slip over the planet into the nightside), and

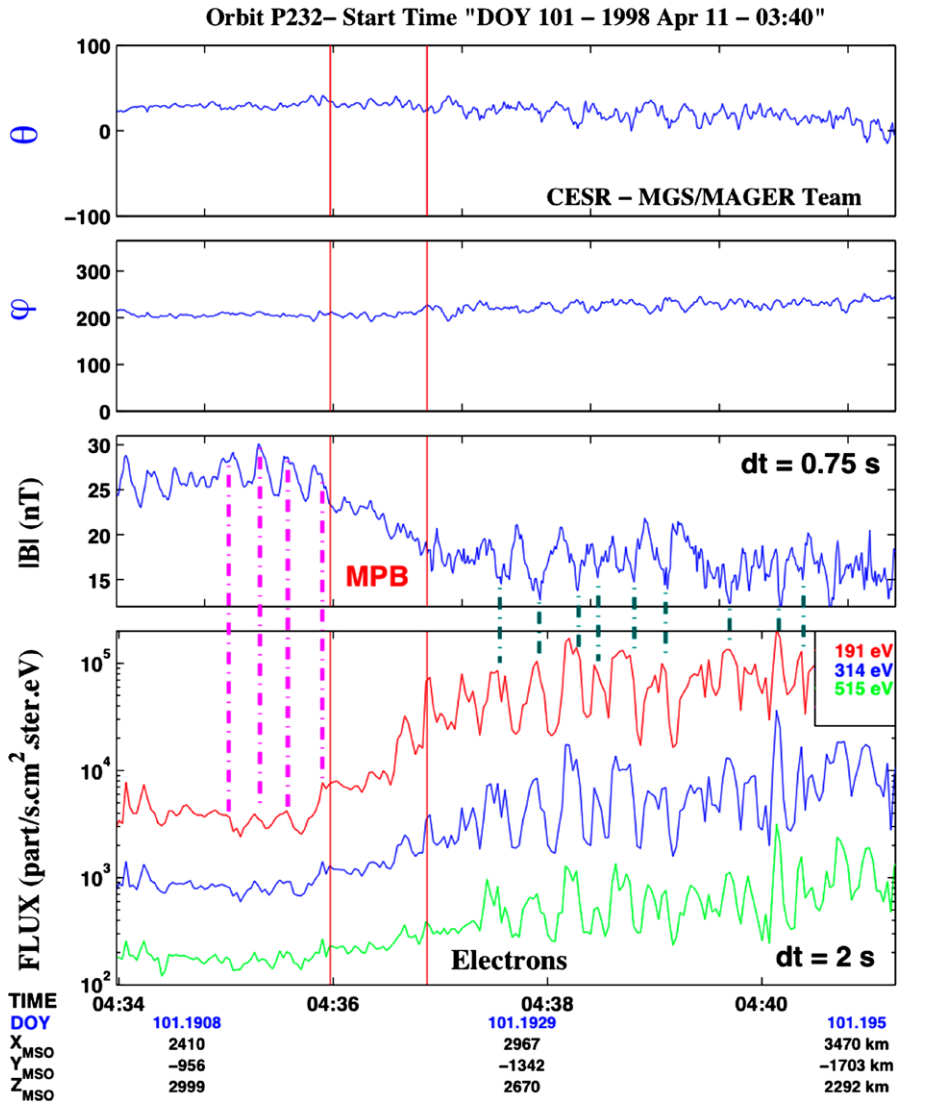

Fig. 13 MGS MAG data in spherical MSO coordinates and ER electron fluxes for 191, 314 and 515 eV during orbit 232. Compressive, magnetic field oscillations occur on either side of the IMB (here identified as MPB): in the IMB (*point-dash lines on the left*) they correlate with the electron fluxes, whereas in the magnetosheath the magnetic field strength is anti-correlated to the electron fluxes (Bertucci et al. 2004)

planetary plasma will be more susceptible to be efficiently accelerated (Fig. 14). This could be the case of the observations reported by Dubinin et al. (2006b, 2006c) where narrow, energetic magnetosheath-like electron events were observed by ASPERA 3 in coincidence with planetary ions (O^+, and O_2^+). In such a scenario, these polar plasma channels would be associated with the gradual formation of a plasma sheet separating the lobes of the magnetotail. The authors also mentioned the reconnection between the IMF and the crustal magnetic fields as an alternative mechanism.

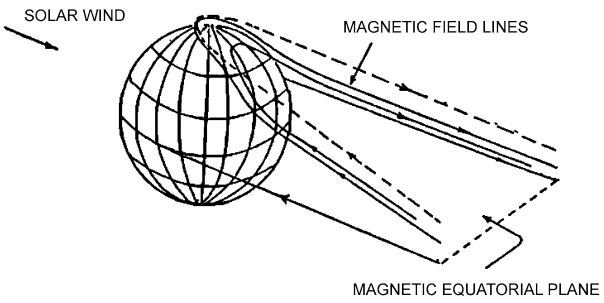

Fig. 14 Schematic of magnetic field lines draping around the ionosphere indicating their entry into the wake over the magnetic polar regions where magnetic stresses become maximum (from Pérez-de-Tejada 1986)

The narrow structures found at Mars could be similar to the tail rays observed around Venus (Brace et al. 1987) and explained as a result of the penetration of the convective electric field into the ionosphere near the terminator (Luhmann 1993). This possibility was mentioned by Dubinin et al. (2006a) for ASPERA-3 ion beams detected near the Martian terminator.

In the nightside, the induced magnetosphere becomes the magnetotail. It consists of two lobes opposite polarity separated by a neutral sheet. The Martian magnetotail has not been extensively explored. However, mid and short-range observations by Phobos-2 and MGS respectively have provided some basic properties about its magnetic structure. Using Phobos-2 observations at $2.86 R_M$, Yeroshenko et al. (1990) and Schwingenschuh et al. (1992), reported that the mid range magnetotail field geometry depends on the IMF clock angle. Halekas et al. (2006) obtained a similar result at 400 km altitude, far from the magnetic crustal sources. Rosenbauer et al. (1994) found a dependence of the magnetic pressure within the magnetotail on the solar wind ram pressure from which they obtained an average flaring angle of $\sim 13°$. Zhang et al. (1994) found a similar result. In a work based on MGS data, Crider et al. (2004) found that the short-range magnetotail flares out from the Mars–Sun direction by 21°.

The Martian crustal sources play an important role in altering the magnetic topology in the low altitude induced magnetosphere at certain latitudes. Brain et al. (2002) found that the influence of crustal sources can be perceived up to 1300–1400 km altitude, depending on the local time, and latitude. They also mention that IMF/Crustal field reconnection may occur. More recently, Eastwood et al. (2008) claims that noncollisional reconnection occurs in the magnetotail. Halekas et al. (2008) on the other hand, suggest that IMF/Crustal field reconnection, if regular, could have important consequences on atmospheric escape, while Brain et al. (2010a) reports evidence of bulk atmospheric escape following reconnection.

The Martian magnetotail plasma inventory was studied in detail by MEX. Following the detection of planetary heavy ions (O^+ and O_2^+) confined inside the IMB (Lundin et al. 2004), a characterization of the different populations of planetary ions within the magnetotail was covered in several works. Fedorov et al. (2006) found that the planetary ion energies above 300 eV decrease from the IMB to the plasma sheet in the center of the magnetotail. In the neutral sheet, Fedorov et al. (2008) reported 1-keV energy heavy ions (Fig. 15). This is in agreement with Phobos-2 observations by Dubinin et al. (1993b) who found that this energy is of the order of that of the solar wind ions, an argument in favor of an efficient transfer of linear momentum and energy from external plasma to the planetary plasma via electrostatic fields. In particular, Dubinin et al. (1993b) estimated the energy gained by the planetary ions within the plasma sheet assuming a $j_e \times B$ force where j_e is the electron current density and found that these estimations are of the same order as those measured by Phobos-2/ASPERA.

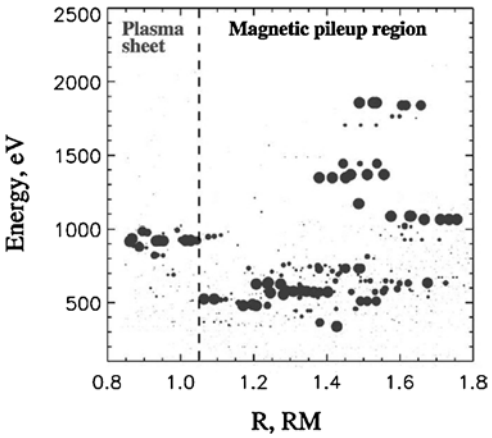

Fig. 15 Scatterplot of the planetary ions energy versus $(Y^2_{MSO} + Z^2_{MSO})^{(1/2)}$. *Each circle* corresponds to the one complete IMA energy-angular spectrum. The diameter of the circle shows the total count rate of the event. The *vertical dashed line* separates the tail lobes from the plasmasheet (Fedorov et al. 2006)

The influence of the convective electric field in the IM plasma morphology was also studied from ASPERA-3 measurements. Fedorov et al. (2008) found a slight asymmetry in the distribution of planetary ions within the plasma sheet, and Dubinin et al. (2008b), reported that the ion fluxes within the IM display asymmetries due to the IMF and the crustal fields.

However, the planetary plasma escape is dominated by the 'cold' ion population (Lundin et al. 2009). This includes not only H^+ but also heavier species, such as molecular ions (e.g. CO_2^+). An interesting conclusion of Lundin et al. (2009) is that there is no appreciable latitude or local time asymmetry in the escaping flux.

2.5 The Ionospheric Boundary

2.5.1 The Photoelectron Boundary (PEB)

In addition to bow shock and IMB, an additional boundary related to the upper limit of the collisional ionosphere was reported at lower altitudes. However, whether this boundary is similar to the Venusian ionopause (Elphic et al. 1981), is still under debate.

Initial observations by MGS well below the IMB and over regions where crustal field influence was negligible displayed a decrease in the magnetic field (Acuña et al. 1998). This led to think that a Venus-type ionopause was indeed present at Mars. However, until a reliable estimation of the thermal pressure within the collisional ionosphere was made, a real comparison with the Pioneer Venus Orbiter observations would be impossible.

In MGS electron reflectometer ER (Mitchell 2001) and more clearly in the ASPERA-3 electron spectrometer (ELS) data (Lundin et al. 2004; Frahm et al. 2006), ionospheric plasma is well traced by the characteristic energy spectrum of photoelectrons. Photoelectron lines are attributed to both carbon dioxide and atomic oxygen, and are theoretically located in energy between 21 eV and 24 eV, and 27 eV (Mantas and Hanson 1979; Fox and Dalgarno 1979). The relevant photoelectron peaks in the energy spectrum are mainly due to ionization by solar 30.4 nm photons.

Photoelectrons are often observed not only near the planet, but also near the IMB, as shown in Fig. 16, where the photoelectron line is observed from periapsis until an altitude of ~900 km, close to the outbound IMB crossing at ~0408 UT (Dubinin et al. 2006a). On the inbound leg photoelectrons are also observed near the IMB, but at much higher altitudes (up

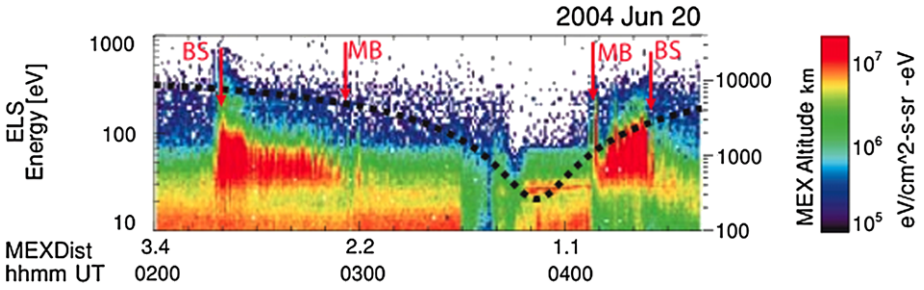

Fig. 16 Electron spectrogram measured by MEX ASPERA-3 ELS on June 20, 2004. The *dotted curve* shows the spacecraft altitude. Crossings of the bow shock, and the IMB (here indicated as MB) (from Dubinin et al. 2006a)

to ∼5000 km ∼0300 UT). However, photoelectrons observed close to Mars on the dayside might be locally produced whereas those in the downstream sector, far from Mars might likely photoelectrons travelling along draped field lines connected to the ionosphere (Frahm et al. 2006). Unfortunately ASPERA-3 ELS cannot discriminate between locally produced and transported photoelectrons (Frahm et al. 2010).

The point in the near Mars space (mostly dayside) where the photoelectron signature sets in defines the photoelectron boundary (PEB). In most MGS and MEX orbits a distinct gap (small or large) exists between the IMB identified by a drop of the sheath electrons and the start of the photoelectron boundary (PEB). The presence of this gap clearly shows that IMB and PEB are indeed two distinct boundaries (Dubinin et al. 2006a).

Finally, it is worth mentioning that the PEB altitude is extremely sensitive to the location of the Martian crustal sources (Brain et al. 2003; Nagy et al. 2004).

2.5.2 MARSIS Ionospheric Electron Density Gradients: Possible Venus-Like Ionopause

Analysis of MARSIS electron density measurements in the ionosphere of Mars revealed the existence of steep gradients similar to the Venusian ionopause. MARSIS ionospheric sounding mode provides electron density measurements from the ionosphere of Mars using two techniques. The remote sounding technique, which provides electron density measurements in the altitude range between 130 and 400 km, involves sending a short radio pulse of frequency f, and measuring the time delay of the returning echo (Gurnett et al. 2005). The second method, which provides electron densities from much higher altitudes, between 275 and 1300 km, is from the excitation of local electron plasma oscillations.

In the ionospheric sounding mode, when the transmitter frequency is near the local electron plasma frequency, electron plasma oscillations are excited at that frequency. Since these oscillations are usually very intense, harmonics of the basic oscillation frequency are introduced in the detector. Ionograms, which are plots of echo intensity as a function of frequency and time delay, then used to display MARSIS data. Electron plasma oscillation harmonics are seen as equally spaced vertical lines at low frequencies. When the plasma frequency is below 100 kHz, the fundamental of the electron plasma frequency cannot be observed. However, the electron plasma frequency can still be determined by measuring the spacing between the harmonics. Once the electron plasma frequencies are obtained, corresponding electron densities can be calculated using the formula $n_e = (f_p/8980)^2$, where the electron density, n_e, is in cm^{-3} and electron plasma frequency, f_p, is in Hz (Gurnett and Bhattacharjee 2005).

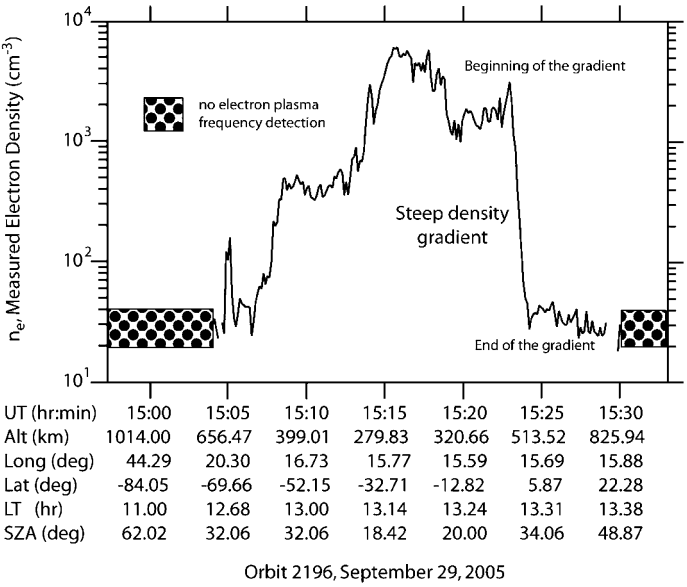

Fig. 17 Pass from September 29, 2005, the electron density in cm^{-3} is presented on the *vertical axis* and *horizontal axis* shows the universal time (UT), altitude (Alt), longitude (Long), latitude (Lat), local time (LT), and solar zenith angle (SZA) (Duru et al. 2009)

Observations Through Excitation of Local Electron Plasma An example of a steep density gradient similar to the ionopause of Venus is shown in Fig. 17 (Duru et al. 2009). The pass starts at around 14:57 UT and ends around 15:33 UT. For the first seven minutes electron plasma oscillations are not detected. The same situation occurs after 15:30 UT. Possible reasons for the disappearance of the electron plasma oscillations are studied extensively by Duru et al. (2009, 2010). After the first detection of the electron plasma oscillations at around 15:04 UT, the electron density increases with decreasing altitude up to about 15:15 UT, where the altitude starts to decrease. A very sharp drop in the electron density is observed at about 15:23 UT. These sharp drops in the ionospheric thermal plasma density are commonly seen at Venus and are identified as the ionopause (Schunk and Nagy 2000; Brace et al. 1980). In this case, the electron density which is 3087 cm^{-3}, decreases to 27 cm^{-3} in about a minute. The beginning of this steep gradient feature is located at an altitude of 419 km and at a SZA of 28°.

In the ionosphere of Venus, steep density gradients are seen very often and are usually observed on both the inbound and the outbound legs of a given pass (Brace et al. 1980). At Mars it was possible to identify only a few MEX passes in which a steep gradient was observed on both legs. In contrast to Venus, Martian steep density gradients occur in only about 18% of the samples studied. This percentage is found by excluding all of the half-passes.

Remote Sounding Observations Remote sounding provides a much better spatial resolution than local plasma density measurements. In an MARSIS ionogram the signature of a Venus-like ionopause is a horizontal line at low frequencies. Out of 132 passes, density drops were detected from remote sounding in 40.

Figure 18 shows four consecutive ionograms from an orbit on November 14, 2005 (Duru et al. 2009). They are separated by 7.54 s, which is the repetition time of the ionospheric sounding. As expected, the steep gradient in n_e is represented by a horizontal line at low frequencies (<0.5 MHz in this case) indicating a rapid increase in density over a short time range. The longer horizontal line seen at around 2.5 ms time delay is the reflection from the horizontally stratified ionosphere. For this pass, the time delay of the steep gradient does not change significantly from one ionogram to the next.

Density Gradient Thickness Drop apparent thickness is calculated by using two methods. In the first method, the local electron density profiles are used and the thickness is defined as the altitude difference between the beginning and the end of the sharp electron density drop. The histogram showing the thicknesses obtained this way is displayed in the top panel of Fig. 19. The mean thickness is calculated to be 37.5 km, with a standard deviation of 20 km.

In the second method, the equation $\Delta h = 1/2\ \Delta t_i\ c$, where $\Delta t_i = t_e - t_b$ is the difference between the time delay at the end of the steep density gradient (t_e) and the time delay at the beginning of the steep density gradient (t_b) (see Fig. 18), and c is the speed of light, is used to calculate the thickness from the remote sounding data. The $1/2$ factor accounts for the fact that the time delay is the time required for the pulse to go and come back from the reflection point. This method should provide a more precise determination of thickness than the method using local plasma oscillations since an ionogram presents data obtained over only 1.26 s, which is the time it takes to complete scan of all the frequencies, between 0.1 MHz and 5.5 MHz, as opposed to the 7.54 s resolution of local plasma frequency data. Spatial and temporal effects are therefore much less likely to affect the results in this method. The altitude resolution of the ionograms is about 14 km with the upper limit of the thickness taken at the calculated value. This method was applied to 55 ionograms. The results are shown in the histogram shown in the bottom panel of Fig. 19. The mean value is about 22 km, with a standard deviation of 8.8 km. The thicknesses obtained from using remote sounding measurements are smaller than those obtained using local electron density measurements. This difference can be attributed to the improved resolution of the remote sounding data eliminating the effect of temporal variations involved in the local density measurements.

It is expected that the thickness of the ionopause boundary should scale with the ion gyroradius (Elphic et al. 1981). The thickness of the crossings and ion cyclotron radius are expected to scale with each other. The ion cyclotron radius varies between 3 km and 22 km with a mean value of 10.31 km and a standard deviation of 4.02 km. The fact that the thickness is usually greater than one ion gyroradius may be due to the ambipolar potential created by the large temperature difference across the regions and layers separating the ionosphere from the magnetosheath.

Spatial Distribution of Density Gradients At Venus, the ionopause altitude changes drastically with changing solar wind conditions (Brace et al. 1980). At Mars, Duru et al. (2009, 2010) reported that ionopause crossings are detected in a large range of altitudes changing between 302 and 979 km. However, most of the crossings lie between about 300 and 600 km. and increase in altitude with increasing solar zenith angle.

The crustal magnetic fields add greatly to the complexity of the ionosphere of Mars and its ionopause (Nagy et al. 2004). Earlier studies show that the crustal magnetic fields can contribute to irregularities in the ionosphere of Mars (Gurnett et al. 2005; Duru et al. 2006). They can also affect the electron distribution and have the effect of raising the boundary between Mars' ionosphere and solar wind. Crider et al. (2002) and Brain et al. (2005) showed that the strong crustal magnetic fields raise the altitude of magnetic pile-up

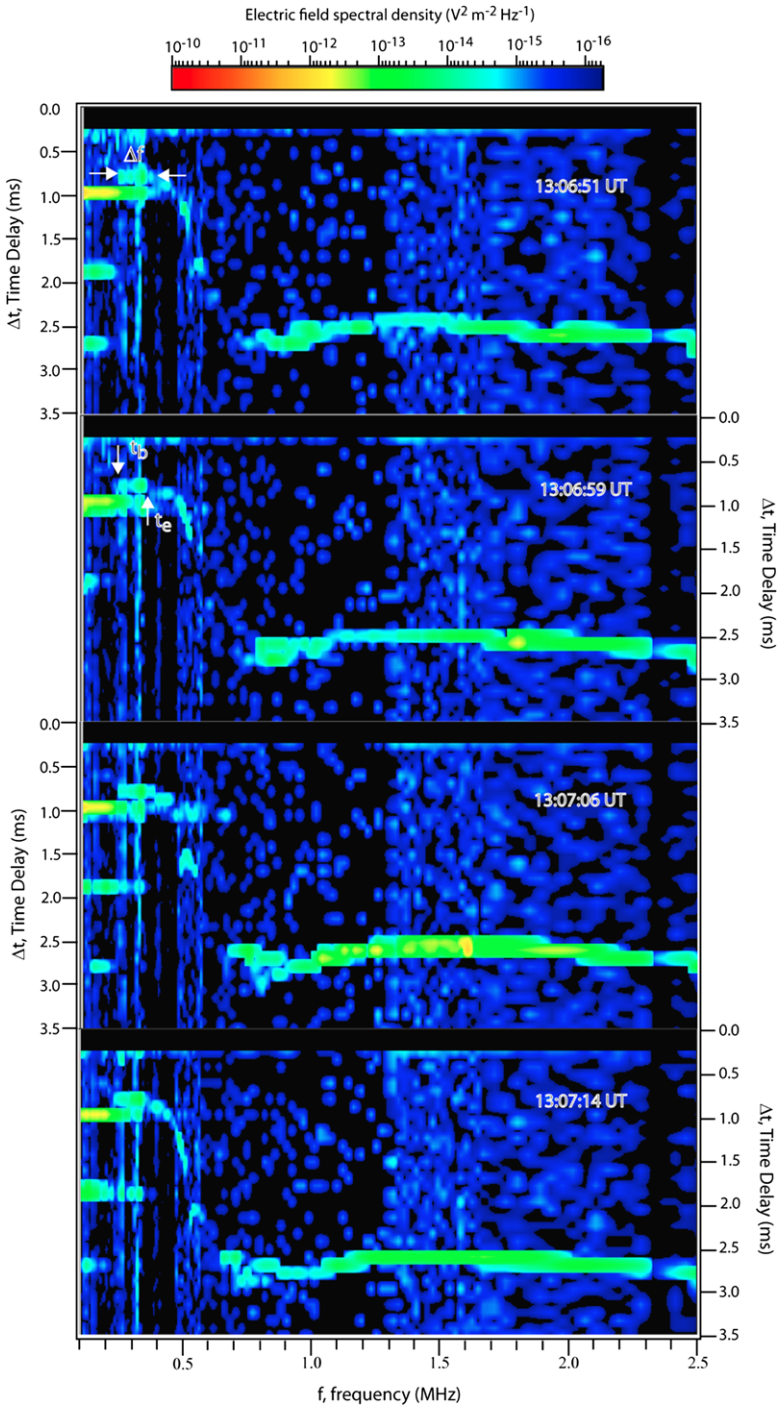

Fig. 18 Ionograms around an ionopause-like signature (Duru et al. 2009)

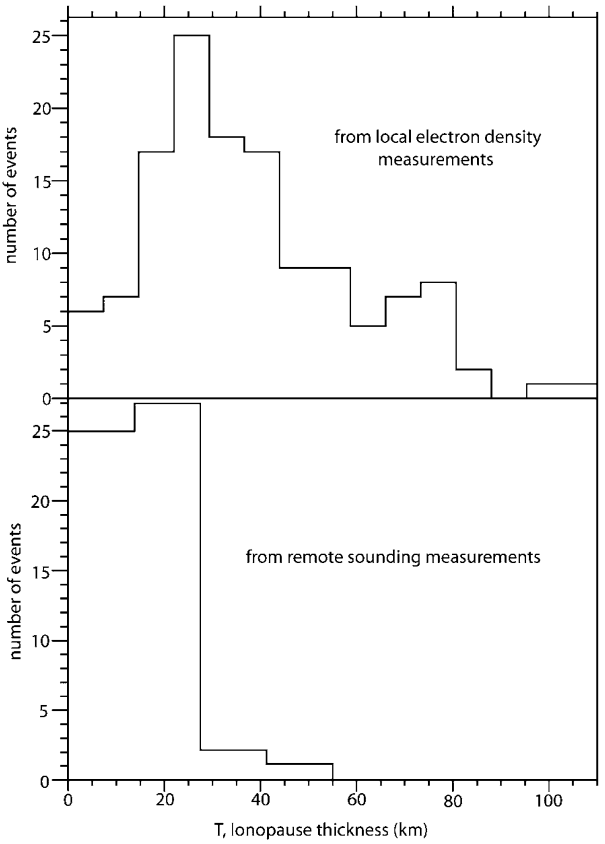

Fig. 19 Distribution of density drop thickness calculated from local n_e measurements (*above*), and remote sounding (*below*) (Duru et al. 2009)

boundary (MPB). Duru et al. (2009) studied the influence of the magnetic crustal sources on the n_e drop location and found that drop altitudes are higher over crustal field regions.

3 Venus

Current knowledge of the solar wind interaction with Venus comes from Venera-9 and Venera-10 measurements (Gringauz et al. 1976; Dolginov et al. 1981; Vaisberg et al. 1976; Zelenyi and Vaisberg 1985), and in much broader extent from the long lasting Pioneer Venus Orbiter (1978–1992) which provided a data set that extended over a complete solar cycle (Russell et al. 2006a). The plasma boundaries at Venus were analyzed using data measured by the PVO magnetometer OMAG (Russell et al. 1980) and plasma analyzers, notably, Orbiter Retarding Potential Analyzer ORPA (Knudsen et al. 1979) because of its higher time resolution.

However, compared with the magnetometer MAG (Zhang et al. 2006) and the ASPERA-4 plasma analyzer Barabash et al. (2007) onboard the Venus Express (VEX) spacecraft PVO had much lower temporal, energy and angular resolution.

Although PVO made observations over the entire solar cycle, no direct measurements of the near Venus plasma environment during solar minimum were possible due to the high PVO orbital altitude (>2000 km) at that time. The VEX spacecraft has a constant periapsis

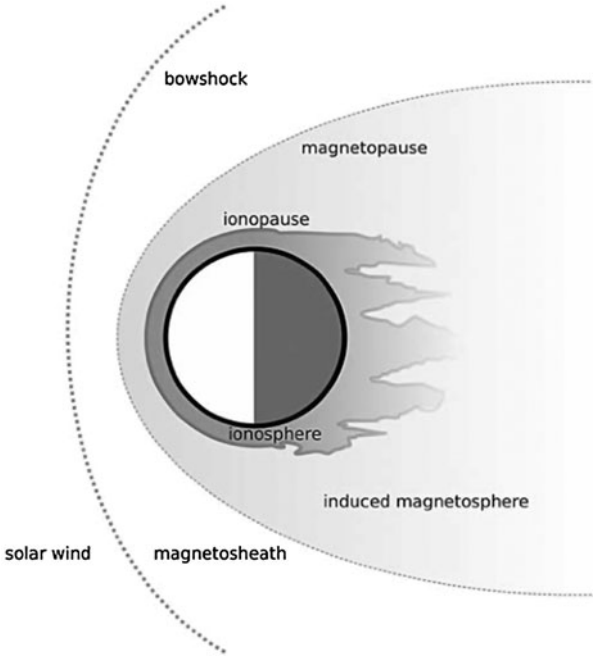

Fig. 20 Schematic of Venus induced magnetosphere and its boundaries (Zhang et al. 2008b)

altitude of about 250 km and thus can sample this region during solar minimum. Just prior to PVO arrival, the Russian Venera 9 and 10 orbiters (1975–1976) observed the Venus solar wind interaction, including the bow shock and tail during solar minimum (Verigin et al. 1978).

Venus' magnetosphere is comparatively smaller than Mars' and proven to be strongly dependent on the Solar cycle phase. It is preceded by a collisionless bow shock that heats, decelerates and compresses the solar wind flow (Fig. 20). Inside the shock, the magnetosheath is characterized by a magnetic field and plasma variability that depends on the IMF cone angle. At the bottom of the magnetosheath, on the dayside, the magnetic field pileup increases (usually gradually) and a magnetic barrier forms. A boundary similar to the Martian IMB marks the entry into the induced magnetosphere, where strong, draped fields coexist with an electron population which is significantly colder than that within the magnetosheath (the plasma mantle). The IMB extends to at least 11 planetary radii downstream and encircles the induced tail where planetary plasma escape is concentrated. The ionospheric boundary is the ionopause, where the thermal ionospheric pressure balances the induced magnetosphere's magnetic pressure. During periods of high solar wind dynamic pressure the shielding effect of the ionopause is diminished and the ionosphere gets magnetized.

3.1 Bow Shock

In the same way as Mars, the interaction between the supermagnetosonic solar wind and the Venusian atmosphere generates a bow shock. Unlike Mars, however, the Venusian bow shock has been investigated over several years by PVO and VEX, leading to an understanding of the influence of the solar wind parameters (depending on the solar cycle phase) on its structure and variability.

As for Mars, ultra low frequency waves at the proton cyclotron frequency in the spacecraft rest frame are also present in the solar wind upstream from the Venusian bow shock (see

companion paper by Delva et al. for more details). However, the smaller extent of Venus' exosphere might lead to a pick up wave corona less extended than the Martian one. In addition, waves related to solar wind backstreaming ions within the planet's foreshock are also present (Wei et al. 2011).

The Venusian bow shock has been systematically observed by all missions so far. Figure 21 shows five crossings of the Venusian bow shock as seen by PVO magnetometer ordered according to increasing plasma beta from top. As shown in the figure, the bow shock is characterized by a strong jump in the magnetic field strength and variability. These features are confirmed by VEX magnetometer (Zhang et al. 2008a). In general, Venus bow shock ramp is more clearly detected than at Mars. This might be a result—at least—of a less important role of the exospheric massloading in the case of more massive Venus. Also, the relatively higher size of the Venusian obstacle and the smaller gyroradii due to a stronger IMF attenuates the kinetic effects believed to be dominant at Mars.

Most of the crossings shown in the figure are quasi-perpendicular and depict the typical substructures arising in supercritical cases: a shock foot, ramp and overshoot. However, well-developed overshoots as the ones in panel 2 and 3 from bottom are rare in PVO measurements. As observed in other planets, the overshoot magnitude seems to increase with increasing M_{MS} (Russell and Vaisberg 1983).

More recently, VEX ASPERA-4 (Barabash et al. 2007) provided high time resolution plasma observations which confirmed the characteristics of a fast shock. Figure 22 displays data obtained on July 15, 2006 showing the main plasma features of the solar wind interaction with Venus about one hour before and after the closest approach of orbit No. 85. The top panel shows an energy spectrogram of measured electrons in the energy range of 0.1 eV–20 keV obtained by ELS. But electrons below 5 eV are reflected to avoid saturation of the counters. The sensor has 16 anodes covering a total field of view of $4° \times 360°$. Shown are counts obtained during 4 s sampling intervals integrated over anodes 5–15 of the sensor because anodes 0–4 are noisier. The data shown in the next two panels represent protons and heavy ions, respectively, measured by IMA, integrated over all 16 anodes and separated into 8 spatial sectors covering a total field of view of $90° \times 360°$. Note that signatures above 50 eV energy in the bottom panel in the solar wind and magnetosheath regions are not caused by heavy ions but by saturation of the proton channels. A spatial scan during 192 s by electrostatic deflection produces the repeatable pattern visible in the spectrogram. The x-axis shows the distance, position and time of the spacecraft along the orbit. First, VEX is located inside the solar wind before crossing the bow shock (BS) at 01:15 UT, identified by an increase in counts of energetic electrons ($E > 35$ eV) in the magnetosheath with respect to the solar wind. Passing the BS, the spacecraft enters the magnetosheath, characterized by the shocked, slowed down and heated solar wind. These signatures are concurrent with an increase in the magnetic field strength (Zhang et al. 2008a). Bow shock's averaged shape, size and controlling factors are covered in Sect. 3.4.2, where they are compared with the IMB.

3.2 Magnetosheath

Venus magnetosheath's size is comparatively larger in terms of gyroradii than that of Mars. Therefore, the solar wind and planetary plasma has more room to properly thermalize within the shock. This thermalization is achieved among other processes via the action of plasma waves which are usually observed in this region.

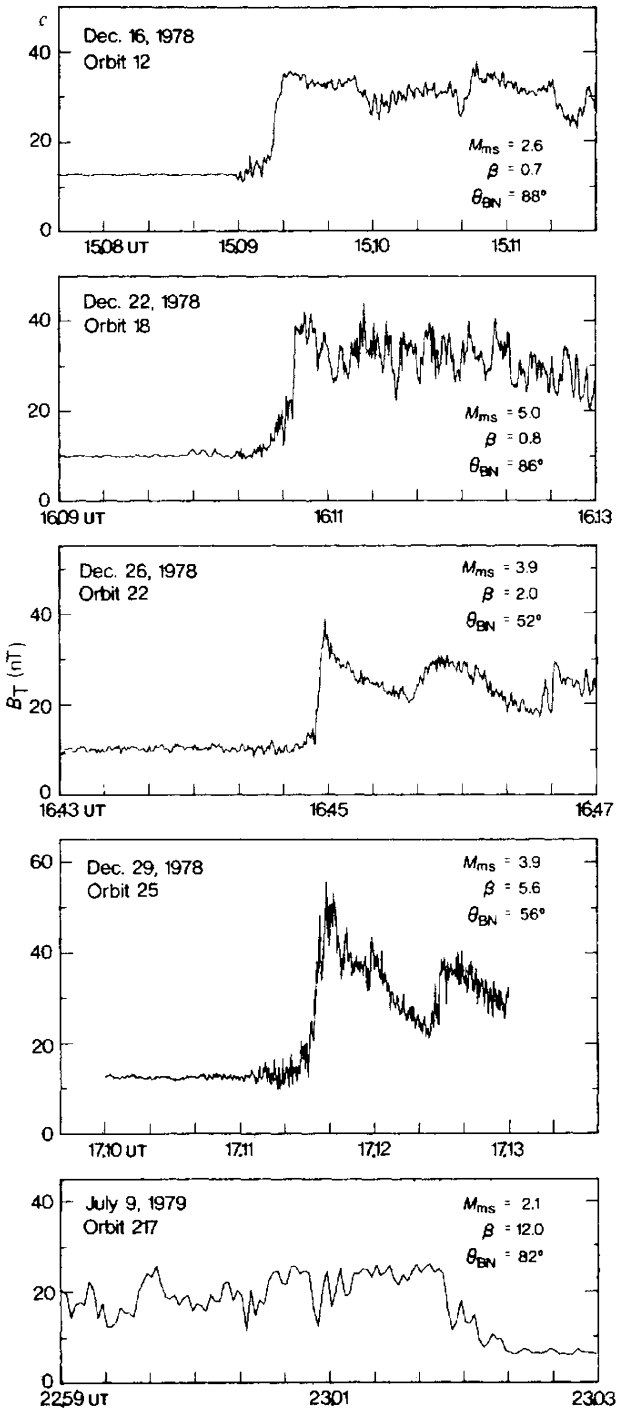

Fig. 21 Magnetic field strength profiles of the Venusian shock for different magnetosonic Mach numbers, shock normal angles, and plasma beta (Russell and Vaisberg 1983)

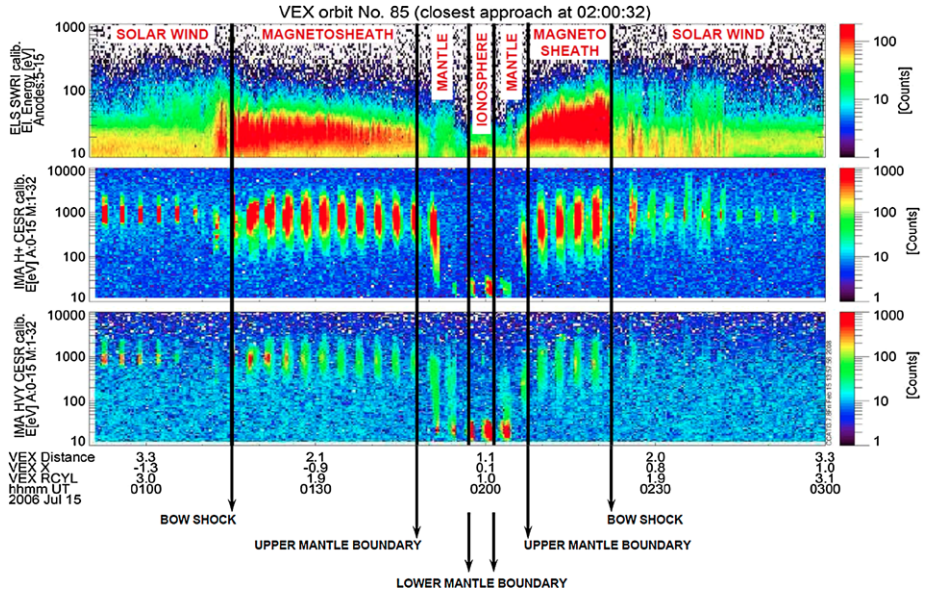

Fig. 22 ASPERA-4 data recorded on July 15, 2006—about an hour before and after the pericenter of that orbit. The *top panel* shows the total counts of energetic electrons measured by the ELS sensor and the two panels below presents the total counts of the proton and heavy ion channels of the IMA sensor, respectively. The heavy ion channel contains proton counts whenever the proton channel saturates. The *black vertical arrows* mark the plasma boundaries separating the different interaction regions (solar wind, magnetosheath, mantle and ionosphere)

The Venusian magnetosheath has been explored in the past by spacecraft Venera 9, 10, and PVO leading to several works on its properties. In particular, a complete review on these observations can be found in Phillips and McComas (1991). Important results obtained by these missions include the dependence of the magnetic field fluctuation level upon the shock normal angle. Luhmann et al. (1983) reported that the magnetic field downstream from a quasi-parallel bow shock fluctuated more intensively. Oscillations with a frequency of 0.05 Hz observed in the magnetosheath were believed to be foreshock waves convected through quasi-parallel shocks (Hoppe and Russell 1982). Also, waves at the proton cyclotron frequency (locally generated, likely) were reported by Russell et al. (2006b).

More recently, VEX identified mirror mode waves in the Venusian magnetosheath (Volwerk et al. 2008), an observation similar to that reported in other magnetospheres, notably Mars (Bertucci et al. 2004). Wavelet analysis also revealed Vörös et al. (2008) found $1/f$ fluctuations, large-scale structures near the terminator and more developed turbulence further downstream in the wake.

The nature of the waves observed within the magnetosheath depending on the shock angle was revisited by Du et al. (2009), who reported that the strength and properties of the fluctuations are strongly controlled by the IMF cone angle: whereas there fluctuations behind a quasi-parallel bow shock are quite strong and turbulent (probably convected foreshock waves), those behind a quasi-perpendicular shock are more coherent, and probably locally generated.

3.3 The Induced Magnetosphere Boundary

3.3.1 Identification and Structure

The existence of a boundary marking the entry into Venus' induced magnetosphere has been under discussion, the main reason being the absence of simultaneous three-dimensional magnetic field measurements and high resolution superthermal and cold plasma measurements. The availability of those measurements combined led to the identification of its main features, which are somehow similar to those listed in the Martian case:

(a) A (sometimes sharp) increase in the magnetic field strength by a factor of 2–3.
(b) Decrease in the magnetic field fluctuations.
(c) Enhancement of the magnetic field draping.
(d) Decrease in the temperature of electrons.
(e) Decrease in the solar wind ion (H^+ and He^{++}) densities.

The increase in the total density reported at Mars is likely to occur at Venus too, but has not been measured so far.

At Venus, the increase in the magnetic field strength that ultimately forms the so-called magnetic barrier is usually gradual. The apparent lack of a sharp jump in the magnetic field strength in PVO OMAG measurements then led to 'ad hoc' IMB definitions based on magnetic pressure (Zhang et al. 1991) which were extremely useful to provide a first estimation of its location on the dayside.

However, more recent analyses of PVO data report that sharp jumps are often observed on the magnetic field strength. Figure 23 shows magnetic field profiles in VSO coordinates in the vicinity of the Venusian IMB. In the Venus-Sun-Orbital (VSO) coordinate system, the positive X_{VSO}-axis points from the center of Venus to the Sun (opposite to the solar wind bulk velocity), the positive Y_{VSO}-axis points opposite to the heliocentric orbital motion of Venus, and the Z_{VSO}-axis completes the right-handed system pointing towards the ecliptic north. Figure 23a shows a profile obtained by PVO OMAG displaying a factor 2–3 jump on $|B|$ similar to the Martian IMB (Bertucci et al. 2003b). Figure 23b shows magnetic field measurements obtained by VEX MAG, revealing a gradual pileup (Zhang et al. 2010). In the second example, the IMB is identified from the stoppage of the magnetic field variability.

In the downstream sector, the IMB as the magnetic tail boundary was easily identified from the onset of a nonzero value for $|B_{XVSO}|$ (Saunders and Russell 1986). However at the time of PVO it was unclear weather the magnetic tail boundary had a dayside counterpart—although certain works like Vaisberg and Zeleny (1984) postulated it. More recently, and following the identification criteria of the Martian IMB by MGS (Bertucci et al. 2003a), Bertucci et al. (2003b) found that the dayside Venusian IMB could be detected from the enhancement of the IMF draping. In a follow-up work Bertucci et al. (2005a) reported that at also at Venus, the IMB structure can manifest itself a boundary with properties comparable to a tangential or a rotational discontinuity depending on the magnitude of the magnetic field component along the minimum variance direction. With the arrival of VEX, Zhang et al. (2008b) systematically identified the Venusian IMB (which is referred to it as 'Magnetopause') as the place where the magnetosheath oscillations stop. The crossings identified in this way were also analyzed using minimum variance analysis and an influence of the direction of the IMB on the normal component of the magnetic field at the boundary location was found.

Induced magnetosphere boundary in downstream region was identified in Venera-9 and Venera-10 data by change of mean ion energy and ion temperature accompanied by change

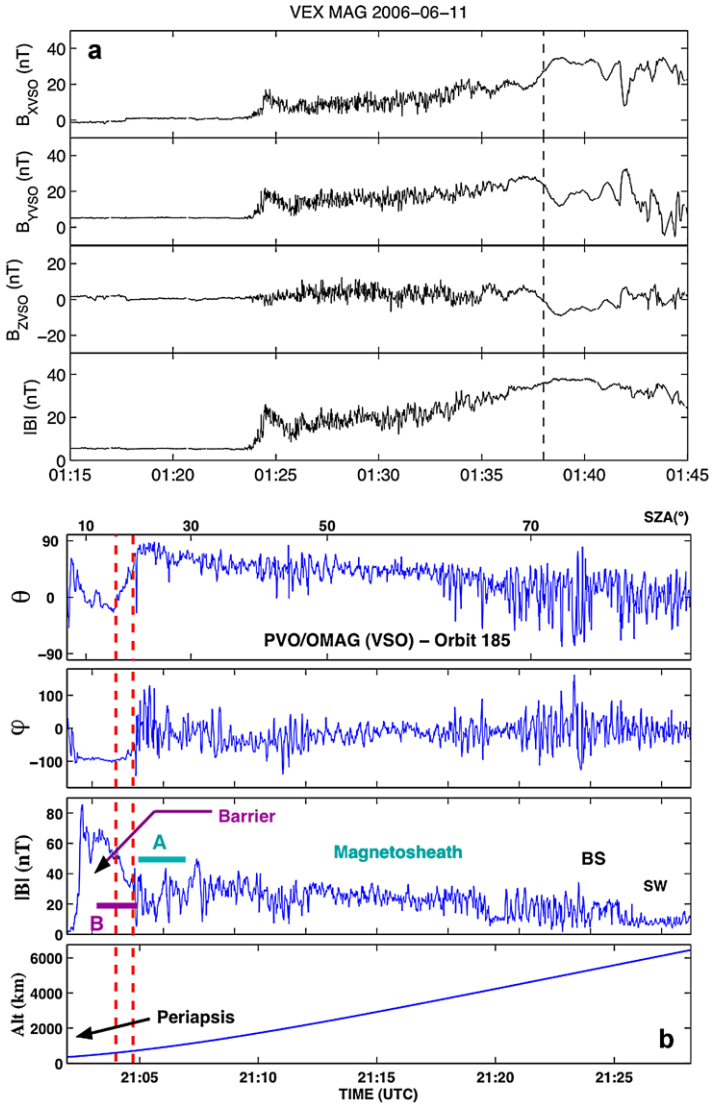

Fig. 23 Magnetic field measurements around Venus in VSO coordinates during an inbound VEX pass (*left*) and an outbound PVO orbit leg (*right*) showing, respectively, a gradual and an abrupt magnetic field pileup. In the first case the IM's (*shaded area*) outer boundary (around 0138 UT) is defined from the stoppage in magnetic field fluctuations (Zhang et al. 2008a), the jump observed in the PVO magnetic field strength a few minutes around 2105 UTC (*red dash lines*) coincides with the stoppage of the fluctuations in the magnetic field direction (Bertucci et al. 2003b)

of magnetic field fluctuations frequency (Vaisberg et al. 1976, 1995). The changes in the spectra of superthermal electrons at the IMB were studied by Spenner et al. (1980), who defined, in the downstream sector a very broad transition zone called 'mantle' where the spectra shape was between that of the magnetosheath (referred to it as ionosheath) and that of the ionosphere. As a result, the so called 'ionosheath boundary' would be the place where

the superthermal electron spectra of the magnetosheath starts to cool down, i.e., a typical signature of the IMB. As a result, the mantle would be co-located with the induced magnetosphere proper.

More recently, Martinecz (2008) and Martinecz et al. (2008, 2009) using VEX ASPERA-4 data and following Spenner et al. (1980) criteria, identified the upper and the lower limits of the Venusian mantle (UMB and LMB), which correspond to the IMB and the ionopause, respectively.

Figure 20 also shows the boundaries and regions inside the Venusian bow shock. At 01:48 UT, VEX crosses the upper mantle boundary (UMB), identified by a strong decrease in electron counts ($E > 35$ eV), and is located in a so-called mantle region or transition zone, where a mixture of solar wind protons and planetary ions is observed. The LMB, crossed at 01:57 UT, is also called Ion Composition Boundary (ICB), because at this boundary the solar wind protons disappear and the planetary ions become the main population. The LMB is identified in ELS by the appearance of ionospheric photoelectrons ($E > 10$ eV). Below the LMB, the spacecraft is located in the ionosphere between 01:57 UT and 02:01 UT. On the outbound pass, VEX crosses again all the mentioned plasma regions and boundaries, but in reverse order, i.e., at 02:01 the LMB, and at 02:08 UT the UMB.

3.3.2 Comparison of Venusian IMB and Bow Shock Sizes, Shapes and Controlling Factors

Russell et al. (1988) and Zhang et al. (1990) investigated the Venus bow shock based on nearly 2000 PVO shock crossings and found that the shock location is modulated by the solar cycle and solar EUV flux, the upstream solar wind parameters and the orientation of the IMF (see also Phillips and McComas (1991) and Russell et al. (2006a)). For modeling the bow shock they have used a simple conic section with its focus at the center of the planet based on PVO data.

More recently, Martinecz et al. (2008) used a 3-parameter fit based on ASPERA-4 measurements to achieve a more realistic shape of this boundary. The same technique, i.e., a conic fit with conic focus along the Sun-planet line as a third free parameter, has already been used by Slavin et al. (1980) based on PVO data and was later applied to Mars by Vignes et al. (2000). From 14 May 2006 to 31 December 2007, 817 Venusian BS crossings, 842 UMB crossings and 798 LMB (ICB) crossings were identified in ELS and IMA data as described above. For the bow shock the curve fitting technique developed by Slavin and Holzer (1981) was applied. This technique has also been used by Trotignon et al. (2006) for modeling the plasma boundaries at Mars. The observed shock locations have first to be transformed into an aberrated solar ecliptic system (X_0, Y_0, Z_0; VSO), assuming a 5° aberration. Then, a conic function in polar coordinates, assuming cylindrical symmetry along the X_0-axis, is least-square fitted to the observed BS positions. In order to get the best fit to the observations an offset of the conic focus along the symmetry axis was used (Slavin et al. 1980). Thus, the shock surface is represented by the following equation where the polar coordinates (r, θ) are measured with respect to a focus located at $(x_0, 0, 0)$. L is the semi-latus rectum and is the eccentricity (see Table 1).

For modeling the positions of UMB and LMB Martinecz et al. (2008) used a somewhat different approach, as the observations on the dayside and on the nightside cannot be represented by single conic functions. This was also noted in the case of the magnetic pile-up boundary (MPB) at Mars (Trotignon et al. 2006). Thus, circular fits for the dayside observations ($X_0 > 0$) and linear regressions ($y = k \cdot x + d$) for the nightside measurements ($X_0 < 0$) were used in order to model the mantle boundaries (see Table 2). The absence of data for the mantle region below about 50° SZA results in boundary fits which are too far

Table 1 Venusian BS fit parameters from ASPERA-4/VEX in comparison with Venera 9/10 (Slavin et al. 1984), PVO (Russell et al. 1988; Zhang et al. 1990) and MAG/VEX (Zhang et al. 2008a) results at solar minimum. L, x_0, ε and r_{tsd} are the semi-latus rectum, eccentricity, conic focus and terminator shock distance, respectively (Martinecz et al. 2008)

	$L\ [R_V]$	ε	$x_0\ [R_V]$	$r_{\mathrm{tsd}}\ [R_V]$
Martinecz et al. (2008)	1.515	1.018	0.664	2.088
Slavin et al. (1984)	1.68	1.03	0.45	2.096
Russell et al. (1988)	2.14	0.609	0.0	2.14
Zhang et al. (1990)	2.131	0.66	0.0	2.131
Zhang et al. (2008a)	2.14	0.621	0.0	2.14

Table 2 UMB and LMB fit parameters from ASPERA-4/VEX at solar minimum (Martinecz et al. 2008)

	Upper mantle boundary	Lower mantle boundary
Circular fit	$r_{\mathrm{UMB}} = 1.130 R_V$	$r_{\mathrm{LMB}} = 1.076 R_V$
Linear regression	$k_{\mathrm{UMB}} = -0.101 R_V$	$k_{\mathrm{LMB}} = 0.122 R_V$
	$d_{\mathrm{UMB}} = 1.130 R_V$	$d_{\mathrm{LMB}} = 1.076 R_V$

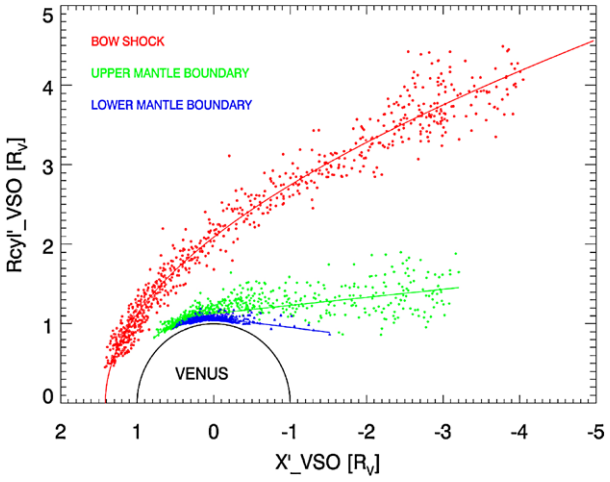

Fig. 24 Axisymmetric bow shock (BS), upper (UMB) and lower (LMB) mantle boundary fits derived using the first 19 months of ASPERA-4 observations in an aberrated VSO coordinate system. The BS crossings (*red circles*) were fitted to a conic function. The UMB (*green diamonds*) and LMB (*blue triangles*) crossings were fitted by a circle on the dayside and by linear regression on the nightside (from Martinecz et al. 2008)

away from the planet on the dayside. More realistic mantle fits will require crossings in the subsolar region, expected later during the VEX mission.

Figure 24 displays the axisymmetric BS, UMB and LMB (ICB) fits derived using the first 19 months of ELS and IMA observations in aberrated VSO coordinates (Martinecz et al. 2008).

Influence of the Solar Wind Dynamic Pressure Martinecz et al. (2008) also studied the variation of the BS position at the terminator as a function of the solar wind dynamic pressure (Fig. 25). All BS crossings (blue plus signs) were extrapolated to the terminator plane

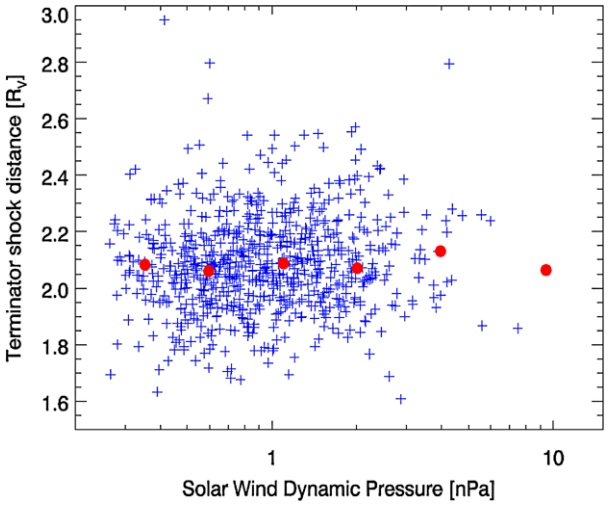

Fig. 25 The dependence of the bow shock position at the terminator on the dynamic pressure of the solar wind derived from ASPERA-4 measurements. All bow shock crossings (*blue plus signs*) were extrapolated to the terminator plane using a conic section curve with a fixed eccentricity ($\varepsilon = 1.018$) and a fixed focus ($x_0 = 0.664$) and with a variable semi-latus rectum. No normalization has been applied to the data. The *red points* represent median values over pressure bins (from Martinecz et al. 2008)

using a conic section curve with a fixed focus ($x_0 = 0.664$) and eccentricity ($\varepsilon = 1.018$) and a variable L value as follows:

$$L = \sqrt{(X' - x_0)^2 + Y'^2 + Z'^2 + \varepsilon \cdot (X' - x_0)}$$

Then the terminator shock distance is given by

$$r_{\mathrm{tsd}} = \sqrt{(L \cdot (L + 2 \cdot \varepsilon \cdot x_0) + x_0^2 \cdot (\varepsilon^2 - 1))}$$

The red points in Fig. 25 represent median values over pressure bins and demonstrate clearly the independence of the BS position from the ram pressure during solar minimum conditions. This finding is in agreement with results obtained by Russell et al. (1988) and by Zhang et al. (2004) based on PVO observations.

Influence of the EUV Flux/Solar Cycle PVO observations revealed that the solar wind interaction with Venus is very dependent on the phase of the solar cycle (Russell et al. 2006a). During solar minimum the BS is found to be closer to the planet than during solar maximum due to lower ionization and ion pickup rates caused by EUV flux changes over the 11-year solar cycle. A comparison between the terminator BS position r_{tsd} and solar EUV flux (F50 index: 0.1–50 nm integrated photons $\mathrm{cm}^{-2}\,\mathrm{s}^{-1}$ and shifted to Venus) derived from SOHO SEM observations shows no apparent dependence (Martinecz et al. 2008). This is probably due to the fact that the EUV flux variation is small over the period of observation, as expected for solar minimum.

Figure 26 shows Martinecz et al. (2008) VEX BS fit in comparison with other shock models based on different data sets at solar minimum. The VEX fit is in good agreement with the BS model of Slavin et al. (1984) based on Mariner 5,10 and Venera 4, 6, 9, 10 observations. They also used a 3-parameter conic section for modeling the upstream and downstream shock location which results in a hyperbola since $\varepsilon > 1$. Russell et al. (1988) investigated the Venusian BS by means of magnetic field measurements on board PVO. They fitted the dayside shock crossings by using a 2-parameter conic function where its focus is fixed at the center of the planet resulting in an ellipse since $\varepsilon < 1$. The dayside BS model from Zhang et al. (2008a), based on Magnetometer data made onboard VEX, is also obtained by using a 2-parameter conic section with a fixed focus at the center of Venus. However,

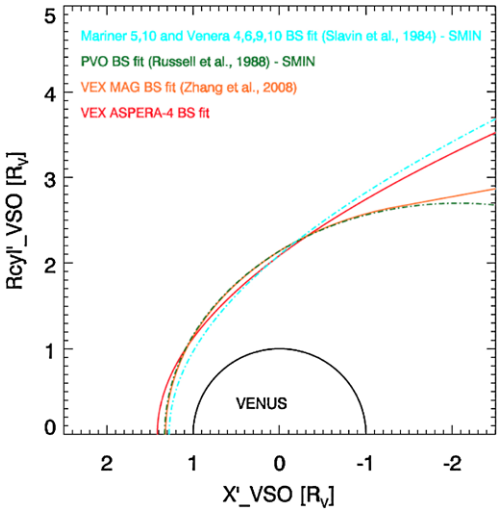

Fig. 26 This plot shows the terminator bow shock position as a function of solar EUV flux (F50 index: 0.1–50 nm integrated photons $cm^{-2}\ s^{-1}$) derived from SOHO SEM observations and shifted to Venus. All bow shock crossings (*orange asterisk signs*) were extrapolated to the terminator plane by means of the conic function

only shock crossings between and 117° solar zenith angle (SZA) were fitted, whereas the distant BS (SZA > 117°) is represented by an asymptotic shock cone determined by an average magnetosonic Mach number of 5.5 at solar minimum. Theoretically, the distant BS should be a Mach cone, but in-situ measurements made by ASPERA-4/VEX provide the counterevidence that this is not the case for the Venusian BS. The same result was found by Trotignon et al. (2006) investigating the location and shape of the Martian BS based on Phobos 2 and Mars Global Surveyor (MGS) data sets. These observations demonstrated that the far downstream BS at Mars does also not meet a Mach cone.

As for the IMB, and the ionopause, the upper and lower boundary positions of the magnetic barrier determined by Zhang et al. (2008b) based on the magnetometer observations on board VEX are only partly in agreement with Martinecz (2008) determination of UMB and LMB locations. At the terminator, the average thickness of the mantle region is around 500 km and hence, 300 km less thick than the magnetic barrier. The thickness of the magnetic barrier in the subsolar region is around 200 km (Zhang et al. 2008b) but currently it is not possible to estimate this thickness for the mantle region due to the lack of mantle crossings below around 50° SZA.

3.4 The Induced Magnetosphere

The magnetic structure of the induced magnetosphere and magnetotail of Venus was exhaustively explored by PVO (Zhang et al. 1991; Phillips and McComas 1991, and references therein) and more recently by VEX (Zhang et al. 2008b, 2010).

On the dayside, the magnetic pressure accumulates gradually inside the induced magnetosphere and generates a magnetic barrier where the plasma is progressively colder and slower as more and more planetary, recently-ionized particles join the flow. As a result, the magnetic pressure term is likely to be dominant in this region. It is still uncertain, however, if the increase in magnetic pressure is associated with a plasma depletion of the piled up flux tubes, as postulated by Zwan and Wolf (1976). High-resolution thermal plasma density measurements within the IM at Mars and Titan (and not available around Venus so far) indicate that flux tubes might be filled with cold planetary plasma and therefore the depletion effect would only be applicable to solar wind plasma.

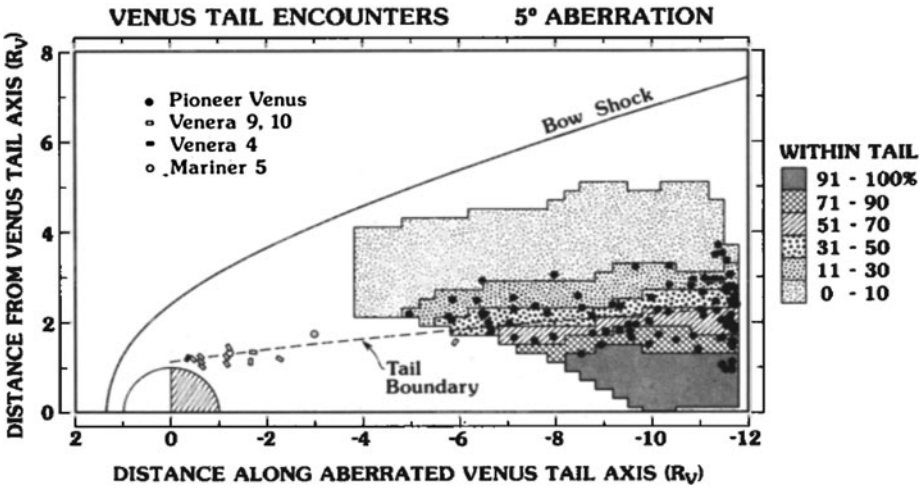

Fig. 27 The average size of Venus magnetotail in aberrated cylindrical VSO coordinates (Saunders and Russell 1986). Note that no dayside counterpart is assumed for the tail boundary (IMB) as such counterpart had not been identified from magnetic field data

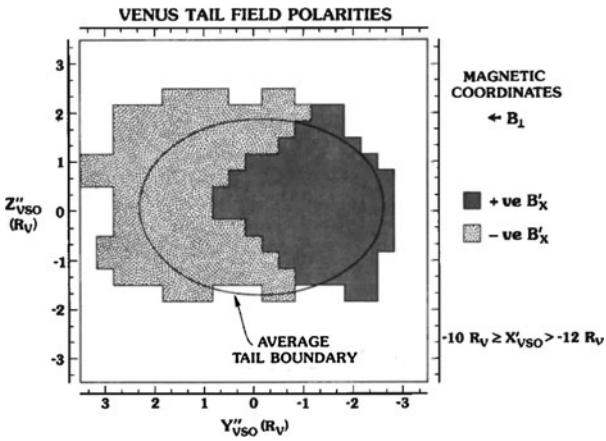

Fig. 28 Magnetic field polarity in magnetic coordinates (cross tail component points in the $+y$ direction) in the distant magnetic tail of Venus (Saunders and Russell 1986). The *ellipse* marks the average tail boundary

In the post terminator region, pressure balance is replaced by a stress balance as field lines become draped. This stress becomes important near the magnetic poles, where $\mathbf{J} \times \mathbf{B}$ force can be efficient in transporting the local plasma across the terminator (Pérez-de-Tejada 1986).

PVO and VEX explored Venus magnetotail in a complementary way. Whereas VEX explored the short-mid ($1.3 > R > 3R_V$) range tail (Zhang et al. 2010), PVO characterized its topology close ($R < 3R_V$) and far ($5 < R < 12R_V$) from the planet (Saunders and Russell 1986; Phillips and McComas 1991).

PVO measurements showed that the although its location is deduced statistically, the IMB/Tail boundary is well defined up to $12R_V$ (Fig. 27) and displays properties of a rotational discontinuity, which may allow the exchange of plasma with the magnetosheath (Saunders and Russell 1986). On the other hand, the cross section of Venus far tail is elongated along the cross-tail component of the background magnetic field ($\mathbf{B}_\perp$) (Fig. 28).

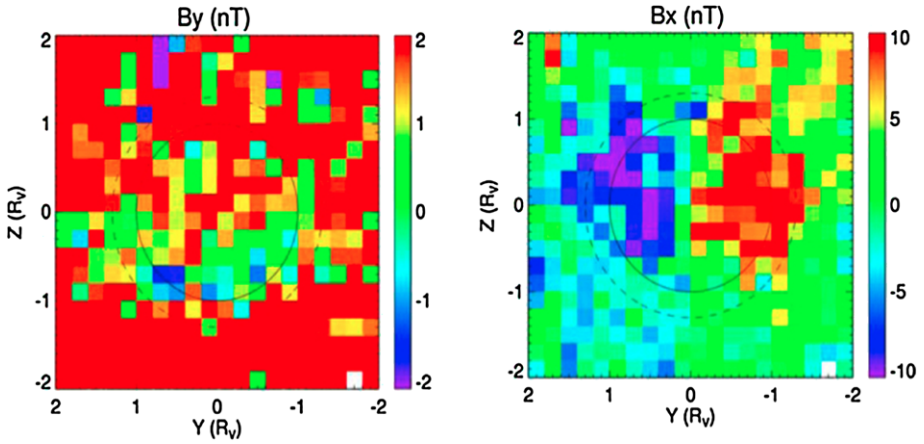

Fig. 29 (*Left*) Cross tail magnetic field component in the near Venusian tail. (*Right*) Sunward component of the magnetic field in the near Venus magnetotail. Upstream IMF points in the $+y$ direction. The view is toward the planet from the tail. The inner circle is the limb of Venus and the outer circle is the approximate magnetotail section deduced by Zhang et al. (2010). In both figures the nominal convective electric field points in the $+z$ direction (Zhang et al. 2010)

Estimates of the cross tail component $\mathbf{B}_\perp$ yielded between 2 nT (Saunders and Russell 1986) and to 4 nT (McComas et al. 1986), and more predominant on the hemisphere where the upstream convective electric field $\mathbf{E}_c = -\mathbf{V} \times \mathbf{B}$ points away from the planet. Tail fluxes were found to be of at least 3 MWb (Saunders and Russell 1986). These high values were interpreted as an indication that most of the magnetotail field lines must close across the tail rather than on the dayside, and that the induced tail is replenished with new IMF lines in only a few minutes, leading to similar transit times for field lines across the interaction region (Phillips and McComas 1991). A more recent work based on VEX MAG data (Zhang et al. 2010) also found an influence of the nominal convective electric field at lower altitudes. Figure 29 shows the cross tail and the sunward magnetic field component distributions in the near Venusian tail (Zhang et al. 2010) revealing more streamlined field lines on the outward pointing convective electric field hemisphere ($Z > 0$).

The planetary ion species dominating Venus IM include H^+, He^+, O^+, and O_2^+ (Fedorov et al. 2008). Figure 30 shows the distributions of protons (above) and heavies ($m/q > 14$, below) for energies larger than 300 eV as measured by VEX ASPERA-4 (Fedorov et al. 2008). The almost mutually exclusive contours shows the differentiation in species within the induced magnetic tail. Also, the protons at the IMB (region called boundary layer) are more energetic than those closer to closer to the magnetotail's neutral sheet. The energy of heavy planetary ions behaves similarly.

Finally, the neutral sheet hosts a thin layer of 500–1000 eV heavy ions surrounded by an envelope of H^+ and He^+ ions (Fedorov et al. 2008).

No recent attempts have been done to study the acceleration mechanisms responsible for the formation of the neutral sheet and the dynamic properties of the planetary ions inside the Venusian tail. McComas et al. (1986) used the average magnetic tail configuration to obtain plasma parameters (velocity and acceleration along the tail axis, density and temperature) from MHD and assuming conservation of the parallel component of the electric field. As a result, the authors find evidence of acceleration compatible with $\mathbf{J} \times \mathbf{B}$ force.

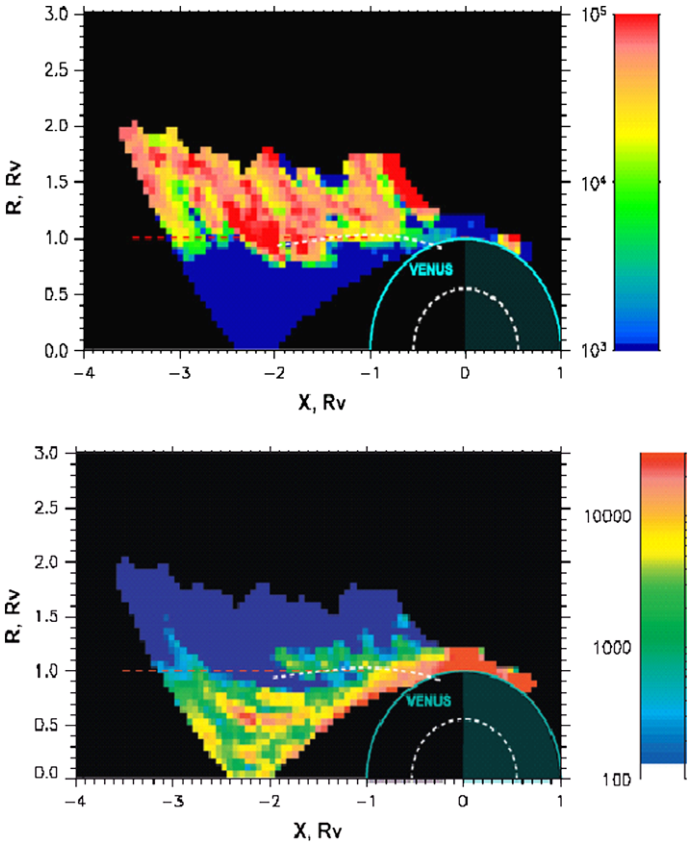

Fig. 30 (*Top*) Spatial distribution of the proton flux with energy greater than 300 eV in VSO cylindrical coordinates. The *color scale* is in arbitrary units. *Blue color* indicates zero flux. *Red dashed line* in the right panel shows the wake boundary at Venus. (*Below*) Same for planetary ions with mass per charge ratio >14 (Fedorov et al. 2008)

Finally, evidence for substorm-type tail reconfiguration likely associated with bulk plasma loss processes was recently presented from VEX data (Volwerk et al. 2009). Unlike Mars, reconfigurations at Venus occur in response to changes in the IMF.

3.5 The Ionospheric Boundary: Ionopause, Photoelectron Boundary

The Venusian ionopause is a well-defined boundary that marks the upper limit of the ionosphere—defined as the region inaccessible for external plasma (Brace et al. 1980).

The Venusian dayside ionopause is characterized by an abrupt change on the plasma density. The thermal plasma measurements required to measure such density changes were provided by the PVO Electron Temperature Probe and ORPA (Brace et al. 1980; Knudsen et al. 1982), but similar measurements are unfortunately not available on VEX.

PVO measurements reveal that during solar maximum, the altitude of the dayside ionopause and increases with SZA, from ∼300 km near the subsolar point to ∼900–1000 km at the terminator. The variability of its altitude also displays similar trend with respect to SZA.

The ionopause is also defined as the boundary where the magnetic pressure in the magnetic barrier is balanced against the thermal pressure within the ionosphere. As a result, it is also characterized by a strong drop in the magnetic field strength. In particular, the altitude of the dayside ionopause was found to increase with decreasing solar wind pressure (Elphic et al. 1980). Also, during periods of high solar wind pressure, the ionospheric thermal pressure is not able to withstand the magnetic pressure at higher altitudes and then the IMF diffuses within the ionosphere.

The solar cycle phase has strong effects on the ionopause location. Comparisons between in situ and remote density measurements at a fixed SZA revealed that the altitude of the ionopause strongly reduced during solar minimum (e.g. Knudsen 1988) likely as a result of the reduction in the peak thermal pressure in the ionosphere.

The ionopause structure is also affected by the solar cycle. Knudsen et al. (1987) reported that at solar maximum, the ionopause density signature is rather sharp, whereas during solar minimum the density gradient is not so clearly defined.

Finally, the nightside ionopause displays a more filamentary structure (Brace et al. 1987) including features such as tail rays and plasma holes (Phillips and McComas 1991).

Local ionospheric photoelectrons were also detected around Venus (Coates et al. 2008). Although PVO Orbiter Retarding Potential Analyzer (ORPA) provided measurements of the integrated electron flux for energies below 50 eV, it did not reproduce the sharp, characteristic spectral peaks of photoelectrons (Knudsen et al. 1980). Energy photoelectron peaks are obtained from models (McCormick et al. 1976; Cravens et al. 1980). In particular, recent models (Gan et al. 1990) predicted multiple photoelectron peaks in the 20–35 eV region, which were compared with data (Spenner et al. 1997).

According to models based on data (Mantas and Hanson 1979) photoelectron signatures at Mars are originated from the ionization of O and CO_2. The presence of O and CO_2 in the Venus atmosphere results in similar ionization potentials. However, at Venus, photoelectrons are primarily produced by ionization of O, due to the lower altitude of the transition region between CO_2 and O at Venus (Schunk and Nagy 2000).

VEX ASPERA-4 electron spectrometer (ELS) detected electrons due to photo-ionization of atomic oxygen and carbon dioxide in the Venus atmosphere by solar helium 30.4 nm photons. Due to its high energy resolution ($\Delta E/E = 7\%$) ELS has been able to improve the detection of these predicted peaks (Coates et al. 2008). Figure 31 shows a time-energy spectrogram showing the counts of electrons measured by ELS for a VEX inbound pass (Coates et al. 2008). Ionospheric photoelectrons start to be observed around 0130 until 0135 UT as a horizontal line around 18 eV. During that interval, VEX altitude varied from 700 to 250 km over the north pole. The photoelectron signatures are on average located below the ionopause (Coates et al. 2008). Coates et al. (2008) also suggest that photoelectrons are likely to be observed far from Venus as a result of their transport along draped IMF lines.

4 Titan

Titan is perhaps the most complex example of the interaction between an atmospheric unmagnetized object and its plasma environment in our solar system. This is due to Titan's orbital location in the confines of Saturn's magnetosphere what makes it prone to excursions into the shocked solar wind of the Kronian magnetosheath, the variability of Saturn's multi species outer magnetospheric plasma, and the moon's complex atmospheric and ionospheric chemistry.

Measurements by Voyager and Cassini (Neubauer et al. 1984; Wei et al. 2011), confirm the absence of a permanent intrinsic magnetic field relevant to the interaction According to

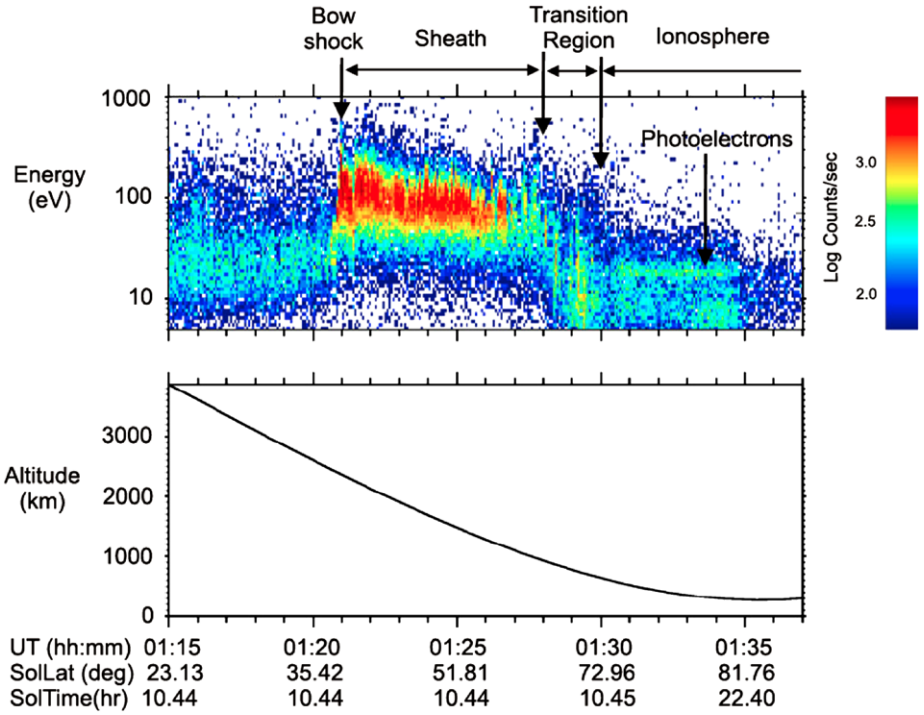

Fig. 31 VEX ELS spectrogram of electron count rate for instrument sector 11. Altitude is shown in the *bottom panel*. The photoelectron peaks are located around 18 eV between 01:30 and 01:35 UT (Coates et al. 2008)

Wei et al. (2011), the upper limit of the permanent dipole moment is 0.78 nT $\times R_T^3$. However, the possible presence of conducting layers on the surface of or within the moon (Beghin et al. 2009) and the ionosphere (Rosenqvist et al. 2009; Cravens et al. 2010b) suggest that the influence of an induced field of variable lifetime might not be negligible in the lower layers of Titan's induced magnetosphere (Wei et al. 2011).

In spite of its heliocentric distance, Titan's obstacle to the incoming plasma strongly depends on photoionization (Ågren et al. 2007). As a result, the angle between the incoming flow (i.e. Saturn's) and the EUV flux from the Sun largely controls the plasma interaction. In the ideal scenario of a magnetospheric plasma co-rotating with Saturn, the plasma flow velocity is tangent to Titan's orbit and therefore the moon's local time with respect to Saturn (Saturn Local Time or SLT) is a reliable parameter to measure the departure of the flow direction from the EUX flux. As a result, these two directions will be parallel around 18:00 SLT (a configuration similar to Mars, Venus and comets), and anti-parallel around 0600.

The first in situ observations of Titan's plasma environment were obtained by Voyager 1 spacecraft during its only flyby on November 12, 1980. The flyby occurred downstream from Titan while the moon was located at a Saturn Local Time (SLT) of 13 hs, with a closest approach distance of 2.71R_T (1R_T = 1 Titan radius = 2575 km) Voyager 1 magnetometer measurements (Ness et al. 1982) detected a well-defined induced magnetosphere with two lobes of opposite magnetic field polarity with and no influence of a significant intrinsic magnetic field. The induced magnetosphere as observed by the magnetometer coincided with a superthermal electron 'bite out' region (Hartle et al. 1982) and populated with cold

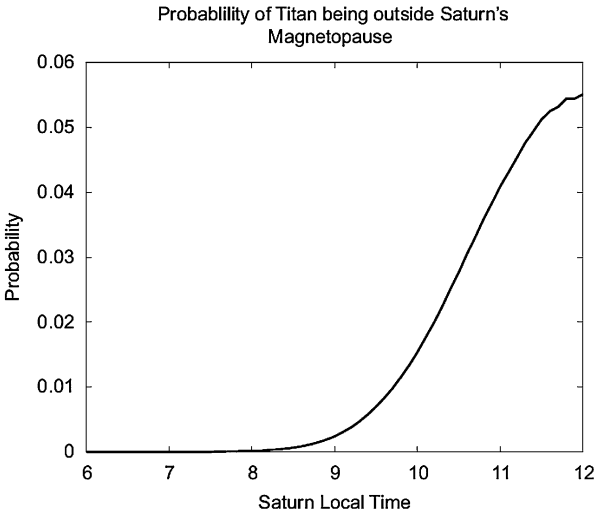

Fig. 32 Probability of Titan's orbit being outside Saturn's magnetopause as a function of SLT (Bertucci et al. 2009)

ions. These results and others are summarized in Neubauer et al. (1984). Cassini is the second spacecraft to provide in situ measurements of Titan's plasma environment. Since its arrival to the Saturnian system, Cassini performed more than 70 Titan flybys exploring Titan's induced magnetosphere at different SLT and local times with respect to the Kronian plasma flow. The latter allowed the exploration of the upstream, flank and tail sectors of the induced magnetosphere.

4.1 Titan's Plasma Context

Titan orbits Saturn at an average distance of $20.2 R_S$ ($1 R_S$ = Saturnian radius = 60330 km). Following pioneering studies on the variability of Titan's plasma environment as a result of the proximity of the Kronian magnetopause (Wolf and Neubauer 1982), a recent empirical model of Saturn's magnetopause (Arridge et al. 2006) led to a statistical study on its standoff distance based on Cassini data, which displays a bimodal stand-off distance (R_{MP}) distribution with means at 22 and $27 R_S$ (Achilleos et al. 2008). Figure 32 from Bertucci et al. (2009) shows the probability of Titan's orbit being outside Saturn's magnetopause as a function of Saturn local time based on the magnetopause stand-off distance probability function inferred in Achilleos et al. (2008). According to these results, Titan is only rarely in the shocked solar wind, however, when this happens it is exposed to a total solar wind pressure of at least 0.0345 nPa, that is approximately more than two times the average (Bertucci et al. 2008).

When inside Saturn's asymmetric disk-shaped outer magnetosphere (Arridge et al. 2008a; Khurana et al. 2009), Titan is exposed to a magnetic plasma flow displaying significant degree of non-uniformity. This results in Titan's induced magnetosphere probably rarely reaching a steady state.

Several works have addressed the variability of Titan's plasma environment. Bertucci (2009) and Bertucci et al. (2009) analyzed the strength and orientation of the magnetic field within Saturn's magnetosphere around $20 R_S$, while Arridge et al. (2008b) did a similar study from Cassini superthermal electron data. These works suggest that Titan's plasma environment is strongly shaped by the proximity of Saturn's magnetodisk. During Saturn's southern summer, the Kronian magnetodisk's central current sheet is systematically pushed

north of Titan's orbit by the solar wind. The dynamics of the disk and ultimately of Titan's plasma environment are then controlled by the solar wind pressure and the effect produced by a rotating magnetic anomaly whose phase is locked to the that of the Saturn kilometric radiation (SKR) emission. The influence of the solar wind is present at all SLT (although dominant in the noon sector), whereas the SKR modulation seems to affect the magnetic field to first-order at least in the dawn sector. Near dawn local times, Titan tends to be farther from the disk at SKR longitudes (Kurth et al. 2008) around 140° and closer to it for longitudes around 320°. Depending on these factors, Titan is exposed to either: a 'magnetodisk lobe' regime where the plasma beta and electron density are low and fields are radially 'stretched' and usually stronger, or a 'current sheet' regime characterized by quasi-dipolar, relatively weak fields and a high-beta plasma and electron density. More recently, Rymer et al. (2009) analyzed CAPS and MIMI electron spectra around Titan for all Cassini flybys until May 2009. They characterized these flybys into four categories: Plasma-sheet, Lobe-like, Magnetosheath and Bimodal. Where as bimodal spectra are associated with local water group products, an additional hot lobe-like environment is also occasionally observed and linked to increased local pick-up. Out of 54 encounters, 34 are associated with one of these groups, while the remaining ones display a combination of them. Simon et al. (2010a, 2010b) investigated the variability of Saturn's magnetic around $20.3 R_S$ and confirmed that it is strongly affected by the presence of Saturn's bowl-shaped and highly dynamic magnetodisk current sheet, In particular, Simon et al. (2010b) discriminated between real (observed by Cassini), and virtual (defined as Cassini passages within $1 R_S$ distance from Titan's orbit) flybys Among the 141 (62 real + 79 virtual) crossings of Titan's orbit between July 2004 and December 2009, only 17 encounters (9 real + 8 virtual) took place within quiet, magnetodisk lobe-type fields. During another 50 encounters (21 real + 29 virtual), rapid transitions between current sheet and lobe fields were observed around the moon's orbital plane. Most of the encounters (54 = 22 real + 32 virtual) occurred when Titan's orbit was within the current sheet.

Regardless of its location with respect to Saturn's magnetodisk, no bow shock has been detected around it so far. This is in agreement with the estimations of the magnetosonic Mach number (Neubauer et al. 1984, 2006).

Plasma moments also display properties different than initially expected. Cassini CAPS estimations of Saturn's magnetospheric flow velocity vector near Titan's orbit show important departures for the co-rotation direction (i.e., tangent to Titan's orbit), especially in the pre-dawn sector of Saturn's magnetosphere (Szego et al. 2007; McAndrews et al. 2009), where a significant anti-Saturn radial component is systematically found. More details on Titan's upstream plasma can be found in Sittler et al. (2010a) and Arridge et al. (this issue)

4.2 The Induced Magnetosphere Boundary

As shown by Voyager 1 and Cassini, Titan's induced magnetosphere is clearly identifiable from plasma instruments. Given the variety of plasma regimes in which Titan can be found, and the limited number of flybys for the entry into the induced magnetosphere is characterized by the following signatures:

(a) A strong change (usually an increase, especially on ram side) in the magnetic field strength.
(b) Enhancement of the magnetic field draping.
(c) Decrease in the temperature of electrons.
(d) Decrease in the external ion density and energy.
(e) Increase in the total plasma density.

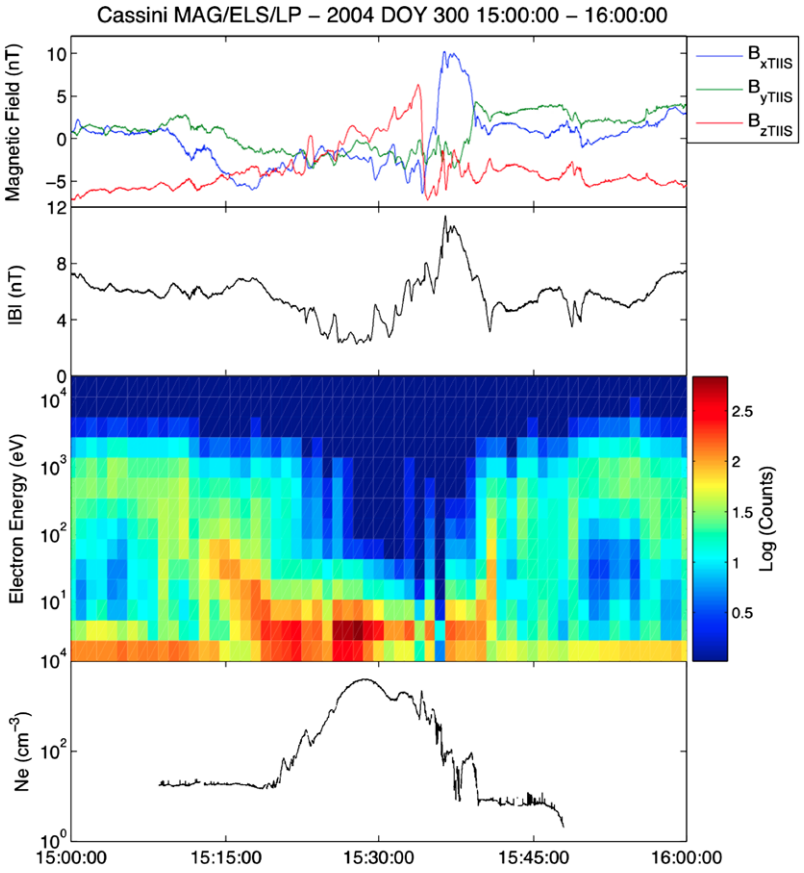

Fig. 33 From top to bottom. Magnetic field vector in TIIS coordinates and strength from MAG, 1 eV–20 KeV electron counts from CAPS/ELS (Anode 5), and electron density (n_e) from RPWS/LP during Cassini's TA encounter. Note that n_e measurements are valid only from ∼1520–1540 (Bertucci et al. 2005c)

Figure 33 shows Cassini magnetometer (Dougherty et al. 2004), CAPS/ELS electron spectrometer (Young et al. 2004), and Langmuir probe (Gurnett et al. 2004) electron density measurements during Cassini's first close encounter (TA flyby). The TA flyby occurred shortly after Cassini entered Saturn's magnetosphere (around 10.6 SLT) and as the spacecraft explored Titan's close magnetic tail from the dayside into the nightside. Cassini TA measurements have been extensively studied in several articles (special issue of Science, 308, 2005; Neubauer et al. 2006; Cravens et al. 2010b; Sittler et al. 2010a). Magnetometer (MAG) data is represented in the Titan Ionospheric Interaction coordinates (TIIS), where the X_{TIIS} axis points in the direction of the co-rotational flow, Y_{TIIS} points towards Saturn, and Z_{TIIS} points north. Closest approach occurs at 1530 UTC, downstream from the moon at an altitude of 1174 km. At both ends of the time interval, the electron distribution is unimodal centered around ∼100 and several hundred eV and the orientation of the magnetic field is mainly southward, suggesting that Titan is within Saturn's magnetodisk current sheet (Rymer et al. 2009; Simon et al. 2010a).

The inbound crossing of Titan's induced magnetosphere occurs around 1513 UTC. First, the magnetic field rotates and becomes anti-parallel to the flow as Cassini enters the 'to-

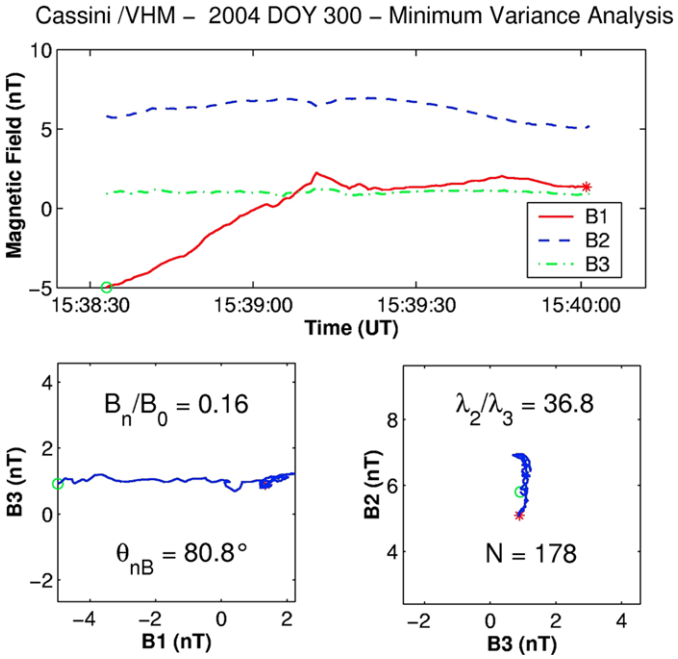

Fig. 34 *Top*: Magnetic field in along maximum (B1), intermediate (B2), and minimum (B3) variance directions across the outbound IMB crossing for TA. *Below*: hodograms indicating magnetic field trajectory on the (B1, B3) and (B3, B2) planes (left and right respectively). Also, the ratio between the normal component and the mean magnetic field strength (B_n/B_0) and the angle between the normal and the mean magnetic field vectors (θ_{Bn}) are indicated (Bertucci et al. 2005c)

ward' lobe of the induced magnetotail. Almost simultaneously, CAPS detects strong electron fluxes at decreasing energies, a signature usually associated with massloading. At the same time, locally produced photoelectrons likely start populating energy ranges inaccessible to CAPS or veiled behind the spacecraft's own photoelectron signal. The increase in the total density due to this added population is not accurately measured in the Langmuir probe data until a few minutes after the IMB crossing (around 1520), where a steep gradient is observed. Also around 1520, locally produced photoelectrons (Coates et al. 2011) start to be observed. On the outbound portion of the flyby, the IMB signatures (around 1539) are sharper. The magnetic field pileup ($|B|$ varies from ∼11 nT in the magnetic barrier to ∼5 nT after 1542) and the draping are pronounced just inside the IMB. In some flybys, the increase in pileup and draping is just inside a drop in the magnetic field magnitude (Neubauer et al. 2006). For TA this drop is evident on the outbound leg, around 1541. These drops are indeed a unique characteristic of Titan's IMB and are observed in the flanks, but not in the upstream region. As shown in Fig. 34, the rotation in the magnetic field direction from around 1539:12 is such that the component of the magnetic field normal to the minimum variance plane is negligible, suggesting that the plasma flow across the IMB might be small as for tangential discontinuities (Knetter et al. 2004). The thickness of the boundary along the normal vector is of the order of the proton inertial length (∼300 km for this flyby) (Bertucci et al. 2005c).

The signature in the superthermal electron counts is similar to that observed in the inbound leg, but sharper, and the increase in the plasma density due to the addition of cold, planetary plasma is clearly visible on the Langmuir probe data above the instrumental noise.

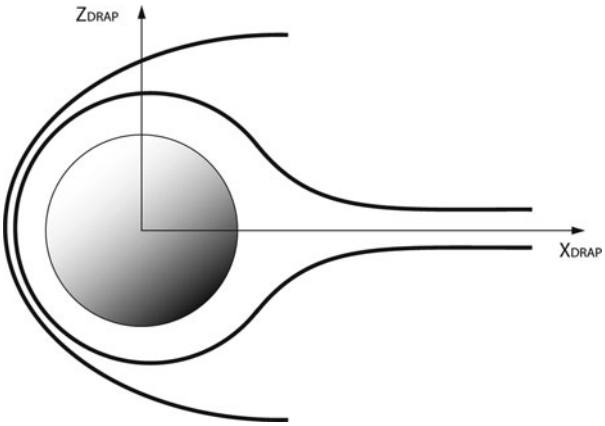

Fig. 35 Schematic illustrating reverse draped field line compared to a weakly draped one. At the flanks of the interaction, a reverse in the Z_{DRAP} component might be related to vertical plasma motion

The mean location and shape of the IMB is difficult to infer due to the variable upstream conditions. In order to compare magnetic field measurements obtained during different upstream conditions, Neubauer et al. (2006) defined the 'draping' coordinate system as follows: X_{DRAP} is along the flow direction (assumed to be perpendicular to the background magnetic field B_0), Z_{DRAP} is anti-parallel to B_0, and Y_{DRAP} completes the right-handed Cartesian system. Based on flybys Cassini MAG data for flybys TA, TB and T3, and an advanced MHD model (Backes et al. 2005), Neubauer et al. (2006) find that the IMB is much more extended on the sunward side than on the opposite side. As this effect is observed in MHD models, this might not be due to finite gyro radius effects of pick up ions (Hartle et al. 1982) but as a direct consequence of the EUV-induced ion production pattern, at least for altitudes inside the IMB. As a result, a study of the average size and shape of the IMB will have to be done from sets of flybys with similar upstream conditions including SLT, SKR phase, and Kronian season.

4.3 The Induced Magnetosphere

Titan's induced magnetosphere is characterized by draped and piled up fields whose geometry is compatible with the direction of the upstream magnetic field and velocity vectors (Ness et al. 1982; Backes et al. 2005; Neubauer et al. 2006; Bertucci et al. 2007). On the upstream side, the magnetic field displays a clear pileup of the field (Simon et al. 2008). On the downstream side, the induced magnetic tail consists of two lobes with field lines parallel and anti-parallel to the flow direction, separated by a neutral sheet theoretically lying on the (X_{DRAP}, Y_{DRAP}) plane. In the case of a Kronian north south field and flow aligned with corotation the DRAP and the TIIS coordinate system coincide.

Contrary to Neubauer et al. (2006), and in agreement with the definition for solar wind interaction, the magnetic equatorial plane will be the plane containing the upstream magnetic field and flow velocity, the (X_{DRAP}, Y_{DRAP}) plane. In general, B_x and B_y change sign when passing through this plane. It is also noted that the onset of nonzero B_y components points at nonzero Y_{DRAP} components of the flow velocity vector, as the external plasma tries to go around the obstacle. Similarly, a change in sign of B_z requires nonzero Z_{DRAP} velocity components. An interesting observation in the flanks of the interaction is the occurrence of "reverse draping" (Neubauer et al. 2006) in the case of positive components B_z in the DRAP system. In reverse draping a drop in the magnetic field strength may occur as draped field

lines become farther apart in the flanks (Fig. 35). Reverse draping is certainly an important piece in understanding the formation of Titan magnetotail's neutral sheet.

Cassini CAPS measurements reported clear signatures of massloading associated with Titan's induced magnetosphere. In a comparison between Voyager 1 and Cassini TA flybys, Hartle et al. (2006) reported a gradual decrease in the 14–16 amu ion energies above the inbound IMB crossing for TA, while energies drop by a factor of 125 in these ions. The authors point out that such a decrease is attributed to the increase in the density—actually observed by RPWS/LP (Wahlund et al. 2005)—and the onset of a strong ion massloading by heavy ions (especially 28 amu ion N_2^+), as exospheric densities start to be dominated by CH_4 and N_2. Other locally pick up species are H^+, H_2^+, probably responsible for the light massloading outside the IMB.

An interesting aspect of Titan's heavy massloading is the low plasma velocities within the IM—Hartle et al. (2006) during TA reports values of the order of 10–15 km/s. Extraordinary evidence of this effect on the transport of draped magnetic flux tubes is provided by the detection of draped magnetic field lines within the IM which correspond to background conditions the moon was exposed to long before the encounter. These fields were named 'fossil fields' because of the analogy to fossil records (Neubauer et al. 2006). Confirmation of the existence and timing of fossil fields were obtained in Titan's first observed excursion into the Kronian magnetosheath during the T32 encounter (Bertucci et al. 2008). Figure 36a shows Cassini MAG data in spherical Kronian magnetic coordinates for the day of the encounter (13 June, 2007). The angle λ is the magnetic latitude and the azimuth ϕ is measured on the magnetic equatorial plane from the sunward direction. Prior to the encounter and as it travels outbound from Saturn, Cassini experiences a nearly 10-hour excursion into the magnetosheath followed by a $\sim$3 hour period within the magnetosphere. Since before the encounter, Cassini's Kronocentric distance is smaller than Titan's, it is reasonable to think that Titan was respectively in the solar wind and the magnetosphere for a similar amount of time. The T32 encounter takes place within the magnetosheath 20 minutes after the third magnetopause crossing (c). Figure 36b shows the magnetic field in spherical TIIS coordinates, RPWS/LP and CAPS/ELS measurements in the vicinity of the encounter, which takes place around 13.6 hours SLT as Cassini flies over the moon's north pole at a minimum altitude of 975 km. The direction of the interplanetary magnetic field surrounding Titan's induced magnetosphere is clearly northward. The IMB is clearly detected around 17:41 and 17:53 (altitudes of 1400 and 1740 km, respectively), where the 100–1000-eV electron count rates suddenly drop showing a strong acceleration of the external flow is strongly decelerated. Around those times, the cold plasma starts to dominate as the plasma density increases above 100 cm^{-3}. As a result of this increase, the ion-neutral collision frequency becomes comparable to the ion gyroradius and therefore the transport of the magnetic field is achieved via the electrons. However, electrons within the IMB are only a few eV and therefore it is expected that the magnetic flux tube convection time is extremely long as compared to that at higher altitudes. It is within the IMB precisely that the draped magnetic flux tubes point in a direction which is not compatible with the draping of the IMF but the Kronian magnetic field Titan was exposed to 20 minutes before closest approach. As a result, the sudden increase in the massloading at the IMB, makes the IM the spatial place where the magnetic history of Titan's environment is stored, in the same way as comets (Raeder et al. 1987). The lifetime of this 'magnetic memory' would range from a few tens of minutes up to 3 hours (Bertucci et al. 2008). This result led to a few theoretical studies based on MHD-Hall (Ma et al. 2009), and hybrid (Simon et al. 2009) simulations with simplified geometry, which gave fossil field lifetimes compatible with the observations.

The removal of fossil fields from Titan's induced magnetosphere can be achieved via diffusion driven processes—such as reconnection between these and new field lines with strong

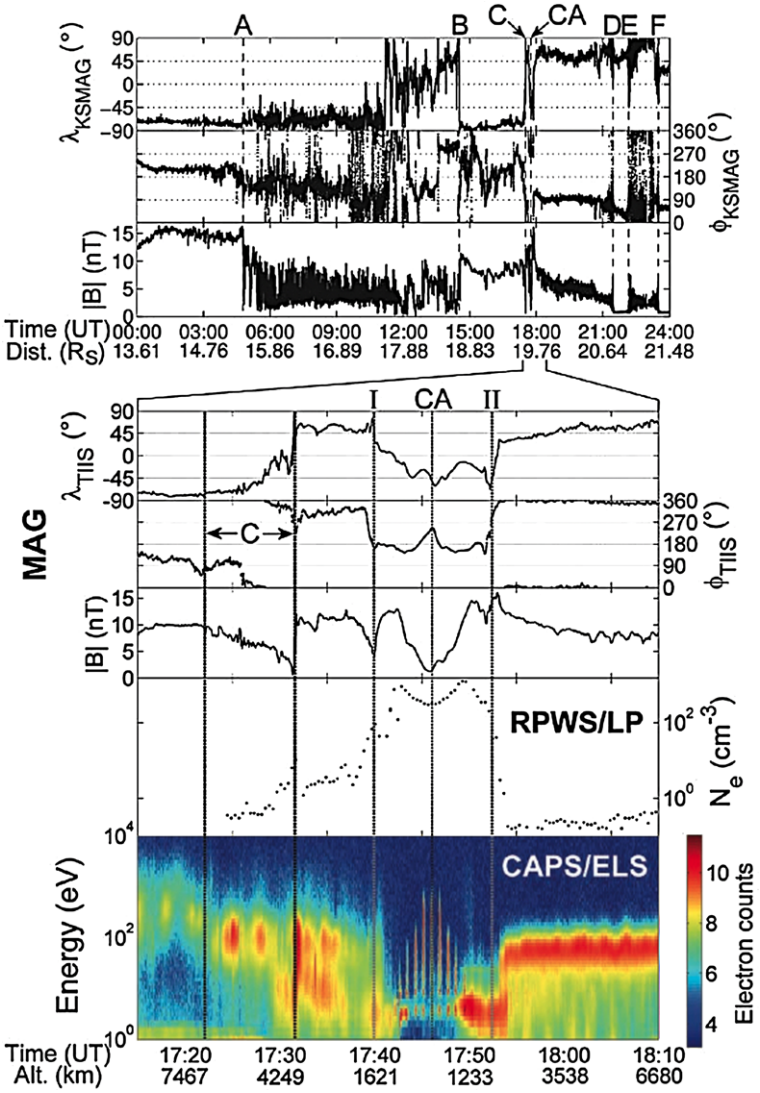

Fig. 36 *Above*: Cassini MAG measurements on 13 June 2007 in spherical KSMAG coordinates. The encounters with the Saturn's magnetopause and bow shock are indicated with the letters *A* to *C* and *D* to *F*, respectively. $|B|$ is the magnetic field strength. Cassini's kronocentric distance is indicated beneath the plots. *Below*: MAG data in spherical TIIS coordinates, plasma density (from RPWS/LP), and electron count rate per energy channel (from CAPS/ELS) during the T32 flyby. Magnetopause crossing C, CA, and the entry (I) and exit (II) of the fossil field region are indicated. Cassini's altitude above Titan is also indicated (from Bertucci et al. 2008)

magnetic shear or diffusion into the ionosphere—or processes involving plasma transport across the magnetic poles of the induced magnetosphere. However, the efficiency of these processes is not well known yet.

Cassini's coverage of Titan's magnetotail at altitudes above $2R_T$ is rather scarce. During the nominal mission, only one flyby covered the mid range tail (around $4R_T$): the

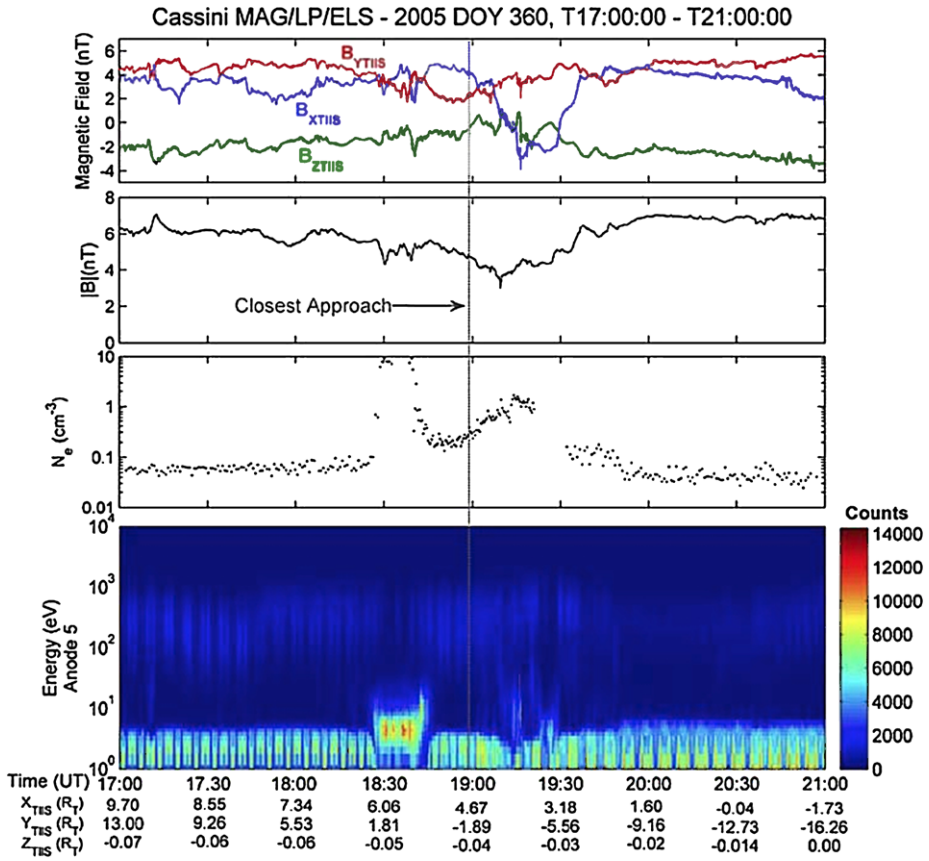

Fig. 37 Magnetic field vector in TIIS coordinates and magnitude (Cassini MAG), electron density (RPWS/LP), and 1 eV–10 KeV electron counts (anode 5) from CAPS/ELS during the T9 flyby (December 26, 2005). Spacecraft position in TIIS coordinates is indicated below the lower panel. Closest approach time is indicated with a *grey line*. The 1832–1838 and 1921–1932 UTC RPWS/LP data gaps are due to a change of mode of the instrument (Bertucci et al. 2007)

T9 flyby. T9 (December 26, 2005) is an outbound, equatorial flyby in Saturn magnetosphere's pre-dawn sector (3.1 hours SLT) at an altitude of 10409.6 km at the time of closest approach (1859 UTC). In the hours leading to the flyby, Cassini has periodic encounters with a probably flapping magnetodisk current sheet (Bertucci 2009). As a result, T9 is likely to have occurred under non-stationary conditions, while Titan and Cassini were temporarily in the magnetodisk's southern lobe (Bertucci et al. 2007; Sittler et al. 2010b). Cassini MAG (TIIS coordinates), RPWS and CAPS/ELS data around T9 are shown in Fig. 37. The first element to note is that the background magnetic field lies almost on the (X_{TIIS}, Y_{TIIS}) plane with B_{YTIIS} the strongest component. This places the tail's neutral sheet on a plane almost parallel to the B_{ZTIIS} and the flow velocity vector, where Cassini can cross it. A second important aspect of this flyby is that the peak of the upstream distribution function is outside the field of view of the CAPS instrument, implying a significant (>40°) displacement of the flow direction from co-rotation (Szego et al. 2007). The resulting geometry is such that Cassini first explores the away lobe (i.e. field lines pointing away from Titan) while it is located downstream from the dayside hemisphere, followed by

the 'toward' lobe, located downstream from the nightside hemisphere. According to MAG data, the IMB/Tail boundary inbound crossing takes place a few minutes before 1830. This coincides with the peak electron energy decrease observed by CAPS/ELS around 1825 and the increase in electron density observed by RPWS/LP. The plasma density reaches a peak value of 10 cm^{-3}, where 16–19 and 28–40 amu ions (Szego et al. 2007), and ∼20 eV ionospheric photoelectrons are observed (Coates et al. 2007). An abrupt change in B_{XTIIS} takes place a few minutes after CA (∼1906) suggesting the crossing of the tail's polarity reversal layer. This signature is immediately followed by a minimum in the magnetic field magnitude (3 nT at 1909:31) after which B_{XTIIS} remains negative until 1935 (magnetotail's toward lobe). During that interval, CAPS and LP data reveal a second region populated with cold plasma from Titan but with a different composition (1–2 amu ions Szego et al. (2007)).

In the light of the difficulties to obtain the upstream flow velocity vector direction from plasma measurements, Bertucci et al. (2007) provided an approximate estimation assuming that Cassini crossed the center of Titan's magnetic tail when the magnetic field strength was the lowest. That led to a unit vector with TIIS components $v = (0.81,\ -0.59,\ -0.01)$, i.e., 36.05° away from the ideal co-rotation towards Saturn, on the equatorial $(X_{\mathrm{TIIS}}, Y_{\mathrm{TIIS}})$ plane. This is consistent with the Kronian plasma velocity vectors reported around $20R_S$ in the pre-dawn sector by McAndrews et al. (2009). The outbound crossing of the IMB occurs around 1936. This signature coincides with the change in the electron temperature around 1930.

Cassini measurements during the T9 flyby represent the first evidence of local plasma escape in the mid-range tail. In particular, clear evidence of escaping heavy plasma along Kronian magnetic field lines draped around Titan (Bertucci et al. 2007; Wei et al. 2007) is observed during the inbound leg. The local plasma signature on the outbound leg, however, is explained as light pick up ions from Titan's exosphere (Sittler et al. 2010b). In the latter, the absence of photoelectron signature suggests that the field lines there are connected to Titan's nightside.

4.4 The Ionospheric Boundary

In spite of its long heliocentric distance, photoionization is largely responsible for the formation of Titan's ionosphere (Ågren et al. 2007). However, unlike Mars and Venus, the EUV flux at Titan is in general not aligned with the upstream flow. As a result, Titan's ionosphere has a varying efficiency in preventing external magnetic fields from accessing the neutral atmosphere.

Nevertheless, Titan's ionosphere is usually associated with attenuated magnetic fields and surrounded by clear drops in the magnetic field strength. These drops are observed for different configurations (Neubauer et al. 2006; Simon et al. 2008; Bertucci et al. 2008), but MAG data hardly ever shows a field free ionosphere (Wei et al. 2011).

It is still uncertain if these magnetic field drops reveal a Venus-like ionopause. Rosenqvist et al. (2009) reports that the magnetic field strength drops coincide with the lowest (∼1000 km altitude) of the two peaks in the altitude profile of the Pedersen conductivity within Titan's ionosphere. However, the electron density is rather constant across the field drop.

During the T32 flyby, both Bertucci et al. (2008) and Garnier (2009) report a gradual increase in the electron density in coincidence with the magnetic field strength drops observed in the collisional ionosphere. However, it is still unclear if pressure balance is satisfied across the field drop.

Signatures of photoelectrons (Coates et al. 2011) have been observed in all sunlit portions of Titan's ionosphere (Hartle et al. 2006), but also in remote locations, indicating transport

along field lines from ionospheric regions (Coates et al. 2007). The signature characterizing these photoelectrons is the spectral line at 22–24 eV when corrected for spacecraft potential (Coates et al. 2007), which corresponds to ionization of N_2 due to solar He 304 nm line (Sittler et al. 2010b). It is very likely that the photoelectron signature is not associated to the IMB signatures mentioned above. Cassini measurements during the T5 flyby where a clear IMB but no photoelectron signature was observed seem to support this idea.

5 Comparisons and Conclusions

In spite of the differences in size, heliocentric distance, atmospheric composition, and plasma environment the induced magnetospheres of Mars, Venus and Titan present clear similarities and differences. In this comparison, it is important to include active comets, which represent a particular example based entirely on massloading (Szego et al. 2000 and references therein).

The first element to consider is the fact that induced magnetospheres are plasma structures which have been shown to be rather permanent over time. This has been unequivocally shown in the case of Mars, Venus and to some extent active comets. However, as this assertion applies to most of the in situ observations, it is worth mentioning that interesting transient alterations of the induced magnetospheres have been reported at Venus (Zhang et al. 2009), where incidentally, the IMF cone angle is small, leading to a negligible upstream convective electric field. In such a scenario, the coupling between the solar wind and the plasma population is likely to be achieved via acceleration processes involving electromagnetic plasma waves probably originating in field-aligned planetary ion beams.

In spite of the important variability of its environment (see Arridge et al., this issue), Cassini plasma measurements also reveal regular features around Titan. However, it is expected that upcoming flybys during the Solstice Mission improve not only the spatial coverage of observations around the moon, but also the range of regimes under which Titan interacts, including post-equinox observations. This will provide additional elements to conclude if the structures within the moon's induced magnetosphere are permanent.

Second, apart from the signatures deriving form the supermagnetosonic nature of the solar wind (bow shock and magnetosheath), the stages in which the momentum and energy transfer from the wind to the atmosphere occurs seem to be spatially ordered in a similar way at all these objects:

(i) Formation of an external boundary of the induced magnetosphere (IMB) with the following common signatures:

(a) A strong change (usually an increase, especially on ram side) in the magnetic field strength.
(b) Enhancement of the magnetic field draping.
(c) Decrease in the temperature of electrons.
(d) Decrease in the external ion density and energy.

These signatures, not exactly co-located but likely interdependent, mark the start of the obstacle to the flow. Both ionosphere and exosphere contribute to the obstacle, but the relative preponderance of these two actors varies from one object to the other. Active comets and Venus will likely be at each end of the spectrum as examples, respectively, of pure a exospheric interaction and an interaction where the ionospheric variability controls the induced magnetosphere.

However, the role that the cold and hot exospheres play in every one of these objects, and how their scale height and composition impacts on the ability to generate massloading is an

issue that remains to be investigated. Perhaps Titan is the most complex and least studied object in this matter, not only because of the different scenarios the interaction can occur, but also because of the complex chemistry that governs its upper atmosphere.

(ii) The induced magnetosphere represents the region where most of the momentum and energy is transferred between the external and the local plasma population. This is the place where local ion acceleration processes operate and for that reason this region is key in the study of planetary ion escape. Some of these acceleration mechanisms have been studied and tested at Mars, Venus, and more recently at Titan. In the case of Mars, agreement has been found between estimates of the forces exerted on planetary charged particles and their energies, validating the presence of those mechanisms. However, this is still one of the aspects on which more advances are expected, and such advances will require multi-instrumental measurements with relatively high time resolution due to its limited size on the ram side.

The magnetic tails of Mars, Venus, Titan and active comets are similar in magnetic structure with two well-defined lobes of opposite magnetic field polarity, and whose orientation depends on that of the upstream field and plasma flow. However, the distribution of plasma populations within the tail seems to be differences probably based on the efficiency of upstream/downstream plasma transport mechanisms, but observations at Mars and Venus both suggest a non-negligible role played by the upstream convective electric field. At Titan, such a role has not been assessed yet, although simulations (Modolo and Chanteur 2008) suggest that more energetic particles would be found on the hemisphere where the convective electric field points outward.

(iii) On the dayside, an ionospheric boundary marks the lower edge of the induced magnetosphere. As for the IMB, the ionospheric boundary is characterized by common signatures:

(a) Appearance of local photoelectron population.
(b) Increase in the electron density.
(c) With the exception of Mars crustal fields, a usual decrease in the magnetic field strength.

Once again, these signatures are not always co-located.

The processes by which the external plasma and magnetic field are prevented from penetrating the ionospheric boundary are different for each object. At Mars, the crustal magnetic field should be considered in the local plasma pressure budget, at Titan collision rate increase with decreasing altitude, leading to diffusion below 1000 km altitude (Cravens et al. 2010b). At Venus, more or less efficient pressure balance occurs, depending on solar cycle phase.

The similarity in the properties found in the plasma regions and discontinuities within the induced magnetospheres of Mars, Venus, Titan and active comets suggest that all these interactions should rest upon basic common processes. One approach to a formulation of a theory of induced magnetospheres based on 'first principles' was explored by Dubinin et al. (2006d), who discussed the formation of 1-D plasma discontinuities in a stationary flow of a plasma consisting of two proton populations and massless and isothermal electrons streaming against a heavy ion cloud. Starting from the standard multifluid equations of continuity and momentum, this work concludes that in a non-magnetized plasma and under specific conditions, a 'heavy ion shock' accompanied by a proton rarefaction is formed. This 'heavy ion shock' has properties similar to the IMB. If a transverse magnetic field is introduced, the differential ion streaming becomes more 'rigid' and a deceleration of the collective plasma flow at superfast speeds is accompanied with an increase of the magnetic field strength. The collective flow stops when the critical loci are reached. This simple model shows that the differential streaming provides an inherent electromagnetic coupling mechanism that leads

to key features which are observed at induced magnetospheres, namely the IMB. Efforts in this type of analytical approach to the problem should be continued.

On the other hand, sophisticated global simulations are increasingly effective in reproducing and explaining many of the features observed around induced magnetospheres (Kallio et al., this issue). In particular, recent efforts to couple these global models with exospheric models are being undertaken. This will significantly improve the description of the interaction in the light of the important role played by the exosphere on these interactions.

On the other hand, efforts such as the SWIM Challenge (Brain et al. 2010b) have been important to test the capacity of models in reproducing these features and should be imitated for other objects.

In summary, in situ measurements around the induced magnetospheres of Mars, Venus, Titan and active comets have revealed common structures and processes. However, there is an urge for simultaneous measurements of basic plasma parameters in order to undertake proper assessments of the properties of their different regions and boundaries. In the near future, this will be hopefully possible with upcoming missions MAVEN and Rosetta. Similar initiatives should be imitated in the case of Venus. In the case of Titan, measurements during the Cassini Solstice Mission are being awaited in order to expand our knowledge on the range of upstream conditions the moon is immersed in as well as their consequences on its plasma environment.

Acknowledgements Authors thank the International Space Science Institute (ISSI) for supporting this work. CB is supported by the National Science and Technology Research Council (CONICET) and the Agency for the Promotion of Science and Technology of Argentina.

NJTE was supported by the Swedish Institute of Space Physics through a grant from the Swedish Science Council (Vetenskapsrådet).

References

N. Achilleos, C.S. Arridge, C. Bertucci, C.M. Jackman, M.K. Dougherty, K.K. Khurana, C.T. Russell, Large-scale dynamics of Saturn's magnetopause: observations by Cassini. J. Geophys. Res. **113**, A11209 (2008). doi:10.1029/2008JA013265

M.H. Acuña et al., Mars Observer magnetic fields investigation. J. Geophys. Res. **97**(E5), 7799–7814 (1992)

M.H. Acuña et al., Magnetic field and plasma observations at Mars: Initial results of the Mars Global Surveyor mission. Science **279**, 1676–1680 (1998)

K. Ågren et al., On magnetospheric electron impact ionization and dynamics in Titan's ram-side and polar ionosphere, a Cassini case study. Ann. Geophys. **25**, 2359 (2007)

A. Albee et al., Overview of the Mars Global Surveyor mission. J. Geophys. Res. **106**(E10), 23291–23316 (2001)

H. Alfven, On the theory of comet tails. Tellus **9**, 92 (1957)

C.S. Arridge, N. Achilleos, M.K. Dougherty, K.K. Khurana, C.T. Russell, Modeling the size and shape of Saturn's magnetopause with variable dynamic pressure. J. Geophys. Res. **111**, A11227 (2006). doi:10.1029/2005JA011574

C.S. Arridge, C.T. Russell, K.K. Khurana, N. Achilleos, S.W.H. Cowley, M.K. Dougherty, D.J. Southwood, E.J. Bunce, Saturn's magnetodisc current sheet. J. Geophys. Res. **113**, A04214 (2008a). doi:10.1029/2007JA012540

C.S. Arridge, N. Andre, N. Achilleos, K.K. Khurana, C.L. Bertucci, L.K. Gilbert, G.R. Lewis, A.J. Coates, M.K. Dougherty, Thermal electron periodicities at 20RS in Saturn's magnetosphere. Geophys. Res. Lett. **35**, L15107 (2008b). doi:10.1029/2008GL034132

H.U. Auster et al., ROMAP: Rosetta magnetometer and plasma monitor. Space Sci. Rev. **128**(1), 221–240 (2007)

H. Backes et al., Titan's magnetic field signature during the first Cassini encounter. Science **308**, 992 (2005)

S. Barabash et al., The analyzer of space plasmas and energetic atoms (ASPERA-3) for the Mars Express Mission. Space Sci. Rev. (2006). doi:10.1007/s11214-006-9124-8

S. Barabash et al., The analyser of space plasmas and energetic atoms (ASPERA-4) for the Venus express mission. Planet. Space Sci. **55**, 1772–1792 (2007)

C. Beghin et al., New insights on Titan's plasma-driven Schumann resonance inferred from Huygens and Cassini data. Planet. Space Sci. **57**(14–15), 1872–1888 (2009)
C. Bertucci, Characteristics and variability of Titan's magnetic environment. Philos. Trans. R. Soc. Lond. A **367**, 789–798 (2009). doi:10.1098/rsta.2008.02502009
C. Bertucci et al., Magnetic field draping enhancement at the Martian magnetic pileup boundary from Mars global surveyor observations. Geophys. Res. Lett. **30**(2), 1099 (2003a). doi:10.1029/2002GL015713
C. Bertucci et al., Magnetic field draping enhancement at Venus: Evidence for a magnetic pileup boundary. Geophys. Res. Lett. **30**(17), 1876 (2003b). doi:10.1029/2003GL017271
C. Bertucci et al., MGS MAG/ER ER observations at the magnetic pileup boundary of Mars: draping enhancement and low frequency waves. Adv. Space Res. **33**(11), 1938–1944 (2004)
C. Bertucci et al., Structure of the magnetic pileup boundary at Mars and Venus. J. Geophys. Res. **110**, A01209 (2005a). doi:10.1029/2004JA010592
C. Bertucci et al., Interaction of the solar wind with Mars from Mars Global Surveyor MAG/ER observations. Journal of Atmospheric and Terrestrial Physics **67**(17–18), 1797–1808 (2005b)
C. Bertucci et al., Titan's interaction with its plasma environment. American Geophysical Union, Fall Meeting 2005, abstract #P52A-02 (2005c)
C. Bertucci, F.M. Neubauer, K. Szego, J.-E. Wahlund, A.J. Coates, M.K. Dougherty, D.T. Young, W.S. Kurth, Structure of Titan's mid-range magnetic tail: Cassini magnetometer observations during the T9 flyby. Geophys. Res. Lett. **34**, L24S02 (2007). doi:10.1029/2007GL030865
C. Bertucci et al., The magnetic memory of Titan's ionized atmosphere. Science **321**(5895), 1475 (2008)
C. Bertucci et al., The variability of Titan's magnetic environment. Planet. Space Sci., 1813–1820 (2009)
L.H. Brace et al., The ionotail of Venus—Its configuration and evidence for ion escape. J. Geophys. Res. **92**(1), 15–26 (1987)
L.H. Brace et al., The dynamic behavior of the Venus ionosphere in response to solar wind interactions. J. Geophys. Res. **85**(A13), 7663–7678 (1980)
D.A. Brain et al., Observations of low-frequency electromagnetic plasma waves upstream from the Martian shock. J. Geophys. Res. **107**(A6), 1076 (2002). doi:10.1029/2000JA000416
D.A. Brain et al., Martian magnetic morphology: Contributions from the solar wind and crust. J. Geophys. Res. **108**(A12), 1424 (2003). doi:10.1029/2002JA009482
D.A. Brain et al., Variability of the altitude of the Martian sheath. Geophys. Res. Lett. **32**, L18203 (2005). doi:10.1029/2005GL023126
D.A. Brain et al., Episodic detachment of Martian crustal magnetic fields leading to bulk atmospheric plasma escape. Geophys. Res. Lett. **37**(14), L14108 (2010a)
D.A. Brain et al., A comparison of global models for the solar wind interaction with Mars. Icarus **206**, 139–151 (2010b)
J.C. Cain et al., An $n = 90$ internal potential function of the martian crustal magnetic field. J. Geophys. Res. **108**(E2), 5008 (2003). doi:10.1029/2000JE001487
L. Gan, T.E. Cravens, M. Horanyi, Electrons in the ionopause boundary layer of Venus. J. Geophys. Res. **95**(1), 19023–19035 (1990)
J.Y. Chaufray, J.L. Bertaux, F. Leblanc, E. Quémerais, Observation of the hydrogen corona with SPICAM on Mars Express. Icarus **195**(2), 598–613 (2008)
A. Chicarro et al., Mars express: a European mission to the red planet, in *Mars Express, The Scientific Payload, SP-1240*, ed. by A. Wilson (ESA Publication Division, Noordwijk, 2004), pp. 3–16
A.J. Coates et al., Ionospheric electrons in Titan's tail: Plasma structure during the Cassini T9 encounter. Geophys. Res. Lett. **34**(24), L24S05 (2007)
A.J. Coates et al., Ionospheric photoelectrons at Venus: initial observations by ASPERA-4 ELS. Planet. Space Sci. **56**(6), 802–806 (2008)
A.J. Coates et al., Ionospheric photoelectrons: comparing Venus, Earth, Mars and Titan planetary and space science. Planet. Space Sci. **59**(10), 1019–1027 (2011)
J.E.P. Connerney, M.H. Acuña, N.F. Ness, G. Kletetschka, D.L. Mitchell, R.P. Lin, H. Rème, Proc. Natl. Acad. Sci. USA **102**(42), 14970–14975 (2005)
T.E. Cravens et al., Model calculations of the dayside ionosphere of Venus: energetics. J. Geophys. Res. **85**, 7778–7786 (1980)
T.E. Cravens, R.V. Yelle, J.-E. Wahlund, D.E. Shemansky, A.F. Nagy, Composition and structure of the ionosphere and thermosphere, in *Titan From Cassini-Huygens*, chap. 11, p. 259. ed. by R.H. Brown, J.-P. Lebreton, J.H. Waite (Springer, Dordrecht, 2010b). ISBN:978-1-4020-9214-5
D.H. Crider et al., Evidence of electron impact ionization in the magnetic pileup boundary of Mars. Geophys. Res. Lett. **27**(1), 45–48 (2000)
D.H. Crider et al., Observations of the latitude dependence of the location of the martian magnetic pileup boundary. Geophys. Res. Lett. **29**(8), 1170 (2002) doi:10.1029/2001GL013860

D.H. Crider et al., Mars global surveyor observations of solar wind magnetic field draping around Mars. Space Sci. Rev. **111**(1), 203–221 (2004)
Sh. Dolginov et al., The magnetic field of Mars according to the data from the Mars 3 and Mars 5. J. Geophys. Res. **81**(19), 3353–3362 (1976)
Sh.Sh. Dolginov, E.M. Dubinin, Ye.G. Yeroshenko, P.L. Israilevich, I.M. Podgorny, S.I. Shkol'nikova, On the configuration of the field in the magnetic tail of Venus. Cosm. Res. **19**, 624 (1981)
M.K. Dougherty et al., The Cassini magnetic field investigation. Space Sci. Rev. **114**, 331–383 (2004). doi:10.1007/s11214-004-1432-2
J. Du, T.L. Zhang, C. Wang, M. Wolwerk, M. Delva, W. Baumjohann, Magnetosheath fluctuations at Venus for two extreme orientations of the interplanetary magnetic field. Geophys. Res. Lett. **36**(9), L09102 (2009)
E. Dubinin et al., Cold ions at the Martian bow shock—PHOBOS observations. J. Geophys. Res. **98**(A4), 5617–5623 (1993a)
E. Dubinin et al., Ion acceleration in the Martian tail: phobos observations. J. Geophys. Res. **98**(A3), 3991–3997 (1993b)
E. Dubinin et al., Plasma morphology at Mars. ASPERA 3 observations. Space Sci. Rev. (2006a). doi:10.1007/s11214-006-9039-4
E. Dubinin et al., Electric fields within the Martian magnetosphere and ion extraction: ASPERA-3 observations. Icarus **182**, 337–342 (2006b)
E. Dubinin et al., Solar wind plasma protrusion into the Martian magnetosphere: ASPERA-3 observations. Icarus **182**(2006), 343–349 (2006c)
E. Dubinin et al., Nonlinear 1-D stationary flows in multi-ion plasmas—sonic and critical loci—solitary and "oscillatory" waves. Ann. Geophys. **24**(11), 3041–3057 (2006d)
E. Dubinin et al., Structure and dynamics of the solar wind/ionosphere interface on Mars: MEX-ASPERA-3 and MEX-MARSIS observations. Geophys. Res. Lett. **35**, 11103 (2008a)
E.M. Dubinin et al., Access of solar wind electrons into the Martian magnetosphere. Ann. Geophys. **26**(11), 3511–3524 (2008b)
F. Duru et al., Magnetically controlled structures in the ionosphere of Mars. J. Geophys. Res. **111**, A11204 (2006). doi:10.1029/2006JA011975
F. Duru et al., Transient density gradients in the Martian ionosphere similar to the ionopause at Venus. J. Geophys. Res. **114**(A12), A12310 (2009) (JGRA Homepage)
F. Duru et al., A plasma flow velocity boundary at Mars from the disappearance of electron plasma oscillations. Icarus **206**, 74–82 (2010)
J.P. Eastwood, D.A. Brain, J.S. Halekas, J.F. Drake, T.D. Phan, M. Øieroset, D.L. Mitchell, R.P. Lin, M. Acuña, Evidence for collisionless magnetic reconnection at Mars. Geophys. Res. Lett. **35**(2), L02106 (2008)
N.J.T. Edberg et al., Statistical analysis of the location of the Martian magnetic pileup boundary and bow shock and the influence of crustal magnetic fields J. Geophys. Res. **113**(A8), A08206 (2008)
N.J.T. Edberg et al., Simultaneous measurements of Martian plasma boundaries by Rosetta and Mars Express. Planet. Space Sci. **57**(8–9), 1085–1096 (2009a)
N.J.T. Edberg, D.A. Brain, M. Lester, S.W.H. Cowley, R. Modolo, M. Fränz, S. Barabash, Plasma boundary variability at Mars as observed by Mars Global Surveyor and Mars Express. Ann. Geophys. **27**(9), 3537–3550 (2009b)
N.J.T. Edberg, M. Lester, S.W.H. Cowley, D.A. Brain, M. Fränz, S. Barabash, Magnetosonic Mach number effect of the position of the bow shock at Mars in comparison to Venus. J. Geophys. Res. **115**, A07203 (2010). doi:10.1029/2009JA014998
R.C. Elphic et al., Observations of the dayside ionopause and ionosphere of Venus. J. Geophys. Res. **85**, 7679 (1980)
R.C. Elphic et al., The Venus ionopause current sheet: thickness length scale and controlling factors. J. Geophys. Res. **86**(A13), 11430–11438 (1981)
J.R. Espley et al., Observations of low-frequency magnetic oscillations in the Martian magnetosheath, magnetic pileup region, and tail. J. Geophys. Res. **109**(A7), A07213 (2004)
A. Fedorov et al., Structure of the Martian Wake. Icarus **182**, 329–336 (2006)
A. Fedorov et al., Comparative analysis of Venus and Mars magnetotails. Planet. Space Sci. **56**, 812–817 (2008)
R.A. Frahm et al., Location of atmospheric photoelectron energy peaks within the Mars environment. Space Sci. Rev. **126**, 389 (2006)
R.A. Frahm et al., Estimation of the escape of photoelectrons from Mars in 2004 liberated by the ionization of carbon dioxide and atomic oxygen. Icarus **206**(1), 50–63 (2010)
M. Fränz, E. Dubinin, E. Roussos, J. Woch, J.D. Winningham, R. Frahm, A.J. Coates, A. Fedorov, S. Barabash, R. Lundin, Plasma moments in the environment of Mars. Mars Express ASPERA-3 observations. Space Sci. Rev. (2006a). doi:10.1007/s11214-006-9115-9

M. Fränz et al., Plasma intrusion above Mars crustal fields—Mars Express ASPERA-3 observations. Icarus (2006b). doi:10.1016/j.icarus.2005.11.016
J.L. Fox, A. Dalgarno, Ionization, luminosity, and heating of the upper atmosphere of Mars. J. Geophys. Res. **84**, 7315–7333 (1979)
P. Garnier, Titan's ionosphere in the magnetosheath: Cassini RPWS results during the T32 flyby. Ann. Geophys. **27**(11), 4257–4272 (2009)
R. Grard et al., First measurements of plasma waves near Mars. Nature **341**(19), 607–609 (1989)
K.I. Gringauz, V.V. Bezrukikh, T.K. Breus, T. Gombosi, A.P. Remizov, M.I. Verigin, G.I. Volkov, Plasma observations near Venus onboard Venera 9 and Venera 10 satellites by means of wide angle plasma detectors, in *Physics of Solar Planetary Environment*, ed. by D.J. Williams (AGU, Boulder, 1976), pp. 918–932
D.A. Gurnett, A. Bhattacharjee, *Introduction to Plasma Physics with Space and Laboratory Applications* (Cambridge University Press, Cambridge, 2005)
D.A. Gurnett et al., The Cassini radio and plasma wave investigation. Space Sci. Rev. **114**, 395–463 (2004)
D.A. Gurnett et al., Radar soundings of the ionosphere of Mars. Science **310**, 1929–1933 (2005)
J.S. Halekas et al., Current sheets at low altitudes in the Martian magnetotail. Geophys. Res. Lett. **33**(13), L13101 (2006)
J.S. Halekas, D.A. Brain, R.P. Lin, J.G. Luhmann, D.L. Mitchell, Distribution and variability of accelerated electrons at Mars. Adv. Space Res. **41**(9), 1347–1352 (2008)
R.E. Hartle et al., Titan's ion exosphere observed from Voyager 1. J. Geophys. Res. **87**, 1383–1394 (1982)
R. Hartle et al., Initial interpretation of Titan plasma interaction as observed by the Cassini plasma spectrometer: comparisons with Voyager 1. Planet. Space Sci. **54**(12), 1211–1224 (2006)
A. Hasegawa, *Plasma Instabilities and Non Linear Effects*, Phys. and in Chem. Space, vol. 8 (Springer, New York, 1975)
M.M. Hoppe, C.T. Russell, Particle acceleration at planetary bow shock waves. Nature **295**, 41–42 (1982)
K.K. Khurana et al., Sources of rotational signals in Saturn's magnetosphere. J. Geophys. Res. **114**(A2), A02211 (2009)
T. Knetter, F.M. Neubauer, T. Horbury, A. Balogh, Four-point discontinuity observations using Cluster magnetic field data: a statistical survey. J. Geophys. Res. **109**(A6), A06102 (2004)
W.C. Knudsen, K.L. Miller, K. Spenner, Improved Venus ionopause altitude calculation and comparison with measurement. J. Geophys. Res. **87**, 2246–2254 (1982)
W.C. Knudsen et al., Retarding potential analyzer for the Pioneer-Venus Orbiter Mission. Space Sci. Instrum. **4**, 351–372 (1979)
W.C. Knudsen et al., Suprathermal electron energy distribution within the dayside venus ionosphere. J. Geophys. Res. **85**(A13), 7754–7758 (1980). doi:10.1029/JA085iA13p07754
W.C. Knudsen et al., Solar cycle changes in the ionization sources of the nightside Venus ionosphere. J. Geophys. Res. **92**, 13391 (1987)
W.C. Knudsen, Solar cycle changes in the morphology of the Venus ionosphere. J. Geophys. Res. **93**, 8756 (1988)
W.S. Kurth et al., An update to a Saturnian longitude system based on kilometric radio emissions. J. Geophys. Res. **113**, A05222 (2008). doi:10.1029/2007JA012861
B. Lembège, P. Savoini, Formation of reflected electron bursts by the nonstationarity and nonuniformity of a collisionless shock front. J. Geophys. Res. **107**(A3), 1037 (2002). doi:10.1029/2001JA900128
J.G. Luhmann, A model of the ionospheric tail rays of Venus. J. Geophys. Res. **98**(A10), 17615–17622 (1993)
J.G. Luhmann et al., Magnetic field fluctuations in the Venus magnetosheath. Geophys. Res. Lett. **10**, 655–658 (1983)
R. Lundin et al., On the momentum transfer of the solar wind to the Martian topside ionosphere. Geophys. Res. Lett. **18**, 1059–1062 (1991)
R. Lundin, E.M. Dubinin, Phobos-2 results on the ionospheric plasma escape from Mars. Adv. Space Res. **12**(9), 255–263 (1992)
R. Lundin et al., Solar wind-induced atmospheric erosion at Mars: first results from ASPERA-3 on Mars Express. Science **305**(5692), 1933–1936 (2004)
R. Lundin, S. Barabash, M. Holmstrom, H. Nilsson, M. Yamauchi, E.M. Dubinin, M. Fraenz, Atmospheric origin of cold ion escape from Mars. Geophys. Res. Lett. **36**, L17202 (2009). doi:10.1029/2009GL039341
Y.J. Ma et al., Time-dependent global MHD simulations of Cassini T32 flyby: From magnetosphere to magnetosheath. J. Geophys. Res. **114**, A03204 (2009). doi:10.1029/2008JA013676
G.P. Mantas, W.B. Hanson, Photoelectron fluxes in the Martian ionosphere. J. Geophys. Res. **84**, 369–385 (1979)
C. Martinecz, The Venus plasma environment: a comparison of Venus Express ASPERA-4 measurements with 3D hybrid simulations. Ph.D. thesis, Uni. Braunschweig (2008)

C. Martinecz et al., Location of the bow shock and ion composition boundaries at Venus-initial determinations from Venus Express ASPERA-4. Planet. Space Sci. **56**, 780–784 (2008). doi:10.1016/j.pss.2007.07.007
C. Martinecz, A. Boesswetter, M. Fränz, E. Roussos, J. Woch, N. Krupp, E. Dubinin, U. Motschmann, S. Wiehle, S. Simon, S. Barabash, R. Lundin, T.L. Zhang, H. Lammer, H. Lichtenegger, Y. Kulikov, The plasma environment of Venus: comparison of Venus Express ASPERA-4 measurements with 3D hybrid simulations. J. Geophys. Res. **114**, E00B30 (2009). doi:10.1029/2008JE003174; Correction: J. Geophys. Res. **114**, E00B98 (2009). doi:10.1029/2009JE003377
C. Mazelle, H. Reme, G. Belmont et al., Ultra low frequency waves at the magnetic pile-up boundary of comet P/Halley. Adv. Space Res. **11**(9), 73–77 (1991)
C. Mazelle et al., Bow shock and upstream phenomena at Mars. Space Sci. Rev. **111**(1), 115–181 (2004)
H.J. McAndrews et al., Plasma in Saturn's nightside magnetosphere and the implications for global circulation. Planet. Space Sci. **57**(14–15), 1714–1722 (2009)
D.J. McComas, H.E. Spence, C.T. Russell, M.A. Saunders, The average magnetic field draping and consistent plasma properties of the Venus magnetotail. J. Geophys. Res. **91**, 7939–7953 (1986)
P.T. McCormick et al., On the energy deposition of photoelectrons in the atmosphere of Venus. J. Geophys. Res. **81**, 5196–5200 (1976)
D.L. Mitchell, Probing Mars' crustal magnetic field and ionosphere with the MGS Electron Reflectometer. J. Geophys. Res. **106**(E10), 23419–23428 (2001)
R. Modolo, G.M. Chanteur, A global hybrid model for Titan's interaction with the Kronian plasma: Application to the Cassini Ta flyby. J. Geophys. Res. **113**, A01317 (2008). doi:10.1029/2007JA012453
R. Modolo et al., Simulated solar wind plasma interaction with the Martian exosphere: influence of the solar EUV flux on the bow shock and the magnetic pile-up boundary. Ann. Geophys. **24**(12), 3403–3410 (2006)
S.L. Moses, F.V. Coroniti, F.L. Scarf, Expectations for the microphysics of the Mars-solar wind interaction. Geophys. Res. Lett. **15**(5), 429–432 (1988). doi:10.1029/GL015i005p00429
A.F. Nagy, D. Winterhalter, K. Sauer, T.E. Cravens, S. Brecht, C. Mazelle, D. Crider, E. Kallio, A. Zakharov, E. Dubinin, M. Verigin, G. Kotova, W.I. Axford, C. Bertucci, J.G. Trotignon, The plasma environment of Mars. Space Sci. Rev. **111**, 33–114 (2004)
N.F. Ness, M.H. Acuna, K.W. Behannon, The induced magnetosphere of Titan. J. Geophys. Res. **87**(1), 1369–1381 (1982)
F.M. Neubauer et al., Titan's magnetospheric interaction, in *Saturn*, ed. by T. Gehrels, M.S. Matthews (University of Arizona Press, Tucson, 1984), pp. 760–787
F.M. Neubauer et al., Titan's near magnetotail from magnetic field and plasma observations and modelling: Cassini flybys TA, TB and T3. J. Geophys. Res. **111**, A10220 (2006). doi:10.1029/2006JA011676
H. Pérez-de-Tejada, Distribution of plasma and magnetic fluxes in the Venus near wake. J. Geophys. Res. **91**, 8039 (1986)
J.L. Phillips, D.J. McComas, The magnetosheath and magnetotail of Venus. Space Sci. Rev. **55**, 1–80 (1991)
G. Picardi et al., Mars Express: a European mission to the red planet. ESA SP **SP-1240**, 51 (2004)
J. Raeder et al., Macroscopic perturbations of the IMF by P/Halley as seen by the Giotto magnetometer. Astron. Astrophys. **187**, 61–64 (1987)
H. Rosenbauer et al., The relationship between the magnetic field in the Martian magnetotail and upstream solar wind parameters. J. Geophys. Res. **99**(A9), 17,199–17,204 (1994)
L. Rosenqvist et al., Titan ionospheric conductivities from Cassini measurements. Planet. Space Sci. **57**(14–15), 1828–1833 (2009)
C.T. Russell, The magnetic field of Mars—Mars 3 evidence re-examined. Geophys. Res. Lett. **5**, 81–84 (1978a)
C.T. Russell, The magnetic field of Mars—Mars 5 evidence re-examined. Geophys. Res. Lett. **5**, 85–88 (1978b)
C.T. Russell et al., Initial Pioneer-Venus magnetic field results: dayside observations. Science **203**, 745–748 (1979)
C.T. Russell et al., Pioneer-Venus flux gate magnetometer. IEEE Trans. Geosci. Electron. **GE-18**, 32–35 (1980)
C.T. Russell, O. Vaisberg, The interaction of the solar wind with Venus, in *Venus*, ed. by D.M. Hunton, L. Colin, T.M. Donahue, V.I. Moroz (University of Arizona Press, Tucson, 1983), pp. 873–940
C.T. Russell, E. Chou, J.G. Luhmann, P. Gazis, L.H. Brace, W.R. Hoegy, Solar and interplanetary control of the location of the Venus bow shock. J. Geophys. Res. **93**, 5461–5469 (1988)
C.T. Russell, J.G. Luhmann, R.J. Strangeway, The solar wind interaction with Venus through the eyes of the Pioneer Venus Orbiter. Planet. Space Sci. **54**, 1482–1495 (2006a)
C.T. Russell, S.S. Mayerberger, X. Blanco-Cano, Proton cyclotron waves at Mars and Venus. Adv. Space Res. **38**, 745–751 (2006b)

A.M. Rymer et al., Discrete classification and electron energy spectra of Titan's varied magnetospheric environment. Geophys. Res. Lett. **36**, L15109 (2009). doi:10.1029/2009GL039427
M.A. Saunders, C.T. Russell, Average dimension and magnetic structure of the distant Venus magnetotail. J. Geophys. Res. **91**, 5589–5604 (1986)
K. Sauer, T. Roatsch, U. Motschmann, K. Schwingenschuh, R. Lundin, H. Rosenbauer, S. Livi, Observations of plasma boundaries and phenomena around Mars with Phobos 2. J. Geophys. Res. **97**, 6227–6233 (1992)
R.W. Schunk, A.F. Nagy, *Ionospheres: Physics, Plasma Physics, and Chemistry* (Cambridge University Press, Cambridge, 2000)
K. Schwingenschuh, W. Riedler, T.-L. Zhang, H. Lichtenegger, H. Rosenbauer, S. Livi, G. Gevai, K. Gringauz, M. Verigin, E. Eroshenko, The Martian magnetic field environment—induced or dominated by an intrinsic magnetic field? Adv. Space Res. **12**(9), 213–219 (1992)
S. Simon et al., Titan's highly dynamic magnetic environment a systematic survey of Cassini magnetometer observations from flybys TA–T62. Planet. Space Sci. **58**(10), 1230–1251 (2010a)
S. Simon et al., Dynamics of Saturn's magnetodisk near Titan's orbit Comparison of Cassini magnetometer observations from real and virtual Titan flybys. Planet. Space Sci. **58**(12), 1625–1635 (2010b)
S. Simon, U. Motschmann, G. Kleindienst, K.-H. Glassmeier, C. Bertucci, M.K. Dougherty, Titan's magnetic field signature during the Cassini T34 flyby: comparison between hybrid simulations and MAG data. Geophys. Res. Lett. **35**, L04107 (2008). doi:10.1029/2007GL033056
S. Simon et al., Titan's plasma environment during a magnetosheath excursion:Real-time scenarios for Cassini's T32 flyby from a hybrid simulation. Ann. Geophys. **27**, 669–685 (2009)
E. Sittler, R.E. Hartle, C. Bertucci, A. Coates, T. Cravens, I. Dandouras, D. Shemansky, Energy deposition processes, in *Titan from Cassini-Huygens*, ed. by R. Brown, J.P. Lebreton, H. Waite (Springer, Dordrecht, 2010a), pp. 393–453. ISBN978-1-4020-9214-5
E.C. Sittler et al., Saturn's magnetospheric interaction with Titan as defined by Cassini encounters T9 and T18: New results. Planet. Space Sci. **58**(3), 327–350 (2010b)
J.A. Slavin, R.C. Elphic, C.T. Russell, F.L. Scarf, J.H. Wolfe, J.D. Mihalov, D.S. Intriligator, L.H. Brace, H.A. Taylor, R.E. Daniell, The solar wind interaction with Venus—Pioneer Venus observations of bow shock location and structure. J. Geophys. Res. **85**, 7625–7641 (1980)
J.A. Slavin, R.E. Holzer, Solar wind flow about the terrestrial planets. I—Modeling bow shock position and shape. J. Geophys. Res. **86**(11), 11401–11418 (1981)
J.A. Slavin, R.E. Holzer, J.R. Spreiter, S.S. Stahara, Planetary Mach cones—theory and observation. J. Geophys. Res. **89**, 2708–2714 (1984)
J.A. Slavin et al., The solar wind interaction with Mars: Mariner 4, Mars 2, Mars 3, Mars 5 and Phobos 2 observations of bow shock position and shape. J. Geophys. Res. **96**, 11235–11241 (1991)
K. Szego et al., Physics of mass loaded plasmas. Space Sci. Rev. **94**(3/4), 429–671 (2000) 2000
B.U.Ö. Sonnerup, M. Scheible, Minimum and maximum variance analysis, in *Analysis Methods for Multi-Spacecraft Data*, ed. by G. Paschmann, P. Daly. ISSI Scientific Reports Series, ESA/ISSI, vol. 1 (1998), pp. 185–220. ISBN1608-280X
K. Spenner, W.C. Knudsen, K.L. Miller, V. Novak, C.T. Russell, R.C. Elphic, Observation of the Venus mantle, the boundary region between solar wind and ionosphere. J. Geophys. Res. **85**, 7655–7662 (1980)
K. Spenner et al., Photoelectron fluxes in the Venus dayside ionosphere. J. Geophys. Res. **102**, 2577–2583 (1997)
K. Szego, Z. Bebesi, C. Bertucci, A.J. Coates, F. Crary, G. Erdos, R. Hartle, E.C. Sittler, D.T. Young, Charged particle environment of Titan during the T9 flyby. Geophys. Res. Lett. **34**(24), L24S03 (2007)
M. Tátrallyay et al., Magnetic field overshoots in the Martian bow shock. J. Geophys. Res. **102**(A2), 2157–2164 (1997)
J.G. Trotignon et al., Position and shape of the martian bow shock: the Phobos 2 plasma wave system observations. Planet. Space Sci. **41**, 189–198 (1993)
J.-G. Trotignon, E. Dubinin, R. Grard, S. Barabash, R. Lundin, Martian planetopause as seen by the plasma wave system onboard Phobos 2. J. Geophys. Res. **101**(A11), 24965–24977 (1996)
J.G. Trotignon, C. Mazelle, C. Bertucci, M.H. Acuña, Martian shock and magnetic pile-up boundary positions and shapes determined from the Phobos 2 and Mars Global Surveyor data sets. Planet. Space Sci. **54**, 357–369 (2006)
B. Tsurutani, G.S. Lakhina, E.J. Smith et al., Mirror mode structures and ELF plasma waves in the Giacobini–Zinner magnetosheath. Nonlinear Process. Geophys. **6**, 229–234 (1999)
O.L. Vaisberg, Mars-plasma environment, in *Physics of Solar Planetary Environment*, ed. by D.J. Williams (AGU, Boulder, 1976), pp. 854–871
O.L. Vaisberg, A.V. Bogdanov, Flow of the solar wind around Mars and Venus—general principles. Cosm. Res. **12**, 253–257 (1974)

O.L. Vaisberg, S.A. Romanov, V.N. Smirnov, I.P. Karpinsky, B.I. Khazanov, B.V. Polenov, A.V. Bogdanov, N.M. Antonov, Ion flux parameters in the solar wind-venus interaction region, in *Physics of Solar Planetary Environment*, ed. by D.J. Williams (AGU, Boulder, 1976), pp. 904–917
O.L. Vaisberg, L.M. Zeleny, Formation of the plasma mantle in the Venusian magnetosphere. Icarus **58**, 412–430 (1984)
O.L. Vaisberg, A.V. Bogdanov, N.F. Borodin, A.A. Zertzalov, B.V. Polenov, S.A. Romanov, Solar plasma interaction with Mars: preliminary results. Icarus **18**, 59–63 (1973)
O. Vaisberg, A. Fedorov, F. Dunjushkin, A. Kozhukhovsky, V. Smirnov, L. Avanov, C.T. Russell, J.G. Luhmann, Ion populations in the tail of Venus. Adv. Space Res. **16**(4), 105–118 (1995)
S. Vennerstrom, N. Olsen, M. Purucker, M.H. Acuña, J.C. Cain, The magnetic field in the pile-up region at Mars, and its variation with the solar wind. Geophys. Res. Lett. **30**(7), 1369 (2003). doi:10.1029/2003GL016883
M.I. Verigin, K.I. Gringauz, T. Gombosi, T.K. Breus, V.V. Bezrukikh, A.P. Remizov, G.I. Volkov, Plasma near Venus from the Venera 9 and 10 wide-angle analyzer data. J. Geophys. Res. **83**, 3721–3728 (1978)
D. Vignes et al., The solar wind interaction with Mars: locations and shapes of the Bow Shock and the magnetic pile-up boundary from the observations of the MAG/ER experiment onboard Mars Global Surveyor. Geophys. Res. Lett. **27**, 49–52 (2000). doi:10.1029/1999GL010703
D. Vignes, M.H. Acuña, J.E.P. Connerney, D.H. Crider, H. Rème, C. Mazelle, Factors controlling the location of the Bow Shock at Mars. Geophys. Res. Lett. **29**(9), 1328 (2002). doi:10.1029/2001GL014513
M. Volwerk et al., Mirror-mode-like structures in Venus' induced magnetosphere. J. Geophys. Res. **113**(15), E0B016 (2008)
M. Volwerk, M. Delva, Y. Futaana, A. Retinò, Z. Vörös, T.L. Zhang, W. Baumjohann, S. Barabash, Substorm activity in Venus's magnetotail. Ann. Geophys. **27**(6), 2321–2330 (2009)
Z. Vörös et al., Intermittent turbulence, noisy fluctuations, and wavy structures in the Venusian magnetosheath. J. Geophys. Res. **113**(A12), E00B21 (2008)
J.E. Wahlund et al., Cassini measurements of cold plasma in the ionosphere of titan. Science **308**(5724), 986–989 (2005)
H.Y. Wei, C.T. Russell, Proton cyclotron waves at Mars: exosphere structure and evidence for a fast neutral disk. Geophys. Res. Lett. **33**(23), L23103 (2006)
H.Y. Wei et al., Cold ionospheric plasma in Titan's magnetotail. Geophys.Res. Lett. **34**, L24S06 (2007). doi:10.1029/2007GL030701
H.Y. Wei et al., Comparative study of ion cyclotron waves at Mars, Venus and Earth. Planet. Space Sci. **59**(10), 1039–1047 (2011). doi:10.1016/j.pss.2010.01.004
D.A. Wolf, F.M. Neubauer, Titan's highly variable plasma environment. J. Geophys. Res. **87**, 881–885 (1982)
Y. Yeroshenko et al., The magnetotail of Mars—PHOBOS observations. Geophys. Res. Lett. **17**, 885–888 (1990)
D.T. Young et al., Cassini plasma spectrometer investigation. Space Sci. Rev. **114**, 1–112 (2004)
L.M. Zelenyi, O.L. Vaisberg, Venusian interaction with the solar wind plasma flow as a limiting case of the cometary type interaction, in *Advances of Space Plasma Physics*, ed. by B. Buti (World Scientific, Singapore, 1985), pp. 59–76
T.-L. Zhang, J.G. Luhmann, C.T. Russell, The solar cycle dependence of the location and shape of the Venus bow shock. J. Geophys. Res. **95**, 14961–14967 (1990)
T.L. Zhang, J.G. Luhmann, C.T. Russell, The magnetic barrier at Venus. J. Geophys. Res. **96**(11), 11145–11153 (1991)
T.-L. Zhang et al., The flaring of the Martian magnetotail observed by the PHOBOS 2 spacecraft. Geophys. Res. Lett. **21**(12), 1121–1124 (1994)
T.L. Zhang, K.K. Khurana, C.T. Russell, M.G. Kivelson, R. Nakamura, W. Baumjohann, On the Venus bow shock compressibility. Adv. Space Res. **33**, 1920–1923 (2004)
T.L. Zhang et al., Magnetic field investigation of the Venus plasma environment: expected new results from Venus Express. Planet. Space Sci. **54**, 1336–1343 (2006)
T.L. Zhang et al., Initial Venus Express magnetic field observations of the Venus bow shock location at solar minimum. Planet. Space Sci. **56**, 785–789 (2008a)
T.L. Zhang et al., Induced magnetosphere and its outer boundary at Venus. J. Geophys. Res. **113**, E00B20 (2008b). doi:10.1029/2008JE003215
T.L. Zhang et al., Disappearing induced magnetosphere at Venus: Implications for close-in exoplanets. Geophys. Res. Lett. **36**(20), L20203 (2009)
T.L. Zhang, W. Baumjohann, J. Du, R. Nakamura, R. Jarvinen, E. Kallio, A.M. Du, M. Balikhin, J.G. Luhmann, C.T. Russell, Hemispheric asymmetry of the magnetic field wrapping pattern in the Venusian magnetotail. Geophys. Res. Lett. **37**(14), L14202 (2010)
B.J. Zwan, R.A. Wolf, Depletion of solar wind plasma near a planetary boundary. J. Geophys. Res. **81**, 1636–1648 (1976)

Space Sci Rev (2011) 162:173–211
DOI 10.1007/s11214-011-9831-7

Ion Energization and Escape on Mars and Venus

E. Dubinin · M. Fraenz · A. Fedorov · R. Lundin · N. Edberg · F. Duru · O. Vaisberg

Received: 10 February 2011 / Accepted: 25 August 2011 / Published online: 14 October 2011

Abstract Mars and Venus do not have a global magnetic field and as a result solar wind interacts directly with their ionospheres and upper atmospheres. Neutral atoms ionized by solar UV, charge exchange and electron impact, are extracted and scavenged by solar wind providing a significant loss of planetary volatiles. There are different channels and routes through which the ionized planetary matter escapes from the planets. Processes of ion energization driven by direct solar wind forcing and their escape are intimately related. Forces responsible for ion energization in different channels are different and, correspondingly, the effectiveness of escape is also different. Classification of the energization processes and escape channels on Mars and Venus and also their variability with solar wind parameters is the main topic of our review. We will distinguish between classical pickup and 'mass-loaded' pickup processes, energization in boundary layer and plasma sheet, polar winds on unmagnetized planets with magnetized ionospheres and enhanced escape flows from localized auroral regions in the regions filled by strong crustal magnetic fields.

Keywords Mars: magnetosphere · Mars: ionosphere · Venus: magnetosphere · Venus: ionosphere · Sun: solar wind

E. Dubinin (✉) · M. Fraenz
MPI für Sonnensystemforschung, 37191 Katlenburg-Lindau, Germany
e-mail: dubinin@mps.mpg.de

A. Fedorov
Centre d'Etude Spatiale des Rayonnements, Toulose, France

R. Lundin
Swedish Institute of Space Physics, Kiruna, Sweden

N. Edberg
Swedish Institute of Space Physics, Uppsala, Sweden

F. Duru
Department of Physics and Astronomy, Iowa University, Iowa, USA

O. Vaisberg
Space Research Institute, Moscow, Russia

1 Introduction

It is believed that the initial atmospheres of Venus, Earth and Mars would have been rather similar in the past. However, presently, atmospheres and water inventory in terrestrial planets of our solar system are drastically different. How did they come to evolve so differently? An important part of the answer is that all terrestrial planets bear evidence of long-term thermal and nonthermal atmospheric escape (see Lammer et al. 2008 and Johnson et al. 2008 for recent reviews).

The main factors which control thermal escape are the exospheric temperature T_{ex} determined by quasi-equilibrium between energy supply from the solar EUV and downward heat conduction, $\frac{J_{EUV}}{K_T mg}$ (Chamberlain and Hunten 1987; Bauer 2002), where J_{EUV} is the intensity of solar EUV radiation, m is the molecular mass of gas, K_T is the thermal conduction coefficient, g is the gravity acceleration. Although the intensity of EUV radiation on Venus is almost four times higher as compared to Mars, the smaller gravitational acceleration ($g_m = 3.31$, $g_v = 8.88$ m s^{-2}) leads to comparable values of T_{ex} (Bauer 2002). The efficiency of the thermal escape is determined by the parameter $\lambda = mg/T_{ex}$ which yields the fraction of particles at the base of the exosphere able to escape when their outward velocity exceeds the escape velocity which is about 10.4 km s^{-1} and 5 km s^{-1} for Venus and Mars, respectively.

At Mars thermal escape of hydrogen is the dominant process. The spacecraft observations of Mars at Lyman-α have shown that the planet is surrounded by a corona of H atoms. The mean flux of atomic hydrogen is about $(1.6 \pm 0.2) \times 10^8$ cm^{-2} s^{-1} (Anderson and Hord 1971, 1972; Chaufray et al. 2008), which is equivalent to the loss of $(1.8 \pm 0.3) \times 10^{26}$ H atoms s^{-1}. Fluxes of molecular hydrogen estimated from the FUSE observations (Krasnopolsky and Feldman 2001) are much weaker (4×10^6 cm^{-2} s^{-1}). Escape of hydrogen supplied by water losses has important implications for the Martian atmosphere. If there were no sinks for oxygen, its concentration would have to be highly enriched. On the other hand, oxygen atoms are too heavy to escape thermally and non-thermal escape processes are required (McElroy et al. 1982). Non-thermal mechanism of dissociative recombination $O_2^+ + e^- \rightarrow O^\star + O^\star$ ($O^\star$ atoms from this process have more energy than the escape energy) was suggested as the main loss process for oxygen atoms at Mars although the differences among the existing models are about two orders of magnitude (Fox and Hać 2009). According to Fox and Hać (2009) the oxygen escape fluxes from dissociative recombination may reach 1.37×10^8 cm^{-2} s^{-1} and 2×10^8 cm^{-2} s^{-1} for low and high solar activities, respectively, which corresponds to a total loss over the dayside of (1.44 and 2.1) $\times 10^{26}$ s^{-1}. However, experimental observations of the hot oxygen corona and such high escape fluxes on Mars are still missing.[1]

At Venus, where the gravity forces are stronger, the temperature in the exosphere is too low for thermal escape even for hydrogen. Dissociative recombination on Venus produces $O^\star$ atoms with $V \sim 6.5$ km s^{-1} which unlike in the case for Mars is not high enough to allow escape of oxygen atoms from the planet. Therefore solar wind induced escape may be the most important mechanism of atmospheric losses.

The question of solar wind erosion of atmospheres of nonmagnetized planets and the evolutionary aspect of this issue were already discussed intensely after the first measurements of ionospheric ions sweeped by solar wind on Venus (Moore et al. 1990; Luhmann and

[1] Recently, Feldman et al. (2011) have detected atomic oxygen emission at 1304 Å at altitudes of 400–1000 km. The density decrease significantly steeper than predicted by exospheric models.

Kozyra 1991; Luhmann and Bauer 1992; Brace et al. 1982) and Mars (Lundin et al. 1989; Rosenbauer et al. 1989). There are several reviews which widely discuss this fundamental problem of atmospheric evolution (e.g. Chassefiere 1997; Chassefiere and Leblanc 2004; Lammer et al. 2006a, 2006b, 2008; Lundin et al. 2007; Johnson et al. 2008).

Most information about solar wind interaction with Venus was obtained by the Pioneer Venus Orbiter (PVO) in 1979–1992. PVO carried instruments surveying the upper atmosphere (UV spectrometer, neutral mass analyzer), the ionosphere (retarding potential analyzer, Langmuir probe, thermal ion spectrometer), the solar wind (plasma analyzer). Reviews of the results are contained in Space Sci. Rev., 'Venus Aeronomy', v. 55, Nos. 1–4, 1991. The space environment near Mars was studied by the Viking-Landers, Mariners, Mars-3,5 as well as Phobos-2 and Mars Global Surveyor (MGS). Reviews are published in the AGU Monograph 'Venus and Mars: Atmospheres, Ionospheres and Solar Wind interactions', 1992 and Space Sci. Rev., 'Mars Magnetism and its Interaction with the solar wind', v. 11, No 1–2, 2004. Although PVO has provided a wealth of in-situ and remote sensing data on the space environment at Venus, the instrument and telemetry constraints limited the capabilities of the plasma measurements. Another unexplored area is the plasma environment and magnetic fields near Venus during low solar activity. The observations on Phobos-2 were also carried out close to solar maximum. Note, that solar activity strongly controls the processes of solar wind/ionosphere/atmosphere interaction.

On the whole, solar wind interactions with Mars and Venus are similar, although some differences appear due to stronger gravity on Venus and finite Larmor radius effects on Mars. Strong local crustal magnetic field on Mars also introduces new features which have counterparts in the solar wind-Earth interaction.

This paper focuses mainly on results obtained from observations on Mars Express (MEX) and Venus Express (VEX) spacecraft, especially those from the IMA/ASPERA-3 and IMA/ASPERA-4 instruments (Barabash et al. 2006; Barabash et al. 2007c), respectively. We present here also some unpublished results concerning ion acceleration and escape. The Ion Mass Analyzer (IMA) on MEX measures ions in the 10 eV/q–30 keV/q energy range and 1–44 amu/charge range, including both solar wind and planetary ions. A new patch uploaded on 1 May 2007 has further improved the IMA performance extending the energy range down to $E/q \leq 10$ eV. At $E/q \geq 50$ eV IMA measures fluxes of different (m/q) ion species with time resolution of 192 s for one 3D scan. The measurements of the low-energy ($E/q \leq 50$ eV) ions are carried out without the elevation steering but with increased time-resolution of 12 s. To get a high time-resolution in the energy range $E/q \geq 50$ eV the electrostatic scanning system was switched off on some orbits enabling to perform the 2D measurements of ion fluxes with a sampling time of 12 s. The MARSIS sounding experiment on MEX essentially complements the capability of MEX for exploring the plasma environment of Mars since it is able to trace not only ionospheric height profiles below the spacecraft from remote radio sounding, but also can measure the local plasma number density and the magnetic field strength from locally generated plasma echoes (Gurnett et al. 2005; Gurnett et al. 2008; Duru et al. 2008).

The ion sensor on ASPERA-4/VEX is almost a replica of IMA/ASPERA-3 but the electrostatic elevation steering operates for the whole energy range. Interpretation of the early observations of ion energization and escape obtained on Mars Express were supported by the availability of magnetometer observations from Mars Global Surveyor (MGS) which ceased working in November 2006. The Mars Express mission has thus far covered a significant portion of the previous solar cycle through the recent minimum. The Venus Express observations supported by magnetometer measurements (Zhang et al. 2006) have been mainly performed in the polar periapsis region at a time of exceptionally low activity, with more coverage expected as the new cycle rises over the next years.

2 General Features of Ion Energization

Mars and Venus do not have a global magnetic field and, as a result, the solar wind interacts directly with their exospheres and ionospheres. The magnetosphere of Venus provided us with the first example of an induced magnetosphere (see more about this type of magnetospheres in Podgorny et al. 1982; Vaisberg et al. 1990; Russell 1991; Russell et al. 2006; Luhmann et al. 2004). Ionospheric ions and neutral atoms ionized by solar UV, charge exchange and electron impact gain momentum and energy from solar wind and escape to space or impact the atmosphere and sputter heavy atoms and molecules off the exosphere which then can also leave the planets.

Processes of ion energization driven by direct solar wind forcing and their escape are intimately related. Charged particles are accelerated by electric fields. In a plasma with one sort of ions, the electric field is composed of the motional electric field, the term related to the thermal pressure gradient and the Hall electric field component:

$$\boldsymbol{E} = -\boldsymbol{V}_i \times \boldsymbol{B} - \frac{\nabla P_e}{n_e e} + \frac{\boldsymbol{j} \times \boldsymbol{B}}{n_e e} \tag{1}$$

If there are two or more ion species the above equation is modified:

$$\boldsymbol{E} = -\sum_i \frac{n_i}{n_e} \boldsymbol{V}_i \times \boldsymbol{B} - \frac{\nabla P_e}{n_e e} + \frac{\boldsymbol{j} \times \boldsymbol{B}}{n_e e}. \tag{2}$$

It will be shown below that in the different regions on Mars and Venus one or another term of the electric field prevails producing specific features of ion acceleration.

There are also numerous mechanisms of particle energization by oscillating electric fields. Particles with velocities close to phase speeds of plasma waves can gain energy due to resonant interactions with electromagnetic fields. These processes are particularly efficient at shocks, plasma boundaries and in the regions with field-aligned currents where plasma often becomes unstable. Oscillatory fields can still exert a time-averaged force on particles in the case of spatially inhomogeneous wave turbulence. The repulsive pondermotive wave force $F \sim -\nabla P_w$, where $P_w = e^2 n / 4m\omega^2 E_\sim^2$ is the wave pressure, can accelerate and push out particles from the region filled by wave turbulence (see e.g. Lundin and Guglielmi 2006).

The classical pick-up process is a result of the action of the motional electric field $\boldsymbol{E} = -\boldsymbol{V}_{sw} \times \boldsymbol{B}$ experienced by a newly generated charged particle in a plasma flow. The maximum energy gain is $W_{pi} = 4W_{sw} \sin^2\theta$, where $W_{sw} = m_p V_{sw}^2/2$ is the bulk energy of the solar wind protons and θ is the angle between the vectors $\boldsymbol{V}_{sw}$ and $\boldsymbol{B}_{IMF}$. The pick-up protons, originating from the extended hydrogen exosphere on Mars, form a ring-beam distribution in velocity space (Dubinin et al. 2006a) and efficiently excite waves which are observed in the spacecraft frame at the proton cyclotron frequency (Brain et al. 2002; Delva et al. 2011, this issue). Due to the relatively small scale of Mars compared to large comets pitch-angle scattering on excited waves is weak and the ring distribution does not evolve to a full shell as it happens near large comets.

A perceptible part of pick-up protons has small normal velocities at the crossing of the bow shock and therefore might be efficiently reflected and trapped between the electrostatic mirror at the shock and the upstream Lorentz force gaining energy in the motional electric field. Figure 1 compares the observed distribution function of pick-up protons in front of the bow shock (Dubinin et al. 2006a) with their expected phase space portrait immediately after a single reflection of PIs at the shock potential (Zank et al. 1996). The small scale of the Martian bow shock and its large curvature decrease the efficiency of the PI energization by

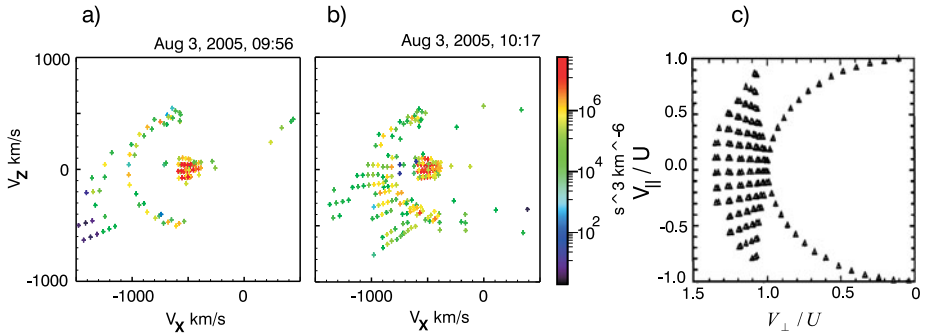

Fig. 1 (**a**,**b**) Typical distribution functions of protons in front of the Martian bow shock. Pick-up protons originating from the extended hydrogen corona form a ring-type distribution in velocity space. Protons with $E \geq 4E_{sw}\sin\theta^2$ are particles reflected from the bow shock and accelerated in the motional electric field (after Dubinin et al. 2006a, 2006b, 2006c). (**c**) Phase space portrait of pick-up ions after the reflection at the shock potential. $V_\perp$, $V_\parallel$ are the velocity components of pickup protons perpendicular and parallel to the magnetic field in the solar wind flow (U) frame, respectively (after Zank et al. 1996)

multiple reflections at the bow shock—after 2–3 reflections ions escape the shock region. Since fluxes of pick-up protons are $<10^6$ cm^{-2} s^{-1} their contribution to hydrogen escape is small as compared to the Jeans escape of neutral hydrogen atoms. Note here that PIs play a much more important role in the outer heliosphere and in the interaction at the heliosphere's termination shock where their pressure becomes comparable with the solar wind dynamic pressure.

It is intuitively clear that the pick-up process of the more heavy and dense ion population at closer distances to the planets can not be described in terms of a simple test-particle approximation and requires the treatment of the momentum and energy exchange between solar wind and the massive planetary plasma. Simple one-dimensional hybrid simulations of plasma flow interaction with a localized cloud of oxygen ions well demonstrate such a coupling and momentum exchange between two plasmas (Dubinin et al. 1998). A weak ion source localized at $X = 0$ with a Gaussian profile was immersed into the incoming plasma flow ($M_A = 5$) with the magnetic field nearly perpendicular to the flow speed (Fig. 2). When oxygen ions are nearly at rest, the electron fluid slows down to provide charge neutrality $v_{ex} \sim n_p V_p/(n_p + n_o)$. Deceleration of electrons leads to a decrease in the motional electric field $E_y = -V_{ex}B_z$ which causes the proton flow to be deflected in the $-Y$ direction which is opposite to the direction of the motional electric field since $\frac{dV_{py}}{dt} = \frac{e}{m_p}(E_y - V_{px}B_z) < 0$, while newly ionized particles originating near the source, begin to move on cycloid-like trajectories accelerating in $+Y$ direction. The deflection of protons in $-Y$ direction is clearly observed in panel (d) of Fig. 2. The arising Lorentz force V_yB_z decelerates the streaming protons which transfer their momentum to oxygen ions. When the velocity of oxygen ions exceeds the proton speed the electrons begin to outrun protons and the motional electric field increases. The proton flow is deflected in the $+Y$ direction and the V_yB_z force accelerates protons taking the momentum from the heavy ions. Both fluids begin to rotate relative each other. Such a periodic momentum exchange is a fundamental feature of ion dynamics in multi-ion plasmas. With increase of the number density in the cloud, the amplitude of a quasi-cycloid decreases and the gain in energy of oxygen ions also decreases. For a more extended source a transition from a modified 'classical pickup' motion of heavy ions to a cometary-like flow occurs. Such a transition is clearly observed in two-ion fluid MHD simulations (Fig. 3) (Sauer et al. 2000; Dubinin and Sauer 1999).

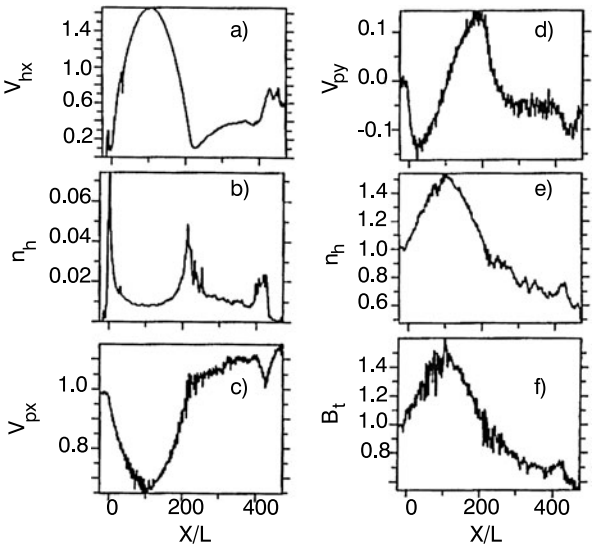

Fig. 2 Variations in plasma parameters in a 1-D hybrid simulation as plasma flows ($M_A = 5$) across a heavy ion source ($m_h = 16$) localized at $X = 0$. The magnetic field was nearly perpendicular to the flow velocity ($\theta = 85°$) and is perpendicular to the XY plane. The parameters are normalized to the upstream values (after Dubinin et al. 1998)

The process of the momentum exchange between two (or more) interacting ion fluids is well described in terms of multi-ion fluid MHD approximation (Chapman and Dunlop 1986; Harold and Hassam 1994; Sauer et al. 1994; Dubinin and Sauer 1999). In the Martian environment, where the Larmor radius of heavy (O^+, O_2^+) ions is large as compared to the characteristic scale of the system, the differential streaming of different ion species is relevant for such an approximation. Note, that in the limit of small Larmor radius all ion species move across the magnetic field with the same $\boldsymbol{E} \times \boldsymbol{B}$ drift velocity. For two ion species, the momentum equations for protons and oxygen ions are (here we neglected the thermal pressure terms):

$$n_p m_p \frac{d\boldsymbol{V}_p}{dt} = e\frac{n_o n_p}{n_e}(\boldsymbol{V}_p - \boldsymbol{V}_o) \times \boldsymbol{B} + n_p \frac{\boldsymbol{j} \times \boldsymbol{B}}{\mu_o n_e} \tag{3}$$

$$n_o m_o \frac{d\boldsymbol{V}_o}{dt} = e\frac{n_o n_p}{n_e}(\boldsymbol{V}_o - \boldsymbol{V}_p) \times \boldsymbol{B} + n_o \frac{\boldsymbol{j} \times \boldsymbol{B}}{\mu_o n_e} \tag{4}$$

The new terms, as compared to the single fluid MHD equations, appear caused by a differential streaming of ion fluids. If we neglect, for a moment, the $\boldsymbol{j} \times \boldsymbol{B}$ terms the velocity gain of oxygen ions is given by $\Delta V_o \sim -\frac{n_p m_p}{n_o m_o}\Delta V_p$, that is it is proportional to the ratio of the mass densities of the interacting fluids. The momentum lost by the solar wind is transferred to the planetary plasma like at collision of two rigid bodies. Lundin and Dubinin (1992) have used the phenomenological expression $V_o = V_p(1 - \exp(-\frac{n_p m_p}{n_o m_o}))$ to describe this process of heavy mass-loading. One can see that in the limit of high mass-density of oxygen ions ($n_o m_o \gg n_p m_p$) this expression coincides with the above expression derived from the multi-ion MHD equations. Conversely, a low mass-density for planetary oxygen ions leads to $V_o \approx V_p$, i.e. to a classical ion pick-up. Figure 4 shows the variations of the velocity ratio V_o/V_p as a function of the density ratio n_p/n_o for two Phobos-2 crossings of the distant boundary layer in the Martian tail. It is observed that the momentum transfer between both ion fluids is reasonably described by a mass-loaded ion pick-up mechanism.

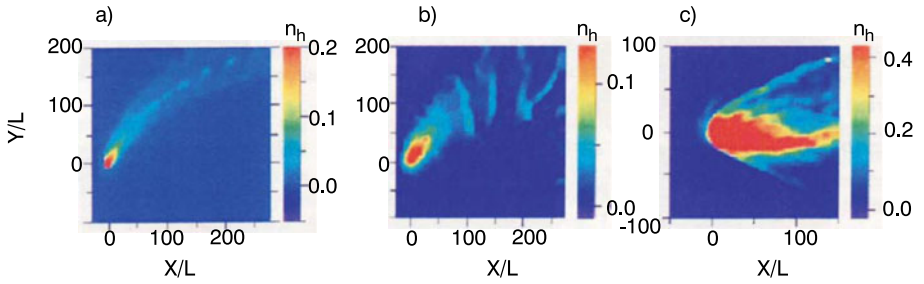

Fig. 3 Interaction of solar wind flow with different types of heavy ion obstacles in 2D two-ion MHD fluid simulations. At the transition from the source localized in space to a more extended and 'heavy' ion cloud ((a) → (c)), the effects of the momentum exchange become more and more important. The classical ion pick-up pattern is transformed to the mass-loaded pickup and a cometary-like interaction. The structuring and filamentation is a result of the instabilities driven by a differential streaming of two ion fluids (after Sauer et al. 2000 and Dubinin and Sauer 1999)

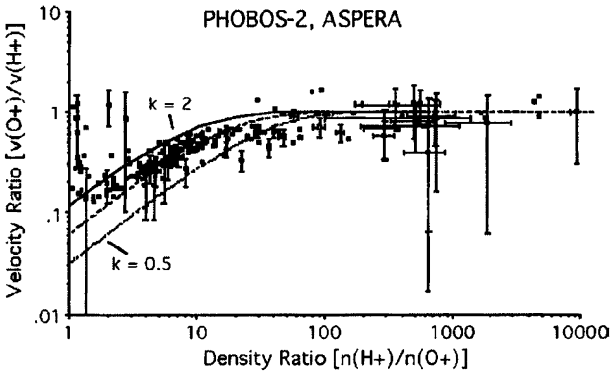

Fig. 4 Mass-loaded ion pick-up observed by the Phobos-2 spacecraft in the Martian boundary layer (after Lundin and Dubinin 1992)

In general, the normal and tangential magnetic field stresses ($\boldsymbol{j} \times \boldsymbol{B}$) can not be neglected and the relationship between the velocities of interacting ion fluids becomes more complicated. Moreover, in some magnetospheric regions, forces related with the compression and the tension of the magnetic field dominate. In this case one can use the standard MHD equation

$$m_o \frac{d\boldsymbol{V}_o}{dt} = -\frac{\nabla \boldsymbol{B}^2}{2\mu_o n_e} + \frac{(\boldsymbol{B} \cdot \nabla)\boldsymbol{B}}{\mu_o n_e}.$$

An important feature is that heavy oxygen ions are often not magnetized and the $\boldsymbol{j} \times \boldsymbol{B}$ force caused by the magnetic shear stresses of the draped field lines acts on the magnetized electrons producing a charge separation. The arising Hall electric field extracts and accelerates planetary ions to reach quasi-neutrality. Hall electric field becomes also important in the regions where solar wind plasma is massloaded by planetary ions and the difference between the ion and electron velocities increases.

3 Momentum Conservation Constraints and Global Morphology of Escape

As it was shown in the previous section conservation of the momentum imposes constraints on the velocity of mass-loaded plasma and the corresponding escape fluxes. A simple estimate of the escape flux from Mars forced by solar wind and based only on the momentum

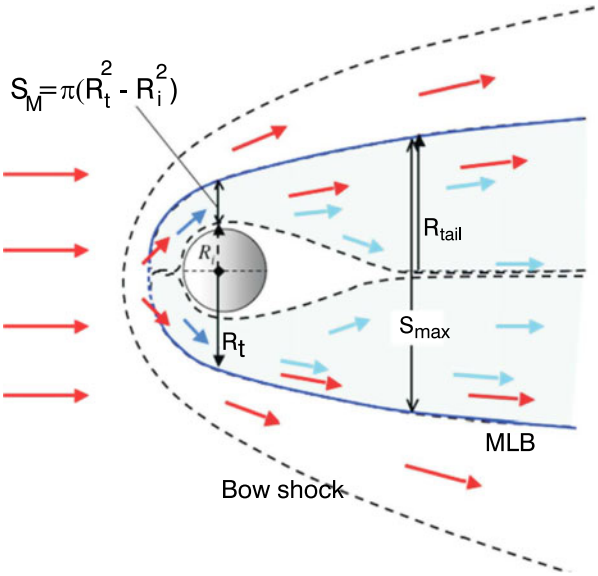

Fig. 5 Diagram of solar wind forcing of a non-magnetized planetary ionosphere/atmosphere. Energy and momentum transfer occurs within the volume extending from the subsolar region to the deep tail. *Red* and *blue arrows* illustrate the solar wind and planetary plasma flows (after Lundin et al. 2007)

conservation (Perez de Tejada 1998; Lundin and Dubinin 1992) gives

$$\Phi_M \sim \frac{m_{sw} V_{sw}}{m_M V_M} \Phi_{sw}, \tag{5}$$

where Φ_{sw} and Φ_M, are the solar wind flux and the flux of Martian ions, respectively, m_{sw} , m_M, V_{sw}, and V_M are the masses and velocities of ion species in solar wind and within the magnetosphere. It is seen that slowly escaping ions carry higher mass losses. If, for example, oxygen ions flow with $V \sim 5$ km s^{-1}, which is close to the escape velocity, then the maximum escape flux is by a factor of ~5 higher than the solar wind flux. Total losses depend on the escape geometry. Since the Phobos-2 measurements were rather short (~2 months) an uncertainty in the determination of the area through which planetary ions escape from Mars remained. Verigin et al. (1991) have assumed that a loss of planetary ions occurs through the plasma sheet. Lundin et al. (1989) and Lundin and Dubinin (1992) have estimated the area as $S_M = \pi(R_t^2 - R_i^2)$. Here R_t and R_i are the radii of the boundary at which onset of the momentum exchange starts (mass-loading boundary) and the unperturbed cold Martian ionosphere, respectively. The important effect of the draping geometry is that the mass of solar wind plasma which effectively takes part in the momentum exchange is higher than that carried by solar wind onto the ionosphere cross-section ($\boldsymbol{j} \times \boldsymbol{B}$ force decelerates the magnetosheath plasma in a broad boundary layer at the flanks transferring the momentum to a planetary plasma via a compressed and sheared magnetic field).

The observations carried out on the Phobos-2 spacecraft have shown that oxygen ions gain energy which is in average close to the energy of solar wind protons. In this case the escape flux is about of 1/4 of the solar wind flux which approximately corresponds to losses of 4×10^{25} s^{-1}. This value can be compared to the flux of 2.5×10^{25} s^{-1} reported by Lundin et al. (1989) for the escape through a cylindrically symmetric boundary layer observed by Phobos-2 or to the flux 1×10^{25} according to the first measurements on Mars by the Mars-4, 5 spacecraft (Vaisberg et al. 1976).

Lundin et al. (2008b) have assumed that the interaction region expands towards the tail, increasing the cross-section area of the momentum exchange to the whole tail area πR_{tail}^2 (Fig. 5). Observations recently performed by Mars Express (MEX) and presented in the

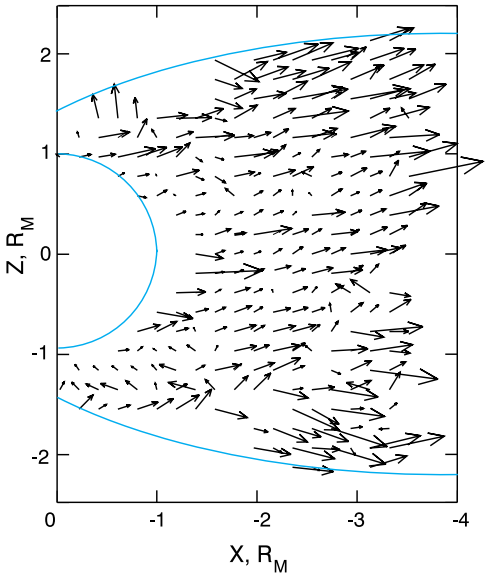

Fig. 6 XZ projections of the velocities of energized oxygen ions ($E_i \geq 50$ eV) within the Martian magnetosphere plotted from the data obtained during the period 2007–2008

MSO coordinates have shown that the whole cross-section of the Martian tail is indeed filled by escaping planetary plasma (Fig. 6) which looks similar to a draped comet-like outflow of modestly energized ions (Lundin et al. 2008b; Dubinin et al. 2008b). But it will be shown below that a global flow pattern for the steady solar wind and IMF conditions is well organized by the motional electric field which splits the tailside plasma into different plasma reservoirs with different energization mechanisms operating therein.

Figure 7a shows the distribution of the tailward fluxes of planetary ions with $m/q \geq 14$ and energies $E_i \geq 30$ eV based on a statistical survey for 2004–2006 (Barabash et al. 2007a; Fedorov et al. 2008). Authors used the IMF coordinate system which is most meaningful for the study of solar wind interaction with planets like Mars or Venus having draped magnetospheric configurations. This system has the $X^\star$-axis antiparallel to the upstream solar wind flow and $Y^\star$-axis along the cross-flow magnetic field component of the IMF. Then the motional electric field $\boldsymbol{E} = -\boldsymbol{V}_{sw} \times \boldsymbol{B}_{IMF}$ is always along the $Z^\star$-axis. Such a system was successfully used in previous studies (Dolginov et al. 1981; Saunders and Russell 1986; Yeroshenko et al. 1990; Dubinin et al. 1996b). Since there is no magnetometer on MEX the only way to get information about the IMF was the Mars Global Surveyor (MGS) measurements at the dayside, at 400 km altitude. Assuming that the clock-angle of the IMF is not changed while the IMF field lines are draped around Mars the proxy direction of the cross-flow component could be inferred. It can seen that most of fluxes are confined in the plasma sheet with a modest contribution in the boundary layer/mantle. Such a map generally resembles the distribution of planetary ions in the Martian tail from Phobos-2 (compare with Plate 2 from Dubinin et al. 1996b), but now, after the extended Mars Express survey, much better statistics are available. The ion escape through the tail shows a very asymmetric distribution which is controlled by the motional electric field (Barabash et al. 2007a; Fedorov et al. 2008, 2011).

The estimated escape rate of oxygen (atomic and molecular) was $\sim 3 \times 10^{23}$ s^{-1} (Barabash et al. 2007a) which is about 50 and 17 times lower than the rates reported by Lundin et al. (1989) and Verigin et al. (1991), respectively, from Phobos-2 taking data during solar maximum while the MEX data are taken close to or at solar minimum (recall

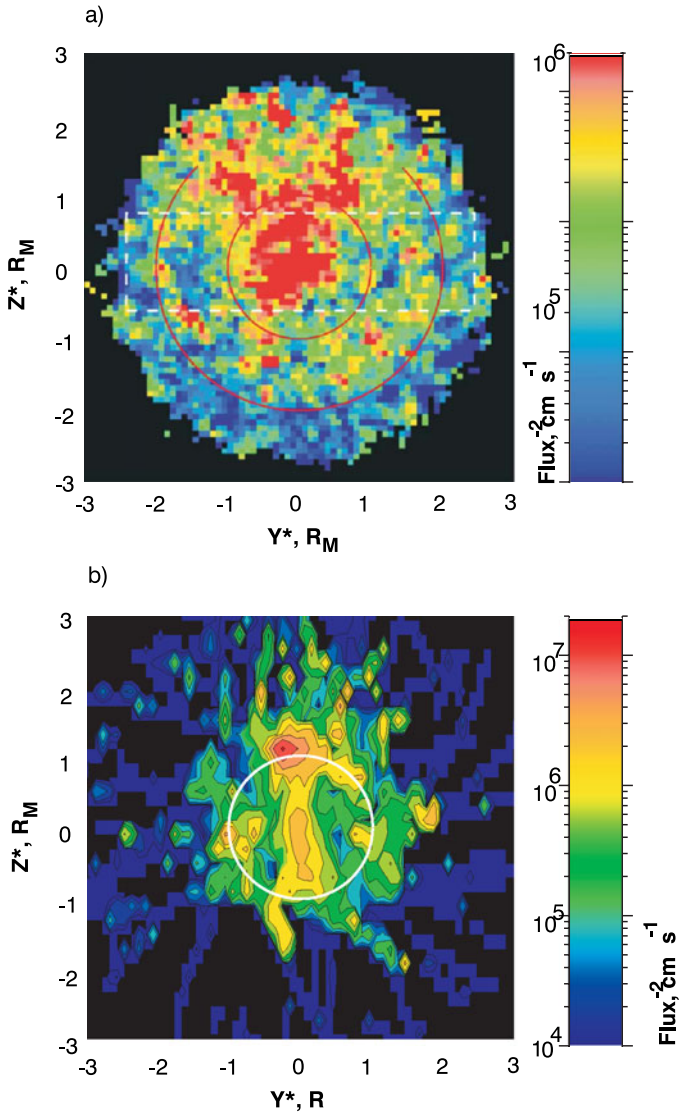

Fig. 7 Distributions of tailward fluxes of planetary ions with $m/q > 14$ in the Y^*Z^* plane, in the Martian tail. (**a**) The data accumulated for the period 2004–2006. (**b**) After a new patch uploaded in May 2007 the performance of the instrument was significantly improved enabling measurements of ion components with lower energy ($E_i \geq 10$ eV) (after Barabash et al. 2007a; Fedorov et al. 2008, 2011)

here that the difference in estimates by Lundin et al. (1989) and Verigin et al. (1991) was caused by the different assumptions on the escape geometry and the differences in the low energy threshold between the ASPERA and TAUS instruments). Another possible reason for a difference between the Phobos-2 and MEX data might be also related to energy range of the measurements. The study by Barabash et al. (2007a) was focused on the observations of tailward fluxes of modestly accelerated ions ($E/q \geq \sim$30–50 eV). Observations made after May 1, 2007, when the new energy table was uploaded, show that the lower energy

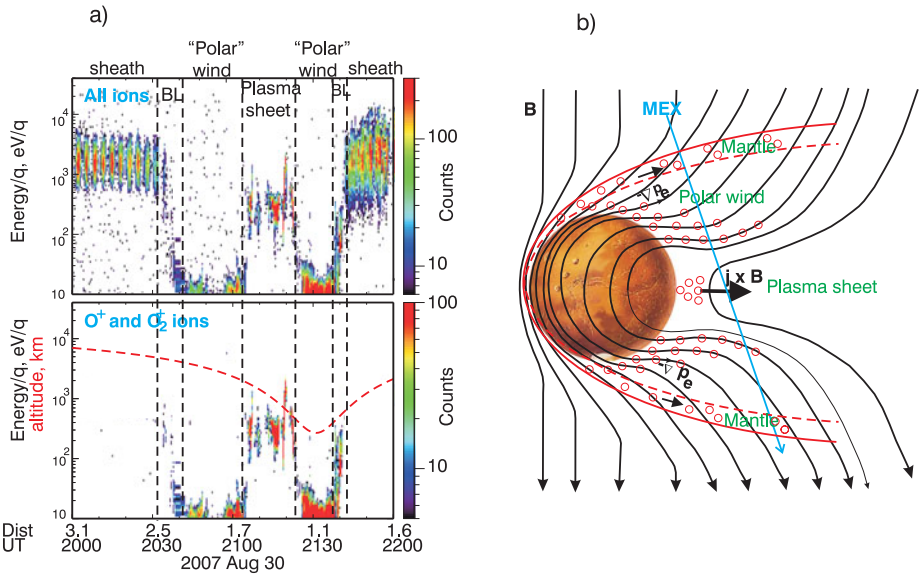

Fig. 8 (**a**) Energy-time spectrograms of ions measured by ASPERA-3 on Mars. The main escape channels: mantle, magnetic lobes filled by polar wind ionospheric ions, and plasma sheet can be clearly seen. (**b**) Sketch of the induced magnetosphere illustrating the topology and driving forces for ion escape in these channels

component significantly contributes to the total escape rate (Fig. 7b, Fedorov et al., private communication). The data are again organized in the IMF reference frame. Since the MGS spacecraft shut down in November 2006 a more sophisticated approach, based on the identification of plasma sheet from the electron measurements, was applied to retrieve this map. It is observed that the tail lobes which were almost empty in the previous study are now filled by cold/low energy ions escaping the planet.

Mean energies of planetary ions occur different in different regions of the induced Martian magnetosphere. Correspondingly, the escape fluxes are also different. The energy-time spectrogram of ion fluxes measured by ASPERA-3 when MEX crossed both lobes of the magnetail (Fig. 8) illustrates the morphology of the escape channels and the energization of planetary ions there. The magnetosphere is bounded by the boundary layer (plasma mantle) adjacent to the magnetosheath filled by shocked solar wind. The mean ion energy in the boundary layer gradually decreases from several hundreds of eVs to tens of eVs when approaching the lobes (see also Fedorov et al. 2006). The lobes of the tail are filled by low-energy atomic and molecular oxygen ions. In the center of tail, ions are again energized up to several hundreds of eV forming the plasma sheet separating two magnetic field lobes.

Although the magnetic topology of the Martian magnetosphere is very different from the topology of the Earth's magnetosphere, there is a similarity between both when looking at the escape routes. Since the ionospheres of Mars and Venus are often magnetized, at least, in solar minimum period, and threaded by the interplanetary magnetic field lines (Acuña et al. 1998; Dubinin et al. 2008a, 2008b; Luhmann 1986; Zhang et al. 2008) an outflow of ionospheric ions along the field lines driven by ambipolar electric fields like for the Earth polar wind (Banks and Holzer 1968) is expected. The plasma sheet is another important channel for transportation of planetary plasma in both types of magnetospheres. An analogue to the boundary layer on Mars and Venus can be also found on Earth. For example, the Earth plasmasphere undergoes erosion by enhanced magnetospheric circulation and the detached

ionospheric plasma is transported out of the inner magnetosphere toward the low latitude boundary layer where it is dragged by solar wind. Below we will try to classify different escape routes and energization processes which operate therein.

4 Main Escape Channels

4.1 Polar Wind

Hartle and Grebowsky (1990) have assumed that the upward fluxes of light ions in the ionospheric holes observed by PVO at Venus are driven by the electric field associated with the thermal and magnetic field pressure gradients along the magnetic field tubes: $E = -\nabla p_e/n_e e - \nabla B^2/8\pi n_e e$. Their analysis has shown that the electric field is sufficient to accelerate H^+ ions up to escape energies resulting in loss rates of 7×10^{25} s^{-1}. Ambipolar electric fields arising due to escape of ionospheric electrons along the field lines can also lead to extraction and acceleration of low-energy ions on Mars. Indirect evidence of polar wind on Mars and Venus was obtained from the observations of CO_2 photoelectrons far in the Martian and Venusian tails (Dubinin et al. 2006b; Frahm et al. 2006b; Coates et al. 2010). Photoelectron energy peaks at ~23–28 eV arising due to the absorption of the strong He II line at 304 Å in the carbon dioxide or oxygen dominated atmospheres of Mars and Venus (Mantas and Hanson 1979) were used for tracing of polar wind.

The magnetic connectivity between the dayside ionosphere and the distant regions in the tail, where CO_2 photoelectrons were recorded, is also confirmed by simulations (Liemohn et al. 2006a). Using the kinetic transport code for superthermal electrons developed for the Earth, Liemohn et al. (2006b) have calculated the expected characteristics of the high-altitude atmospheric photoelectrons. which are in a reasonable agreement with the observations. Statistics of their occurrence is shown in Fig. 9 (see also Fig. 12 in Dubinin et al. 2006b). Photoelectrons occupy a large region which approximately coincides with the magnetic pile-up region (MPR) adjacent to the induced magnetospheric boundary. Frahm et al. (2010) have estimated the escape fluxes of these photoelectrons as $\sim 4 \times 10^6$ cm^{-2} s^{-1} and the total losses to match the escape of the suprathermal electrons to be 3×10^{23} s^{-1}. Since only 'peaked' electrons could be traced and referred to polar wind, this value should be regarded only as the lower limit of polar wind losses.

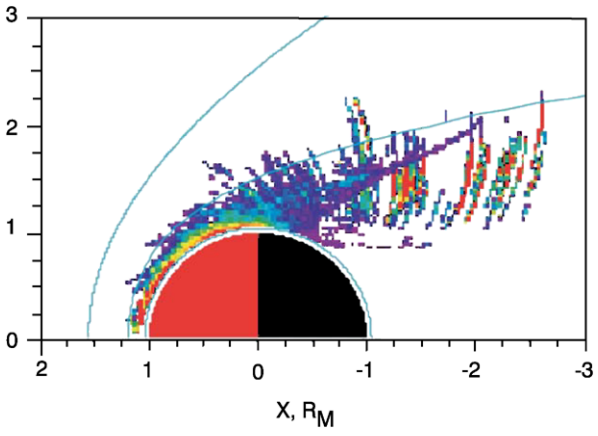

Fig. 9 Fractional occurrence of atmospheric photoelectrons illustrating the existence of polar wind on Mars (after Frahm et al. 2006a, 2006b)

Presently, there is not yet an adequate theory of 'polar wind' on Mars and Venus. Such a theory must include (a) the multi-ion composition of the topside ionosphere (the presence of gravitationally bounded heavy ion components increases the ambipolar electric field), (b) photochemistry and transport processes in the upper ionosphere, (c) entry of magnetosheath electrons along the field lines (which can also lead to increase in extraction of oxygen ions), (d) suprathermal photoelectrons in the sunlit hemisphere (their escape leads to an increase in the ambipolar electric field and polar wind outflow velocities), (e) a finite time of convection of the magnetic flux tubes through the ionosphere imposing the constraints on loss fluxes, (f) energization by wave absorption.

Observations of photoelectrons can be used not only for tracing. A shift of their energy peaks provide us with an estimate of the spacecraft potential which reaches up to -9 V in a dense ionospheric plasma. This implies that low-energy ions ($E_i \sim 10$ eV) measured by IMA/ASPERA-3 comprise to the core distribution accelerated in the floating voltage drop. Analyzing the effect of the field-of-view offset of the IMA instrument, ion trajectories influenced by the spacecraft motion and its charging Fraenz et al. (2010) have found a reasonable fitting between the measurements of the cold ion component by IMA and the measurements of the total electron density from the frequency of electron plasma oscillations detected by MARSIS. Moreover, it was shown that the ionospheric plasma at the altitudes $\geq$300 km is not in a rest but is moving tailward. Horizontal transport of the ionospheric plasma from the dayside to the terminator region and further to tail is also confirmed by the measurements of the altitude profiles of the electron number density (Duru et al. 2008). While in the photo-chemical equilibrium region the densities decrease with increasing solar zenith angle as $\cos^{1/2}$(SZA), at higher altitudes ($\geq$300 km) the densities are almost independent of solar zenith angle.

This motion might be the result of (a) the manifestation of polar wind, (b) trans-terminator ionospheric flow from day to night side driven by day/night asymmetry in the thermal pressure (Knudsen et al. 1980), (c) cometary-like tailward expansion driven by the magnetic field tensions, (d) wave acceleration (Lundin et al. 2011). Probably all these mechanisms contribute to the bulk ion motion in the top-side ionosphere of Mars. Figure 10 shows that low-energy ($10 \leq E_i \leq 50$ eV) oxygen ions are observed almost at all distances from Mars sampled by the MEX spacecraft within the induced magnetosphere. Estimate of the total losses which takes into account the field-off-view offset yields $\sim 3 \times 10^{25}$ s^{-1} (Fraenz et al. 2010) that is approximately one order of magnitude higher than the escape fluxes evaluated by Lundin et al. (2008a, 2008b). In this respect the MARSIS measurements in the tail

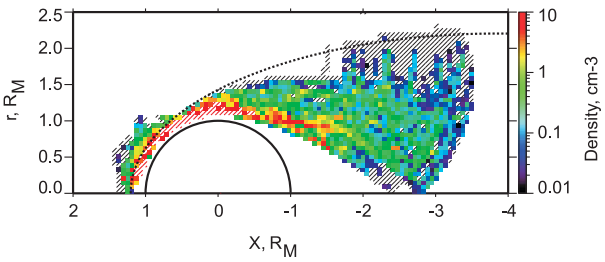

Fig. 10 Map of 2D number densities of low-energy ($E \leq 50$) oxygen ions at Mars. The color-coded values are maximum densities measured over 0.06×0.06 R_M bins in cylindrical coordinates. Since the measurements have been made without elevation scanning ($6^\circ \times 360^\circ$) the data provide us only with a qualitative picture. The total number densities might be significantly higher (see e.g. Fraenz et al. 2010). Despite of the absence of 3D measurements the observations clearly demonstrate an expansion of cold/low energy planetary plasma into the tail

would be vitally important for assess in the escape of the cold ionospheric component which might be missed by particle spectrometers.

The PVO observations on Venus have also shown that the trans-terminator ionospheric flow persists further at the nightside but becomes increasingly filamentary with distance downstream. Ions gain sufficient energies ($E_i \sim 9$–16 eV) for escape. Brace et al. (1987) have estimated the loss rates of the ionospheric material from Venus to be 5×10^{25} s^{-1}.

4.2 Plasma Sheet

Figure 11 shows how energy of ions varies when MEX goes from the lobes filled by polar wind ions to the plasma sheet and back to the lobes. Since the $\boldsymbol{j} \times \boldsymbol{B}$ force due to the magnetic shear stresses of the draped field lines is the strongest in the center of tail, the energy gradually increases, reaches maximum and then again decreases. Such a bell-like shape of energy variation can be easily explained. If the magnetic field across the current sheet varies as $B_x \sim \tanh(y/\delta)$, where y and δ are the distance of MEX to the center and the width of the plasma sheet, respectively, then the tangential forces $(\boldsymbol{B} \cdot \nabla)\boldsymbol{B}$ and the energy of accelerated ions will vary with distance as $\frac{1}{\cosh^2(y/\delta)}$ (dotted curve in Fig. 11) (see also Dubinin et al. 1993).

Since the magnetic tensions on the nightside are determined by pile-up of the field lines at the dayside, which in their turn vary with solar wind dynamic pressure, the energy gained by ions in the plasma sheet also changes with solar wind variations. Figure 12 compares the variations in solar wind dynamic pressure with the velocities and temperatures of O^+ and O_2^+ ions in the center of the plasma sheet. The results confirm the hypothesis of a chain of processes whereby the solar wind momentum (black symbols on the top panel of Fig. 12) is transferred to the magnetic field pressure on the dayside (blue symbols) and then via the magnetic field stresses on the night side to the momentum of planetary ions $n_{sw} m_{sw} V_{sw}^2 \Rightarrow B^2/2\mu_o \Rightarrow n_M m_M V_M^2 + n_M T_M$. Here m_{sw}, n_{sw}, V_{sw} and m_M, n_M, V_M are the masses, number densities and velocities of solar wind protons and plasma sheet ions, respectively. T_M is the ion temperature in the energy units. Comparison of the observed energies of oxygen ions E_M in the plasma sheet and the values inferred from the simple expression $E_M \sim \frac{2k P_{dyn}}{n_M}$, where P_{dyn} is solar wind dynamic pressure, and k is the efficiency of the momentum transfer, gives a reasonable agreement at $k \approx 0.1$. Note that the above expression can be easily obtained.

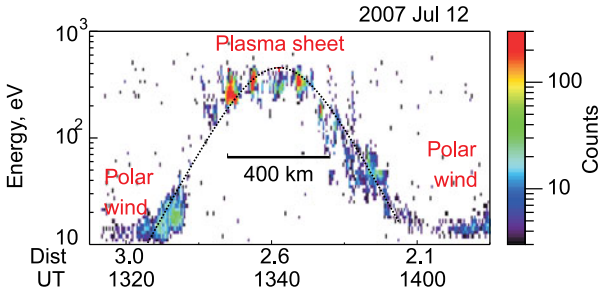

Fig. 11 Transition from lobes to the plasma sheet is characterized by ion acceleration driven by the magnetic field tensions. The imposed *dotted curve* shows that a bell shaping of the energy gain is well described by the function $\sim \frac{E_{peak}}{\cosh^2(y/\delta)}$, where E_{peak} is the peak energy in the center, and $\delta = 200$ km, which exemplifies how the magnetic stresses vary across the current sheet

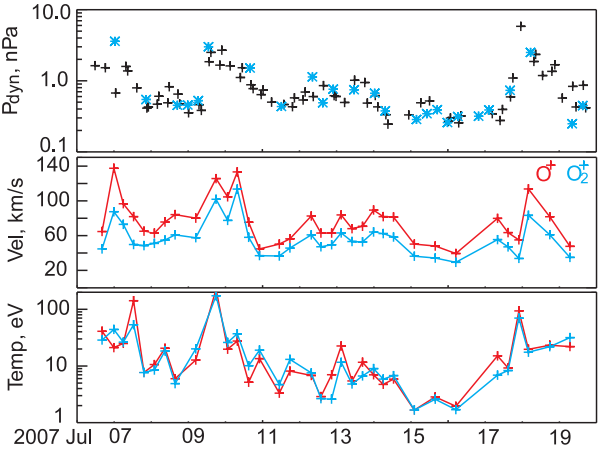

Fig. 12 Bulk speed and temperature of oxygen ions in the center of the plasma sheet vary with the dynamic pressure of the incoming solar wind. *Black and blue symbols* on the top panel show the observed values of the dynamic pressure and the peak values of $B^2/8\pi$ in the magnetic barrier on the dayside inferred from the ASPERA-3 and MARSIS measurements, respectively

Indeed, the equation of a force balance

$$\frac{1}{2} n_M m_M \frac{dV_M^2}{dx} = -\nabla \frac{B_{tail}^2}{\mu_o} \tag{6}$$

(factor 2 at the right hand side appears due to addition of the normal and tangential magnetic tension forces) yields $n_M E_M \sim B_{tail}^2/\mu_o$. Since $B_{tail} \sim 3B_{sw}$ (Crider et al. 2004) and $P_{dyn} = B_{mb}^2/2\mu_o$, where B_{mb} is the magnetic field in the magnetic barrier at the dayside, then using $B_{mb} \sim 10B_{sw}$ we come to the above expression with $k \sim 0.1$.

Correspondingly, for two sorts of ions (O^+ and O_2^+) in the plasma sheet the above equation is modified:

$$n_{O^+} E_{O^+} + n_{O_2^+} E_{O_2^+} = 2k m_{sw} n_{sw} V_{sw}^2. \tag{7}$$

Here we neglected thermal pressures of extracted and accelerated O^+ and O_2^+ ions which are smaller than their bulk momentums. This equation can be also written in the form:

$$m_{O^+} f_{O^+}^2/2 + m_{O_2^+} f_{O_2^+}^2/2r = 2k m_{sw} f_{sw}^2 n_{O^+}/n_{sw}, \tag{8}$$

where f_{O^+}, $f_{O_2^+}$ and f_{sw} are fluxes ($n_i V_i$) of atomic and molecular oxygen ions in the center of plasma sheet, and protons in solar wind, respectively, n_{sw} is the number density of the solar wind protons and $r = n_{O_2^+}/n_{O^+}$. Then using $E_{O_2^+} \approx E_{O^+}$ (the energies of the atomic and molecular oxygen ions occur approximately equal since they are accelerated by the Hall electric field) yields that the escape flux through the plasma sheet is proportional to the solar wind flux,

$$f_{O^+} \sim f_{sw} \left(4k \frac{n_{O^+}}{n_{sw}} \frac{m_{sw}}{m_{O^+}} \right)^{1/2} \frac{1}{(1+r)^{1/2}}, \qquad f_{O_2^+} \sim f_{O^+} r/\sqrt{2}.$$

Comparison of the observed fluxes ($E_i > 50$ eV) and values inferred from the above expressions gives a reasonable agreement (Fig. 13) supporting the above scenario of particle energization and escape in the plasma sheet. It is also important that ion fluxes in the plasma sheet vary at $\geq$10 times in response to solar wind variations.

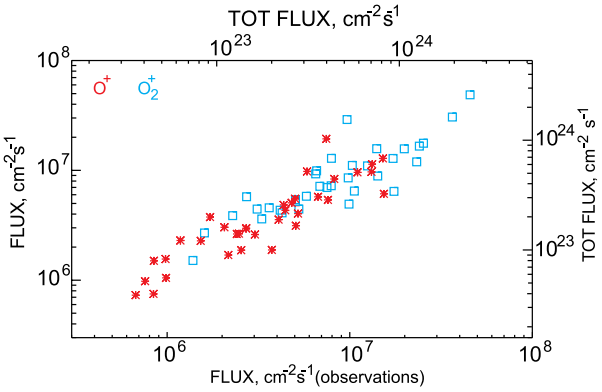

Fig. 13 Comparison of the observed fluxes of oxygen (O^+ and O_2^+) ions in the center of the plasma sheet and values inferred from a model

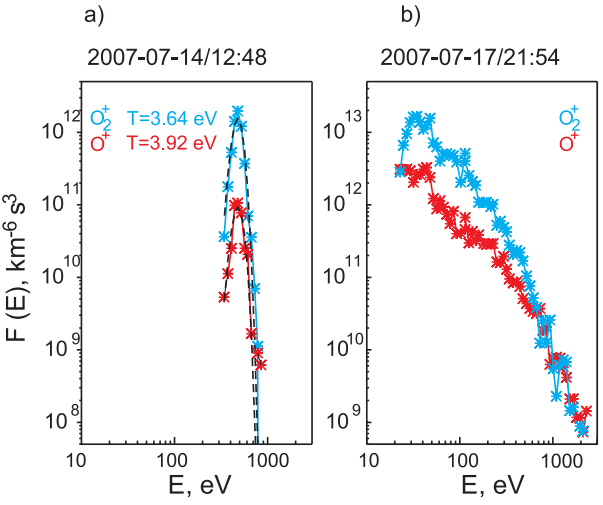

Fig. 14 Examples of distribution functions of oxygen ions in the plasma sheet

For nominal solar wind dynamic pressure ion beams in the plasma sheet are usually very cold ($T_i \leq 5$ eV). With increase in P_{dyn} the temperature increases implying that a part of the momentum is transferred to ion heating (see Figs. 12, 14).

McComas et al. (1986) have suggested a similar $\boldsymbol{j} \times \boldsymbol{B}$ acceleration model for Venus and calculated a map of the forces and speeds as a function of distance. The magnetic forces push plasma toward the center and accelerate it tailward. McComas et al. (1986) have estimated the escape flux of oxygen ions through the plasma sheet of Venus to be 6×10^{24} s^{-1}. However, the PVO spacecraft carried a limited plasma analyzer, and more comprehensive plasma measurements in the plasma sheet were made only recently on VEX.

Maps of O^+, He^+ and H^+ fluxes and energies of these ions in the Venus tail are shown in Fig. 16 (Barabash et al. 2007b). The data organized in the IMF reference system using the simultaneous measurements of magnetic field show a well-ordered distribution with major fluxes in the central tail. Figure 17 shows the velocity map of O^+ ions in the X^*Y^* plane of the same frame. The plasma sheet with accelerated ions streaming tailward ions is clearly seen.

Fedorov et al. (2011) have used the superposed epochs technique to estimate the total loss rates of different ion species with energies $E_i \geq 10$ eV through the Venus tail during solar

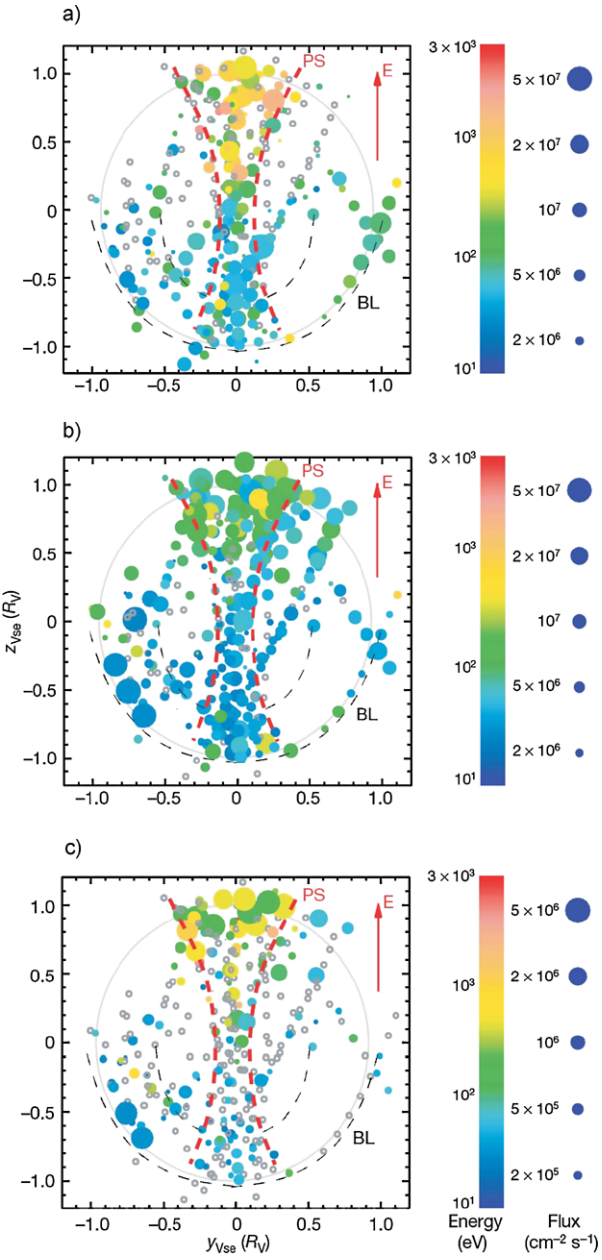

Fig. 15 Maps of the measured O^+ (**a**), H^+ (**b**) and He^+ (**c**) fluxes in the tail of Venus (after Barabash et al. 2007b)

minimum conditions in 2006–2007. The rates are $Q(H^+) = 7.1 \times 10^{24}$ s^{-1}, $Q(He^+) = 7.9 \times 10^{22}$ s^{-1}, $Q(O^+) = 2.7 \times 10^{24}$ s^{-1}. The ratio of hydrogen and oxygen escape was observed to be ~1.9–2.9, i.e. rather close to the stoichiometric ratio corresponding to water (Barabash et al. 2007b; Fedorov et al. 2011). The fluxes are still less than the values estimated from the PVO data for the solar maximum (5×10^{25} s^{-1}, Brace et al. 1987). It is also worth noting that Brace et al. (1987) have assumed that escape went on through the entire cross-

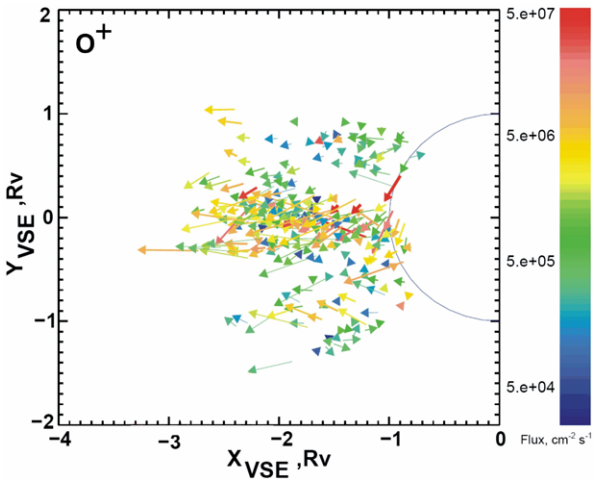

Fig. 16 Map of the velocities of O^+ ions in the tail of Venus (after Fedorov et al. 2011). The length of each vector is proportional to the velocity vector. *Color shows* the flux

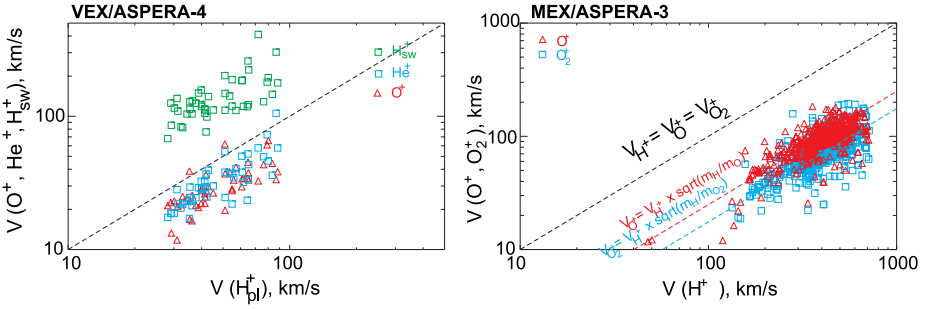

Fig. 17 (**a**) Relationship between the bulk speeds of planetary protons and solar wind protons, oxygen and helium ions in the Venusian boundary layer. (**b**) Distribution of the velocities of O^+ and O_2^+ ions as a function of the proton velocities accumulated over 50 MEX orbits across the Martian boundary layer. Velocities of different species are roughly proportional to $\sqrt{m_p/m_M}$, where m_p and m_M are the masses of the protons and planetary ions, respectively

section of the Venus disk while the calculations by Fedorov et al. (2011) show that they are inhomogeneous but well organized.

4.3 Boundary Layer/Mantle

The boundary layer is a region where the momentum lost by the solar wind is coupled to the planetary plasma. A coupling occurs via the normal and tangential magnetic field stresses and (or) anomalous processes of plasma transport (anomalous diffusion and viscosity). The existence of boundary layers on Mars and Venus was already observed in the first space missions (Vaisberg et al. 1976; Spenner et al. 1980; Taylor et al. 1981; Kaspzak et al. 1982; Vaisberg and Zelenyi 1984; Vaisberg et al. 1995). These observations have identified slow and heavy planetary plasma moving tailward in the intermediate transition between the magnetosheath and the ionosphere. Vaisberg et al. (1995) have interpreted a confinement of accelerated planetary ions in the boundary layer by their specific trajectories in the shear velocity layer. Test particles launched into such a configuration and moving in mutually perpendicular electric and magnetic fields field were con-

fined in the boundary layer for a long distance. Their maximum velocity was close to the flow velocity of the magnetosheath plasma. Similar trajectories of test oxygen pick-up ions launched into the field pattern inferred from the MHD model were also observed in global simulations (Luhmann et al. 2006). Later the boundary layer on Mars was comprehensively studied using ion composition measurements on the Phobos-2 spacecraft (Rosenbauer et al. 1989; Lundin et al. 1990a, 1990b, 1991; Lundin and Dubinin 1992; Dubinin et al. 1996b).

Recent MEX and VEX observations also show the importance of boundary layers for ion energization and escape. For example, in Fig. 16 besides the ions streaming tailward in the plasma sheet, oxygen fluxes in the boundary layer are clearly seen.

Solar wind plasma, which enter a boundary layer, is decelerated by the $\boldsymbol{j} \times \boldsymbol{B}$ forces at the magnetic barrier. Since ions are not magnetized on such scales they respond only to polarization electric fields. Observations of a gradual deceleration of the solar wind ions in the boundary layers (see, e.g. Fig. 8) can be interpreted as their retardation while entering the magnetic barrier with outward pointing electric field. In contrast, a local planetary plasma gain energy by passing through this potential drop. Some fraction of ions enter the magnetosheath and gain more energy in the motional electric field. A differential streaming of solar wind and planetary ions also leads to the appearance of $\Delta \boldsymbol{V} \times \boldsymbol{B}$ forces. Interplay of these two driving forces makes interpretation of multi-ion dynamics in the boundary layer more difficult.

In some cases differential streaming is observed even for the same sort of ion species. Figure 17a shows an example of the relationship between the bulk speeds of the planetary protons (H^+_{pl}) and O^+, He^+ and protons of solar wind origin (H^+_{sw}) in the Venusian boundary layer. Planetary protons move faster than oxygen and helium ions but slower than the solar wind protons.

Differential streaming of different ion species is also observed in the Martian boundary layer (Fig. 17b). Atomic and molecular oxygen ions move slower than protons. Their bulk speeds are grouped around the lines $V_{O^+} = V_{H^+}\sqrt{m_H/m_O}$ and $V_{O_2^+} = V_{H^+}\sqrt{m_H/m_{O_2}}$, implying that O^+ and O_2^+ ions gain approximately the same energy.

Ion populations moving with different velocities with respect to the net center of charge experience different electric fields. In effect, the different ion fluids intermittently gain or lose energy while exchanging their momentum. As a result plasma in the boundary layer is often striated consisting of alternating bunches of solar wind protons and oxygen ions. Figure 18 shows an example of such a structuring of the Martian boundary layer when the ion sensor has operated in the 'fast' mode providing the 2D bulk parameters with 12 s resolution. It is seen that a periodic acceleration/deceleration of the oxygen ions is accompanied by deceleration/acceleration of solar wind protons. Correspondingly, the plasma distribution is also stratified by different species. Such large amplitude 'bi-ion' waves were observed on Phobos-2 too (Dubinin et al. 1996a).

The interface between the magnetosheath and ionospheric plasmas is also a site for possible fluid-like MHD instabilities (Wolff et al. 1980; Dubinin et al. 1980; Elphic and Ershkovich 1984; Thomas and Winske 1991; Arshukova et al. 2004). The observations of the surface waves near the Venusian ionopause and detached clouds of ionospheric plasma in the magnetosheath (Brace et al. 1982) confirm this suggestion. Plasma clouds are transported to the tail and escape the ionosphere. Using some assumptions about their geometry and velocities, Brace et al. (1982) have estimated the loss rate of the dayside ionosphere to be $\sim 1.7–7 \times 10^{26}$ s^{-1}. Note, that these values are higher than the total escape rates (5×10^{25} s^{-1}) reported by Brace et al. (1987) using the PVO measurements downstream

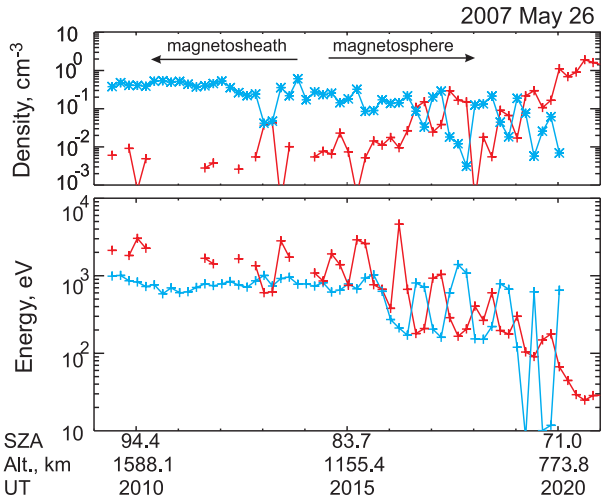

Fig. 18 Fine structure of the boundary layer on Mars. *Red* and *blue symbols* correspond to O^+ and H^+, respectively. MEX is approaching Mars and observes alternating structures dominated either by solar wind protons or planetary ions

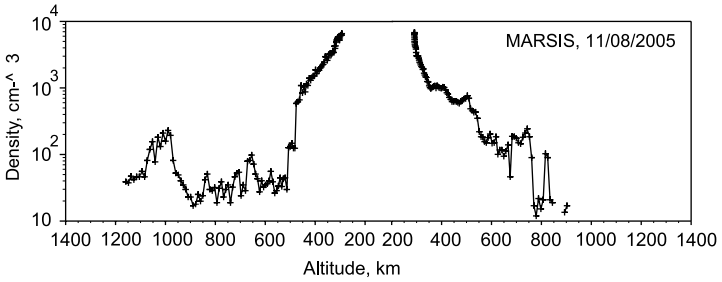

Fig. 19 Example of plasma clouds in the transition region of Mars

in the tail. The remaining trans-terminator flux appears responsible for the production of the nightside Venus ionosphere.

Similar 'detached' structures are observed on the electron density profiles inferred from the radar sounding experiment MARSIS onboard MEX. Figure 19 presents an example of n_e along the MEX orbit. Although the measurements were made only at altitudes $\leq$1300 km plasma clouds in the interface region between the magnetosheath and the ionospheric plasmas are clearly seen. The differential potential measurements of the electron density enhancements made at much higher altitudes ($\sim 6R_M$) (Pedersen et al. 1991) support the assumption that such plasma structures are detached and removed from the ionosphere.

The MARSIS data also show the existence of large-amplitude fluctuations in the electron number density in the upper ionosphere of Mars, sometimes as much as a factor of three or more (Gurnett et al. 2010). These wave-like structures are very similar to the ones observed on Venus (Brace et al. 1982). The amplitude of fluctuations reaches very high levels ($\delta n_e/n_e \sim 1$) at altitudes of 400 km and above and decreases with decreasing altitude. The Kelvin-Helmholtz (K-H) instability due to velocity shear between the solar wind and the ionopause is one of the candidates to explain these observations on Mars and Venus. The estimates of losses of O^+ ions in detached plasma clouds, formed at the nonlinear stage of the K-H instability on Mars yield escape rates of $0.2–3.0 \times 10^{24}$ s^{-1} (Penz et al. 2004).

The observations of large density fluctuations near the sub-solar region, where the conditions for K-H instability are not favorable, assume also the existence of other type of MHD instabilities. Among possible candidates we mention the modified Rayleigh-Taylor instability for plasma with unmagnetized ions (Hassam and Huba 1987; Dubinin et al. 1996a) which is driven by the ion acceleration in the Hall electric field where $\boldsymbol{E} \cdot \nabla n < 0$.

Another probable mechanism for collisionless momentum coupling between interpenetrating plasmas in the boundary layers could be plasma instabilities driven by the relative motion of ions and electrons. For example, ion-ion instabilities can provide anomalous friction between two plasmas (Papadopoulos et al. 1971). The 'modified two-stream-instability', which is, in fact, an electron-ion instability can also lead to the momentum exchange between different ion components since the friction between electrons and ions affects the other fluid component via the quasineutrality condition (McBribe et al. 1972). The instability is analogous to the usual Buneman two-stream instability but the velocity threshold is much lower ($V \geq V_{i,th}$), where $V_{i,th}$ is the thermal ion velocity.

For waves propagating almost perpendicular to the magnetic field, $(k_z/k) \sim (m_e/m_i)^{1/2}$ (k and k_z are the wave number and the projection of the vector $\boldsymbol{k}$ along magnetic field, respectively), the friction between electrons and ions can be large since the effective electron mass becomes comparable to the ion mass, $\bar{m_e} \sim (k_z/k)m_e \sim m_i$. Shapiro et al. (1995) have applied this mechanism to explain the characteristics of the plasma mantle on Venus. The model predicts the heating of electrons along the magnetic field and pick-up and heating of the ionospheric ion component. Dobe et al. (1999) have modified this model considering the interaction between the unmagnetized ionospheric oxygen ions extracted by the motional electric field and cold ionospheric electrons drifting in $\boldsymbol{E} \times \boldsymbol{B}$ fields. The free energy source for the instability is the solar wind flow across the magnetic field and, correspondingly, the motional electric field penetrating towards the boundary layer. The instability leads to strong deceleration of the magnetosheath protons and acceleration of planetary ions to superthermal energies. Although the observations of strong wave activity in the boundary layers of Venus and Mars (Scarf et al. 1980; Grard et al. 1989) and of electron heating (Dubinin et al. 2006b) are consistent with a friction-like interaction of two interpenetrating plasmas the role of high frequency plasma waves in the energization process needs further investigation.

4.4 Ion Pick-Up

Although the PVO measurements have identified pickup oxygen ions only indirectly, from the secondary peaks in energy (E/q) spectra, their existence in the Venusian plasma environment have been consistently shown (Mihalov and Barnes 1981; Intriligator 1989; Luhmann et al. 2006). Because of the large Larmor radius of ions their distribution was strongly asymmetrical with respect to the direction of the motional electric field in the solar wind (Intriligator 1989; Moore et al. 1990). Pickup ions form a plume in the inner part of the magnetosheath adjacent to the magnetosphere (Moore et al. 1990). This plume is well reproduced in simple test particle simulations (see e.g. Lichtenegger and Dubinin 1998) implying the exact recognition of their origin. A plume of pickup ions is also clearly observed by ASPERA-3 on MEX. Pickup ions are located both inside the magnetosphere and in the adjacent magnetosheath. Figure 20a,b shows a collection of 33 orbital segments in the inner magnetosheath with simultaneous observations of shocked protons and pickup oxygen ions. Although oxygen ions are generally streaming as the magnetosheath plasma their radial velocity is higher than the radial velocity of the protons (Fig. 21). A flux of pickup oxygen ions is strongly asymmetrical producing a plume on the magnetospheric surface (Fig. 20b). In a certain sense this plume can be regarded as an extension of the plasma

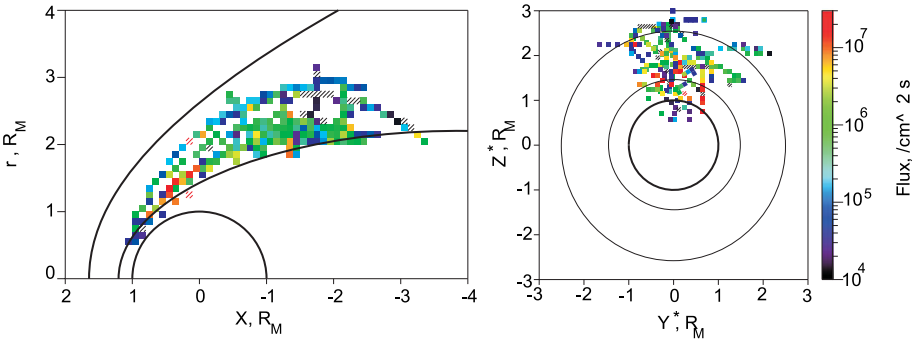

Fig. 20 (**a**) Flux of pickup oxygen ions in the Martian magnetosheath adjacent to the induced magnetosphere (cylindrical coordinates). Average positions of the magnetospheric boundary and the bow shock are shown. (**b**) The data are plotted in the IMF coordinate system. *Thin curves* show the average positions of the magnetospheric boundary and the bow shock in the terminator plane. Pickup ions form a peculiar plume on the magnetospheric surface due to asymmetry caused by the motional electric field

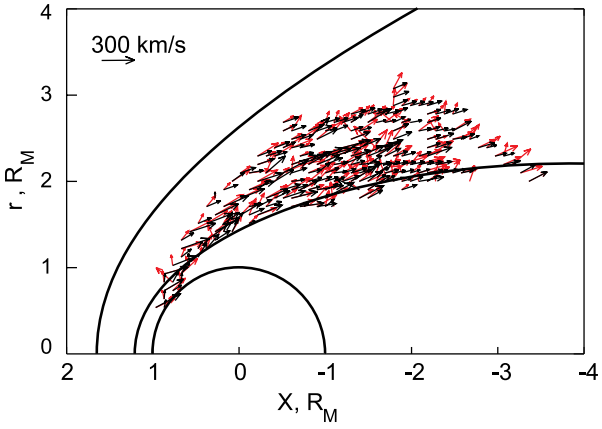

Fig. 21 Vectors of the bulk speed of the protons (*black arrows*) and oxygen ions (*red arrows*) plotted in cylindrical coordinates

sheet to the magnetosheath. The mean escape flux through such a plume is about 0.5–$1R_M \times 1R_M \times 10^6 \sim 5 \times 10^{22}$–$10^{23}$ s^{-1}.

Mass-dependent acceleration of different ion species is also a clear manifestation of the pickup mechanism. Particularly, this effect is noticeable in the plasma sheet adjacent to the boundary layer, in the hemisphere pointed in the direction of the $-\boldsymbol{V} \times \boldsymbol{B}$ electric field where planetary and solar wind ions coexist. Figure 22a shows an example of such a mass-dependent acceleration in the plasma sheet of Mars—H^+, He^{++} and O^+ ions have approximately the same speed. On Venus, the asymmetry in ion energies between the E^+ and E^- hemispheres, also favours the classical pickup process. However, the ratio of the $O^+/He^+/H^+$ energies in the plasma sheet is often not 16 : 4 : 1 as one would expect for a pure pick-up acceleration but rather about 4 : 2 : 1 (Fig. 22b).

Dubinin et al. (2006c) and McEnulty et al. (2010) have found a linear dependence of pick-up ion energy on distance which might be attributed to acceleration in an electric field (Fig. 23). The required electric fields are close to the typical values of the motional electric field. Enhancements in the motional electric field due to, for example, a passage of interplanetary disturbances (ICME) increase the ion energy gain. The $E^+ - E^-$ asymmetry in

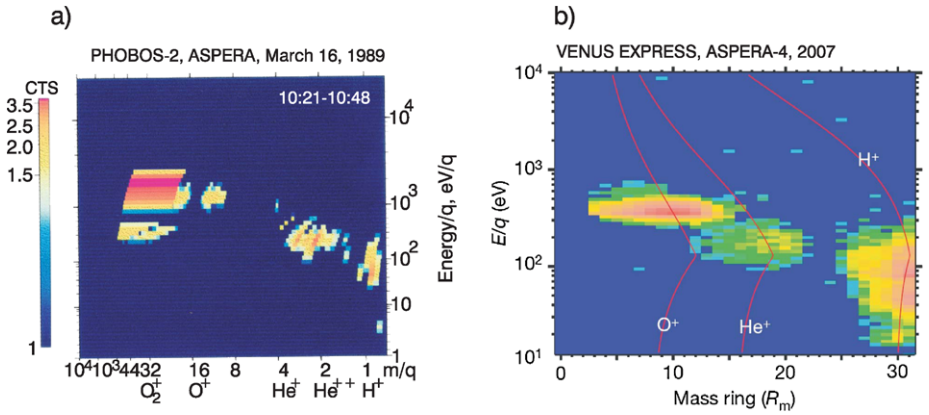

Fig. 22 Mass-dependent acceleration in the plasma sheet on Mars and Venus observed from the energy–mass matrices accumulated by ASPERA-1 and ASPERA-4 onboard Phobos-2 and VEX, respectively (from Phobos-2 data and Barabash et al. 2007b)

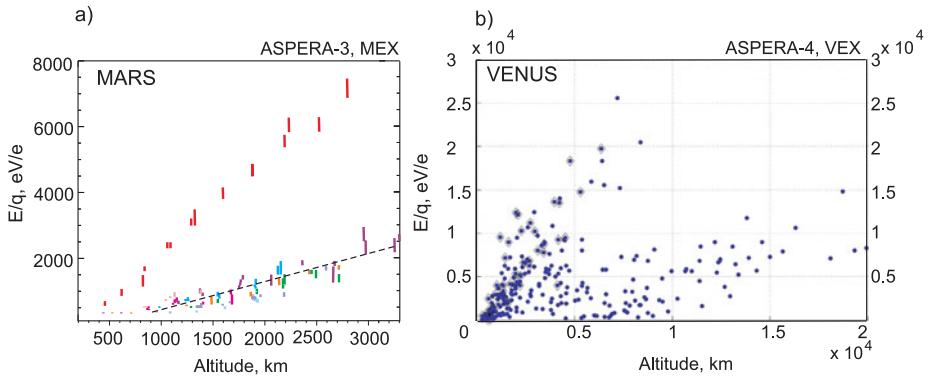

Fig. 23 (**a**) Energy of oxygen ions as a function of altitude for nine MEX orbits. *Different color* shows different orbits. The electric field inferred from these observations is close to the typical value (∼1 mV/m) of the motional electric field in solar wind. A group of the data points apart from the main cluster data corresponds to an extreme solar event. (**b**) Pick-up ions near Venus plotted in energy and altitude coordinates. *Diamond symbols* correspond to the observations during an ICME event in the solar wind (after Dubinin et al. 2006c and McEnulty et al. 2010)

escape fluxes (Nilsson et al. 2010) and ion energy in the plasma sheet (Fedorov et al. 2008) is also the manifestation of the protruded motional electric field inside the induced magnetospheres.

Note, that we use the expression 'protrusion (penetration) of electric field' only to make things clearer. Actually the electric field is produced by a bulk plasma flow across the magnetic field, which is driven by the $\boldsymbol{j} \times \boldsymbol{B}$ forces i.e. by the magnetic field tensions (Vasyliunas 2001), and can not be simply projected to the ionosphere because of polarization fields in a dense planetary plasma.

It is worth noting that test particle simulations which often use the field distributions from the empirical or MHD models (e.g. Luhmann and Schwingenschuh 1990; Lichtenegger et al. 1995; Luhmann et al. 2008) often fail to reproduce some observational

features of oxygen fluxes within the induced magnetospheres. Indeed, Moore et al. (1991) have shown that in the 3D hybrid simulations oxygen ions originating deep within the magnetic barrier behave in a fluid fashion while ions originating at higher altitudes where their number densities are much lower can be treated as test particles moving on cycloidal trajectories. The key question of the transition from a classical pickup to a fluid-like motion needs further investigation.

4.5 Bursty Energization and Escape

Wavy behavior of plasma is a typical feature of the Martian space. This phenomenon is revealed during the time periods when IMA is operating with a high temporal resolution (12 s). Bursts of tailward streaming ions are observed not only in the boundary layer where solar wind and planetary plasmas are in a direct contact but also in the magnetosheath (see e.g. Winningham et al. 2006) and deep inside the magnetospheric cavity. A bursty dynamics is clearly exposed in Fig. 24 which shows periodic jets of accelerated oxygen ions in the Martian tail. Accompanying strong variations in the electron fluxes show that the bursts are not related to possible field-of-view offset of the instrument. The amplitude of flux variations reaches a factor of 10–30. Frequency of oscillations is about 15 mHz which is close to the oxygen gyrofrequency in the magnetic field $B \sim 15$ nT.

There are several possible mechanisms which can be responsible for the observed periodic bursts. Large-amplitude coherent pressure pulses generated upstream the bow shock by ion beams (Mazelle et al. 2004) impact the magnetosphere and produce periodic pulses in forces pushing planetary plasma tailward. Pressure pulses can also arise downstream the bow shock—in the magnetosheath, which becomes to be decomposed into a sequence of periodic compressive waves (Winningham et al. 2006). Figure 25a shows how compressive waves from the magnetosheath propagate to the subsolar transition region in which two plasmas come in to direct contact and the planetary plasma gradually predominates. Strong oscillations ($f \sim 50$ mHz, $\Delta n_e/n_e \sim 30\%$) are observed not only on the spectrogram of the sheath electrons but also on the total electron density profile inferred from the variations in the electron plasma frequency (ω_{pe}) measured by MARSIS. ULF waves can be transported even to the ionosphere (Fig. 25b) producing large fluctuations in the density and escape fluxes. Lundin et al. (2011) have suggested that ULF waves (3–20 mHz) penetrating into the Martian magnetosphere not only modulate the external forces but directly accelerate low-energy ions supplying polar wind. A close relationship was found between solar wind dynamic pressure, the magnetosheath ULF wave power and outflow of oxygen ions.

Wave-like dynamics can also appear due to the multiple-ion origin of plasma in the transition region. Such a plasma behaves like a specific rotator with the characteristic frequency close to the low-frequency cutoff (see e.g. Dubinin and Sauer 1999). An example of bi-ion waves was shown in Fig. 18.

In addition, K-H or other MHD instabilities probably excited in the interface region can generate surface waves which will modulate the tension forces. In Fig. 26a the total electron density (MARSIS) is plotted along the MEX trajectory in the XZ_{MSO} coordinates. The topside ionosphere occurs very fragmented consisting of intermittent cold and energized ionospheric plasmas. Tongues of ionospheric plasma alternate with penetrating tapering jets of magnetosheath plasma (Fig. 26b) resembling large-amplitude surface waves propagating on the boundary surface (Fig. 26c). Note that large-amplitude surface waves in the subsolar region also appear in hybrid simulations (Terada et al. 2002). The event was related to the

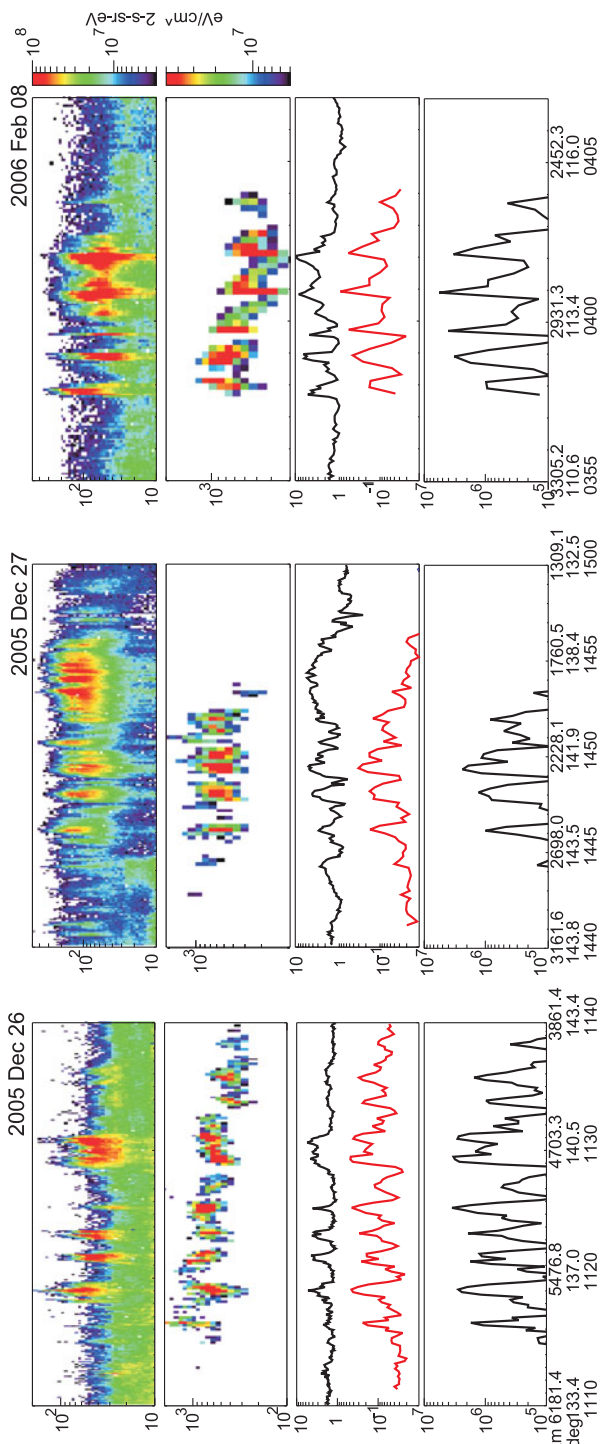

Fig. 24 Examples of bursts of accelerated and escaping oxygen ions in the Martian tail. From top to bottom are: energy-time spectrograms of electrons and oxygen ions, partial number densities of the electrons ($E = 10$–1000 eV) *(black curves)* and oxygen ions *(red curves)*, fluxes of oxygen ions

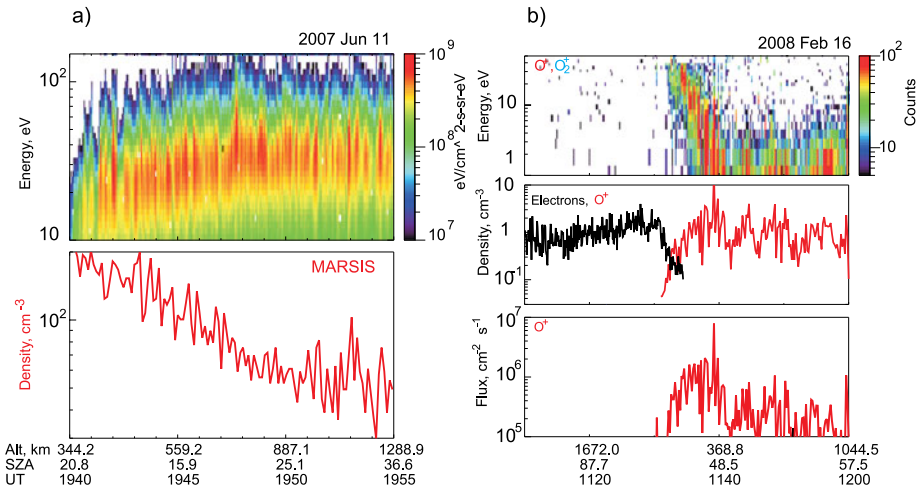

Fig. 25 (**a**) Simultaneous observations of large-amplitude compressive waves in the magnetosheath and transition region by ASPERA-3 and MARSIS instruments. (**b**) From top to bottom: spectrogram of fluxes of oxygen ions in the boundary layer and ionosphere of Mars, partial number densities of electrons and oxygen ions, fluxes of oxygen ions. Penetrating into the ionosphere ULF waves produce strong fluctuations in the density and escape fluxes

impact of a corotating interaction region (CIR) on Mars (Dubinin et al. 2009a). Simple estimates by Dubinin et al. (2009a) show that losses of the ionospheric component during such events can easily reach 2×10^{25} s^{-1}.

4.6 Protrusion of Blobs of Solar Wind and Ion Scavenging

Although the Martian and Venusian ionospheres lack a shielding by the intrinsic magnetic field, as in the case of Earth, the induced magnetic fields formed by pile-up of the IMF rather efficiently screen the ionospheres and atmospheres of these planets. The draping of the IMF increases the magnetic pressure on the dayside, just sufficiently to balance the solar wind dynamic pressure and to terminate the solar wind at a certain distance from the planets (Dubinin et al. 2008a) with the effect that only a minor fraction of solar wind enters inside the induced magnetospheric cavity. However, in some cases, mainly related to the solar wind conditions, the magnetic barrier on the dayside ceases to be a shield for the incoming solar wind. Small and large blobs of solar wind penetrate into the magnetosphere and sweep out a dense plasma from the ionosphere. Figure 27 shows the different stages of the dayside upper ionosphere of Mars. Typically, in the interface region between the shocked solar wind (magnetosheath) and the ionosphere, void of solar wind, where the IMF is piled up, the electron number density increases and reaches 2–5 $\times$ 10^3 cm^{-3} at an altitude of 270–300 km (Fig. 27a). Penetration of large blobs of solar wind plasma results in a local ionospheric erosion caused by ion scavenging (Fig. 27b,c). The ASPERA-3 measurements show that the process of penetration is accompanied by strong energization of planetary ions indicating their escape rather than a simple contraction and redistribution of the ionospheric plasma. Figure 27d demonstrates even a more striking event when the dense and high pressure solar wind penetrates much deeper inside the ionosphere, down to the pericenter altitude. It is observed that local electron number density inferred from MARSIS remains much lower ($\sim 10^2$ cm^{-3}) than its typical value ($>10^3$ cm^{-3}) at $h \sim$ 250–300 km implying a strong scavenging of the ionospheric plasma.

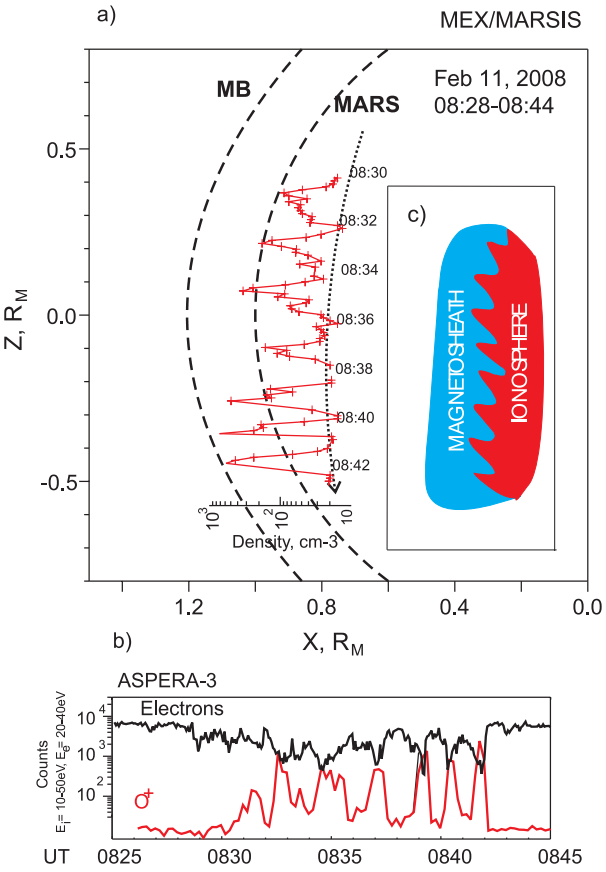

Fig. 26 (**a**) The total electron number density of the ionospheric plasma plotted along the MEX orbit. (**b**) Fluxes of magnetosheath electrons and cold oxygen ions show the appearance of intermittent tongues of solar wind and planetary plasmas. (**c**) Sketch of large-amplitude surface waves propagating on the ionosphere surface and scavenging the ionospheric matter

4.7 Energization and Escape through Auroral Flux Tubes

The discovery of a strong localized crustal magnetic field on Mars (Acuña et al. 1998) suggests that the Martian magnetosphere comprises also some features typical for the Earth magnetosphere. Although the crustal fields act mainly as an additional shield for solar wind (Fraenz et al. 2006; Dubinin et al. 2008d) narrow channels (mini-cusps), through which a hot plasma has an access to low altitudes, also appear (Soobiah et al. 2006; Dubinin et al. 2008d). Precipitation of the magnetosheath electrons through mini-cusps and the effects of local ionospheric erosion are clearly seen in Fig. 28 which compares the measurements of the electron number density (MARSIS) and the fluxes of electrons with $E_e > 5$ eV (ASPERA-3) over the regions with strong crustal fields. The dips in electron number density probably arise due to increase of thermal outflows caused by heating in the O^+ ionospheric layer. The energy source for heating might be related to electron precipitation and wave absorption at the cyclotron frequency of oxygen ions (Ergun et al. 2006). Note, that the ionospheric heating from 0.2 eV to 1 eV increases thermal outflows by ~10 times. Figure 29 compares the distribution functions of molecular oxygen ions at the altitudes ~300 km within and away of the mini-cusp. The distribution in the cusp contains a cold ionospheric core ($T \approx$ 0.2 eV) and a heated component. Energy of the energized O_2^+ ions reaches several hundred eV. These ions can be rejected from the ionosphere by 'magnetic moment pumping'.

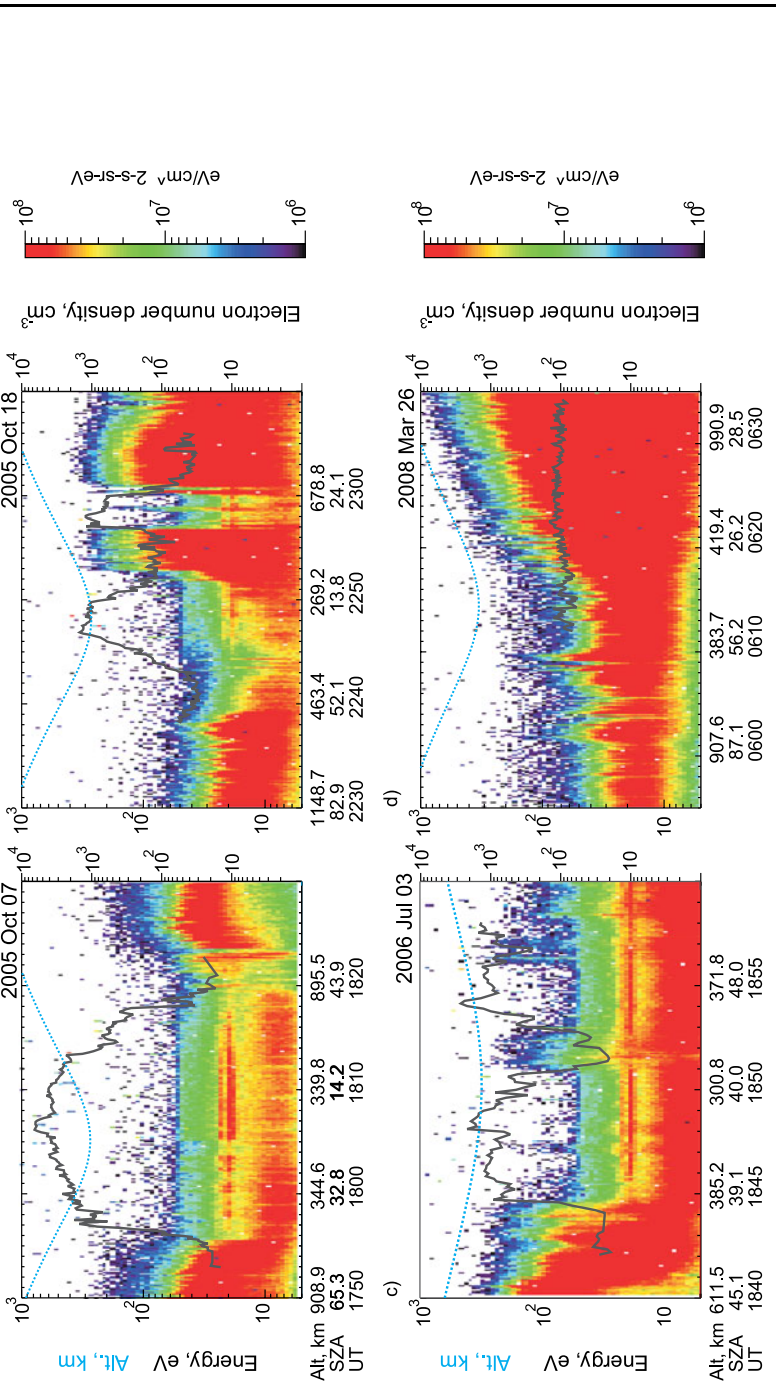

Fig. 27 Penetration of the solar wind plasma inside the Martian magnetosphere affects the altitude profiles of the ionospheric plasmas. Examples of spectrograms of electron fluxes measured by ASPERA-3 with imposed profiles of the electron number density inferred from MARSIS data. Plasma protrusion into the ionosphere creates large and small-scale depressions in the electron number density. These depressions indicate a scavenging of the ionospheric plasma by solar wind

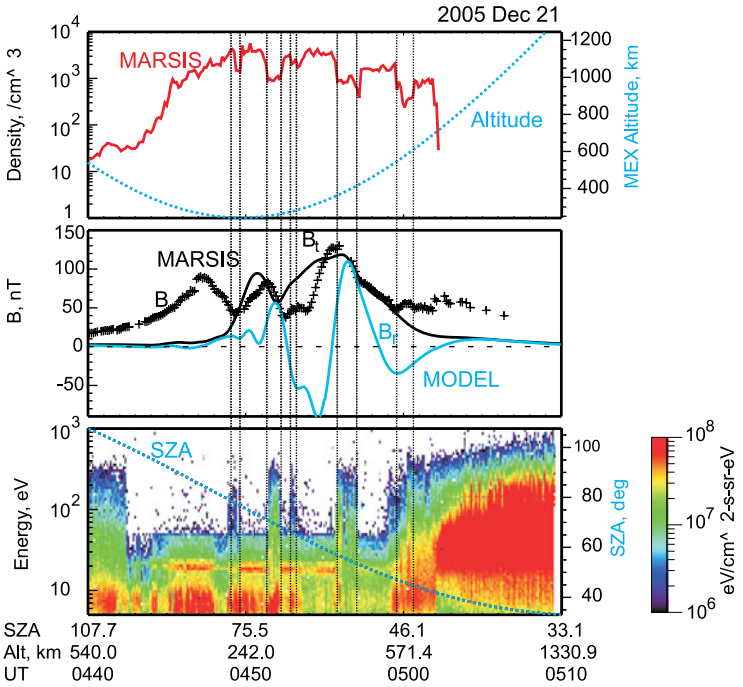

Fig. 28 From top to bottom: the electron number density, the magnetic field measured by MARSIS (*black symbols*) and the model crustal magnetic field (the total strength B_t and the radial component B_r), spectrogram of electron fluxes. Protrusions of solar wind through multiple narrow channels (minicusps) in the crustal magnetic field configuration heat and accelerate the ionospheric ions enhancing their escape along open field lines. Dips in the electron number density observed during such events and ion energization signatures confirm that such a mechanism, which is typical for the cusp and auroral oval on Earth, also operates on Mars

It is worth noting that protrusion of solar wind plasma through mini-cusps is not a continuous process. Figure 30 compares the observations made over the same region of the crustal magnetization on two successive orbits. One of them (30 September 2005) was characterized by several electron injections accompanied by the local dips in the ionospheric electron number density and the magnetic field depressions due to the diamagnetic effect, while on the another orbit (3 October 2005) the ionosphere remained undisturbed. Dubinin et al. (2008d) have observed that the protrusion of the magnetosheath plasma into the ionosphere depends on the IMF orientation. Negative values of the $B_{y,IMF}$ assist an access to the regions with strong crustal magnetization.

Although the most intense fluxes of oxygen ions are observed at the dayside of the Martian magnetosphere in the southern hemisphere over the regions with strong crustal fields there is no clear correspondence between oxygen fluxes at the day and night sides (Lundin et al. 2010). Lundin et al. (2010) suggested that the dayside minimagnetospheres reduce the transport of oxygen ions to the nightside by trapping plasma at closed field lines.

When reconnected with the IMF, the crustal magnetic field lines can be stretched in the antisunward direction producing an intricate magnetic field configuration with access of plasma sheet or magnetosheath electrons into the ionosphere/atmosphere. Therefore auroral phenomena similar as on Earth might be expected on Mars too. Note here, that signatures of aurora on Mars were observed by the UV spectrometer SPICAM onboard MEX (Bertaux

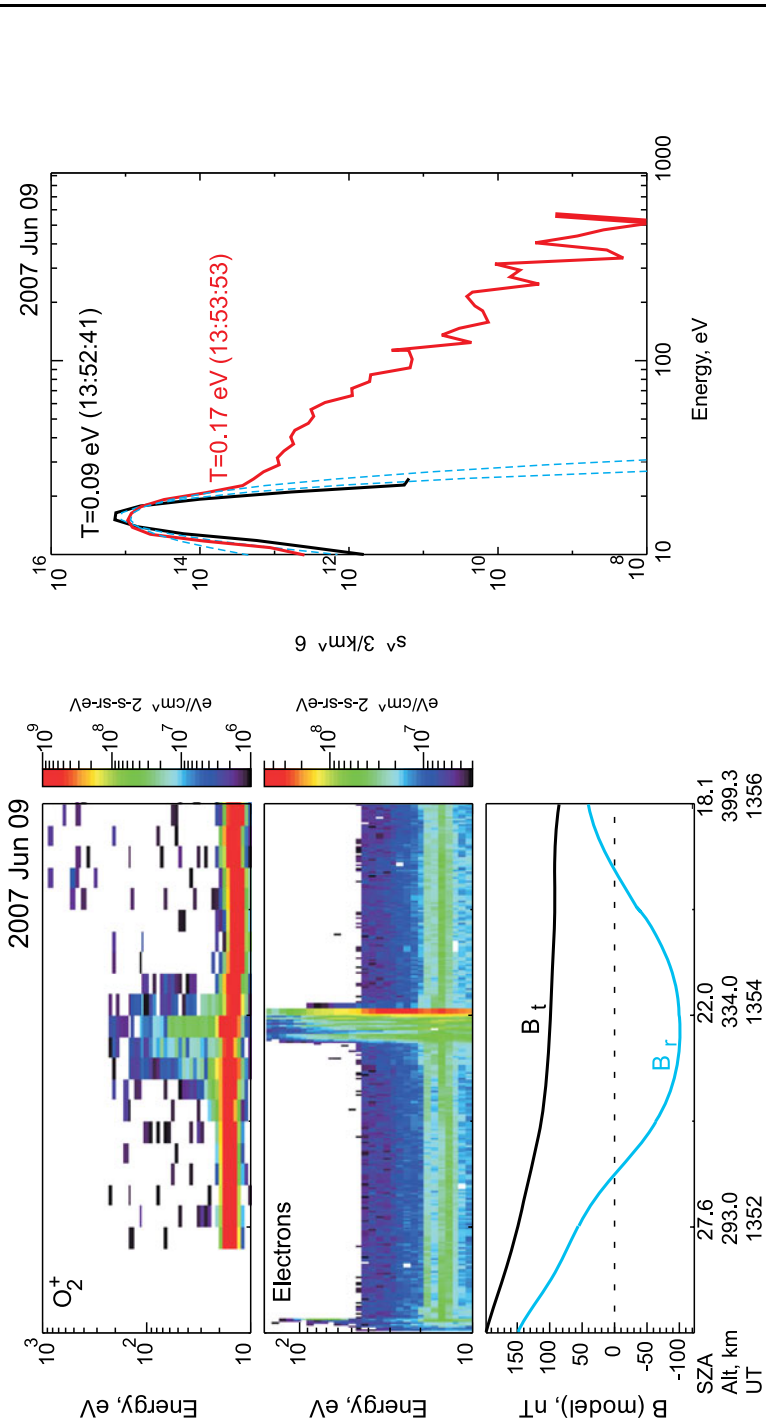

Fig. 29 Ionospheric plasma is heated in narrow local regions—mini-cusps through which the magnetosheath electrons intrude into the Martian magnetosphere (the total strength B_t and the radial component B_r of the model crustal field is shown). Heating is well seen by the comparison of the ion distribution functions inside and outside of one of the mini-cusps (*red* and *black curves*, respectively). *Blue dashed curves* show the Maxwellian fittings of the cold core components

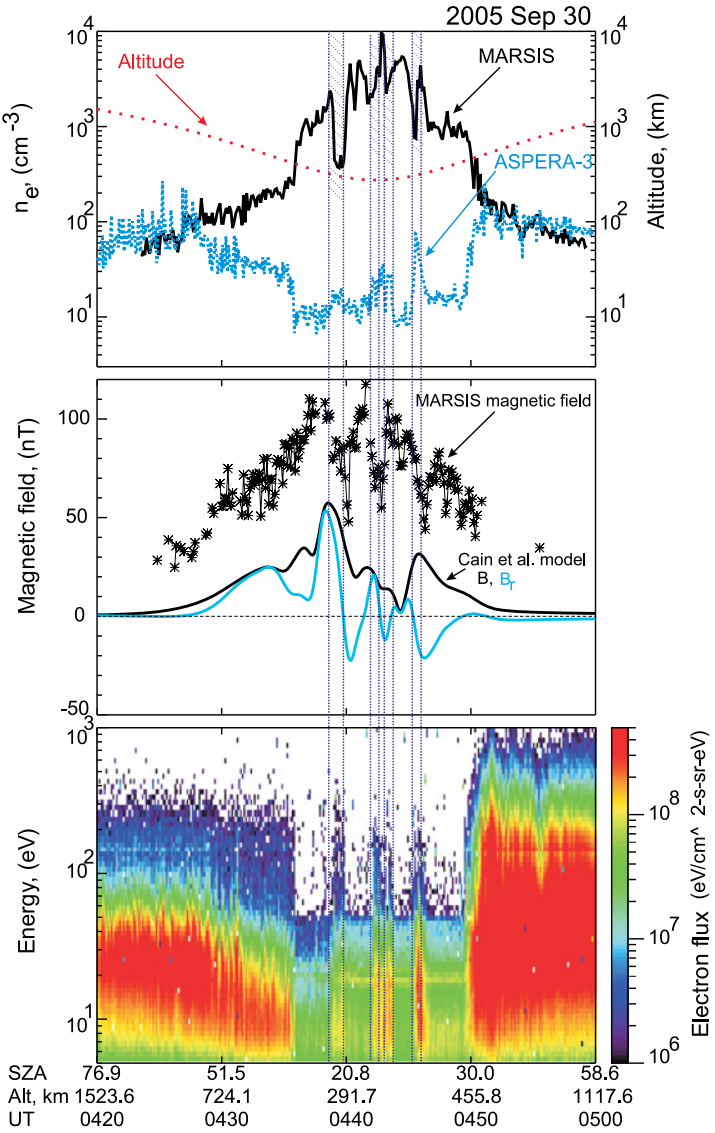

Fig. 30 Comparison of two orbits over the same region with strong crustal magnetization demonstrates variability in the plasma protrusion through mini-cusps. The injection process is probably controlled by conditions in the solar wind and the IMF

et al. 2005; Leblanc et al. 2008). The inverted '*V*' structures on spectrograms of electron fluxes (Brain et al. 2006; Lundin et al. 2006a, 2006b) collocated with upward field-aligned currents imply the existence of electric potential drops and related energization processes. Mechanisms of ion energization in the auroral regions of Earth are well documented (André and Yau 1997) and are not discussed in this paper. Although the electrodynamics of the magnetosphere/ionosphere coupling on Mars can be different than on Earth due to much higher Pedersen conductivity (Dubinin et al. 2008c), active auroral processes on the red planet may

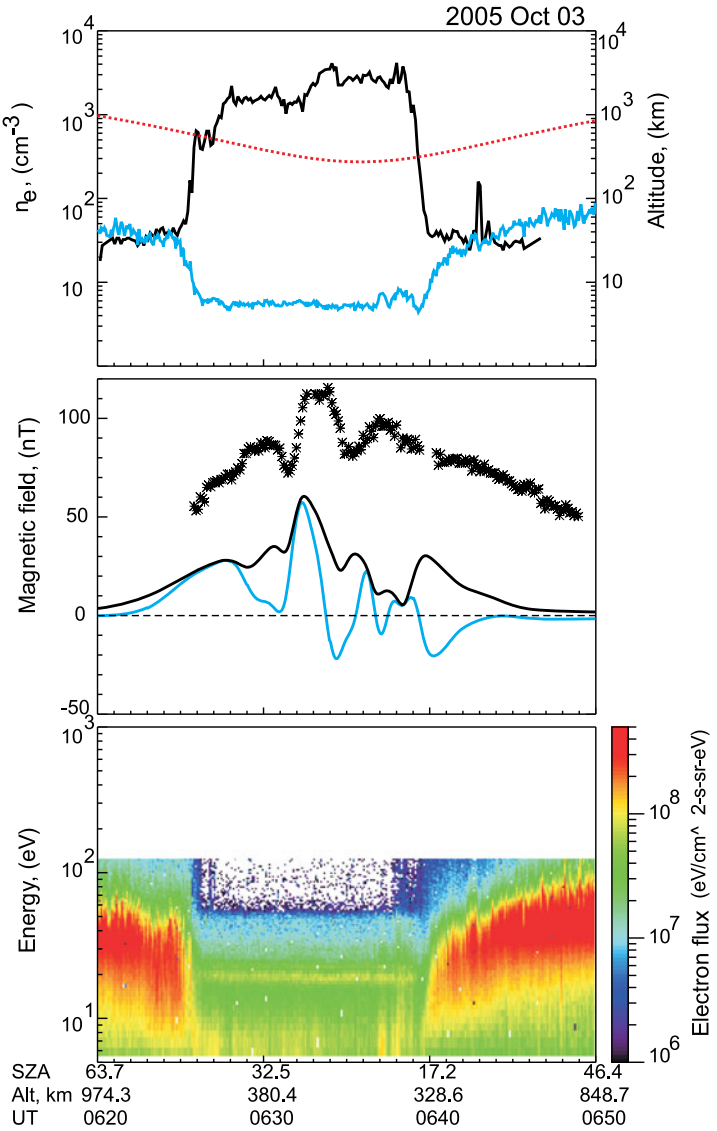

Fig. 30 (*Continued*)

contribute to atmospheric loss. Ergun et al. (2006) have examined the role of waves carried by shocked solar wind or excited by the field-aligned currents or electron beams in ion heating/energization. Estimates of losses driven by these processes give values of $\sim 10^{25}$ s^{-1}. Dubinin et al. (2009b) have observed long-lived auroral structures on Mars characterized by large electron energy fluxes ($\geq 10^{-4}$ $W\,m^{-2}$) and a heating/energization of the ionospheric ions. The local ionospheric 'troughs' at these sites indicate escape processes. An estimate of outward fluxes through a single auroral flux tube yields a loss of $\sim 10^{23}$ s^{-1}. The uncertainty in the total area of active auroras on Mars does not allow to estimate accurately the total

losses driven by auroral processes. A global image of the UV emissions on Mars by the MAVEN spacecraft to be launched in 2013 will help to resolve this problem.

4.8 Escape During the Impact of CIRs/CMEs

The erosion of the Martian and Venusian atmospheres/ionospheres is a continuous, but not a constant, process. Sporadic large losses of planetary matter can take place during the passage of coronal mass ejections (CMEs) or co-rotating interaction regions (CIRs). A CIR is created when high and low-speed solar wind streams emitted, respectively, from high latitude and equatorial regions on Sun collide. An interaction region is characterized by an increase in magnetic field strength, a magnetic field rotation and an increase in plasma density. It takes a CIR about 36 hours, on average, to pass by Mars and they occur on average 2.4 times every solar rotation (27 days), which means that during 15% of the time the Martian plasma environment is exposed to 'stormy' space weather. During solar minimum, when the Sun is relatively quiet, CIRs are the dominant interplanetary disturbance outside of ∼1 AU although at the orbit of Venus CIRs have not developed fully.

A CIR effectively acts as a pressure pulse in the solar wind, which propagates radially outward in the solar wind and occasionally impacts on the solar system bodies. The increase in solar wind dynamic pressure temporarily enhances the solar forcing on the plasma environment of the planet such that more plasma is being accelerated away. Lundin et al. (2008a) have analyzed ASPERA-3 data from 17 months in 2004–2006 (prior the new energy setting) for different solar wind conditions and found approximately one order of magnitude changes of the ion outflow directly connected with the solar wind variations. Evaluating the total escape fluxes authors assumed an azimuthal symmetry of ion outflow. Similar variations, at least of one order of magnitude, were found using a different approach when analyzing the effectiveness of escape in the plasma sheet (see Sect. 4.2).

Edberg et al. (2010) have performed a statistical study of 41 CIR events observed over 14 months during the solar minimum interval of 2007–2008 using the measurements of ions with $E_i \geq 10$ eV made after the new energy patch. Figure 31 shows anti-sunward fluxes of heavy planetary ions as measured by MEX separated into times when CIRs impact on Mars (top panels) and when there are 'normal' solar wind conditions (lower panels). Despite a reduction of obstacle size due to a contraction of the magnetosphere, seen on the YZ cross-sections, the fluxes of escaping heavy planetary ions are observed to increase by a factor of ∼2.5, on average, when a CIR impacts on Mars. The difference in the amplification factor between these results and previous estimates which accentuated on the whole range of flux variations (Lundin et al. 2008a, previous section) is probably explained by a different response of escape efficiency on solar wind variations in plasma sheet and boundary layer as compared to the lobes. For example, if the main driving force for the escape of low energy ions in lobes is the gradient of thermal pressure governed rather by EUV flux than by solar wind variations then variations in escape forced by solar wind pulses are smeared out by statistics of total fluxes averaged over the whole cross-section. On the other hand, the difference in total outflow is somewhat less than the difference in flux values since the outflow area is reduced during the impact events (see also Nilsson et al. 2010).

However, even an increase by a factor of 2.5 which should be seen as a lower bound in the escape rate, means that a third of the total mass lost into space is lost during CIRs. One can expect that an impact of a CME should have the same kind of effect on Mars' atmosphere and enhance the escape rate. Depending on how active the Sun was in the past and how many CME-like events there were, this could have important consequences for the evolution of the Martian atmosphere through time. If more CMEs occurred in the past, then the atmosphere

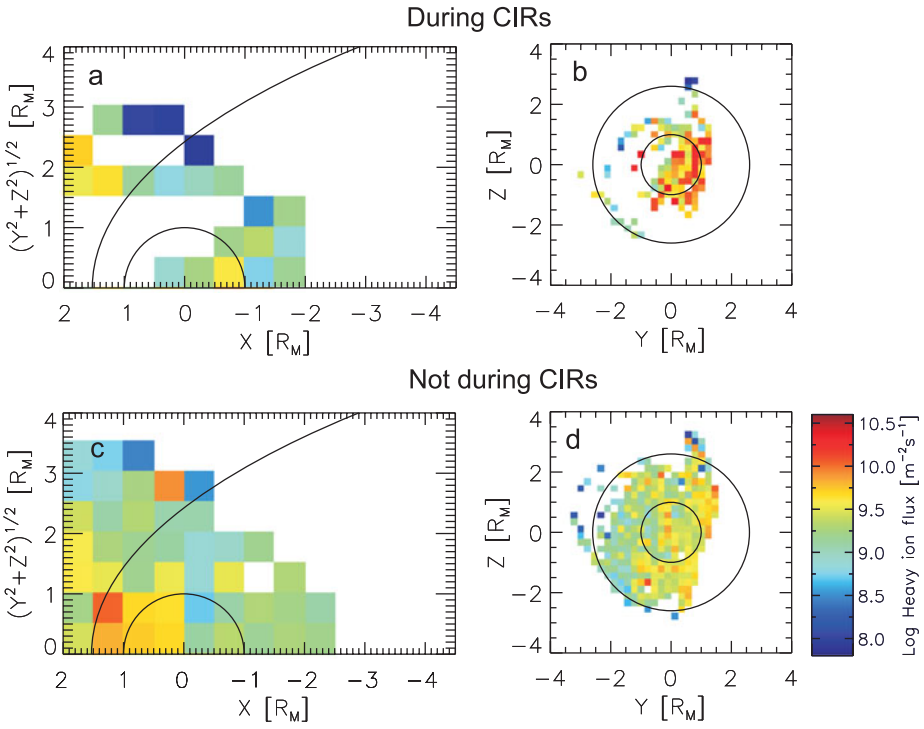

Fig. 31 Average anti-sunward fluxes of heavy planetary ions from Mars during the impact of CIRs (**a**) and (**b**) and during 'normal' solar wind conditions (**c**) and (**d**). The measured fluxes are averaged over $0.25 \times 0.25 R_M$ bins in MSO coordinates. Bins with fewer than 3 samples are colored white. (after Edberg et al. 2010)

would have been eroded more rapidly. If the solar wind were generally higher, the escape rate from Mars would also be higher.

Recently Edberg et al. (2011) have performed a similar analysis of impact of CIR/ICMEs on atmospheric escape on Venus. As compared to quiet solar wind conditions, the escape rate increases on average by factor of 1.9, although in some spatial bins the increase in fluxes is larger by two orders of magnitude.

During solar maximum the frequency of CMEs usually increases by a factor of 5–7. Solar wind dynamic pressure also increases. Therefore we can anticipate a strong enhancement of solar wind forcing of escape processes during the next increasing period of the solar cycle. For Venus, the same kind of influence from CIRs and CMEs as has been reported for Mars would be expected. The dynamic pressure associated with CMEs should be even higher at Venus as the solar wind density falls off as $1/r^2$. The observations on VEX show enhancements in ion escape related to interplanetary coronal mass ejections (Luhmann et al. 2008) although respective observations of escape fluxes and their variations are still missing.

5 Conclusions

The fundamental problem of Mars and Venus dehydration directly relates to the problem of solar wind induced escape and mechanisms of ion energization. Interaction of solar

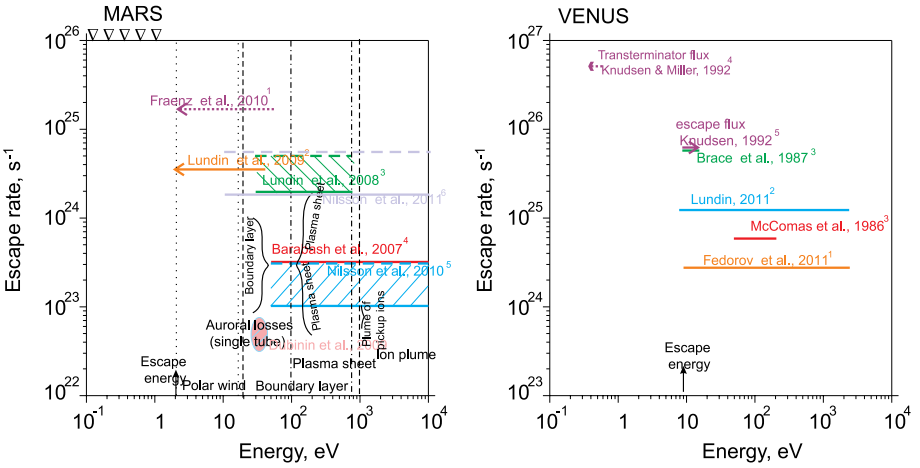

Fig. 32 Summary of oxygen loss fluxes on Mars and Venus evaluated by different authors on the base of ASPERA-3,4 observations at different energies. The results from the PVO observations are also added. *Mars*: [1] Authors have used 2D IMA observations near the terminator assuming axial symmetry of ion fluxes. They have shown that local escape fluxes can be obtained as a product of the total plasma density measured by MARSIS and bulk speed inferred from the IMA observations. The value provides us the upper limit of 'polar wind' losses. [2] Authors also assumed axial symmetry of plasma transport and used the average value of spacecraft potential of −9 V. [3] 43 orbits from 2004 through 2006 were selected to separate mechanisms which provide a large variability in escape. It was assumed cylindrical symmetry of escape fluxes. [4] Authors have transformed the data to the IMF coordinate system and performed the statistical study of observations made in 2004–2006. Total escape of O^+ and O_2^+ is shown. [5] Authors have assumed cylindrical symmetry of ion fluxes (2004–2005). [6] Authors have built average distribution functions in different spatial bins using 4 years of the observations and calculated the bulk parameters and escape fluxes assuming cylindrical symmetry. *Venus*: [1] Authors report the total escape rates at solar minimum conditions (May 2006–December 2007) covering all ion acceleration processes in the energy range 10 eV/q–25 keV/q. The data were sorted in the IMF reference frame. [2] Author does not sort the data (Jun 2006–Jun 2009) and use the VSO coordinate system, and shifts the energy table to lower energies (spacecraft potential). [3] Authors used the densities of electrons of the ionospheric plasma in the terminator region along with the ion speeds and assumed a hemispheric symmetry. [4] Hemispherically averaged transterminator flow of the cold ionospheric plasma. Most of it converges to the planet forming the nightside ionosphere. [5] Approximately 10% of the transterminator flux might be lost in tail. [6] Authors used the MHD momentum equation to evaluate the bulk parameters of plasma in the tail (8–10R_V) and the corresponding escape fluxes

wind with ionospheric shells of unmagnetized Mars and Venus lead to the momentum exchange between both plasmas, mediated by the magnetic field tensions, and losses of the ionized planetary matter. The major source of acceleration of planetary ions is related to the $-\boldsymbol{V}_e \times \boldsymbol{B}$ electric field which can be decomposed into different terms, the motional electric field, the Hall electric field and the gradient of the thermal pressure. Each of them can prevail in different regions providing specific observational features and different effectiveness of escape. Multi-ion composition of plasmas and wave acceleration also add new important aspects to the interaction and momentum transfer. Space weather effects and solar cycle variations in solar wind have a strong influence on the atmospheric and ionospheric losses at Mars and Venus. Local crustal magnetization at Mars introduces the additional energization mechanisms and escape routes typical for the Earth magnetosphere.

Figure 32 summarizes values of escape rates of oxygen ions on Mars and Venus estimated by different authors on the base of IMA/ASPERA-3 observations in different energy

intervals. Since little has been published recently concerning ion acceleration and escape on Venus values inferred from the PVO observations are also inserted. Solid and dashed horizontal bars mark the averaged and maximum total losses, respectively. Dotted bars correspond to case studies. Different authors have used different methods and assumptions which are briefly listed in the caption. Typical energies gained by ions passing different energization routes are tentatively shown by the vertical curves. The observed variations of fluxes in the boundary layer and plasma sheet are also given. Triangles on the top show the fluxes of oxygen ions which would be necessary to adjust thermal losses of hydrogen atoms if one assumes that escaping oxygen ions originate from water and do not return back to the planet.

It is observed that cold ionospheric ions dominate the plasma escape from Mars. However the constraints associated with the 2D field-of-view and spacecraft potential reduce the instrument capabilities at low energies and uncertainties remain in the escape fluxes. The probe observations can contribute essentially to exploring the processes of low-energy plasma scavenging. Strong variability inherent to induced magnetospheres also set hurdles for in-situ measurements of escape fluxes and calls for a continuous solar wind monitoring. The bursty origin of ion fluxes impose requirements on the temporal resolution of plasma detectors. These and other lessons must be addressed by future missions to Mars and Venus.

Acknowledgements The authors acknowledge the support of EUROPLANET RI project (grant 228319) funded by EU, and also the support of ISSI (Bern). E.D. and M.F. wish to acknowledge the DLR and DFG for supporting this work by grants FKZ 50 QM 0801, MO539/17-1, SPP 1488 W0910/3-1, respectively. NJTE was supported through a grant from the Swedish Science Council (Vetenskapsrådet).

References

M.H. Acuña, J. Connerney, P. Wasilewski et al., Science **279**, 1676 (1998)
M. André, A.W. Yau, Space Sci. Rev. **80**, 27 (1997)
D.E. Anderson, C.W. Hord, J. Geophys. Res. **76**, 6666 (1971)
D.E. Anderson, C.W. Hord, J. Geophys. Res. **77**, 5638 (1972)
I.L. Arshukova, N. Erkaev, H.K. Biernat et al., Adv. Space Res. **33**, 182 (2004)
P.M. Banks, T.E. Holzer, J. Geophys. Res. **73**, 6846 (1968)
S. Barabash, R. Lundin, H. Andersson et al., Space Sci. Rev. **126**, 113 (2006)
S. Barabash, A. Fedorov, R. Lundin et al., Science **315**, 501 (2007a). doi:10.1126/science.1134358
S. Barabash, A. Fedorov, J.-A. Sauvaud et al., Nature **450**, 650 (2007b). doi:10.1038/nature06434
S. Barabash et al., Planet. Space Sci. **55**, 1772 (2007c). doi:10.1016/j.pss.2007.01.014
S.J. Bauer, in *Proceedings of the Second European Workshop on ExoAstrobiology*, Graz, Austria (2002), p. 21
J.-L. Bertaux, F. Leblanc, O. Witasse et al., Nature **435**, 790 (2005). doi:10.1038/nature03603
L.H. Brace, T.F. Theis, W.R. Hoegy, Planet. Space Sci. **30**, 29 (1982)
L.H. Brace, W.T. Kasprzak, H.A. Taylor, T.F. Theis et al., J. Geophys. Res. **92**, 15 (1987)
D.A. Brain, F. Bagenal, M.H. Acuna et al., J. Geophys. Res. **107**, 1076 (2002). doi:10.1029/2000JA000416
D.A. Brain, J.S. Halekas, L.P. Peticolas et al., Geophys. Res. Lett. **33**, L01201 (2006). doi:10.1029/2005GL024782
J.W. Chamberlain, D.M. Hunten, in *Theory of Planetary Atmospheres: An Introduction to Their Physics and Chemistry* (Academic Press, New York, 1987), p. 481
S.C. Chapman, M.W. Dunlop, J. Geophys. Res. **91**(7), 8051 (1986)
E. Chassefiere, Icarus **126**, 229 (1997)
E. Chassefiere, F. Leblanc, Planet. Space Sci. **52**, 1039 (2004)
J.Y. Chaufray, J.-L. Bertaux, F. Leblanc, E. Quemerais, Icarus **195**, 598 (2008). doi:10.1016/j.icarus.2008.01.009
A. Coates, S. Tsang, A. Wellbrock et al., Planet. Space Sci. (2010). doi:10.1016/j.pss2010.07.019
D. Crider et al., Mars Global Surveyor observations of solar wind magnetic field draping around Mars. Space Sci. Rev. **111**(1–2), 203 (2004). doi:10.1023/B:SPAC.0000032714.66124.4e
Z. Dobe, K.B. Quest, V.D. Shapiro, K. Szego, J.D. Huba, Phys. Rev. Lett. **83**, 260 (1999)
M. Delva et al., Space Sci. Rev. (2011, this issue)

S.S. Dolginov, E. Dubinin, R. Yeroshenko et al., Cosm. Res. **19**, 624 (1981)
E. Dubinin, P. Israelevich, I. Podgorny, S. Shkolnikova, Lett. Astron. J. **6**, 253 (1980)
E. Dubinin, R. Lundin, H. Koskinen, N. Pissarenko, J. Geophys. Res. **98**, 3991 (1993)
E. Dubinin, K. Sauer, R. Lundin et al., J. Geophys. Res. Lett. **23**, 785 (1996a)
E. Dubinin, K. Sauer, R. Lundin, O. Norberg et al., J. Geophys. Res. **101**, 27061 (1996b)
E. Dubinin, K. Sauer, K. Baumgaertel, K. Srivastava, Earth Planets Space **50**, 279 (1998)
E. Dubinin, K. Sauer, Astrophys. Space Sci. **264**, 273 (1999)
E. Dubinin, M. Fraenz, J. Woch et al., Geophys. Res. Lett. **33**, L22103 (2006a). doi:10.1029/2006GL027799
E. Dubinin, M. Fraenz, J. Woch et al., Space Sci. Rev. **126**, 209 (2006b). doi:10.1007/s11214-006-9039-4
E. Dubinin, R. Lundin, M. Fraenz, J. Woch et al., Icarus **182**, 337 (2006c). doi:10.1016/j.icarus.2005.09.022
E. Dubinin, R. Modolo, M. Fraenz, J. Woch et al., Geophys. Res. Lett. **35**, L11103 (2008a). doi:10.1029/2008GL033730
E. Dubinin, R. Modolo, M. Fraenz, J. Woch et al., J. Geophys. Res. **113**, A10217 (2008b). doi:10.1029/2008JA013355
E. Dubinin, G. Chanteur, M. Fraenz, J. Woch, Planet. Space Sci. **56**, 868 (2008c). doi:10.1016/j.pss2007.01.019
E. Dubinin, M. Fraenz, J. Woch et al., Ann. Geophys. **26**, 3511 (2008d). www.ann-geophys.net/26/3511/2008/
E. Dubinin, M. Fraenz, J. Woch et al., Geophys. Res. Lett. **36**, L01105 (2009a). doi:10.1029/2008GL0365595
E. Dubinin, M. Fraenz, J. Woch et al., Geophys. Res. Lett. **36**, L08108 (2009b). doi:10.1029/2009GL038209
F. Duru, D.A. Gurnett, D.D. Morgan, R. Modolo et al., J. Geophys. Res. **113**, A07302 (2008). doi:10.1029/2008JA013073
N. Edberg, H. Nilsson, A.O. Williams et al., Geophys. Res. Lett. (2010). doi:10.1029/2009GL041814
N. Edberg, H. Nilsson, Y. Futaana et al., J. Geophys. Res. (2011). doi:10.1029/2011JA016749
R.C. Elphic, A.I. Ershkovich, J. Geophys. Res. **89**, 997 (1984)
R.E. Ergun, L. Andersson, W.K. Peterson, D. Brain et al., Geophys. Res. Lett. **33**, L14103 (2006). doi:10.1029/2006GL025785
A. Fedorov, E. Budnik, J.-A. Sauvaud, C. Mazelle et al., Icarus **182**, 329 (2006). doi:10.1016/j.icarus.2005.09.021
A. Fedorov, C. Ferrier, J.-A. Sauvaud, S. Barabash et al., Planet. Space Sci. **56**, 812 (2008). doi:10.1016/j.pss2007.12.012
A. Fedorov, S. Barabash, J.-A. Sauvaud et al., J. Geophys. Res. **116**, A07220 (2011). doi:101029/2011JA016427
P.D. Feldman, A.J. Steffl, J.W. Parker et al., Icarus (2011, in press)
J.L. Fox, A. Hać, Icarus **204**, 527 (2009). doi:10.1016/j.icarus.2005.09.021
M. Fraenz, J.D. Winningham, E. Dubinin, E. Roussos et al., Icarus **182**, 406 (2006). doi:10.1016/j.icarus.2009.07.005
M. Fraenz, E. Dubinin, E. Nielsen et al., Planet. Space Sci. **58**, 1442 (2010). doi:10.1016/j.pss.2010.06.009
R. Frahm, J.D. Winningham, J.R. Sharber et al., Icarus **182**, 371 (2006a). doi:10.1016/j.icarus.2006.01.014
R. Frahm, J.R. Sharber, J.D. Winningham et al., Space Sci. Rev. **126**, 389 (2006b). doi:10.1007/s11214-006-9119-5
R. Frahm, J.R. Sharber, J.D. Winningham et al., Icarus (2010). doi:10.1016/j.icarus.2009.03.024
R. Grard, A. Pedersen, S. Klimov et al., Nature **341**, 607 (1989)
D.A. Gurnett, D.L. Kirchner, R.L. Huff, D. Morgan et al., Science **310**, 1929 (2005)
D.A. Gurnett, R.L. Huff, D.D. Morgan et al., J. Adv. Space Res. (2008). doi:10.1016/j.asr.2007.01.062
D.A. Gurnett, D.D. Morgan, F. Duru et al., Icarus **206**, 83 (2010). doi:10.1016/j.asr.icarus.2009.02019
J.B. Harold, A.B. Hassam, J. Geophys. Res. **99**, 19,325 (1994)
R.E. Hartle, J.M. Grebowsky, J. Geophys. Res. **95**, 31 (1990)
A.B. Hassam, J.D. Huba, Geophys. Res. Lett. **14**, 60 (1987)
D.S. Intriligator, Geophys. Res. Lett. **91**, 167 (1989)
R.E. Johnson et al., Space Sci. Rev. **16**(2), 355 (2008)
W.T. Kaspzak, H.A. Taylor, L. Brace, H.B. Niemann, Planet. Space Sci. **30**, 1107 (1982)
W.C. Knudsen, K. Spenner, K.L. Miller, V. Novak, J. Geophys. Res. **85**, 8039 (1980)
W.C. Knudsen, in *Venus and Mars: Atmospheres, Ionospheres and Solar wind interactions*. AGU Monograph, 66 (AGU, Washington, 1992), p. 237
W.C. Knudsen, K.L. Miller, J. Geophys. Res. **97**, 17165 (1992)
V. Krasnopolsky, P.D. Feldman, Science **294**, 1914 (2001)
H. Lammer et al., Planet. Space Sci. **54**, 1445 (2006a)
H. Lammer et al., Icarus **165**, 9 (2006b)
H. Lammer et al., Space Sci. Rev. **139**, 399 (2008)
F. Leblanc, O. Witasse, J. Lilensten et al., J. Geophys. Res. **113**, A08311 (2008). doi:10.1029/2008JA013033

M.W. Liemohn, Y. Ma, R. Frahm et al., Space Sci. Rev. **126**, 63 (2006a). doi:10.1007/a11214-006-9116-8
H. Lichtenegger, K. Schwingenschuh, E. Dubinin, R. Lundin, J. Geophys. Res. **100**, 21659 (1995)
H. Lichtenegger, E. Dubinin, Earth Planets Space **50**, 445 (1998)
M.W. Liemohn, R. Frahm, J.D. Winningham, S. Barabash et al., Icarus **182**, 383 (2006b). doi:10.1016/j.icarus.2005.10.036
J.G. Luhmann, S. Bauer, in *Venus and Mars: Atmospheres, Ionospheres and Solar wind interactions*. AGU Monograph, 66 (AGU, Washington, 1992)
J.G. Luhmann, Space Sci. Rev. **44**, 241 (1986)
J.G. Luhmann, J.U. Kozyra, J. Geophys. Res. **96**, 5457 (1991)
J.G. Luhmann, K. Schwingenschuh, J. Geophys. Res. **95**, 939 (1990)
J.G. Luhmann, S.A. Ledvina, C.T. Russell, Adv. Space Res. **33**, 1905 (2004)
J.G. Luhmann, S.A. Ledvina, J.G. Lyon, C.T. Russell, Planet. Space Sci. **54**, 1457 (2006). doi:10.1016/j.pss.2005.10.009
J.G. Luhmann, A. Fedorov, S. Barabash et al., J. Geophys. Res. **113**, E00B04 (2008). doi:10.1029/2008JE003092
R. Lundin, E. Dubinin, Adv. Space Res. **12**(9), 255 (1992)
R. Lundin, A. Zakharov, R. Pellinen et al., Nature **341**, 609 (1989)
R. Lundin, A. Zakharov, R. Pellinen et al., Geophys. Res. Lett. **17**, 873 (1990a)
R. Lundin, A. Zakharov, R. Pellinen et al., Geophys. Res. Lett. **17**, 877 (1990b)
R. Lundin, E. Dubinin, H. Koskinen, O. Norberg, N. Pissarenko, S. Barabash, Geophys. Res. Lett. **18**, 1059 (1991)
R. Lundin, J.D. Winningham, S. Barabash et al., Science **311**, 980 (2006a). doi:10.1126/science.1122071
R. Lundin, J.D. Winningham, S. Barabash et al., Space Sci. Rev. **126**, 333 (2006b). doi:10.1007/s11214-006-9086-x
R. Lundin, A. Guglielmi, Space Sci. Rev. **127**, 1 (2006). doi:10.1007/s11214-006-8314-8
R. Lundin, H. Lammer, I. Ribas, Space Sci. Rev. **129**, 245 (2007). doi:10.1007/s11214-007-9176-4
R. Lundin, S. Barabash, A. Fedorov et al., Geophys. Res. Lett. **35**, L09203 (2008a). doi:10.129/2007GL032884
R. Lundin, S. Barabash, M. Holmstrom et al., Geophys. Res. Lett. **35**, L18203 (2008b). doi:10.129/2008GL034811
R. Lundin, S. Barabash, M. Yamauchi et al., Geophys. Res. Lett. (2010, in press)
R. Lundin, S. Barabash, E. Dubinin et al., Geophys. Res. Lett. (2011, in press)
G.P. Mantas, W.B. Hanson, J. Geophys. Res. **84**, 369 (1979)
C. Mazelle, D. Winterhalter, K. Sauer et al., Space Sci. Rev. **111**, 115 (2004)
J.B. McBribe, E. Ott, J.P. Boris, J.H. Orens, Phys. Fluids **15**(12), 2367 (1972)
D.J. McComas, H.E. Spence, C.T. Russell et al., J. Geophys. Res. **91**, 7939 (1986)
M.B. McElroy, M.J. Prather, J.M. Rodriguez, Science **215**, 1614 (1982)
T.R. McEnulty, J.G. Luhmann, I. de Pater et al., Planet. Space Sci. **58**, 1794 (2010). doi:10.1016/j.pss2010.07.019
J.D. Mihalov, A. Barnes, Geophys. Res. Lett. **8**(12), 1277 (1981)
K.R. Moore, D.J. McComas, C.T. Russell, J.D. Mihalov, J. Geophys. Res. **95**, 12005 (1990)
K.R. Moore, V.A. Thomas, D.J. McComas, J. Geophys. Res. **96**(A5), 7779 (1991)
H. Nilsson, E. Carlsson, D. Brain et al., Icarus **206**, 40 (2010)
H. Nilsson, N. Edberg, G. Stenberg et al., Icarus (2011, in press)
K. Papadopoulos, R.C. Davidson, J.M. Dawson et al., Phys. Fluids **14**, 849 (1971)
A. Pedersen, C. Nairn, R. Grard, K. Schwingenschuh, J. Geophys. Res. **96**, 11243 (1991)
T. Penz, N.V. Erkaev, H.K. Biernat et al., Planet. Space Sci. **52**, 1157 (2004)
H. Perez de Tejada, J. Geophys. Res. **103**, 31499 (1998)
I. Podgorny, E. Dubinin, P. Israelevich, Moon Planets **27**, 397 (1982)
H. Rosenbauer et al., Nature **341**, 612 (1989)
C.T. Russell, in *Venus Aeronomy* (Kluwer Academic, Dordrecht, 1991), p. 489
C.T. Russell, J.G. Luhmann, R.J. Strangeway, Planet. Space Sci. **54**, 1482 (2006)
K. Sauer, A. Bogdanov, K. Baumgaertel, Geophys. Res. Lett. **21**, 2255 (1994)
K. Sauer, J.F. McKenzie, E. Dubinin, in *Waves in Dusty, Solar and Space Plasmas*, ed. by F. Verheest et al. (AIP, New York, 2000), p. 327
M.A. Saunders, C.T. Russell, J. Geophys. Res. **91**, 5589 (1986)
F. Scarf et al., J. Geophys. Res. **85**, 7599 (1980)
Y. Soobiah, A. Coates, D.R. Linder, D.O. Kataria et al., Icarus **182**, 396 (2006). doi:10.1016/j.icarus.2005.10.034
V.D. Shapiro, K. Szego, S. Ride et al., J. Geophys. Res. **100**, 21289 (1995)

K. Spenner, W.C. Knudsen, K.L. Miller, V. Novak, C.T. Russell, R.C. Elphic, J. Geophys. Res. **85**, 7655 (1980)
H.A. Taylor et al., Adv. Space Res. **1**, 247 (1981)
V.A. Thomas, D. Winske, Geophys. Res. Lett. **18**, 1943 (1991)
N. Terada, S. Machida, H. Shinagawa, J. Geophys. Res. **107**(A12), 1471 (2002). doi:10.1029/2001JA009224
O. Vaisberg et al., in *Physics of Solar Planetary Environment*. Geophys. Monogr. Ser., vol. 2 (AGU, Washington, 1976), p. 904
O. Vaisberg, L. Zelenyi, Icarus **58**, 412 (1984)
O. Vaisberg, J. Luhmann, C.T. Russell, J. Geophys. Res. **95**, 14,841 (1990)
O. Vaisberg, A. Fedorov, F. Dunjushkin et al., Adv. Space Res. **16**(4), 105 (1995)
V.M. Vasyliunas, Geophys. Res. Lett. **28**(11), 2177 (2001)
M. Verigin, N. Shutte, A. Galeev, K.I. Gringauz et al., Planet. Space Sci. **39**, 131 (1991)
J.D. Winningham, R. Frahm, J.R. Sharber et al., Icarus **182**, 360 (2006). doi:10.1016/j.icarus.2005.10.033
R.S. Wolff, B.E. Goldstein, C.M. Yeates, J. Geophys. Res. **85**, 7697 (1980)
Ye. Yeroshenko, W.R. Riedler, K. Schwingenschuh, J.G. Luhmann, M. Ong, C.T. Russell, Geophys. Res. Lett. **17**, 885 (1990)
G.P. Zank, H.L. Pauls, I.H. Cairns, G.M. Webb, J. Geophys. Res. **101**, 457 (1996)
T.L. Zhang, M. Delva, W. Baumjohann et al., Planet. Space Sci. **54**, 1336 (2006). doi:1016/j.pss.2006.04.018
T.L. Zhang, M. Delva, W. Baumjohann et al., Planet. Space Sci. **56**, 790 (2008)

Space Sci Rev (2011) 162:213–266
DOI 10.1007/s11214-011-9834-4

Exospheres and Energetic Neutral Atoms of Mars, Venus and Titan

Yoshifumi Futaana · Jean-Yves Chaufray · H. Todd Smith · Philippe Garnier · Herbert Lichtenegger · Magda Delva · Hannes Gröller · Alessandro Mura

Received: 9 February 2011 / Accepted: 12 September 2011 / Published online: 8 November 2011

Abstract Our understanding of the upper atmosphere of unmagnetized bodies such as Mars, Venus and Titan has improved significantly in this decade. Recent observations by in situ and remote sensing instruments on board Mars Express, Venus Express and Cassini have revealed characteristics of the neutral upper atmospheres (exospheres) and of energetic neutral atoms (ENAs). The ENA environment in the vicinity of the bodies is by itself a significant study field, but ENAs are also used as a diagnostic tool for the exosphere and the interaction with the upstream plasmas. Synergy between theoretical and modeling work has also improved considerably. In this review, we summarize the recent progress of our understanding of the neutral environment in the vicinity of unmagnetized planets.

Y. Futaana (✉)
Swedish Institute of Space Physics, Box 812, Kiruna 98128, Sweden
e-mail: futaana@irf.se
url: http://www.irf.se/~futaana

J.-Y. Chaufray
LMD/IPSL, CNRS, 4 place Jussieu, 75005 Paris, France
e-mail: jyclmd@lmd.jussieu.fr

H.T. Smith
Johns Hopkins University Applied Physics Laboratory, 11100 Johns Hopkins Road, Laurel, MD 20723, USA

P. Garnier
UPS, CESR, Universite de Toulouse, 9 ave colonel Roche, 31028 Toulouse cedex 9, France

P. Garnier
UMR5187 CNRS, 31028 Toulouse, France

H. Lichtenegger · M. Delva · H. Gröller
Institut für Weltraumforschung, Österreichische Akademie der Wissenschaften, Schmiedlstrasse 6, 8042 Graz, Austria

A. Mura
Institute of Interplanetary Space Physics/INAF, Via del Fosso del Cavaliere 100, 00133 Roma, Italia

Keywords Mars · Venus · Titan · Exosphere · Energetic neutral atom

1 Introduction

1.1 Exosphere

The upper atmosphere of planetary bodies can be characterized by three different domains: the thermosphere, the ionosphere, and the exosphere. The thermosphere is a neutral atmospheric region where the temperature strongly increases with altitude due to the absorption of the solar ultraviolet (UV) flux. This absorption is responsible for a complex chemistry producing supra-thermal populations (McElroy et al. 1982; Nagy and Cravens 1988; Cravens et al. 1997) and UV emissions called airglow (Barth et al. 1971; Fox and Dalgarno 1979; Fox and Bougher 1991; Leblanc et al. 2006; Ajello et al. 2008). In the thermosphere, the molecular diffusion is the main process for vertical transport and explains why the lighter species become dominant. The ionosphere is composed of electrons and ions resulting mainly from the photoionization of the neutral upper atmosphere. Because of the presence of electric fields, the electron temperature becomes generally higher than the neutral temperature in the high thermosphere. Ion-neutral reactions are other sources of supra-thermal populations in the upper atmospheres (Hodges 1999). The exosphere is the region of the upper atmosphere where collisions become negligible. The exosphere is separated from the thermosphere by a boundary called the exobase. The exobase can be defined mathematically as an infinitely thin boundary where the scale height is equal to the mean free path, but physically there is a transition region where collisions are still present but not sufficient to use the hydrodynamics equations. A kinetic approach is therefore needed to describe this region. The temperature at the exobase, and therefore the scale height of the exospheric thermal species, depends on the heating and cooling processes occurring in the thermosphere (Bougher et al. 2000; González-Galindo et al. 2009). A fraction of the exosphere may also be ionized by different processes forming what is sometimes called an exo-ionosphere. In the low thermosphere, the newly created hot populations are quickly thermalized by collisions, while in the upper thermosphere and in the exosphere these hot populations are not fully thermalized and will form a hot component or escape. These reactions are probably the source of the hot hydrogen population observed on Venus (Hodges 1999) and could produce the hot population of CH_4, N_2 and H_2 observed on Titan (De La Haye et al. 2007a). According to current models, these kinds of reactions should produce a hot oxygen population on Mars and Venus (Hodges 2000; Lichtenegger et al. 2006; Chaufray et al. 2007; Cipriani et al. 2007; Valeille et al. 2009) as observed at Venus by Pioneer Venus Orbiter (Nagy et al. 1981) and possibly by Venera 11 (Bertaux et al. 1981) and at Mars by ROSETTA-ALICE during its fly-by of Mars (Feldman et al. 2011).

Because of the lack of a global magnetic field on Mars, Venus and Titan, the solar wind or Saturn's plasma interacts with the low exosphere and sometimes even with the upper thermosphere (Lundin et al. 2004). This interaction is characterized by several processes such as charge exchange between plasma protons and the neutral exosphere, leading to energetic neutral atoms (ENA) observed recently by the ASPERA-3 and ASPERA-4 instruments on board Mars Express and Venus Express at Mars (Futaana et al. 2006a) and Venus (Galli et al. 2008a) respectively and by the MIMI experiment on board Cassini at Titan (Smith et al. 2009). These charge exchange reactions are also an additional source of ionization of the exosphere. The charge exchange between highly charged ions of the solar wind and the neutral atmosphere is a source of X-ray predicted and observed both

on Mars and Venus (Holmström et al. 2001; Dennerl 2006, 2008). Such X-ray emission has also been detected from the terrestrial exosphere (e.g. Wargelin et al. 2004; Snowden et al. 2004) and is used as a diagnostic tool for the interaction between the exosphere and the upstream plasma. Another ionization process in the exosphere is due to solar wind electron impact as observed at Mars near the magnetic pileup boundary (Crider et al. 2000). Ions produced in the exosphere can escape to the interplanetary medium or reimpact the planetary atmosphere producing additional neutral escape through atmospheric sputtering (Johnson et al. 2008). Finally, the interaction between the exosphere and the solar wind is also characterized by numerous plasma processes such as the generation of upstream ion cyclotron waves which can be interpreted as the signature of the existence of specific planetary ion in the exosphere (Brain 2002; Delva et al. 2009). Most of these processes are discussed in more detail in other sections.

1.2 Energetic Neutral Atoms

1.2.1 ENA Imaging: A History

The first evidence of the existence of Energetic Neutral Atoms (ENAs), arising from the interaction of terrestrial ionospheric plasma with the local exospheric gas, was discovered in the early 1950s. During an aurora activity, Meinel (1951) detected a blue-shifted Hα line, indicating that some precipitating hydrogen ions were being neutralized. Moritz (1972) reported the detection of protons of about 200 keV at equatorial low altitudes and suggested that they could have come from the outer radiation belt. Such protons could have been neutralized by exchanging their charge with an ambient neutral thermal population, and then reaching low altitudes without being affected by the magnetic field, and finally been re-ionized just before detection.

A few years later, the ion detectors on board IMP 7, IMP 8 and ISEE-1 detected some energetic particle flux coming from the Earth while the spacecraft were orbiting out of the magnetospheric environment. Again, the charge exchange process was invoked, since no ion flux is expected in these regions (Roelof et al. 1985).

1.2.2 Application of ENA Imaging to Space Plasma Sciences

The innovative technique of ENA imaging permits the interaction between energetic plasma and a neutral thermal population to be studied using global remote sensing through detecting the produced ENAs. ENA imaging is now used as a diagnostic tool for the upstream plasma and neutral thermal population. The main advantage of using global remote sensing, when compared to the direct ion detection, is that it is possible to have an instantaneous survey of the whole magnetosphere of a planet (e.g. Gruntman 1997; Wurz 2000). Before the first ENA data, for example, most of the knowledge about the Earth's magnetospheric plasma came from *in situ* measurements of ions, electrons and electromagnetic fields. Those local measurements could not, of course, represent the global information instantaneously, but only provide an averaged picture of it, mainly because the temporal and spatial variation could not be easily distinguished. Moreover, some short time scale phenomena, such as substorms, have been found difficult to comprehend without global and continuous imaging. Even if some information about the plasma may be extracted from other sources, such as UV imaging of aurorae (e.g. Horwitz 1987), some populations (for example, the ring current) remain invisible if not observed with the ENA imaging technique. ENA investigation technique usually requires dedicated unfolding techniques to recover the 3D plasma distributions from the 2D ENA images (e.g. Roelof and Skinner 2000).

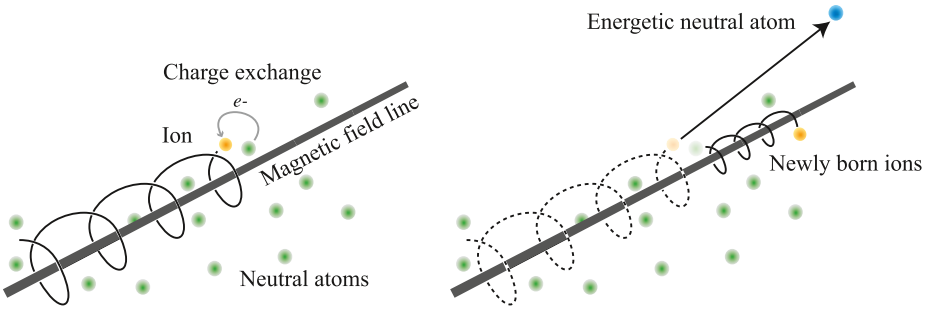

Fig. 1 Scheme of the charge exchange process. Energetic ion gyrating around the magnetic field line hits a neutral target (*left*) and gets an electron from it. After the charge exchange, the generated energetic neutral atom proceeds with a straight-line trajectory (*right*)

Furthermore, ENA imaging also gives information about thermal neutral populations, i.e. the exosphere of the planet (Galli et al. 2008a, 2008b). Garnier et al. (2007), for example, starting from MIMI observations of ENA fluxes at Titan, compared them with simulations to obtain a reconstructed model of the exosphere of Titan.

1.2.3 Generation Mechanism of ENAs

The most important generation mechanism of ENAs from space plasma is the so-called charge exchange process, which is schematically illustrated in Fig. 1. In this process, an energetic ion projectile collides with a neutral target particle. By transferring an electron from the energetic ion to the neutral particle, the energetic ion is neutralized to become an ENA. Since it is no longer affected by magnetic or electric fields, the ENA travels along ballistic trajectories (approximated by straight lines for ENAs with energies above 100 eV), and can be detected outside the charged particles interaction region.

A small amount of the kinetic energy is also exchanged between the neutral and the ion along with the electron. The energy defect of the process is equal to the difference of the two atomic ionization potentials (Hasted 1964); the amount of exchanged energy is usually small with respect to that of the incoming ion. Typically the energy loss of the projectile charged particle of $\sim$1 keV is below $\sim$10 eV (e.g. Rees 1989; Basu et al. 1993). Therefore, one can assume that the newly created ENA has approximately the same energy and direction as the colliding energetic ion.

Energies of ENAs in the vicinity of Mars, Venus and Titan are usually higher than the corresponding gravitational binding energies. The escape energy is of the order of a few eV while the energy of ENAs is usually of the order of several hundred eV to several MeV. Therefore, one can assume that the ENAs travel along straight lines. Hence, the differential ENA flux to be observed at a point S_0 coming from the direction $\hat{v}$ is generated by the interaction of the energetic ion fluxes with one or more ambient neutral populations for all points S along the line of sight $(S_0, \hat{v})$. The ENA flux is obtained by integrating the ENA source rate along the line of sight. At the location S, the infinitesimal ion flux dJ_+ directed toward S_0 is:

$$dJ_+ = n_+(l) v f(l, \mathbf{v})\, d\mathbf{v}, \tag{1}$$

where $n_+(l)$ is the ion density, v is the velocity vector, $f(l, \mathbf{v})$ is the ion velocity distribution function and l is the distance along the line of sight.

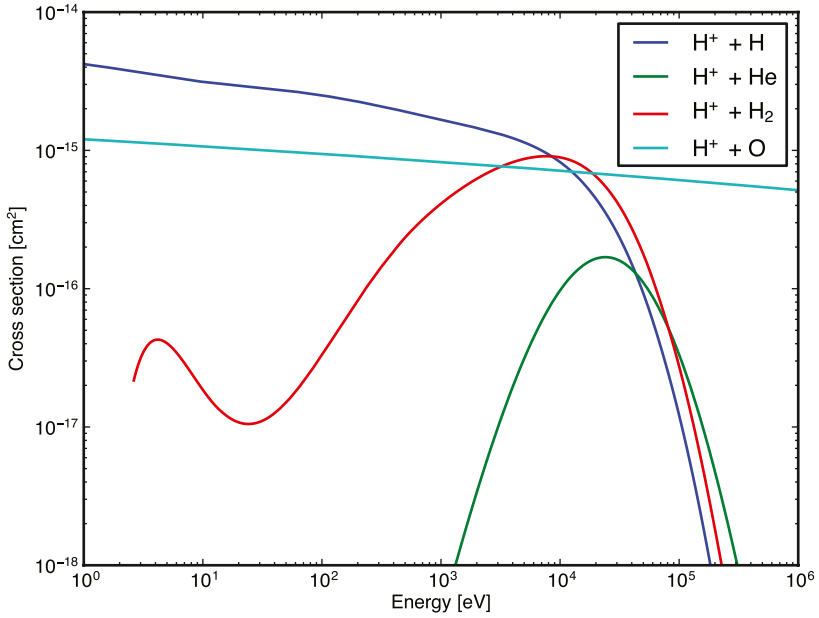

Fig. 2 Cross sections of charge exchange processes between a proton and various target species, as functions of the energy. Data are obtained from Barnett et al. (1990) (for He and H_2) and Lindsay and Stebbings (2005) (for other species)

Using the mean free path of ions of energy E regarding the charge exchange process with all the neutral species, k,

$$\lambda_+(l, E) = \frac{1}{\sum_k \sigma_k(E) n_k(l)}, \tag{2}$$

where n_k and σ_k is the density and the charge exchange cross section for species k, the ENA differential flux $dJ_{\mathrm{ENA}}(E, \hat{v})$ is:

$$dJ_{\mathrm{ENA}}(E, \hat{v}) = \int_{l=0}^{\infty} dJ_{H^+} \frac{1}{\lambda_+(l, E)} dr = \int_{l=0}^{\infty} f(l, \mathbf{v}) \frac{1}{\lambda_+(l, E)} n_+(l)\, dl\, dE\, d\Omega. \tag{3}$$

The ENA flux moving towards S_0 may be reduced by other processes, such as photon ionization or stripping (Brandt 1999). In this case, it is easy to include a destruction function by means of the mean free path λ_{ENA} in (3).

The cross sections for charge exchange processes of protons with typical energies between 1 eV–1 MeV are shown in Fig. 2 as examples. They vary between 10^{-15} and 10^{-18} cm^{-2} or even less depending on the energy and the species of the target particles (Fig. 2). Even if such values are not very high, the integration path may be long enough (typically of the order of the planetary radius of 10^3 km $= 10^8$ cm) to cause relevant ENA fluxes.

In many domains in the upper atmospheres of Mars, Venus and Titan, the medium can be considered "optically thin" to ENAs, i.e. the mean free path of ENAs is long enough that ENAs can transport information out of the generation region, thus allowing remote sensing of the interaction volume. However, special treatment is needed in some regions

where the neutral density is high, such as in the thermosphere, for example, when one treats atmospheric effects for Titan (see Sect. 5).

1.2.4 ENA Sensors in Space

Because ENAs fly along straight lines after their emission without perturbations by electromagnetic fields as photons do, the scientific community initiated studies of the feasibility of "ENA imaging" already in the 1970s. The first ENA image of the Earth's magnetosphere was obtained serendipitously by using an ion detector on ISEE-1 (Roelof et al. 1985; Roelof 1987; Roelof and Williams 1988). This image opened the way to ENA remote sensing both of planetary magnetospheres and of neutral populations.

In the magnetosphere of a planet or a moon, the charge exchange process may be responsible for increasing the erosion rate of the atmosphere, resulting in the loss of both mass and energy from the planets. This is true both for magnetized and unmagnetized bodies. However, the cases of Mars, Venus and Titan may be quite peculiar because these bodies lack of a strong intrinsic magnetic field. Such bodies are known to have comet-like "induced" magnetotails and have been the subject of many comparative studies (i.e. Luhmann et al. 1991; Bertucci et al. this issue). The properties of this specific interaction depend on the impacting plasma and the atmosphere of the body itself. In this respect, Mars, Venus and Titan together form an extremely interesting ensemble. Mars and Venus have recently been explored by the ESA Mars Express (MEX) and Venus Express (VEX) missions. The ASPERA-3 and -4 instruments on board these missions collected (and are still collecting) the first ENA data on Mars and Venus. Titan is inside the Saturn's magnetosphere for most of its orbit, and the plasma is sub-magnetosonic, thus no bow shocks forms (Neubauer et al. 2006; Arridge et al. this issue). The dense atmosphere of Titan neutralizes part of the plasma, thus leading to ENA production; such ENAs have been detected by the MIMI/INCA sensor on board the Cassini spacecraft (Mitchell et al. 2005).

2 Energetic Neutral Atoms close to Mars and Venus

2.1 Solar Wind Interaction with Mars and Venus

The signatures of the upstream plasma (the solar wind or magnetospheric plasma) interaction with a planetary body depend mainly on the strength of a possible intrinsic magnetic field, and on the density of the atmosphere and the ionosphere.

In this sense, the solar system bodies can be categorized into four groups (Table 1). In the case of the Earth and the gas giant planets such as Jupiter or Saturn, their strong intrinsic magnetic fields extend far beyond the dense ionosphere. The extended magnetospheres deflect the solar wind before it reaches their ionospheres. Mercury possesses a moderate intrinsic magnetic field, which creates a magnetosphere similar in shape but smaller than the

Table 1 Categorization of solar wind-planetary body interaction signatures

	Dense atmosphere	Tenuous atmosphere
Strong magnetic field	Earth, Jupiter, Saturn	Mercury
Weak magnetic field	Mars, Venus, comets, Titan[a]	Moon, Phobos, asteroids

[a]Most of the time Titan is in the subsonic corotating magnetosphere of Saturn

Earth's (Ness et al. 1974; Anderson et al. 2008). Due to the absence of a substantial atmosphere or a dense ionosphere, the magnetospheric particles interact directly with the surface of Mercury (e.g. Kallio and Janhunen 2003; Orsini et al. 2007). There are many solar system bodies that lack substantial intrinsic magnetic fields and atmospheres, e.g. the Moon, Phobos and many asteroids. When such planetary bodies are exposed to the solar wind, they directly absorb the solar wind protons and electrons without forming a bow shock. It would be worth noting here that the Moon (and many atmosphere-less bodies) has an exosphere (sometimes called as surface boundary exosphere; Stern 1999). While its density is extremely low, owing to the long flight distance over the lunar terminator region, a detectable ENA flux originating from the charge exchange with the solar wind is predicted (Futaana et al. 2008a). Dust in the exosphere may also produce an ENA flux of the solar wind origin (Collier and Stubbs 2009).

On the other hand, Mars, Venus, and some comets (particularly when they are close to the Sun) have sufficiently dense atmospheres to form strong ionospheres, while lacking an intrinsic magnetic field. The solar wind comes very close to the ionosphere, where ionospheric currents are induced which prevent a bulk penetration of the solar wind plasma is prevented. This separates the plasma domain of the planetary ionosphere from the solar wind, and thus this region is sometimes called "induced magnetosphere" (Lundin et al. 2004). Obviously, the nightside structures of the induced magnetosphere are also quite different from those of the Earth. No trapped particles exist in the induced magnetosphere in the case of Mars and Venus. Observations of substorm-like accelerations have been reported at Venus by using magnetometer and plasma data (Volwerk et al. 2009), where the acceleration of the ions was up to 1.5–2 keV. The main plasma population inside the induced magnetospheres is either of solar wind or of planetary ionosphere origin, and the energy range of the particles is up to the solar wind energy, typically $\sim$1 keV $(M/q)^{-1}$, where M and q are, respectively, the mass and the charge of the ions. The pickup process can accelerate the planetary ions up to twice the solar wind velocities. However, the particles need to travel long distances to be accelerated, typically of the order of one Martian radius ($\sim$3400 km) (e.g. Luhmann and Kozyra 1991).

The ENAs close to non-magnetized planets are mainly generated through the charge exchange mechanism as explained in the Introduction section, but scattering and sputtering processes also contribute to the generation of ENAs in the vicinity of non-magnetized bodies.

The scattering and sputtering processes may occur after the collision of an ion with a surface or a dense atmosphere. When a charged particle reaches the solid surface or dense atmosphere, it can collide with atoms from the surface or the atmosphere elastically or non-elastically. After the collision, the energy and the directions of the impinging particles will be deviated from the original states. This is called the scattering process. During the collisions, the charged particles may lose their initial charged state and become neutralized. On the other hand, in the collision process a fraction of the atoms of the surface or the atmosphere may get enough momentum and energy from an impinging charged or neutral particle to fly into space; this process is called sputtering. The energy of the scattered and sputtered particles does not exceed the energy of the incoming particle. Nominally, the peak energy of the sputtered particles is a few eV (e.g. Betz and Wien 1994; Wurz et al. 2007, 2010). For the charge exchange processes, the energy loss can be neglected, and the charge exchanged ENAs have about the same energies as the original ions. For the cases of Mars and Venus, this is the solar wind proton energy, i.e. $\sim$1 keV.

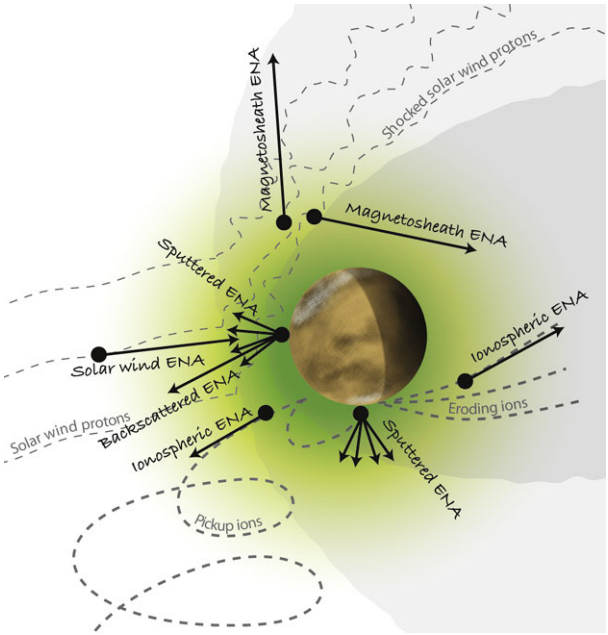

Fig. 3 Illustration of five ENA generation mechanisms (1, 2, 3, 6 and 7 in the text) in the vicinity of Mars. The dashed lines are ion trajectories and the *dark arrows* are the predicted ENAs in the vicinity of Mars. The extended exosphere is illustrated by the *green area*, and the plasma regions called the induced magnetosphere and the magnetosheath are represented by the *dark and light gray fill*, respectively

2.2 Theoretical Prediction of ENA Generation at Mars

For the Mars Express mission study, ENA production in the vicinity of Mars has been investigated using theoretical, fluid and hybrid models. Possible sources of ENA fluxes are: (1) undisturbed solar wind plasma charge exchanged with the hydrogen exosphere of Mars (Barabash et al. 1995; Holmström et al. 2002); (2) the shocked solar wind plasma charge exchanged with the exosphere (Barabash et al. 1995; Holmström et al. 2002); (3) accelerated ions of solar and planetary origin (e.g. Lundin et al. 1989; Luhmann and Kozyra 1991) in the induced magnetosphere boundary (Barabash et al. 2002); (4) nonthermal energetic particles (Barabash et al. 1995); (5) solar wind particles interacted with the hypothetical Phobos and Deimos tori (Barabash et al. 1995; Mura et al. 2002); (6) ENAs of solar wind proton or the solar wind ENA origin backscattered from the Martian atmosphere (Kallio and Barabash 2001; Kallio and Janhunen 2001); (7) heavy ion neutral flux of energies of $<$100 eV sputtered by accelerated heavy ions (Luhmann and Kozyra 1991; Barabash et al. 2006).

Figure 3 illustrates a cartoon of theoretical predictions of the ENA generation in the vicinity of Mars. Barabash et al. (1995) calculated the expected ENA flux for each mechanism. Holmström et al. (2002) also estimated the expected ENA fluxes and images by using the empirical model developed in Kallio (1996). The solar wind hydrogen ENAs are estimated to have a flux as high as 10^6–10^7 cm^{-2} sr^{-1} s^{-1} keV^{-1}. Note that oxygen ions in the solar wind are highly charged (typically O^{6+} or O^{7+}), and thus the oxygen ENAs of the solar wind oxygen ions may rarely exist. In addition, helium ENAs from the solar wind alpha particles (He^{2+}) are also barely expected, particularly in the solar wind and the magnetosheath. Even though the expected solar wind hydrogen ENA flux is high, detection of those ENAs is quite difficult in general because strong solar photon fluxes come from the same direction, and can easily enter the instrument aperture causing strong contaminations. There are observations of the solar wind ENAs around the Earth by the IM-

AGE/LENA instrument (Collier et al. 2001) owing to the hemispherical deflection system and the TOF system, but ENA sensors on board Mars Express and Venus Express were not designed to measure the solar wind ENAs. On the other hand, it is more feasible to observe ENAs from other mechanisms. Using the charge exchange rate between solar wind protons and the Martian exosphere extending into the solar wind region, Barabash et al. (1995) predicted the intense flux (10^5–10^6 $cm^{-2}\,sr^{-1}\,s^{-1}\,keV^{-1}$) of hydrogen ENAs with energy of 0.1–1 keV for mechanism 2) from the shocked solar wind ENAs. Holmström et al. (2002) updated the flux of the order of 10^7 $cm^{-2}\,sr^{-1}\,s^{-1}\,keV^{-1}$. They also mentioned that the ENA fluxes are highly depending on the spacecraft position and sensor FoV in addition to the solar wind condition and Martian plasma environment, particularly the IMB altitude. The flux of the charge exchanged planetary ENAs for mechanism 3), originating from the accelerated planetary oxygen ions may reach up to 10^8 $cm^{-2}\,sr^{-1}\,s^{-1}\,keV^{-1}$ for an energy range of 0.1–1.7 keV (Barabash et al. 2002). The planetary hydrogen ENAs are estimated as 10^{10} $cm^{-2}\,s^{-1}\,keV^{-1}$ (Lichtenegger et al. 2002). The high energy (>10 keV) ENA flux is quite low (<5 $cm^{-2}\,s^{-1}\,sr^{-1}$). A hypothetical gas-tori of the Martian moons may generate an ENA flux with 6×10^3 $cm^{-2}\,s^{-1}$. Even though the Phobos interaction with the solar wind can be categorized into different types (non-magnetized and non-atmospheric) in Table 1, it will be discussed briefly in the next section. Kallio and Barabash (2001) and Kallio and Janhunen (2001) proposed a possible measurement of energetic neutral atoms backscattered from the atmosphere. Since a fraction of the undisturbed solar wind protons charge exchanges with the part of the exosphere extending beyond the bow shock (mechanism 1), solar wind hydrogen ENAs are created flowing toward the Martian atmosphere. These ENAs, which do not feel an electromagnetic force, can travel down to the exobase, where collisions become significant. Kallio and Barabash (2001) modeled in total 30 mechanisms of elastic and inelastic collisions, and concluded that ~58% of the impinging ENAs will be scattered back.

2.3 ENAs from Phobos

Charge exchange processes may also occur with neutral atoms outgassing from small bodies, or gaseous rings. This is expected for the case of the Martian satellite Phobos. The hypothetical neutral oxygen outgassing from the surface of Phobos has enough energy to escape the very weak gravitation field of the satellite, but is not fast enough to escape the Martian gravity. Hence, this population may fill a torus along the orbit of Phobos. Oxygen atoms are removed by photoionization; the total amount of oxygen atoms in the torus is equal to the global outgassing rate multiplied by the photon ionization lifetime. The neutral density in the torus may be up to 10^4–10^5 cm^{-3} (Mura et al. 2002), which is comparable to that of the Martian exosphere, so that the charge exchange mechanism may be relevant in this region, and especially close to Phobos, where the density is higher (Fig. 4). However, the small volume of the torus, and hence the short line-of-sight integration, leads to a relevant ENA flux only for particular configurations of Phobos and the vantage point. So far, no clear ENA signatures have yet been reported related to the Phobos gas torus.

On the other hand, recent observations close to the Earth's moon revealed that a fraction of the solar wind is scattered back from the regolith-covered lunar surface as protons (Saito et al. 2008) and as ENAs (Wieser et al. 2009). Similar backscattered process would occur at the surface of Phobos. Recently Futaana et al. (2010) reported measurement of backscattered protons from the surface of Phobos, and thus, so backscattered ENAs from Phobos are very likely to be expected.

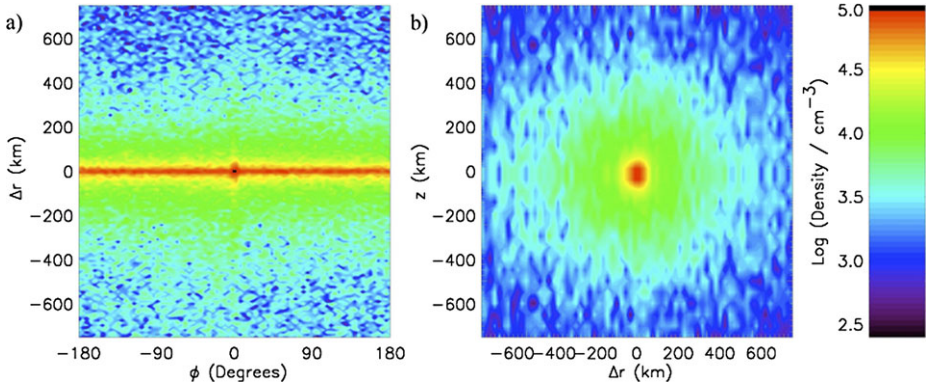

Fig. 4 Color-coded map of simulated neutral oxygen density near the orbit of Phobos ϕ versus r, $z = 0$; $Q = 10^{23}$ s^{-1}. Phobos' position is at $r = 0$, $\phi = 0$, $z = 0$. After Mura et al. (2002)

2.4 Observed ENA Fluxes in Mars and Venus Environment

The first ENA measurement close to a non-magnetized body was conducted by the Analyser of Space Plasmas and Energetic Atoms (ASPERA-3) on board Mars Express (MEX). ASPERA-3 aims to investigate the solar wind-atmosphere interaction by characterization of the plasma and neutral gas environment near Mars space. One of the most important scientific objectives is to understand the solar wind induced escape in the form of pickup ions and of bulk escape (Barabash et al. 2006; Dubinin et al. this issue). Even though the escape in the form of ENAs may be very small, the neutral particle environment is also relevant to an understanding of the physical processes of the escape, because the interaction between the plasma and neutral atmosphere is important in particular close to the non-magnetized bodies.

Two types of ENA sensors are part of the ASPERA-3 instrument: the neutral particle imager (NPI) and the neutral particle detector (NPD). Summarizing the specification (Barabash et al. 2006), NPI has a wide angular aperture of $9 \times 344°$ with a good angular resolution of $4 \times 11.5°$, but no energy resolution is available. NPD has a time of flight (TOF) system and therefore can resolve the velocity of the ENAs. Using the time difference between two signals from two micro channel plates (MCPs) separately placed inside the sensor, one can measure the velocity of the impinging ENA. In addition, by using the pulse height distribution that depends on the mass composition of impinging particles, one can in principle obtain mass information of the ENAs in a statistical way. However in practice, the TOF information has only been used for the mass separation for the NPD data analysis. The physical distance of the MCP is optimized to separate the TOF signals between 0.1–10 keV hydrogen ENAs and >0.1 keV oxygen ENAs. A limitation of NPD is the coarse resolution of the sensor channels of $\sim 10 \times 40°$ (FWHM). The total field of view is $10 \times 180°$. The ENA sensors onboard VEX are basically replicas of those onboard MEX (Barabash et al. 2007a).

2.4.1 Solar Wind Interaction with Mars

Past ENA observations have been used to investigate the plasma-neutral interaction occurring in the vicinity of the Earth. For example, the IMAGE (Imager for Magnetopause-to-Aurora Global Exploration) satellite carried three ENA sensors to cover a wide energy range: HENA for the energy range of 30–500 keV (Mitchell et al. 2000), MENA for 1–30 keV

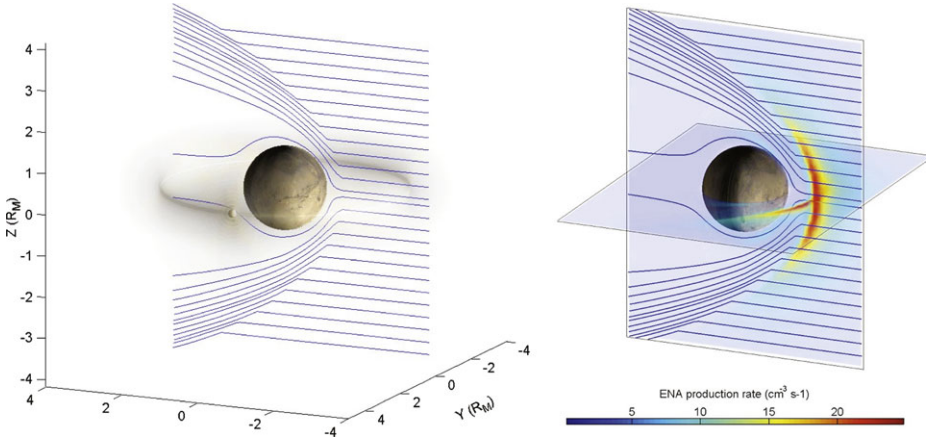

Fig. 5 *Left panel*: solar wind flows around Mars (*blue streamlines*), and the Phobos' gas torus. *Right panel*: ENA production rate simulated from the same analytical model as in Mura et al. (2002). Exospheric densities have been taken from Krasnopolsky and Gladstone (1996). Plasma flow around Mars is modeled by Kallio (1996)

(Pollock et al. 2000) and LENA for 10–750 eV (Moore et al. 2000). These sensors on the IMAGE satellite provided a large dataset of ENAs from the Earth's magnetosphere so that our understanding of dynamics of the terrestrial magnetosphere system has greatly improved (e.g. Burch 2003). It is a natural idea to use the ENA measurement technique to investigate the solar wind-exosphere interaction also at Mars, since analyzing the ENA data allows us to understand how the solar wind plasma interacts with the Martian plasma. The subsolar region is the place where the strongest ENA fluxes are expected because it is the area of the densest neutral exospheric population (e.g. Holmström et al. 2002). Figure 5 shows an example of ENA generation at the dayside of Mars simulated with the same analytical Mars magnetosphere model as in Mura et al. (2002).

The first analyses of ENAs flying from the subsolar region were conducted by using ENA data recorded by NPD (Futaana et al. 2006b) and NPI (Gunell et al. 2006). As has been already discussed, both sensors complement each other. Gunell et al. (2006) used NPI data to show the existence of a strong ENA flux of 1.3×10^7 cm^{-2} sr^{-1} s^{-1} from the subsolar region when MEX is at the flank side of Mars. They reported strong signals in the NPI data when ENAs of shocked solar wind proton origin have been expected. To prove that such signals indicate ENA fluxes, they compared the observed flux with the predicted ENA flux at the spacecraft position using an empirical model of the plasma flow around Mars (Kallio 1996) together with the Chamberlain exospheric model (Chamberlain and Hunten 1987). The similarity of the ENA fluxes between the model prediction and the observation indicates that those signals are indeed of ENA origin. Since NPI is also sensitive to Lyman-α (Brinkfeldt et al. 2006), they also modeled the UV flux from the Martian atmosphere. The signature of the modeled UV flux could not explain the observed signals recorded by NPI, making them unlikely to arise from UV contamination.

Concurrently, Futaana et al. (2006b) used NPD data to investigate the ENAs from the same region. Under similar position and field of view configurations as NPI, NPD also detected a strong flux of hydrogen ENAs from the subsolar region, with energies between 0.3–3 keV and a flux corresponding to 4–7 $\times 10^5$ cm^{-2} sr^{-1} s^{-1}. The flux measured by NPD is smaller by approximately one to two orders of magnitude with respect to NPI and the

discrepancy is not yet understood, though other quantitative characteristics of the ENA signatures agree. One possible explanation of the lower flux is that due to the limited FoV of NPD, the flux obtained by NPD is underestimated because NPD may miss the direction of the main peak of the ENA jet flux. A small angular spread in the ENA flux (as discussed later) may also lead to an underestimation of the flux derived from a sensor with wide angular resolution. In addition, the field of view planes are not precisely coaligned (the FoVs of NPD and NPI have 15° offset). Temporal variations might be another possible reason for the discrepancy. Comparing with models, the observed flux is consistent with the flux of 10^5–10^6 $\mathrm{cm^{-2}\,sr^{-1}\,s^{-1}\,keV^{-1}}$ estimated by Barabash et al. (1995), but not with the flux of the order of 10^7 $\mathrm{cm^{-2}\,sr^{-1}\ \ s^{-1}\,keV^{-1}}$ by Holmström et al. (2002). The discrepancy in the flux is still an open question.

The TOF system is useful not only for knowing the velocity of the incoming particles, but also for subtracting background signals arising from UV photons or from internal electric noises (Futaana et al. 2006b; Galli et al. 2006a). The TOF system takes the time difference within a certain time window (2048 ns for the NPD case) between two signals called *start* and *stop*. Assuming that these signals are white noises with count rates of C_{start} and C_{stop}, the resulting probability function of the TOF distribution, $fc(\mathrm{tof})$ [/s^2], theoretically follows the exponential distribution:

$$fc(\mathrm{tof}) = C_{start} \cdot C_{stop} \cdot \exp(-C_{start} \cdot \mathrm{tof}) \tag{4}$$

This can be derived from the fact that the time series of white noises follows a Poisson process. Using typical values $C_{start} = 10000$ [/s] and $C_{stop} = 300$ [/s] (Futaana et al. 2006b) for NPD, $fc(\mathrm{tof})$ can be approximated by a constant distribution over the TOF range of interest (<2048 ns). According to the observed mass spectra, the ENA flux from the subsolar point is only composed of hydrogen. The oxygen flux was below the detection level of the NPD sensor.

Considering that the composition of the ENA jet is only hydrogen and that the flux only comes from the subsolar region, the most probable source of these ENAs is charge exchange between shocked solar wind protons and the exospheric neutral atoms in the subsolar region.

These ENA fluxes are commonly found in the NPD dataset when the spacecraft was located at the flank side of the subsolar point and the sensor's FOV pointed toward the subsolar region. Futaana et al. (2006b) also made statistics of the observation occurrence of subsolar ENAs when MEX and NPD were under optimal observation configurations during the time period between April to June 2004. Subsolar ENA fluxes can be found in ∼95% of the observational opportunities. Around Venus, a subsolar ENA flux has not yet been reported because quite high UV photon-originated count rates in VEX/NPI and VEX/NPD data made the subsolar ENA jet investigation quite difficult.

Mura et al. (2008) performed a comparison of statistical data analysis of Martian ENA jets with results from model calculations using the analytical model proposed by Kallio (1996) combined with the exospheric profiles of H, H_2 and O by Krasnopolsky and Gladstone (1996). Considering the smaller exospheric density profiles during the period of observations (Galli et al. 2006b) they assumed an exospheric density 10 times less than that of the theoretical model by Krasnopolsky. The simulated ENA flux resembles well the statistics of the ENA flux generated at the subsolar region at an altitude of ∼700 km above the surface (∼1.2 Rm from the center, where Rm = 3390 km is the Martian radius).

There are also unexpected features in the subsolar ENA measurements. Futaana et al. (2006b) pointed out that ∼64% of the observed ENA fluxes show a rather sharp decrease in magnitude as MEX goes farther out into the solar wind, even though its FoV pointed

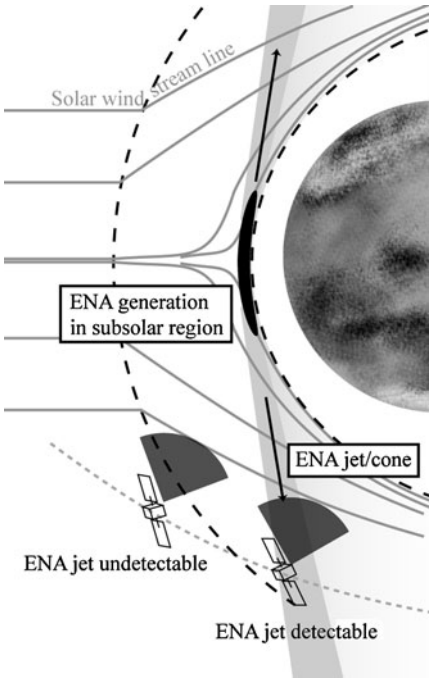

Fig. 6 An illustration of the ENA jet. Relatively quick decrease of the ENA signal observed by NPD indicates a directional flow of the ENA flux from the subsolar region (Futaana et al. 2006b). The generation region is estimated at ∼700 km above the surface (Mura et al. 2008) and the horizontal spread is estimated to be ∼2 Rm (Futaana et al. 2006c)

towards the subsolar region for all observations. This means that the subsolar ENAs flow only directionally flankward (Fig. 6). Therefore, they called this ENA flux "the subsolar ENA jet." Similar signatures of a sharp decrease in the subsolar ENA flux can also be found in the NPI data published in Gunell et al. (2006). Note that if we consider the fact that such ENA jets can be found in almost all the orbits (95%) for a certain time period of more than two months, the name "ENA cone" may be more appropriate (Grigoriev et al. 2006) because the ENA flux is expected to exist in any direction from the subsolar region. However, we use the term "ENA jet" here, because 3-D signatures of the ENA flux have not yet been investigated, and are one of the important future tasks.

Another open question regarding the subsolar ENA jet remains: How can such directional flows be generated in the shocked solar wind? From a perspective of magneto-hydrodynamic (MHD) theory, the supersonic solar wind plasma flow is decelerated and heated at the Martian bow shock in the subsolar region, and the flow becomes subsonic. The velocity distribution function of the shocked solar wind plasma is not directional, i.e. the thermal velocity is larger than the bulk velocity. The rather high bulk energy of the observed ENAs also cast doubts on whether the fluid theory can be applied to the subsolar region. Most probably, fluid theories, which consider the subsolar point as a singular point, cannot describe the plasma dynamics in the subsolar magnetosheath near the IMB due to the large gyro-radius of solar wind protons comparable to the size of the subsolar region. Thus, kinetic effects may play a significant role in this region. Such kinetic effects around the subsolar region must also be investigated by, for example, comparing the observed ENA flux with global hybrid models or global particle simulations in the near future. In situ plasma measurements in this region will also give us hints to understand the plasma dynamics.

Strong temporal variations of the subsolar ENA jet fluxes were also a distinct signature of the ENA jet, which was further investigated by the analysis of NPD data. Grigoriev et al. (2006) statistically analyzed periodic fluctuations in the intensity of the ENA jet flux.

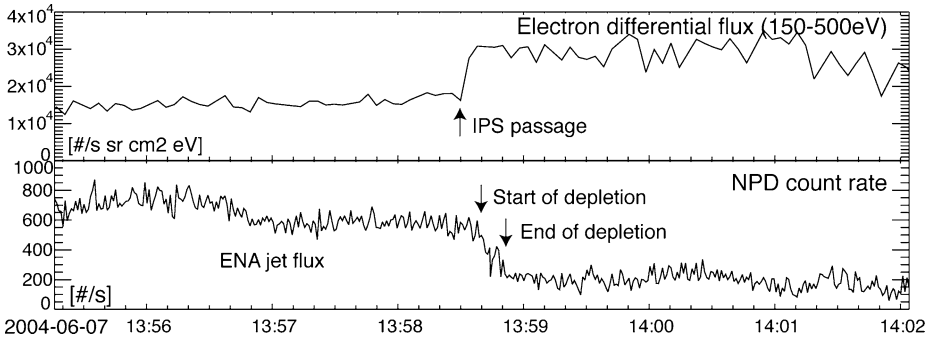

Fig. 7 ENA jet signature during an interplanetary shock (IPS) passage on June 7, 2006. (*Top*) Electron differential flux. The sharp increase of the flux at 13:58:30 is associated with the IPS passage. (*Bottom*) Subsequent depletion of the ENA jet flux between 13:58:40-48, which can be interpreted as a quick replacement of the jet signature due to the shrinking of the Martian induced magnetosphere caused by higher dynamic pressure. After Futaana et al. (2006c)

They categorized the fluctuations into two types by their peak-to-peak periods: 'fast' and 'slow' oscillations. The periods of the two types of variation in the ENA flux intensity in the spacecraft reference frame were on average 50 s (0.02 Hz) and 300 s (0.003 Hz), respectively. Both types of oscillations were detected quite frequently: fast oscillations appeared in all orbits, and slow oscillations could be identified in ∼40% of the orbits. Because of the rather coarse angular resolution of the NPD sensors, it is difficult to determine whether these variations are due to spatial or temporal variations. Possible mechanisms for ENA flux oscillations are due to: (1) Low frequency ion oscillations seen in the magnetosheath such as the mirror mode instabilities found in the magnetic field data by Mars Global Surveyor at about 0.04 Hz (Espley et al. 2005) or cyclotron instabilities found in the electron data by Mars Express at 0.01–0.02 Hz (Winningham et al. 2006). Grigoriev et al. (2006) claims that the cyclotron instabilities might be a plausible explanation because the ENA jet oscillation exhibits the same frequency range (0.02 Hz) as the cyclotron instabilities (0.01–0.02 Hz); (2) Temporal variations of the ENA generation region, e.g. by global oscillations of the Martian induced magnetosphere (Futaana et al. 2006c) or Kelvin-Helmholtz instabilities at the magnetic pile-up boundary (MPB) (e.g. Terada et al. 2002); or (3) Spatial variations of the ENA jet structure such as hair-like ENA sub-jet structures. Grigoriev et al. (2006) mention that the 'slow' oscillations may be due to either mechanisms (2) or (3), but is not certain.

On June 7, 2004, a distinct event occurred, which was relevant for studying the ENA jet signature and the associated Martian ENA environment (Futaana et al. 2006c). They reported the event of the quick ENA jet flux depletion associated with an interplanetary shock passage through the Martian plasma environment (Fig. 7). From the ion mass analyzer (IMA) and the electron spectrometer (ELS) observations (Barabash et al. 2006), the velocity distribution functions of the solar wind plasma showed an increase in the temperature for both protons and electrons. At the same time, Mars Global Surveyor also detected an increase in the magnetic pressure inside the Martian induced magnetosphere, indicating an increase of the dynamic pressure in the solar wind. All these plasma and magnetic field observations are evidence of the passage of an interplanetary shock through the Martian plasma environment. Simultaneous observations by NPD exhibited a strong flux of the ENA jet followed by a quick depletion of the flux within 10 s. After the depletion, three sporadic flux bumps could be observed with peak-to-peak time of ∼60 s. The quick ENA flux depletion can be explained by a displacement of the induced magnetosphere boundary caused by the change

of the dynamic pressure of the solar wind. Such a displacement of the boundary causes a change of the geometry of the ENA jet toward the anti-sunward direction, and the MEX position moved out of the jet region. Therefore, the ENA signal disappeared. Futaana et al. (2006c) estimated the extent of the ENA generation region along the line of sight (ΔL) using the signature of the decrease in the ENA jet flux during this event:

$$\left(\frac{\Delta L}{L}\right)^2 \sim \left(\frac{\Delta T}{T}\right)^2 + \left(\frac{\Delta V}{V}\right)^2,$$

where L and T is the average distance and travel time of ENAs between the source region and observation point, V and ΔV are the average and deviation of the ENA velocity respectively, and ΔT is the decrease time of the ENA jet flux. Using observed parameters, they estimated $\Delta L \sim 2$ Rm.

This observation and analysis indicates that the Martian induced magnetosphere responds to the solar wind structure very quickly. Moreover, the ENA jet is potentially used for monitoring the induced magnetosphere boundary (IMB) position at the subsolar region.

Indeed, a similar analysis has been conducted for the terrestrial magnetopause to understand its response to changes in the IMF direction and solar wind dynamic pressure. Collier et al. (2005) reported an event of solar wind ENA flux enhancement, which is produced mainly at the magnetopause because of the charge exchange between the geocorona (the exosphere of the Earth) and the shocked solar wind, observed by the LENA instrument (Moore et al. 2000) on board the IMAGE spacecraft. They developed a simple analytic model of ENA emission and by comparing it with the observation they concluded that the ENA enhancement is caused by the increase of the charge exchange between the solar wind and the geocorona due to the southward turning of the IMF, which moved the magnetopause inward. Hosokawa et al. (2008) reported a response of the magnetopause location by the change of the solar wind dynamic pressure. They used the ENA data on April 13, 2001, and reported that the high dynamic pressure of the solar wind compressed the terrestrial magnetopause to the geosynchronous orbit on that day. They found a good agreement between the retrieved magnetopause positions and the in situ measurement of the magnetopause crossings by the LANL-01A spacecraft. Recently, by using IBEX spacecraft (McComas et al. 2009), ENA fluxes from the terrestrial subsolar magnetopause (Fuselier et al. 2010) and cusp regions (Petrinec et al. 2011) that originated from the interaction between the shocked solar wind plasma and the geocorona were reported.

The observations and analyses of ENAs of magnetosheath solar wind plasma origin close to different planets, where different physical mechanisms are ongoing, have proven that ENA measurements can be used for a potential investigation of the global response of the solar wind-obstacle boundaries. The physics of the induced magnetosphere boundary has been intensively investigated mainly by analysis of in situ data (Bertucci et al. this issue and references therein), which is very useful for understanding in detail what is going on inside or very close to the boundary. The ENA measurement can provide complementary global information about the boundary structure.

2.4.2 ENAs in the Wake of Mars and Venus

In addition to the ENA fluxes generated on the dayside of Mars, there are also predictions of ENA generation on the Martian nightside (Fok et al. 2004; Kallio et al. 2006). The most productive components are charge exchanged hydrogen ENAs, which were originally protons in the solar wind and the magnetosheath. Due to the thermal velocities of those protons,

the hydrogen ENAs have an angular spread, and a part of them can penetrate into the wake (Fig. 1). Thus, the ENAs behind the wake potentially have information on the temperatures of the upstream solar wind and shocked solar wind protons and the exospheric ENAs.

Brinkfeldt et al. (2006) discussed NPI data obtained inside the wake boundary during the spacecraft's entry into and exit from the shadow of Mars. The planetary shadow is one of the favorable regions for investigating ENA signals in the near Martian environment because the expected UV contamination is small due to the shadowing of the UV by the planetary body. In the NPI data, there are strong signals found at the wake boundary. The signature of the signals changes orbit by orbit even though the examined orbits are in a similar geometry in the Sun-Mars reference frame. Since NPI may still suffer from scattered UV contamination, Brinkfeldt et al. (2006) modeled the UV flux from the Martian exosphere in the same manner as in the ENA jet study in Gunell et al. (2006) and claimed that the expected UV flux is too low to explain the recorded signals by NPI. In addition, simultaneously observed photoelectron counts of spacecraft origin by ELS were used as a proxy of the UV flux at the spacecraft location, and they also showed the lack of a correlation. As a result, they could conclude that these counts are from ENAs, not from UV photons. Brinkfeldt et al. (2006) suggested that the ENAs are solar wind ENAs produced upstream of the bow shock. Milillo et al. (2009), using a statistical study, reported possible ENA signals ($\sim 5 \times 10^6$ cm^{-2} sr^{-1} s^{-1}) coming from the terminator direction above the atmosphere toward the wake when the spacecraft was in shadow.

These ENAs are presumably of solar wind proton origin charge exchanged by exospheric neutral atoms. Due to the non-zero thermal velocity of the solar wind protons, the trajectories of the produced ENAs are not exactly anti-sunward, but have a small angle, depending on the solar wind bulk velocity and the temperature. Some of the particles can penetrate into the wake and were observed by NPI.

The ENA fluxes in the Martian wake were also reported by Galli et al. (2006a). They analyzed hydrogen ENA data recorded by the NPD sensor on board Mars Express. The intensity of the hydrogen ENA flux was 10^5 cm^{-2} sr^{-1} s^{-1}. From a compilation of all NPD data recorded in the shadowed region, Galli et al. (2008c) generated maps of the ENA fluxes in order to understand global signatures of ENA generation. The maximum flux in the maps is in the order of 10^5 cm^{-2} sr^{-1} s^{-1}. The maps are compared with those predicted by an empirical model (Kallio 1996) and an MHD model (Ma et al. 2002) combined with the Chamberlain exospheric model (Chamberlain and Hunten 1987). The biggest uncertainties in the models are the exospheric parameters such as density and temperature. Galli et al. (2006b) derived the very low density of hot H-corona, 10^4 cm^{-3}, at the North Pole region. UV observations by the SPICAM instrument performed about one year later at the sub-solar point gave a density of a few 10^5 cm^{-3} (Chaufray et al. 2008). The difference might be due to the spatial difference, or to an underestimation of the exospheric density due to the optically thin assumption used in Galli et al. (2006b). Such an assumption may lead to an overestimation of the temperature, and consequently to an underestimation of the density. Later, Galli et al. (2008c) made a parametric survey of the nightside ENAs generated by the charge exchange mechanism in the exosphere, and concluded that the optimized density was 10^5 cm^{-3}. The predicated image qualitatively agrees with the observation; in particular, the intensity of the ENA flux was within the error by a factor of two. However, there was also a discrepancy in the characteristics between the observation and the model. The observed ENA flux was spread angularly more widely than in the prediction by the plasma model. One possible explanation for this spread is that the ENAs are generated not only by charge exchange mechanisms, but also by elastic collisions (Kallio and Barabash 2001).

Galli et al. (2008b) reported ENA fluxes in the Venusian wake as well. The same approach as in the Martian wake study was used to compile maps of the ENA flux observed inside the shadowed region of Venus. Up to the spacecraft positions, they generated three maps of tailward flowing hydrogen ENAs. The maximum ENA flux was 1.4×10^5 cm^{-2} sr^{-1} s^{-1}. Those maps are compared with predicted maps using MHD simulations (Tanaka and Murawski 1997) and exospheric VIRA model (Keating et al. 1985) that is extended by Chamberlain model (Chamberlain and Hunten 1987). The comparison indicates that the observed ENA flux can be reproduced by selecting reasonable parameters for the VIRA model, while the modeled flux is slightly higher than the observations. The flux could be optimized if the exobase temperature was reduced by 20% from the default parameters, or if the exobase density was halved. Obviously, the plasma flow models affect the ENA flux, but unfortunately, Galli et al. (2008b) could not manage to change the parameters in the plasma models. The dependence of the ENA flux on the upstream plasma conditions is an important task towards understanding how the ENA flux is generated in the vicinity of the Martian atmosphere.

2.4.3 Atmospheric Effect on Mars

A part of the solar wind protons and the solar wind ENAs may reach the Martian exosphere. Classically the induced magnetosphere boundary is defined as a boundary that separates the solar wind plasma and the plasma of planetary origin (sometimes referred to the name 'mass composition boundary'). However, in reality some of the solar wind protons can get through the boundary. Even though the reason for the penetration is under discussion, such protons have been detected in the lower altitude by MEX (Lundin et al. 2004). A part of those protons that reach down to the exobase may also be scattered back as ENAs after a cascade of collisions with the atmospheric particles (Kallio and Janhunen 2001) thereby losing a fraction of their energy and momentum.

The measurement of the backscattered ENAs from the exosphere combined with backscattering models may open a new window for investigating the energy, momentum, and mass transfer from the solar wind to the planetary upper atmosphere. For example, the energy transfer from the solar wind may heat the planetary upper atmosphere and ionosphere locally or possibly globally, in an analogous way to the auroral particle precipitation and heating occurring in the terrestrial polar region. This interaction between the solar wind and the upper atmosphere is therefore sometimes called "atmospheric effect." The measurement of solar wind ENAs flowing directly along the Sun direction is always troublesome because the incoming flux in the ionosphere or the atmosphere of unmagnetized bodies is contaminated by the UV flux from the Sun. Instead of measuring the solar wind ENAs, the measurement of the backscattered ENAs coming from the upper atmosphere can be used to estimate the incoming flux and the deposition site. Another advantage of using the backscattered ENAs is that the global coverage of the precipitation and the deposition rate may be retrieved. Obviously, detailed modeling of microphysics of collisions in the upper atmosphere and the ionosphere is very important for this study.

Futaana et al. (2006a) discussed the atmospheric effect from ENA data recorded by the NPD sensor. When MEX was in front of the subsolar point at very low altitude (∼570 km), significant H-ENA signals could be detected. The observed total flux is $0.9–1.3 \times 10^7$ cm^{-2} s^{-1}. On the other hand, a theoretical flux of the backscattered flux of 3.2×10^6 cm^{-2} s^{-1} was obtained by assuming that 10% of the solar wind protons are neutralized before reaching the induced magnetosphere boundary, and that 58% of precipitated ENAs are backscattered at the exobase. The observed flux is 3 times more than that of the theoretical prediction. Futaana et al. (2006a) suggested a significant flux of the solar

wind proton penetration inside the boundary because of the similarity of the distribution functions between their observations and those in calculation in the model by Kallio and Barabash (2001).

The generation mechanism of the observed higher ENA flux is an open question. Moreover, there is a discussion that the flux modeled by Kallio and Barabash (2001) may be overestimated. In that model, scattering angles after each collision are independent of the collision processes. They adopt the scattering angle model from Noël and Prölss (1993), which is based on laboratory measurement by Newman et al. (1986). The minimum scattering angle after a collision was assumed to be 0.12°. However, this may hardly occur because the scattering angle for some collision mechanisms, such as the charge exchange process, is almost negligible in theory (e.g. Basu et al. 1993). Since a smaller scattering reduces the backscattering rate, a much higher precipitating flux must be assumed to explain the observed ENA flux as backscattering ENAs.

2.4.4 Oxygen ENAs at Mars and Venus

According to the estimations in Barabash et al. (2002), an oxygen ENA flux of $\sim 10^5$ cm^{-2} sr^{-1} s^{-1} eV^{-1} was predicted to exist in the vicinity of Mars, which should be detectable by the existing ENA sensors. In addition, NPD is capable of separating the oxygen ENAs from hydrogen ENAs from its TOF range. The main source of the oxygen ENAs close to Mars and Venus is the charge exchange mechanism between the accelerated oxygen ions of planetary origin and the exosphere. After intensive searches in the MEX/NPD data, the oxygen ENA flux at Mars was found to be below the NPD detection level ($\sim 10^4$ cm^{-2} sr^{-1} s^{-1}). Even if Galli et al. (2008c) found the best candidate of oxygen fluxes in the dataset, the signal only corresponds to $3 \pm 2 \times 10^4$ cm^{-2} sr^{-1} s^{-1}. Figure 8 shows the energy spectra of the ENA jet together with mass information as an example. This result indicates that the direct contribution of oxygen ENAs to the outflow is at most of the order of 10^{22} s^{-1}, which is significantly less than the total oxygen outflow (e.g. Barabash et al. 2007b; Dubinin et al. this issue). The same conclusion was derived for Venus (Galli et al. 2008b).

The overestimate of the oxygen ENAs in previous models may be due to a combination between the assumed higher O^+ distribution and higher exospheric density around Mars and Venus. In the oxygen ENA flux model of Barabash et al. (2002), an oxygen ion outflow flux was estimated based on the knowledge from PHOBOS spacecraft data (Lundin et al. 1990). However, recent MEX observations indicate that the O^+ outflow flux is less by one order of magnitude (Barabash et al. 2007b) compared with PHOBOS observations.

Other observations imply a lower density of the exosphere than has been considered. Galli et al. (2006b) evaluated the exospheric density at the polar region to be $\sim 10^4$ cm^{-3}, while most of the simulations had used a density of 10^6 cm^{-3} based on Krasnopolsky and Gladstone (1996). By analyzing data from the SPICAM instrument on board MEX, Chaufray et al. (2008) concluded that the exobase density at the subsolar point is $1–4 \times 10^5$ cm^{-3}, which is one order less than the prediction by Krasnopolsky and Gladstone (1996).

However, one should note that the solar activity might control the plasma environment, especially the escaping O^+ ion fluxes in the vicinity of Mars and Venus (Futaana et al. 2008b; Luhmann et al. 2008; Lundin et al. 2008; Edberg et al. 2010; Dubinin et al. this issue). The ENA observations and analysis were only conducted using data obtained between 2004 (MEX) and 2006–2007 (VEX). In this period, the solar activity was declining from the solar cycle 23 (peak in 2001–2003) and went down to solar minimum. For the period between

Table 2 Summary of the ENA observations by ASPERA-3 and -4 instruments close to Mars and Venus

ENA generation mechanisms	Mars	Venus
Solar wind ENA	N/A	N/A
Magnetosheath ENA (ENA jet)	1.3×10^7/cm^2 sr s from NPI (Gunell et al. 2006) $(4–7) \times 10^5$/cm^2 sr s from NPD (Futaana et al. 2006b)	N/A
Planetary ENA (including nightside)	Below the detection level of NPD (Galli et al. 2008c). Upper limit of 10^{22}/s	Below the detection level of NPD (Galli et al. 2008b). Upper limit of 10^{22}/s
Phobos tori	Not yet reported	
Backscattered ENA from the exobase	$0.9–1.3 \times 10^7$/cm^2 s (Futaana et al. 2006a)	N/A
Nightside ENAs	5×10^6/cm^2 sr s from NPI (Milillo et al. 2009) 10^5/cm^2 sr s from NPD (Galli et al. 2006a)	1.4×10^5/cm^2 sr s from NPD (Galli et al. 2008b)

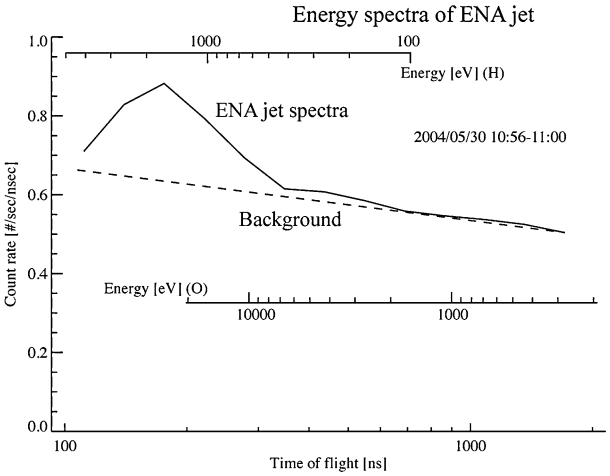

Fig. 8 Typical TOF spectra (equivalent to the energy spectra) of the subsolar ENA jet. Corresponding energies for hydrogen and oxygen atoms are superimposed. Hydrogen with energy less than 100 eV cannot be detected because of the extremely low efficiency in this low energy range. Therefore the main contribution of the TOF steps greater than ~700 ns is oxygen ENAs with energies of several hundreds of eV. After Futaana et al. (2006b)

2006 and 2009, the Sun was extremely quiet. There is a possibility that a more active Sun may strongly increase the oxygen ENA flux close to Mars and Venus.

2.5 Summary of ENA Environment Close to Mars and Venus

After the orbit insertions of Mars Express in 2003 and Venus Express in 2005, a unique dataset of ENA signals from Mars and Venus has been obtained. Table 2 summarizes the detected ENA fluxes together with a comparison with the expected ENA generation mechanisms. Due to the limitation of the energy and angular resolution, the UV contamination, the FOV conditions, etc, there are still many open questions concerning the ENA environment and associated plasma and exospheric environment. A list of the open issues is given at the end of this paper.

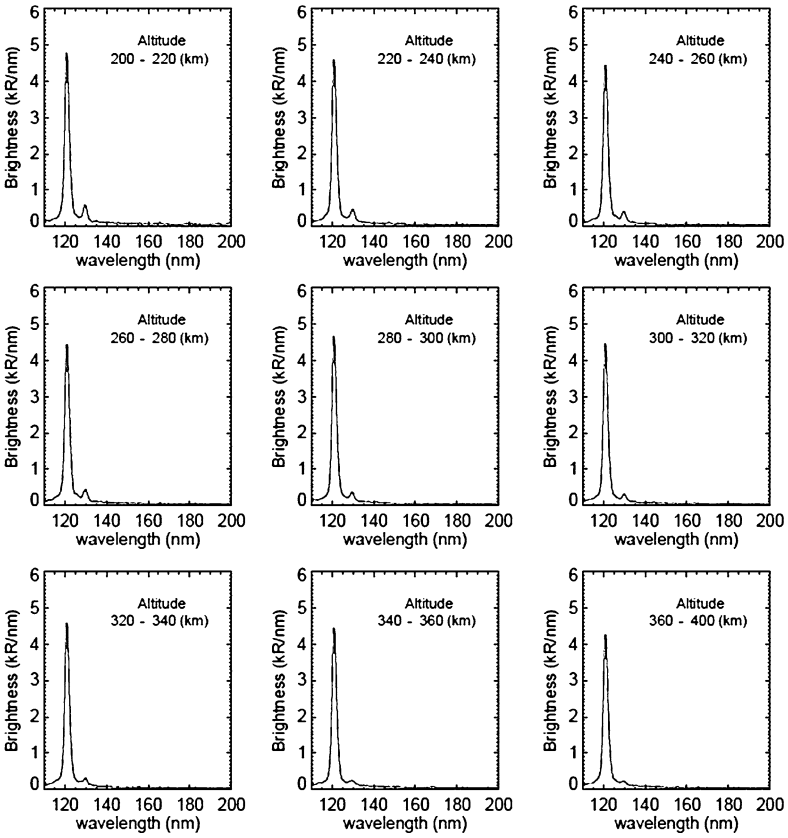

Fig. 9 Averaged UV spectra obtained by SPICAM-MEX at different altitudes in the Martian exosphere. H Lyman-α emission line is observed at 121.6 nm. O emission line is observed at 130.4 nm

3 Recent Observations of the Martian and Venusian Exospheres

In this section, we will focus on the neutral exospheres of Mars and Venus. Their composition, recent observations from space and the characteristics of the two main atomic components, i.e. atomic hydrogen and oxygen, are reviewed.

3.1 Composition

While the atmosphere of Venus (with a surface pressure of ~ 93 bar) is much denser than the Martian atmosphere (where the surface pressure is ~ 7 mbar), both atmospheric compositions are similar. The thermosphere is composed mainly of CO_2 with a few percent of N_2 and Ar. Because diffusion is the dominant process for vertical transport at higher altitude, O, H_2 and H become the dominant species (Krasnopolsky 2002; Fox 2003). Atomic hydrogen and oxygen in the Martian and Venusian exospheres were observed for the first time by the UV spectrometers on the Mariner missions forty years ago (e.g. Barth et al. 1969; Broadfoot et al. 1974). The exospheric UV spectra with the H and O lines observed by the Mars Express UV spectrometer SPICAM are displayed in Fig. 9. The H Lyman-α emission line at 121.6 nm and the oxygen emission line at 130 nm are clearly visible. While

the hydrogen line is visible from 200 to 400 km, the oxygen line falls below the instrument detection limit at 400 km.

Molecular hydrogen H_2 has been detected on Mars with the Far Ultraviolet Spectrometer Experiment (FUSE). Krasnopolsky and Feldman (2001) derived a H_2 column density of $(1.17 \pm 0.13) \times 10^{13}$ cm^{-2} above 140 km corresponding to a mixing ratio of 15 ppm in the lower atmosphere. No H_2 has been reported in the Venusian thermosphere. Other minor species, such as atomic deuterium, D, have also been found in the Martian atmosphere (Krasnopolsky et al. 1998). Using the Goddard high-resolution spectrograph (GHRS) on board the Hubble Space Telescope (HST), a deuterium line was detected on Mars at an intensity of 23 ± 6 Rayleigh corresponding to the ratio in DH/H_2 equal to $1.5 \pm 0.6 \times 10^{-4}$. This was lower than the D/H ratio observed in the water vapor in the Martian mesosphere from infrared data (Owen et al. 1988). The D/H ratio is useful to estimate the loss of water along the planetary history assuming that the deuterium enrichment compared to the Earth D/H ratio is due to preferential escape of hydrogen atoms in the upper atmosphere (Gurwell 1995; Donahue 1999; Hodges 1999; Krasnopolsky 2000, Krasnopolsky and Feldman 2002; Bertaux and Montmessin 2001). Helium has also been observed on Venus (Bertaux et al. 1981) and Mars (Krasnopolsky and Gladstone 1996). It is partly supplied by the capture of solar wind He^{++} ions and surface outgassing (Krasnopolsky and Gladstone 2005; Chanteur et al. 2009). In addition, emission lines from atomic carbon and nitrogen have also been finally observed on Mars and Venus (Feldman et al. 2000; Krasnopolsky 2002; Gérard et al. 2011).

3.2 Observations of the Neutral Exospheres

Among several methods used to observe the neutral exospheres, UV spectroscopy is an important method. The absorption of solar photons can excite an atom or molecule by causing an electric transition. The excited state atom or molecule subsequently relaxes to a lower energy state by emitting a photon. The wavelength of the emitted photon can be the same (resonant scattering) or larger (fluorescent scattering) than the wavelength of the photon absorbed. Several detections of exospheric neutral species have been made using remote sensing observations. Mass spectrometers have also provided information on the composition of the upper atmosphere of Mars (Nier and Mcelroy 1977) and Venus (von Zahn et al. 1979, 1980). Aerobraking data are often used to derive the total mass density in the thermosphere (Keating et al. 1998), and more recently, radio tracking data to perform precise orbit determination has been used from the Mars Odyssey mission to derive a mass density $\sim 10^{-15}$–10^{-14} kg m^{-3} and a scale height between 25–45 km in the exosphere at 400 km (Mazarico et al. 2007), or with Mars Global Surveyor to derive the exospheric temperature and mass density at 390 km and their variations with the solar flux (Forbes et al. 2008).

X-rays from Venus and Mars were first detected in 2001 by Chandra (Dennerl 2002; Dennerl et al. 2002). These observations show the presence of a strong X-ray emission due to solar scattering by the Martian upper atmosphere but also an extended halo produced by charge exchange between heavy solar wind ions in high charge states and atmospheric constituents (Dennerl 2006, 2008). ENA imaging has been used successfully on Mars and Venus Express to detect the presence of hot hydrogen produced by the charge exchange process between solar wind protons and the neutral exosphere as reviewed in the previous section. Finally numerous observations of the ionosphere and thermosphere are also useful to study the exosphere and its possible variations. Recent observations of the Martian thermosphere by stellar occultation (Forget et al. 2009) or UV airglow (Leblanc et al. 2006; Simon et al. 2009) have shown a strong seasonal variability. Oscillations of the electron peak

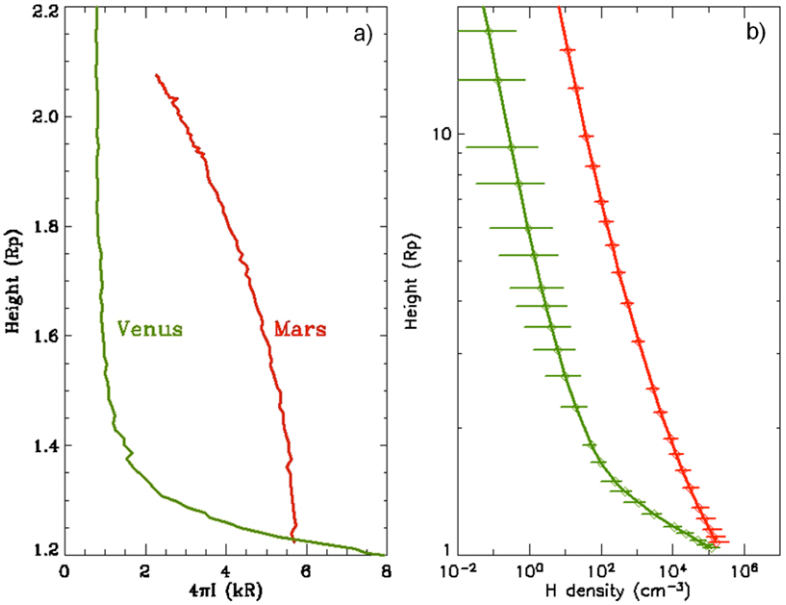

Fig. 10 (**a**) Height profile of the Lyman-α brightness obtained by SPICAM-MEX in the Martian exosphere (*red line*) and by SPICAV-VEX in the Venusian exosphere (*green line*). R_p is the planet radius (3390 km and 6051 km for Mars and Venus respectively); (**b**) H density profiles derived from Lyman-α published observations (see text for details)

density as a function of longitude have been observed from the MGS radio occultation experiment and accelerometer measurements (Bougher et al. 2001; Withers et al. 2003). These oscillations, produced by thermal tides resulting from the interaction of solar radiation and Mars topography, have been confirmed by Mars Odyssey accelerometer density retrievals (Wang et al. 2006).

Because the exosphere is directly coupled to the thermosphere and ionosphere, these variabilities should also affect the exobase altitude as well as the exospheric density.

3.3 Recent Observations of Hydrogen Coronae by UV Remote Sensing

The hydrogen coronae have been observed since the Mariner missions in the 1970s. More recently the Martian hydrogen corona has been observed by the UV spectrometer SPICAM (Bertaux et al. 2006) on Mars Express, by the ALICE instrument on Rosetta during its fly-by in February 2007 (Feldman et al. 2011) and from Earth by FUSE (Feldman et al. 2000) and the Hubble Space Telescope (Clarke et al. 2009). The Venus hydrogen corona has been observed by the UV instruments SPICAV (Bertaux et al. 2007) on Venus Express and UVIS on Cassini during its fly-by of Venus (Gérard et al. 2011). In this section, we focus on the recent observations performed by the SPICAM-UV and SPICAV-UV instruments.

Figure 10a displays typical brightness profiles of the Lyman-α intensity on Mars and Venus observed by SPICAM and SPICAV during grazing limb observations at dayside. The altitude is referring to that of the tangent point. The profiles are quite different. The Venusian profile presents two scale heights corresponding to a cold hydrogen population dominant below 2000 km (∼1.3 Rv; where Rv is the Venus radius of 6051 km) and a

hot hydrogen population dominant above 4000 (∼1.7 Rv) km. These two scale height profiles have already been observed by several previous missions to Venus (Anderson 1976; Bertaux et al. 1978, 1982; Takacs et al. 1980; Paxton et al. 1988). On Mars, the Lyman-α brightness profile is rather constant between 400 km and 1000 km (1.2–1.4 Rm). This is a sufficient (but not necessary) condition to show that the emission is optically thick, because if the emission were optically thin, the intensity profile would decrease exponentially. The Venusian emission is in fact also optically thick at least below 4000 km as deduced from radiative transfer models taking into account auto-absorption and multiple scattering. The fact that the emissions on both Venus and Mars are optically thick (with a vertical thickness of ∼10–20 above the absorption level by CO_2 at ∼110 km on Venus and ∼85 km on Mars) prevents a direct inversion of the profile to derive the hydrogen density, because in this case, effects of multiple scattering cannot be neglected and there is no simple analytical relation between the brightness and the column density integrated on a line of sight. The general method used to derive the hydrogen density is to compare the expected brightness profiles from different hydrogen density profile models to the observed profiles (e.g. Anderson and Hord 1971; Paxton et al. 1988; Chaufray et al. 2008). To compute the theoretical brightness profiles, taking into account the multiple scattering, the radiative transfer equation must be solved. Chaufray et al. (2008) used several assumptions such as complete frequency redistribution function (where the wavelength of the outgoing photon is independent of the wavelength of the incoming photon), and used a Gaussian profile rather than the widely-used Voigt profiles to simplify the problem. These assumptions are justified for the Lyman-α emission on Mars and Venus by the fact that the optical thickness is not very large (∼10–20) and therefore the wings of the absorption profile have a negligible effect on the observed brightness. This method allows deriving a parameterization of the hydrogen density profile. The first Martian hydrogen profiles obtained by SPICAM have been studied in detail by Chaufray et al. (2008) showing that they could be reproduced by a single cold population when assuming a large uncertainty in the models (Fig. 10b). However, the authors show that models including a hot population provide a better fit, especially on the dayside of Mars. Unfortunately, the method used to analyze these observations only provide a parameterization of the density profile but does not allow the source of this putative hot hydrogen population to be identified. Observations of the H Lyman-α and Lyman-β lines obtained by the ALICE-UV spectrometer during the Rosetta fly-by show no evidence of a hot hydrogen population (Feldman et al. 2011).

The main uncertainty on the Martian exobase temperature derived from Lyman-α brightness profiles comes from the uncertainty in the absolute photometric calibration of the SPICAM sensor. Chaufray et al. (2008) showed that some observed profiles could be reproduced well when the calibration was changed by 25%. The second limit of this process comes from the modeled hydrogen density profiles used to derive the best profile using a χ^2 minimization process. Models with few parameters are justified to reduce the numbers of modeled brightness profiles, but this approach could produce bias and still needs to be validated using more realistic 3D hydrogen density profiles such as those provided by the modern version of the Martian Global Circulation Model (MGCM) describing the Martian atmosphere up to the exobase (González-Galindo et al. 2009; Valeille et al. 2009). Numerous hydrogen corona observations have been performed but not yet published. The analysis of these data as well as the future observations by the Mars Atmospheric and Volatile EvolutioN (MAVEN) mission (Mitchell 2010) will help us to understand the physics controlling the Martian hydrogen corona.

A systematic study was conducted by Chaufray et al. (2011). These observations show diurnal variations of the thermal hydrogen density whereas the hot hydrogen density is rather

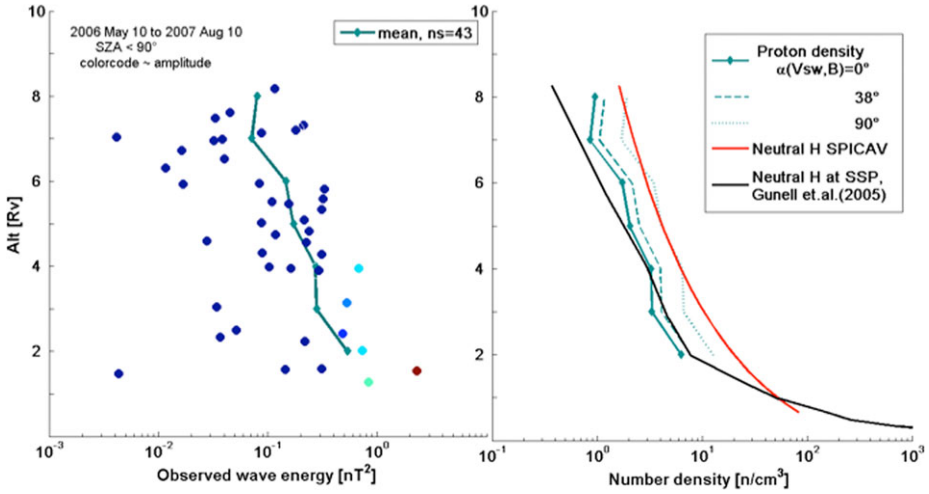

Fig. 11 Observed wave energy on the Venus dayside as a function of altitude and required proton density. (*Left*) Wave energy for newly generated PCWs for SZA <90°. (*Right*) Proton density required to generate the observed waves for SZA <90° maximum energy transfer efficiency and different pitch angles α. The *black line* denotes the neutral hydrogen density from atmospheric models, the *red line* is the neutral hydrogen density determined from SPICAV Lyman-α observations. After Delva et al. (2009)

well reproduced by the model of Hodges (1999). These observations were made below 10,000 km and hydrogen density above 10,000 km is not strongly constrained. H Lyman-α observations at higher altitudes need to be carefully corrected from the interplanetary emission component, which contributes to more than 70% of the signal above 10,000 km. Hydrogen observations by UVIS on Cassini during its Venus fly-by have been reported by Gérard et al. (2011) but no detailed study has been performed yet. Hydrogen density profiles derived from published SPICAM-UV (one population model) and SPICAV-UV (near noon; Chaufray et al. 2008, 2011) are displayed on Fig. 10b. The scale height of the thermal hydrogen density on Mars is much larger than the scale height of the thermal hydrogen density on Venus due to the lower gravity.

3.4 Venus Hydrogen Corona Implied from Magnetometer Data

As already mentioned, the actual content of hydrogen in the Venus exosphere is still an open issue, mainly because no *in situ* direct measurements are available yet. Instead, Delva et al. (2009) applied an indirect method for the detection of planetary hydrogen in the region upstream of the bow shock, using the presence of proton cyclotron waves (PCW) as an early tracer of ionized planetary hydrogen picked up by the solar wind. Recent long-term observations over two full Venus-years of upstream PCWs by the magnetometer on the Venus Express spacecraft indicate permanent ionization and pickup of hydrogen by the solar wind upstream of the bow shock up to large distances ~8 Rv. A density profile for the pickup protons was derived from the observed wave energy and is shown in Fig. 11. Despite consideration of energetic neutral hydrogen from precipitating solar wind protons and from interstellar hydrogen as possible additional sources for local pickup, no significant neutral hydrogen density with the required low velocity in the regions of PCW observations could be identified. Therefore, the authors concluded that the observation of the waves at the local proton cyclotron frequency in the Venus upstream region can only be explained by

pickup of local neutral hydrogen from an extended reservoir of planetary origin. This conclusion contradicts the neutral hydrogen density derived from UV emissions but as pointed out in the previous subsection, the neutral hydrogen density above 10,000 km is not well constrained by UV observations analyzed by Chaufray et al. (2011). Therefore, the nature of the extended Venusian exosphere with frequent high local densities is still an open issue and needs further investigation.

3.5 Hot Hydrogen Coronae

Several sources of hot hydrogen in the Venusian exosphere have been proposed in the past. Rodriguez et al. (1984), using a two-stream approach to describe the transport of hot hydrogen in the Venusian atmosphere, suggested charge exchange between ambient hydrogen and H^+ is the dominant source of hydrogen on the nightside while collisions between ambient hydrogen and hot oxygen (produced by dissociative recombination of O_2^+) are the dominant source on the dayside. Shizgal (1999) studied this last process (but focusing more on the escape flux than the structure of the exosphere) showing that the hydrogen and deuterium escape induced by collisions with hot oxygen should be significant on Venus and very sensitive to the amount of hot oxygen and cold hydrogen in the thermosphere. Reactions involving H bearing molecules such as H_2 were not considered in these studies due to the absence of measurements of H_2 on Venus. Hodges (1999), using a Monte Carlo model coupled iteratively to an ionospheric model, suggested that momentum transfer between ambient H and H^+ and O^+ was the main source of hot hydrogen but did not consider collisions between hot oxygen and ambient hydrogen. This study was able to reproduce the hydrogen density profile derived from Lyman-α emissions of the outer exosphere by the missions Mariner 5 (Anderson 1976) and Mariner 10 (Takacs et al. 1980) as well as recent observations made by SPICAV on Venus Express (Chaufray et al. 2011) while the dayside hydrogen density profile recently derived from the magnetometer on VEX (Delva et al. 2009) is significantly higher than predicted by the model of Hodges (1999). Models including both momentum transfer between ambient hydrogen and ions as well as energization of ambient hydrogen by hot oxygen will be helpful to quantify the importance of each source on Venus in terms of escape flux and hot hydrogen density.

Recent analysis based on MEX observations claims that a hot hydrogen population, denser than expected, is present on Mars (Galli et al. 2006b; Chaufray et al. 2008). This conclusion is supported by the fact that high temperatures are needed to reproduce the Lyman-α observations made by Mariner. The Mariner missions observed the Martian corona during a period of high solar activity. The variations of the exobase temperature with the solar activity are not well known but recent analysis of precise orbit determination of the Mars Global Surveyor spacecraft from 1999 to 2005 provides the variations of the exospheric temperature (T_{exo}) with the 81 days averaged value of the solar $F_{10.7}$ index ($F_{10.7}$) and the solar longitude (L_s) at Mars by the relation (Forbes et al. 2008)

$$T_{\mathrm{exo}} = 130.7 + 1.53 \cdot F_{10.7} - 13.5 \cos(L_s - 85^\circ). \tag{5}$$

During the observations studied by Chaufray et al. (2008) at $L_s \sim 180^\circ$ and $F_{10.7} \sim 40$–50, the above equation leads to an exospheric temperature of 190–210 K, which is close to the value assumed by these authors for the cold population in their model with two populations and is in good agreement with temperatures derived from the CO_2^+ UV emission line (Leblanc et al. 2006). During the Mariner 6 and 7 observations, the $F_{10.7}$ solar index at Mars was equal to 88 and the solar longitude equal to 200° (Bougher et al. 2000). For

these conditions, (5) gives an exospheric temperature equal to 271 K close to the lower limit of the exospheric temperature derived from Mariner's observations. Therefore, in the light of recent observations by Mars Global Surveyor, the 350 K temperature derived from the Mariner's Lyman-α observations appears too high and could be due to the presence of an additional hot population (Lichtenegger et al. 2006).

However, other uncertainties in the absolute calibration of sensors on board Mariner could also explain this large value. The presence of a substantial hot hydrogen population is not supported by the recent Lyman-α and -β observations made over a larger altitude range by ROSETTA-ALICE during its flyby (Feldman et al. 2011). It is possible that a hot hydrogen population is produced on Mars as on Venus, but on Mars, due to the low gravity, it escapes directly and therefore does not contribute very much to the exospheric density.

Anyway, very few studies have investigated the source of hot hydrogen by momentum transfer and collisions between ambient hydrogen with hot oxygen on Mars. Lichtenegger et al. (2006), using a Monte Carlo model, suggested that these reactions were negligible compared to reactions involving H_2 molecules that are the important species in the Martian exosphere (Krasnopolsky 2002; Fox 2003). Models could also be useful to estimate more accurately the difference between the Martian and Venusian hydrogen coronae.

3.6 Oxygen Coronae

The oxygen in the exospheres of Mars and Venus has been detected since the first remote sensing UV observations (Barth et al. 1969; Broadfoot et al. 1974). The most important oxygen line is the optically thick line at 130 nm (Fig. 9). Other oxygen emissions have been observed such as the lines at 98.9 nm, 135.6 nm and 297.2 nm (Barth et al. 1971; Feldman et al. 2000; Leblanc et al. 2006) but these lines are generally much weaker than that at 130 nm and not resonantly excited making them more difficult to investigate in the exosphere. For Mars, the first detailed oxygen data analysis was provided by Strickland et al. (1972, 1973) and using the data from Mariner 6, 7 and 9. These authors found that the emission was produced mainly by resonant scattering of the solar light, but a non-negligible source was provided by the impact of photoelectrons. These data were reanalyzed later by Stewart et al. (1992) using an updated radiative transfer model and cross sections for electronic impact. They found that a mixing ratio [O]/[CO_2] of $\sim$0.7% at the 1.2 nbar level ($\sim$115–130 km) was needed to reproduce the intensity profile observed, while a mixing ratio of $\sim$0.2% was found to provide the best fit of the relative latitude/local time variations. The O/CO_2 mixing ratio is an important parameter controlling the cooling of the Martian thermosphere and therefore the exobase temperature (Bougher et al. 1999). Chaufray et al. (2009) have analyzed the oxygen population using the Mars Express data and found a density of 1.2×10^7 cm^{-3} at the exobase altitude (200 km) for solar zenith angle (SZA) $\sim$20–55° and a decrease by a factor 2 for SZA $\sim$55–90°. The mixing ratio derived near the homopause (135 km) was 0.6–1.2% and thus in good agreement with Mariner's observations but the CO_2 density profile was not constrained in this study and its density in the thermosphere is variable (Forget et al. 2009).

If we assume that the dominant species at 400 km are H, H_2, He and O and assume same densities $\sim 10^5$ cm^{-3} for H, H_2 and He (Krasnopolsky 2010), that is $\rho(\mathrm{H} + \mathrm{H_2} + \mathrm{He}) \sim 10^{-18}$ g cm^{-3}, we can compare these results to the densities retrieved from the precise orbit determination of Mars Odyssey (MO) between March 2002 and November 2005 (Mazarico et al. 2007) and Mars Global Surveyor (MGS) between February 1999 and July 2005 (Forbes et al. 2008). MO and MGS are in nearly sun-synchronous polar orbits with a periapsis in the southern hemisphere, near 85° latitude for MO and 40–60° latitude for MGS and a local time

for MGS equal to 2 am/pm and varying from 4 am/pm to 6 am/pm for MO corresponding to SZA near 90° for MGS and 60° for MO. The densities $\rho \sim 2 \times 10^{-18}$–$10^{-17}$ g cm^{-3} derived from the first set of measurements give an oxygen density between 10^4–4×10^5 cm^{-3} at 400 km. The densities at 390 km obtained from the relation between the density and the solar flux fitted to the second set of observations, after correction in the sign as pointed out by Krasnopolsky (2010), given by

$$\rho_{390} = -3.72 + 0.28 F_{10.7} - 4.5 \cos(L_s - 72°), \tag{6}$$

in the unit of 10^{-18} g cm^{-3}. This relation leads to oxygen densities of (1–4) $\times 10^5$ cm^{-3}, that is slightly larger than the densities derived from the MO dataset. These values are also slightly larger than the oxygen density at 400 km derived by Chaufray et al. (2009), (2–8) $\times 10^4$ cm^{-3} without including the hot oxygen population from O_2^+ dissociative recombination (see the next section). For an exospheric temperature of 200 K, the oxygen density decreases by ~33% from 390 to 400 km and cannot totally explain the difference. Krasnopolsky (2010) suggested that the density derived from MGS measurements could be overestimated at low solar activity due to a low signal to noise ratio. He found that the observed annual mean density values at 390 km (n_{390}) vary by a factor of 3 with solar index $F_{10.7}$ varying from 40 to 100, i.e.

$$\frac{n_{390}(F_{10.7} = 100)}{n_{390}(F_{10.7} = 40)} = 3 \tag{7}$$

while using his 1D photochemical model at SZA = 60° with the temperature variation given by (6) for the same $F_{10.7}$ variations, he found

$$\frac{n_{390}(F_{10.7} = 100)}{n_{390}(F_{10.7} = 40)} = 8 \tag{8}$$

Chaufray et al. (2009) found a decrease by a factor 2 in the oxygen density from SZA ~35–70° consistent with the decrease of the density derived from both datasets. Chaufray et al. (2009) used 1D models to derive the oxygen density from the 130 nm emission line, while 3D GCM models show strong spatial variations in the oxygen density (Valeille et al. 2009; González-Galindo et al. 2009) in the thermosphere. The 1D models could produce bias in the interpretation of the O emission lines and this should be investigated. A hot oxygen population has been observed by ALICE on board ROSETTA during its fly-by of Mars (Feldman et al. 2011); such a population has been predicted on Mars and observed on Venus (Nagy et al. 1981) and should result mainly from dissociative recombination of O^{2+} ions in the ionosphere (see next section). The observed scale height of this hot oxygen population on Mars is not consistent with models and the reason for this discrepancy is unknown.

No observations of the Venusian oxygen corona from Venus Express have been published yet but the observations from past missions have been summarized by Fox and Bougher (1991).

4 Monte Carlo Modeling of the Venusian Hot Oxygen Corona

Here we briefly look through a recent development of exospheric oxygen corona generation theories and models and discuss some of the open problems.

Among the various processes that can produce suprathermal particles, such as sputtering of upper atmospheric species by the impact of high energetic particles or exothermic photochemical reactions, dissociative recombination (DR) of O_2^+ appears to be the dominant source for the Venusian hot exosphere. Despite the lack of a substantial amount of O_2 atoms in the Venusian thermosphere, O_2^+ is the major ion in the lower ionosphere of Venus. While ionization of O_2 by photons or by electron impact is negligible, O_2^+ is predominately formed by means of the two fast exothermic reactions

$$O + CO_2^+ \rightarrow CO + O_2^+(v \leq 6) + 1.33\ \text{eV}, \tag{9}$$

$$O^+ + CO_2 \rightarrow CO + O_2^+(v \leq 5) + 1.20\ \text{eV}, \tag{10}$$

where (9) is mainly important below 150 km and (10) above 150 km (Fox 1985). As indicated, these reactions can produce vibrational levels up to $v = 6$ and $v = 5$, respectively. At zero collision energy, DR of ground state O_2^+ can proceed via the following 5 different channels

$$O_2^+ + e \rightarrow \begin{cases} O(^3P) + O(^3P) + 6.99\ \text{eV}, & \text{(11a)} \\ O(^3P) + O(^1D) + 5.02\ \text{eV}, & \text{(11b)} \\ O(^3P) + O(^1S) + 2.80\ \text{eV}, & \text{(11c)} \\ O(^1D) + O(^1D) + 3.06\ \text{eV}, & \text{(11d)} \\ O(^1D) + O(^1S) + 0.84\ \text{eV}, & \text{(11e)} \end{cases}$$

where the energy values correspond to the energy released by the process in the center of mass frame and shared by the two oxygen dissociation fragments. These exothermicities are considered to be valid for the ground electronic state of the initial O_2^+ ions and do not include the vibrational or rotational energies of these ions. The lifetimes of the excited internal states ^1D and ^1S amount to 100 s and 0.79 s, respectively.

4.1 Dissociative Recombination Rates, Branching Ratios and Vibrational Distribution

The overall rates for dissociative recombination (DR) of O_2^+ have been measured extensively during the past (e.g. Mehr and Biondi 1969; Peverall et al. 2001; Petrignani et al. 2005a, 2005b) and are believed to be known within a factor of ~2. Sheehan and St.-Maurice (2004) recommend a rate coefficient k for DR of O_2^+ for $v = 0$ of the ground electronic state and $T_e < 1200$ K of

$$k = 1.95 \times 10^{-7} \left(\frac{300}{T_e}\right)^{0.7}\ \text{cm}^3\,\text{s}^{-1} \tag{12}$$

and for ions with vibrational levels populated according to the Frank-Condon distribution

$$k = 0.90 \times 10^{-7} \left(\frac{300}{T_e}\right)^{0.49}\ \text{cm}^3\,\text{s}^{-1}. \tag{13}$$

The branching ratios for the different channels in (11) depend both on the vibrational level of O_2^+ and on the collision energy. Table 3 summarizes the values of the branching ratios

Table 3 Branching ratios for dissociative recombination of O_2^+ for various vibrational levels at zero electron collision energy. The branching fraction of reaction (11c) is negligible and therefore not shown in the table

Reference	v	(A)	(B)	(C)	(D)
Kella et al. (1997)	0	0.22 ± 0.10	0.42 ± 0.05	0.31 ± 0.07	0.05 ± 0.02
Peverall et al. (2001)	0	0.204 ± 0.02	0.44 ± 0.03	0.315 ± 0.02	$0.041^{+0.007}_{-0.004}$
Petrignani et al. (2005a, 2005b)	0	0.265 ± 0.008	0.473 ± 0.008	0.204 ± 0.003	0.058 ± 0.005
	1	0.073 ± 0.75	0.278 ± 0.051	0.510 ± 0.054	0.139 ± 0.031
	2	0.0002 ± 0.0003	0.764 ± 0.022	0.025 ± 0.021	0.211 ± 0.025

obtained by heavy-ion storage ring experiments at zero collision energy and for $v \leq 2$. It should be noted that the branching fraction of reaction (11c) is almost zero at low electron energies (Guberman 1997; Kella et al. 1997; Peverall et al. 2001; Petrignani et al. 2005a, 2005b) and is therefore not listed in the table. The dependence of the branching ratios on the collision energy is still unclear, since two independent experiments with non-zero energy have revealed quite different results (Peverall et al. 2001; Petrignani et al. 2005a).

In order to account for the different branching ratios for different vibrational levels, the vibrational distribution of O_2^+ ions as a function of altitude must be known. Fox (1985) has calculated the vibrational distribution of O_2^+ in the ionosphere of Venus based on data from Pioneer Venus mass spectrometer and the assumption of photochemical equilibrium. Fox (1985) calculated the relative populations of vibration levels $v \leq 2$ and $3 \leq v \leq 10$ between 115 and 270 km altitude. According to Fig. 1 in Fox (1985), below ~ 140 km quenching (mainly by CO_2 and O) dominates and thus limits the fractional population, while at high altitudes the fraction for $v = 0$–5 approaches 0.16 because these levels are assumed to be produced with equal probability in (7). It should be noticed that the vast majority of the hot particles produced at 140 km altitude (i.e. several scale heights below the exobase) is quickly thermalized before reaching the exobase level, hence their contribution to the energy distribution function at the exobase is negligible.

Another contribution to the initial energy distribution of the O atoms comes from the rotational distribution of $O_2^+(v, J)$. Therefore, the rotational energy for each vibrational level has to be calculated by including a sufficient number of rotational levels that are characterized by the angular momentum quantum number J (e.g. Fox and Hac 2009).

Figure 12 shows the energy spectrum of oxygen products generated by DR of O_2^+ at three different altitudes. The red lines account for the ion and electron temperature and are based on the branching ratios of Kella et al. (1997), while the other dashed lines include in addition the vibrational and rotational energy contributions. Although these contributions are relatively small with respect to the exothermicities of (11a)–(11e), any uncertainties in their calculation may introduce some error in the corresponding exosphere density results. A larger error, however, may be introduced by the use of different collision cross sections and will be discussed in the following section.

4.2 Collision Cross Sections

Hot atoms generated by DR in the thermosphere will exchange energy due to elastic, inelastic and quenching collisions with the background constituents. While some total cross sections for elastic collisions are available, no such values seem to exist for inelastic and quenching collisions. The modeling of the thermalization of hot O atoms ideally requires

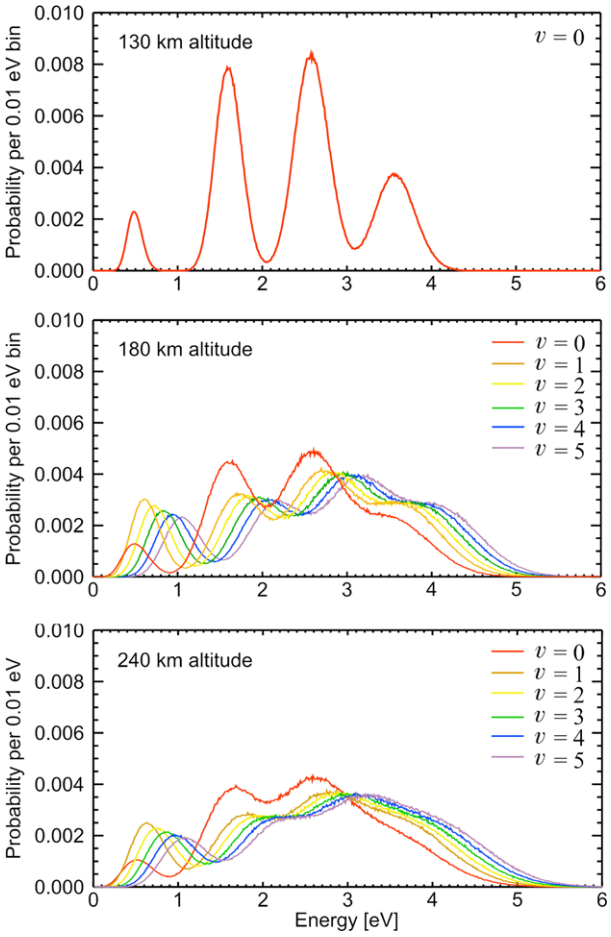

Fig. 12 Initial energy spectra of atomic oxygen produced via DR of O_2^+ at three different altitudes. The *red line* corresponds to the energy obtained by DR alone, the other lines also include the energy released by the vibrational and rotational states. At 130 km altitude, all ions are in the $v = 0$ state, therefore only the distribution corresponding to this state is shown

not only the total scattering cross sections but also its energy and angular dependence. In most models, however, the same constant value has been used for all species and the scattering angles were assumed to be isotropically distributed (e.g. Nagy and Cravens 1988; Kim et al. 1998; Hodges 2000; Valeille et al. 2010). The proper choice of the cross sections, however, may have a significant effect on the energy distribution functions and hence the exosphere density since it determines the rate of thermalization of the hot particles. Total cross sections for O–O collisions in the low energy range have been calculated by Tully and Johnson (2001) and Kharchenko et al. (2000). However, for O–CO_2 collisions, the other most relevant collisions in the Venusian exosphere modeling, no relevant data are available. In a Monte Carlo model, Lichtenegger et al. (2009) have used the total O–O cross section of Kharchenko et al. (2000) and the O–N_2 total cross sections published by Balakrishnan et al. (1998), the latter being a substitute for O–CO_2 collisions. Upon still assuming isotropic scattering angles, they arrived at notably lower oxygen exosphere densities than previous models based on a single constant total cross section. These results can be considered as a lower limit of the exosphere densities since they neglect the expected preference for scattering at small angles (Kharchenko et al. 2000). On the other hand, an upper limit can be found by using a constant cross section and adopting a forward scattered angular distribution; such

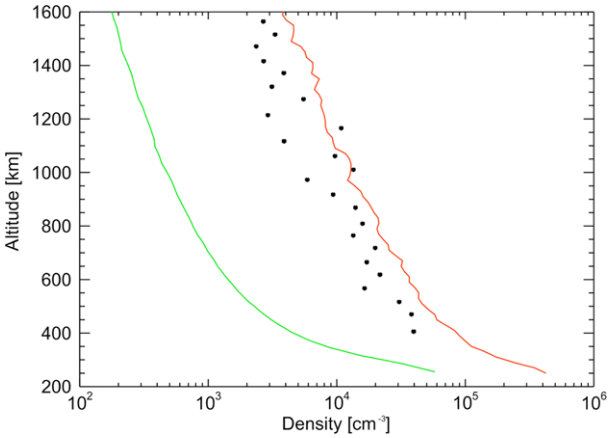

Fig. 13 Oxygen density profiles at Venus for two different scattering models. *Both lines* are obtained by means of energy dependent cross sections with the left profile (*green*) based on an isotropic scattering model and the right profile (*red*) based on a forward scattering model. The *black dots* denote the density inferred from PVO observations (Nagy et al. 1981)

an approach was recently suggested by Fox and Hac (2009) for modeling the oxygen escape from Mars.

Figure 13 shows the oxygen density profiles at Venus calculated by means of a Monte Carlo model for the two limiting cases, where the atmospheric and ionospheric input is based on the model of Fox and Sung (2001). The left profile (green line) is obtained by invoking the energy dependent total cross sections of Kharchenko et al. (2000) for O–O collisions and of Balakrishnan et al. (1998) for O–CO_2 collisions (as a proxy for O–NO_2 collisions) and assuming isotropically distributed scattering angles in the center of mass frame. The right density profile (red line) results from using the same total cross sections as for the green line, but the scattering angles are extracted from the differential cross sections of Kharchenko et al. (2000) (for O–O collisions) and of Balakrishnan et al. (1998) (for O–CO_2 collisions). The total cross sections for elastic collisions are also used for the corresponding inelastic and quenching collisions, the latter being assumed to occur somewhat arbitrarily with a probability of 1% each. It should be noted that a different probability would also modify the density profile.

Figure 13 also indicates the oxygen density inferred from Pioneer Venus Orbiter UV spectrometer measurements (Nagy et al. 1981). These are the only oxygen exosphere data published and may not be representative of the average oxygen density at Venus (Lichtenegger et al. 2009). Due to the uncertainties concerning both the proper use of the total and differential cross sections and the little known inelastic and quenching collision rate, the actual exosphere density profile of hot oxygen may lie anywhere between the two extreme cases in Fig. 13. Indeed, modern ENA instrumentation would be able to detect a density comparable to the one reported by Nagy et al. (1981) and predicted by former exosphere modeling. However, the so far unavailing attempts to observe the hot oxygen corona at Venus (Galli et al. 2008b) suggest that its density may be lower than hitherto expected.

5 Exosphere and ENA Environment of Titan

5.1 Titan and the Cassini Spacecraft

The largest satellite in the Saturnian system, Titan, is of major interest for its dense nitrogen rich atmosphere, as well as for its role in the Saturnian magnetosphere dynamics. With a radius of ∼2575 km, Titan is the second largest moon in our solar system and even larger

than the planet Mercury. As mentioned in Sect. 1, Titan differs from the Earth because no intrinsic magnetic field has been observed. Without such a field, Titan's atmosphere is relatively unprotected from the surrounding charged particle environment. Such interactions can strip atmospheric particles providing a source for Saturn's magnetosphere (Michael et al. 2005; De La Haye et al. 2007a). Since Titan's atmosphere is still robust, it is important to understand the role of charged particle energy deposition and sputtering. Describing the penetration of plasma particles into Titan's atmosphere is a critical first step.

Prior to 2004, *in situ* data collected in the Saturnian system was limited to three brief Saturnian fly-bys (Pioneer 11 and Voyagers 1 & 2). However, the Cassini spacecraft has been in orbit around Saturn for over 7 years. The Cassini mission has substantially progressed our knowledge of the Saturn environment since its Saturn Orbit Insertion in July 2004. Titan is one of the main objectives of the mission, with over 75 flybys performed by April 2011, and approaching Titan to a minimum altitude of 900–1000 km.

5.2 Description of the Cassini Experiments

Two main instruments on board Cassini have been able to investigate the Titan thermosphere and exosphere: the Ultraviolet Imaging Spectrograph (UVIS) (Esposito et al. 2004; Hedelt et al. 2010) and the Ion and Neutral Mass Spectrometer (INMS) (Waite et al. 2004). Cassini also has the capability of detecting *in situ* high energy plasma particles using the Magnetospheric Imaging Instrument (MIMI). This experiment (Krimigis et al. 2004) comprises three sensors: CHEMS (Charge Energy Mass Spectrometer) and LEMMS (Low Energy Magnetospheric Measurement System) for ions, and INCA (Ion and Neutral Camera) for ions or ENAs.

The Ion and Neutral Camera (INCA) instrument aboard Cassini is an imager which, depending on its mode of operation, can detect ions and/or neutrals with energies (per nucleon) between 7 keV and 3 MeV and is able to separate H, O and heavy species (Krimigis et al. 2004). It is a time-of-flight (TOF) energetic particle instrument, with a large field of view ($120 \times 90°$). This instrument has a charged particle rejection system, the INCA collimator, which filters out charged particles when the instrument is used to measure ENAs ("ENA mode"). When the INCA collimator is turned on, the sensor deflects charged particles away from the instrument's entrance system and measures mainly ENAs in the energy range of a few keV to hundreds of keV, with separation of hydrogen from heavy neutrals. INCA results based on this observational mode have provided important insights into the processes and complexities of energetic plasma interactions with Titan's upper atmosphere (Mitchell et al. 2005).

Cassini/LEMMS is designed to measure both energetic ion and electron fluxes but is not able to determine composition. As a subsystem in LEMMS, the low energy telescope (LET) measures protons collected through a conical collimator of 15° full angle with energies from 27 keV to 2.2 MeV over 8 energy channels (Krimigis et al. 2004). With these data, one can estimate the total energetic proton flux as well as its energy flux incident on Titan's atmosphere.

5.3 Titan's Exosphere and Energetic Neutral Atoms

Titan interacts strongly with the incident plasma from the Saturn environment and even from the solar wind through various phenomena (Brecht et al. 2000; Kallio et al. 2004), giving rise to a Mars- or Venus-like interaction due to the absence of an intrinsic magnetic field (Backes et al. 2005). The exception is the absence of a bow shock for Titan because the

upstream plasma is most often the sub-sonic magnetospheric flow of Saturn (composed of H^+ and O^+ ions), even around noon in magnetospheric local time. Titan may be outside the magnetopause in the magnetosheath, or even in the solar wind during large solar wind pressure events (Bertucci et al. 2008; Garnier et al. 2009).

Spectroscopic analyses performed by Kuiper (1944) led to the first clues about the composition of Titan's atmosphere. Although Pioneer 11 was the first probe to visit Saturn, the subsequent Voyager 1 and 2 missions provided more information in 1980 and 1981 through the analysis of radio wave absorption or infrared/ultraviolet observations. These data allowed the detection of the most important species (molecular nitrogen, methane, hydrogen and numerous hydrocarbons) and gave values for the molecular nitrogen density and temperature up to high altitudes (Hanel et al. 1981; Broadfoot et al. 1981; Smith et al. 1982; Lindal et al. 1983).

Titan has an extended corona or exosphere. Smith et al. (1982) and Atreya (1986) determined the position of the exobase at respectively 1400 and 1595 km altitude. Following these results, several authors developed atmospheric models for Titan up to 2000 km altitude (Yung et al. 1984; Keller et al. 1992; Toublanc et al. 1995). However, no information or model was available about the exosphere above this limit until Amsif et al. (1997) proposed a first model in preparation for the Cassini-Huygens mission. Vervack et al. (2004) revisited the Voyager 1 UVS results by solar occultation and obtained significant differences from the initial estimates for some neutral densities and the thermospheric temperature.

The energetic ions of the Saturn's magnetosphere may undergo charge exchange reactions with Titan's cold exospheric neutrals, producing ENAs. These can then be detected like photons by ENA imagers like the INCA instrument of the MIMI experiment (Krimigis et al. 2004). The analysis of the ENA environment of Titan allows us to infer information on both the neutral and ion populations, in particular in the upper part of the Titan atmosphere, where the neutral densities cannot be measured directly.

5.4 Titan Exosphere

The Titan atmosphere has a large column density of 7×10^{27} amu/cm^2 (ten times larger than at Earth), where amu is the atomic mass unit, and a low gravitational binding energy (Johnson 2004). The combination leads to a very extended exosphere for Titan. Its Hill sphere radius (Hill 1878), which gives the limit of its gravitational influence and thus a good estimation for the upper limit of its exosphere, is about 50,000 km. As a consequence, the measurements available today (up to 2000 km altitude, for an exobase around 1400–1500 km) are only able to provide information in the lower part of the corona, except for molecular hydrogen with observations up to 7000 km altitude (Cui et al. 2008) or atomic hydrogen with the UVIS experiment (Hedelt et al. 2010).

5.4.1 First Cassini Results

Preparation of the Cassini mission required the development of a new exosphere model for Titan up to high altitudes (Amsif et al. 1997). The exobase characteristics were derived from the Voyager observations and the model by Keller et al. (1992): an exobase altitude around 1525 or 1600 km and a temperature of 166, 186 and 206 K. The Chamberlain's (1963) formalism was used to calculate the exospheric densities from the conditions at the exobase and the species concerned were: N_2, CH_4, H_2, H and N. However, Vervack et al. (2004) recently revisited the Voyager results (e.g. Smith et al. 1982) and changed some previous estimates near the exobase: the N_2 densities were increased, the CH_4 densities

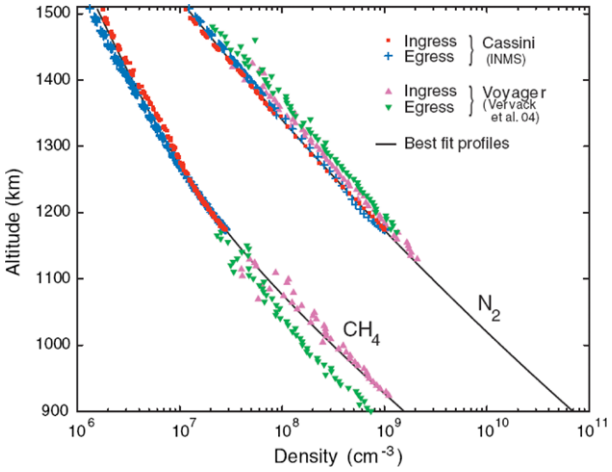

Fig. 14 Density profiles versus altitude for N_2 and CH_4 (after Waite et al. 2005) from Cassini/INMS data during the first Titan flyby Ta (26 October 2004). The data are compared to profiles shown by Vervack et al. (2004). Figure from Waite et al. (2005). Reprinted with permission from AAAS

Table 4 Conditions at the exobase used for the Garnier et al. (2007) thermal exospheric model: exobase altitude (H_c), temperature (T_c) and neutral densities (N_c) for five major species

Parameter	Value
H_c	1425 km
T_c	148.5 K
N_c(N)	7.1×10^4 cm^{-3}
N_c(H)	4.6×10^4 cm^{-3}
N_c(H_2)	5×10^5 cm^{-3}
N_c(N_2)	5.9×10^7 cm^{-3}
N_c(CH_4)	4.9×10^6 cm^{-3}

were significantly decreased and the temperature decreased by about 20–40 K (down to 153–158 K).

The first results for the lower exosphere derived from Cassini measurements were remarkably similar to the Voyager observations. UVIS data obtained during the second Titan flyby (Tb; 13th December 2004) provided neutral densities for 6 hydrocarbons up to 1600 km altitude as well as a temperature profile ($T \sim 151$ K near 1500 km altitude) (Shemansky et al. 2005). The first INMS data during the first encounter (Ta; 26th October 2004) published by Waite et al. (2005) showed neutral densities for N_2, CH_4 and H_2 in the upper atmosphere. Figure 14 displays some of these first results for both ingress and egress legs of the Ta flyby, combined with the Vervack et al. (2004) profiles derived from the Voyager missions.

Garnier et al. (2007) then developed a new Titan exospheric model for the five main species (N_2, CH_4, H_2, H and N) and for the Cassini conditions, based on the Chamberlain approach. They used as input both INMS results obtained during Ta (Waite et al. 2005) and the photochemical atmospheric model by Toublanc et al. (1995), with conditions at the exobase summarized in Table 4. The resulting profiles are shown in Fig. 15 and compared with those by Amsif et al. (1997) for altitudes up to 10,000 km altitude. The different characteristics considered near the exobase region (mainly the temperature), due to different conditions (solar cycle, orbit of Saturn, magnetospheric activity) and instruments for the Cassini and Voyager missions, lead to large discrepancies at high altitudes for heavy species.

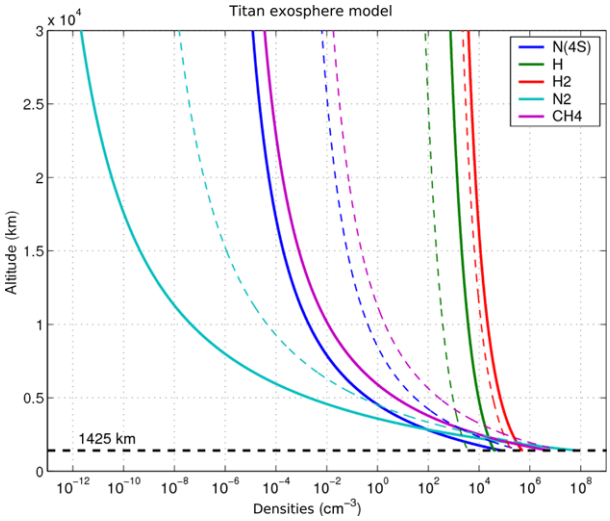

Fig. 15 Density profiles for the 5 main neutral species in the extended exosphere, with a comparison between the models of Garnier et al. (2007) and Amsif et al. (1997) models with *continuous* and *dashed lines*, respectively

The first Titan encounters (Ta, Tb and T5) were also analyzed in detail by Yelle et al. (2006) and De La Haye et al. (2007b). Globally, the INMS data revealed a remarkably isothermal structure for the upper atmosphere, with a temperature of about 145–160 K. The exobase is around 1400–1450 km altitude (1429 ± 5 km during Ta). It is noteworthy that during these flybys Cassini observed exospheric profiles very similar to Voyager, whereas the respective solar activities were very different, with more than a factor two of difference for the net EUV solar flux below 800 Å.

However, a significant variability was observed in the upper atmosphere, depending on latitude/longitude and local time (Müller-Wodarg et al. 2008). In particular, there appeared to be a 5 K difference between night (hotter) and dusk temperatures, which is opposite to a pure solar heating driver, and thus needs a detailed understanding of time lags and other sources of heating (such as the magnetospheric interaction, with a specific geometry). Müller-Wodarg et al. (2006) revealed key elements for the dynamics of the thermosphere, with density perturbations observed by INMS for N_2 and CH_4 revealing the propagation of waves with large amplitudes and spatial scales.

The most recent results (Bell et al. 2011; Westlake et al. 2011) now provide significant evidence that the horizontal variations observed in the upper atmosphere of Titan are actually driven by the variability of the magnetospheric plasma, with Titan passing through different magnetospheric regions (i.e. lobes and plasmasheet).

5.4.2 Titan Exospheric Populations

The structure of the Titan corona is not yet fully understood. Even considering the simplified case with thermal profiles for exospheric neutrals (see below for more details about nonthermal observations), only the populations crossing the exobase can be estimated rigorously with the Liouville theorem (Chamberlain and Hunten 1987). Thus, it is not really known how large the contribution of Titan-originated particles with satellite orbits (i.e. particles trapped by Titan's gravity field with a periapsis above the exobase originating from ballistic particles that underwent a collision in the exosphere) is, and their contribution has thus often been neglected. Garnier (2007) showed however that, if we consider conditions

leading to maximum phase space densities for such satellite particle populations, these satellite particles will dominate at high altitudes (above 8000 km altitude) against the ballistic populations. A realistic estimation needs the rigorous calculation of sources and losses for those particles in the corona (Richter et al. 1979).

Several observations brought key information about this issue. First, Cui et al. (2008) provided molecular hydrogen densities up to 7000 km altitude from numerous Titan flybys. They successfully fitted the measured profiles without introducing satellite populations, which thus suggests that such populations are not significant. Schaufelberger et al. (2011), using a Monte-Carlo code, suggested rare collisions in the Titan's exosphere, which would indicate a low production of satellite particles. However, as mentioned above, they can only dominate at higher altitudes. Brandt et al. (2011) recently used the inversion of ENA images of the extended corona (up to 40,000 km) to infer density profiles for the main neutral source of ENAs H_2 (see Sect. 5.5.4). The results of their fits would actually suggest that high altitude exospheric hydrogen particles mainly follow satellite trajectories. However, the precision of the density profiles obtained is critical for this issue and needs to be confirmed. Future analysis, using rigorous calculations, will help to resolve this apparent contradiction and confirm or disprove the expected absence of significant satellite particles.

5.4.3 Nonthermal Corona

The most important questions today about Titan's exosphere are: what is the escape rate to space, and what are the processes responsible for it (see Johnson 2009 for a detailed discussion). Yelle et al. (2006) analyzed INMS observations during the Ta flyby of Titan and derived an escape flux for H_2 much higher (by a factor of 3–4) than the simple thermal Jeans escape ($\sim 2 \times 10^{28}$ amu s^{-1}), as well as possible large upward fluxes for methane. They suggested that nonthermal processes (such as pickup ions, sputtering, etc.) play a significant role in the evolution of neutrals species such as H_2 and CH_4. Moreover, De La Haye et al. (2007b) also found evidence for suprathermal populations in the N_2 and CH_4 INMS density profiles.

The large H_2 fluxes observed by INMS were interpreted by Cui et al. (2008) without any nonthermal mechanisms as resulting from heat conduction near Titan's exobase, thus balancing the energy loss induced by escaping particles. Two main mechanisms were used to investigate the sources of the large loss rates (up to 5×10^{28} amu s^{-1}) observed for heavier species (i.e. N_2 and CH_4): nonthermal processes and slow hydrodynamic escape. De La Haye et al. (2007a) studied in detail some of the basic mechanisms, the exothermic ion and neutral chemistry, whereas Strobel (2008, 2009) as well as Yelle et al. (2008) inferred upward fluxes due to a thermally-driven escape with a heat conduction still acting above the exobase. However, Tucker and Johnson (2009) obtained opposite conclusions to Strobel (2008, 2009): they developed direct Monte Carlo models to estimate the possible influence of a thermally-driven escape, and concluded that the escape rates derived from INMS data could not be explained by such mechanisms, and thus require either nonthermal processes or global transport phenomena with net transport towards other regions of the atmosphere.

We should also remember that recent studies (Bell et al. 2011; Westlake et al. 2011) have identified the magnetospheric plasma as the main driver for the horizontal variations observed in the upper atmospheric densities. Garnier (2007) used the INMS results from the Ta, Tb and T5 flybys (De La Haye et al. 2007b) to develop nonthermal profiles for heavy species (N, N_2 and CH_4) in the extended exosphere (up to 30,000 km altitude). They considered kappa distributions (Vasyliunas 1968), commonly used for space plasmas and based on solid theoretical characteristics (Collier 1993, 2004), instead of maxwellians to

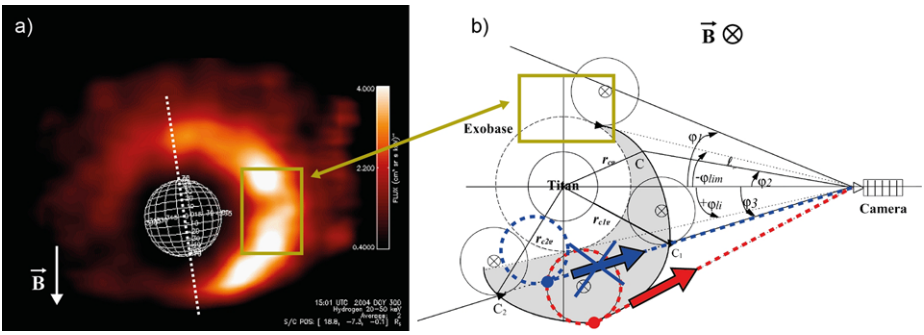

Fig. 16 (**a**) H ENA image by INCA during Ta, at an altitude of about 8000 km, an energy range of 24–55 keV and a time duration of ∼8 minutes (after Garnier et al. 2007); (**b**) finite gyroradii effects for energetic protons in the vicinity of Titan (after Dandouras and Amsif 1999; see text for details). Reprinted from Garnier et al. (2007) and Dandouras and Amsif (1999) with permissions from Elsevier

take into account a larger number of particles in the suprathermal part of the distribution. They obtained an average profile for these flybys, with a kappa parameter of ∼12–13, and showed the significant influence of such distributions on the heavy species at high altitudes, due to a velocity filtering increasing with altitude.

However, at the time of writing of this article, the calibrations of the INMS instrument have been updated, with densities corrected by a factor of 3, to account for a cross calibration between the INMS, NAV and AACS systems (Bell et al. 2010). This may significantly change the results concerning the structure and the dynamics of the Titan exosphere as drawn from the initial calibrations.

5.5 The ENA Environment of Titan

ENA imaging is very effective in the Saturn context since a dynamic magnetospheric plasma interacts with many neutral sources (bodies, atmospheres and surfaces as well as dust rings). In this section we review the ENA environment of Titan.

5.5.1 Pre-Cassini Studies

Prior to the arrival of the INCA ENA imager in the Titan environment, Amsif (1996) modeled the production of ENAs with energies of 10–50 keV in the vicinity of Titan. The first step of this thesis was the development of an exosphere model up to high altitudes and based on the Voyager observations (see Sect. 5.4). Then, he calculated the finite gyroradii effects induced by the large gyroradii of the energetic parent ions. An $E = 50$ keV proton has indeed a gyroradius of $R_g = (2mE)^{1/2}/qB \sim 6300$ km (for 90° pitch angle and $B = 5$ nT as given by Neubauer et al. (1984)), which is large compared to the Titan radius (Rt = 2575 km). These gyroradii effects are summarized in Fig. 16b and were described in detail by Dandouras and Amsif (1999): considering circular trajectories in the plane perpendicular to the ambient magnetic field, ions gyrate and may create ENAs directed towards the imager; the large dots illustrate two virtual examples for the location of ENA production, with the red particle being able to reach the detector, whereas we would have to assume that its parent ion (with the blue circular trajectory) had previously crossed the dense atmosphere or even the surface of the Moon if the blue ENA reached the detector. There thus appears a "shadow"

region where no created ENA can reach the camera, leading to asymmetries in the ENA observations determined by the parent ion gyration direction, which depends on the direction of the magnetic field.

The last step performed by Amsif (1996) was the development of a 3D ENA production model, based on homogeneous electric and magnetic fields, as well as circular ion trajectories. This showed that the ENA images should exhibit a limb brightening, i.e. a maximum flux at the lower limit for the ENA emission where the integrated optical depth is maximized: below, absorption mechanisms are too important, and above, neutral densities decrease rapidly.

5.5.2 First ENA Observations by Cassini

The Cassini spacecraft performed its first Titan flyby on 26 October 2004, with a closest approach altitude of about 1200 km. Figure 16a shows an ENA image for hydrogen atoms (initially magnetospheric protons) obtained during this encounter, for energies of 24–55 keV and an accumulation time of ~ 8 minutes. These first results, discussed in detail by Mitchell et al. (2005) and Garnier et al. (2007) confirmed the main features expected from the work by Amsif (1996): a limb brightening effect and a strong asymmetry probably related to finite gyroradii effects. Indeed, the image displays strong ENA fluxes on the right side (see Fig. 16a), which corresponds to the region where no shadow exists for ENA parent ions (see Fig. 16b), whereas lower fluxes are seen on the other side where gyroradii effects are active.

However, these first observations needed closer investigation. First, the flux values were lower than expected, thus requiring an update of both exospheric and magnetospheric conditions from previous Voyager results. Then, the observed ENA halo was located at a higher altitude than modeled, corresponding to an ENA emission limit far above the exobase. Finally, the next flybys revealed very dynamic ENA fluxes, both in structure and in value. As a consequence, a statistical analysis among numerous images (see Sect. 5.5.5) as well as detailed modeling of the complex interaction between Titan's exosphere and Saturn's magnetosphere (see Sects. 5.5.3 and 5.5.4) were essential to understand the dynamics.

5.5.3 Absorption of ENAs by Titan's Atmosphere

Garnier et al. (2008), using reprocessed images with final ephemeris data, confirmed that the exobase is the lower limit altitude for ENA emission according to INCA data. They used an ENA exospheric analytical theory developed by Roelof (2005) as well as a 2D numerical approach (with Cassini conditions, provided by MIMI/LEMMS for incident ions fluxes and exospheric profiles by Garnier et al. (2007) for neutrals), and obtained a maximum flux altitude around 2000 km altitude, which corresponds to emissions from the exobase ($H_c = 1425$ km altitude) after the angular scattering by the instrument carbon foil has been taken into account.

Garnier et al. (2008) also investigated the absorption of ENAs in the upper atmosphere of Titan, in order to determine the theoretical lower limit for ENA emission. They first analyzed the finite gyroradii effects in more detail, still using homogeneous electric and magnetic fields, but introducing the influence of the corotating plasma flow that leads to cycloidal trajectories rather than circular. The most important absorption process for ENAs is the charge stripping on atmospheric neutrals, with H ENAs potentially ionized up to an impact parameter (distance between the Titan surface and the altitude of closest approach of the ENA trajectory) of 1550 km altitude. At very low altitude, the ionized ENAs can be neutralized again by charge exchange with the atmospheric neutrals. As a consequence

of multiple ionization and neutralization, a full thermalization of the particles will occur below a certain altitude (<700 km for 20–50 keV ENAs; Smith et al. 2009). While such ENAs have been observed below the exobase, they have not been detected at high altitudes (∼ 10,000 km or above). This contradiction may indicate the existence of unknown loss processes in between.

5.5.4 Global Modeling of the Titan Interaction Region

The global interaction between Titan and the incident plasma, under the condition of non-homogeneous electromagnetic fields, was investigated by Wulms et al. (2010) with 3D MHD (magneto-hydrodynamics) models and for the conditions of the first moon encounters (Ta and Tb). They emphasized the influence of draped magnetic field lines on the parent ions dynamics, and thus the ENA emissions, compared to homogeneous fields. Wulms et al. (2010) specifically compared the ENA emissions for homogeneous and draped field lines, revealing the production of large ENA fluxes in the Titan wake due to the magnetic field draping, whereas a uniform electromagnetic configuration leads to a void of emissions in this region. We may remark that no hybrid modeling for ENA imaging close to Titan is available today, which could show different results since finite gyroradii effects may have been underestimated. Moreover, further developments are needed in order to appropriately couple the modeling of draped field lines appropriately with an accurate description of the ENA dynamics through multiple collisions in the upper atmosphere.

As described in Sect. 5.4, the Titan exosphere extends up to several 10,000 km, but the Cassini instruments cannot provide neutral densities in this upper part of the exosphere (except for atomic hydrogen up to 10,000 km; Hedelt et al. 2010). Brandt et al. (2009, 2011) studied the ENA images of the extended H_2 corona during several moon encounters among 3 years of observations. They used a parametric neutral atmosphere model consisting of molecular hydrogen in order to simulate hydrogen and oxygen ENA images in the 24–55 keV energy range by the Cassini INCA instrument. Figure 17 shows a comparison between observed (upper panel) and modeled (lower panel) ENA images for a specific encounter. Assuming a power law for the evolution of H_2 density with altitude, their best fit with observations induced an exponent for this power law of ∼2. Such a distribution would favor the scenario where satellite populations (see also Sect. 5.4.2) dominate the exosphere at high altitudes (Brandt et al. 2011).

5.5.5 Statistical Observations of the Titan ENA Halo

In addition, Garnier (2007) and Garnier et al. (2010) performed statistical analyses of the ENA environment of Titan with the Cassini spacecraft located at intermediate altitudes (above the source region, not far enough to study the extended corona) in order to better understand the structure and dynamics of the ENA halo shown in Fig. 16. All H ENA images for 24–55 keV energies obtained by INCA during the Cassini Titan flybys before June 2006 were studied. The authors showed that the variability of the ENA fluxes between the flybys is mainly driven by the dynamics of the parent magnetospheric protons (and not by the exosphere) or by the distance from the moon (though the source of Titan's ENAs is rather extended). The average ENA halo position (maximum ENA flux altitude) was found to be very stable, around 2000 km altitude, as during the Ta flyby, which induces a lower limit for the ENA emissions roughly around the exobase (1425 km altitude) when corrected for instrumental scattering. Moreover, a phenomenological study of the ENA halo asymmetries confirmed that the bright semi-circle observed during Ta is an almost permanent feature mostly due to the finite gyroradii effects and not influenced by the sunlight.

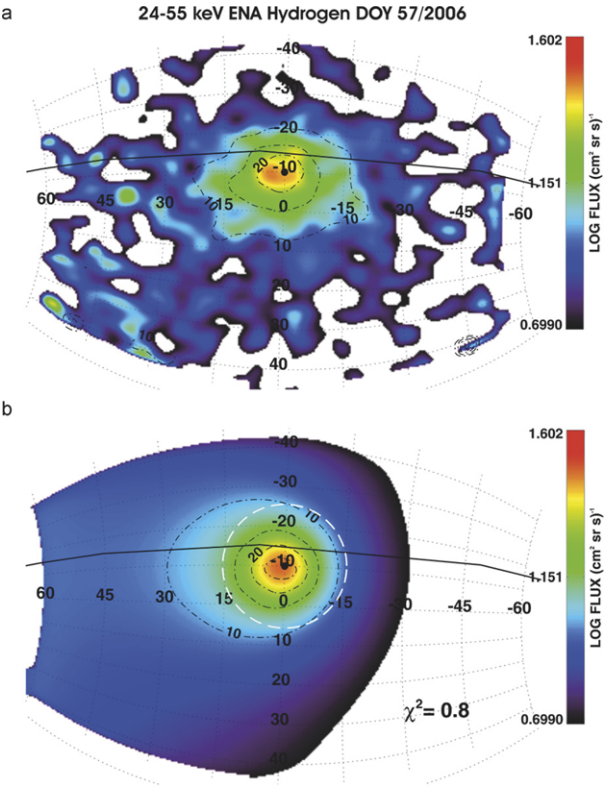

Fig. 17 This figure gives a comparison between observed (*upper panel*) and simulated (*lower panel*) ENA emissions in the extended Titan corona, for H ENAs images with a 24–55 keV energy range. The Sun and Saturn were located behind the reader during the event, whereas the corotating flow came from the left side of the field of view. Larger fluxes are observed on the left, due to both border and Compton-Getting effects (Brandt et al. 2011). The conditions correspond to DOY 57 in 2006, with a r^2 altitude distribution for the H_2 exospheric density. Reprinted from Brandt et al. (2011), with permission from Elsevier

5.6 Atmospheric Effects on Titan

The energy deposition into the Titan atmosphere by Saturn's magnetospheric plasma is a key issue for our understanding of the history and evolution of Titan's atmosphere. The incident plasma may induce significant escape from Titan, but it is also a significant source of energy for the complex chemistry and dynamics of the Titan atmosphere (e.g. Bell et al. 2011; Westlake et al. 2011), in particular the production of heavy hydrocarbons in the upper atmosphere (Coates et al. 2007; Waite et al. 2007; Sittler et al. 2009).

The energy deposition by energetic magnetospheric ions has been investigated by several authors (Luna et al. 2003; Mitchell et al. 2005; Cravens et al. 2008; Smith et al. 2009), using ion fluxes derived during specific Titan encounters. In particular, Smith et al. (2009) used the INCA H ENA images during the T18 flyby to calculate altitude profiles of the energy deposited by energetic protons in the atmosphere In this section, we focus on the first observational report by Smith et al. (2009).

5.6.1 Background

Cassini data have indicated that H^+ is the dominant ion species in the outer magnetosphere with O^+ also noticeably contributing to the plasma (Young et al. 2005) in the order of ∼1–10%. Luna et al. (2003) first compared the energetic proton energy deposition as a function of the altitude above Titan's surface to the energy deposited by the solar UV flux based on Voyager data. They determined cross sections for protons and nitrogen ions incident on molecular nitrogen (N_2) and then used these cross sections to model the impact

of such energetic particles on Titan's atmosphere. Using the measurement of energetic flux by Voyager, they modeled energetic proton (>10 keV) penetration and energy deposition in Titan's atmosphere for altitudes between 1000–1700 km. They found that protons carry an energy flux comparable to energetic magnetospheric electrons and thermal plasma but a factor of four lower than the flux carried by UV photons.

Subsequently, Cravens et al. (2008) used modeling combined with Cassini MIMI energetic particle data to examine ion production in Titan's atmosphere. They identified two levels of incident proton fluxes: a lower 'typical' flux observed by Cassini when the spacecraft is outside the current sheet of Saturn and a higher flux when inside the current sheet. They used the Cassini T5 encounter data which appeared consistent with the higher flux scenario for their calculations. Additionally, the fluxes measured by Voyager were consistent with being inside the current sheet. They reported ion production rates in Titan's atmosphere by solar photons, low energy electrons and oxygen ions as well as energetic protons for the typical and T5 fluxes. They showed the photon penetration peaking at ∼1100 km with thermal electrons and ions peaking around 900 km. Interestingly, they also reported that high energy protons (>30 keV) can penetrate at least to 650 km above Titan's surface.

This is a significant result because Cravens et al. (2005) showed that at altitudes > ∼900 km above Titan's surface solar radiation interactions deposit most of this mechanism's energy. They used a model along with the Cassini Radio and Plasma Wave Experiment (RPWS) and Ion and Neutral Mass Spectrometer (INMS) data to examine Titan's ionosphere during the initial encounter (Ta) in October 2004. With only solar photons, their model did not produce electron densities consistent with measurements while their model compared well when energetic electrons were included. This indicated the importance of energetic electrons for ion production in Titan's atmosphere at altitudes above 1174 km (the altitude of the spacecraft's closest approach during the Ta encounter).

Concurrently, Mitchell et al. (2005) showed that lower energy plasma (<several keV) deposits energy at altitudes above 1100 km. They used a Monte Carlo model to examine pickup ion energy deposition in Titan's atmosphere along with the resulting nitrogen particle escape and upper atmosphere heating. Their research suggested that energy deposition of the pickup ions peaks at ∼1200 km and can be significant even near Titan's exobase (∼1500 km). This result is significant because earlier papers incorrectly assumed photons to be the dominant source of heating in Titan's thermosphere. However, pickup ions are indeed a more significant source of energy at higher altitudes.

Thus, understanding the importance of lower altitude energy deposition by energetic plasma is needed to fully consider all energy inputs into Titan's upper atmosphere. Such an investigation requires confirmation and updating using Cassini data. For the purpose of investigating the precipitation flux, Smith et al. (2009) used MIMI/INCA instrument data. INCA images Titan's atmosphere via ENAs and therefore can observe to depths below those actually visited by the spacecraft. While the MIMI LEMMS is capable of detecting *in situ* energetic charged particles, Cassini's closest approach to Titan never passes lower than ∼950 km above the surface, which is too high an altitude to investigate the precipitation flux, because most of the energy is likely being deposited at altitudes below 800 km (Cravens et al. 2008).

Additionally, the work of Rymer et al. (2009) showed that the plasma environment near Titan can vary significantly. Their paper used Cassini thermal and energetic electron observations by CAPS and MIMI to categorize the plasma environment discretely during 54 encounters of the Cassini spacecraft with Titan from October 2004 until May 2009. Even though their observations have significant variability, they were able to classify the encounter environments into four broad categories: plasmasheet, lobe-like, magnetosheath

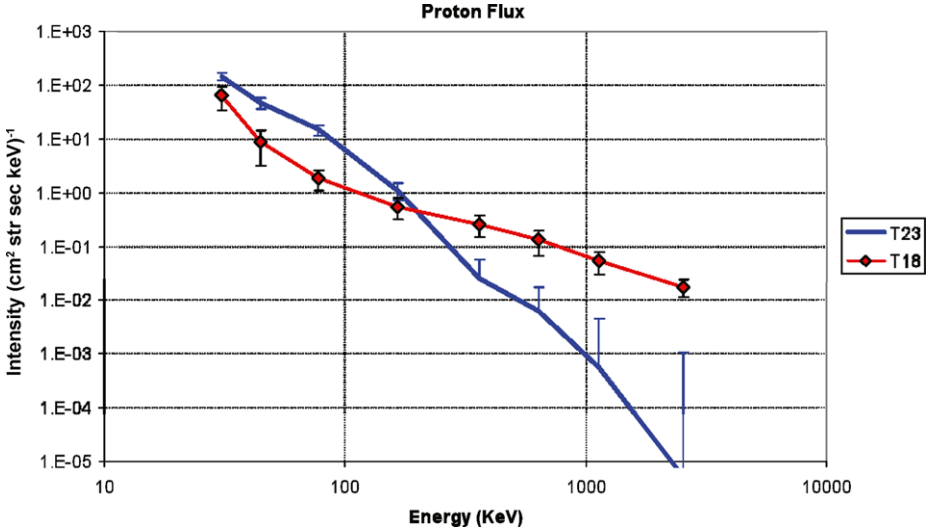

Fig. 18 Energetic proton flux in intensity ($cm^{-2}\ s^{-1}\ sr^{-1}\ keV^{-1}$) by energy (keV) for low intensity encounter (T18 in *red*) and a high intensity encounter (T23 in *blue*)

and bimodel. The highest plasma intensities are found during the plasmasheet encounters while the lowest fluxes occur during the lobe-like encounters. Figure 18 shows how the energetic proton fluxes vary between high intensity periods (T23 Titan encounter; plasmasheet encounter) and lower intensity periods (T18 Titan encounter; lobe-like encounter) between encounters.

5.6.2 Saturn High Energy Proton Interaction with Titan Atmosphere

Smith et al. (2009) used INCA data to investigate the altitude profile of the energy deposition of the energetic protons into Titan's atmosphere. Figure 19 illustrates the observational geometry and the plasma interaction process. An incident energetic proton enters Titan's atmosphere (left side of the figure) and continues to travel into the atmosphere until it interacts with an atmospheric particle. Because ∼97% of Titan's atmosphere above 960 km is N_2 (Waite et al. 2005), the dominant interaction below about 50 keV is charge exchange whereas above ∼50 keV it is ionization of N_2 that dominates (Luna et al. 2003). The energy loss of each charge exchange process and deposition into the atmosphere was assumed to be ∼30 eV (Schowengerdt and Park 1970; Jasperse and Basu 1982). The most likely subsequent interaction is electron stripping of the energetic H by N_2 (Garnier et al. 2008). This collision causes the particle to return to its original charge state with another loss (deposition) of ∼30 eV of its energy at the atmospheric interaction location further reducing the total energy of energetic hydrogen. Eventually, the incident particle loses all its energy and does not exit the atmosphere, or else it exits the atmosphere, reaches the INCA instrument and is observed if its energy exceeds the INCA energy threshold.

Figure 20 (top row) shows examples of the INCA images collected during the T18 encounter measured in terms of intensity ($cm^{-2}\ s^{-1}\ sr^{-1}\ keV^{-1}$) for the 20–50 keV energy range (Smith et al. 2009). The INCA total flux image in ion mode illustrates that the total ion flux remains a maximum until the paths traveled by incident particles penetrate into

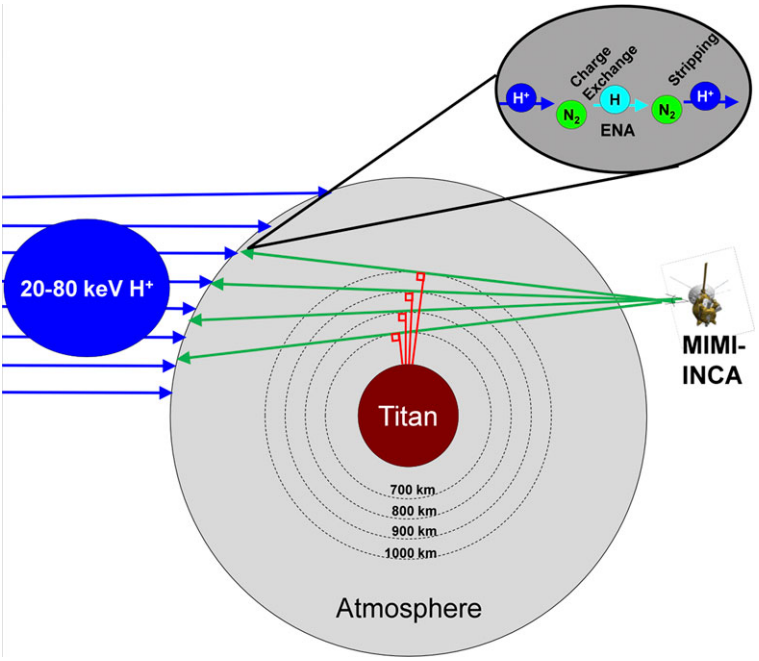

Fig. 19 Diagram showing INCA observational viewing geometry and atmospheric interactions. Incident energetic proton flux approaches Titan from the left and these particles interact with the atmosphere through alternating charge exchange, ionization and stripping reactions. The INCA (*rightside*) observes these particles traveling along observational lines of sight (*light blue lines*) identified by their altitude of closest approach to Titan's surface or impact parameter (700–1000 km). After Smith et al. (2009)

Titan's atmosphere. However, the ENA intensity peak is located below ∼1400 km. Figure 20 (middle row) shows the average quantitative intensities for each line of sight altitude. The peak intensity is observed around 1400 km consistent with Titan's exobase. Although Fig. 16 shows the peak intensity at ∼2000 km, Garnier et al. (2007) explain that this peak emission is also consistent with the exobase once instrument effects (the scattering by the instrument carbon foil) are taken into consideration. The data in Fig. 20 is not affected by such a limitation because observations were taken much closer to Titan.

5.6.3 Energy Deposition of the High Energy Particle in the Atmosphere

Smith et al. (2009) also modeled the energy deposition of the magnetospheric high energy particles into the Titan atmosphere due to charge exchange, ionization and stripping. They used LEMMS energetic ion observations as the initial input into Titan's atmosphere, and later the spectra of ions are modified in order to reproduce the INCA observations. The particles are then tracked considering the predominant electric processes below the exobase (with only ∼ 30 eV as the average energy loss per collision) in which angular deflections of these energetic particles are negligible for particles with the observed energies higher than 20 keV. Each particle was traced until it loses all of its energy to the atmosphere or arrives at the instrument. The comparison between the INCA observed intensity profiles (separated by the altitude above Titan's surface) and these model intensity profiles shows a good agreement (bottom row in Fig. 20).

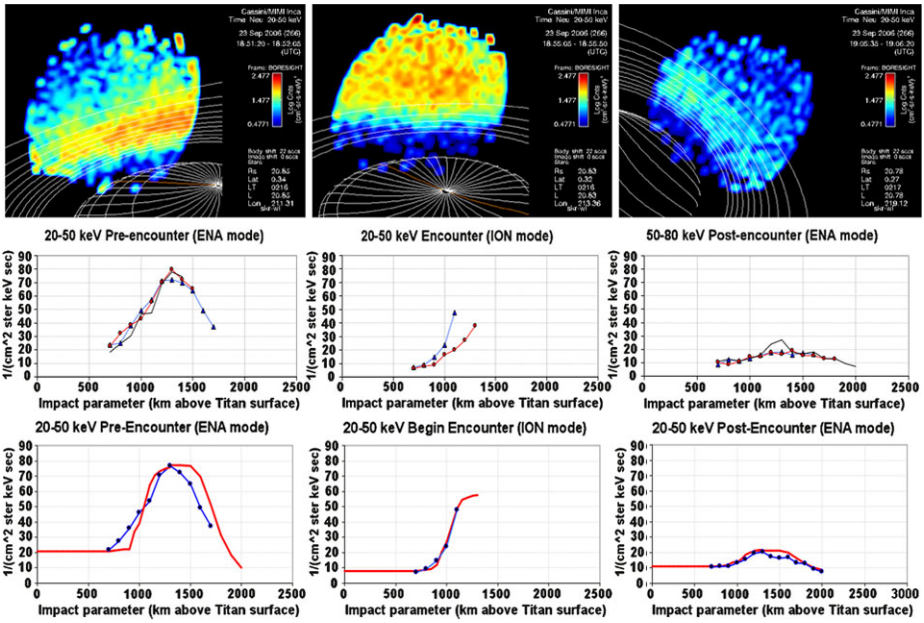

Fig. 20 Observation data and model results of the ENA and ion flux. (*Top*) INCA 20–50 keV hydrogen images measured in intensity ($cm^{-2}\ s^{-1}\ sr^{-1}\ keV^{-1}$) with the left panel on approach in neutral mode, middle panel during the encounter when INCA is in the ion mode, and the right panel during egress in the neutral mode; (*middle*) Atomic 20–50 keV hydrogen average intensities for the INCA images dependence on the impact parameter (km above the Titan's surface, different colored lines represent data from individual INCA images); and (*bottom*) Comparison of intensities (*blues lines* from the middle row) with modified model prediction (*red lines*). After Smith et al. (2009)

Fig. 21 Energy deposition for INCA observed proton flux through Titan's atmosphere by altitude above Titan's surface (km) for Cassini's approach to Titan (*thick line*), during the encounter (*dashed line*) and the egress (*thin line*) (after Smith et al. 2009)

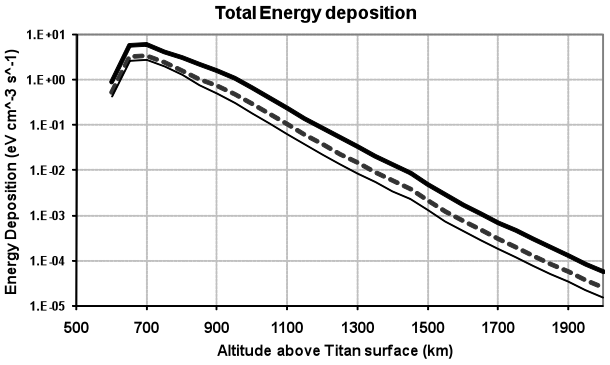

The above model by Smith et al. (2009) could also compile the atmospheric energy deposition profiles for energetic protons during the T18 encounter (Fig. 21).

The deposition rates calculated were lower by an order of magnitude than those predicted by Luna et al. (2003). This discrepancy may be explained by the higher incident proton flux assumed by Luna et al. (2003), since they used the proton energy flux derived from the Voyager 1 fly-by ($\sim 5 \times 10^9$ eV $cm^{-2}\ s^{-1}$) which is significantly higher than that observed during T18 (~ 5–9×10^8 eV $cm^{-2}\ s^{-1}$). Cravens et al. (2008) address such differences in

incident proton flux when they point out that the T5 Titan encounter showed a much higher incident proton flux and one that is similar to the value used by Luna et al. (2003). Additionally, Cravens et al. (2008) show a "typical" incident flux that is more consistent with the flux as observed for T18. The peak in the ion penetration depth profile generated by Cravens et al. (2008) when using this typical spectrum is similar to the modeled penetration (∼700–800 km; Smith et al. 2009). Therefore, it appears that Voyager crossed Titan's orbit during a period of significantly higher proton flux than observed during T18, causing Luna et al. (2003) to predict higher than "typical" energy deposition profiles. Time varying changes in the incident energetic proton flux and possible anisotropies in the distribution are other possible contributions to the observed ENA intensity variation. Such variation in Titan's interaction with the surrounding plasma environment over a short period of time hints at long term variations as well and will be the topic of further study.

6 Summary and Open Questions

Recent *in situ* and remote sensing measurements of the exosphere and ENAs close to the unmagnetized bodies Mars, Venus and Titan, conducted by Mars Express (at Mars since 2003), Cassini (at Titan since 2004) and Venus Express (at Venus since 2006), have contributed to a significant increase in our knowledge regarding the neutral and plasma environment in the upper atmosphere and its interaction with the solar wind. The first ENA measurements opened up a new way of investigating the planetary upper atmosphere and the ambient plasma flow (the solar wind in cases of Mars and Venus, and the Saturn's corotating plasma in case of Titan).

On the other hand, it is natural that new questions come up as we increase our knowledge about the exosphere and the ENA environment close to these bodies. Here we summarize the open questions, which are also a challenge and will further enhance research and missions investigating the plasma environment of unmagnetized bodies in the solar system:

- What are the temporal (seasonal and/or solar activity) variations of the neutral exospheres of Mars, Venus and Titan?
- What are the spatial variations of the neutral density in the exosphere and how do variations in the thermosphere and ionosphere affect the exosphere?
- Does a hot hydrogen corona exist in the vicinity of Mars and Venus? If yes, what are the typical parameters? How is it formed?
- How are the directional ENA jets generated in the subsonic magnetosheath of Mars?
- What is the source of the oscillation in the Martian subsolar ENA jet? In particular, the source of slow oscillations with a period of ~ 300 s is not clear.
- What is the source of a strong ENA flux coming from the Martian exobase? Does the exobase backscatter ENAs?
- Can we detect oxygen ENAs during the solar maximum? What is the solar activity dependence of the oxygen ENA contribution to atmospheric escape?
- What is the origin of the observed ENA variation at Titan and along Titan's orbit?
- Which are the processes leading to the observed large neutral upward fluxes in the lower Titan exosphere? What is the influence of nonthermal mechanisms?
- Where are the expected cyclotron waves associated with the pickup ions at Titan?
- What kind of dynamics (e.g. the loss processes) is acting for ENAs in the Titan upper atmosphere, particularly below or around the exobase?
- Are the satellite populations the dominant exospheric particles in the Titan extended corona?

Acknowledgements The authors acknowledge the support of EUROPLANET RI project (Grant agreement No. 228319) funded by EU; and also the support of the International Space Science Institute (Bern).

References

J.M. Ajello et al., Titan airglow spectra from the Cassini ultraviolet imaging spectrograph: FUV disk analysis. Geophys. Res. Lett. **35**, L06102 (2008). doi:10.1029/2007GL032315

A. Amsif, Etude et modélisation de la production d'atomes énergétiques neutres dans l'exosphère de Titan, Ph.D. thesis, University Toulouse III (1996)

A. Amsif, J. Dandouras, E.C. Roelof, Modeling the production and the imaging of energetic neutral atoms from Titan's exosphere. J. Geophys. Res. **102**(A10), 22181–22184 (1997)

B.J. Anderson, M.H. Acuna, H. Korth, M.E. Purucker, C.L. Johnson, J.A. Slavin, S.C. Solomon, R.L. McNutt, The structure of Mercury's magnetic field from MESSENGER's first flyby. Science **321**(5885), 82–85 (2008)

D.E. Anderson Jr., C.W. Hord, Mariner 6 and 7 ultraviolet spectrometer experiment: Analysis of hydrogen Lyman-alpha data. J. Geophys. Res. **76**(28), 6666–6673 (1971)

D.E. Anderson Jr., The Mariner 5 ultraviolet photometer experiment: Analysis of hydrogen Lyman alpha data. J. Geophys. Res. **81**(7), 1213–1216 (1976)

S.K. Atreya, *Atmospheres and Ionospheres of the Outer Planets and Their Satellites* (Springer, Berlin, 1986)

H. Backes et al., Titan's magnetic field signature during the first Cassini encounter. Science **308**(5724), 992–995 (2005)

N. Balakrishnan, V. Kharchenko, A. Dalgarno, Slowing of energetic O(3P) atoms in collisions with N_2. J. Geophys. Res. **103**(A10), 23393–23398 (1998)

S. Barabash, R. Lundin, T. Zarnowiecki, S. Grzedzielski, Diagnostic of energetic neutral particles at Mars by the ASPERA-C instrument for the Mars 96 mission. Adv. Space Res. **16**(4), 81–86 (1995)

S. Barabash, M. Holmström, A. Lukyanov, E. Kallio, Energetic neutral atoms at Mars. IV. Imaging of planetary oxygen. J. Geophys. Res. **107**(A10), 1280 (2002). doi:10.1029/2001JA000326

S. Barabash et al., The analyzer of space plasmas and energetic atoms (ASPERA-3) for the Mars Express mission. Space Sci. Rev. **126**(1), 113–164 (2006)

S. Barabash et al., The analyser of space plasmas and energetic atoms (ASPERA-4) for the Venus Express mission. Planet. Space Sci. **55**(12), 1772–1792 (2007a)

S. Barabash, A. Fedorov, R. Lundin, J.-A. Sauvaud, Martian atmospheric erosion rates. Science **315**(5811), 501–503 (2007b)

C.F. Barnett, H.T. Hunter, M.I. Fitzpatrick, I. Alverez, C. Cisneros, R.A. Phaneuf, Collisions of H, H_2, He and Li atoms and ions with atoms and molecules, in *At. Data Fusion*, vol. 1 (Oak Ridge Natl. Lab, Oak Ridge, 1990)

C.A. Barth, W.G. Fastie, C.W. Hord, J.B. Pearce, K.K. Kelly, A.I. Stewart, G.E. Thomas, G.P. Anderson, O.F. Raper, Mariner 6: ultraviolet spectrum of Mars upper atmosphere. Science **165**(3897), 1004–1005 (1969)

C.A. Barth, C.W. Hord, J.B. Pearce, K.K. Kelly, G.P. Anderson, A.I. Stewart, Mariner 6 and 7 ultraviolet spectrometer experiment: upper atmosphere data. J. Geophys. Res. **76**(10), 2213–2227 (1971)

B. Basu, J.R. Jasperse, D.J. Strickland, R.E. Daniell Jr., Transport-theoretic model for the electron-proton-hydrogen atom aurora. I. Theory. J. Geophys. Res. **98**(A12), 21517–21532 (1993)

J.M. Bell et al., Simulating the one-dimensional structure of Titan's upper atmosphere. I. Formulation of the Titan global ionosphere-thermosphere model and benchmark simulations. J. Geophys. Res. **115**(E12) (2010). doi:10.1029/2010JE003636

J.M. Bell, J. Westlake, J. Waite, J. Hunter, Simulating the time-dependent response of Titan's upper atmosphere to periods of magnetospheric forcing. Geophys. Res. Lett. **38**(6), L06202 (2011). doi:10.1029/2010GL046420

J. Bertaux, F. Montmessin, Isotopic fractionation through water vapor condensation: the deuteropause, a cold trap for deuterium in the atmosphere of Mars. J. Geophys. Res. **106**(E12), 32879–32884 (2001)

I.L. Bertaux, J. Blamont, M. Marcelin, V.G. Kurt, N.N. Romanova, A.S. Smirnov, Lyman-alpha observations of Venera-9 and 10. I. The non-thermal hydrogen population in the exosphere of Venus. Planet. Space Sci. **26**(9), 817–831 (1978)

J.L. Bertaux, J.E. Blamont, V.M. Lepine, V.G. Kurt, N.N. Romanova, A.S. Smirnov, Venera 11 and Venera 12 observations of E.U.V. emissions from the upper atmosphere of Venus. Planet. Space Sci. **29**(2), 149–166 (1981)

J.L. Bertaux, V.M. Lepine, V.G. Kurt, A.S. Smirnov, Altitude profile of H in the atmosphere of Venus from Lyman alpha observations of Venera 11 and Venera 12 and origin of the hot exospheric component. Icarus **52**(2), 221–244 (1982)

J. Bertaux et al., SPICAM on Mars Express: Observing modes and overview of UV spectrometer data and scientific results. J. Geophys. Res. **111**, E10S90 (2006). doi:10.1029/2006JE002690
J. Bertaux et al., SPICAV on Venus Express: Three spectrometers to study the global structure and composition of the Venus atmosphere. Planet. Space Sci. **55**(12), 1673–1700 (2007)
C. Bertucci et al., The magnetic memory of Titan's ionized atmosphere. Science **321**(5895), 1475–1478 (2008)
G. Betz, K. Wien, Energy and angular distributions of sputtered particles. Int. J. Mass Spectrosc. Ion Proces. **140**, 1–110 (1994)
S.W. Bougher, S. Engel, R.G. Roble, B. Foster, Comparative terrestrial planet thermospheres. 2. Solar cycle variation of global structure and winds at equinox. J. Geophys. Res. **104**(E7), 16591–16611 (1999)
S.W. Bougher, S. Engel, R.G. Roble, B. Foster, Comparative terrestrial planet thermospheres. 3. Solar cycle variation of global structure and winds at solstices. J. Geophys. Res. **105**(E7), 17669–17692 (2000)
S. Bougher, S. Engel, D. Hinson, J. Forbes, Mars Global Surveyor radio science electron density profiles: neutral atmosphere implications. Geophys. Res. Lett. **28**(16), 3091–3094 (2001)
D.A. Brain, Observations of low-frequency electromagnetic plasma waves upstream from the Martian shock. J. Geophys. Res. **107**(A6) (2002)
C.P. Brandt, ENA imaging of planetary magnetospheres. IRF Sci. Rep. 259 (1999)
P. Brandt, K. Dialynas, I. Dandouras, D.G. Mitchell, P. Garnier, S.M. Krimigis, Titan's extended atmosphere: INCA results, in Geophysical Research Abstract, vol. 11. EGU General Assembly (2009)
P.C. Brandt, K. Dialynas, I. Dandouras, D.G. Mitchell, P. Garnier, S.M. Krimigis, The distribution of Titan's high-altitude (out to $\sim 50,000$†km) exosphere from energetic neutral atom (ENA) measurements by Cassini/INCA. Planet. Space Sci. (2011, in press). doi:10.1016/j.pss.2011.04.014
S.H. Brecht, J.G. Luhmann, D.J. Larson, Simulation of the Saturnian magnetospheric interaction with Titan. J. Geophys. Res. **105**(A6), 130 (2000)
K. Brinkfeldt et al., First ENA observations at Mars: Solar-wind ENAs on the nightside. Icarus **182**(2), 439–447 (2006)
A.L. Broadfoot, S. Kumar, M.J.S. Belton, M.B. McElroy, Ultraviolet observations of Venus from Mariner 10: preliminary results. Science **183**(4131), 1315–1318 (1974)
A.L. Broadfoot et al., Extreme ultraviolet observations from Voyager 1 encounter with Saturn. Science **212**(4491), 206–211 (1981)
J. Burch, The first two years of image. Space Sci. Rev. **109**, 1–24 (2003). doi:10.1023/B:SPAC.0000007510.32068.68
J.W. Chamberlain, Planetary coronae and atmospheric evaporation. Planet. Space Sci. **11**(8), 901–960 (1963)
J.W. Chamberlain, D.M. Hunten, *Theory of Planetary Atmospheres, an Introduction to Their Physics and Chemistory*, 2nd edn. International Geophysics Series, vol. 36 (Academic Press, Orlando, 1987), p. 481
G.M. Chanteur, E. Dubinin, R. Modolo, M. Fraenz, Capture of solar wind alpha-particles by the Martian atmosphere. Geophys. Res. Lett. **36**(23), L23105 (2009). doi:10.1029/2009GL040235
J.Y. Chaufray, R. Modolo, F. Leblanc, G. Chanteur, R.E. Johnson, J.G. Luhmann, Mars solar wind interaction: formation of the Martian corona and atmospheric loss to space. J. Geophys. Res. **112**(E9), E09009 (2007). doi:10.1029/2007JE002915
J. Chaufray, J. Bertaux, F. Leblanc, E. Quémerais, Observation of the hydrogen corona with SPICAM on Mars Express. Icarus **195**(2), 598–613 (2008)
J.Y. Chaufray, F. Leblanc, E. Quémerais, J.L. Bertaux, Martian oxygen density at the exobase deduced from O I 130.4-nm observations by spectroscopy for the investigation of the characteristics of the atmosphere of Mars on Mars Express. J. Geophys. Res. **114**(E2), E02006 (2009). doi:10.1029/2008JE003130
J.-Y. Chaufray, J.-L. Bertaux, E. Quémerais, E. Villard, F. Leblanc, Hydrogen density in the dayside Venusian exosphere derived from Lyman-alpha observations by SPICAV on Venus Express. Icarus (2011, in press). doi:10.1016/j.icarus.2011.09.027
F. Cipriani, F. Leblanc, J.J. Berthelier, Martian corona: nonthermal sources of hot heavy species. J. Geophys. Res. **112**(E7), E07001 (2007). doi:10.1029/2006JE002818
J.T. Clarke, J. Bertaux, J. Chaufray, R. Gladstone, E. Quemerais, J.K. Wilson, HST observations of the extended hydrogen corona of Mars, in *AAS/Division for Planetary Sciences Meeting Abstracts*, vol. 41 (2009), p. 49.11
A.J. Coates, F.J. Crary, G.R. Lewis, D.T. Young, J.H. Waite Jr., E.C. Sittler Jr., Discovery of heavy negative ions in Titan's ionosphere. Geophys. Res. Lett. **34**, L22103 (2007). doi:10.1029/2007GL030978
M.R. Collier, On generating kappa-like distribution functions using velocity space Lévy flights. Geophys. Res. Lett. **20**(15), 1531–1534 (1993)
M. Collier, Are magnetospheric suprathermal particle distributions (κ functions) inconsistent with maximum entropy considerations? Adv. Space Res. **33**(11), 2108–2112 (2004)
M.R. Collier, T.J. Stubbs, Neutral solar wind generated by lunar exospheric dust at the terminator. J. Geophys. Res. **114** (2009). doi:10.1029/2008JA013716

M.R. Collier et al., Observations of neutral atoms from the solar wind. J. Geophys. Res. **106**(A11), 24893–24906 (2001). doi:10.1029/2000JA000382
M.R. Collier, T.E. Moore, M.-C. Fok, B. Pilkerton, S. Boardsen, H. Khan, Low-energy neutral atom signatures of magnetopause motion in response to southward B_z. J. Geophys. Res. **110**(A2) (2005). doi:10.1029/2004JA010626
T.E. Cravens, C.N. Keller, B. Ray, Photochemical sources of non-thermal neutrals for the exosphere of Titan. Planet. Space Sci. **45**(8), 889–896 (1997)
T.E. Cravens et al., Titan's ionosphere: Model comparisons with Cassini Ta data. Geophys. Res. Lett. **32**(12), L12108 (2005). doi:10.1029/2005GL023249
T.E. Cravens, I.P. Robertson, S.A. Ledvina, D. Mitchell, S.M. Krimigis, J.H. Waite Jr., Energetic ion precipitation at Titan. Geophys. Res. Lett. **35**(3), L03103 (2008). doi:10.1029/2007GL032451
D. Crider et al., Evidence of electron impact ionization in the magnetic pileup boundary of Mars. Geophys. Res. Lett. **27**(1), 45–48 (2000)
J. Cui, R.V. Yelle, K. Volk, Distribution and escape of molecular hydrogen in Titan's thermosphere and exosphere. J. Geophys. Res. **113**, E10004 (2008). doi:10.1029/2007JE003032
J. Dandouras, A. Amsif, Production and imaging of energetic neutral atoms from Titan's exosphere: a 3-D model. Planet. Space Sci. **47**(10–11), 1355–1369 (1999)
V. De La Haye et al., Cassini ion and neutral mass spectrometer data in Titan's upper atmosphere and exosphere: observation of a suprathermal corona. J. Geophys. Res. **112**, A07309 (2007a). doi:10.1029/2006JA012222
V. De La Haye, J.H. Waite Jr., T. Cravens, A. Nagy, R. Johnson, S. Lebonnois, I. Robertson, Titan's corona: the contribution of exothermic chemistry. Icarus **191**(1), 236–250 (2007b)
M. Delva, M. Volwerk, C. Mazelle, J.Y. Chaufray, J.L. Bertaux, T.L. Zhang, Z. Vörös, Hydrogen in the extended Venus exosphere. Geophys. Res. Lett. (2009). doi:10.1029/2008GL036164
K. Dennerl, V. Burwitz, J. Englhauser, C. Lisse, S. Wolk, Discovery of X-rays from Venus with Chandra. Astron. Astrophys. **386**, 319–330 (2002)
K. Dennerl, Discovery of X-rays from Mars with Chandra. Astron. Astrophys. **394**(3), 1119–1128 (2002)
K. Dennerl, X-rays from Mars. Space Sci. Rev. **126**(1), 403–433 (2006)
K. Dennerl, X-rays from Venus observed with Chandra. Planet. Space Sci. **56**(10), 1414–1423 (2008)
T.M. Donahue, New analysis of hydrogen and deuterium escape from Venus. Icarus **141**(2), 226–235 (1999)
N.J.T. Edberg, H. Nilsson, A.O. Williams, M. Lester, S.E. Milan, S.W.H. Cowley, M. Fränz, S. Barabash, Y. Futaana, Pumping out the atmosphere of Mars through solar wind pressure pulses. Geophys. Res. Lett. **37**, L03107 (2010). doi:10.1029/2009GL041814
J.R. Espley, P.A. Cloutier, D.H. Crider, D.A. Brain, M.H. Acuña, Low-frequency plasma oscillations at Mars during the October 2003 solar storm. J. Geophys. Res. **110**, A09S33 (2005). doi:10.1029/2004JA010935
L.W. Esposito et al., The Cassini ultraviolet imaging spectrograph investigation. Space Sci. Rev. **115**(1), 299–361 (2004)
P.D. Feldman, E.B. Burgh, S.T. Durrance, A.F. Davidsen, Far-ultraviolet spectroscopy of Venus and Mars at 4 Å resolution with the Hopkins ultraviolet telescope on Astro-2. Astrophys. J. **538**(1), 395–400 (2000)
P. Feldman et al., Rosetta-Alice observations of exospheric hydrogen and oxygen on Mars. Icarus (2011, submitted)
M.C. Fok, T.E. Moore, M.R. Collier, T. Tanaka, Neutral atom imaging of solar wind interaction with the Earth and Venus. J. Geophys. Res. **109** (2004). doi:10.1029/2003JA010094
J.M. Forbes, F.G. Lemoine, S.L. Bruinsma, M.D. Smith, X. Zhang, Solar flux variability of Mars' exosphere densities and temperatures. Geophys. Res. Lett. L01201 (2008). doi:10.1029/2007GL031904
F. Forget, F. Montmessin, J. Bertaux, F. González-Galindo, S. Lebonnois, E. Quémerais, A. Reberac, E. Dimarellis, M.A. López-Valverde, Density and temperatures of the upper Martian atmosphere measured by stellar occultations with Mars Express SPICAM. J. Geophys. Res. **114**(E1), E01004 (2009). doi:10.1029/2008JE003086
J.L. Fox, The O_2^+ vibrational distribution in the Venusian ionosphere. Adv. Space Res. **5**(9), 165–169 (1985)
J.L. Fox, Effect of H_2 on the martian ionosphere: implications for atmospheric evolution. J. Geophys. Res. **108**(A6), 1223 (2003). doi:10.1029/2001JA000203
J.L. Fox, A. Dalgarno, Ionization, luminosity, and heating of the upper atmosphere of Mars. J. Geophys. Res. **84**(A12), 7315–7333 (1979)
J.L. Fox, S.W. Bougher, Structure, luminosity, and dynamics of the Venus thermosphere. Space Sci. Rev. **55**(1), 357–489 (1991)
J.L. Fox, K.Y. Sung, Solar activity variations of the Venus thermosphere/ionosphere. J. Geophys. Res. **106**(A10), 21305–21335 (2001)

J.L. Fox, A.B. Hac, Photochemical escape of oxygen from Mars: A comparison of the exobase approximation to a Monte Carlo method. Icarus **204**(2), 527–544 (2009)
S.A. Fuselier et al., Energetic neutral atoms from the Earth's subsolar magnetopause. Geophys. Res. Lett. **37**(13) (2010). doi:10.1029/2010GL044140
Y. Futaana et al., First ENA observations at Mars: ENA emissions from the Martian upper atmosphere. Icarus **182**(2), 424–430 (2006a)
Y. Futaana et al., First ENA observations at Mars: subsolar ENA jet. Icarus **182**(2), 413–423 (2006b)
Y. Futaana, S. Barabash, A. Grigoriev, D. Winningham, R. Frahm, M. Yamauchi, R. Lundin, Global response of Martian plasma environment to an interplanetary structure: from ENA and plasma observations at Mars. Space Sci. Rev. **126**(1), 315–332 (2006c)
Y. Futaana, S. Nakano, M. Wieser, S. Barabash, Energetic neutral atom occultation: new remote sensing technique to study the lunar exosphere. J. Geophys. Res. **113**, A11204 (2008a). doi:10.1029/2008JA013356
Y. Futaana et al., Mars Express and Venus Express multi-point observations of geoeffective solar flare events in December 2006. Planet. Space Sci. **56**(6), 873–880 (2008b)
Y. Futaana, S. Barabash, M. Holmström, A. Fedorov, H. Nilsson, R. Lundin, E. Dubinin, M. Fränz, Backscattered solar wind protons by Phobos. J. Geophys. Res. **115**(A10), A10213 (2010). doi:10.1029/2010JA015486
A. Galli, P. Wurz, S. Barabash, A. Grigoriev, H. Gunell, R. Lundin, M. Holmstrom, A. Fedorov, Energetic hydrogen and oxygen atoms observed on the nightside of Mars. Space Sci. Rev. **126**(1), 267–297 (2006a)
A. Galli, P. Wurz, H. Lammer, H. Lichtenegger, R. Lundin, S. Barabash, A. Grigoriev, M. Holmstrom, H. Gunell, The hydrogen exospheric density profile measured with ASPERA-3/NPD. Space Sci. Rev. **126**(1), 447–467 (2006b)
A. Galli et al., First observation of energetic neutral atoms in the Venus environment. Planet. Space Sci. **56**(6), 807–811 (2008a)
A. Galli et al., Tailward flow of energetic neutral atoms observed at Venus. J. Geophys. Res. **113**, E00B15 (2008b). doi:10.1029/2008JE003096
A. Galli et al., Tailward flow of energetic neutral atoms observed at Mars. J. Geophys. Res. (2008c). doi:10.1029/2008JE003139
P. Garnier, The exosphere of Titan and its interaction with the kronian magnetosphere, with the use of MIMI data onboard Cassini, Ph.D. thesis, Universite Toulouse III (2007)
P. Garnier et al., The exosphere of Titan and its interaction with the kronian magnetosphere: MIMI observations and modeling. Planet. Space Sci. **55**(1–2), 165–173 (2007)
P. Garnier et al., The lower exosphere of Titan: energetic neutral atoms absorption and imaging. J. Geophys. Res. **113**, A10216 (2008). doi:10.1029/2008JA013029
P. Garnier et al., Titan's ionosphere in the magnetosheath: Cassini RPWS results during the T32 flyby. Ann. Geophys. **27**, 4257–4272 (2009)
P. Garnier et al., Statistical analysis of the energetic ion and ENA data for the Titan environment. Planet. Space Sci. **58**, 1811–1822 (2010)
J.C. Gérard, B. Hubert, J. Gustin, V.I. Shematovich, D. Bisikalo, G.R. Gladstone, L.W. Esposito, EUV spectroscopy of the Venus dayglow with UVIS on Cassini. Icarus **211**(1), 70–80 (2011)
F. González-Galindo, F. Forget, M.A. López-Valverde, M.A. Coll, A ground-to-exosphere Martian general circulation model. 2. Atmosphere during solstice conditions-thermospheric polar warming. J. Geophys. Res. **114**(E8), E08004 (2009). doi:10.1029/2008JE003277
A. Grigoriev, Y. Futaana, S. Barabash, A. Fedorov, Observations of the Martian subsolar ENA jet oscillations. Space Sci. Rev. **126**(1), 299–313 (2006)
M. Gruntman, Energetic neutral atom imaging of space plasmas. Rev. Sci. Instrum. **68**, 3617–36561 (1997)
S.L. Guberman, Mechanism for the green glow of the upper ionosphere. Science **278**(5341), 1276–1278 (1997)
H. Gunell et al., First ENA observations at Mars: charge exchange ENAs produced in the magnetosheath. Icarus **182**(2), 431–438 (2006)
M.A. Gurwell, Evolution of deuterium on Venus. Nature **378**(6552), 22–23 (1995)
R. Hanel et al., Infrared observations of the Saturnian system from Voyager 1. Science **212**(4491), 192–200 (1981)
J. Hasted, *Physics of Atomic Collisions* (Butterworths, London, 1964)
P. Hedelt, Y. Ito, H. Keller, R. Reulke, P. Wurz, H. Lammer, H. Rauer, L. Esposito, Titan's atomic hydrogen corona. Icarus **210**(1), 424–435 (2010). doi:10.1016/j.icarus.2010.06.012
G.W. Hill, Researches in the lunar theory. Am. J. Math. **1**(1), 5–26 (1878)
R.R. Hodges, An exospheric perspective of isotopic fractionation of hydrogen on Venus. J. Geophys. Res. **104**(E4), 8463–8471 (1999)
R.R. Hodges, Distributions of hot oxygen for Venus and Mars. J. Geophys. Res. **105**(E3), 6971–6981 (2000)

M. Holmström, S. Barabash, E. Kallio, X-ray imaging of the solar wind-Mars interaction. Geophys. Res. Lett. **28**(7), 1287–1290 (2001)
M. Holmström, S. Barabash, E. Kallio, Energetic neutral atoms at Mars. 1. Imaging of solar wind protons. J. Geophys. Res. **107**, 1277–1285 (2002)
J. Horwitz, Core plasma in the magnetosphere. Rev. Geophys. **25**(3) (1987)
K. Hosokawa, S. Taguchi, S. Suzuki, M.R. Collier, T.E. Moore, M.F. Thomsen, Estimation of magnetopause motion from low-energy neutral atom emission. J. Geophys. Res. **113**, A10205 (2008)
J.R. Jasperse, B. Basu, Transport theoretic solutions for auroral proton and H atom fluxes and related quantities. J. Geophys. Res. **87**(A2), 811–822 (1982)
R.E. Johnson, The magnetospheric plasma-driven evolution of satellite atmospheres. Astrophys. J. **609**, L99–L102 (2004)
R. Johnson, M. Combi, J. Fox, W.H. Ip, F. Leblanc, M. McGrath, V. Shematovich, D. Strobel, J. Waite, Exospheres and atmospheric escape. Space Sci. Rev. **139**(1), 355–397 (2008)
R.E. Johnson, Sputtering and heating of Titan's upper atmosphere. Philos. Trans. R. Soc. Lond. A **367**, 753–771 (2009)
E. Kallio, An empirical model of the solar wind flow around Mars. J. Geophys. Res. **101**(A5), 11133–11147 (1996)
E. Kallio, S. Barabash, Atmospheric effects of precipitating energetic hydrogen atoms on the Martian atmosphere. J. Geophys. Res. **106**(A1), 165–177 (2001)
E. Kallio, P. Janhunen, Atmospheric effects of proton precipitation in the Martian atmosphere and its connection to the Mars-solar wind interaction. J. Geophys. Res. **106**(A4), 5617–5634 (2001)
E. Kallio, P. Janhunen, Solar wind and magnetospheric ion impact on Mercury's surface. Geophys. Res. Lett. **30**(17), 1877–1880 (2003). doi:10.1029/2003GL017842
E. Kallio, I. Sillanpää, P. Janhunen, Titan in subsonic and supersonic flow. Geophys. Res. Lett. L15703 (2004). doi:10.1029/2004GL020344
E. Kallio et al., Energetic neutral atoms (ENA) at Mars: properties of the hydrogen atoms produced upstream of the martian bow shock and implications for ENA sounding technique around non-magnetized planets. Icarus **182**(2), 448–463 (2006)
G.M. Keating et al., Models of Venus neutral upper atmosphere: structure and composition. Adv. Space Res. **5**(11), 117–171 (1985)
G.M. Keating et al., The structure of the upper atmosphere of Mars: In situ accelerometer measurements from Mars Global Surveyor. Science **279**(5357), 1672–1676 (1998)
D. Kella, L. Vejby-Christensen, P.J. Johnson, H.B. Pedersen, L.H. Andersen, The source of green light emission determined from a Heavy-Ion storage ring experiment. Science **276**(5318), 1530–1533 (1997)
C.N. Keller, T.E. Cravens, L. Gan, A model of the ionosphere of Titan. J. Geophys. Res. **97**(A8), 12117–12135 (1992)
V. Kharchenko, A. Dalgarno, B. Zygelman, J. Yee, Energy transfer in collisions of oxygen atoms in the terrestrial atmosphere. J. Geophys. Res. **105**(A11), 24899–24906 (2000)
J. Kim, A.F. Nagy, J.L. Fox, T.E. Cravens, Solar cycle variability of hot oxygen atoms at Mars. J. Geophys. Res. **103**(A12), 29339–29342 (1998)
V. Krasnopolsky, On the deuterium abundance on Mars and some related problems. Icarus **148**(2), 597–602 (2000)
V.A. Krasnopolsky, Mars' upper atmosphere and ionosphere at low, medium, and high solar activities: Implications for evolution of water. J. Geophys. Res. **107E**(12), 5128 (2002)
V.A. Krasnopolsky, Solar activity variations of thermospheric temperatures on Mars and a problem of CO in the lower atmosphere. Icarus **207**(2), 638–647 (2010)
V.A. Krasnopolsky, P.D. Feldman, Detection of molecular hydrogen in the atmosphere of Mars. Science **294**(5548), 1914–1917 (2001)
V.A. Krasnopolsky, P.D. Feldman, Far ultraviolet spectrum of Mars. Icarus **160**(1), 86–94 (2002)
V.A. Krasnopolsky, G.R. Gladstone, Helium on Mars: EUVE and PHOBOS data and implications for Mars' evolution. J. Geophys. Res. **101**(A7), 15765–15772 (1996)
V.A. Krasnopolsky, G.R. Gladstone, Helium on Mars and Venus: EUVE observations and modeling. Icarus **176**(2), 395–407 (2005)
V.A. Krasnopolsky, M.J. Mumma, G.R. Gladstone, Detection of atomic deuterium in the upper atmosphere of Mars. Science **280**(5369), 1576–1580 (1998)
S.M. Krimigis et al., Magnetosphere imaging instrument (MIMI) on the Cassini mission to Saturn/Titan. Space Sci. Rev. **114**(1), 233–329 (2004)
G.P. Kuiper, Titan: a satellite with an atmosphere. Astrophys. J. **100**, 378–383 (1944)
F. Leblanc, J. Chaufray, J. Lilensten, O. Witasse, J. Bertaux, Martian dayglow as seen by the SPICAM UV spectrograph on Mars Express. J. Geophys. Res. **111**(E9), E09S11 (2006). doi:10.1029/2005JE002664

H. Lichtenegger, H. Lammer, W. Stumptner, Energetic neutral atoms at Mars. 3. Flux and energy distributions of planetary energetic H atoms. J. Geophys. Res. **107**(A10), 1279 (2002). doi:10.1029/2001JA000322
H. Lichtenegger, H. Lammer, Y. Kulikov, S. Kazeminejad, G. Molina-Cuberos, R. Rodrigo, B. Kazeminejad, G. Kirchengast, Effects of low energetic neutral atoms on Martian and Venusian dayside exospheric temperature estimations. Space Sci. Rev. **126**(1), 469–501 (2006)
H.I.M. Lichtenegger, H. Gröller, H. Lammer, Y.N. Kulikov, V.I. Shematovich, On the elusive hot oxygen corona of Venus. Geophys. Res. Lett. **36**, L10204 (2009). doi:10.1029/2009GL037575
G.F. Lindal, G.E. Wood, H.B. Hotz, D.N. Sweetnam, V.R. Eshleman, G.L. Tyler, The atmosphere of Titan: an analysis of the Voyager 1 radio occultation measurements. Icarus **53**(2), 348–363 (1983)
B.G. Lindsay, R.F. Stebbings, Charge transfer cross sections for energetic neutral atom data analysis. J. Geophys. Res. **110**(A12) (2005). doi:10.1029/2005JA011298
J.G. Luhmann, J.U. Kozyra, Dayside pickup oxygen ion precipitation at Venus and Mars: spatial distributions, energy deposition and consequences. J. Geophys. Res. **96**(A4), 5457–5467 (1991)
J.G. Luhmann, C.T. Russell, K. Schwingenschuh, E. Eroshenko, A comparison of induced magnetotails of planetary bodies—Venus, Mars, and Titan. J. Geophys. Res. **96**(A7), 11199–11208 (1991)
J.G. Luhmann et al., Venus Express observations of atmospheric oxygen escape during the passage of several coronal mass ejections. J. Geophys. Res. **113**, E00B04 (2008). doi:10.1029/2008JE003092
H. Luna, M. Michael, M.B. Shah, R.E. Johnson, C.J. Latimer, J.W. McConkey, Dissociation of N_2 in capture and ionization collisions with fast H^+ and N^+ ions and modeling of positive ion formation in the Titan atmosphere. J. Geophys. Res. **108**(E4), 5033 (2003). doi:10.1029/2002JE001950
R. Lundin et al., First measurements of the ionospheric plasma escape from Mars. Nature **341**(6243), 609–612 (1989)
R. Lundin et al., Aspera/Phobos measurements of the ion outflow from the Martian ionosphere. Geophys. Res. Lett. **17**(6), 873–876 (1990)
R. Lundin et al., Solar wind-induced atmospheric erosion at Mars: First results from ASPERA-3 on Mars Express. Science **305**(5692), 1933–1936 (2004)
R. Lundin, S. Barabash, A. Fedorov, M. Holmström, H. Nilsson, J.A. Sauvaud, M. Yamauchi, Solar forcing and planetary ion escape from Mars. Geophys. Res. Lett. **35**, L09203 (2008). doi:10.1029/2007GL032884
Y. Ma, A.F. Nagy, K.C. Hansen, D.L. DeZeeuw, T.I. Gombosi, K.G. Powell, Three-dimensional multispecies MHD studies of the solar wind interaction with Mars in the presence of crustal fields. J. Geophys. Res. **107**(A10) (2002). doi:10.1029/2002JA009293
E. Mazarico, M.T. Zuber, F.G. Lemoine, D.E. Smith, Martian exospheric density using Mars Odyssey radio tracking data. J. Geophys. Res. **112**(E5) (2007). doi:10.1029/2006JE002734
D. McComas et al., IBEX—interstellar boundary explorer. Space Sci. Rev. **146**(1), 11–33 (2009). doi:10.1007/s11214-009-9499-4
M.B. McElroy, M.J. Prather, J.M. Rodriguez, Escape of hydrogen from Venus. Science **215**(4540), 1614–1615 (1982)
F.J. Mehr, M.A. Biondi, Electron temperature dependence of recombination of O^{2+} and N^{2+} ions with electrons. Phys. Rev. **181**(1), 264 (1969)
A.B. Meinel, Doppler-shifted auroral hydrogen emission. Astrophys. J. **113**, 50 (1951)
M. Michael, R. Johnson, F. Leblanc, M. Liu, J. Luhmann, V. Shematovich, Ejection of nitrogen from Titan's atmosphere by magnetospheric ions and pick-up ions. Icarus **175**(1), 263 (2005)
A. Milillo et al., Statistical analysis of the observations of the MEX/ASPERA-3 NPI in the shadow. Planet. Space Sci. **57**(8–9), 1000–1007 (2009)
D. Mitchell, The Mars atmosphere and volatile evolution mission, in *Aerospace Conference, 2010 IEEE* (2010), pp. 1–7
D. Mitchell et al., High energy neutral atom (HENA) imager for the IMAGE mission. Space Sci. Rev. **91**(1), 67–112 (2000)
D.G. Mitchell, P.C. Brandt, E.C. Roelof, J. Dandouras, S.M. Krimigis, B.H. Mauk, Energetic neutral atom emissions from Titan interaction with Saturn's magnetosphere. Science **308**(5724), 989–992 (2005)
T. Moore et al., The low-energy neutral atom imager for IMAGE. Space Sci. Rev. **91**(1), 155–195 (2000)
J. Moritz, Energetic protons at low equatorial altitudes (energetic protons detection below radiation belt at equatorial latitudes from Azur satellite measurements, hypothesizing exospheric and upper atmospheric charge exchange processes). Z. Geophys. **38**, 701–717 (1972)
I.C.F. Müller-Wodarg, R.V. Yelle, N. Borggren, J.H. Waite Jr., Waves and horizontal structures in Titan's thermosphere. J. Geophys. Res. **111**, A12315 (2006)
I.C.F. Müller-Wodarg, R.V. Yelle, J. Cui, J.H. Waite, Horizontal structures and dynamics of Titan's thermosphere. J. Geophys. Res. **113**, E10005 (2008). doi:10.1029/2007JE003033
A. Mura, A. Milillo, S. Orsini, E. Kallio, S. Barabash, Energetic neutral atoms at Mars. 2. Imaging of the solar wind-Phobos interaction. J. Geophys. Res. **107**(A10), 1278 (2002). doi:10.1029/2001JA000328

A. Mura et al., ENA detection in the dayside of Mars: ASPERA-3 NPD statistical study. Planet. Space Sci. **56**(6), 840–845 (2008)
A.F. Nagy, T.E. Cravens, Hot oxygen atoms in the upper atmospheres of Venus and Mars. Geophys. Res. Lett. **15**(5), 433–435 (1988)
A.F. Nagy, T.E. Cravens, J. Yee, A.I.F. Stewart, Hot oxygen atoms in the upper atmosphere of Venus. Geophys. Res. Lett. **8**(6), 629–632 (1981)
N.F. Ness, K.W. Behannon, R.P. Lepping, Y.C. Whang, K.H. Schatten, Magnetic field observations near Mercury: preliminary results from Mariner 10. Science **185**(4146), 151–160 (1974). doi:10.1126/science.185.4146.151
F.M. Neubauer, D.A. Gurnett, J.D. Scudder, R.E. Hartle, Titan's magnetospheric interaction, in *Saturn*, ed. by T. Gehrels, M.S. Matthews (University of Arizona Press, Tuscon, 1984), pp. 760–787
F.M. Neubauer et al., Titan's near magnetotail from magnetic field and electron plasma observations and modeling: Cassini flybys TA, TB, and T3. J. Geophys. Res. **111**, A10220 (2006). doi:10.1029/2006JA011676
J.H. Newman, Y.S. Chen, K.A. Smith, R.F. Stebbings, Differential cross sections for scattering of 0.5-, 1.5-, and 5.0-keV hydrogen atoms by He, H_2, N_2, and O_2. J. Geophys. Res. **91**(A8), 8947–8954 (1986)
A.O. Nier, M.B. Mcelroy, Composition and structure of Mars' upper atmosphere: results from the neutral mass spectrometers on Viking 1 and 2. J. Geophys. Res. **82**(28), 4341–4349 (1977)
S. Noël, G.W. Prölss, Heating and radiation production by neutralized ring current particles. J. Geophys. Res. **98**(A10), 325 (1993)
S. Orsini, L.G. Blomberg, D. Delcourt, R. Grard, S. Massetti, K. Seki, J. Slavin, Magnetosphere-exosphere-surface coupling at Mercury. Space Sci. Rev. **132**, 551–573 (2007)
T. Owen, J.P. Maillard, C. de Bergh, B.L. Lutz, Deuterium on Mars: the abundance of HDO and the value of D/H. Science **240**(4860), 1767 (1988)
L.J. Paxton, D.E. Anderson Jr., A.I.F. Stewart, Analysis of pioneer Venus orbiter ultraviolet spectrometer Lyman α data from near the subsolar region. J. Geophys. Res. **93**(A3), 1766–1772 (1988)
A. Petrignani, F. Hellberg, R.D. Thomas, M. Larsson, P.C. Cosby, W.J. van der Zande, Electron energy-dependent product state distributions in the dissociative recombination of O_2^+. J. Chem. Phys. **122**(23), 234,311-8 (2005a)
A. Petrignani, W.J. van der Zande, P.C. Cosby, F. Hellberg, R.D. Thomas, M. Larsson, Vibrationally resolved rate coefficients and branching fractions in the dissociative recombination of O_2^+. J. Chem. Phys. **122**(1), 014,302-11 (2005b)
S.M. Petrinec et al., Neutral atom imaging of the magnetospheric cusps. J. Geophys. Res. **116**(A7) (2011). doi:10.1029/2010JA016357
R. Peverall et al., Dissociative recombination and excitation of O_2^+: cross sections, product yields and implications for studies of ionospheric airglows. J. Chem. Phys. **114**(15), 6679–6689 (2001)
C. Pollock et al., Medium energy neutral atom (MENA) imager for the IMAGE mission. Space Sci. Rev. **91**(1), 113–154 (2000)
M.H. Rees, *Physics and Chemistry of the Upper Atmosphere* (Cambridge University Press, Cambridge, 1989)
E. Richter, H.J. Fahr, H.U. Nass, Satellite particle exospheres of planets: application to Earth. Planet. Space Sci. **27**(9), 1163–1173 (1979)
J. Rodriguez, M. Prather, M. McElroy, Hydrogen on Venus: exospheric distribution and escape. Planet. Space Sci. **32**(10), 1235–1255 (1984)
E.C. Roelof, Energetic neutral atom image of a storm-time ring current. Geophys. Res. Lett. **14**(6), 652–655 (1987)
E.C. Roelof, Theory of "optically-thick" ENAS emission from Titan's exosphere, in *AGU Fall Meeting* (2005)
E. Roelof, A. Skinner, Extraction of ion distributions from magnetospheric ENA and EUV images. Space Sci. Rev. **91**(1), 437–459 (2000)
E. Roelof, D. Williams, The terrestrial ring current-from in situ measurements to global images using energetic neutral atoms. Johns Hopkins APL Tech. Dig. **9**, 144–163 (1988)
E.C. Roelof, D.G. Mitchell, D.J. Williams, Energetic neutral atoms (E $\sim$ 50 keV) from the ring current: IMP 7/8 and ISEE 1. J. Geophys. Res. **90**(11), 10991–11008 (1985)
A.M. Rymer, H.T. Smith, A. Wellbrock, A.J. Coates, D.T. Young, Discrete classification and electron energy spectra of Titan's varied magnetospheric environment. Geophys. Res. Lett. **36**, L15109 (2009). doi:10.1029/2009GL039427
Y. Saito et al., Solar wind proton reflection at the lunar surface: low energy ion measurement by MAP-PACE onboard SELENE (KAGUYA). Geophys. Res. Lett. **35**, L24205 (2008). doi:10.1029/2008GL036077
A. Schaufelberger, P. Wurz, H. Lammer, Y.N. Kulikov, Is hydrodynamic escape from Titan possible? Planet. Space Sci. (2011, in press). doi:10.1016/j.pss.2011.03.011

F.D. Schowengerdt, J.T. Park, Energy-loss spectra and collision cross sections for impact of 20–120-keV positive ions on molecular nitrogen. Phys. Rev. A **1**(3), 848–855 (1970)
C.H. Sheehan, J. St.-Maurice, Dissociative recombination of N_2^+, O_2^+, and NO^+: rate coefficients for ground state and vibrationally excited ions. J. Geophys. Res. **109**, A03302 (2004). doi:10.1029/2003JA010132
D.E. Shemansky, A.I.F. Stewart, R.A. West, L.W. Esposito, J.T. Hallett, X. Liu, The Cassini UVIS stellar probe of the Titan atmosphere. Science **308**(5724), 978–982 (2005)
B.D. Shizgal, Escape of h and d from Mars and Venus by energization with hot oxygen. J. Geophys. Res. **104**(A7), 14833–14846 (1999)
C. Simon, O. Witasse, F. Leblanc, G. Gronoff, J. Bertaux, Dayglow on Mars: kinetic modelling with SPICAM UV limb data. Planet. Space Sci. **57**(8–9), 1008–1021 (2009)
E.C. Sittler, R.E. Hartle, C. Bertucci, A. Coates, T. Cravens, I. Dandouras, D. Shemansky, Energy deposition processes in Titan's upper atmosphere and its induced magnetosphere, in *Titan from Cassini-Huygens* (Springer, Berlin, 2009), pp. 393–453
G.R. Smith, D.F. Strobel, A.L. Broadfoot, B.R. Sandel, D.E. Shemansky, J.B. Holberg, Titan's upper atmosphere: composition and temperature from the EUV solar occultation results. J. Geophys. Res. **87**(A3), 1351–1359 (1982)
H.T. Smith, D.G. Mitchell, R.E. Johnson, C.P. Paranicas, Investigation of energetic proton penetration in Titan's atmosphere using the Cassini INCA instrument. Planet. Space Sci. **57**(13), 1538–1546 (2009)
S. Snowden, M. Collier, K. Kuntz, XMM-Newton observation of solar wind charge exchange emission. Astrophys. J. **610**, 1182–1190 (2004)
S.A. Stern, The lunar atmosphere: History, status, current problems, and context. Rev. Geophys. **37**(4), 453–491 (1999)
A.I.F. Stewart, M.J. Alexander, R.R. Meier, L.J. Paxton, S.W. Bougher, C.G. Fesen, Atomic oxygen in the martian thermosphere. J. Geophys. Res. **97**(A1), 91–102 (1992)
D.J. Strickland, G.E. Thomas, P.R. Sparks, Mariner 6 and 7 ultraviolet spectrometer experiment: Analysis of the O I 1304- and 1356-A emissions. J. Geophys. Res. **77**(22), 4052–4068 (1972)
D.J. Strickland, A.I. Stewart, C.A. Barth, C.W. Hord, A.L. Lane, Mariner 9 ultraviolet spectrometer experiment: Mars atomic oxygen 1304-A emission. J. Geophys. Res. **78**(22), 4547–4559 (1973)
D.F. Strobel, Titan's hydrodynamically escaping atmosphere. Icarus **193**(2), 588–594 (2008)
D.F. Strobel, Titan's hydrodynamically escaping atmosphere: escape rates and the structure of the exobase region. Icarus **202**(2), 632–641 (2009)
P. Takacs, A. Broadfoot, G. Smith, S. Kumar, Mariner 10 observations of hydrogen Lyman alpha emission from the Venus exosphere: evidence of complex structure. Planet. Space Sci. **28**(7), 687–701 (1980)
T. Tanaka, K. Murawski, Three-dimensional MHD simulation of the solar wind interaction with the ionosphere of Venus: results of two-component reacting plasma simulation. J. Geophys. Res. **102**(A9), 19805–19821 (1997)
N. Terada, S. Machida, H. Shinagawa, Global hybrid simulation of the Kelvin-Helmholts instability at the Venus ionosphere. J. Geophys. Res. **107**(A12), 1471 (2002)
D. Toublanc, J.P. Parisot, J. Brillet, D. Gautier, F. Raulin, C.P. McKay, Photochemical modeling of Titan's atmosphere. Icarus **113**(1), 2–26 (1995)
O.J. Tucker, R. Johnson, Thermally driven atmospheric escape: Monte Carlo simulations for Titan's atmosphere. Planet. Space Sci. **57**(14–15), 1889–1894 (2009)
C. Tully, R.E. Johnson, Low energy collisions between ground-state oxygen atoms. Planet. Space Sci. **49**(6), 533–537 (2001)
A. Valeille, M.R. Combi, S.W. Bougher, V. Tenishev, A.F. Nagy, Three-dimensional study of Mars upper thermosphere/ionosphere and hot oxygen corona. 2. Solar cycle, seasonal variations, and evolution over history. J. Geophys. Res. **114**(E11), E11006 (2009). doi:10.1029/2009JE003389
A. Valeille, M.R. Combi, V. Tenishev, S.W. Bougher, A.F. Nagy, A study of suprathermal oxygen atoms in Mars upper thermosphere and exosphere over the range of limiting conditions. Icarus **206**(1), 18–27 (2010)
V.M. Vasyliunas, A survey of low-energy electrons in the evening sector of the magnetosphere with OGO 1 and OGO 3. J. Geophys. Res. **73**(9), 2839–2884 (1968)
R.J. Vervack, B.R. Sandel, D.F. Strobel, New perspectives on Titan's upper atmosphere from a reanalysis of the Voyager 1 UVS solar occultations. Icarus **170**(1), 91–112 (2004)
M. Volwerk, M. Delva, Y. Futaana, A. Retino, Z. Voros, T.L. Zhang, W. Baumjohann, S. Barabash, Substorm activity in Venus's magnetotail. Ann. Geophys. **27**, 2321–2330 (2009)
U. von Zahn, D. Kankowsky, K. Mauersberger, A.O. Nier, D.M. Hunten, Venus thermosphere: in situ composition measurements, the temperature profile, and the homopause altitude. Science **203**(4382), 768–770 (1979)
U. von Zahn, K.H. Fricke, D.M. Hunten, D. Krankowsky, K. Mauersberger, A.O. Nier, The upper atmosphere of Venus during morning conditions. J. Geophys. Res. **85**(A13), 7829–7840 (1980)

J.H. Waite et al., The Cassini ion and neutral mass spectrometer (INMS) investigation. Space Sci. Rev. **114**(1), 113–231 (2004)
J.H. Waite et al., Ion neutral mass spectrometer results from the first flyby of Titan. Science **308**(5724), 982–986 (2005)
J.H. Waite, D.T. Young, T.E. Cravens, A.J. Coates, F.J. Crary, B. Magee, J. Westlake, The process of tholin formation in Titan's upper atmosphere. Science **316**(5826), 870–875 (2007)
L. Wang, D. Fritts, R. Tolson, Nonmigrating tides inferred from the Mars Odyssey and Mars Global Surveyor aerobraking data. Geophys. Res. Lett. **33**, L23201 (2006). doi:10.1029/2006GL027753
B. Wargelin, M. Markevitch, M. Juda, V. Kharchenko, R. Edgar, A. Dalgarno, Chandra observations of the "dark" moon and geocoronal solar wind charge transfer. Astrophys. J. **607**, 596–610 (2004)
J.H. Westlake, J.M. Bell, J.H. Waite Jr., R.E. Johnson, J.G. Luhmann, K.E. Mandt, B.A. Magee, A.M. Rymer, Titan's thermospheric response to various plasma environments. J. Geophys. Res. **116**(A3) (2011) doi:10.1029/2010JA016251
M. Wieser et al., Extremely high reflection of solar wind protons as neutral hydrogen atoms from regolith in space. Planet. Space Sci. **57**, 2132–2134 (2009)
J. Winningham et al., Electron oscillations in the induced Martian magnetosphere. Icarus **182**(2), 360–370 (2006)
P. Withers, S. Bougher, G. Keating, The effects of topographically-controlled thermal tides in the martian upper atmosphere as seen by the MGS accelerometer. Icarus **164**(1), 14–32 (2003)
V. Wulms, J. Saur, D.F. Strobel, S. Simon, D.G. Mitchell, Energetic neutral atoms from Titan: Particle simulations in draped magnetic and electric fields. J. Geophys. Res. **115**, A06310 (2010). doi:1029/2009JA014893
P. Wurz, Detection of energetic neutral particles, in *The Outer Heliosphere: Beyond the Planets*, ed. by K. Scherer, H. Fichtner, E. Marsch, pp. 251–288 (Copernicus Gesellschaft e. V., Katlenburg-Lindau, 2000)
P. Wurz, U. Rohner, J.A. Whitby, C. Kolb, H. Lammer, P. Dobnikar, J.A. Martín-Fernández, The lunar exosphere: the sputtering contribution. Icarus **191**(2), 486–496 (2007)
P. Wurz, J. Whitby, U. Rohner, J. Martín-Fernández, H. Lammer, C. Kolb, Self-consistent modelling of Mercury's exosphere by sputtering, micrometeorite impact and photon-stimulated desorption. Planet. Space Sci. **58**(12), 1599–1616 (2010). doi:10.1016/j.pss.2010.08.003
R.V. Yelle, N. Borggren, V. de la Haye, W. Kasprzak, H. Niemann, I. Müller-Wodarg, J. Waite, The vertical structure of Titan's upper atmosphere from Cassini ion neutral mass spectrometer measurements. Icarus **182**(2), 567–576 (2006)
R. Yelle, H. Lammer, W.-H. Ip, Aeronomy of extra-solar giant planets. Space Sci. Rev. **139**(1), 437–451 (2008)
D.T. Young et al., Composition and dynamics of plasma in Saturn's magnetosphere. Science **307**(5713), 1262–1266 (2005)
Y.L. Yung, M. Allen, J.P. Pinto, Photochemistry of the atmosphere of Titan—comparison between model and observations. Astrophys. J. Suppl. Ser. **55**, 465–506 (1984)

Space Sci Rev (2011) 162:267–307
DOI 10.1007/s11214-011-9814-8

Modeling of Venus, Mars, and Titan

Esa Kallio · Jean-Yves Chaufray · Ronan Modolo · Darci Snowden · Robert Winglee

Received: 9 February 2011 / Accepted: 19 July 2011 / Published online: 6 October 2011

Abstract Increased computer capacity has made it possible to model the global plasma and neutral dynamics near Venus, Mars and Saturn's moon Titan. The plasma interactions at Venus, Mars, and Titan are similar because each possess a substantial atmosphere but lacks a global internally generated magnetic field. In this article three self-consistent plasma models are described: the magnetohydrodynamic (MHD) model, the hybrid model and the fully kinetic plasma model. Chamberlain and Monte Carlo models of the Martian exosphere

E. Kallio (✉)
Finnish Meteorological Institute, Helsinki, Finland
e-mail: esa.kallio@fmi.fi

J.-Y. Chaufray
Laboratoire de Météorologie Dynamique, Institut Pierre Simon Laplace, Centre National de la Recherche Scientifique, Paris, France
e-mail: jyclmd@lmd.jussieu.fr

R. Modolo
Université de Versailles Saint-Quentin, 45 avenue des Etats-Unis, 78035 Versailles cedex, France
e-mail: ronan.modolo@latmos.ipsl.fr

R. Modolo
Laboratoire Atmosphères, Milieux et Observations Spatiales, Quartier des Garennes, 11 bd d'Alembert, 78280 Guyancourt, France

R. Modolo
Centre National de la Recherche Scientifique, Quartier des Garennes, 11 bd d'Alembert, 78280 Guyancourt, France

D. Snowden
Lunar and Planetary Laboratory, University of Arizona, Tucson, AZ, USA
e-mail: dsnowden@u.washington.edu

R. Winglee
Department of Earth and Space Sciences, University of Washington, Johnson Hall, Box 351310, Seattle, WA 98195-1310, USA
e-mail: winglee@ess.washington.edu

are also described. In particular, we describe the pros and cons of each model approach. Results from simulations are presented to demonstrate the ability of the models to capture the known plasma and neutral dynamics near the three objects.

Keywords Numerical modeling · Full kinetic model · Hybrid model · Magnetohydrodynamic model · Exosphere model · Venus · Mars · Titan · Planetary magnetospheres · Planetary exospheres

1 Introduction

Numerical simulations are commonly used to study ionized and neutral particles near Venus, Mars and Titan (VMT) because they provide a simple description of plasma phenomena and cover a wide range of temporal and spatial scales. Simulating all of the physical processes that take place in the Solar System with a single model is currently not possible. For this reason, several types of models have been developed. Each model includes approximations depending on the physical phenomena being studied. These approximations must be understood in order to interpret simulation results correctly.

In this paper we first describe three self-consistent plasma models that have been used to model the plasma and neutral dynamics in the atmospheres of VMT: (1) the magnetohydrodynamic (MHD) model, (2) the hybrid model, and (3) the fully kinetic model. MHD models simulate the dynamics of both the ions and electrons as fluids, hybrid models simulate the dynamics of ion particles and electron fluids, and fully kinetic models simulate the dynamics of ions and electrons as individual particles. Each model is used to study the plasma interaction at a different spatial and temporal scale. Roughly speaking, MHD models are used to study relatively slow, large-scale fluid processes while fully kinetic models are employed to study fast, small-scale particle processes, with hybrid models falling in between fully kinetic and MHD methods. Results are presented to demonstrate the basic phenomena simulated by each type of model. It is important to note that numerical simulations are run in discrete space and time. Therefore, a model cannot include the effects of physical processes that are not resolved spatially or temporally by the simulation, even when the processes are explicitly expressed in the model. Therefore, the spatial and temporal scales of relevant physical processes, such as the inertial lengths, gyroradius, and plasma frequencies must be considered in relation to the grid size and time step of the model.

2 Self-consistent Plasma Modeling Methods

In this section, we introduce MHD and hybrid models, which are three-dimensional (3D) numerical methods frequently used to analyze the plasma interactions near VMT. We also introduce fully kinetic models, which simulate positively charged ions and electrons as particles. Although, fully kinetic models have not been used to simulate the global interaction near VMT, they are introduced for theoretical completeness. Another model not discussed in depth but may be of interest to the reader is the Vlasov model. In this model each species, s, is described by a velocity distribution function $f_s(\mathbf{x},\mathbf{v},t)$. Interested readers can find descriptions of the Vlasov model and its usage in planetary atmospheres/ionospheres (e.g. Schunk and Nagy 2009) as well as recent reviews of MHD and hybrid modeling approaches (Ma et al. 2008; Ledvina et al. 2008) from the literature.

2.1 Magnetohydrodynamic Methods

Magnetohydrodynamic (MHD) models are important tools for studying the plasma interactions of Venus, Mars, and Titan (VMT). In this section we briefly review the methods of several fluid models. Ledvina et al. (2008) is a more comprehensive review of MHD modeling methods, assumptions, and limitations. We start with ideal MHD, which is the basis for all MHD models but is rarely used to study the plasma interactions of VMT today. Next we describe multi-species MHD models, which include important mass loading and ion-neutral friction terms. Hall MHD models simulate the electrodynamics more accurately by including a Hall term in the electric field equation. Multi-fluid models include the Hall term, differentiate light and heavy ion dynamics, and can include the same source and loss terms as multi-species MHD. Finally, results from various three-dimensional simulations of the plasma interaction at VMT are discussed.

The plasma interactions of VMT are described in detail in Bertucci et al. (2011, this issue). In summary, the solar wind or magnetospheric plasma and magnetic field piles-up upstream of VMT. The magnetic field drapes around the body and solar wind (or magnetospheric) plasma and field is diverted around a cavity called the induced magnetosphere. For Venus and Mars the very outer boundary of the interaction is the bow shock. This boundary does not form around Titan unless it exits Saturn's magnetosphere and enters the solar wind. Downstream of the bow shock, the next boundary layer is the induced magnetosphere boundary (IMB), also known as the magnetic pile-up boundary (MPB), where there is a strong increase in the magnetic field. Another lower boundary occurs when collision processes begin to dominate in the ionosphere. As described in Bertucci et al. (2011, this issue), the aspects of the lower boundary are significantly different for VMT.

Models of the plasma interaction at VMT are useful tools for understanding the three-dimensional characteristics of induced magnetospheres and how they are affected by changes in the upstream conditions, the properties of the ionosphere, or, in the case of Mars, crustal magnetic fields. Simulations have also quantified the loss of ionospheric ions to better understand how the plasma interaction erodes the upper atmosphere.

2.1.1 Assumptions of MHD Models

Compared to fully kinetic or hybrid models, fluid models make the most assumptions, however these assumptions allow MHD models to be numerically simple enough to simulate even large global magnetospheres with good resolution with modest computational resources. While finer details of the magnetospheric interactions such as chemical reactions, charge exchange, and intrinsic crustal magnetic fields (in the case of Mars) can be included in hybrid models, MHD simulations are often the first to describe these physical interactions.

The core assumption of any MHD model is that the plasma acts like a fluid, bound together either by frequent collisions or by electromagnetic forces. A fluid model can only simulate the bulk parameters (velocity, density, temperature) of the interaction; therefore, it is assumed that kinetic processes stemming from the generation of energetic tails in the particle distributions or from temperature anisotropies are not important (at least to the processes that are being studied), and that the plasma behavior is well described by a single Maxwellian distribution in ideal MHD or by multiple Maxwellian distributions in the multi-fluid approach. In addition, all fluid models assume: quasi-neutrality $n_e = n_i$, $m_i/m_e \gg 1$ (neglect $d\mathbf{J}/dt$), and isotropic temperatures ($T_\perp \approx T_{||}$, relative to the magnetic field). Here m and n are the mass and number density and the subscripts e and i refer electrons and ions; $T_\perp$ and $T_{||}$ are the temperatures perpendicular and parallel to the magnetic field; and $\mathbf{J}$ is the current.

There are two fundamental areas where fluid models differ: the treatment of Ohm's law and the treatment of ion dynamics. Ohm's law, which relates the bulk plasma properties to the induced electric field, can be derived from the electron momentum equation under the assumptions of quasi-neutrality and $m_i/m_e \gg 1$. Different versions of Ohm's law have been developed, depending on the relevant scale sizes of structures incorporated within the model. Ideal MHD and resistive MHD treatments neglect the differential acceleration of ions with different masses and assume all species have the same bulk velocity, i.e. $\mathbf{V}_i = \mathbf{V}_e = \mathbf{V}$. The resulting Ohm's law is given by either:

$$\mathbf{E} = -\mathbf{V} \times \mathbf{B} \quad \text{(ideal MHD)} \tag{2.1}$$

$$\mathbf{E} = -\mathbf{V} \times \mathbf{B} + \eta \mathbf{J} \quad \text{(ideal resistive MHD)} \tag{2.2}$$

where $\mathbf{V}$ is the velocity vector, $\mathbf{E}$ is electric field, $\mathbf{B}$ is the magnetic field, and η is the plasma resistivity (only included in resistive MHD models). If the system includes structures on the order of the ion gyroradius or ion skin depth then higher order corrections, specifically the Hall and ∇p_e terms should be included:

$$\mathbf{E} = -\mathbf{V} \times \mathbf{B} + \frac{\mathbf{V} \times \mathbf{B}}{q n_e} - \frac{1}{q n_e} \nabla p_e + \eta \mathbf{J} \quad \text{(Generalized Ohm's Law)} \tag{2.3}$$

where p_e is the scalar electron pressure and q is the elementary charge. Some treatments neglect the ∇p_e term if the electrons are cold. The effects of the Hall and ∇p_e terms are greatest when the ion skin depth (c/ω_{pi} where ω_{pi} is the ion plasma frequency and c is the speed of light) is comparable to the scale length of the structure (L).

In addition, many fluid models assume that all ion species have the same bulk speed $\mathbf{V}$. This assumption means the model includes only one equation of motion for all of the ions, which greatly reduces the numerical complexity. However, the acceleration of different ion species depends on the ion mass and temperature. For example, low-energy ionospheric outflows can exhibit differential acceleration and propagation between light and heavy ions. Ideal, multi-species and Hall MHD methodologies neglect these effects. Multi-fluid models include them by incorporating a separate equation of motion for each ion species.

Of course, the various models also make fundamentally different assumptions about which magnetosphere-ionosphere interactions are important to the interaction region that they are studying. Some models include detailed chemistry and ionizations sources in the ionosphere, while others include relatively simple inner boundary conditions. The treatment of ion-neutral, ion-ion collisions, charge exchange, photoionization, and electron impact ionization are important when describing features that occur close to or below the planets exobase and ion outflow.

Some of the underlying assumptions of MHD models are invalid in regions near VMT. To determine whether an assumption is valid, the grid size of the simulations should be compared to the implicit length scale of the assumption. The simulation grid size is usually constrained by computational resources and the size of features of the plasma interaction. In the case of Earth's magnetosphere the bow shock should be included in the simulation. The bow shock is ~15 Earth radii from the center of the Earth at the sub-solar point and can flare out ~100 Earth radii at the flanks. Therefore, the volume of the simulation limits the grid size to a significant fraction of an Earth radius. Simulations of the induced magnetospheres of VMT are smaller relative to the planetary radius. The sub-solar locations of the bow shocks of Venus and Mars are ~1.5 planetary radii (R) from

Table 1 Comparison of plasma relevant scale sizes at VMT and simulation grid sizes

	Venus	Mars	Titan
Radius	6052 km	3395 km	2575 km
$L = 0.1R, r_l/L$	0.063	0.43	1.6
λ_D/L	9.3×10^{-7}	6.4×10^{-6}	7.4×10^{-5}
λ_{mfp}/L	2.2×10^{4}	5.5×10^{5}	1.4×10^{9}
$c/\omega_{pi}/L$	9.7×10^{-3}	0.047	0.79
$c/\omega_{pe}/L$	2.2×10^{-4}	1.1×10^{-3}	3.8×10^{-3}

the center of the planet with flare distances of less than 10 planetary radii. This means that simulation grid sizes can be on the order of $\sim 0.1R$ or less. For the smaller bodies, Mars and Titan, the grid size is often smaller than the ion skin depth and boundary layers of the interaction can be resolved. For example, the thickness of the bow shock and magnetic pile-up boundary at Mars and Venus are on the order of the ion skin depth (Mazelle et al. 2004) as is the current sheet thickness at Titan and Mars (Halekas et al. 2006; Wahlund et al. 2005). However, resolving the ion skin depth violates the assumptions of some models. In Table 1, the implicit length scales of various MHD assumptions are compared to a typical scale size of simulations at VMT, $L \sim 0.1R$. The scale sizes in Table 1 are taken from Ledvina et al. (2008) and are calculated for values applicable to the solar wind (for Mars and Venus) and for magnetospheric O^+ for Titan. The term in the first row of the table, r_l/L, compares the Lamour radius of ions in the induced magnetosphere to the simulation scale length. From this comparison it is evident that neglecting ion gyroradius effects of incident ions is acceptable at Venus, somewhat invalid at Mars, and completely invalid at Titan. However, it is important to note that these values are representative of the H^+ ions in the solar wind and not the heavy ions in each body's upper atmosphere. Even for Venus, the gyroradius of planetary ions can be large relative to the simulation scale length depending on the strength of the magnetic field and the origin of the planetary ions (see, for example, Kallio and Jarvinen 2011, Fig. 2). The large gyroradius of ions in VMT's ionospheres can lead to large asymmetries in the plasma interaction. For example, the convective electric field in the solar wind (or Saturn's magnetosphere) accelerates ions away on one side of VMT's ionosphere forming an asymmetric wake region. On the other side, the convective electric field accelerates ions towards the ionosphere, depositing energy into the upper atmosphere.

In each case comparing the Debye length to the simulation scale length, $\lambda_D/L \ll 1$, validates the assumption of quasi-neutrality. The comparison of the mean free paths, λ_{mfp}/L, and the simulation scale size shows that outside the dense regions of the atmospheres the plasma becomes collisionless; therefore, it is not valid to assume the plasma has a thermal distribution and isotropic pressure. The next two length scales, $c/\omega_{pi}/L$ and $c/\omega_{pe}/L$, are the characteristic length scales of waves that oscillate near the ion plasma frequency and electron plasma frequency. While it is a valid assumption to neglect all waves with frequencies on the order of the electron plasma frequency, neglecting waves on the order of the ion plasma frequency, such as ion cyclotron waves, is not valid at the typical resolutions of simulations of Mars and Titan.

Comparing the length scales of each of the fundamental assumptions indicates that MHD models of Venus break the fewest assumptions because of the large size of Venus compared to Mars and Titan and the relatively stronger magnetic field (which decreases the Lamour radius). MHD models of Titan's induced magnetosphere break the most assumptions. Not only is Titan small compared to Venus and Mars, Titan's ionosphere contains very massive

ion species (Waite et al. 2005). Furthermore, the plasma in Saturn's magnetosphere contains ions that gyrate with a radius on the order of the diameter of Titan (Hartle et al. 2006).

In particular, assumptions that the plasma has a Maxwellian distribution and that ion cyclotron effects are not important become invalid in the near collisionless regions near VMT's atmospheres and in VMT's ion tails.

However, useful model-data comparisons have been made using fluid models when the authors were aware of how the limitations of their fluid simulation affected their results. Furthermore, there are several advantages to fluid models that make certain types of simulations more convenient to implemented MHD rather than fully kinetic or hybrid models. MHD models require less computational resources therefore fluid simulations typically have faster simulation times, larger simulation volumes, and good resolution inside the ionosphere of the target object. In addition, the most resolved regions in fluid simulations are often in regions where ion-neutral collisions validate the assumptions of neglecting the ion gyroradius and anisotropic pressure. Outside of the dense regions of the atmospheres it is better to use a Hall MHD or multi-fluid models to study the interaction because these models include ion cyclotron effects, although not as explicitly as hybrid models. Of course, Hall MHD and multi-fluid simulations also assume isotropic pressure and thermal plasma distributions. To simulate non-thermal distributions, it is necessary to use a kinetic or hybrid model.

2.1.2 Ideal MHD

The ideal MHD equations self-consistently solve for the evolution of the gas dynamics of the plasma (through the continuity, energy, and momentum equations) and the evolution of the magnetic field (through the induction equation). Here we assume the reader is familiar with MHD theory. For more detail the reader is referred to text such as Schunk and Nagy (2009). The basic form of the ideal MHD equations is:

$$\text{Continuity equation:} \quad \frac{\partial \rho}{\partial t} + \nabla \cdot \rho \mathbf{V} = 0, \tag{2.4}$$

$$\text{Momentum equation:} \quad \frac{\partial \rho \mathbf{V}}{\partial t} + \nabla \cdot (\rho \mathbf{V}\mathbf{V}) = \mathbf{J} \times \mathbf{B} - \nabla p, \tag{2.5}$$

$$\text{Energy equation:} \quad \frac{\partial e}{\partial t} + \nabla \cdot (e\mathbf{V}) = -p \nabla \cdot \mathbf{V}, \tag{2.6}$$

$$\text{Induction equation:} \quad \frac{\partial \mathbf{B}}{\partial t} = \nabla \times (\mathbf{V} \times \mathbf{B}) \tag{2.7}$$

where ρ is the plasma mass density, $\mathbf{V}$ is the velocity vector, $\mathbf{J}$ is the current, $\mathbf{B}$ is the magnetic field, e is internal energy density, and p is the scalar thermal pressure. The thermal pressure is related to the internal energy density by $p = (\gamma - 1)e$ and γ is the adiabatic index, which is $5/3$ for an adiabatic flow.

The ideal MHD equations are written in conservative form, meaning that mass, pressure, and momentum is strictly conserved. However, sometimes the MHD equations used in models are not conservative but are in "primitive form". Primitive equations do not strictly conserve energy but can be easier to solve numerically. Some MHD equations such as the multi-fluid equations cannot be conservative. The errors resulting from using non-conservative forms of MHD equations are not well understood and we refer the reader to Ledvina et al. (2008) for a more detailed description of this issue.

2.1.3 Resistive MHD

The diffusion of the magnetic field due to electron-neutral collisions in the atmospheres of VMT can be accounted for by using resistive MHD. The induction equation in resistive MHD is:

$$\text{Induction equation:} \quad \frac{\partial \mathbf{B}}{\partial t} = \nabla \times (\mathbf{V} \times \mathbf{B}) + \eta \nabla^2 \mathbf{B}. \tag{2.8}$$

The final term on the right hand side is a resistive term that simulates the diffusion of the magnetic field inside the atmosphere due to electron-neutral collisions, where the resistivity is:

$$\eta = \frac{1}{\sigma_0 \mu_0} = \frac{\sum_{n=\text{neutrals}} \upsilon_{en} m_e}{q^2 n_e \mu_0}. \tag{2.9}$$

Here σ_0 is the conductivity, μ_0 is the permeability of free space, and υ_{en} is the electron-neutral collision frequency. Including this term is particularly important when studying the lifetime and structure of the magnetic field in the ionosphere. The resistive term can also be included in the multi-species and multi-fluid models below. Whether or not it is included varies from model to model.

2.1.4 Multi-species MHD

Multi-species MHD models improve ideal MHD by including the effects of mass loading and ion-neutral drag. Unlike ideal MHD, multi-species MHD models also calculate the relative abundance of ion species in each cell of the simulation, which depends on ion source and loss terms. The relative abundance of ion species is tracked by incorporating a separate continuity equation for each ion species:

$$\frac{\partial \rho_i}{\partial t} + \nabla \cdot \rho_i \mathbf{V} = S_i - L_i, \tag{2.10}$$

where i denotes different ion species, S_i is the ion source term, and L_i is the ion loss term. The source and loss terms can include elastic and inelastic collisions with the background neutral gas, photoionization, photoelectron ionization, electron impact ionization, and dissociative recombination. For more details about the source and loss terms the reader is referred to Schunk and Nagy (2009) or the papers referenced in this review.

After the continuity equations are solved the mass density of all species is summed, i.e. $\rho = \sum_{i=\text{ions}} \rho_i$. A single momentum equation forces the resulting single-fluid plasma:

$$\frac{\partial \rho \mathbf{V}}{\partial t} + \nabla \cdot \left(\rho \mathbf{V}\mathbf{V} + p\mathbf{I} + \frac{B^2}{2\mu_0}\mathbf{I} - \frac{1}{\mu_0}\mathbf{B}\mathbf{B} \right) - \rho G = \frac{\partial M}{\partial t}, \tag{2.11}$$

where $\mathbf{I}$ is the identity matrix, and $\mathbf{G}$ is gravity. Collisions between ions and the planets neutral atmosphere transfers momentum from the plasma to the neutral gas, slowing the incident plasma. In addition, ions from the ionosphere are picked up by the interplanetary or planetary magnetic field. The added mass slows the propagation of the magnetic field near the body in a process known as mass loading. In the momentum equation the frictional effects of ion-neutral collisions and mass loading effect of photoionization, electron impact ionization, and charge exchange would be included in the term $\frac{\partial M}{\partial t}$, which varies from model to model.

Similar to ideal MHD it is assumed that the dynamics of the plasma can be described by a single-fluid and that the electrons and all ions have the same bulk velocity. Therefore, the Hall term is not included in Ohm's law:

$$\mathbf{E} = -\mathbf{V} \times \mathbf{B} + \eta \mathbf{J}. \tag{2.12}$$

This is the resistive form of Ohm's law. However, it is important to note that most of the multi-species MHD models that have been used to study the interaction at VMT neglect this resistive term. Ohm's law is substituted into the induction equation:

$$\frac{\partial \mathbf{B}}{\partial t} = -\nabla \times \mathbf{E} \tag{2.13}$$

to solve for the magnetic field.

The final equation describing the dynamics of the plasma is the energy or, as shown here, the pressure equation:

$$\frac{1}{\gamma - 1}\frac{\partial p}{\partial t} + \frac{1}{\gamma - 1}(\mathbf{V} \cdot \nabla) p + \frac{1}{\gamma - 1} p(\nabla \cdot \mathbf{V}) = \frac{\partial E}{\partial t}. \tag{2.14}$$

The relation $p = (\gamma - 1)e$ can be used to find the corresponding energy equation. On the right hand side of the equation, heating/cooling terms due to ion-neutral, ion-ion, and ion-electron collisions would be added. In this case we have simplified the equation by representing various heating and cooling terms with the transport function, $\frac{\delta E}{\delta t}$. In multi-species models the temperatures of all ion species are averaged together and typically it is assumed that the electron and ion temperatures are equal, i.e. $\sum_{i=\text{ions}} T_i = T_e = T_p/2$.

2.1.5 Hall MHD

The Hall term modifies the magnetic field topology and produces asymmetries in the plasma flow near VMT. For the Hall term to be non-zero $v_i \neq v_e$. Since MHD models do not solve for the ion and electron velocity independently, the relative velocity of the ions and electrons, or the current, must be calculated by taking the curl of the magnetic field, $\mathbf{v}_H = -\frac{\mathbf{J}}{ne} = -\frac{\nabla \times \mathbf{B}}{ne\mu_o}$. Then the electric field equation (Ohm's law) can be modified to include the Hall term,

$$\mathbf{E} = -\mathbf{V} \times \mathbf{B} + \eta \mathbf{J} + \frac{1}{nq}\mathbf{J} \times \mathbf{B}. \tag{2.15}$$

The set of Hall MHD equations are then (Tóth et al. 2008):

$$\frac{\partial \rho}{\partial t} + \nabla \cdot \rho \mathbf{V} = S - L \tag{2.16}$$

$$\frac{\partial \rho \mathbf{V}}{\partial t} + \nabla \cdot \left(\mathbf{V}\rho\mathbf{V} + \mathbf{I}p + \mathbf{I}\frac{B^2}{2\mu_0} - \frac{1}{\mu_0}\mathbf{B}\mathbf{B} \right) = \frac{\partial M}{\partial t} \tag{2.17}$$

$$\frac{\partial e}{\partial t} + \nabla \cdot \left(\mathbf{V}(\varepsilon + p) + (\mathbf{V} + \mathbf{v}_H) \cdot \left(\bar{\mathbf{I}}\mathbf{B}^2 - \mathbf{B}\mathbf{B} \right) - \mathbf{B} \times \eta \mathbf{J} \right) = \frac{\partial E}{\partial t} \tag{2.18}$$

$$\frac{\partial \mathbf{B}}{\partial t} = \nabla \times \left((\mathbf{V} + \mathbf{v}_H) \times \mathbf{B} - \eta \mathbf{J} \right) \tag{2.19}$$

$$e = \varepsilon + \frac{\mathbf{B}^2}{2} = \frac{p}{\gamma - 1} + \frac{\rho \mathbf{V}^2}{2} + \frac{\mathbf{B}^2}{2} \tag{2.20}$$

where ε is the hydrodynamic energy density. Including the additional term in the electric field equation decouples the ions from the magnetic field (and the electrons which are still strictly coupled to the magnetic field). Other variations of Hall MHD have also been applied to study Mars (Harnett and Winglee 2003, 2005). In this case the methodology was referred to as non-ideal MHD and the equations of this model included the ideal MHD continuity, momentum, and energy equations but similar to Hall MHD the Ohm's law included Hall and electron pressure gradient terms that needed to be scaled by 1/3 for stability.

2.1.6 Multi-fluid

Multi-fluid models are fundamentally different from what is typically considered an MHD model because multi-fluid models solve for the dynamics of each ion species with a separate momentum and energy equation. This means that ion and electrons are not co-added to form a single-component-plasma, requiring all ion species and electrons to have the same speed. In addition, the Ohm's law used in multi-fluid models can include the Hall and electron pressure gradient (∇p_e) terms.

For simplicity we show the form of the multi-fluid model used by Harnett and Winglee (2006) with the addition of source and loss terms. The continuity equation is:

$$\frac{\partial \rho_i}{\partial t} + \nabla \cdot \rho_i \mathbf{V}_i = S_i - L_i \tag{2.21}$$

The Ohm's Law is derived from the electron momentum equation, assuming the electrons are in steady-state drift motion. The Ohm's Law used in multi-fluid models can include the Hall term, the pressure gradient term, and a resistive term:

$$\mathbf{E} = -\sum_i \frac{n_i}{n_e}\mathbf{V}_i \times \mathbf{B} + \frac{\mathbf{J}\times\mathbf{B}}{qn_e} - \frac{1}{qn_e}\nabla p_e + \eta \mathbf{J} \tag{2.22}$$

A momentum and pressure equation is solved for each of the ion species, denoted by the subscript i:

$$\rho_i \frac{d\mathbf{V}_i}{dt} - qn_i\left[(\mathbf{V}_i \times \mathbf{B}) - \sum_i \frac{n_i}{n_e}\mathbf{V}_i \times \mathbf{B}\right] - \mathbf{J}\times\mathbf{B} + \nabla(p_i + p_e) - \rho_i g(r) = \frac{\partial M_i}{\partial t} \tag{2.23}$$

$$\frac{\partial p_i}{\partial t} + \gamma \nabla \cdot (p_i \mathbf{V}_i) - (\gamma - 1)\mathbf{V}_i \cdot \nabla p_i = \frac{\partial E_i}{\partial t} \tag{2.24}$$

The current is $\mathbf{J} = \mu_o^{-1}\nabla \times \mathbf{B}$ and the electron velocity is $\mathbf{V}_e = \sum_i \frac{n_i}{n_e}\mathbf{V}_i - \frac{\mathbf{J}}{en_e}$.

The equations are closed with a pressure equation for the electron fluid and the induction equation:

$$\frac{\partial p_e}{\partial t} + \gamma \nabla \cdot (p_e \mathbf{V}_e) - (\gamma - 1)\mathbf{V}_e \cdot \nabla p_e = \frac{\partial E_e}{\partial t} \tag{2.25}$$

$$\frac{\partial \mathbf{B}}{\partial t} = -\nabla \times \mathbf{E} \tag{2.26}$$

The advantage of multi-fluid models is that they simulate mass dependent-asymmetric behavior. The asymmetry in ion outflow produced by the convective electric field in multi-fluid models is similar to those of hybrid models. Multi-fluid models also include the electric fields arising from pressure gradients and ion-demagnetization across boundary layers. A disadvantage compared to hybrid models is that multi-fluid models are unable to include non-Maxwellian particle distributions as well as temperature anisotropies.

Recently, Najib et al. (2011) used a different form of the multi-fluid equations to simulate the Mars interaction. The Ohm's law (Eq. (2.22)) used by Najib et al. (2011) did not include the resistive, Hall, and pressure gradient terms. Najib et al. (2011) also assumed that the electron pressure was equal to the total ion pressure and did not solve the electron pressure equation. The multi-fluid method used by Najib et al. (2011) includes source and loss terms as well as ion-neutral and ion-ion collision terms in the continuity, mass, and pressure equations. As described in Ledvina et al. (2008), there are questions related to how multi-fluid models simulate shocks. When one species shocks in a hybrid simulation waves are produced that interact with other ion particles. Although the full spectrum of waves are not simulated in multi-fluid models, the ion fluids in a multi-fluid model are still coupled through the electric field equation. However, due to this concern, Najib et al. (2011) solved for the hydrodynamic energy density, $e_s = \rho_s \mathbf{V}_s^2/2 + p_s/(\gamma - 1)$, instead of the pressure equations (Eq. (2.24)) outside of and near where the bow shock forms, by solving:

$$\frac{\partial e_s}{\partial t} + \nabla \cdot [(e_s + p_s)\mathbf{V}_S] - \mathbf{V}_s \left[\frac{n_s q_s}{n_e e} (\mathbf{J} \times \mathbf{B} - \nabla p_e) + n_s q_s (\mathbf{V}_S - \mathbf{V}_+) \times \mathbf{B} \right] = \frac{\partial E_e}{\partial t}, \quad (2.27)$$

where $\mathbf{V}_+$ is the average velocity of all ion fluids. Although, this method is not strictly conservative, Glocer et al. (2009) claims it gives "roughly correct jump conditions across shocks when the magnetic energy density is small relative to the kinetic and thermal energy densities". Glocer et al. (2009) also couples the ion fluids in their multi-fluid model by approximating the two-stream instability along field lines by adding an additional friction term to the momentum equation. This term is not included in the model in Najib et al. (2011).

2.1.7 MHD Models of Venus' Interaction with the Solar Wind

Venus was the first planet to be studied in depth with 3D fluid models. The ideal, single-fluid MHD model by Tanaka (1993) simulated many features of induced magnetospheres that are well known today. For example, the model was used to determine how magnetic field lines and solar wind plasma pile-up upstream of Venus and how the magnetic field slowly slips around the flanks of the planet. Tanaka (1993) showed that the field lines are bent into U-shapes as they move from the day side to the night side of the ionosphere and that $\mathbf{J} \times \mathbf{B}$ force of the bent magnetic field lines accelerates plasma along the poles of Venus' ionosphere. Eventually the mass loaded, deformed field lines were shown to convect to the night-side of Venus and detach. The detachment of the U-shaped field formed a magnetotail with a neutral sheet of ionospheric plasma separating lobes of oppositely directed magnetic field lines. Therefore, Tanaka (1993) was the first to simulate the outflow of plasma in the solar wake of an un-magnetized object. These results agreed with data from the Pioneer Venus Orbiter, which had already observed a wake of plasma and draping of magnetic fields in Venus' ionosphere (e.g. Luhmann and Cravens 1991).

A single-fluid, two-species (multi-species), MHD model (Tanaka and Murawski 1997) improved on the model published in Tanaka (1993) by adding source and loss terms to the continuity equation to represent the production and loss of O^+ in Venus' ionosphere by

photoionization and charge exchange collisions with CO_2. The model also included gravity and ion-neutral friction in the momentum and energy equations. The simulation results were used to investigate the location of the bow shock and the MPB and the 3D flow patterns of ionospheric O^+ above and below Venus' ionopause. Tanaka and Murawski (1997) showed that horizontal flow due to the magnetic tension force transports plasma from the day side to the night side. The horizontal plasma flow is fastest near the terminator where strongly bent field lines occur and slows significantly on the night side. In addition, Tanaka and Murawski (1997) further described ion outflow in Venus' magnetotail. They showed that ionospheric O^+ lost from Venus forms a cross-shaped ion tail with features that resembled tail rays observed by the Pioneer Venus Orbiter (e.g. Brace and Kliore 1991).

The next sequence of models focused on quantifying how mass loading due to photoionization, electron impact ionization, and charge exchange affects the location of Venus' boundary layers. Observations showed that the bow shock and MPB were located further from Venus during solar maximum than solar minimum. It was hypothesized that mass loading from higher EUV ionization caused the bow shock to move out during solar maximum, however previous 3D MHD models (Murawski and Steinolfson 1996) had not been able to show this effect. However, the simulation by Murawski and Steinolfson (1996) used an unrealistic IMF direction.

Kallio et al. (1998) used an ideal MHD model with a source term included in the continuity equation to determine if mass loading from photoionization, charge exchange, and electron impact ionization could account for the bow shock distances. At the time the mass loading rate due to charge exchange and electron impact ionization was not well known so Kallio et al. (1998) simply tripled the photoionization rate of oxygen in Venus atmosphere. Kallio et al. (1998) found that the additional mass loading caused the bow shock to move outward in agreement with theory. The peak magnetic field in the magnetic pile-up region was also stronger.

Bauske et al. (1998) also used a single-fluid MHD model to simulate the effect of mass loading due to photoionization, charge exchange, and electron impact ionization on the location of the bow shock and magnetic field barrier near Venus. Kallio et al. (1998) only included a mass loading term in the continuity equation. Bauske et al. (1998) included mass loading terms in the continuity, momentum, and energy equations. They showed that charge exchange and electron impact ionization had only a small effect, however the mass loading due to photoionization significantly changed the location of the bow shock in agreement with observations. Bauske et al. (1998) saw a larger increase in the distance of the bow shock for the same mass loading rate used in the simulation of Kallio et al. (1998) indicating that mass loading terms should be included in the momentum and energy equation in addition to the continuity equation.

Similar to Kallio et al. (1998), Bauske et al. (1998) found that additional mass loading caused the peak magnetic field in the sub-solar direction to increase. Kallio et al. (1998) argued that this effect may be due to vortices that were produced on the on the wake side of Venus. However, the model by Bauske et al. (1998) did not produce these vortices. Instead, Bauske et al. (1998) reasoned that slower convection of plasma and field slipping around the obstacle due to ion-neutral drag leads to a higher magnetic field in the magnetic pile-up region.

The first resistive, multi-species model to be applied to Venus was developed by Terada et al. (2009). The multi-species MHD model included ten ion species, a comprehensive chemical scheme and ion-neutral collisions. This model is the first three-dimensional model to include an appropriate thermal conductivity term and they were able to reproduce realistic plasma temperatures in Venus' ionosphere.

More recently, a single-fluid, multi-species semi-time dependent MHD model was used to interpret data taken during MESSENGER's flyby of Venus (Benna et al. 2009). Venus Express was observing the properties of the solar wind outside of Venus' induced magnetosphere and observed strong rotations in the magnetic field during the MESSENGER flyby. Benna et al. (2009) combined results from four simulations, ran with upstream conditions characteristic of four rotations of the IMF. The simulations showed that Venus' magnetotail responded and rotated within minutes of rotations in the IMF.

2.1.8 MHD Models of Mars' Interaction with the Solar Wind

The small scale of Mars relative to Venus and the reduced strength of the IMF at Mars means that the Lamour radius of solar wind ions and ionospheric ions are large compared to Mars' radius and, therefore, may have a larger impact on the features of the interaction. However, many features of the interaction between Mars and the solar wind have been correctly simulated by fluid models.

Most three-dimensional simulations of Mars' interaction with the solar wind have been used to study how the intrinsic crustal magnetic fields affect the location of boundary layers, ionospheric plasma flow, and ion loss rates. Quantifying atmospheric escape is particularly important at Mars because quantifying the loss of Mars' atmosphere through solar wind erosion helps answer the question: where did the water go? Nagy et al. (2004) provided a detailed review of Mars' interaction with the solar wind including results based on observation and numerical modeling. In this section we review some of that material and update it with results from numerical models published since 2004.

Similar to the model of Tanaka and Murawski (1997), Liu et al. (1999) developed a two-species, MHD model of the plasma interaction at Mars, which included simple chemistry and source and loss terms in the continuity, momentum, and energy equations. This model simulated boundary layers with sub-solar distances that were in good agreement with observations by Mars Global Surveyor (Vignes et al. 2000). The model predicted an ionospheric outflow of O^+ equal to 2.5×10^{25} s^{-1}. Liu et al. (2001) described the results from an updated version of this model including an additional ionospheric species (O^+). This model found a similar ionospheric loss rate (3.06×10^{25} s^{-1}) and boundary layer locations as the previous model. Anomalous magnetic field had been observed near Mars, so Liu et al. (2001) used the model to investigate the effects of crustal magnetic fields by adding a small surface dipole. They found that an intrinsic crustal field can significantly perturb the ionosphere and the rotation of the fields may cause the large variability observed in the location of Mars' bow shock.

Ma et al. (2002) published the first of several three-dimensional, multi-species, single-fluid MHD studies of the interaction between Mars' exosphere and the solar wind. The first model included 3-ion species (H^+, O^+, and O_2^+) and major chemical reactions, photoionization, electron impact ionization, and charge exchange interactions with Mars' extended neutral oxygen corona. One objective was to simulate how crustal magnetic fields affect the location of the bow shock and MPB. Unlike the dipole field approximation used in Liu et al. (2001), Ma et al. (2002) used a crustal field modeled after spacecraft measurements of Mars' crustal field. The strongest of the magnetic fields (which occur mostly in the southern hemisphere) were placed in the sub-ram direction. Ma et al. (2002) found that crustal magnetic fields did not effect the location of the bow shock but did effect the location of the MPB. The interaction between the piled-up IMF field in the MPB and the crustal magnetic fields also produced small-scale magnetic structures known as magnetocylinders, which had been observed by spacecraft (Mitchell et al. 2001). Ma et al. (2002) also described the general

circulation of ionospheric plasma which, in agreement simulations of Venus' plasma interaction, was upward on the day side ionosphere, day to night at higher altitudes, downward on the night side below about 250 km altitude, and down Mars magnetotail at higher altitudes.

Ma et al. (2004) improved on the model published in Ma et al. (2002) by including a new spherical grid structure, better resolution near the inner boundary, and an additional species (CO_2^+). This model was used to quantify ion outflow from Mars for several orientations of crustal magnetic field and for different solar wind conditions. The fluxes reported in Ma et al. (2007) ranged from 2.7×10^{23} to 2.4×10^{24} s^{-1} for nominal solar wind conditions. The range of simulated outflow is in agreement with the flux measured by Mars Express, which was estimated to be 3.2×10^{23} s^{-1} (Barabash et al. 2007). Different orientations of the crustal magnetic field caused the outflow to change by a factor of $\sim$2 to 3. Forcing Mars' atmosphere with strong storm like conditions lead to an order of magnitude increase in ionospheric loss rates (3×10^{25} s^{-1}).

Harnett and Winglee (2003) applied a single-fluid, "non-ideal" (Hall), resistive MHD model to Mars. The model was non-ideal because it included the Hall term and the electron pressure gradient term in the Ohm's law (reduced by 1/3). Including the full terms led to unstable results. Harnett and Winglee (2003) showed that mini-magnetopauses form around the crustal magnetic fields. The inclusion of Hall term and electron pressure gradient allowed for ion demagnetization to occur across the boundary layers, which induced additional electric fields that cannot be captured with ideal MHD. Harnett and Winglee (2005) used the same model to study the effect of crustal magnetic fields when the strongest magnetic fields are located on the night side and on the dawn and dusk terminators of Mars. The crustal magnetic fields were shown to cause large perturbations in the magnetotail, much larger than the magnetic structures themselves. In particular, the crustal magnetic fields were shown to lead to asymmetries, strong density depletions, and density enhancements in Mars' magnetotail that were in good agreement with measurements made by Phobos 2 spacecraft (Lundin et al. 1990).

The first 3D resistive, multi-fluid model applied to Mars was presented in Harnett and Winglee (2006). This model included three ion species (H^+ (solar wind), H^+ (ionosphere), O^+ or O_2^+ (ionosphere)) each with a separate, continuity, momentum, and pressure equation. Harnett and Winglee (2006) did not include coupling chemistry or collision terms between the ion species or the neutral exosphere. For this reason the inner boundary of the model was placed well above the exobase where collisions are infrequent. However, charge exchange collisions between solar wind protons and Mars' extended neutral exosphere occur at those altitudes ionizing Mars' extended neutral corona and mass loading the plasma. Harnett and Winglee (2006) accounted for this by placing a static density of O^+ at the inner boundary, which replicates a continuous source of O^+ but unlike the model of Ma et al. (2004) the inclusion of O^+ due to charge exchange was not done in a self consistent way.

By simulating the separate dynamics of ionospheric and solar wind ions, Harnett and Winglee (2007) were able to determine how the crustal magnetic fields affected the access of solar wind protons to the surface of Mars. Similar to the findings of Brain et al. (2010), that were based on Mars Global Surveyor measurements, in regions where the magnetic field was oriented horizontal to the surface the penetration of solar wind protons was minimal, however where the field lines were radial to the surface the density and temperature of solar wind protons was enhanced. This effect was studied for several solar wind velocities and densities as well as magnetic field orientations and for one extreme storm-like event. Harnett and Winglee (2006) found that an increase in solar wind density causes a large increase in the outflow of heavy ions relative to an increase in the solar wind speed

(resulting in identical kinetic pressures). Although, locally, the crustal magnetic fields had a large effect on the penetration and heating of solar protons, any enhanced outflow due to regions of heating were balanced by regions of cooling since the location of the strongest crustal magnetic fields did not have a large effect on the total loss rates.

Harnett and Winglee (2006) also discussed the complexity of quantifying ion loss rates from Mars. Harnett and Winglee (2006) showed that ion loss rates depend non-linearly on a multitude of factors. The Hall term in the model caused heavy ions to be accelerated in the direction of the convective electric field of the solar wind (ion pick-up). The number of ions lost through this process depends on the gyroradius of the ionospheric ions and, therefore, scales with the mass of the ions and the strength of the IMF. A stronger IMF reduces this effect because the ion gyroradius is small. However, Harnett et al. (2006) showed that a stronger IMF also causes higher loss ions rates of in the magnetotail plasma sheet.

Harnett and Winglee (2007) also published a version of the multi-fluid model of Mars that included high resolution across the day side of Mars. These higher resolution studies were able to show that crustal magnetic fields effect the MPB not just in the southern hemisphere but when the strongest crustal fields are in the sub-ram direction the MPB is higher across the entire day side. These results are in agreement with the findings of Brain et al. (2010).

Finally, Harnett (2009) used a multi-fluid model with high-resolution ($\sim$40 km) across Mars night side to study the development and dynamics of magnetic flux that form due to reconnection between IMF field and crustal magnetic fields. The energy spectra from a sample satellite flying through a simulated flux rope were similar to inverted-V type spectra that had been observed near Mars (Lundin et al. 2006). Harnett (2009) also showed that flux ropes significantly enhanced the ionospheric loss rate.

Recently, Najib et al. (2011) used a three-dimensional, multi-fluid model that included the same ion source and loss terms and ion-neutral and ion-ion collision terms as the multi-specie MHD model of Ma et al. (2007). Unlike the model of Harnett and Winglee (2006), the model did not include an electron pressure equation, but instead set the electron pressure gradients to be equal to the total ion pressure gradients. Najib et al. (2011) found that, compared to a single-fluid simulation, the multi-fluid simulation produced asymmetric results in agreement with previous multi-fluid simulations by Harnett and Winglee (2006). Within 300 km altitude, the ion density and temperature calculated by the simulation was in good agreement to the Viking data, as was previous single-fluid, multi-species simulations (Ma et al. 2007). Najib et al. (2011) noted that the Hall term only contributed small differences to the ion density at altitudes lower than 300 km. This result is expected as below 250 km the ionosphere is collisional and therefore the Hall effect should be minimal (Ma et al. 2007). Results Harnett and Winglee (2006) and hybrid simulations (e.g. Modolo et al. 2005) described in the subsequent section suggest that the Hall term is more important at further radial distances.

Najib et al. (2011) noted that the asymmetries simulated by multi-fluid models due to the individual Lorentz forcing of ion species are similar to the asymmetries observed in hybrid models. However, a comparison paper by Brain et al. (2010) shows that the ion outflow predicted by hybrid, multi-fluid and MHD simulations can be quite different. Brain et al. (2010) presented a comprehensive comparison of MHD, multi-fluid, and hybrid modeling techniques that have been recently used to study Mars' plasma interaction. Brain et al. (2010) showed that even with identical upstream conditions and similar inner boundary conditions various MHD, multi-fluid, and hybrid models can produce noticeably different results, and that the differences from model to model are not always easy to explain. For example, in MHD models most ions escape directly downstream in the solar wake. In the hybrid models the plasma escaped mostly from the flank of the ionosphere where ion pick-up occurs.

The multi-fluid results had significant ion escape both in the tail and on the pick-up flank. Based on these results, Brain et al. (2010) questioned whether the large-scale downstream outflow of ions in fluid models was physically realistic at all. Not surprisingly, the different mechanisms of ion outflow and the differences in ionospheric configuration lead to large differences in the calculated ion escape rates. In general, the results of the comparison of the models suggest that hybrid models may be better at describing ion behavior on a large scale, while the fluid models may be better at describing physics that occurs near or inside the planetary atmospheres were the plasma undergoes frequent collisions.

2.1.9 MHD Models of Titan's Interaction with Saturn's Magnetosphere

Titan's interaction with Saturn's magnetosphere is challenging to model because Titan's upper atmosphere is home to some of the most complex chemistry in the solar system and the plasma and magnetic field characteristics in Saturn's magnetosphere can vary with time scales of tens of minutes to hours. Additionally, frozen-in magnetic field can persist within Titan's ionosphere for more than an hour (Ma et al. 2009). Furthermore, Titan also occasionally exits Saturn's magnetosphere and enters the magnetosheath or even the unshocked solar wind. Titan is also challenging to model because ion scale lengths near Titan are similar to or even exceed Titan's radius. Similar to Mars and Venus, the large gyroradius of ions in Saturn's outer magnetosphere and in Titan's ionosphere can lead to large asymmetries in the plasma interaction.

First we briefly mention several three-dimensional models used to study the interaction before Cassini. Ledvina and Cravens (1998) was first to simulate Titan's interaction with Saturn's magnetosphere with an ideal 3D MHD including a source term in the continuity equation. Kabin et al. (1999, 2000) also used an ideal 3D MHD model with mass loading terms in the continuity, momentum, and energy equations to simulate the basic features of Titan's interaction. However, the model in Kabin et al. (1999) included a dipole field (since little was known about Titan's interaction at that time).

Nagy et al. (2001) published the first multi-species, MHD model of Titan's interaction with Saturn's magnetosphere. This model considered three light ion species (H^+, H_2^+, and H_3^+), two medium (N^+, CH_5^+), and two heavy (N_2^+ and $HCNH^+$) ion species. The relative distribution of the species was determined by major chemical reaction based on a 2D model by Cravens et al. (1998) and the effects of mass loading and ion-neutral collisions were considered. The results of the model were compared with data from Voyager's flyby of Titan. The results of the simulation suggested that below an altitude of ~1425 km the ionosphere was chemically controlled rather than dynamically controlled. The loss rate calculated from the model was 6.5×10^{24} s^{-1}. Since the results were in reasonable agreement with the more simple single-fluid models of Ledvina and Cravens (1998) and Kabin et al. (1999), Nagy et al. (2001) concluded that the structure of Titan's ionosphere did not have a large impact on the general features of Titan's induced magnetosphere.

Using a single-species MHD model with mass loading and ion-neutral friction, Backes et al. (2005) found good agreement between simulation results and magnetic field observations from Cassini's TA flyby and Backes et al. (2005) used the simulation to determine the main features of Titan's magnetic tail. Subsequently, Neubauer et al. (2006) compared results from the same model magnetic field to observations from Cassini's TB and T3 flybys and found similar agreement with the bulk features of the magnetometer data. However, for each model-data comparison the model could not reproduce small-scale features in the data and the exact amplitude and timing of the major features. Neubauer et al. (2006) explained that some of the failure of the model to capture the magnetic field observations could be due to the variability of Saturn's magnetosphere, which was evident

in the data, and fossil magnetic fields within Titan's ionosphere. Fossil magnetic fields make it difficult (if not impossible) to correctly reproduce Cassini observations with any type of plasma model. However, MHD models offer some advantages over kinetic or hybrid models when simulating the affects of fossil magnetic fields. MHD models have good resolution in the ionosphere, where ion-neutral collisions make kinetic affects less important, and the numerical simplicity of MHD models means that they can be ran relatively quickly and for long periods of time, sampling a variety of changing upstream conditions.

MHD simulations of Cassini's T32 flyby showed that MHD models are able to simulate fossil fields within Titan's ionosphere. It has long been presumed that during high solar wind pressure, Titan may find itself outside of the magnetosphere when it is near noon on Saturn's day side. The T32 flyby, which took place on 13 June 2007, indicates that this is indeed possible. During the flyby, Titan was found outside of Saturn's magnetopause, draped in northwardly directed magnetic field that could only have been the interplanetary magnetic field (Bertucci et al. 2008). The magnetic field observed deep within Titan's ionosphere indicated draping of a southward field and was likely the fossil remnants Saturn's draped magnetic field (Bertucci et al. 2008). Ma et al. (2009) used a multi-species MHD model to simulate Titan crossing a boundary where the magnetic field transitioned from being southward to northward. Indeed, MHD simulations of Ma et al. (2009) were able to reproduce the fossil fields within Titan's ionosphere and showed that fossil fields remain within Titan's ionosphere for several hours.

Ma et al. (2006) also compared results from multi-species MHD simulations to data from Cassini's magnetometer, plasma spectrometer, and Langmuir Probe from the TA and TB flybys. The simulation reproduced the asymmetric electron density measured by the Langmuir Probe, indicating that the asymmetry was due to photoionization and electron impact ionization asymmetries, which were included in the model. The results show that multi-species MHD models do a good job simulating regions of Titan's ionosphere where ion-neutral collisions are significant. One aspect of the model that did not correlate well with the data was the deceleration region on the inbound trajectory. The simulation underestimated the spatial extent of Titan's disturbance of incident plasma. This disagreement is likely due to the neglect of ion gyroradius effects. The large gyroradius of ions in Saturn's magnetosphere means magnetospheric ions can impact Titan's ionosphere even if their guiding center is several thousand kilometers from Titan (Hartle et al. 2006).

Snowden et al. (2007) simulated the interaction between Titan and Saturn's magnetosphere using a resistive, multi-fluid model. The multi-fluid simulation used upstream parameters that were an average of the TA, TB, and T3 flyby observations and found good correlation with the bulk features of the magnetic field data from each of the flybys. Figure 1 shows results from this simulation. The blue and magenta surfaces are surfaces constant density (isosurfaces) of Titan's ionosphere and ion tail. The magenta isosurface shows the extent of Titan's heavy (28 amu) ion tail and the blue isosurfaces shows the extent of Titan's light (1 amu) ion tail. The isosurfaces show significant differences near Titan. Unlike, the MHD simulations the multi-fluid model was able to capture the asymmetric ion pick-up on the flanks of Titan's induced magnetosphere. Similar to the hybrid results of Modolo and Chanteur (2008) the model shows that heavy ions gyrate far from Titan on the anti-Saturn side of Titan's ionosphere, as seen in the magenta isosurface in Fig. 1. On the Saturn facing side of the ionosphere, ions are accelerated back into the atmosphere and are heated.

Not unexpectedly, given the direction of the magnetic field, the well-confined beam of heavy pick-up ions was found to be located below each of the flybys (as seen in Fig. 1). This explains why large asymmetric features were not observed in the data and why the

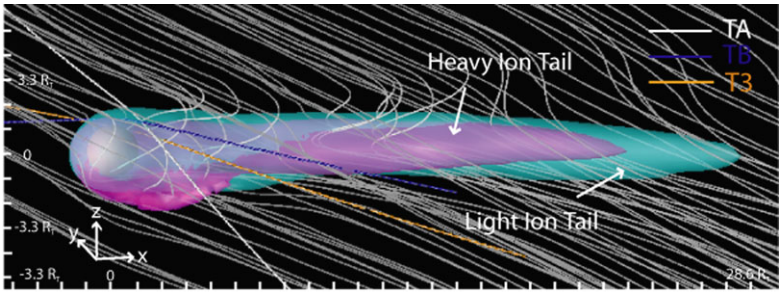

Fig. 1 Titan in Saturn's magnetosphere based on a multi-fluid model. Magnetic field lines, shown in white, interact with Titan's ionosphere. In the near Titan region the heavy ion tail (magenta) is very asymmetric. The heavy ion isosurface is drawn at a density of $10^{-1.7}$ cm^{-3} and the light ion density is shown at $10^{-1.2}$ cm^{-3} (Snowden et al. 2007)

symmetric single-fluid MHD models of Backes et al. (2005) and Ma et al. (2006) could simulate the basic features of the magnetic field data. However, the results of Snowden et al. (2007) show that asymmetric pick-up of ions on the anti-Saturn side of Titan changes the global configuration of the induced magnetosphere. The pick-up ions extend the size of Titan's ionosphere on the anti-Saturn side, causing the shielding currents to form at higher altitudes. The asymmetric pick-up also extends the mass loading and magnetic pile-up of the magnetospheric plasma and magnetic field.

Cassini's T9 flyby took place several Titan radii downstream of Titan, observing Titan's mid-wake region. The plasma instrument observed two separate ion tail regions. One region was composed of cold, heavy plasma (∼16 amu). The other region was composed of warmer less massive plasma (1 and 2 amu). Analysis by Coates et al. (2007) and Wei et al. (2007) indicated that both regions contained plasma from Titan's ionosphere. Ma et al. (2007) simulated the T9 flyby using a Hall MHD model and a non-Hall MHD model. Ma et al. (2007) found better agreement between Cassini's magnetic field data and results from the Hall MHD simulation, indicating the importance of including the Hall term in the electric field equation. In addition, the decrease in velocity in the tail region was much better matched when the Hall term was included in the MHD model. However, the Hall MHD model still simulates all ions as a single fluid, which averages out the dynamics of ionospheric ions and ions from Saturn's magnetosphere. Therefore, the model was not able to reproduce the two compositionally distinct ion tails like the hybrid model of Modolo et al. (2007).

2.1.10 Multi-scale Simulations of the Saturn-Titan Interaction

The variability of Saturn's magnetosphere can strongly affect the morphology of Titan's induced magnetosphere. However, the limited scale of local models (that only simulate the region near Titan) makes realistically simulating the variability of Titan's environment difficult. To address this problem, Winglee et al. (2009) developed a multi-fluid/multi-scale model with Titan embedded within Saturn's magnetosphere. The multi-fluid aspect of the model allows the incorporation of the differential dynamics of solar wind protons, Saturn's ionospheric plasma, ions from Enceladus' plume, and Titan's ionospheric plasma. The multi-scale aspect allows Titan to be placed within a model of Saturn's magnetosphere while still maintaining sufficient resolution near Titan.

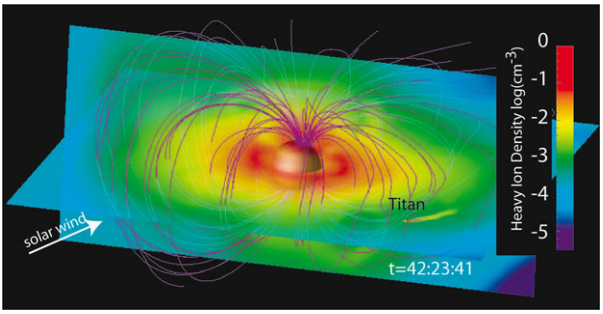

Fig. 2 Titan embedded in a multi-fluid model of Saturn's magnetosphere. The image shows Saturn's magnetic field lines (*purple*) and heavy (32 amu) ion density in the orbital plane and in a plane parallel to the solar wind. Titan is placed at 21 Saturn local time and Titan's ion tail can be seen as a streak of enhanced ion density in Saturn's magnetotail

Winglee et al. (2009) examined the coupled interaction with Titan located at 21 Saturn local time. The simulation showed that Titan's induced magnetosphere is affected by the direction of the interplanetary magnetic field (IMF), because the IMF direction affects the global characteristics of Saturn's magnetosphere. Results from this simulation are shown in Fig. 2. In this figure, the heavy (32 amu) ion density is imaged in Titan's orbital plane. A streak of heavy ions can been seen downstream of Titan. The heavy ions are Titan's ion tail, which forms due to Titan's interaction with the rotating magnetic field and plasma in the Saturn simulation. Although, not shown, the finest resolution near Titan is $0.18R_T$, so that the simulation can also be used to study some aspects of Titan's induced magnetosphere.

When the IMF is parallel to Saturn's planetary magnetic field, Saturn's magnetosphere near Titan was relatively stable with a thick plasma sheet. In this case, Titan's ion tail was well confined and grew to a length of over $10R_S$ over several hours of simulated time. When the IMF is anti-parallel to Saturn's planetary magnetic field, the situation is more dynamic. Enhanced convection within Saturn's magnetosphere leads to an enhancement of the Rayleigh-Taylor instability between cold, dense plasma in Saturn's plasma disk and hot, tenuous plasma in the outer magnetosphere, which is driven by the outward centrifugal force of the rapidly rotating plasma. As shown by Kidder et al. (2009) and Winglee et al. (2009), the instability causes regions of cold, dense plasma to extend into Saturn's outer magnetosphere. The regions of plasma sweep past Titan and cause strong variability in the plasma and magnetic field characteristics near Titan. The variability causes Titan's ion tail to flap, impeding the formation of a complete ion torus at Titan's orbit. The outflow rate of heavy ions from Titan's ionosphere also increased from $3{-}4 \times 10^{24}$ s^{-1} for parallel IMF to 1.2×10^{25} s^{-1} for anti-parallel IMF.

2.1.11 Summary of MHD Methods

Although, the Larmor radius of ions modeled in Venus', Mars' and Titan's interaction are significant, turbulence or wave-particle interactions may act as pseudo-collisions, particularly inside of the bow shock, reducing global asymmetries due to gyrating ions (Nagy et al. 2001). This is certainly occurring to some extent as the results of MHD simulations are in good agreement with satellite observations of the locations of boundary layers such as the bow shock and MPB. However, there are also many features of the interaction such as an extended pick-up region that cannot be simulated with a symmetric single-fluid MHD model. In fact, more groups are adopting some variation of the multi-fluid techniques to account for physics due to mass depended acceleration of ions and the Hall and electron pressure gradient term in Ohm's law. However, even these models cannot account fully for the kinetic effects of gyrating plasma, including non-Maxwellian plasma distributions and anisotropic pressure gradients, which are frequently observed near VMT. In order to account for these effects a hybrid or fully kinetic approach must be taken.

2.2 Hybrid Methods

In this section, the hybrid approach is briefly detailed, emphasizing its advantages and limitations. Hybrid models are used to describe phenomena occurring at smaller ion spatial and temporal scales than simulated by MHD models, however hybrid models cannot simulate processes occurring at electron scales such as the Debye length, electron inertia length and electron cyclotron frequency. As described in the next section, a description of phenomena taking place on electron scales requires a fully kinetic model in which each species, s, is described by a distribution function $f_s(\mathbf{x},\mathbf{v},t)$ satisfying the Vlasov equation or when the dynamics of both ion and electron particles are simulated. However, the relatively high computational requirements needed to simulate large numbers of particles, electron length and time scales, and plasma transit times means that, currently, fully kinetic models generally cannot simulate complete magnetospheric interactions and are reserved to study local processes. Typically, the physical dimension of the simulation box is about six to ten times the radius of the obstacle in models of the plasma interaction of Venus, Mars or Titan. Fully kinetic models must resolve the electron scale (which can be of the order of few km or even less). In addition, the transit time of solar wind particles, corresponding to several hundred proton cyclotron periods, are required to reach a quasi-steady state. Therefore, to study phenomena occurring on global scales it is necessary to simplify the fully kinetic model by abandoning the description of all the detailed particle behavior.

Hybrid formalism is thus an intermediate approach between MHD (Sect. 2.1) and fully kinetic (Sect. 2.3) models. In a hybrid model, electrons are described as a mass-less charge-neutralizing fluid, whereas ions are treated as individual charged simulation particles. Simulation particles, also called macroparticles, have a volume corresponding to a simulation cell volume and their positions are identified by the center of the particle. A macroparticle can be viewed as a cloud of identical charged particles traveling together at the same velocity. Macroparticles do not have any internal degrees of freedom and cannot be considered as an elementary volume of plasma. Owing to their finite size and their ability to interpenetrate each other, macroparticles do not suffer close binary collisions. In order to represent major and minor ion species with sufficient statistical sampling, macroparticles are statistically weighted. The weight of each macroparticle determines the total particle distribution. The use of weighted macroparticles enables hybrid models to simulate regions with large density differences.

Temporal evolution of the position and speed of macroparticle number p satisfies the equation of motion of individual charged particles, similar to the full particle equations:

$$\frac{d\mathbf{x}_p}{dt} = \mathbf{v}_p \tag{2.28}$$

$$\frac{d\mathbf{v}_p}{dt} = \frac{q_p}{m_p}(\mathbf{E} + \mathbf{v}_p \times \mathbf{B}). \tag{2.29}$$

Electrons are modeled by a mass-less neutralizing fluid, leading to $n_e = \sum_s n_s = \rho$, where n_e is the electron number density and n_s is the ion number density of species s. This assumption is valid for scale lengths larger than the Debye length, which is generally the case for plasma interactions with planetary atmospheres. The models in Simon et al. (2006) and Modolo and Chanteur (2008) used two electron fluids to represent incoming plasma and planetary plasma with different densities and temperatures while Brecht and his coworkers solve the electron energy equation for the electron temperature (see Ledvina et al. 2008, and references therein). Moments (density, velocity, ionic current, etc.) are derived from

macroparticle information collected on a grid (Birdsall and Langdon 1985). Electric field is a function of state computed from the electron momentum equation:

$$\mathbf{E} = -\frac{\mathbf{J}_i \times \mathbf{B}}{\rho} + \frac{(\nabla \times \mathbf{B}) \times \mathbf{B}}{\mu_o \rho} - \frac{\nabla p_e}{\rho} \tag{2.30}$$

where $\mathbf{J}_i = \sum_s q_s n_s \mathbf{V}_s$ is the ionic current, $\mathbf{V}_s$ and n_s are the speed and the density of ion species s. The total current is calculated from Ampère's equation without the current displacement term. Neglecting the current displacement term is valid as long as low frequency phenomena are of interest. Faraday's law gives the time evolution of the magnetic field, while satisfying conservation of magnetic flux:

$$\frac{\partial \mathbf{B}}{\partial t} = -\nabla \times \mathbf{E} \tag{2.31}$$

$$\nabla \cdot \mathbf{B} = 0. \tag{2.32}$$

E and **B** can be computed on two identical grids shifted relative to each other by half a grid size in all directions allowing the simulation to resolve the conservation of the magnetic flux to the second order of approximation (Birdsall and Langdon 1985).

Time integration schemes used for the solar wind interaction with a weakly magnetized body are mainly the algorithms developed by Harned (1982), Matthews (1994) and Kallio and Janhunen (2001).

The morphology of the simulation grid varies from Cartesian grid to non-structured grid with higher spatial resolution close to the obstacle or curvilinear grid (Modolo et al. 2005; Kallio et al. 2010; Boesswetter et al. 2007).

2.2.1 Hybrid Models of Mars' Interaction with the Solar Wind

Since Mars does not possess a global intrinsic magnetic field, Mars' upper atmosphere and ionosphere acts as an obstacle to the solar wind flow. This property implies a strong coupling between the neutral environment, the exosphere and atmosphere, and the solar wind plasma. In addition, highly localized crustal magnetic fields have been discovered on the surface of Mars (Acuña et al. 2001), indicating that Mars possessed a strong active dynamo at some time in the past.

Several hybrid models have been adapted to investigate the solar wind interaction with the Martian atmosphere (Brecht and Ferrante 1991; Kallio and Janhunen 2001; Shimazu 1999; Boesswetter et al. 2004; Modolo et al. 2005). Each of these models has their own specifics on both numerical (simulation grid, average number of particles per cell, algorithm, etc.) and physical processes (implementation of ionization processes or ion planetary production, ionospheric chemical model, number of ion species, etc.) and they are detailed in their original article listed above. However, all of them self-consistently describe the dynamics of each ion species (solar wind/planetary ions). Since the original papers, the models have been improved either by adding a chemistry scheme (Brain et al. 2010; Brecht et al. 2010), or by improving their spatial resolution (Kallio et al. 2010), or including crustal fields (Brecht et al. 2011).

Although, Mars' crustal magnetic fields have not been incorporated into most hybrid models, mainly due to the model's limited spatial resolution, the models reproduce the most distinct plasma regions and boundaries observed near Mars with respect to *in-situ* observations (Figs. 3(a)–(d)). For example, the bow shock can be clearly identified in Figs. 3(a)

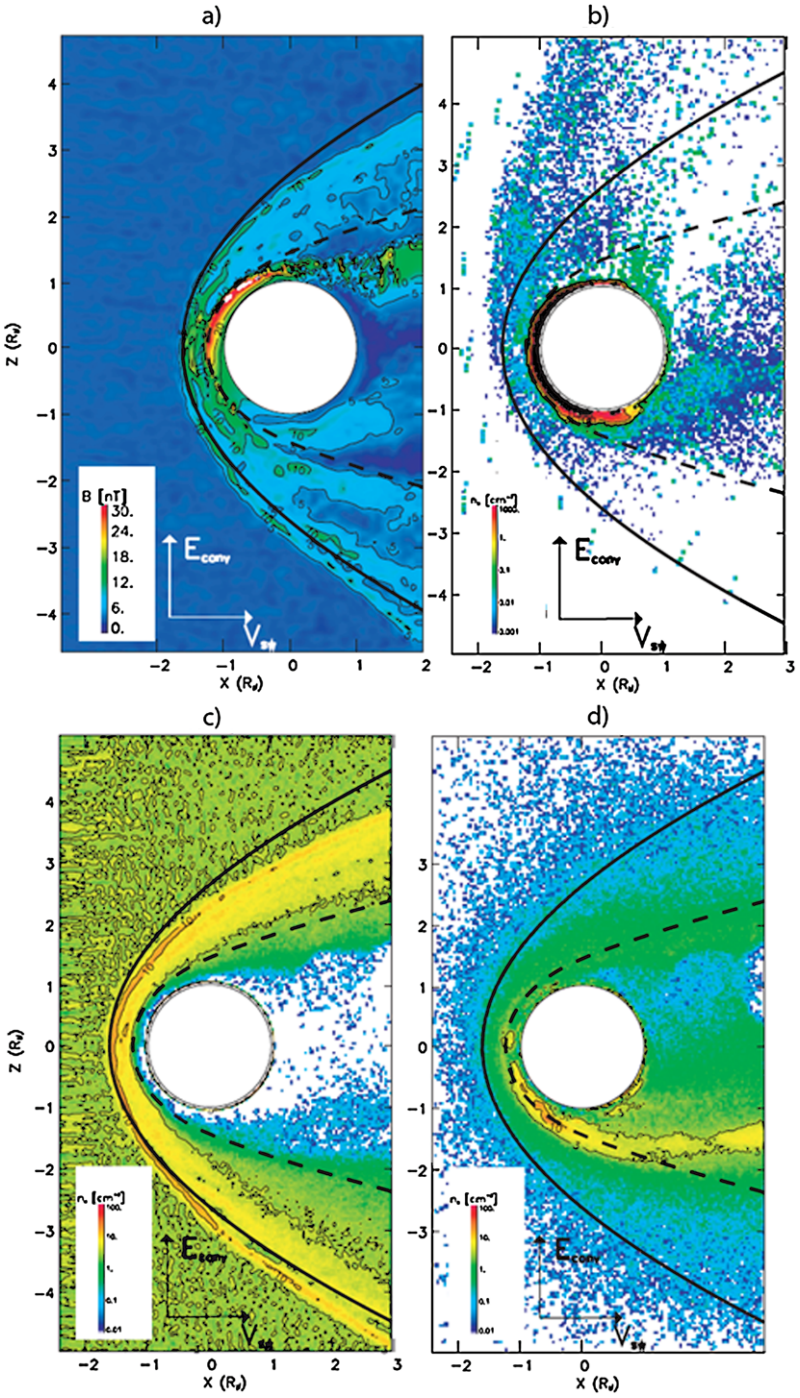

Fig. 3 Maps of total magnetic field (**a**) in the plane containing the motional electric field E_{conv} and the solar wind flow direction V_{SW}. Panels (**b**)–(**d**) represent density maps of O^+ ions, solar wind protons and planetary protons respectively, in the same plane than panel (**a**). Simulated results extracted from the SWIM challenge (Brain et al. 2010) by Modolo et al. (2005)

and 3(c). At the bow shock, the increase in magnetic field strength (Fig. 3(a)) coincides with an increase in solar wind proton density (Fig. 3(c)) and a decrease in the bulk plasma velocity (not shown). The position and shape of the bow shock are in good agreement with the average location of the bow shock deduced from Mars Global Surveyor observations, which are indicated by a black full line (Vignes et al. 2000). Multiple shock structures are usually present in hybrid simulations and are often associated with kinetic effects and multiple ion species. In addition, closer to the planet, a region of strong total magnetic field, reaching about 30 nT, is also shown (Fig. 3(a)) and corresponds to the Magnetic Pile-up Boundary (Bertucci et al. 2003) or Induced Magnetospheric Boundary (Lundin et al. 2004). The so-called Ion Composition Boundary (ICB), instead, indicates the transition from a region governed by solar wind plasma (Fig. 3(c)) to a region mainly populated by planetary plasma consisting of O^+ and H^+ ions (Figs. 3(b) and 3(d)). Hybrid models also simulate the deposition of energy into the Martian atmosphere by precipitating solar wind plasma (Brecht 1997; Kallio and Janhunen 2001; Boesswetter et al. 2004; Modolo et al. 2005) as is evident in Mars Express observations (Lundin et al. 2004; Dubinin et al. 2006).

One common feature seen in hybrid simulations is asymmetric boundary layers. The symmetry in the system is broken by the Hall term, which is included consistently in the hybrid approach. The asymmetry of the induced magnetospheric boundary is particularly apparent in the $+\mathbf{E}_{\mathrm{conv}}$ hemisphere, in agreement with Vennerstrom et al. (2003). The density map of O^+ ions (Fig. 3(b)) clearly shows the asymmetric forcing of the convective electric field. In the $-\mathbf{E}_{\mathrm{conv}}$ hemisphere the electric field points radially inward, towards Mars, while in the $+\mathbf{E}_{\mathrm{conv}}$ the electric field points outward. The acceleration of ionospheric plasma by $\mathbf{E}_{\mathrm{conv}}$ produces a heavy plasma plume along the $+\mathbf{E}_{\mathrm{conv}}$ direction. Magnetic field curvature and gradients, which are due to the draping of magnetic field lines around the planet, exert magnetic tension and pressure which forces the solar wind and planetary plasma tail-ward (Figs. 3(b) and 3(d)). The different dynamics of planetary O^+ and planetary H^+ seen in Fig. 3 illustrates the necessity of modeling multiple ion species. For example, planetary O^+ ions in Mars' ion tail are mainly concentrated in the plasma sheet while planetary H^+ are concentrated in the lobe regions. Closer to the planet, where the ionosphere is in chemical equilibrium, the plasma is more fluid-like and MHD or multi-fluid models can be more advantageous than kinetic models because they are computationally simpler and can more finely resolve the ionosphere. However, even in the ionosphere, hybrid models reproduce the global density gradients observed by Mars Express (Duru et al. 2008, 2010). In many ways, such models are in good agreement with spacecraft observations (e.g. Kallio et al. 2006; Modolo et al. 2006; Boesswetter et al. 2007; Dubinin et al. 2008).

Although hybrid models are in good agreement with recent Martian observations, significant improvements can still be made. For example, hybrid models can be improved by including a better description of the induced magnetospheric region, self-consistent ionospheric chemistry, remnant surface magnetic fields and improved coupling between charged and neutral species. A first attempt to use a 3D exospheric model coupled to a 3D hybrid model have been performed by Chaufray et al. (2007), as described in Sect. 3. The results of Chaufray et al. (2007) emphasize the need to include multiple species and kinetic effects to properly account for the plasma dynamics of each species. However, the results also illustrated how the low spatial resolution of hybrid models makes it difficult to properly include the coupling between the neutral atmosphere and the plasma. Including realistic coupling between the neutral plasma and the neutral atmosphere requires a spatial resolution lower or equal to the neutral and ionospheric scale height, which is of the order of 25–45 km. Such spatial resolution is not yet accessible for sequential hybrid models due to computational limitations. A parallel hybrid model is needed.

2.2.2 *Hybrid Models of Titan's Interaction with Saturn's Magnetosphere*

In the last ten years, most of the hybrid models developed to study the Mars' plasma interaction have been adapted to investigate the interaction between Saturn's magnetospheric and Titan (Brecht et al. 2000; Kallio et al. 2004; Sillanpää et al. 2007; Simon et al. 2007, 2009; Modolo and Chanteur 2008; Ledvina et al. 2011). MHD and multi-fluid models of Titan's plasma interaction have been somewhat advantageous in the dense regions of Titan's ionosphere since some models include chemical reaction and thus have a more complete description of this region (e.g. Ma et al. 2006). However, more recently, hybrid models have been developed that include a similar set of ionospheric chemistry equations (Ledvina et al. 2011). MHD and multi-fluid models can not take into account finite ion gyroradius effects. These effects cannot be ignored in remote regions beyond the exobase, since the Larmor radii of magnetospheric O^+ ions and heavy pick-up ions (CH_4^+ and N_2^+ for example) are larger than the radius of the satellite itself. The importance of kinetic effects was first investigated with test particle simulations (Luhmann 1996; Ledvina et al. 2005). Newly born pick-up ions are accelerated by the motional electric field $\mathbf{E}_{\text{conv}} = -\mathbf{v} \times \mathbf{B}$ and move in cycloidal trajectories in a plane perpendicular to the undisturbed magnetospheric magnetic field (Hartle et al. 1982). The initial distribution of pick-up ions in velocity space is a ring distribution. This is the main reason why multi-fluid cannot take into account self-consistently the dynamic of pick-up, since these models assume a Maxwellian distribution function for ion species. However hybrid models do not make this assumption and can simulate the behavior of pick-up ions.

In a hybrid simulation, two different regions can be identified in Titan's wake, the main part of the planetary plasma wake which have an elliptical-like shape elongated in the direction of the undisturbed magnetic field and a second region more limited in size, associated to a plume-like structure with a density of fraction of ions per cm^3. The main elliptical shape of Titan's plasma wake agrees well with MHD simulation (Backes et al. 2005). The plume of the so-called pick-up ions, occurs in a region governed by the magnetospheric plasma and is relatively narrow and aligned the motional electric field. In addition, the energy of these ions is significantly high (few keV). Outflowing ions in the main plasma wake region are cold (up to hundreds of eV). The difference in energy between the 'pick-up' region and the main plasma wake is due to the difference of the speed flow in these two regions. Ions in the main wake region are not accelerated as quickly as the pick-up ions in the magnetospheric region. This feature agrees well with the CAPS Cassini observations (Harnett and Winglee 2006).

Moreover, the multi-species observed by Cassini observations are reproduced well by hybrid models. While multi-fluid models have to resolve a set of equation for each ion species in order to take into account the difference in density, speed and temperature, hybrid models include multiple species by adjusting the mass ratio for the different macroparticles. The main limitation of hybrid models is that a large number of particles must be included to obtain reasonable statistical sampling of each ions species.

Figure 4 emphasizes the different dynamic behavior of each ion species. Density maps of magnetospheric plasma (Fig. 4(a)–(c)) show that O^+ (2 keV) and energetic H^+ (30 keV) do not penetrate below the exobase level, except in a limited region where energetic magnetospheric ions can precipitate (Fig. 4(a), (c)). However, hybrid models are usually not well designed to study collisional region such as the atmosphere (Modolo and Chanteur 2008). On the other hand thermal protons (200 eV) show a completely different pattern and are mainly excluded from the induced magnetospheric region (Fig. 4(b)), similarly to the Martian picture. Energetic protons have larger gyroradii than thermal protons and thus are less

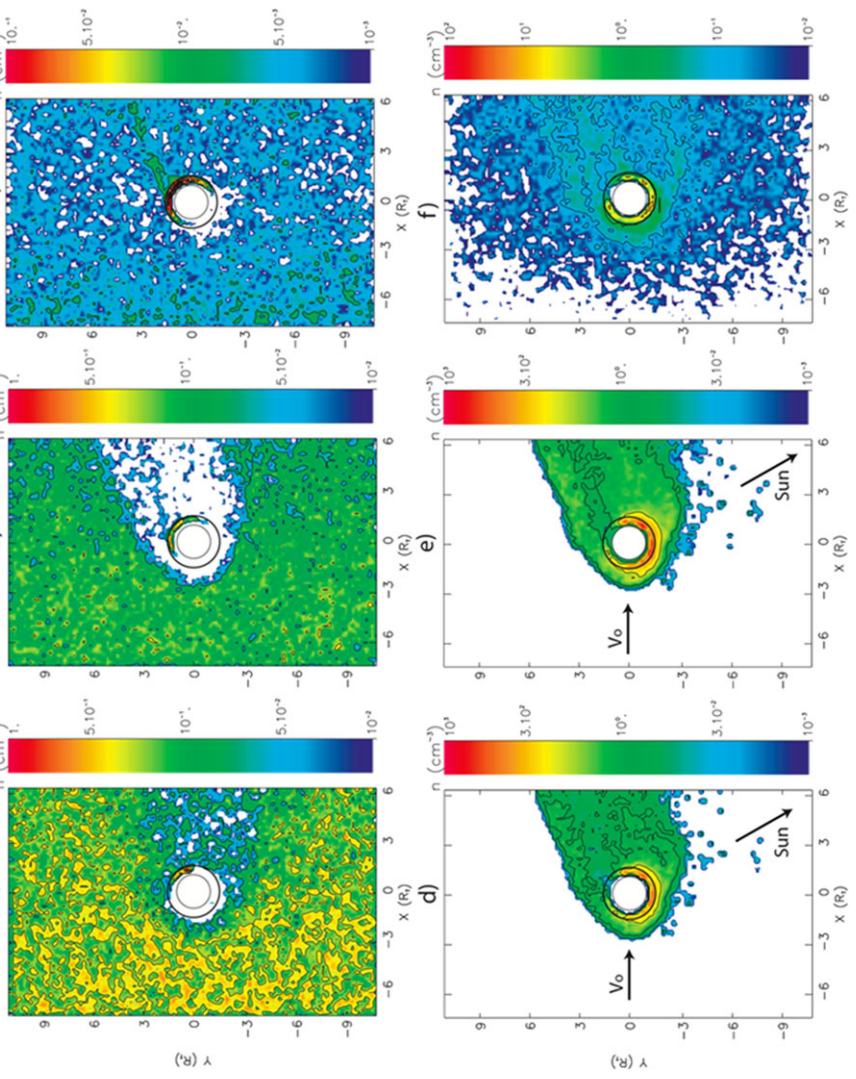

Fig. 4 Density map of magnetospheric ion species (**a**)–(**c**) and exospheric origin ion species (**d**)–(**f**) in the XY plane of the TIIS coordinate system. The simulation has been performed in the Ta flyby conditions (Modolo and Chanteur 2008). The projection of the Sun direction in this plane is indicated by the *arrow* on figures (**d**), (**e**). The magnetospheric plasma is composed of O^+ (**a**), thermal H^+ (**b**) and energetic H^+ (**c**) while the "planetary" plasma is composed in the simulation of N_2^+ (**d**), CH_4^+ (**e**) and H_2^+ (**f**)

sensitive to draped magnetic field lines, since they required more time to adjust their trajectory to the magnetic field direction. The planetary plasma is mainly confined in the induced magnetospheric region (Figs. 4(d)–(f)). The largest ionospheric density is observed on the sunlight side of the ionosphere. The heavy planetary plasma (CH_4^+ and N_2^+) extends 2.5–3 Titan radii on the ram-side and fills the plasma wake of the induced magnetospheric region while the planetary light ion (H_2^+) shows a larger spread even in the magnetospheric region, and contributes to the mass loading region (Fig. 4(f)). The dissimilarity between light and heavy ion structure can be explained by the difference of the production source. The main source of ionization for H_2^+ is charge exchange, efficient in the magnetospheric region, while the main source of ionization for heavy planetary ions is photoionization and electron impact ionization (Modolo et al. 2007).

2.2.3 Hybrid Models of Venus' Interaction with the Solar Wind

Only a few hybrid models have been adapted to study Venus' plasma interaction. One of the main reasons is that the size of the obstacle is much larger than the typical solar wind ion scale. Therefore, the interaction is more fluid-like.

Moore et al. (1991) developed the first two-dimensional hybrid model used to study the solar wind interaction with Venus. It emphasized the asymmetry of the O^+ dynamics in the direction of the motional electric field, which is in many ways similar to the Martian case. With a three-dimensional model, Kallio et al. (2006) showed that asymmetry in the escape of O^+ was due to the motional electric field, in agreement with Moore et al. (1991) . Hybrid simulations are in good agreement with Pioneer Venus Orbiter observations (Jarvinen et al. 2008) and Venus-Express observations (Kallio et al. 2008; Zhang et al. 2010) and reproduce the main boundaries and regions.

2.3 Fully Kinetic Methods

Fully kinetic models provide a comprehensive description of the plasma. This method has not yet been used in global VMT model but it is informative to describe its basic properties for a theoretical completeness.

In fully kinetic model, all ions and electrons are modeled as particles that are accelerated by the Lorentz force and possible non-Lorentz forces ($\mathbf{F}$):

$$\frac{d\mathbf{v}_p}{dt} = \frac{q_p}{m_p}(\mathbf{E} + \mathbf{v}_p \times \mathbf{B}) + \mathbf{F} \tag{2.33}$$

$$\frac{d\mathbf{x}_p}{dt} = \mathbf{v}_p \tag{2.34}$$

Here $\mathbf{v}_p$, $\mathbf{x}_p$, m_p and q_p are the velocity, position, mass and charge of an ion or electron denoted by the subscript p. The forces in (2.33) can include gravitational forces and forces associated with ion-ion, ion-electron, ion-neutral or electron-neutral collisions.

The magnetic field is propagated in time by Faraday's law

$$\frac{\partial \mathbf{B}}{\partial t} = -\nabla \times \mathbf{E} \tag{2.35}$$

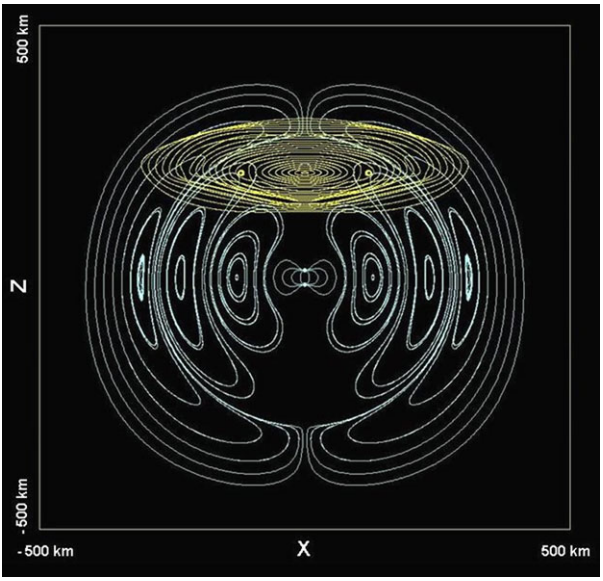

Fig. 5 A three-dimensional spherical electromagnetic wave in a fully kinetic model. The run includes an oscillating point source in a vacuum located at the center of the figure and the source generates a sinusoidal electric field. The *white lines* and the *yellow lines* are the electric and the magnetic field lines, respectively, which are added to illustrate the electromagnetic field in 3D. The vantage point is slightly below of the source in order to see the circular magnetic field-lines about the vertical axis. (Pohjola and Kallio 2010)

and the electric field by Ampere-Maxwell's law

$$\frac{\partial \mathbf{E}}{\partial t} = \nabla \times \mathbf{B}/\varepsilon_o \mu_o - \mathbf{j}/\varepsilon_o. \tag{2.36}$$

In (2.36), $\mathbf{j}$, ε_o and μ_o are the electric current, the electric permittivity and the magnetic permeability, respectively.

As seen in from (2.35) and (2.36), the plasma is coupled to $\mathbf{E}$ and $\mathbf{B}$ fields through the electric current. There are several ways to derive $\mathbf{j}$ from particles. The electric current can be derived from the macroscopic plasma parameters:

$$\mathbf{j} = \sum_i q_i n_i \mathbf{V}_i - e n_e \mathbf{V}_e, \tag{2.37}$$

where the subscript i refers to ions and e to electrons, $\mathbf{V}$ and n are the bulk velocity and the number density, q_i is the charge of a ion and e is the elementary charge (1.6×10^{-19} C) (see, e.g. Pohjola and Kallio 2010). The plasma densities and bulk velocities can be derived from the individual particle positions and velocities (Pohjola and Kallio 2010) but also other techniques can be used (see Umeda 2010, and ref. therein).

As can be seen from (2.33)–(2.37), the basic equations are straightforward, however several issues make solving these equations challenging. First, (2.36) can be rearranges to include the displacement current term ($\equiv \varepsilon_o \mu_o \frac{\partial \mathbf{E}}{\partial t}$). Therefore, fully kinetic models include high frequency electromagnetic waves which can lead to numerical instabilities. Figure 5 shows an example of a fully kinetic simulation in which a point source is emitting electromagnetic waves in a vacuum.

Secondly, fully kinetic models do not require the assumption of quasi-neutrality, that is, the assumption that the electron density is equal the total charge density of ions. This means that the electric field can be derived from Ampere-Maxwell's law (Eq. (2.36)) and not from the electron momentum equation as in the hybrid model (cf. Sect. 2.2). It is also important to note that if the electric field is derived from (2.36), then Gauss' law does not

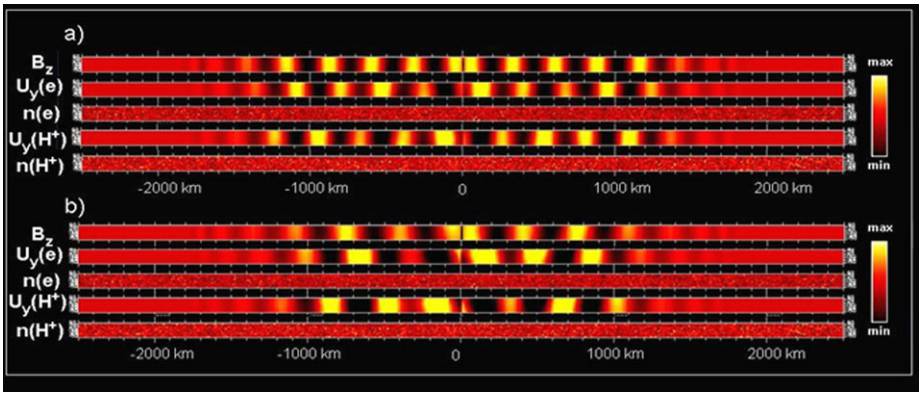

Fig. 6 The propagation of an electromagnetic wave in a electron-proton plasma based on a fully kinetic model. The horizontal axis is the x-axis and a plane wave is generated at $x = 0$. In panel (**a**) the initial electron density in the simulation box was 0.016 cm^{-3} and in panel (**b**) it was 0.021 cm^{-3}. In panel (**a**) the tables from top to bottom are: B_z from -1×10^{-12} T to 1×10^{-12} T, the velocity of electrons in the y-direction ($U_y(e)$) from -10 km/s to 10 km/s, the electron density ($n(e)$) from 0 to 0.03 cm^{-3}, the velocity of protons in the y-direction ($U_y(\mathrm{H}^+)$) from -5 m/s to 5 m/s and the proton density ($n(\mathrm{H}^+)$) from 0 to 0.03 cm^{-3}. In panel (**b**) the tables from top to bottom are: B_z from -1×10^{-12} T to 1×10^{-12} T, $U_y(e)$ from -10 km/s to 10 km/s, $n(e)$ from 0 to 0.04 cm^{-3}, $U_y(\mathrm{H}^+)$ from -5 m/s to 5 m/s and $n(\mathrm{H}^+)$ from 0 to 0.04 cm^{-3}. In both panels the *color map on the right hand side* is a linear color map from the minimum value (min) of the variable to the maximum value (max) of the variable (Pohjola and Kallio 2010)

need to be solved explicitly. It can be seen, by taking the divergence of Ampere-Maxwell's law (Eq. (2.36)), that Gauss' law is fulfilled during the simulation (if it is fulfilled initially). However, deriving the electric field this way means that the model must solve the continuity equation (e.g. Pohjola and Kallio 2010), which can be done by adopting a specific accurate charge accumulation scheme (e.g. Villasenor and Buneman 1992, or Umeda et al. 2003) or by cleaning the electric field with a Poisson solver (Birdsall and Langdon 1985).

Third, the spatial (ion inertial length and gyroradius) and temporal (gyrofrequency and plasma frequency) scales of a fully kinetic model are determined by both the mass of ions and electrons. Electron spatial and temporal scales are very small compared to the ion scales because of the mass difference between the electron and ions. To properly simulate electron inertial scales and the electron plasma and gyro frequency, one has to use a small grid size and small time step. One also has to adopt small spatial and temporal scales to model fast propagating electromagnetic waves and to reach the Debye length scale. In plasma physics one way to speed up the simulations in a specific application is to replace the fully electromagnetic code described above by a so-called Darwin electromagnetic code, where the transverse displacement current is omitted from (2.36), or to use implicit time integration (see, for example, Langdon 1986; Birdsall and Langdon 1985; Besse et al. 2007). These limitations mean that, in practice, fully kinetic models are more applicable for small-scale local simulations rather than large-scale global simulations.

However, fully kinetic models contain very rich physics and do not contain any "subscales". Fully kinetic models also include fewer approximations than hybrid and MHD models and give a more comprehensive description of particles dynamics and electromagnetic fields. For example, fully kinetic models can be used to study the stability of various planetary plasma regions in three-dimensional space. They can also be used to analyze the propagation of waves in various plasma environments. Figure 6 shows results from a fully kinetic

simulation of electromagnetic waves propagating in plasma. Similarly, fully kinetic models could be used to study the propagation of naturally or artificially produced electromagnetic waves in planetary ionospheres or surfaces.

3 Models of Mars' Neutral Exosphere

Developing a comprehensive global model of the interaction of the atmosphere of VMT and their space environments is challenging because the model should include not only charged particles but also neutrals particles. The flowing plasma near VMT interacts directly with the atmospheres of the non-magnetized bodies; therefore, a comprehensive model has to take into account charged particle-neutral reactions. Moreover, ions are generated from the neutrals by charge exchange processes, electron impact ionization, photoionization and chemical processes. A comprehensive unified model should therefore contain both a global plasma model and a global model for planetary neutrals. The goal of this section is to describe how this approach has been used to model the exosphere of Mars.

3.1 The Neutral Exosphere of Mars

The exosphere is the collisionless region of the upper atmosphere, extending from the exobase (near 200 km altitude for Mars) into interplanetary space. The exosphere of Mars is important by itself but it is also important because it is formed through the same processes that cause atmospheric escape. Therefore, understanding Mars' exosphere helps us understand Martian atmospheric escape and its effect on Martian climatic change (Chassefière et al. 2007). This section can be considered as a complement of the recent review about escape modeling done by Johnson et al. (2008), which focuses on the Martian neutral exosphere.

The exosphere of Mars is composed of two oxygen populations, a cold or thermal population produced by vertical diffusion of oxygen atoms from the lower thermosphere and a hot population resulting from the dissociative recombination of the O_2^+ ions in the upper thermosphere and exosphere (McElroy 1972; Nagy and Cravens 1988). The hot oxygen atoms formed by dissociative recombination of O_2^+ can produce a recoil population through a cascade of collisions with the thermal oxygen population (Shematovich et al. 1994). Other sources of hot neutral oxygen such as sputtering, due to the precipitation of accelerated pick-up O^+ ions into the Martian atmosphere, are less important in current conditions (Chaufray et al. 2007) but could have played a more important role in the past (Leblanc and Johnson 2001; Johnson et al. 2008). Moreover, recent detections of energetic neutral atoms (ENAs) produced by charge exchange between energetic ions and the neutral exosphere require accurate coupling between the neutral exosphere and solar wind (Futaana et al. 2011). It is therefore important to couple an exospheric model to a plasma model to accurately describe processes related to the solar wind interaction but also to study the effect of pick-up ions precipitation into the Martian upper atmosphere and the additional escape produced by sputtering. This may be particular important when studying past escape on Mars.

The O_2^+ dissociative recombination is divided into 5 channels:

$$O_2^+ \rightarrow O(^3P) + O(^3P) + \Delta E = 6.95 \text{ eV } (0.22 \pm 0.10) \tag{3.1}$$

$$O(^1D) + O(^3P) + \Delta E = 4.99 \text{ eV } (0.42 \pm 0.05) \tag{3.2}$$

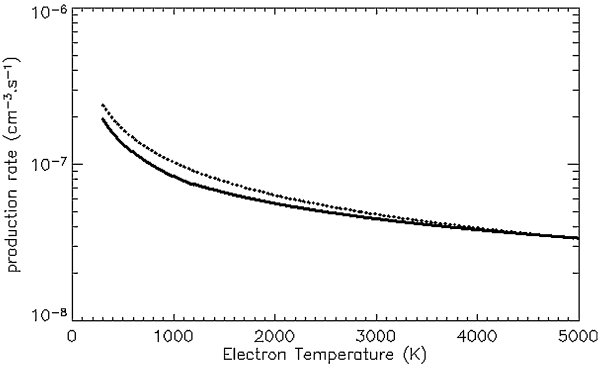

Fig. 7 Production rates of the O_2^+ ground state dissociative recombination function of the temperature from Mehr and Biondi (1969) (*solid line*) and Peverall et al. (2001) (*dashed line*)

$$O(^1D) + O(^1D) + \Delta E = 3.02 \text{ eV } (0.31 \pm 0.07) \tag{3.3}$$

$$O(^3P) + O(^1S) + \Delta E = 2.77 \text{ eV } (<0.01) \tag{3.4}$$

$$O(^1D) + O(^1S) + \Delta E = 0.80 \text{ eV } (0.05 \pm 0.02) \tag{3.5}$$

For the ground state, the branching ratios have been measured by Kella et al. (1997) using the ASTRID heavy ion storage ring and are given in parenthesis. The fourth branching ratio has efficiency equal to 0 (Kella et al. 1997). The energy in the center of mass is indicated for each channel (Kella et al. 1997). If this energy is divided equally between the two oxygen atoms produced, only the first two channels will produce atoms with energy larger than the escape velocity (~2 eV at the exobase). The production rates, the branching ratios and the exothermicity, ΔE, of the reaction depend on the vibrational state of the O_2^+ ions (Guberman 1983, 1989). The addition of one vibrational quantum adds about 0.23 eV to the exothermicity (Fox and Hac 1997). The vibrationally excited states of O_2^+ ions are controlled by ion-neutral reactions in the thermosphere (Fox and Hac 1997) and their altitude distributions have been modeled in the Martian ionosphere by Fox and Hac (2009) at a 60° solar zenith angle (see also Futaana et al. 2011, this issue). The production rates from Mehr and Biondi (1969) and Peverall et al. (2001) are displayed in Fig. 7 for typical electron temperatures in the Martian upper atmosphere between 300 and 5000 K. There is a systematic difference of 20% below 1200 K and a good agreement for electron temperature larger than 3000 K.

Mars' cold oxygen population has been observed through its 130 nm emission line (Barth et al. 1971; Strickland et al. 1972, 1973; Stewart et al. 1992; Leblanc et al. 2006; Chaufray et al. 2009) at altitudes below 400 km. The profile of the 130 nm oxygen emission observed by ALICE onboard Rosetta during its Mars flyby present a change in slope, indicating two oxygen populations (Feldman et al. 2011). The cold oxygen population is dominant below 500 km while the hot oxygen population is dominant above 500 km (Feldman et al. 2011). In the last decades, several models have been developed to study the Martian exosphere. Most of the work has focused on oxygen density. No model currently describes, in a single consistent approach, the full exospheric oxygen distribution. Currently, exospheric models solve Boltzmann equations for cold and hot oxygen populations separately. Several approaches have been used to study the hot oxygen population such as the two-stream model method (Nagy and Cravens 1988) or Monte Carlo models (Hodges et al. 2000). In the 1D two-stream approach, the hot oxygen flux is divided into an upward flux $\Phi^+(E, z)$ and a downward flux $\Phi^-(E, z)$ where z is the altitude and E the energy of the oxygen atoms. The linear coupled equations of these two fluxes are solved below the exobase and the velocity distribution

function at the exobase altitude z_c is computed as $f(V) = [\Phi^+(E, z_c) + \Phi^-(E, z_c)]/V(E)$ where V is the velocity associated to the energy E. Then, the Liouville equation is solved above the exobase to describe the density in the exosphere (Zhang et al. 1993; Kim et al. 1998). In Monte Carlo models, the hot oxygen atoms simulated by "representative" particles or test particles, which are followed along their trajectory. This approach uses more realistic 2D or 3D thermospheric-ionospheric environments (Hodges 2000; Leblanc and Johnson 2002; Chaufray et al. 2007; Valeille et al. 2009a, 2009b) or realistic cross sections to describe the collision between hot oxygen atoms and the background atmosphere (Krestyanikova and Shematovich 2005; Cipriani et al. 2007; Fox and Hac 2009). The collision cross sections of hot oxygen and cold thermospheric species are crucial parameters, as shown by several studies (Shizgal 1999a; Johnson et al. 2000; Cipriani et al. 2007; Fox and Hac 2009; Lichtenegger et al. 2009).

While numerous studies have analyzed hydrogen in Earth's (e.g., Chamberlain 1963, 1977, 1980; Vidal-Madjar and Bertaux 1972; Bertaux 1978; Shizgal and Blackmore 1986; Hodges 1994) and Venus' exosphere (e.g., Rodriguez et al. 1984; Shizgal 1987; Nagy et al. 1990; Hodges 1999; Shizgal 1999a), few studies have described Mars' hydrogen exosphere. Nagy et al. (1990) studied the production of hot hydrogen produced by charge exchange using a two-stream model approach. Shizgal (1999a) studied the hydrogen and deuterium escape caused by energization due to collisions with hot oxygen but focused more on Venus' exosphere rather than Mars' exosphere due to the lack of observations. Chen and Cloutier (2003) developed a 3D Monte Carlo model that included radiation pressure, photoionization and charge exchange with solar wind protons and found density profiles similar to Chamberlain's approach without satellite particles. More recently Lichtenegger et al. (2006) used a Monte Carlo model to estimate the energy distribution of hot hydrogen at the exobase. They considered the exothermic reactions in McElroy et al. (1982) and found that hot hydrogen was negligible on Mars.

A comparative study of the Venusian and Martian hydrogen exospheres is needed since the differences and similarities have not been examined since the work of Nagy et al. (1990) who did not consider the full set of reactions. First, we will present Chamberlain's method, which is usually used to describe the hydrogen in the Martian exosphere, and then the Monte Carlo approach, which widely used to study the hot oxygen population in the Martian exosphere.

3.2 Chamberlain's Method

Chamberlain's approach (Chamberlain 1963) is based on the solution of the Liouville equation in a collisionless exosphere. Once this equation is solved, the velocity distribution is integrated in the region of velocity space consistent with trajectories coming from the exobase in a gravitational field. The velocity space can be divided into different regions, which represent different classes of trajectories (Fahr and Shizgal 1983). Figure 8 displays a cut of the velocity space. The conditions for each class of trajectory are summarized in Table 2. In this section, a particle will be identified by its trajectory. For example, an escaping particle is a particle with an escaping trajectory.

The parameters (using the notation of Chamberlain 1963) are defined as follows, λ is the escape parameter defined by

$$\lambda(r) = \frac{GMm}{kT_c r} = \frac{V_{\rm esc}^2}{U^2}, \tag{3.6}$$

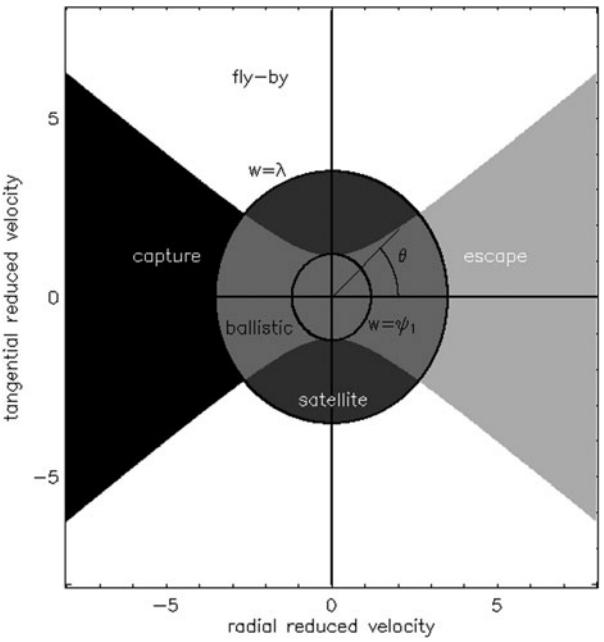

Fig. 8 Repartition of the different classes of particle in the velocity space adapted from Fahr and Shizgal (1983). The reduced velocity w is defined as the ratio of the velocity and the thermal velocity. The parameters λ, ψ_1 and θ are defined by (3.6), (3.7), (3.8) respectively

Table 2 Different classes of particles and their distribution in the velocity space, adapted from Fahr and Shizgal (1983)

Class of particle	Orbit	w_{range}	θ_{range}	Domain of velocity space
Balistic (B)	Elliptic crossing the exobase	$0 \le w \le \psi_1^{1/2}$ $\psi_1^{1/2} \le w \le \lambda^{1/2}$	$0 \le \theta \le \pi$ $0 \le \theta \le \theta_m(w)$	Between the two circles and outside the hyperbolae
Satellite (S)	Elliptic not crossing the exobase	$\psi_1^{1/2} \le w \le \lambda^{1/2}$	$\theta_m(w) \le \theta \le \pi$	Inside the largest circle and inside the hyperbolae
B + S	Elliptic	$0 \le w \le \lambda^{1/2}$	$0 \le \theta \le \pi$	Inside the largest circle
Escaping (E)	Hyperbolic crossing the exobase	$w > \lambda^{1/2}$ $w_r > 0$	$0 \le \theta \le \theta_m(w)$	Outside the largest circle and outside the hyperbolae in the field $w_r > 0$
Capture (C)	Hyperbolic crossing the exobase	$w > \lambda^{1/2}$ $w_r < 0$	$0 \le \theta \le \theta_m(w)$	Outside the largest circle and the hyperbolae, in the field $w_r < 0$
Fly-by	Hyperbolic not crossing the exobase	$w > \lambda^{1/2}$	$\theta_m(w) \le \theta \le \pi$	Outside the largest circle and inside the hyperbolae
E + C + F	Hyperbolic	$w > \lambda^{1/2}$	$0 \le \theta \le \pi$	Outside the largest circle

where G is the gravitational constant, M the mass of the planet, m the mass of the specie, k the Boltzmann constant, T_c the exobase temperature, r the radial distance from the center of the planet, V_{esc} the escape velocity and $U = (2kT_c/m)^{1/2}$ is the thermal velocity. The

equation of the hyperbolae delimitating the satellite and flyby particles from the escape, ballistic and capture particles is

$$w_t^2 - \frac{\lambda^2}{\lambda_c^2 - \lambda^2} w_r^2 = \frac{\lambda^2}{\lambda + \lambda_c} = \psi_1, \tag{3.7}$$

where, w_r and w_t are the radial and the tangential components of the reduced velocity which is the ratio between the velocity and the thermal velocity U. The parameter θ_m is given by

$$\cos\theta_m(w) = \frac{(\lambda_c^2 - \lambda^2)^{1/2}}{\lambda_c}\left(1 - \frac{\psi_1}{w^2}\right)^{1/2} = \left[1 - \frac{\lambda^2}{\lambda_c^2}\left(1 + \frac{\lambda_c - \lambda}{w^2}\right)\right]^{1/2}. \tag{3.8}$$

In the exosphere, if collisions were totally neglected, only particles with trajectories crossing the exobase (ballistic and escaping) would be present. To take into account long-lived satellite particles, which can exist in the lower exosphere due to rare collisions, Chamberlain (1963) introduced the satellite critical radius. Satellite particles are included below this radius and excluded above it.

In spherically symmetric exospheres without collisions, the Liouville equation can be written under the form

$$v_r \frac{\partial f}{\partial r} + \left(\frac{P_x^2}{mr^3} - \frac{GMm}{r^2}\right)\frac{\partial f}{\partial p_r} = 0, \tag{3.9}$$

where (r, θ) are the standard spherical coordinates, $P_\chi = mr^2(d\theta/dt)$ is a constant according to Kepler's second law, f is the velocity distribution function, v_r is the radial velocity and $p_r = mv_r$. Assuming a function with a form $f = A(r)\exp(-p_r^2/2mkT_c)$, the equation can be written as

$$\frac{d(\ln f)}{dr} = -\left(\frac{GMm}{kT_c r^2} - \frac{P_x^2}{MkT_c r^3}\right). \tag{3.10}$$

This equation is then solved using a Maxwellian distribution as the boundary condition at the exobase. The velocity distribution at an altitude r is therefore given by

$$f(r, p_r, P_x) = \frac{n_c \exp(-(\lambda_c - \lambda))\exp(-p_r^2/2mkT_c)\exp(-P_x^2/2mkT_c r^2)}{(2\pi kT_c/m)^{3/2}}, \tag{3.11}$$

The velocity distribution is integrated over the velocity region allowed by the trajectory in a gravitational field (Table 2) and leads to the density given by

$$n(r) = n(r_c)\exp[-(\lambda_c - \lambda)]\zeta(\lambda), \tag{3.12}$$

where $\zeta(\lambda)$ equal to 1 when the distribution given by (3.11) is integrated over the full velocity space leading to the hydrostatic density profile. This means that the barometric law, usually derived from equilibrium between gas pressure and gravitation (and should be valid only below the exobase) is still valid in the exosphere provided the moments extend over all possible values and assuming a Maxwellian distribution at the exobase (Chamberlain 1963).

Analytical expressions of the ζ function for each class of particle can be found in Chamberlain (1963). The Jeans escape formula can be derived from the integration of the first moment of the velocity function distribution over the escape particles velocity space do-

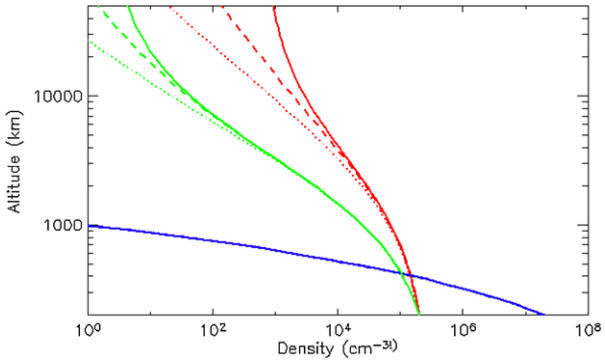

Fig. 9 Examples of density profiles for atomic hydrogen (*red*), molecular hydrogen (*green*) and atomic oxygen (*blue*) derived under different assumptions for an exobase temperature of 250 K. *Solid lines* represent the barometric law with the specie scale height, *dashed lines* represent density profiles including ballistic, satellite and escaping particles, *dotted lines* represent the density profile including only ballistic and escaping particles

main (Chamberlain 1963). Examples of hydrogen density profiles under different assumptions are displayed in Fig. 9 with $T_c = 250$ K. For atomic oxygen there is no difference in the density profile when all classes of particles are included (hydrostatic) and when only escape and ballistic particles are included. For atomic hydrogen the hydrostatic assumption overestimates the density above 2000 km compared to the density derived with only escape and ballistic particles, while including satellite particles changes the distribution above 4000 km. For H_2, departure from the hydrostatic law occurs near 4000 km altitude. The hydrostatic assumption used by some 1D collisional models above the exobase, until 400 km (e.g. Krasnopolsky 2010), is therefore justified. Above ∼400 to 500 km, non-thermal populations, especially non-thermal oxygen, cannot be neglected (Valeille et al. 2009a).

3.3 Monte Carlo Method

The first Monte Carlo simulations of planetary exospheres were performed to determine how to correct Jeans' escape so that it takes into account the perturbation of the velocity distribution due to escaping H and He at the exobase of Earth (see Brinkman 1971 and references therein). Later, this approach was used to model the structure of the hydrogen and helium exospheres of the Moon and Mercury (Hodges 1973, 1980; Curtis and Hartle 1978; Smith et al. 1978). Since then, Monte Carlo models have been used extensively to study different processes in several exospheric environments. In this section, we illustrate the Monte Carlo approach, by describing the models used to study the oxygen exosphere and escape rate on Mars.

Monte Carlo simulations have been used to describe exospheric hot oxygen density and escape produced by the dissociative recombination of O_2^+ ions (Hodges 2000; Krestyanikova and Shematovich 2005; Cipriani et al. 2007; Chaufray et al. 2007; Valeille et al. 2009a; Fox and Hac 2009) and sputtering (Leblanc and Johnson 2001, 2002; Cipriani et al. 2007; Chaufray et al. 2007). The main inputs of Monte Carlo models are the thermospheric-ionospheric background and collisions cross-sections between hot oxygen atoms and thermospheric species (mainly CO_2 and thermal O). Table 3 summarizes the assumptions used by different authors and the processes described.

Table 3 Assumptions made by the recent Monte Carlo studies of the hot oxygen coronae. DR: Dissociative Recombination of O_2^+ ions, CE: Charge Exchange between energetic O^+ ions and ambient H or O. HS: Hard Sphere, UP: Universal Potential, MD: Molecular Dynamics Model from Johnson et al. (2002), FSDCS: Forward Scattering Differential Cross Section. 1D means that density depends only on the radius *r*, 2D means a dependence on *r* and *sza* (solar zenith angle). For sputtering models, the ionosphere is not needed

Authors	Processes	Thermosphere/Ionosphere	Collisions
Hodges et al. (2000)	DR, CE	2D/2D, winds, rotation	HS
Leblanc and Johnson (2001)	Sputtering	2D	UP
Leblanc and Johnson (2002)	Sputtering	1D	MD
Krestyanikova and Shematovich (2005)	DR	1D/1D	FSDCS/HS-isotropic
Cipriani et al. (2007)	DR, sputtering	1D/1D	MD-UP-HS
Chaufray et al. (2007)	DR, sputtering	2D/1D, rotation	UP
Valeille et al. (2009)	DR	3D/3D, winds, rotation	HS-isotropic
Fox and Hac (2009)	DR	1D/1D	FSDCS/HS-isotropic

To describe Mars' hot oxygen corona, which is produced by O_2^+ dissociative recombination, first a realistic O_2^+ density profile, electron temperature profile, and a neutral density profile (to calculate collisions) are assumed to compute the production rates of hot oxygen. Cipriani et al. (2007), Krestyanikova et al. (2005) and Fox and Hac (2009) assume a spherically symmetry O_2^+ and neutral density profile based on 1D photochemical models (Krasnopolsky 2002; Fox and Hac 2009). To describe sputtering, Leblanc and Johnson (2001) only need neutral density profiles, taken from Zhang et al. (1993), and include a day/night asymmetry in the temperature profile. Hodges (2000) introduces ions and neutral profiles that vary with solar zenith angle, while Chaufray et al. (2007) only uses such variations for O_2^+ ions. Currently, Valeille et al. (2009a) uses the most sophisticated ion and neutral profiles. They use 3D data from the MTGCM model (Bougher et al. 1999), which includes thermospheric winds and planetary rotation. Most of the studies have used the electron temperature profile derived from Viking mission (Hanson and Mantas 1988) except Fox and Hac (2009) who compute the profile. Finally, the erosion of the ionosphere above ~180 km, not included in the MTGCM model or in the photochemical model of Krasnopolsky (2002), should also be taken into account (Fox and Hac 2009).

The easiest way to simulate collisions between hot oxygen and the neutral atmosphere is to use a total cross section and assume an isotropic distribution of scattering angles (hard sphere model). Hodges (2000) and Valeille et al. (2009a) used this approach, and Fox and Hac (2009) tested it. The total cross section used in simulations varies from $1-3 \times 10^{-15}$ cm^2. The isotropic assumption is the main limitation of the hard sphere approach. An accurate description of the O-O collisions needs to use 18 separate ground state potential curves for O_2 (Tully and Johnson 2001). Kharchenko et al. (2000) derived scattering cross sections between two oxygen atoms by solving the Schrodinger equation of the relative motion of two oxygen atoms in a potential field for different channels corresponding to different states of the O_2 molecule. Previously, Hodges (1993) and Shizgal (1999b) used a similar approach to derive scattering cross sections between O and H or D atoms. Kharchenko et al. (2000) found that the statistically averaged (over channels) cross sections are highly peaked at small scattering angles, χ, for energies of few eV. This agrees with the results of Tully and Johnson (2001). They also show that the Landau-Schiff approximation reproduced the statistically averaged (over scattering angles) cross sections as function of

the energy. Therefore, as pointed out by Fox and Hac (2009), isotropic cross sections overestimate the effect of large scattering angles and therefore the loss of energy for hot atoms (Eq. (3.13)):

$$\Delta E = E\frac{2m_1m_2}{(m_1+m_2)^2}(1-\cos\chi), \tag{3.13}$$

where m_1 and m_2 are the masses of the two particles and E is the initial energy of the system.

Using differential cross sections from Kharchenko et al. (2000), Krestyanikova and Shematovich (2005) and Fox and Hac (2009) show that more realistic cross sections could increase the oxygen escape rate by one order of magnitude compared to the isotropic assumption. Another approach used to compute the scattering angles of collisions consists of solving the movement equation of two particles in a potential field. For collisions involving significant energy transfer (∼1 keV), the repulsive part of the potential is dominant and a universal potential can be used to describe O collisions (Johnson et al. 2000). This universal potential (Ziegler et al. 1985) is defined by

$$\Phi(r) = \frac{Z_1Z_2q^2}{r}\varphi(r/a_u) \tag{3.14}$$

$$\varphi(x) = 0.181\exp(-3.2x) + 0.5099\exp(-0.9423x) + 0.2802\exp(-0.4029x) + 0.02817\exp(-0.2016x) \tag{3.15}$$

where Z_1 and Z_2 are the charge number of the particles (8 for oxygen), q the elementary charge, R the distance between the oxygen atoms and $a_U = 0.8853a_0/(Z_1^{0.23}+Z_2^{0.23})$ where a_0 is the Bohr radius (0.529 nm). Knowing, the impact parameter b and the total energy E, the scattering angle χ can be then computed using the usual relation

$$\chi = \pi - 2b\int_{r_0}^{\infty}\left(r^2\left(1-\frac{\Phi}{E}\right)-b^2\right)^{-1/2}\frac{dr}{r}, \tag{3.16}$$

where r_0 is the positive root of the equation $r^2(1-\Phi/E)-b^2=0$.

The impact parameter is derived by

$$\frac{\pi b^2}{\pi b_{\max}^2} = \alpha, \tag{3.17}$$

where $b_{\max}$ is the maximum impact parameter value and α is a random number between 0 and 1. In the simulations done by Chaufray et al. (2007), $b_{\max} = 4$ Å corresponding to a maximal total cross section $\sim 5\times10^{-15}$ cm^2. The universal potential has been used to describe the sputtering of an oxygen atmosphere by O^+ pick-up ions (Johnson et al. 2000; Leblanc and Johnson 2001; Cipriani et al. 2007; Chaufray et al. 2007). The universal potential has also been used by Chaufray et al. (2007) to describe collisions between hot oxygen (produced by the dissociative recombination of O_2^+ ions) and the ambient atmosphere. However, for energies of few eV, Cipriani et al. (2007) showed that this approach overestimates thermalization compared to differential cross sections calculated from quantum approach (Kharchenko et al. 2000) as used by Krestyanikova and Shematovich (2005).

In Monte Carlo simulations, the environment is divided into several audit cells, where all the macroscopic parameters (velocity distribution function, density, flux, temperature) can be estimated. For 3D approaches (Hodges 2000; Chaufray et al. 2007; Valeille et al.

2009a), spherical coordinates have been used. In all Monte Carlo simulations, the translational movement is decoupled from intermolecular interactions.

Chaufray et al. (2007) used the algorithm of Bird (1994) to determine the number of collisions in each cell at each time step. In each cell M, the maximum number of collisions produced by each individual test particle is

$$N_{\text{coll}}^{\max}(M) = n(M)(\sigma V)_{\max} dt, \tag{3.18}$$

where $n(M)$ is the local density, $(\sigma V)_{\max}$ is an upper value of the product between the cross section and the relative velocity of the test particle and atmospheric particle, and dt the time step of the simulation. Then, for each possible collision, the velocity of the neutral particle is estimated assuming a Maxwellian distribution at the local temperature $T(M)$. The collision is finally taken into account if it satisfies the condition

$$\frac{\sigma V_r}{(\sigma V)_{\max}} < \alpha, \tag{3.19}$$

where α is a random number between 0 and 1, σ the cross section of the collision and V_r is the relative velocity between the test particle and the atmospheric particle. After a long time simulation the average number of collisions for a given relative velocity V_r, during dt, corresponds to

$$N_{\text{coll}}(M) = n(M)\sigma V_r dt \tag{3.20}$$

For each selected collision, the impact parameter is determined from (3.17), and (3.16) and (3.21) are used to derive the angles (χ and ε) that define the post-collisional direction of the two test particles.

$$\varepsilon = 2\pi\alpha \tag{3.21}$$

The most important results given by Monte Carlo simulations are oxygen escape flux and hot oxygen density. Figure 10 shows an example of hot oxygen density, obtained by Chaufray et al. (2007), in the equatorial plane and the velocity distributions at altitudes between 560 and 890 km for three local times. As expected from the exospheric theory presented above, no satellite, capture or flyby particles are present in the collisionless region. The velocity distribution functions have opposite asymmetries at 6 h and 18 h local time. This asymmetry can be explained easily. Most of the hot oxygen atoms are produced at 12 h. These hot atoms come back to the planet in the rotation direction or anti-rotation direction. When they move in the rotation direction ($Vt > 0$) they return to the evening hemisphere and when they move in anti-rotation direction ($Vt < 0$) they return to the morning hemisphere.

Chaufray et al. (2007) coupled a 3D Monte Carlo model, describing the Martian corona, to a 3D hybrid model, describing the corona's interaction with the solar wind (Modolo et al. 2005). The coupled model was used to compare oxygen escape processes. Escaping fluxes determined by this model are summarized in Table 4. More recently, Valeille et al. (2009b) coupled a 3D MTGCM model to a 3D exospheric model to determine the escape of oxygen due to dissociative recombination for several seasons, solar activity levels and at different epochs in the past. They have shown that oxygen can vary by a factor ~5 to 7 along with season and solar activity and by a factor ~6 to 9 historically. These authors also estimate the oxygen escape due to other processes, using simpler assumptions. Valeille et al. (2009b) found that dissociative recombination is the main process of oxygen escape in agreement with Chaufray et al. (2007). However, full coupling between a 3D Martian global circulation model extended to the exobase, a 3D exospheric model and a 3D model describing Mars'

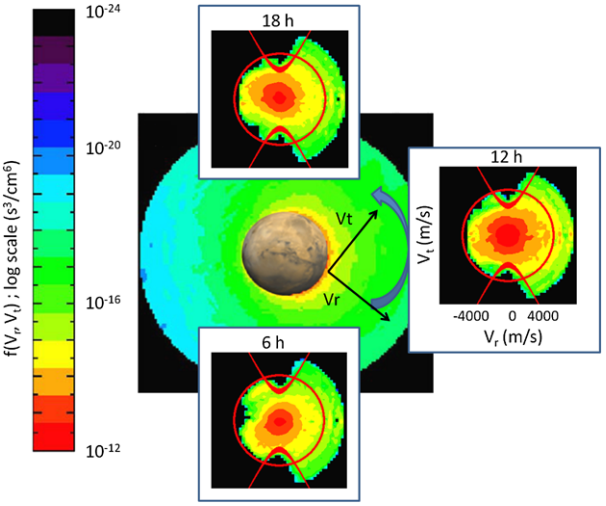

Fig. 10 Equatorial density and velocity distribution functions for the hot oxygen component obtained at altitudes between 560 and 890 km at three local times obtained by Chaufray et al. (2007). The *red circle* and the *red hyperbolae* on velocity distribution function figures indicate the boundaries for escaping particles and closed trajectories (satellite or flyby see also Fig. 8). The positive sense of the tangential velocity is the direction of the planetary rotation indicated by the *blue arrow*. More details can be found in Chaufray et al. (2007)

Table 4 Oxygen escape flux estimated by the Monte Carlo simulations of Chaufray et al. (2007) at low and high solar activity for different processes

Process	Low solar activity	High solar activity
Dissociative recombination	1×10^{25}	4×10^{25}
Pick-up ions escape	2×10^{23}	3×10^{24}
ENA escape	4×10^{22}	4×10^{23}
Sputtering	2×10^{23}	7×10^{23}

interaction with the solar wind is still needed to accurately and self-consistently investigate the evolution of oxygen escape processes. This type of model could determine the amount of water that has escaped to space historically, and in particular in past epochs when the solar wind was likely denser and faster.

4 Summary

Numerical simulations help us understand the dynamics of ionized and neutral particles near Venus, Mars, and Titan. The modeling approach that should be used to study plasma and neutral phenomena depends on the relevant scales of the interaction. This paper describes the methodology, advantages, and limitations of several self-consistent plasma models that have been used to model the plasma and neutral dynamics near Venus, Mars, and Titan.

Fully kinetic models, which simulate ions and electrons as particles, were shown to make the fewest assumptions and therefore include the most accurate physics. However, these models must resolve electron inertial scales and include fast electromagnetic waves. Therefore, fully kinetic models are typically used to studying small regions or fast processes. MHD models simulate ions and electrons as fluids. These models include the most assumptions; therefore they often neglect important physical processes, particular in collisionless regions where the fluid assumptions begin to fail and ion cyclotron effects become important. However, the numerical simplicity of MHD models allows them to simulate large regions over long time scales. Hybrid models are an intermediate between fully kinetic models and

MHD models. In hybrid models, ions are simulated as macroparticles and electrons are simulated as a mass-less fluid. Hybrid simulations can be used to study much larger regions than fully kinetic models and include both phenomena that occur at ion scales and non-thermal ion distributions; however, compared to MHD models they are still somewhat limited in resolution and/or simulation time.

This paper also describes Chamberlain's method and the Monte Carlo method, which are used to describe the dynamics of neutral particles in planetary exospheres. These models are important because they help us understand Martian atmospheric escape both today and historically. Efforts are currently underway to couple various exospheric models to plasma models in order get a complete description of the interaction of the atmosphere's of unmagnetized bodies with the plasma and electromagnetic fields in their space environment.

Acknowledgements The authors acknowledge the support of EUROPLANET RI project (Grant agreement no.: 228319) funded by EU; and also the support of the International Space Science Institute (Bern). RM acknowledges support from the ANR (ANR-09-JCJC-0038 and ANR-09-BLAN-223).

References

M.H. Acuña et al., J. Geophys. Res. **106**(E10), 23403–23418 (2001)
H. Backes et al., Science **308**, 992 (2005). doi:10.1126/science.1109763
S. Barabash et al., Science **315**(5811), 501–503 (2007). doi:10.1126/science.1134358
C.A. Barth et al., J. Geophys. Res. **76**, 2213 (1971)
R. Bauske et al., J. Geophys. Res. **103**(A10), 23635–23638 (1998)
M. Benna et al., Geophys. Res. Lett. **36**, L04109 (2009). doi:10.1029/2008GL036718
J.-L. Bertaux, Planet. Space Sci. **26**, 431 (1978)
C. Bertucci et al., Geophys. Res. Lett. **30**(2), 1099 (2003). doi:10.1029/2002GL015713
C. Bertucci et al., Science **321**, 1475 (2008). doi:10.1126/science.1159780
C. Bertucci et al., Space Sci. Rev. (2011, submitted)
N. Besse et al., Int. J. Appl. Math. Comput. Sci. **17**, 361–374 (2007). doi:10.2478/v10006-007-0030-3
G.A. Bird, *Molecular Gas Dynamics and the Direct Simulation of Gas Flows* (Clarendon, Oxford, 1994)
C.K. Birdsall, A.B. Langdon, *Plasma Physics via Computer Simulation* (McGraw-Hill, New York, 1985)
A. Boesswetter et al., Ann. Geophys. **22**, 4363–4379 (2004)
A. Boesswetter et al., Ann. Geophys. **25**, 1851–1864 (2007)
S.W. Bougher et al., J. Geophys. Res. **104**, 16591 (1999)
L.H. Brace, A.J. Kliore, Space Sci. Rev. **55**(1–4), 81–163 (1991). doi:10.1007/BF00177136
D. Brain et al., Icarus **206**, 139–151 (2010)
S.H. Brecht, J.R. Ferrante, J. Geophys. Res. **96**(A7), 11209–11220 (1991)
S.H. Brecht, J. Geophys. Res. **102**(A3), 4743–4750 (1997)
S.H. Brecht et al., J. Geophys. Res. **105**(A6), 13119–13130 (2000)
S.H. Brecht et al., Icarus **206**, 164–173 (2010)
S.H. Brecht et al., Earth, Planets and Space. (2011, accepted)
R.T. Brinkman, Planet. Space Sci. **19**, 791–794 (1971)
J.W. Chamberlain, Planet. Space Sci. **11**, 901 (1963)
J.W. Chamberlain, J. Geophys. Res. **82**, 1 (1977)
J.W. Chamberlain, Icarus **44**, 651 (1980)
E. Chassefière et al., Planet. Space Sci. **55**, 343 (2007)
J.-Y. Chaufray et al., J. Geophys. Res. **112**, E09009 (2007). doi:10.1029/2007JE002915
J.-Y. Chaufray et al., J. Geophys. Res. **114**, E02006 (2009)
Y. Chen, P.A. Cloutier, J. Geophys. Res. **108**, 1382 (2003)
F. Cipriani et al., J. Geophys. Res. **112**, E7001 (2007)
A.J. Coates et al., Geophys. Res. Lett. **34**, L24S05 (2007). doi:10.1029/2007GL030919
T.E. Cravens et al., Planet. Space Sci. **46**, 1193 (1998)

S.A. Curtis, R.E. Hartle, J. Geophys. Res. **83**, 1551 (1978)
E. Dubinin et al., Space Sci. Rev. **206**, 209–238 (2006)
E. Dubinin et al., Planet. Space Sci. (2008)
F. Duru et al., J. Geophys. Res. **113**, A07302 (2008). doi:10.1029/2008JA0130373
F. Duru et al., Icarus **206**(1), 74–82 (2010)
H.J. Fahr, B. Shizgal, Rev. Geophys. Space Phys. **21**, 75 (1983)
P.D. Feldman et al., Icarus **214**, 394 (2011)
J.L. Fox, A.B. Hac, J. Geophys. Res. **102**, 24,005 (1997)
J.L. Fox, A.B. Hac, Icarus **204**, 527 (2009)
Y. Futaana et al., Space Sci. Rev. (2011, submitted)
A. Glocer et al., J. Geophys. Res. **114**, A12203 (2009). doi:10.1029/2009JA014418
S.L. Guberman, in *Physics of Ion–Ion and Electron–Ion Collisions*, ed. by F. Brouillard, J.W. McGowan (Plenum, New York, 1983), pp. 167–200
S.L. Guberman, in *Dissociative Recombination: Theory Experiment and Applications*, ed. by J.B.A. Mitchell, S.L. Guberman (World Scientific, Singapore, 1989), pp. 45–60
J.S. Halekas et al., Geophys. Res. Lett. (2006). doi:10.1029/2006GL026229
W.B. Hanson, G.P. Mantas, J. Geophys. Res. **93**, 7538 (1988)
D.S. Harned, J. Comput. Phys. **47**, 452–462 (1982)
E. Harnett, R. Winglee, Geophys. Res. Lett. 30 (2003). doi:10.1029/2003GL017852
E. Harnett, R. Winglee, J. Geophys. Res. **110**, A07226 (2005). doi:10.1029/2003JA010315
E.M. Harnett, R.M. Winglee, J. Geophys. Res. **111**, A09213 (2006). doi:10.1029/2006JA011724
E.M. Harnett, R.M. Winglee, J. Geophys. Res. **112**, A05207 (2007). doi:10.1029/2006JA012001
E.M. Harnett, J. Geophys. Res. **114**, A01208 (2009). doi:10.1029/2008JA013648
R.E. Hartle et al., J. Geophys. Res. **87**, 1383–1394 (1982). doi:10.1029/JA087iA03p01383
R.E. Hartle et al., Geophys. Res. Lett. **33**, L08201 (2006). doi:10.1029/2005GL024817
R.R. Hodges, J. Geophys. Res. **78**, 8055 (1973)
R.R. Hodges, J. Geophys. Res. **85**, 164 (1980)
R.R. Hodges, J. Geophys. Res. **98**, 3799 (1993)
R.R. Hodges, J. Geophys. Res. **99**, 23229 (1994)
R.R. Hodges, J. Geophys. Res. **104**, 8463 (1999)
R.R. Hodges, J. Geophys. Res. **105**, 6971 (2000)
R. Jarvinen et al., Adv. Space Res. **41**, 1361–1374 (2008)
R.E. Johnson et al., J. Geophys. Res. **105**, 1659 (2000)
R.E. Johnson et al., Space Sci. Rev. **139**, 355 (2008)
K. Kabin et al., J. Geophys. Res. **104**, 2451 (1999)
K. Kabin et al., J. Geophys. Res. **105**, 10,761 (2000)
E. Kallio et al., J. Geophys. Res. **103**, 4723 (1998)
E. Kallio, P. Janhunen, J. Geophys. Res. **106**, 5617–5634 (2001)
E. Kallio et al., Geophys. Res. Lett. **31**, L15703 (2004). doi:10.1029/2004GL020344
E. Kallio et al., Planet. Space Sci. **54**, 1472–1481 (2006)
E. Kallio et al., Planet. Space Sci. **56**, 796–801 (2008)
E. Kallio et al., Icarus **206**, 152–163 (2010)
E. Kallio, R. Jarvinen, Earth, Planets and Space (2011, submitted)
J. Kella et al., Science **276**, 1530 (1997)
V. Kharchenko et al., J. Geophys. Res. **105**, 24,899 (2000)
A. Kidder et al., J. Geophys. Res. **113**, A02205 (2009). doi:10.1029/2008JA013100.
J. Kim et al., J. Geophys. Res. **103**, 29339 (1998)
V.A. Krasnopolsky, Icarus **107**, 5128 (2002)
V.A. Krasnopolsky, Icarus **207**, 638 (2010)
M.A. Krestyanikova, V.I. Shematovitch, Sol. Syst. Res. **39**, 22 (2005)
A.B. Langdon, Part. Accel. **19**, 223–225 (1986)
F. Leblanc, R.E. Johnson, Planet. Space Sci. **49**, 645 (2001)
F. Leblanc, R.E. Johnson, J. Geophys. Res **107** (2002). doi:10.1029/2000JE001473
F. Leblanc et al., J. Geophys.Res. **111**, E09S11 (2006). doi:10.1029/2005JE002664
S.A. Ledvina, T.E. Cravens, Planet. Space Sci. **46**, 1175 (1998)
S.A. Ledvina et al., J. Geophys. Res. **110**, A06211 (2005). doi:10.1029/2004JA010771
S.A. Ledvina et al., Space Sci. Rev. (2008). doi:10.1007/s11214-008-9384-6
S.A. Ledvina et al., Earth Planet. Sci. (2011, submitted)
H.I.M. Lichtenegger et al., Space Sci. Rev. **126**, 469 (2006)
H.I.M. Lichtenegger et al., Geophys. Res. Lett. **36**, L10204 (2009)
Y.J. Liu et al., Geophys. Res. Lett. **26**(17), 2689–2692 (1999)

Y.J. Liu et al., Adv. Space Res. **27**, 1837 (2001)
J.G. Luhmann, J. Geophys. Res. **101**(E12), 29387–29393 (1996)
J.G. Luhmann, T.E. Cravens, Space Sci. Rev. **55**, 1 (1991). doi:10.1007/BF00177138
R. Lundin et al., Geophys. Res. Lett. **17**, 877 (1990)
R. Lundin et al., Science **305**, 1933–1936 (2004)
R. Lundin et al., Science **311**(5763), 980–983 (2006). doi:10.1126/science.1122071
Y.J. Ma et al., J. Geophys. Res. **10**, A10 (2002). doi:10.1029/2002JA009293
Y.J. Ma et al., J. Geophys. Res. **109**, A07211 (2004). doi:10.1029/2003JA010367
Y. Ma et al., J. Geophys. Res. **111**, A05207 (2006). doi:10.1029/2005JA011481
Y.J. Ma et al., Geophys. Res. Lett. (2007). doi:10.1029/2007GL031627
Y.-J. Ma et al., Space Sci Rev. **139**(1–4) (2008). doi:10.1007/s11214-008-9389-1
Y.J. Ma et al., J. Geophys. Res. **114**, A03204 (2009). doi:10.1029/2008JA013676
C. Mazelle et al., Space Sci. Rev. **111**, 115–181 (2004)
A. Matthews, J. Comput. Phys. **112**, 102–116 (1994)
M.B. McElroy, Science **175**, 443–445 (1972)
M.B. McElroy et al., Science **215**, 1614 (1982)
F.J. Mehr, M.A. Biondi, Phys. Rev. **181**, 264 (1969)
D.L. Mitchell et al., J. Geophys. Res. **106**, 23419 (2001)
R. Modolo et al., Ann. Geophys. **23**, 433–444 (2005)
R. Modolo et al., Ann. Geophys. **24**, 3403–3410 (2006)
R. Modolo et al., Geophys. Res. Lett. **34**, L24S07 (2007). doi:10.1029/2007GL030489
R. Modolo, G.M. Chanteur, J. Geophys. Res. **113**, A01317 (2008). doi:10.1029/2007JA012453
K. Moore et al., J. Geophys. Res. **96**, 7779–7791 (1991)
K. Murawski, R.S. Steinolfson, J. Geophys. Res. **101**, 2547 (1996)
A.F. Nagy, T.E. Cravens, Geophys. Res. Lett. **15**, 433 (1988)
A.F. Nagy et al., Ann. Geophys. **8**, 251 (1990)
A.F. Nagy et al., J. Geophys. Res. **106**(A4), 6151–6160 (2001)
A.F. Nagy et al., Space Sci. Rev. **111**, 1 (2004). doi:10.1023/B:SPAC.0000032718.47512.92
D. Najib et al., J. Geophys. Res. **116**, A05204 (2011). doi:10.1029/2010JA016272
F. Neubauer et al., J. Geophys. Res. **111**, 10220 (2006)
R. Peverall et al., J. Chem. Phys. **114**, 6679 (2001)
V. Pohjola, E. Kallio, Ann. Geophys. **28**, 743–751 (2010)
J.M. Rodriguez et al., Planet. Space Sci. **32**, 1235 (1984)
R.W. Schunk, A.F. Nagy, *Ionospheres: Physics, Plasma Physics, and Chemistry* (Cambridge University Press, New York, 2009)
V.I. Shematovich et al., J. Geophys. Res. **99**, 23,217 (1994)
H. Shimazu, Earth Planets Space **51**, 383–393 (1999)
B. Shizgal, Adv. Space Sci. **7**, 73 (1987)
B. Shizgal, J. Geophys. Res. **107**, 14833 (1999a)
B. Shizgal, Planet. Space Sci. **47**, 163 (1999b)
B.D. Shizgal, R. Blackmore, Planet. Space Sci. **34**, 279 (1986)
I. Sillanpää et al., J. Geophys. Res. **112**, A12205 (2007). doi:10.1029/2007JA012348
S. Simon et al., Ann. Geophys. **24**, 1113–1135 (2006)
S. Simon, A. Boesswetter, T. Bagdonat, U. Motschmann, J. Schuele, Ann. Geophys. **25**, 117–144 (2007) doi:10.5194/angeo-25-117-2007
S. Simon et al., Planet. Space Sci. **57**, 2001–2015 (2009)
G.R. Smith et al., J. Geophys. Res. **83**, 3783 (1978)
D. Snowden et al., J. Geophys. Res. **112**, A1221 (2007). doi:10.1029/2007/JA012393
A.I. Stewart et al., J. Geophys. Res. **97**, 91 (1992)
D.J. Strickland et al., J. Geophys. Res. **77**, 4052 (1972)
D.J. Strickland et al., J. Geophys. Res. **78**, 4547 (1973)
T. Tanaka, J. Geophys. Res. **98**, 17251–17262 (1993)
T. Tanaka, K. Murawski, J. Geophys. Res. **102**, 19,805 (1997). doi:10.1029/97JA01474
N. Terada et al., J. Geophys. Res. **114**, A09208 (2009). doi:10.1029/2008JA013937
G. Tóth et al., J. Comput. Phys. **227**, 6967–6984 (2008)
C. Tully, R.E. Johnson, Planet. Space Sci. **49**, 533 (2001)
T. Umeda et al., Comput. Phys. Commun. **156**(1), 73–85 (2003). doi:10.1016/S0010-4655(03)00437-5
T. Umeda, J. Geophys. Res. **115**, A01204 (2010). doi:10.1029/2009JA014643
A. Valeille et al., J. Geophys. Res. **114**, E11005 (2009a)
A. Valeille et al., J. Geophys. Res. **114**, E11006 (2009b)
S. Vennerstrom et al., Geophys. Res. Lett. **30**, 1369 (2003)

A. Vidal-Madjar, J.-L. Bertaux, Planet. Space Sci. **20**, 1147 (1972)
D. Vignes et al., Geophys. Res. Lett. **27**, 49 (2000)
J. Villasenor, O. Buneman, Comput. Phys. Commun. **69**, 306 (1992)
J.H. Waite et al., Science **308**(5724), 982–986 (2005)
J.E. Wahlund et al., Science **308**, 986–989 (2005)
H.Y. Wei et al., Geophys. Res. Lett. **34**, L24S06 (2007). doi:10.1029/2007GL030701
R.M. Winglee et al., J. Geophys. Res. **114**, A05215 (2009). doi:10.1029/2008JA013343
M.H.G. Zhang et al., J. Geophys. Res. **98**, 10,915 (1993)
T.L. Zhang et al., Geophys. Res. Lett. **37**, L14202 (2010). doi:10.1029/2010GL044020
J.F. Ziegler et al., *The Stopping and Ranges of Ions in Matter* (Pergamon, New York, 1985)

Space Sci Rev (2011) 162:309–334
DOI 10.1007/s11214-011-9811-y

Ion Acceleration and Outflow from Mars and Venus: An Overview

Rickard Lundin

Received: 4 March 2011 / Accepted: 7 July 2011 / Published online: 23 August 2011

Abstract Solar wind forcing of Mars and Venus results in outflow and escape of ionospheric ions. Observations show that the replenishment of ionospheric ions starts in the dayside at low altitudes (≈300–800 km), ions moving at a low velocity (5–10 km/s) in the direction of the external/ magnetosheath flow. At high altitudes, in the inner magnetosheath and in the central tail, ions may be accelerated up to keV energies. However, the dominating energization and outflow process, applicable for the inner magnetosphere of Mars and Venus, leads to outflow at energies ≈5–20 eV.

The aim of this overview is to analyze ion acceleration processes associated with the outflow and escape of ionospheric ions from Mars and Venus. Qualitatively, ion acceleration may be divided in two categories:

(a) Modest ion acceleration, leading to bulk outflow and/or return flow (circulation).
(b) Acceleration to well over escape velocity, up into the keV range.

In the first category we find a processes denoted "planetary wind", the result of e.g. ambipolar diffusion, wave enhanced planetary wind, and mass-loaded ion pickup. In the second category we find ion pickup, current sheet acceleration, wave acceleration, and parallel electric fields, the latter above Martian crustal magnetic field regions. Both categories involve mass loading. Highly mass-loaded ion energization may lead to a low-velocity bulk flow—A consequence of energy and momentum conservation. It is therefore not self-evident what group, or what processes are connected with the low-energy outflow of ionospheric ions from Mars.

Experimental and theoretical findings on ionospheric ion acceleration and outflow from Mars and Venus are discussed in this report.

Keywords Mars and Venus · Ionospheric ion acceleration · Plasma escape

R. Lundin (✉)
Swedish Institute of Space Physics, Teknikhuset, 90187 Umea, Sweden
e-mail: rickard@irf.se

1 Introduction

Our present understanding of the solar wind interaction with non-magnetized planets have evolved from *in-situ* measurements on space probes orbiting Mars and Venus, for Mars: Phobos-2, Mars Global Surveyor (MGS), and Mars Express (MEX), and for Venus: Pioneer Venus Orbiter (PV and Venus Express (VEX). In analogy with the plasma in the Earth's magnetosphere, magnetized by an intrinsic dipole field, the plasma near non-magnetized planets is also magnetized, but now as a result of the solar wind interaction with the planetary ionosphere. The interaction gives rise to an induced magnetosphere, a notion coined by Alfvén (1953). A contemporary view of the induced magnetosphere is that of a pileup of solar wind magnetic field and shocked plasma on the front side (see e.g. Nagy et al. 2004 for a review). As a result of the solar wind interaction with the planet the solar wind magnetic field lines are draped over the obstacle, while the solar wind plasma maintain a slightly deflected antisunward motion. Behind the obstacle magnetized plasma tail is formed, constituting a mix of escaping planetary plasma and penetrating solar wind plasma. A current sheet maintains the geometry of the elongated plasma tail. From an MHD perspective, Fig. 1a (Nagy et al. 2004), the outer boundary of an induced magnetosphere is the magnetic pileup boundary, MPB, (Zhang et al. 1991; Vignes et al. 2000). Inside the MPB is the magnetic pileup region where solar wind and planetary plasma can intermix. The plasma sheet in Fig. 1a also constitutes a current sheet that maintains the magnetic tail. Figure 1b also display the solar wind interaction with Mars, but now from a planetary plasma perspective based on Phobos-2, MGS and MEX findings. The main difference between Figs. 1a and 1b is related with boundary terminology, MPB versus IMB (Induced Magnetosphere Boundary). The latter relates to planetary plasma outflow boundary, while the former is related with a magnetic boundary. In addition, Fig. 1b depicts a wave-like modulation of the outflow, and "auroral" plasma acceleration (Brain et al. 2006; Lundin et al. 2006a, 2006b) on the nightside above magnetic anomalies (Acuña et al. 1999). Average flow vectors describe the transport of dayside low-velocity ionospheric plasma towards the nightside, and the subsequent ion acceleration in the Plasmasheet and the tail boundaries.

Solar EUV and solar wind forcing have a strong influence on the ionosphere and atmosphere of the non-magnetized planets Mars and Venus. The lack of a strong intrinsic/dipole magnetic field means that the solar wind has relatively easy access to the planetary ionosphere and atmosphere. The induced magnetic field in the magnetic pileup region provide some magnetic shielding, but not sufficient to prohibit solar wind energy and momentum from having direct access to the Martian upper ionosphere (e.g. Lundin et al. 2004; Dubinin et al. 2006b). This leads to scavenging of ionospheric ions from the dayside, over the terminator, and into the nightside/tail, as was first observed on Venus (Brace et al. 1987). Outflow velocities are close to or just above escape velocity, by and large resembling the outflow from a comet (e.g. Gombosi et al. 1996). Planetary ions in the tail and in the magnetosheath are subsequently energized to solar wind velocities at Mars (Dubinin et al. 1993) and Venus (Mihalov and Barnes 1981; Intriligator et al. 1979). The overall solar wind interaction with Venus and Mars is analogous with the solar wind interaction with a comet (Brandt et al. 1997), but there are certainly contrasting elements as noted by Luhmann (1991) and Dubinin et al. (1991).

Atmospheric/ionospheric escape and the long-term consequences of mass loss is a theme of major interest for Mars and Venus. Two main groups of escape processes are discussed in connection with planetary atmospheric mass loss, *thermal escape,* and *non-thermal escape* (e.g. Chassefière et al. 2007). Global escape rates and planetary mass-loss are derived from observational data as well as from theory and simulations. Publications on non-thermal

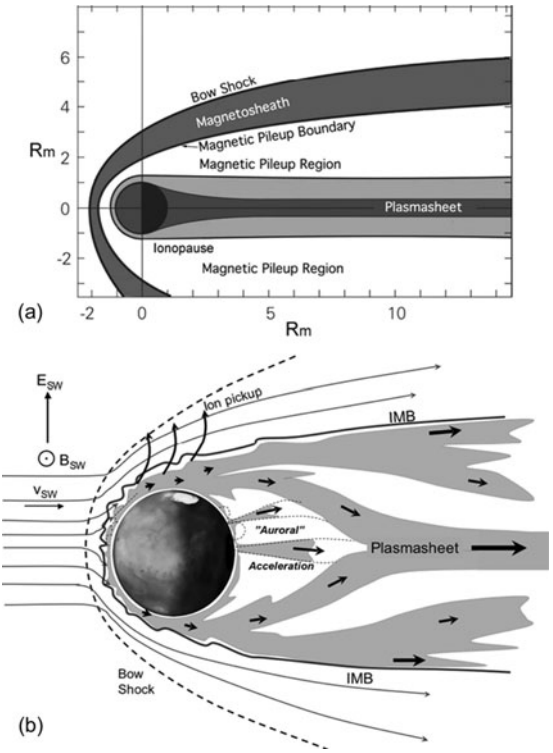

Fig. 1 Solar wind interaction with Mars. (**a**) Structure of the Martian plasma environment based on primarily Phobos-2 and MGS results (Nagy et al. 2004). (**b**) Diagram illustrating the energization and average flow of ionospheric plasma escape based on recent ASPERA3 measurements from Mars Express

plasma escape derived from simulations spans over two decades (Brecht and Ferrante 1991; Brecht et al. 1993; Ma et al. 2002; Kallio and Janhunen 2002; Luhmann et al. 2006; Järvinen et al. 2009; Terada et al. 2009). Simulation results offer large differences in plasma escape rates. On the other hand, neither has observational data offered a clear picture of plasma escape rates. For instance, ion escape rates measured/estimated from Mars may differ by up to two orders of magnitude (e.g. Barabash et al. 2007a; Lundin et al. 1989, 2008a). Venus escape rates inferred from data have also varied (Luhmann and Bauer 1992; Fedorov et al. 2011). To some extent these differences can be understood by solar variability and instrument limitations. Other non-thermal escape processes, such as photochemical-, and sputtering induced escape, are not considered in this overview. These processes are connected with measurement difficulties and great uncertainties.

Solar forcing of the Martian and Venusian atmosphere leads to a gradual erosion of atmospheric atoms and molecules. The net mass loss is directly related with the solar evolution, how solar forcing varies with time. Energization and escape of matter depends on the planetary resilience against solar forcing, where proximity to the Sun, gravity, magnetic shielding, atmospheric composition and the related photochemistry play a role. Despite major differences between Mars and Venus, such as gravity, ground pressure and temperature, and the existence crustal magnetic fields (Mars), the upper atmosphere and ionosphere of today at Mars and Venus display similar properties. Both atmospheres are dominated by CO_2 (95–98%). The upper ionospheres (>300 km) are dominated by ionized oxygen, mainly O^+ for Venus but also O_2^+ for Mars (e.g. Hanson et al. 1977; Nagy et al. 1980; Fox and Hac 2009). Ionized carbon molecules (CO_2^+ and CO^+) are minor species in the upper ionosphere. Hydrogen (protons) displays a more complex altitude distribution. However, a substantial out-

flow of H^+ is observed on both Venus (Barabash et al. 2007c), and Mars (Lundin et al. 2009). Notice that the ion escape from the carbon rich atmospheres of Mars and Venus is dominated by H^+, O^+, and O_2^+ (Mars). Carbon ions (e.g. CO_2^+) constitute less than 10% of the ion escape from Mars, even less than that from Venus. This is perhaps not surprising in view our present understanding the ionospheric ion composition (Nagy et al. 1980; Fox and Hac 2009). The ratio of the escape flux (hydrogen versus oxygen), and the minute carbon ion content implies that the ultimate origin of the escape is water—a minor constituent in the atmosphere of Mars and Venus. Water is apparently a molecule very much prone to escape.

Plasma acceleration is responsible for essentially all of the outflow and escape of ionospheric plasma measured at Mars and Venus. Theoretical modeling and simulations are laden by a number of constraints, the most important one being a scant data basis on in-situ plasma measurements to compare with. A comparison with the well-documented Terrestrial plasma environment has certain limitations; because the ground rooted dipole field magnetizes plasma everywhere near the Earth. Terrestrial analogies are feasible over crustal field regions at Mars, but they introduce instead further large-scale morphological complexity. Until we have access to more detailed in-situ measurement results of particles, fields, and waves, the solar-wind ionosphere coupling at Mars and Venus will continue to be subject of speculations. The level of ionospheric plasma magnetization is an issue, because anisotropic (non-stochastic) plasma acceleration is a magnetized plasma phenomenon. The directional flow of energized ionospheric ions at Mars and Venus therefore suggests magnetic connection to the ionosphere. In this way, there is an analogy with the Earth's magnetized ionosphere, albeit not by an intrinsic dipole field.

Plasma acceleration and escape has been studied in-situ for now some 40 years in the Terrestrial plasma environment, the Earth's ionosphere and magnetosphere. There is a wealth of information available on this topic. For further details, see e.g. the ISSI books by Hultqvist et al. (1999), and Paschmann et al. (2002).

Plasma acceleration may be ordered in separate categories, but from a physics point of view it boils down to the fundamental forces: gravity-, inertia-, and the Coulomb-force. From these we may derive the Lorentz force ($\underline{F}_L = q \cdot (\underline{E} + \underline{v} \times \underline{B})$, the wave/Ponderomotive force (e.g. $\underline{F}_P \propto \underline{\nabla} E^2$), and many other relative forces acting on plasma particles. Six categories of plasma acceleration process, is proposed:

1. Particle-particle interaction—energy and momentum transfer between particles
2. Wave-particle interaction—wave acceleration (ponderomotive forcing)
3. Plasma pressure forcing—ambipolar diffusion—polar wind
4. Field-aligned electric fields—quasi electrostatic
5. Ion pickup—electric drift acceleration
6. Current sheet acceleration—jxB forcing

The first (1) requires collisions, rare in tenuous space plasmas. Nevertheless, conservation of energy and momentum between driver plasma (solar wind) and load plasma (ionosphere) must apply. Instead of direct collisions, indirect collisions may occur via waves and electric fields. The second (2), wave forcing, is a prominent plasma forcing mechanism in the auroral region at the Earth, considered the perhaps most important ion acceleration and escape mechanism. Plasma pressure forcing (3) leads to plasma energy and momentum transfer between neighboring plasma domains, creating for instance the Polar Wind (Banks and Holzer 1968). Magnetic field-aligned quasi-static electric fields (4) were controversial when introduced, but is now recognized as an important acceleration process in auroral physics. Ion-pickup (5) is a widely accepted acceleration process for the plasma of weakly magnetized objects such as Mars, Venus, and comets (e.g. Luhmann and Kozyra 1991; Coates 1991).

It is also a process simple to model and simulate. However, except for in the deep magnetotail, the process is less frequently referred to in the Terrestrial magnetosphere. Finally, acceleration of plasma in/near a current sheet (6) is applied for Earth as well for Mars and Venus. Magnetic reconnection is a process that falls into this category, although the focus is more on global aspects. Finally, mass-loading has a relevance for all acceleration processes discussed. We will return to mass-loading in Chap. 3.

Considering that wave acceleration is such an important mechanism for the outflow and escape of ionospheric plasma at the Earth, this report will focus on wave acceleration at Mars and Venus, a "missing link" in understanding the plasma escape from weakly magnetized planets. Old and new experimental findings from Mars and Venus, will be discussed. Focus will be on data from MEX and VEX, and their context with theoretical considerations regarding energization and escape of ionospheric ions. However, the discoveries from the very first Mars- and Venus missions, such as Mars-2, -3, and -5 (e.g. Gringauz et al. 1976a, 1976b; Vaisberg 1976), Venera-9, and -10 (Vaisberg et al. 1976; Gringauz et al. 1976a), and Pioneer Venus Orbiter, PVO, (e.g. Intriligator et al. 1979; Mihalov and Barnes 1981; Russell et al. 1985; Brace et al. 1987) paved the way for the new discoveries. Moreover, they delivered the environmental constraints required for more in-depth investigations such as MGS, MEX and VEX. The observational data to be discussed in this report are obtained mainly from the ASPERA instruments on MEX and VEX (Barabash et al. 2006, 2007b).

2 Solar Wind Energy and Momentum Transfer

The solar wind energy and momentum transfer may be discussed in the framework of a direct/fluid interaction (Pérez-de Tejada 1987), or as an indirect electric field and wave coupling to the external solar wind/magnetosheath flow. Both ways, a kinetic means may be used to describe acceleration, outflow and escape of a magnetized ionospheric plasma.

Acceleration processes widely discussed at Mars and Venus are e.g. ion pickup by the solar wind motional electric field (e.g. Luhmann and Kozyra 1991), and current sheet acceleration (e.g. Dubinin et al. 1993). Mass loading leads to a local weakening of the motional electric field, and a correspondingly weaker acceleration (Lundin and Dubinin 1992).

Solar wind forcing may be described from general particle kinetics, i.e. conservation of energy and momentum in the interaction between solar wind and ionospheric plasma (e.g. Pérez-de Tejada 1987, 1998). Since the plasma is collisionless, another means of "collisional" energy and momentum transfer is required. Waves produced by the source plasma represent such a means in magnetized plasma. In fact, wave-acceleration represents a major means for the energization and escape of ionospheric plasma from the Earth (e.g. Moore et al. 1999). Wave acceleration has been proposed for ion acceleration at Mars (Ergun et al. 2006) as well. Waves are observed in the shocked solar wind plasma (e.g. Russell et al. 1990, 2006; Brain et al. 2002; Espley et al. 2004; Delva et al. 2008) but also inside the induced magnetospheres of Mars and Venus (e.g. Espley et al. 2004; Winningham et al. 2006; Gunell et al. 2008).

A simple fluid dynamic description of the interaction region above a non-magnetized planet is given in Fig. 2. The solar wind and planetary/ionospheric plasma interaction is expected to take place everywhere inside the MPB/IMB. Ionospheric plasma removal from the dayside involves a comparison between total flux, Φ, through A_M and $A_{\max}$. If some of the dayside ions are recycled, returning back to the planet in the nightside ionosphere, the tail flux through $A_{\max}$ is less than the terminator A_M flux. Ionospheric plasma flow through $A_{\max}$ constitutes the escape rate for non-magnetized planets. Interaction (i.e., transfer of solar wind energy and momentum to the planetary plasma embedded in the flow) is expected

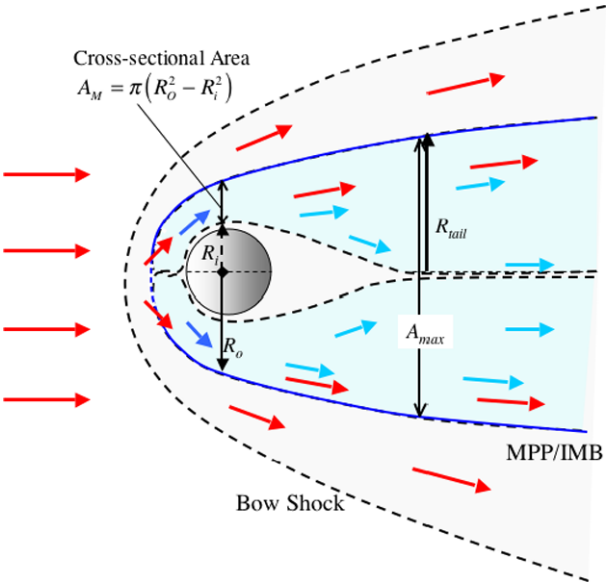

Fig. 2 Diagram of solar wind plasma forcing of a non-magnetized planetary atmosphere/ionosphere. The *cross-sectional area* and depth constitute the region of solar wind energy and momentum transfer. *Blue arrows* illustrate planetary ion escape

to continue until balance in momentum flux is achieved between the solar- and planetary tail plasma. The cross section area A_M ($A_M = \pi(R_o^2 - R_i^2)$) in Fig. 2 may be used as a minimum cross-section area for the solar wind input, by Lundin and Dubinin (1992) obtained from the experimentally determined "mass loading boundary" (R_o) and the altitude of the unperturbed/cold Martian ionosphere (R_i). Notice that momentum balance is not expected to be instantaneous at the cross-section area (A_M). It should be achieved further tailward along a flow channel defined by the cross section areas A_M and $A_{\max}$ (Fig. 2).

Pérez-de Tejada (1987, 1998) derived an expression for the solar wind energy and momentum transfer to the upper atmosphere and ionosphere, valid for most weakly magnetized objects in the solar system. The model is local, but also useful in a global context. From the conservation of energy and momentum in the transfer of energy and momentum flux for the solar wind (Φ_{SW}) and planetary ions (Φ_P) one gets:

$$\Phi_P = \frac{v_{SW} \cdot m_{SW}}{v_P \cdot m_P}\left(\Phi_{SW} - \frac{v_{i,SW}}{v_{SW}}\Phi_{i,SW}\right) \cdot \delta \tag{1}$$

Where $\Phi_{i,SW}$ and $v_{i,SW}$ is the local/decelerated solar wind flux and velocity respectively, and $\delta(0 < \delta \leq 1)$ is the relative momentum exchange thickness, describing the efficiency of the solar wind energy and momentum transfer to planetary ions along the flow channel. If the momentum transfer involves waves, δ may be referred to as a wave-particle coupling function. Equation (1) illustrates that the Martian ion flux is strongly coupled to speed (v_P) and mass (m_P) of the outflowing ions. The ratio between the solar wind velocity and the planetary ions v_{SW}/v_P, provides flux amplification for ions of equal masses, i.e. a low velocity ion escape leads to higher mass loss than a high velocity escape. Figure 3 demonstrates that for Mars the maximum H^+ escape flux for a solar wind velocity of 400 km/s may be amplified by up to 80 times the solar wind flux in the Martian environment ($v_{esc} = 5$ km/s). The corresponding O^+ escape flux may become five times higher than the solar wind flux. Enhanced escape rates for low energy ion outflow is therefore a theoretical consequence. The same applies for Venus, but the higher escape velocity for Venus reduces the maximum amplification factor to 40 for H^+ and 2.5 for O^+ respectively.

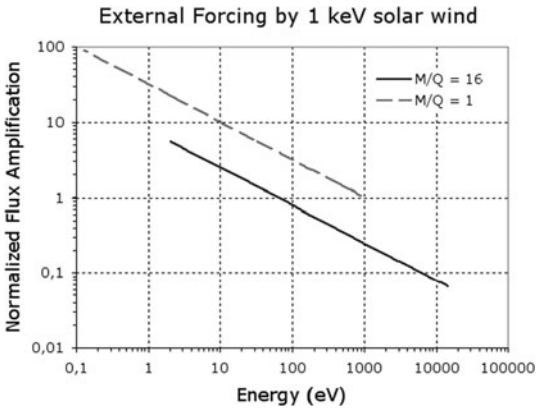

Fig. 3 Normalized momentum exchange by external solar wind forcing, illustrating the amplification of escape flux for O^+ ($m/q = 16$) and H^+ ($m/q = 1$) with decreasing outflow velocity (1)

Using the above model (1), the theoretical mass escape rate from a planet, S_P, can be derived from $S_P = A \cdot m_P \cdot \Phi_P$ (kg/s), where Φ_P is related to the solar wind input (Φ_{SW}) and A is the cross-sectional area for inflow ($A \rightarrow A_m$) and outflow ($A \rightarrow A_{\max}$) respectively. Comparing measured quantities with the model gives the efficiency (δ) of the energy and momentum transfer.

3 Mass-Loaded Ion Energization

A local plasma at rest acts as a load for a moving plasma. Mass loaded ion pickup may be described as an energy and momentum transfer process that leads to differential ion drift. The process can be understood from basic electromagnetic theory of ion momentum transfer in an electric dynamo subject to internal loading (Lundin and Dubinin 1984). The outset is a differential equation derived from Ohm's law for dynamo plasma (solar wind) affecting (accelerating) load plasma. Under the assumption that a dynamo current is driven by plasma inertia, we obtain the differential equation:

$$S_{xy}\sigma(E_y - v_x B_z) = \frac{nm}{B_z}\frac{dv_x}{dt} \tag{2}$$

Where S_{xy} is a spatial parameter, E the (motional) electric field, m the ions mass, B the magnetic field, and σ is a phenomenological conductivity in the interaction region. For an isotropic σ in the interaction region and with planetary/load ions initially at rest, one obtains the following velocity relation between planetary ions (v_P) and solar wind ions (v_{SW}):

$$v_P = v_{SW}\left(1 - \exp\left(-k\frac{n_{SW}m_{SW}}{n_P m_P}\right)\right) \tag{3}$$

Where k is a scalar for the number of gyroperiods. This expression, describing the "internal loading" of an MHD dynamo, shows that a high mass density of planetary ions relative to the injected solar wind ions leads to a low pickup velocity ($v_P \ll v_{SW}$). Conversely, a low mass-density for the boundary layer ions leads to $v_P \approx v_{SW}$, i.e. to test-particle ion pickup (convection). Equation (3) therefore describes the mass loading characteristics of ion pickup.

An experimental verification of the mass-loaded ion pickup process is displayed in Fig. 4 (Lundin and Dubinin 1992). Notice that a high-density ratio between the dynamo plasma

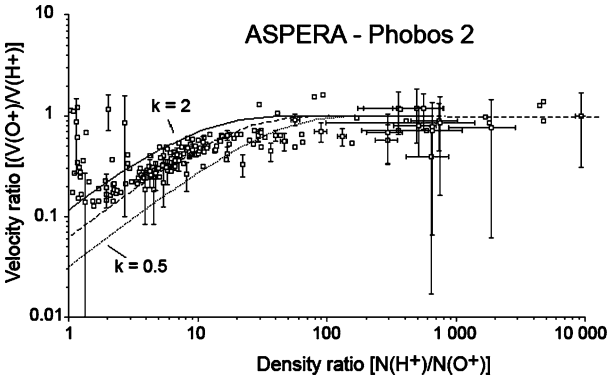

Fig. 4 Momentum exchange between solar wind ions and planetary ions ((2), Lundin and Dubinin 1992)

(solar wind H^+) and the ionospheric (O^+) plasma gives $v_P \approx v_{SW}$. Conversely, low-density ratios (Fig. 4) leads to low velocity ratios, approaching equal energy for H^+ and O^+. The upward turn for low densities was by Lundin and Dubinin (1992) interpreted as a central tail phenomenon, the O^+ ion flow now becoming the source of energy, transferring energy and momentum to cold H^+ ions.

Mass-loaded ion pickup scales with mass-density of individual ion species. A single particle at rest, immersed in convecting plasma, provides a finite (albeit minute) mass loading. This means that an identification of O^+ and H^+ in the Venus tail by PVO (e.g. Mihalov and Barnes 1981), assuming the ions had the same velocity, is less applicable in mass-loaded ion acceleration. A more general characteristic is that different ion species flow at different speed. The ion outflow velocity is certainly mass dependent, but in a more complex way than simple mass-loaded ion pickup can explain (Lundin et al. 2011), in particular at low altitudes and in the nightside wake of the planet.

Energy-time spectra exemplifying the low-energy multispecies ion outflow in the nightside wake of Mars is displayed in Fig. 5. The low energy (<10 eV), and rather cool (1–3 eV) ion outflow extend into the tail, apparently without further acceleration. As noted by Lundin et al. (2008a), low-energy ions dominate the outflow near the planet. This does not imply the lack of ion energization in the tail. On the contrary, there are ample evidences for central-tail/plasma sheet acceleration (e.g. Dubinin et al. 1993, 2006b). However, as will be described in the section on plasma escape, the average outflow velocity near the planet is low. For Mars the trend is a gradual comet-like energization further down the tail. The low-velocity erosion of dayside ionospheric plasma to the nightside at Mars resembles that for Venus, as described by Brace et al. (1987).

Data from the ASPERA-4 ion mass analyzer on VEnus Express (VEX) are in general agreement with the Brace et al. (1987) findings, i.e. a scavenging of low-energy ionospheric ions (H^+ and O^+) from the dayside moving towards the nightside/tail, as illustrated by the noon-midnight pass in Fig. 6. The H^+ and O^+ outflow peak energy increase very little (10–30 eV) up to $X \approx -2\ R_V$. Energetic/pickup (keV) ions are found in the time interval 08:50-09:10 UT, when the spacecraft approaches the IMB and enters the magnetosheath. That time interval is also characterized by an entry of solar wind H^+ to the Venus inner magnetosphere, suggesting that further acceleration of O^+ is associated with solar wind H^+. At the same time MAG-data indicates that VEX traversed the tail current sheet twice. A close inspection shows that B_x changed sign at 08:51 and 08:59 UT. i.e. VEX stayed most of the time in the Northern tail lobe (VSE), accessing the Southern tail lobe during 8 minutes. This is consistent with a current sheet oriented essentially parallel to the ecliptic plane, the solar

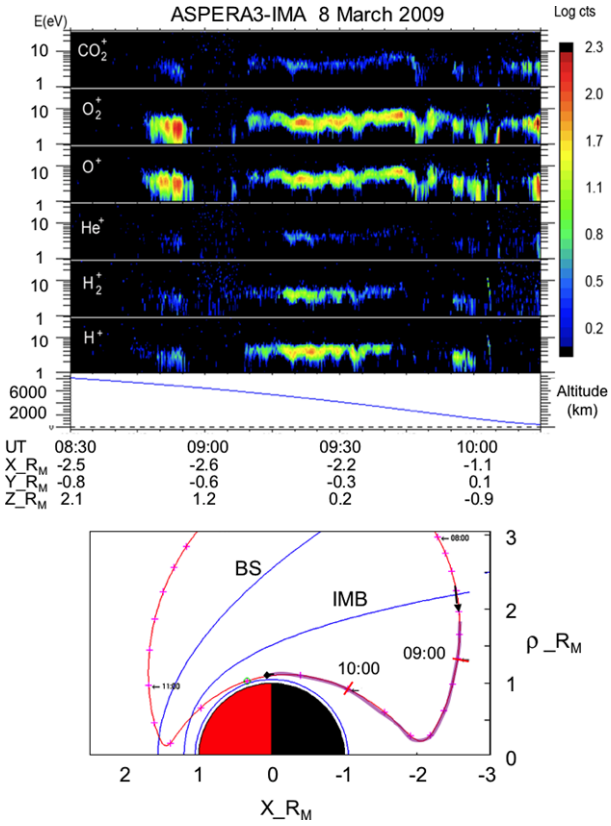

Fig. 5 Energy-time spectrogram of low-energy (<50 eV) ionospheric ion (CO_2^+, O_2^+, O^+, He^+, H_2^+, H^+) outflow from Mars (*top panel*). The MEX orbit in a cylindrical coordinate system is shown in the *bottom panel*. *Bold magenta curve* marks the time period of low-energy ion outflow

wind motional electric field directed towards Y (VSO). Notice that accelerated O^+ occur on primarily the $B_x < 0$ side, with modest acceleration before 08:51, but acceleration up to keV-energies after 08:59. The clear asymmetry of the ion acceleration with respect to the plasma sheet/current sheet may result from a combination of the solar wind motional electric field direction (e.g. Kallio et al. 2006; Järvinen et al. 2009), and a tailward evolving pickup process (e.g. Luhmann et al. 2006). Enhanced solar wind motional electric field towards the magnetospheric boundary (Dubinin et al. 2006a, 2006b) is also consistent with the gradual increased outflow energy. The fact that the acceleration takes place near the current sheet is an argument for current sheet acceleration (e.g. (Dubinin et al. 1993)). Gradually increasing energy for escaping ionospheric ions with distance is also consistent plasma acceleration by waves, as discussed in Sect. 4. Whatever the process, it must be consistent with observations of the ionospheric acceleration and escape from Venus (and Mars)—a gradual energy gain (10–100 eV inside a radial distance of $\approx 2\ R_V$).

In what follows, we will analyze in more detail the characteristics of ion energization and their related acceleration processes. Four panels with energy-mass spectra from the ion mass analyzer (IMA) on MEX in Fig. 7 illustrate the ion energization at Mars to just above escape velocity, i.e. 0.15 eV for H^+, 2.5 eV for O^+, and 5 eV for O_2^+. Energization to equal energy per charge, regardless of mass (e.g. at 06:24 UT) may be interpreted as quasi-electrostatic ion acceleration. An ambipolar electric field driven by the thermal ionospheric plasma pressure and density gradients (e.g. Banks and Holzer 1968) may contribute, but is generally insufficient to raise heavy ions to escape velocities. A negative spacecraft potential, up to

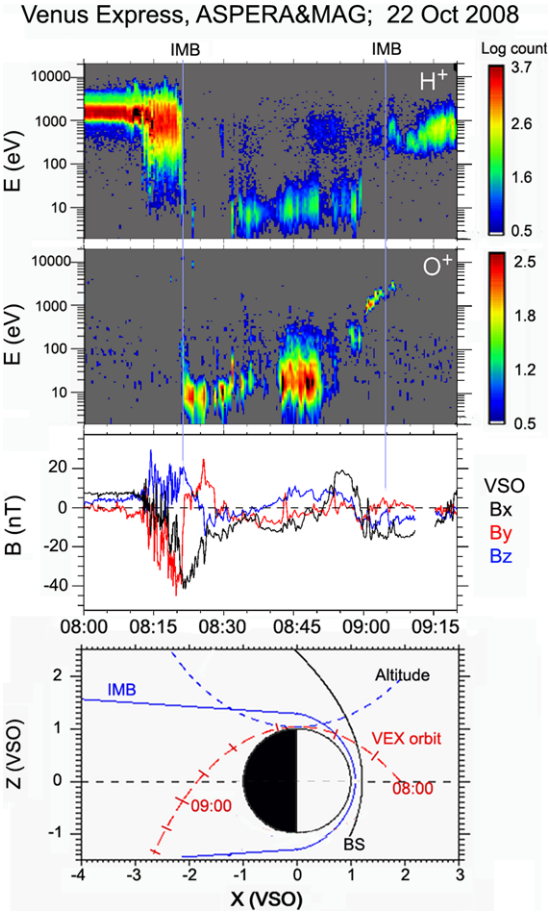

Fig. 6 Energy-time spectrogram of H^+ and O^+, and vector magnetic field components (VSO) from a VEX pericenter pass October 22, 2008. *Vertical blue lines* mark the Induced magnetosphere boundary (IMB). *Bottom panel* display the Venus Express orbit projected onto the *X Z*-plane (VSO). *BS* marks the average Bow Shock

−9 V, plays an important role here in being able to measure cold ionospheric ions. In fact, any electrostatic acceleration in the few eV-range may rather be attributed to an error in determining the spacecraft potential. As for the two middle panels, a mass-dependent acceleration is observed, which is inconsistent with an electrostatic process. We will return to this issue later.

The two flux-energy spectra from another MEX traversal of the upper (≈500 km) ionosphere, displayed in Fig. 8, demonstrate the mass-dependent ion energization in more detail. Notice that the H^+ peak has lowest energy, with heavier ion (H_2^+, He^+, O^+, O_2^+, and CO_2^+) energy peaks increasing with mass. Based on the peak energies it is also clear that the ions are neither accelerated to equal energy, nor to equal velocity. This is consistent with a momentum exchange process under heavy mass loading as described in Fig. 4. However, the spacecraft is now well inside the ionosphere, with no measurable flux of solar wind ions. The ions are therefore subject to acceleration processes coupled indirectly to the external energy source (the solar wind). Downward propagating waves, generated by solar wind/magnetosheath plasma, and/or a corresponding electric field access (solar wind motional emf) are candidates for such an indirect ion energization in the Martian ionosphere.

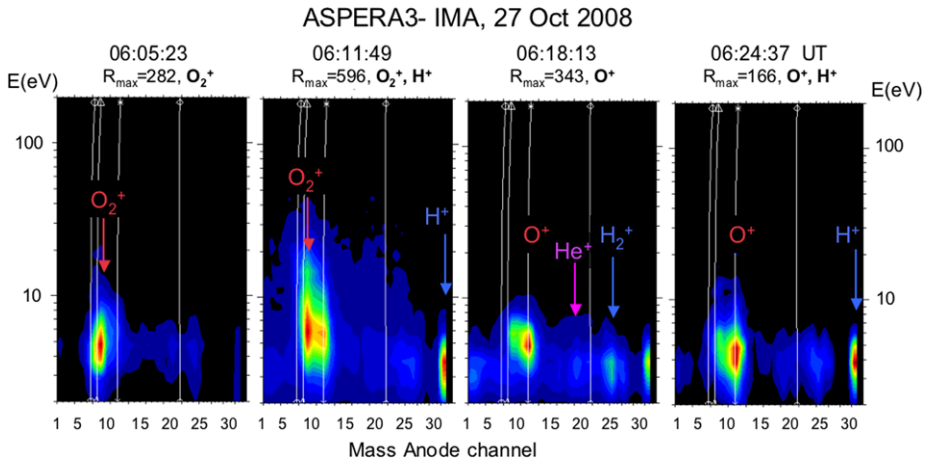

Fig. 7 Four panels with IMA energy-mass anode spectra of ionospheric ions from a Mars Express pericenter pass. Color indicates counts on a linear scale normalized to maximum count ($R_{\max}$) in each panel. *Vertical curves* show the nominal mass lines; from right to left for m/q 4, 16, 32, and 44, respectively. Notice that the actual mass-lines is displaced; light ions to the left, and ions heavier than O^+ slightly to the right. The figure display the gradual mass-dependent ionospheric ion energization

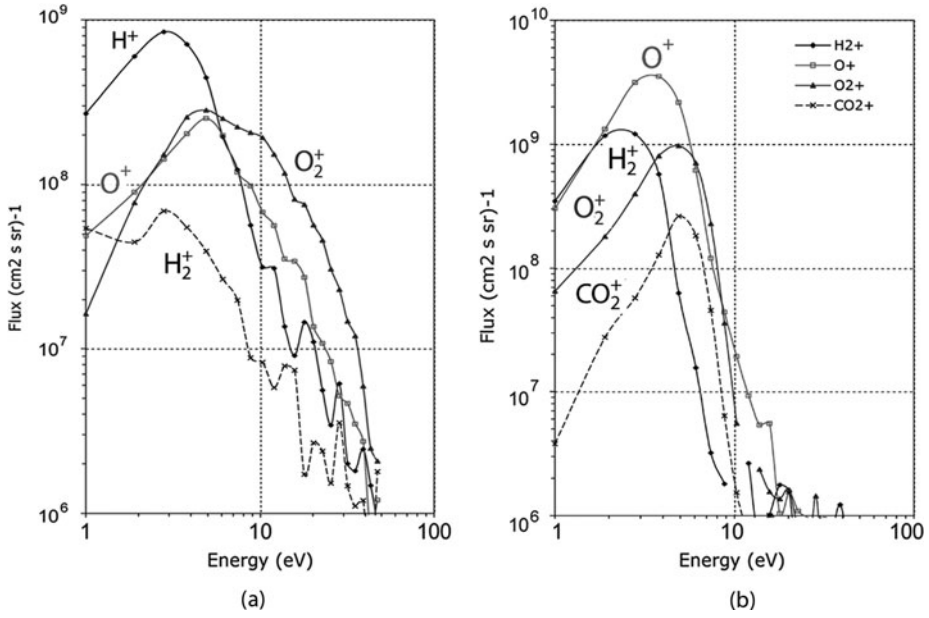

Fig. 8 Two ion energy spectra, displaying the mass dependent energization of the Martian ionospheric ion outflow. Notice that the energy gain increases with increasing mass

As already noted above, the energization and outflow of ionospheric ions from Mars have been subject to detailed analysis using data from Phobos-2, and now recently also from MEX. Conversely, previous ion measurements from Venus did not enable such a detailed analysis like that for Mars. The new IMA ion data obtained by ASPERA-4 on VEX has

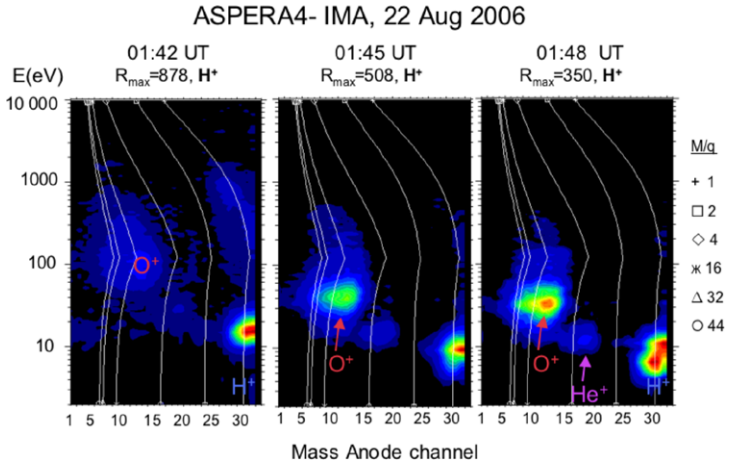

Fig. 9 Three panels with IMA energy-mass spectra of ionospheric ions from a Venus Express approach to pericenter. Color indicates counts on a linear scale normalized to maximum count ($R_{\max}$) in each panel. Bended curves give nominal mass lines; from right to left for m/q 1, 2, 4, 16, 32, and 44, respectively. Notice the slight displacement of the actual mass-lines to the left. The figure displays a consistent mass-dependent ionospheric ion energization

changed that (e.g. Barabash et al. 2007c; Fedorov et al. 2008, 2011; Martinecz et al. 2009). However, concerning ion acceleration processes very little has been published. For this discussion we therefore present some unpublished material from the ion mass analyzer (IMA) on ASPERA-4. These measurements indicate many similarities between ion energization at Mars and Venus.

Figure 9 shows three panels with energy-mass ion spectra from an inbound traversal of the high-altitude ionosphere. The formats of the panels are identical to those in Fig. 7, i.e. it is possible to identify ion species and peak energies. Minor shifts in ion mass peaks versus the mass lines marks differences between nominal and in-flight mass identifications. Data in Fig. 9 was taken in the altitude range 13 000–11 000 km. The plasma contains an admixture of sheath H^+ (100–1500 eV) and ionospheric H^+ (peak $\approx$15 eV) at 01.42 UT. With decreasing altitude the sheath ion flux weakens, and has at 01:48 UT essentially disappeared. A mass dependent ion energization, as described above for Mars, is also apparent here. This kind of energization signature in fact repeats for every orbit. The difference between Figs. 7 and 9 is that Fig. 9 display acceleration in a transition region, from mixed sheath and ionospheric plasma to only ionospheric plasma. The high altitude contact with the sheath (01:42 UT) leads to higher acceleration, but a significant acceleration remains at lower altitudes (01:48 UT). A question regarding the degree of acceleration and the nature of the ion acceleration processes, therefore remains. Does the local existence of sheath ions matter (direct interaction and/or pickup), or is ion acceleration caused by indirect means, a remote transfer of energy and momentum by e.g. electric fields and waves? No doubt a local mix of solar wind- and ionospheric ions plays a role. This is in particular evident from Fig. 7, i.e. pickup ion energies in the keV range are mainly observed in an environment with magnetosheath plasma. On the other hand, ion acceleration without direct contact with plasma of solar wind origin requires some further analysis. In what follows we will discuss waves as an indirect coupling mechanism.

4 Plasma Acceleration by Waves

The interaction between plasma and electrostatic/electromagnetic waves is a topic of major impact in space plasma physics, let alone in fundamental plasma physics. Some fifty years of in-situ measurements demonstrates that plasma waves are a characteristic property of space plasmas. Observations near the Earth, in particular over the auroral and polar region, shows that waves are heavily involved in-, if not dominating, the acceleration and outflow of ionospheric plasma. Plasma waves have also been observed near Mars (e.g. Wang and Nielsen 2002; Espley et al. 2004; Ergun et al. 2006), but lacking simultaneous particle, field, and wave measurements we must rely on theory and a qualitative analysis. The relation between waves and the wavelike modulation of ions and electrons, was considered by Winningham et al. (2006), Gunell et al. (2008) and Lundin et al. (2006b), the latter in an analysis of the auroral plasma acceleration above regions of crustal magnetic field at Mars. The question is therefore to what degree waves may contribute to plasma acceleration and, if so, where the waves are generated and how they access the ionosphere. Wang and Nielsen (2002) reported on what they interpreted as hydrodynamic waves in the topside ionosphere of Mars, i.e. strong electron density modulations reaching down to some 200 km altitude. Similar modulations are reported from ASPERA-MEX data (Lundin et al. 2011), but now interpreted as waves actively involved in ion acceleration.

In the further discussion we assume that the plasma accelerated near Mars and Venus is magnetized. In fact, one may go even further by stating that magnetization is required for collision-less plasma to become steadily accelerated. Wave energization in a collisionless magnetized plasma, is usually based on plasma resonance, specifically gyro-resonance. For instance, ions may be energized by the wave electric field at frequencies near the ion cyclotron frequency, preferentially also by circular polarized waves. An alternative, non-resonant, approach is the theory of ponderomotive forcing. Notice that the ponderomotive force theory is in essence just a way to describe energy and momentum transfer by waves, electrostatic or electromagnetic, in magnetized plasma. The theory includes resonance, but also non-resonant forcing. By non-resonant is meant any frequency outside resonance, from quasi-static to high frequency electric fields.

A ponderomotive force can be defined as an *average* force unique for oscillating fields resulting in an exchange of wave energy and momentum to particles. The theory is quite general and relates to gradients of the wave electric field in time and space. From the general theory (Guglielmi and Lundin 2001) four forces may be derived, but two of them turn out to be most useful, the Magnetic Moment Pumping, MMP, and the Miller force. These two forces boils down to the following simple equation for traveling Alfvén waves at frequencies less than the gyro-frequency:

$$F = -\frac{mc^2}{B^2}\left(\frac{E^2}{B}\frac{\partial B}{\partial z} - \frac{1}{2}\frac{\partial E^2}{\partial z}\right) \tag{4}$$

where E is the wave electric field and B the ambient magnetic field in the plasma. The MMP force is governed by the magnetic field gradient along z (along the magnetic field line), while the Miller force is determined by the gradient (damping) of the wave electric field in the z direction. Under the assumption that E changes slowly with z, we may focus on the first, MMP, term of (4). From the equation of motion and the ponderomotive potential, one may derive the following expression for the velocity, $V(z)$, acquired by wave forcing (Lundin and Gugliemi 2006, equation 2.40)

$$V(z) = \frac{cE}{\sqrt{2}B_0}\left\{\left[\frac{B_0}{B(z)}\right]^2 - 1\right\}^{1/2} \tag{5}$$

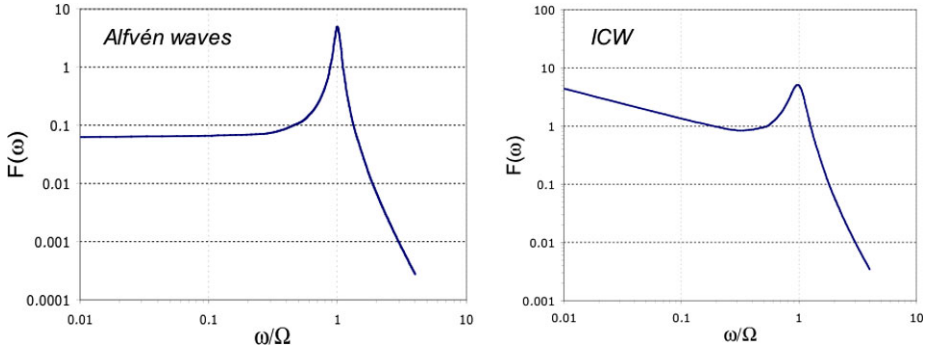

Fig. 10 Frequency dependence of the ponderomotive MMP force for Alfvén waves and ion cyclotron waves, normalized to the ion cyclotron frequency

The velocity increase is described by the convective term (E/B_0), where E is the electric field of the Alfvén wave and B_0 is the initial ambient magnetic field, times the magnetic field gradient $(\approx B_0/B(z))$. While the wave electric field represents the main driver, the magnetic field gradient determines the amplification and direction of the MMP ponderomotive acceleration. Notice that the force is along B, i.e. magnetic field aligned, and provides equal velocity independent of mass below resonance frequency.

Consider now the case of Mars and the solar wind magnetic field pileup on the front side of the obstacle. Magnetic pileup reaches its maximum in the subsolar region, decreases toward the flank and reaches a minimum in the wake and distant flanks of Mars (see e.g. Crider et al. 2004). Taking the average values of normalized $|B|$ from the subsolar/pileup region to the wake/flank, one obtains $B_0/B(tail) \approx 3$. This gives an amplification of the E/B_0 by a factor of $\approx$3, and accordingly also of the ion velocity V. Considering Alfvén waves in the ULF regime (1–20 mHz) near Mars, ponderomotive acceleration therefore enhances the ion velocity by a factor of three above the convective term E/B_0, where the electric field (E) is the most decisive term. For Alfvén waves the velocity increase is proportional to E, while for e.g. low frequency ion cyclotron waves and near resonance the effect of E is greatly enhanced. The frequency dependence of the MMP force for Alfvén waves, using a regularizing "collision" term $\Lambda = (2\nu\omega)^{1/2}$ is given by the following equations (Lundin and Guglielmi 2006):

$$F_Z = -\left(\frac{e^2E^2\Omega^2}{2m}\frac{\partial}{\partial z}\ln B\right)F(\omega) \tag{6}$$

where m and Ω is the ion mass and cyclotron frequency respectively, and

$$F(\omega) = -\frac{1}{(\Omega^2-\omega^2)^2+\Lambda^4}, \tag{7}$$

and $\Lambda = (2\nu\omega)^{1/2}$is a regularizing term here assumed to be due to "collisions".

The MMP force for ion cyclotron waves (ICW) may be derived in a similar way. From the normalized frequency dependence of the MMP force for Alfvén waves and ion cyclotron waves, displayed in Fig. 10, we find a flat response below resonance for Alfvén waves, while for ICW the MMP force increase toward low frequencies. At high frequencies, above resonance, the force goes to zero for both wave modes.

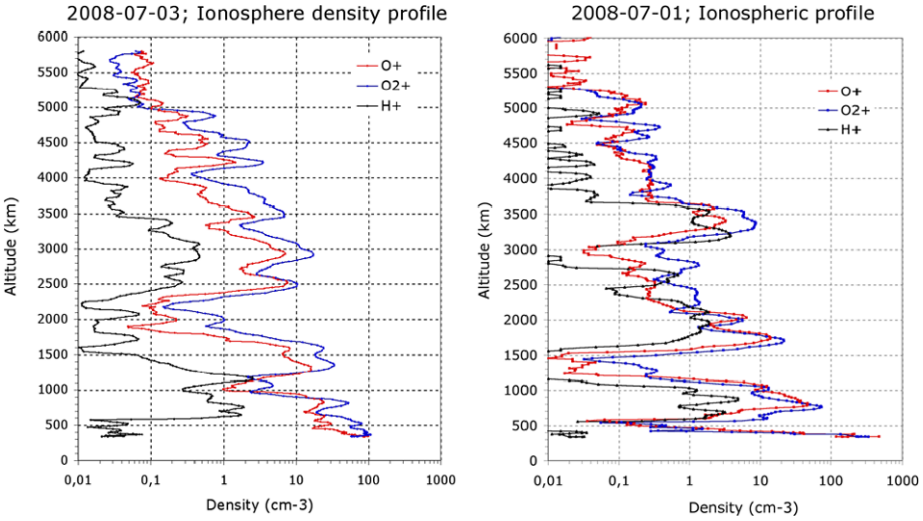

Fig. 11 Mars Express/IMA high time resolution (12 s) ion composition measurements for energies <40 eV, displaying a flank/nightside ionospheric number density height profile. Notice the apparent density striation versus height, which is in reality represents temporal density modulations, and the expansion of ionospheric ions into the tail

Characteristic for the ponderomotive MMP force (and the Miller force) is, that the force not only peaks at resonance, but also maintains high force values at frequencies below resonance. Finally, because the ponderomotive force primarily derives from the wave electric field, it will also be subject to mass loading derived from (2), but now affecting the wave electric field.

Our next task is to identify and characterize waves near Mars and Venus. We focus on Mars, with the most adequate time resolution to detect ULF oscillations in the ion data. Figure 11 shows ion density versus altitude data from two MEX outbound orbits on the nightside of Mars. Densities are computed from 2D distributions obtained every 12 s, for three ion species with energies <40 eV. Because of the 2D coverage, the instrument may miss the ram direction. An order of magnitude or more frequently underestimates the number densities. However, the diagrams are yet useful for ionospheric density profile studies, in particular with regard to the ion composition and the density variability. Two important features stands out in the profiles, the extension of the nightside/flank ionosphere deep into the tail, and the strong density variability. The density variations may also be species dependent. The question is, are the variations temporal or spatial? Plotting densities with time instead of in space/altitude, we find that the densities are modulated persistently in the 3–20 mHz range. This explains the short-range variability at low altitudes, MEX spending a longer time within a given altitude range near pericenter. Considering that the spacecraft near pericenter covers an in-orbit range of about 200–600 km during one wave cycle, with no obvious Doppler shift of the density modulation, implies that modulations below 1 mHz probably represent traversals of large-scale structures. However, the existence of narrow band features in the wavelet spectrum at frequencies above 3–5 mHz suggests temporal oscillations. Moreover, remote sensing of modulated fluxes of energetic neutral atoms (Futaana et al. 2006) suggest that ULF modulations may even be a global phenomenon. Obvious questions are therefore, what causes large-scale modulations of the Martian ionosphere, and what are the implications?

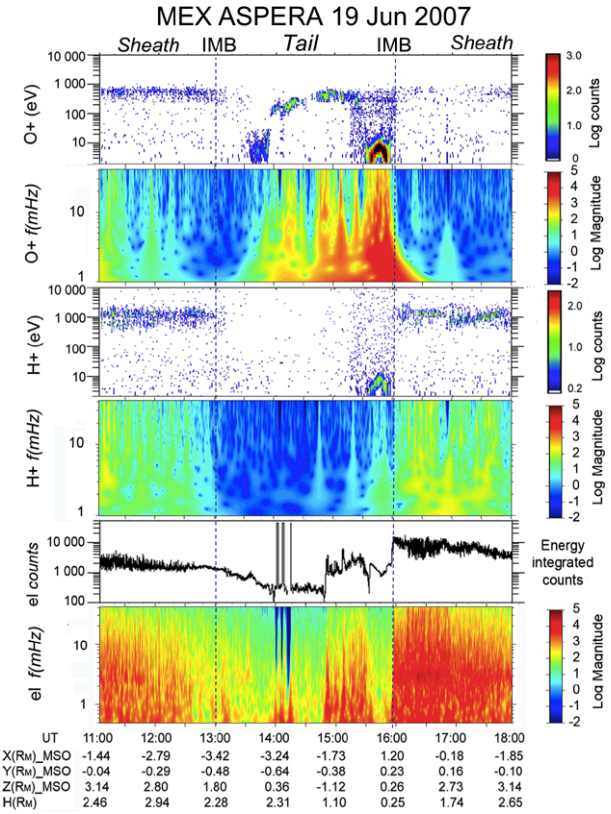

Fig. 12 Energy-time spectra for O^+ and H^+ (panels 1 and 3), energy-sweep intergrated counts for electrons (panel 5), and their corresponding frequency-time wavelet spectra. Data was taken from a noon-midnight pass on June 19, 2007. IMB marks the induced magnetosphere boundary. Wavelet spectra for O^+, H^+ and electrons were obtained from energy-sweep accumulated counts. From Lundin et al. (2011)

To answer these questions, we have analyzed ion and electron modulations during entire passes of the Martian plasma environment, from the solar wind to the ionosphere. Lacking electric-, magnetic field-, and wave data, we can only refer to the ULF modulations, as plasma oscillations.

Figure 12 display ion and electron data from a MEX orbit close to the noon-midnight meridian (from Lundin et al. 2011). The spacecraft passes from the nightside sheath through the inner magnetosphere/ionosphere, and out into the dayside sheath. The first and third panel give energy-time spectra of ionospheric O^+ ions with 12 s time resolutions. The fifth panel shows energy-integrated counts of electrons with 1 s time resolution. Wavelet analysis is performed for energy-integrated counts of O^+ (<50 eV), H^+ (>10 eV), and electrons (>20 eV). The power of the wavelet oscillations (panels 2, 4, and 6) is given in arbitrary units, representing the magnitude ($W(f,t)$) of particle oscillations. We note that the wavelet spectra of O^+ in the frequency range 1–40 mHz bears certain similarities with the sheath H^+ and electron wavelet spectra, such as a temporarily variable broad-band noise and resonant features in the 2–5 mHz range. The sheer magnitude of the oscillation, and their overall similarity, indicates that the magnetosheath must be the source of the waves inside the magnetosphere. In fact, all orbits analyzed by wavelet methods, display the same pattern with modulations in the abovementioned frequency regime. The question is, how do waves access the inner magnetosphere of Mars, and what impact do they have on the planetary/ionospheric plasma?

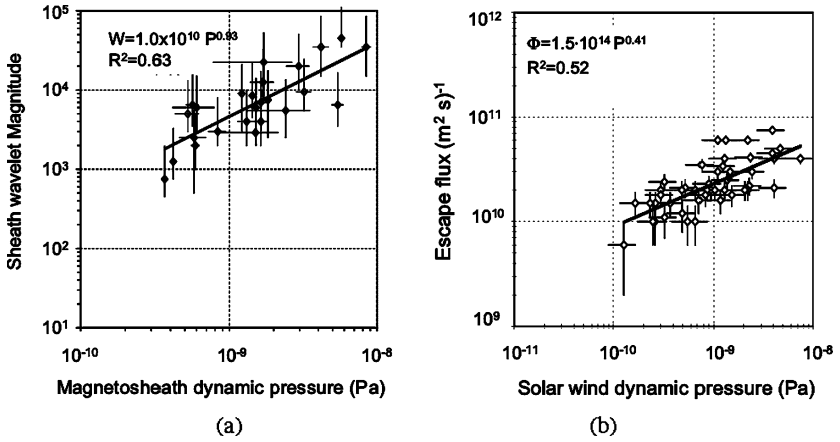

Fig. 13 Magnetosheath wavelet power, and average escape flux plotted versus solar wind dynamic pressure: (**a**) Average magnetosheath wave power plotted against magnetosheath dynamic pressure (after Lundin et al. 2011). (**b**) Average ion escape flux in the Martian tail, normalized to the effective tail cross section, plotted against solar wind dynamic pressure (after Lundin et al. 2008b)

A more detailed analysis shows that ions and electrons oscillate simultaneously. The modulations for different species are, however, not necessarily phased (Fig. 11), but the sheer magnitude of the density oscillations indicates magnetized plasma oscillations, i.e. MHD waves A more detailed analysis of the plasma oscillations is certainly required to understand the type of waves responsible for the particle oscillations. Above all, electric and magnetic field data is required for such an analysis. The question is now, what other implications do the ULF waves have on ionospheric plasma, besides leading to density fluctuations? How deep into the tail can ULF waves propagate? To what extent are these waves involved in the acceleration of ionospheric plasma?

The mass-dependent energization of ions illustrated in Figs. 7 and 9 illustrates a gradual mass-dependent energization in the lower ionosphere from a background/cold distribution. At such low altitudes, a mass-dependent energization by the solar wind electric field motional emf is less likely. Moreover, there is in the case of Fig. 7a net tailward flow of heavy ions in this time interval with velocity 5–6 km/s with minor differentiation with respect to mass (06:24 UT). It is doubtful whether such velocities for O^+ and O_2^+ can be explained by ambipolar electric fields caused by escaping electrons (e.g. Soobiah et al. 2006), considering the voltage required for O_2^+ escape. However, the most important argument against ambipolar outflow of heavy ions is that the heaviest element has the highest peak energy (Figs. 7, 8, 9). On the other hand, heavy ion acceleration to 5–6 km/s velocities can be achieved by a ponderomotive wave enhanced "polar wind" (Guglielmi and Lundin 2001). Ponderomotive wave acceleration is consistent with the velocity dependent ion energization observed.

Having established the connection between ULF oscillations in the magnetosheath ULF oscillations deep down in the ionosphere, the question remains about the cause of ULF oscillations in the magnetosheath, and to what extent they are involved in the acceleration of ionospheric ions. The Bow Shock is the boundary within which intense magnetosheath wave activity initiates. An intense wave activity then stays within the entire dayside magnetosheath. The solar wind energy flux, or the dynamic pressure, is solar wind parameters important for wave generation. A comparison between wavelet intensities at 10–20 mHz from electrons in the magnetosheath (Lundin et al. 2011) give a positive correlation between

ULF wave activity and solar wind dynamic pressure, i.e. enhanced solar wind dynamic pressure leads to enhanced wave activity. In relation to this we note the relation between solar wind dynamic pressure and ion escape from Mars (Lundin et al. 2008b; Edberg et al. 2010), i.e. there is a positive correlation between ion outflow and solar wind dynamic pressure. The fact that both ion escape and magnetosheath ULF activity correlates with solar wind dynamic pressure does not in itself prove a physical connection. However, Alfvén waves generated in the dayside magnetosheath represent an adequate energy source for the acceleration of ionospheric ion at the Earth (e.g. Chaston 2005). In a similar manner, penetrating magnetosheath waves should be involved in the acceleration and outflow of ionospheric ions at Mars (Lundin et al. 2011). Two graphs relevant to the abovementioned hypothesis is displayed in Fig. 13. Figure 13a shows the wavelet intensity, M, versus solar wind dynamic pressure (Lundin et al. 2011), and Fig. 13b the ion escape flux versus solar wind dynamic pressure (after Lundin et al. 2008a, 2008b). Notice that Figs. 13a and 13b were obtained from two different data sets. This means that only a qualitative relation between wavelet magnitude and ion escape rates can be derived, using the least-square fitted curves. From Figs. 13a and 13b, we now derive the relation between escape flux, Φ, and wave intensity, M:

$$\Phi = 1.1 \times 10^9 \exp(\ln M \times 0.355)\ (\mathrm{m^2\ s})^{-1}$$

Using the above expression, one finds that two orders of magnitude change of wavelet magnitude (M) give one order of magnitude change of ion escape flux. Notice that lacking adequate wave instruments on MEX, we may only refer to the magnitude/ power of the plasma oscillations in relative units rather than in physical units. However, it is yet clear that solar wind dynamic pressure changes leads to changes of the magnetosheath wave activity as well as of the ionospheric ion escape flux from Mars.

5 Plasma Escape from Mars and Venus

As indicated in the Fig. 1b, the outflow leading to escape is due to different processes, ion pickup, mass-loaded ion pickup (streaming along the external sheath flow), tail current sheet acceleration, and on Mars upward acceleration above magnetic anomalies (auroral acceleration). To this should be added scavenging of cold/low energy ions from the dayside, subsequently moving into the tail. This applies to both Mars and Venus (e.g. Lundin et al. 2008a; Brace et al. 1987), but with some differences, as noted below. To illustrate the symmetric scavenging of cold plasma from Mars we have in Fig. 14 plotted the distribution of average fluxes and flow velocities of low energy (<200 eV) O^+ ions in the Mars rest frame. A conical ρZ coordinate system is used, $+Z$ representing ecliptic North, the ordinate, $\rho = \pm\sqrt{X^2 + Y^2}$ (the sign from Y) giving the distance from the planet. The panels in Fig. 14 illustrate two important findings: (1) The O^+ flux is more or less axi-symmetric. (2) The velocity distribution is also axi-symmetric near the planet, and generally below 10 km/s at altitudes up to 1500 km. Figure 14 therefore demonstrates that the average low-altitude, low-energy ion outflow from Mars is effectively axi-symmetric.

The ion outflow from Mars is summarized in Fig. 15, the upper panel showing the tailward flux of <200 eV heavy ions (O^+ and O_2^+) within 500 × 500 km quadrants, plotted in a cylindrical coordinate system (after Lundin et al. 2008a). The panel below display escape rates of heavy ions <200 eV and >200 eV, near the terminator (A1 in Fig. 2), at $X = -1.5\ R_M$, and at $X = -2.7\ R_M$. Escape rates were derived assuming an axi-symmetric

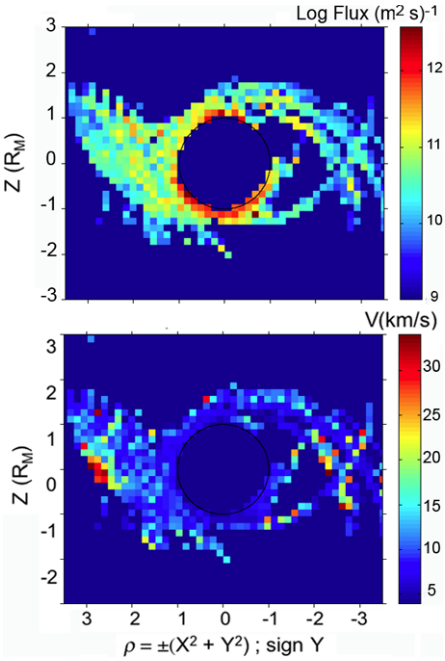

Fig. 14 Low energy (<200 eV) flux and velocity distribution of O^+ at Mars, averaged in 500 × 500 km quadrants, and plotted in a conical Solar oriented coordinate system (MSO). ρ marks the distance from the planet in XY, maintaining the sign of Y. (**a**) O^+ flux averaged in 500 × 500 km quadrants and projected onto the ρZ plane. (**b**) O^+ average tailward flow velocities projected onto the ρZ plane. Notice the low velocities (<10 km/s) near the planet

distribution in the YZ-plane. Notice the gradual tailward change from low energy to high-energy ion escape rates. Near the planet, low-energy ions dominates completely, while a cross-over to energetic ions (>200 eV) is reached at about $X \approx -3\ R_M$. The characteristic is similar to the plasma tail of a comet, i.e. a gradual energization, from low velocities (few km/s, Gombosi et al. 1996) near the comet, to high (solar wind) velocities in the distant tail (Brandt et al. 1997). In this respect, the ion outflow and escape from Mars is comet-like—a dayside erosion of ionospheric plasma, moving antisunward and forming a comet-like tail. The mass-loss by non-thermal escape depends on the dynamic solar wind input, and atmospheric ionization processes, such as solar EUV, charge exchange, and electron impact. The escape rate from Mars depends on the solar wind dynamic pressure (Lundin et al. 2008b; Edberg et al. 2010), and to some extent also solar EUV (Lundin et al. 2008a, 2008b; Nilsson et al. 2010).

The atmospheric evolution in relation to ionospheric plasma escape from Venus has also been subject of interesting discussions in contemporary planetology. PVO provided measurement results of the ion escape from Venus (see e.g. Luhmann et al. 2006). However, lacking energetic ion mass analyzer on PVO, these measurements provided an incomplete picture of the outflow/escape of ionospheric plasma. The cold ionospheric ion outflow observed by Brace et al. (1987) indicated a filamentary tailward draping of the Venus ionosphere, and a loss of cold ionospheric plasma. The minimum escape rate of cold ionospheric outflow, inferred by Brace et al. (1982), was $\approx 5 \times 10^{25}\ s^{-1}$. Results from the ion mass analyzer (IMA) on Venus Express (VEX) corroborate the tailward expansion of low-energy ionospheric plasma at Venus. With IMA we may now analyze the composition, energy, and angular distribution of the ion outflow from Venus. For instance, the ionospheric ion outflow comprises mainly H^+ and O^+, in a stoichiometric ratio 2:1 (Barabash et al. 2007c), suggesting that the ultimate origin of the ion escape is water.

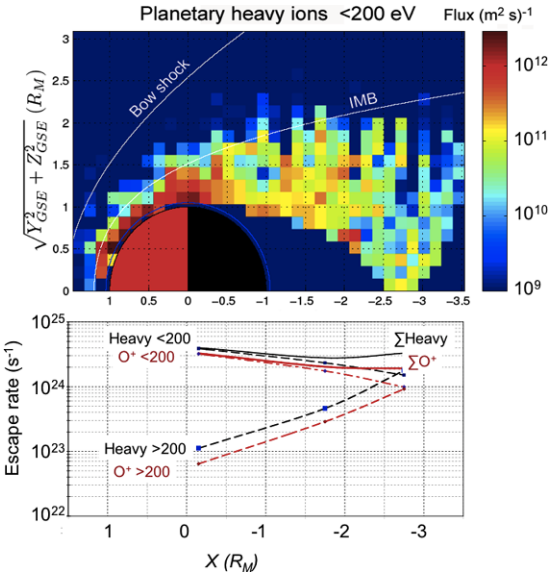

Fig. 15 *Upper panel*: Low-energy (<200 eV) planetary heavy ion (O^+, O_2^+, CO_2^+) fluxes near Mars. Color scale represents average fluxes in the 500 × 500 km quadrants. *Lower panel*: Ionospheric escape rates derived for two different energy ranges (<200 eV; >200 eV) at different distances along X (Mars-Sun line)

The VEX orbital coverage impose some global measurement restrictions. They include no access to the subsolar region, and a partial North-South hemisphere coverage. With a polar orbit, the pericenter located near the North Pole, certain assumptions have to be made. One working assumptions is to introduce the Venus Solar Electric (VSE) coordinate system. The VSE-system creates a new asymmetry with regard to North-South. VSE North is determined by the direction of the solar wind motional electric field E_{SW}, positive E_{SW} defining "North" (Z positive) in VSE coordinates. Because E_{SW} depends on the direction of the interplanetary magnetic field (IMF), it may in principle point in any direction perpendicular to the planet-Sun line. Ion data organized in the VSE coordinate system introduces a new asymmetry, with the result that VSE "North" and "South" is covered by VEX. However, this is not the case in the ecliptic coordinate system, the Venus Solar Oriented (VSO) system. Barabash et al. (2007c) and Fedorov et al. (2011) presented the first results on the ion outflow from Venus in VSE system, the latter offering the first results on escape rates of H^+, He^+, and O^+ from Venus.

The VSE coordinate system takes preference not only on the morphology of the solar wind interaction with Venus, but also with regard to the ionospheric ion acceleration processes, the ion pickup process (see e.g. Luhmann et al. 2006; Russell et al. 2006; Kallio et al. 2006; Järvinen et al. 2009). The ionospheric ion acceleration and outflow follow a distinct "North-South" asymmetry (VSE). Ion pickup is certainly an important process at Mars and Venus, but as mentioned in the introduction, and in relation to the low-energy outflow from Mars (e.g. wave-acceleration), ion pickup represents but one of several optional ion acceleration processes. Another option is wave acceleration. Because waves are essentially omnipresent in the magnetosheath, encompassing the induced magnetosphere, wave penetration and wave acceleration should be distributed axi-symmetric around the X-axis in induced magnetospheres. Assuming an axi-symmetric low-energy ion escape like for Mars, data may be organized and analyzed in cylindrical VSO coordinates ($\rho = \sqrt{Y^2 + Z^2}$). Figure 16 displays the outflow morphology of O^+ ions from Venus in such a cylindrical coordinate system. Lower panel shows the O^+ flux in 1000 × 1000 km quadrants, the upper panel depicting O^+ velocity vectors. Notice that the O^+ fluxes are somewhat higher

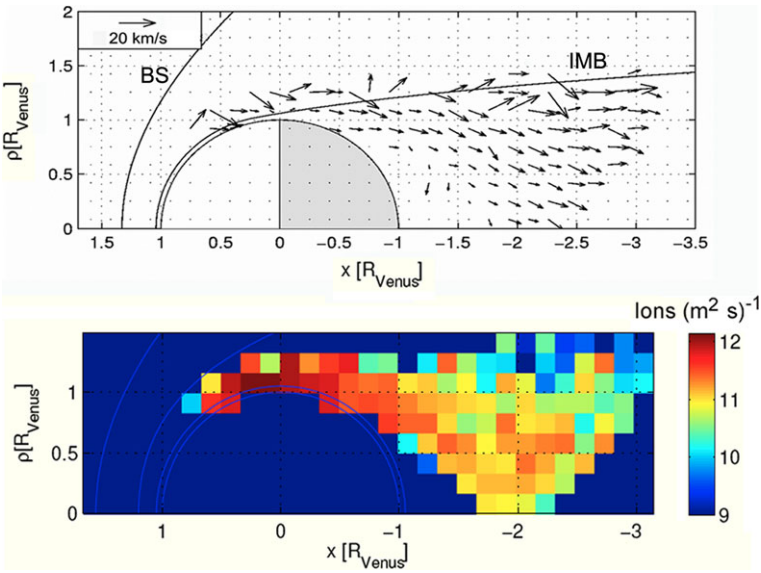

Fig. 16 Venus O^+ with energies <300 eV. Data from 390 orbits are binned in quadrant sizes 1000 × 1000 km, the average values subsequently plotted in a cylindrical coordinate system ($\rho = (Y^2 + Z^2)^{-1/2}$). *Upper panel* show velocity vectors in the Venus rest frame, the longest arrow corresponding to about 20 km/s. *Lower panel* display average O^+ fluxes within each pixel. Notice the existence of back-streaming O^+ in the inner tail

for Venus compared to Mars. However, as the velocity vector diagram shows, the outflow is also more complex on Venus. We find a turbulent flow with an eddy in the nightside/tail. A sunward/return flow may be observed near the nightside central tail. The turbulence/ return flow breaks at $X \approx -2\ R_V$. Beyond $-2\ R_V$, the flow is persistently tailward.

The ionospheric ion escape rates derived using the VSE coordinate system are according to Fedorov et al. (2011): $\Phi(O^+) = 2.7 \times 10^{24}\ s^{-1}$; $\Phi(H^+) = 7.1 \times 10^{24}\ s^{-1}$. These rates were derived from 114 (out 540) orbits from June 2006 to December 2007. As already noted, there are arguments for an axi-symmetric outflow of low-energy ions, i.e. to derive the ionospheric plasma escape rate, one might as well project flux data in VSO cylindrical coordinates. The escape rates for O^+ and H^+ ions less that 300 eV are here derived from 390 (out of 1100) VEX orbits from June 2006 to June 2009. Tailward fluxes are averaged in 1000 × 1000 km quadrants as shown in Fig. 16. The escape rates are: $\Phi(O^+) = 1.2 \times 10^{25}\ s^{-1}$; $\Phi(H^+) = 3.9 \times 10^{25}\ s^{-1}$. This is a factor of four higher O^+ escape rate compared to the Fedorov et al. (2011) values, yet four times lower that the cold O^+ escape estimated by Brace et al. (1982). The main reason for the different escape rates in the VEX data probably rests in the difference in methodologies used, the VSE versus the VSO coordinate system. The latter also relates to preferences in ion acceleration processes, ion pickup versus wave acceleration. It would lead too far to analyze differences in escape rates any further here. We simply conclude that the two methods used to determine the Venus ionospheric O^+ escape rate is in the range ≈ 0.3–$1 \times 10^{25}\ s^{-1}$, i.e. in the range estimated for pickup escape from PVO (Luhmann et al. 2006), the latter in agreement with simulations (e.g. Järvinen et al. 2009), but well below the cold ion escape rates inferred by Brace et al. (1982).

6 Discussions and Conclusions

Energization and escape of ionized atoms and molecules from the atmosphere on Mars and Venus, the consequence of solar wind and solar EUV forcing, has become an issue in contemporary planetology, with implications on theories regarding the evolution of planetary atmospheres and hydrospheres. While light atoms, such as hydrogen, can more easily escape from a planet by thermal processes (e.g. hydrodynamic escape), thermal escape processes are inefficient for heavier atoms and molecules. Removing e.g. oxygen and nitrogen requires more powerful energization mechanisms. Electromagnetic forcing and acceleration of ionized heavy atoms and molecules, is an effective way to remove heavy atoms and molecules from comets and the terrestrial planets. In fact, the escape of accelerated heavy ions, primarily O^+, dominates the atmospheric mass loss from Earth, Mars and Venus. Ion composition measurements from Earth (e.g. Yau et al. 1988), Venus (e.g. Barabash et al. 2007c), and Mars (e.g. Barabash et al. 2007a; Lundin et al. 2009), indicates that H^+, O^+, and for Mars also O_2^+, dominates the planetary ion escape. For Mars and Venus this may seem enigmatic, considering that their atmospheres are completely dominated by CO_2, water being a minor atmospheric constituent. However, the composition of the ion outflow simply reflects the ion composition of the upper ionosphere at Venus and Mars (e.g. Taylor et al. 1980; Fox and Hac 2009). With water as the ultimate origin of planetary ion escape, it follows that water is the molecule most prone to escape from the terrestrial planets.

The above said should be put in context with the "Sun in time", the solar evolution (e.g. Wood et al. 2002, 2005; Ribas et al. 2005; Güdel 2007). The terrestrial planets, in particular Venus and Mars, must have experienced a dramatic period under the young Sun (e.g. Lundin et al. 2007). Plasma escape may have contributed greatly to the loss of hydrosphere at Venus (Kulikov et al. 2006)), with Mars loosing most of the water that modified its surface in the past (Carr and Head 1996).

Loss of water does not necessarily require non-thermal escape, e.g. plasma escape. Hydrodynamic escape is capable of removing massive amounts of hydrogen (e.g. Chassfiére 1996), while oxygen can remain on the planet as minerals (oxides) (e.g. Lammer et al. 2003). However, the fact that the loss of H^+ and O^+ is close to the stoichiometric 2:1 ratio (Barabash et al. 2007c; Lundin et al. 2009) implies that plasma escape is an efficient loss process for all ion species subject to direct or indirect solar wind forcing.

The exchange of momentum between solar wind and planetary ions implies that the escape flux of planetary ions increases with decreasing outflow velocity. Acceleration processes leading to low-velocity ion escape therefore governs the most efficient mass loss. In fact, the outflow of low-velocity heavy ions dominates the primary escape from Venus and Mars. This implies that the primary energization process is quite efficient in favoring mass removal instead of ion speed. High velocity pickup is preferentially taking place in the deep tail and in the sheath/solar wind.

Mass-loaded ion pickup by the solar wind motional electric field is also consistent with the low-speed removal of planetary ions. A characteristic feature of mass-loaded ion pickup is that ions of different masses are subject to a mass-dependent acceleration versus energy. Mass-loaded acceleration also differs from single particle ion pickup in that the accelerated ions flow along the external (sheath) flow, which is consistent with observations. Mass-loaded ion pickup is therefore a feasible process that can explain the multitude of speeds acquired by planetary ions.

Similar arguments in favor for mass-loaded ion pickup also apply for wave acceleration. According to the theory of ponderomotive forcing, ponderomotive acceleration is effective over a broad frequency range below resonance. Acceleration of planetary ions is expected to

continue along the wave propagation direction, i.e. tailward and along the external (sheath) flow. The characteristics of ponderomotive acceleration are in many respects similar to the mass-loaded ion pickup process. Ions are ideally accelerated to the same speed, regardless of mass. Mass loading applies to ponderomotive acceleration as well, but in this case to the wave electric field instead of the (solar wind) motional electric field. The main difference is that mass-loaded pickup ions, like solar wind ions, is expected to move/convect at an angle with respect to B, while for wave acceleration by ponderomotive MMP ions move along magnetic field-lines. Acceleration and escape by ion pickup in the solar wind motional electric field, is best described in the VSE coordinate system. Conversely, for wave acceleration driven by penetrating ULF waves from the dayside magnetosheath of Mars, an axisymmetric (cylindrical) coordinate system may be applied to describe acceleration and escape. We note that the low-energy ion outflow from Mars and Venus (Brace and Kliore 1990) initiates in the dayside ionosphere. The ion outflow is characterized by strong ULF ion density oscillations, observed also deep in the ionosphere. The similarity in wavelet spectra between magnetosheath ion/electron oscillations and the accelerated ionospheric ion oscillations, suggests that waves from the magnetosheath are omnipresent in the induced magnetospheres of Mars and Venus.

In conclusions, the acceleration and escape of planetary ions from Mars and Venus may be described by a *local/direct* solar wind/magnetosheath energy and momentum transfer to planetary ions (by local electric fields and waves), and an *indirect* transfer of solar wind/magnetosheath energy and momentum, whereby waves and electric fields can penetrate deep into the planetary ionosphere. In both cases, mass loading leads to low outflow velocity and enhanced mass loss. In this report focus have been on processes that lead to the low velocity ion outflow observed at Mars and Venus, i.e. mass-loaded ion pickup, and wave acceleration. A third process, pressure induced ambipolar diffusion may act as a cooperative primary "lifting" force, but it cannot explain the observational characteristics of the heavy ion outflow at Mars and Venus.

Acknowledgements ASPERA-3 and ASPERA-4 on ESA's Mars Express and Venus Express is a joint effort between 15 laboratories in 10 countries. We are indebted to the national agencies, e.g. the Swedish National Space Board, CNRS in France, and NASA (contract # NASW00003), for supporting ASPERA-3, and to the European Space Agency for making MEX a great success. The author acknowledges the support of EUROPLANET RI project (Grant agreement No. 228319) funded by EU; and also the support of the International Space Science Institute (Bern). Finally, the author wants to express his deep appreciation to Pär-Ola Nilsson, Leif Kalla, Jan Karlsson, and Emmanuel Penou for providing software support and excellent data analysis tools.

References

M.H. Acuña et al., Magnetic field and plasma observations at Mars: initial results of the Mars Global Surveyor mission. Science **279**, 1676 (1999)

H. Alfvén, *On the Origin of the Solar System* (Oxford University Press, London, 1953)

P.M. Banks, T.E. Holzer, The polar wind. J. Geophys. Res. **73**, 6846 (1968)

S. Barabash, R. Lundin, H. Andersson, K. Brinkfeldt et al., The Analyzer of Space Plasmas and Energetic Atoms (ASPERA-3) for the Mars Express Mission. Space Sci. Rev. **126**(1–4), 113–164 (2006)

S. Barabash, J.-A. Sauvaud, and the ASPERA-4 Team, The analyzer of space plasmas and energetic atoms (ASPERA-4) for the Venus Express Mission. Planet. Space Sci. **55**(12), 1772–1792 (2007a)

S. Barabash, A. Fedorov, R. Lundin, J.-A. Sauvaud, Martian atmospheric erosion rates. Science **315**, 501–503 (2007b)

S. Barabash, A. Fedorov, J.J. Sauvaud, R. Lundin, C.T. Russell, Y. Futaana, T.L. Zhang, H. Andersson, K. Brinkfeldt, A. Grigoriev, M. Holmström, M. Yamauchi et al., The loss of ions from Venus through the plasma wake. Nature **450**, 770, 650–653 (2007c). doi:10.038/nature06434

D.A. Brain, F. Bagenal, M.H. Acuña, J.E.P. Connerney, D.H. Crider, C. Mazelle, D.L. Mitchell, N.F. Ness, Observations of low-frequency electromagnetic plasma waves upstream from the Martian shock. J. Geophys. Res. **107**(A6), SMP 9-1 (2002). doi:10.1029/2000JA000416
D.A. Brain, J.S. Halekas, L.M. Peticolas, R.P. Lin, J.G. Luhmann, D.L. Mitchell, G.T. Delory, S.W. Bougher, M.H. Acuña, H. Rème, Geophys Res Lett, 33(1) (2006). doi:10.1029/2005GL024782
J.C. Brandt, Y. Yi, C.C. Petersen, M. Snow, Comet de Vico (122P) and latitude variations of plasma phenomena. Planet. Space Sci. **45**, 813–819 (1997)
S.H. Brecht, J.R. Ferrante, Global hybrid simulation of unmagnetized planets: comparison of Venus and Mars. J. Geophys. Res. **96**, 11209 (1991)
S.H. Brecht, J.R. Ferrrante, J.G. Luhmann, Three-dimensional simulations of the solar wind interaction with Mars. J. Geophys. Res. **98**, 1345 (1993)
L.H. Brace, A.J. Kliore, The structure of the Venus ionosphere. Space Sci. Rev. **55**, 81–164 (1990)
L.H. Brace, R.F. Theis, W.R. Hoegy, Plasma clouds above the ionopause of Venus and their implications. Planet. Space Sci. **30**, 29–37 (1982)
L.H. Brace, W.T. Kasprzak, H.A. Taylor, R.F. Theis, C.T. Russell, A. Barnes, J.D. Mihalov, D.M. Hunten, The ionotail of Venus: its configuration and evidence for ion escape. J. Geophys. Res. **92**, 15 (1987)
M.H. Carr, J.W. Head, Oceans on Mars: an assessment of the observational evidence and possible fate. J. Geophys. Res. **108**, 5042 (1996). doi:10.1029/2002JE001963
E. Chassefière, Hydrodynamic escape of oxygen from primitive atmospheres: application to the cases of Venus and Mars. Icarus **124**, 537–552 (1996)
D.H. Crider, D.A. Brain, M.H. Acuña et al., Mars Global Surveyor observations of solar wind magnetic field draping around Mars. Space Sci. Rev. **111**, 203–221 (2004)
A.J. Coates, Cometary plasma energization. Ann. Geophys. **9**, 158–169 (1991)
E. Chassefière, F. Leblanc, B. Langlais, The combined effects of escape and magnetic field histories at Mars. Planet. Space Sci. **55**(3), 343–357 (2007)
C.C. Chaston, L.M. Peticolas, C.W. Carlson, J.P. McFadden et al., Energy deposition by Alfveń waves into the dayside auroral oval:Cluster and FAST observations. J. Geophys. Res. **110**, A02211 (2005). doi:10.1029/2004JA010483
M. Delva, T.L. Zhang, M. Volwerk, C.T. Russell, H.Y. Wei, Upstream proton cyclotron waves at Venus. Planet. Space Sci. **56**(9), 1293–1299 (2008)
E.M. Dubinin, R. Lundin, W. Riedler, K. Schwingenshuh, J.G. Luhmann, C.T. Russell, L.H. Brace, Comparison of observed plasma and magnetic field structures in the wakes of Mars and Venus. J. Geophys. Res. **96**, 11189 (1991)
E. Dubinin, R. Lundin, H. Koskinen, N. Pissarenko, Ion acceleration in the martian tail: PHOBOS observations. J. Geophys. Res. **98**, 3991 (1993)
E. Dubinin, D. Winningham, M. Fränz, the ASSPERA-3 team, Solar wind plasma protrusion into the martian magnetosphere—ASPERA-3 observations. Icarus **182**(2), 343 (2006a)
E. Dubinin, R. Lundin, M. Fränz, J. Woch et al., Electric fields within the martian magnetosphere and ion extraction—ASPERA-3 observations. Icarus **182**(2), 337 (2006b)
N.J.T. Edberg, D.A. Brain, M. Lester, S.W.H. Cowley, R. Modolo, M. Fraenz, S. Barabash, Plasma boundary variability at Mars as observed by Mars Global Surveyor and Mars Express. Ann. Geophys. **27**, 3537–3550 (2010)
R.E. Ergun, L. Andersson, W.K. Peterson, D. Brain, G.T. Delory, D.L. Mitchell, R.P. Lin, A.W. Yau, Role of plasma waves in Mars' atmospheric loss. Geophys. Res. Lett. **33**, 14 (2006). doi:10.1029/2006GL025785
J.R. Espley, P.A. Cloutier, D.H. Crider, D.A. Brain, M.H. Acuña, Low frequency plasma oscillations at Mars during the October 2003 solar storm. J. Geophys. Res. (2005). 2004AGUFMSA13A1120E
Y. Futaana, S. Barabash, A.A. Grigorieva, M. Holmström et al., Sub solar ENA jet at Mars. Icarus **182**(2), 413 (2006)
A. Fedorov et al., Comparative analysis of Venus and Mars magnetotails. Planet. Space Sci. **56**, 812–817 (2008). doi:10.1016/j.pss.2007.12.012
A. Fedorov, S. Barabash, J.-A. Sauvaud, Y. Futaana et al., Venus Express measurement of ion escape rates for solar minimum. J. Geophys Res. **116**, A07220 (2011). doi:10.1029/2011JA016-427
J. Fox, A. Hac, Photochemical escape of oxygen from Mars: a comparison of the exobase approximation to a Monte Carlo method. Icarus **204**(2), 527–544 (2009)
K.I. Gringauz, V.V. Bezrukikh, M.I. Vergin, A.P. Rezimnov, On the electron and ion components of plasma in the antisolar part of near-martian space. J. Geophys. Res. **81**, 3349–3352 (1976a)
K.I. Gringauz, V.V. Bezrukikh, T.K. Berus, T. Gombosi et al., Plasma observations near Venus on board the Venera 9 and 10 satellites by means of wide-angle plasma detectors, in *Physics of Solar Planetary environment*, vol. 2, ed. by D.J. Williams (AGU, Washington, 1976b), p. 918

A. Guglielmi, R. Lundin, Ponderomotive upward acceleration of ions by ion-cyclotron and Alfvén waves over the polar regions. J. Geophys. Res. **106**, 13219–13236 (2001)
T.I. Gombosi, D.L. De Zeeuw, R.M. Häberli, K.G. Powell, Three-dimensional multiscale MHD model of cometary plasma environments. J. Geophys. Res. **101**(A7), 15233–15252 (1996)
H. Gunell, U.V. Amerstorfer, H. Nilsson, C. Grima, M. Koepke, M. Fränz, J.D. Winningham, R.A. Frahm, J.-A. Sauvaud, A. Fedorov, N.V. Erkaev, H.K. Biernat, M. Holmström, R. Lundin, S. Barabash, Shear driven waves in the induced magnetosphere of Mars. Plasma Phys. Control. Fusion **50**, 074018 (2008). (9 pp.). doi:10.1088/0741-3335/50/7/074018
M. Güdel, The Sun in time: activity and environment. Living Rev. Solar Physics, **4**, 1–137 (2007)
W.B. Hanson, S. Sanatani, D.R. Zuccaro, The martian ionosphere as observed by the Viking retarding potential analyzer. J. Geophys. Res. **82**, 4351–4363 (1977)
B. Hultqvist, M. Oieroset, G. Paschmann, R. Treumann (eds.), Magnetospheric plasma sources and losses. Space Sci.Rev. **88**, 1–2 (1999)
D.S. Intriligator, H.R. Collard, J.D. Mihalov, R.C. Whitten, J.H. Wolfe, Electron observations and ion flows from the Pioneer Venus Orbiter plasma analyzer experiment. Science **205**, 116–119 (1979)
R. Järvinen, E. Kallio, P. Jahnunen, et al., Oxygen ion escape from Venus in a global hybrid simulation: role of the ionospheric O^+ ions. Ann. Geophys. **27**, 4333–4348 (2009)
E. Kallio, P. Janhunen, Ion escape from Mars in a quasi-neutral hybrid model. J. Geophys. Res. **107**, 1035 (2002). doi:10.1029/2001JA000090
E. Kallio, R. Järvinen, P. Janhunen, Venus solar wind interaction: asymmetries and the escape of O^+ ions. Planet. Space Sci. **54**, 1472–1481 (2006). doi:10.1016/j.pss.2006.04.030
Y.N. Kulikov, H. Lammer, H.I.M. Lichtenegger, N. Terada, I. Ribas, C. Kolb, D. Langmayr, R. Lundin, E.F. Guinan, S. Barabash, H.K. Biernat, Atmospheric and water loss from early Venus. Planet. Space Sci. **54**(13–14), 1425–1444 (2006)
H. Lammer, H.I.M. Lichtenegger, C. Kolb, I. Ribas, E.F. Guinan, R. Abart, S.J. Bauer, Loss of water from Mars: implications for the oxidation of the soil. Icarus **106**, 9–25 (2003)
J.G. Luhmann, The solar wind interaction with Venus and Mars: cometary analogies and contrasts. Geophys. Monogr. **61**, 5 (1991)
J.G. Luhmann, S.J. Bauer, Solar wind effects on atmospheric evolution at Venus and Mars, in *Venus and Mars: Atmospheres, Ionospheres, and Solar Wind Interactions*, AGU Monograph, vol. 66, pp. 417–430 (1992)
J.G. Luhmann, J.U. Kozyra, Dayside pickup oxygen ion precipitation at Venus and Mars: spatial distributions, energy deposition and consequences. J. Geophys. Res. **96**, 5457 (1991)
J.G. Luhmann, S.A. Ledvina, J.G. Lyon, C.T. Russell, Venus O^+ pickup ions: collected PVO results and expectations for Venus Express. Planet. Space Sci. **54**, 1457–1471 (2006)
R. Lundin, E. Dubinin, Solar wind energy transfer regions inside the dayside magnetopause. I. Evidence for magnetosheath plasma penetration. Planet. Space Sci. **32**, 745–755 (1984)
R. Lundin, E.M. Dubinin, Phobos-2 results on the ionospheric plasma escape from Mars. Adv. Space Res. **12**(9), 255 (1992)
R. Lundin, A. Guglielmi, Ponderomotive forces in Cosmos. Space Sci. Rev. **127**(1–4), 1–116 (2006). doi:10.1007/s11214-006-8314-8
R. Lundin, A. Zakharov, R. Pellinen, B. Hultqvist, H. Borg, E.M. Dubinin, S. Barabasj, N. Pissarenko, H. Koskinen, I. Liede, First results of the ionospheric plasma escape from Mars. Nature **341**, 609 (1989)
R. Lundin, S. Barabash, H. Andersson, M. Holmström et al., Solar wind induced atmospheric erosion at Mars—first results from ASPERA-3 on Mars Express. Science **305**, 1933 (2004)
R. Lundin, D. Winningham, S. Barabash and the ASPERA-3 Team, Plasma acceleration above martian magnetic anomalies. Science **311**, 980–983 (2006a)
R. Lundin, D. Winningham, S. Barabash et al., Auroral plasma acceleration above martian magnetic anomalies. Space Sci. Rev. **126**(1–4), 333–354 (2006b)
R. Lundin, H. Lammer, I. Ribas, Planetary magnetic fields and solar forcing: Implications for atmospheric evolution. Space Sci. Rev. **129**(1–3), 245–278 (2007)
R. Lundin, S. Barabash, M. Holmström, H. Nilsson, M. Yamauchi, M. Fraenz, E.M. Dubinin, A comet-like escape of ionospheric plasma from Mars. Geophys. Res. Lett. **35**, L18203 (2008a). doi:10.1029/2008GL034811
R. Lundin, S. Barabash, A. Fedorov, M. Holmström, H. Nilsson, J.-A. Sauvaud, M. Yamauchi, Solar forcing and planetary ion escape from Mars. Geophys. Res. Lett. **35**, L09203 (2008b). doi:10.1029/2007GL032884
R. Lundin, S. Barabash, M. Holmström, H. Nilsson, M. Yamauchi, E.M. Dubinin, M. Fraenz, Atmospheric origin of cold ion escape from Mars. Geophys. Res. Lett. **36**, L17202 (2009). doi:10.1029/2009GL039341

R. Lundin, S. Barabash, E. Dubinin, D. Winningham, M. Yamauchi, Low-altitude acceleration of ionospheric ions at Mars. Geophys. Res. Lett. **38**, L047064 (2011) doi:10.1029/2011GL047064
Y.A. Ma, A.F. Nagy, K.C. Hansen, D.L. DeZeeuw, Three-dimensional multispecies MHD studies of the solar wind interaction with Mars in the presence of crustal fields. J. Geophys. Res. **107**, 1282 (2002). doi:10.1029/2002JA009293
C. Martinecz, A. Boesswetter, M. Fränz et al., Plasma environment of Venus: comparison of Venus Express ASPERA-4 measurements with 3-D hybrid simulations. J. Geophys. Res. **114**, E00B30 (2009). doi:10.1029/2008JE003174
J.D. Mihalov, A. Barnes, Evidence for the acceleration of ionospheric O^+ in the magnetosheath of Venus. Geophys. Res. Lett. **8**, 1277–1280 (1981). doi:10.1029/GL008i012p01277
T.E. Moore, R. Lundin, D. Alcayde, M. Andre, S.B. Ganguli, M. Temerin, A. Yau, Source processes in the high-latitude ionosphere. Space Science Review **88**, 7–84 (1999)
A.F. Nagy, T.E. Cravens, S.G. Smith, H.A. Taylor, H.C. Brinton, Model calculations of the dayside ionosphere of Venus—Ionic composition. J. Geophys. Res. **85**, 7795–7801 (1980)
A.F. Nagy, D. Winterhalter, K. Sauer et al., The plasma environment of Mars. Space Sci. Rev. **111**(1), 33–114 (2004)
H. Nilsson, E. Carlsson, D. Brain, A. Yamauchi, M. Holmström et al., Ion escape from Mars as a function of solar wind conditions: a statistical study. Icarus **206**(1), 40–49 (2010)
G. Paschmann, S. Haaland, R. Treumann (eds.), Auroral Plasma Physics. Space Sci. Rev. **103**, 1–4 (2002)
H. Pérez-de Tejada, Plasma flow in the Mars magnetosphere. J. Geophys. Res. **92**, 4713 (1987)
H. Pérez-de-Tejada, Momentum transport in the solar wind erosion of the Mars ionosphere. J. Geophys. Res. **103**, 31499–31508 (1998)
C.T. Russell, J.G. Luhmann, K. Schwingenschuh, W. Riedler, Ye. Yeroshenko, Upstream waves at Mars—PHOBOS observations. Geophys. Res. Lett. **17**, 897–900 (1990)
Y. Soobiah, A.J. Coates, D.R. Linde, D.O. Kataria et al., Icarus **182**(2), 396 (2006). doi:10.1016/j.icarus.2005.10.034
N. Terada, Y.N. Kulikov, H. Lammer, H.I.M. Lichtenegger, T. Tanaka, H. Shinagawa, T. Zhang, Atmosphere and water loss from early Mars under extreme solar wind and extreme ultraviolet conditions. Astrobiology **9**(1), 55–70 (2009)
H.A. Taylor, H.C. Brinton, S.J. Bauer, R.E. Hartle, Global observations of the composition and dynamics of the ionosphere of Venus: implications for the solar wind interaction. J. Geophys. Res. **85**(A13), 7765–7777 (1980)
J.S. Wang, E. Nielsen, Possible hydrodynamic waves in the topside ionosphere of Mars and Venus. J. Geophys. Res. **107**(A4), 1039 (2002). doi:10.1029/2001JA900142
J.D. Winningham, R.A. Frahm, J.R. Sharber, the ASPERA-3 Team, Electron oscillations in the induced Martian magnetosphere. Icarus **182**(2), 360 (2006)
B.E. Wood, H.-R. Müller, G. Zank, J.L. Linsky, Measured mass loss rates of solar-like stars as a function of age and activity. Astrophys. J. **574**, 412–425 (2002)
B.E. Wood, H.-R. Müller, G.P. Zank, J.L. Linsky, S. Redfield, New mass-loss measurements from astrospheric Ly-*a* absorption. Astrophys. J. **628**, L143–L146 (2005)
I. Ribas, E.F. Guinan, M. Güdel, M. Audard, Evolution of the solar activity over time and effects on planetary atmospheres. I. High-energy irradiances (1-1700 Å). Astrophys. J. **622**, 680–694 (2005)
C.T. Russell, M.A. Saunders, J.G. Luhmann, Mass-loading and the formation of the Venus tail. Adv. Space Res. **5**, 177 (1985)
C.T. Russell, J.G. Luhmann, R.J. Strangeway, The solar wind interaction with Venus through the eyes of the Pioneer Venus Orbiter. Planet. Space Sci. **54**, 1482–1495 (2006)
O.L. Vaisberg, Mars-plasma environment, in *Physics of Solar Planetary Environment*, vol. 2, ed. by D.J. Williams (AGU, Washington, 1976), p. 845
O.L. Vaisberg, S.A. Romanov, V.N. Smirnov, I.P. Karpinsky et al., Ion flux parameters in the solar wind-Venus interaction region according to Venera-9 and Venera-10 data, in *Physics of Solar Planetary Environment*, vol. 2, ed. by D.J. Williams (AGU, Washington, 1976), p. 904
D. Vignes et al., The solar wind interaction with Mars: locations and shapes of the bow shock and the magnetic pile-up boundary from the observations of the MAG/ER experiment onboard Mars global surveyor. Geophys. Res. Lett. **27**, 49 (2000)
A.W. Yau, W.K. Peterson, E.G. Shelley, Quantitative parametrization of energetic ionospheric ion outflow, modeling magnetospheric plasma. In: *Proceedings of the First Huntsville Workshop on Magnetosphere/Ionosphere Plasma Models*, Guntersville, AL, 14–16 October 1987 (A89-13779 03-46) (American Geophysical Union, Washington, 1988), pp. 211–217
T.L. Zhang, J.G. Luhmann, C.T. Russell, The magnetic barrier at Venus. J. Geophys. Res. **96**, 11145–11153 (1991)